

**RIKEN**  
**Accelerator**  
**Progress Report**

1988

vol. 22

理化学研究所  
*the Institute of Physical and Chemical Research*

**RIKEN Accelerator Progress Report**  
**January-December 1988**

理化学研究所  
**the Institute of Physical and Chemical Research**  
**Wako-shi, Saitama, 351-01 JAPAN**

## Editors

S. Ambe	K. Asahi
M. Hara	T. Kambara
S. Kitayama	Y. Miyazawa
N. Sakai	I. Shimamura
I. Tanihata	S. Yamaji
Y. Yano	

This volume contains recent information of the accelerators at RIKEN (IPCR), informal reports and abstracts of papers which will be published at scientific meetings or in publications by staff members, guests, and visitors.

All rights reserved. This report or any part thereof may not be reproduced in any form (including photostatic or microfilm form) without written permission from the publisher.

# C O N T E N T S

	Page
<b>I. INTRODUCTION .....</b>	<b>1</b>
<b>II. OPERATION OF ACCELERATORS</b>	
1. RRC Operation .....	2
2. RILAC Operation .....	4
3. Cyclotron Operation .....	6
4. Tandetron Operation .....	7
<b>III. RESEARCH ACTIVITIES</b>	
1. Nuclear Physics	
1. Negative Pion Production in Heavy-Ion Collisions at $E_{\text{lab}}/A = 42 \text{ MeV}$ .....	8
2. Search and Identification of New Isotopes .....	10
3. Nuclear Studies with Secondary Radioactive Beams .....	12
4. Projectile Fragmentation of an Extremely Neutron-Rich Nucleus $^{11}\text{Li}$ at 0.79 GeV/nucleon .....	14
5. Nuclear-Matter Radii of $^7\text{Be}$ and $^7\text{Li}$ and the Astrophysical S-Factors for Radiative Alpha-Capture Reactions .....	16
6. Angular Momentum Transfer and Spin Alignment in the Reaction $^{40}\text{Ar} + ^{209}\text{Bi}$ at 26 MeV/u .....	18
7. Multiple Coulomb Excitation of $^{157}\text{Gd}$ .....	20
8. A Candidate for the $K^\pi = 4^+$ Double-Gamma Vibrational Band Head in $^{168}\text{Er}$ .....	21
9. Dipole Moment of $^{222}\text{Ra}$ in the Two-Center Configuration .....	23
10. Estimation of the Decay Rates of Cluster Emissions in $^{222}\text{Ra}$ .....	25
11. Master Equations in the Microscopic Theory of Nuclear Collective Dynamics .....	27
12. Dissipative Collective Motion in the Non-Linear Dynamics of the Nuclear Time-Dependent Hartree-Fock Theory .....	29
13. Microscopic Derivation of Transport Equation in the Time-Dependent Hartree-Fock Theory .....	31
14. Average Partial Level Density Including the Effect of Residual Interaction .....	33
2. Atomic and Solid-State Physics	
1. Cross Sections for Radiative Electron Capture Calculated by a Relativistic Impulse Approximation—Formulation .....	35
2. Cross Sections for Radiative Electron Capture Calculated by a Relativistic Impulse Approximation—Total and Differential Cross Sections and Linear Polarization .....	38

	Page
3. Circularly Polarized X Ray Emission Due to Radiative Electron Capture .....	40
4. Dynamic Electron Correlation in Double Ionization by Charged Particle Impact and Photon Impact .....	42
5. Calculation of Stopping Powers for Energetic Heavy Ions in Solids and Plasmas .....	45
6. The Form Factors of the Hydrogenlike Atoms Revisited.....	47
7. Gamma-Ray Spectrum Due to the De-Excitation of a Muonic Molecule $p\alpha\mu$ .....	49
8. State Densities and Ionization Equilibrium of Atoms in Dense Plasmas.....	52
9. Charge-State Distribution Measurements of 26-MeV/u Ar Ions .....	54
10. Multiple Inner-Shell Ionization of Target Atoms by 0.8–26 MeV/u Heavy-Ion Impact .....	55
11. Resonant Transfer and Excitation (RTE) in $\text{Ge}^{31+}$ on $\text{H}_2$ Collisions .....	57
12. Studies on the Continuum X Rays Produced by Heavy-Ion-Atom Collisions .....	60
13. Target Thickness Dependence of Charge State Fractions of Ar Ions after the Passage through C-Foil, $\text{CH}_4$ , and $\text{H}_2$ .....	62
14. Charge Distributions of the Recoil Ions Accompanied with Multiple Ionization of Heavy Projectile Ions .....	65
15. K-LL Auger Spectra of Nitrogen Projectiles .....	68
16. Analysis of the Mg IX 2s3d-2s4f Transition of Beam-Foil Spectra .....	70
17. Impact Parameter Dependence of Ne K-X Ray Emission in 10 MeV $\text{Ne}^{7+}$ on Ne Collisions .....	72
18. K Auger Spectra of Doubly-Excited Helium-Like Carbon .....	74
19. Observation of the Velocity Distribution of a Sodium Atomic Beam Irradiated by a Resonant CW Dye Laser .....	75
20. Resonance Ionization Spectroscopy of Lantanoid Elements .....	77
21. Incident Angle Dependence of Al-LVV Auger Spectra for $\text{Ar}^{12+}$ Impact .....	79
22. Excitation of Convoy-Like Electrons by Glancing-Angle Incident Heavy-Ion Impact .....	81
23. $^{61}\text{Ni}$ Mössbauer Studies of Heusler Alloys.....	83
24. $^{57}\text{Fe}$ Mössbauer Study on Superconductor Oxides .....	84
25. Motion of Kr-Bubbles in Krypton-Implanted Aluminum .....	86
26. Lattice Location Study on Kr Atoms in Aluminium by Means of a Channelling Method .....	88
27. Evaluation of Crystalline Quality and Irradiation Effects of a Bi-Sr-Ca-Cu-O System High Transition Temperature Superconductor by Rutherford Backscattering Spectroscopy .....	91
28. RBS Investigation of N-Implanted $\text{AlN}_x$ Film Deposited on Silicon .....	93

	Page
29. RBS Investigation of N-Implanted Iron .....	95
30. Hydrogen Trapping by Solute Atoms in Nb-Mo Alloys as Observed by a Channelling Method .....	97
31. Radiation Damage in Ion-Implanted CaF <sub>2</sub> Observed by Channeling .....	99
32. PIXE-Channeling Analysis of Ga in the Ge Epitaxial Layer on a Si Substrate .....	100
33. Chemical Erosion of Molybdenum Disulphide (MoS <sub>2</sub> ) by Hydrogen Plasma .....	102
34. Charge Collection Measurements for the Study on Single Event Upset .....	104
35. Correlation of Particle-Induced Displacement Damage in Si and GaAs .....	105
<b>3. Radiochemistry and Nuclear Chemistry</b>	
1. Study on Incorporation of Carbon, Boron, and Oxygen in LEC-GaAs Using Charged Particle Activation .....	107
2. Profiling of Light Elements in the Surface Layer of Solid by Means of the Elastic Recoil Detection .....	109
3. Depth Profiling of Light and Heavy Elements—Application to the Study on the Compositions of Anodic Oxide Films on Titanium— .....	111
4. Behavior of a Releasing Agent Coated on a Heated Substrate as Studied by Heavy-Ion Rutherford Scattering .....	113
5. Cross-Check of He Profiles by ERDA Method with <sup>16</sup> O and <sup>40</sup> Ar Beams .....	115
6. Application of PIXE Analysis to Materials Sciences (I) .....	117
7. Multielement Analysis of Human Spermatozoa by PIXE .....	119
8. Mössbauer Emission Spectroscopy of <sup>57</sup> Fe Arising from <sup>57</sup> Mn .....	121
9. <sup>99</sup> Ru Mössbauer Spectroscopic Studies of Heusler Alloys.....	122
10. Mössbauer Study of Organic Ruthenium Clusters .....	124
11. $\gamma$ -Rays Perturbed Angular Correlation of <sup>111m</sup> Cd in CdO, Cd(OH) <sub>2</sub> , and $\alpha$ -Fe(2 at. % Cd) <sub>2</sub> O <sub>3</sub> .....	125
12. Preparation of No-Carrier-Added <sup>111m</sup> Cd for the Measurement of $\gamma$ - $\gamma$ Perturbed Angular Correlation .....	127
<b>4. Radiation Chemistry and Radiation Biology</b>	
1. High-Density Excitation by Heavy Ion: Techniques and Measurement of the Fast Emission Decay of BaF <sub>2</sub> Single Crystal .....	128
2. LET Dependence of Cellulose Triacetate Film Dosimeter Response for Ion Beams .....	130
3. Proton Irradiation Effects on Mechanical Properties of Aromatic Polymers .....	131
4. An Irradiation System for Biological Samples and Dosimetry at RIKEN Ring Cyclotron .....	133

	Page
5. Parallel Plate Avalanche Counter for Dosimetry in the RIKEN Ring Cyclotron Biology Facility .....	135
6. Combined Effect of <i>cis</i> -Diamminedichloroplatinum and Heavy Ions on Mammalian Cells <i>In Vitro</i> .....	137
7. Dependence of the Strand Breakage in DNA on Radiation Quality .....	139
8. <i>In Vitro</i> Cell Transformation and Mutation by Heavy Ions .....	141
 5. Instrumentation	
1. Network in the RIKEN Accelerator Facility .....	144
2. Large Scattering Chamber at RIKEN Ring Cyclotron Facility .....	147
3. RIKEN Swinger-Spectrometer System .....	148
4. Facilities for Atomic Physics at RIKEN Ring Cyclotron .....	149
5. Falling-Ball Irradiation System and the Hot Laboratory .....	150
6. Target Transportation System for the One-Meter Diameter Scattering Chamber .....	152
7. Test of a Superconducting Secondary Beam Transport System with Large Solid Angle (SLΩ) .....	153
8. Construction of a New Type of Low Energy Radioisotope Beam Channel "SLOW" for Surface Studies .....	155
9. Performance of the Stop Detector for Time-of-Flight (T.O.F) System .....	157
10. Timing Property of New Type Time Pick-Up Detector .....	159
11. Timing Properties of a Time-of-Flight Detector .....	162
12. Compact and Gridless Channel Plate Start Detector .....	164
13. A Position Sensitive Ionization Chamber .....	166
14. Performances of a Two-Dimensional Position-Sensitive Silicon Detector with a Large Effective Area .....	168
15. Calibration of Si-Detector Telescopes for Heavy-Ion Measurements in Space .....	170
16. Measurements of Some Characteristics of Thin Position-Sensitive Silicon Detectors .....	172
17. Test of a Si Two-Dimensional Position-Sensitive Detector for Unbound Particle Measurements .....	174
18. Resonance Ionization Spectroscopy of a Fe Atomic Beam Generated by a Spark Discharge Method .....	176
19. Resonance Ionization Spectroscopy of Neutral Atoms Generated by a Spark Discharge Method .....	178
20. Resonance Ionization Spectroscopy with a Sputtering Atomic Beam Source .....	180
21. A Radiation-Detected Optical Pumping System for the Achievement of Nuclear Orientation in Solids .....	182
22. An Attempt for a Local Loop Network Using an MC6854 ADLC .....	184

	Page
23. Spectral Analysis with a Graphic Terminal .....	186

#### **IV. NUCLEAR DATA**

1. Status Report of the Nuclear Data Group .....	187
2. On the Cross Sections for the $^{12}\text{C}(\text{p}, \text{pn})^{11}\text{C}$ Reaction .....	189
3. The Nuclear Data for $^{13}\text{N}$ Production.....	191
4. Excitation Function Data for $^{15}\text{O}$ Production .....	194

#### **V. DEVELOPMENT OF ACCELERATOR FACILITIES**

##### **1. Ion Accelerator Development**

1. Performance of New Grid Bypass Capacitors of the Final RF Amplifier for RIKEN Ring Cyclotron .....	196
2. Present Status of the Vacuum System for RIKEN Ring Cyclotron .....	199
3. Present Status of the Control System for RIKEN Ring Cyclotron.....	200
4. Status of Construction of the Injector AVF Cyclotron .....	202
5. Magnetic Field Measurement of the Injector AVF Cyclotron .....	203
6. Design of the Central Region of the Injector AVF Cyclotron .....	205
7. Calculation of the Extraction Orbit for the Injector AVF Cyclotron .....	207
8. Measurement of the Characteristics of a Resonator of the Injector AVF Cyclotron .....	209
9. Power Test of the RF System for the Injector AVF Cyclotron .....	211
10. Beam Buncher in the Injection Beam Line for the Injector AVF Cyclotron .....	213
11. Model Study of the Beam Rebuncher for the Injector AVF Cyclotron and RIKEN Ring Cyclotron .....	215
12. Rotational Beam Scanner .....	217
13. Status of the RIKEN Electron Cyclotron Resonance Ion Source (ECRIS) for an Injector AVF Cyclotron .....	219
14. Basic Study of a Polarized $^3\text{He}$ Ion Source by Laser Optical Pumping. I .....	222
15. Basic Study of a Polarized $^3\text{He}$ Ion Source by Laser Optical Pumping. II .....	225

##### **2. Synchrotron Radiation Source Development**

1. A Preliminary Design of the 8 GeV Chasman-Green Lattice .....	227
2. Correction of the Closed Orbit Distortion (COD) for an 8 GeV Storage Ring (1) .....	231
3. Correction of the Closed Orbit Distortion (COD) for an 8 GeV Storage Ring (2) .....	235
4. Effect of Insertion Devices on Beam Dynamics of 8 GeV Light Source Storage Rings .....	238

	Page
5. Nonlinear Dynamics with Sextupoles .....	242
6. Particle Tracking in Harmonic Expanded Sextupole Fields .....	245
7. Computer Code CATS: A Code for Sextupole Optimization .....	248
8. Study of the Beam Injection to a 6 GeV Storage Ring .....	253
9. Beam Lifetime of the 6 GeV Electron Storage Ring .....	257
10. Beam Stability of the 8 GeV Electron Storage Ring .....	259
11. Design of the Sextupole Magnets for the 8 GeV Storage Ring .....	262
12. RF System for 8 GeV SR .....	265
13. 500 MHz Model Cavities for the 8 GeV SR Ring .....	268
14. Study of Multi-Cell Cavity with Inductive Coupling Slots for the 8 GeV SR Ring .....	271
15. Calculation of the RF Electromagnetic Field for 8 GeV SR Ring Components .....	273
16. Estimate of the Coupling Impedance for the Storage Ring .....	276
17. Pumping System for the 8 GeV Storage Ring .....	279
18. Stress Analysis of the Vacuum Chamber for the 8 GeV Storage Ring .....	281
19. Pumping Characteristics of NEG Strip .....	283
20. Synchrotron Radiation Power Distribution at the 8 GeV Storage Ring .....	286
21. Pressure Gradient Profile in the 8 GeV Storage Ring .....	288
22. Outgassing Rate of an Extruded Aluminum Alloy Chamber .....	290
23. Thermal Analysis of the Crotch at the 8 GeV Storage Ring .....	292
24. Design of the Low-Frequency Cavity for the Synchrotron .....	295
25. Conceptual Design of Linac for the RIKEN SR .....	297
26. Positron Injection System for RIKEN SR .....	299
<b>VI. RADIATION MONITORING</b>	
1. Routine Monitoring of the Cyclotron, RILAC, and TANDETRON .....	301
2. Leakage-Radiation Measurements in the Cyclotron Building .....	303
3. Shielding Calculation for the Facility of RIKEN Ring Cyclotron Using RILAC as an Injector .....	305
4. Radiation Monitoring in RIKEN Ring Cyclotron Facility .....	307
<b>VII. LIST OF PUBLICATIONS</b> .....	309
<b>VIII. LIST OF OUTSIDE USERS AND THEIR THEMES</b> .....	321
<b>IX. LIST OF SEMINARS</b> .....	322
<b>X. LIST OF PERSONNEL</b> .....	324
<b>AUTHOR INDEX</b>	

## I. INTRODUCTION

A variety of collaborative research work using heavy-ion beams was extensively carried out in the past year in the field of nuclear and atomic physics, nuclear and radiation chemistry, material engineering, and radiation biology at the Institute of Physical and Chemical Research (RIKEN). The main facilities dedicated to this collaborative research work are a 160 cm cyclotron, a variable-frequency heavy-ion linac (RILAC), a 1 MV electrostatic accelerator (TANDETRON), and a separated-sector cyclotron (RIKEN Ring Cyclotron, RRC). The 160 cm cyclotron, which has been in operation for 23 years and used for studies in many research fields, was decided to be shut down at the end of fiscal 1989 (March, 1990).

RILAC has been operated as an injector to RRC as well as an independent accelerator for its own users. The beam time for the injection to RRC was nearly a half of the total beam time of RILAC. To reduce troubles associated with a PIG source, we decided to introduce NEOMAFIOS, an ECR soured developed at CEN, Grenoble, for an ion source of RILAC; NEOMAFIOS will be delivered at the end of 1989.

RRC has been in routine operation this year. Ions of  $^{15}\text{N}$ ,  $^{20}\text{Ne}$ ,  $^{22}\text{Ne}$ ,  $^{40}\text{Ca}$ ,  $^{64}\text{Zn}$ , and  $^{84}\text{Kr}$  were newly accelerated in this period. The highest energy was 44 MeV/u for light heavy ions whereas the lowest energy was 10.6 MeV/u of  $^{84}\text{Kr}$  ions. The lower energy can be obtained by increasing the harmonic number of RRC. RRC was shut down March through June to extend beam lines to three new experimental halls. It was reshot down again in December to extend the beam lines to three other experimental halls.

Construction of the second injector, an AVF cyclotron, was continued. Field mapping has been finished and the beam dynamical calculations of injection, acceleration and extraction orbits were performed. The power test of an RF system was successfully pursued. An ECR source for the AVF cyclotron was completed and test operation showed its high-performance; it was used on trial for experiments on atomic collisions.

From this year the RRC is open for outside users and twelve teams of inside and outside users have performed experiments. Studies on nuclear physics were carried out using RRC. Measurements of high-energy  $\gamma$ -ray and the subthreshold pion production cross sections were extensively performed.

H. Kamitsubo

Reaction cross sections by radioactive nuclei were measured at Bevalac and RRC. The search for new isotopes led to the successful identification of new proton-rich nuclei,  $^{61}\text{Ga}$  and  $^{63}\text{Ge}$ .

Theoretical studies of heavy-ion reactions and fission processes were performed on the basis of transport calculations. Nuclear structure studies of largely deformed nuclei were continued this year. Theoretical studies on atomic collision processes have been pursued in connection with various phenomena such as radiative electron capture at high energy, ionization processes of highly ionized atoms in gas and solid, and formation and decay of muonic molecules.

Experimental studies were carried out on atomic collision processes and on beam foil spectroscopy by using various kinds of ions at RILAC and RRC. Energy spectra of photons and Auger electrons, charge-state distributions of colliding and recoiled ions, and angular distributions of X-rays and scattered ions were measured to study the structure of highly ionized atoms, the ionization processes, and charge transfer process. Subnanosecond measurement of light emission along a heavy-ion trajectory in gaseous materials was also continued.

Mössbauer spectroscopy and perturbed angular correlation techniques were applied to the studies on the properties of alloys, high-temperature superconducting oxide, and other materials. Analysis of the distributions of implanted or dissolved impurities was continued by using a Rutherford back-scattering method, elastic recoil detection method, and nuclear reaction method. Activation analysis of light-element impurities in high-purity materials was continued as before. PIXE analysis was applied to the composition analysis of medical samples. The study of the radiation effects of heavy ions on mammalian cells was also continued.

Construction of experimental equipments and devices was continued. Performance tests and test experiments were done for the devices completed in the preceding years by using high energy beams from RRC.

Design and fabrication of a high-resolution spectrograph and a projectile fragment separator (RIPS) were continued.

The R & D work on a high-brilliance synchrotron radiation source was continued and the design of an 8-GeV storage ring was pursued.

## II. OPERATION OF ACCELERATORS

### 1. RRC Operation

Y. Yano, K. Hatanaka, M. Kase, A. Goto, H. Takebe, H. Nonaka,  
H. Isshiki,\* R. Abe,\* S. Otsuka,\* H. Akagi,\* and T. Ishikawa\*

The 1988 RRC experiment programs accepted by the nuclear and the other field users' PAC's were carried out for 21 days in January-March and for 36.5 days in September-November. In these runs, with a few exceptions, the starting up and tuning of the machine was done on Monday, and the beam was offered to one or two groups from Tuesday morning until Saturday morning without changing the particle and its energy.

This year we had scheduled shutdowns three times: from mid March to June, in August and in December. During the first period, the beam distributing lines were extended to E2, E3, and E7 experiment halls, and new experimental setups were installed in each. In July, after this shutdown, the study of beam transportation was performed for every new beam line to obtain the optimal-value data of magnet currents. On July 19 the extended radiation-controlled areas underwent the inspection by the authorities. In the following two periods regular machine overhauls were carried out.

New beams used for the experiments are listed

in Table 1. Among them a  $^{64}\text{Zn}^{20+}$  beam was difficult to tune, because its input beam intensity to the cyclotron was not enough. Our non-interceptive phase measuring system, the timing data from which are used for optimizing the rf-phase of the rebuncher and creating the isochronous sector magnet field, require at least 100 enA to obtain the clear beam-phase data. Thus, for tuning the machine, the idea of accelerating a  $^{16}\text{O}^{5+}$  beam, which has a very close  $m/q$ -value to the  $^{64}\text{Zn}^{20+}$  beam and enough intensity, was adopted. The isochronous field of the former beam is biased by approximately 7.7 gauss to the latter. This bias field was easily removed by adjusting a main coil current. It took nearly 17 hours since starting the sector field setting for the oxygen beam till extracting the zinc beam.

An experiment group measured the beam energy of  $^{18}\text{O}^{7+}$  by the TOF technique in use of double PPAC's placed about 7.4 m apart from each other in the E1 hall, and obtained  $41.46 \pm 0.08$  MeV/u. This beam was accelerated at an rf frequency of 35 MHz and in a  $h=9$  mode. On

Table 1. New RRC beams in January-December 1988.

$F$ (MHz)	RILAC			RRC			
	$Q_1$	$E_1$ (MeV/u)	$T_N$	$Q_2$	$h$	$E_2$ (MeV/u)	$i$ (enA)
$^{12}\text{C}$	35	3	2.48	6	5	9	42
$^{13}\text{C}$	35	3	2.48	6	6	9	42
$^{14}\text{N}$	35	3	2.48	6	6	9	42
$^{15}\text{N}$	20.187	2	0.648	5	5	10	10.65
	35	3	2.48	6	6	9	42
$^{16}\text{O}$	25	2	1.22	6	5	9	20.6
$^{40}\text{Ca}$	28	4	1.58	6	14	9	26
$^{64}\text{Zn}$	25	5	1.22	6	20	9	20.6
							10

$F$ , RF frequency;  $Q_1$ , Charge state;  $E_1$ , Beam energy;  $T_N$ , Number of tanks;  $Q_2$ , Charge state;  $h$ , Harmonic number;  $E_2$ , Beam energy;  $i$ , Maximum beam intensity during the experimental run.

(\*) , This beam was accelerated for creating the isochronous field of  $^{64}\text{Zn}^{20+}$  beam (in detail see the text).

\* Sumijyu Accelerator Service, Ltd.

the other hand, we estimated the beam energy to be 41.5 MeV/u from then-set coil current of the extraction bending magnet EBM2 whose radius of curvature and magnetic excitation curve are known. It was found that the estimation of the beam energy from the EBM2 coil current is quite reliable. The relation among the rf frequency  $F$  (MHz), harmonic number  $h$ , and beam energy  $E$  (MeV/u) is given by

$$A(F/h)^2 = 1 - (1 + E/931.5)^{-2}$$

Summing up the beam energies so far accelerated, we obtained the most probable value of  $A$  to be 0.00552. This empirical expression gives the beam energy within the error of  $\pm 1.2\%$  for given  $F$  and  $h$ .

Some of the user groups demand that the lower limit of the RRC beam energy decreases to about 5 MeV/u while the nominal value is 10.6 MeV/u.

This low energy beam can be obtained in a 20 MHz,  $h=14$  operational mode. But the present rebuncher has a drift-tube structure suited to a  $h=9$  operational mode, and cannot give enough bunching power for such a beam; a double buncher system is necessary. To investigate the other crucial problems, we made a preliminary test for a  $^{132}\text{Xe}^{19+}$  beam of 0.33 MeV/u injection energy corresponding to 5.3 MeV/u extraction energy. The lifetimes of charge-stripper carbon foils of  $10\mu\text{g}/\text{cm}^2$  and  $20\mu\text{g}/\text{cm}^2$  were about 2 hours and 5 hours in average, respectively. The vertical and horizontal emittances were measured to be 79 mm•mrad and 82 mm•mrad, while they were 25 mm•mrad and 28 mm•mrad without the thicker foil. The energy spread of the beam was acceptable. The study of resolving these problems is under way.

## II-2. RILAC Operation

Y. Miyazawa, M. Hemmi, T. Inoue, M. Yanokura, M. Kase, E. Ikezawa,  
T. Aihara,\* T. Ohki,\* H. Hasebe,\* and Y. Chiba

This year, RILAC has been in steady operation, and various kinds of ion beams were supplied for experiments. Table 1 gives the statistics of operation. The total beam time increased by 16% compared with that of the last year, because of the shorter periods for overhaul and improvement. One day of the scheduled beam-time was cancelled owing to the trouble in a cooling pipe of the PIG source. Table 2 gives the beam time for individual research groups. The total beam-time for RIKEN Ring Cyclotron (RRC) was 80 days, which is about 27% longer than that for the last year. Ions,  $^{13}\text{C}$ , N,  $^{15}\text{N}$ ,  $^{18}\text{O}$ , Ar, Ca, Zn, and Xe accelerated by RILAC were injected to RRC. Table 3 gives the statistics of the ions used this year. Ion beams of 22 species have been used for experiments and 50% of total beam-time was devoted to Ar ions.

Table 1. Statistics of operation for Jan. 1-Dec. 31, 1988.

	Day	%
Beam time	176	48.1
Frequency change	15	4.1
Overhaul and improvement	44	12.0
Periodic inspection and repair	28	7.6
Machine trouble	1	0.3
Scheduled shut down	102	27.9
Total	366	100

Table 2. Beam time for individual research groups.

	Day	%
Atomic physics	31	17.6
Solid-state physics	17	9.7
Nuclear physics	0	0
Radiochemistry and nuclear chemistry	15	8.5
Radiation chemistry and radiation biology	12	6.8
Accelerator research	21	11.9
Beam transportation to RRC	80	45.5
Total	176	100

\* Sumijyu Accelerator Service, Ltd.

Table 3. Statistics of ions used in this year.

Ion	Mass	Charge state	Day
C	12	3	9
C	12	4	1
C	13	3	7
N	14	2	5
N	14	3	17
N	15	1	3
N	15	3	5
Ne	20	2	7
Ne	20	3	2
Mg	24	3	3
Si	28	3	2
Ar	40	4	87
Ca	40	4	7
Ti	48	3	2
Zn	64	3	0.5
Zn	64	5	5.5
Zr	90	4	0.5
Ag	107	5	1.5
Sn	120	5	1
Xe	132	7	8
Xe	132	8	1
Ta	181	7	0.5

To investigate the possibility of beam acceleration in the frequency region above 40 MHz,  $\text{C}^{3+}$  and  $\text{C}^{4+}$  ions were accelerated at frequencies of 40 and 43 MHz, respectively. In the 43 MHz operation, glass-epoxy rods used to support a variable vacuum capacitor at the output port of a final amplifier were burned off by RF-heating and were replaced by ones made of Teflon. This year, we began accelerating  $\text{Zr}^{4+}$ ,  $\text{Ag}^{5+}$ ,  $\text{Sn}^{5+}$ , and  $\text{Ta}^{7+}$  at 18 MHz.

We have made several improvements as follows:

- 1) The cooling tower and water pump for 500 kV injector operating used for the past eleven years were replaced with new types.
- 2) Seven phase-lock circuits to suppress fluctuation in the phase of accelerating voltages were equipped with a buncher and six resonators. These circuits have been used for

extracting beams from RILAC very stably for long time runs.

3) In exchange for a mechanical relay, a MOS transistor switch was introduced in the coil circuit of a vacuum contactor used in the primary power lines of the plate power supply for the final tube. The exchange aimed to relieve a shock of crowbar action to the power supply by cutting off the primary lines with a minimum delay after crowbar protector firing. The delay time was reduced to 35 ms from the inherent delay of the vacuum contactor of 70 ms.

4) Since the control units (HP2240A), which is connected through GPIB to the RILAC control computer system, had been outmoded and over a

period of guarantee to be replaced with their spare parts, one of the five units was replaced tentatively with a new type. If it works satisfactory, all other units will be replaced.

5) An electrostatic quadrupole doublet lens was installed at the exit of a 500 kV accelerating column. Thus, the beam intensity at the entrance of the linac was doubled by use of this lens.

6) This year, we observed frequent spark discharges along the surface of the cylindrical insulator housing of the 500 kV injector power supply, they were due to pollutant deposited on the insulator surface. We cleaned the surface and sprayed silicone varnish on it to suppress the sparks completely.

### II-3. Cyclotron Operation

I. Kohno, K. Ogiwara, T. Kageyama, and S. Kohara

The 160 cm cyclotron was operated on a 24 h-a-day basis during the period XXIII from Jan. 1, to Dec. 31, 1988. The statistics of the machine operation time is shown in Table 1.

Table 2 shows the beam-time allotment to various activities during this period. Table 3 shows the distribution of the scheduled beam-time among various particles.

Table 1. Cyclotron operation in the period XXIII.

	Oscillator	Ion source	Beam
Reading of the time			
meter on			
Jan. 06 1988 (h)	95,270.1	100,416.4	59,837.6
Reading of the time			
meter on			
Jan. 06 1989 (h)	97,380.8	103,421.5	61,453.9
Deference (h)	2,110.7	3,005.1	1,616.3
Schedule in this period:			
Beam-time	176 d		
Overhaul and installation	60		
Periodical inspection and repair	28		
Schedule shutdown	97		
Machine trouble	5		

Table 2. Scheduled beam-time and research subjects in period XXIII.

Subject	Heavy ion	Light ion	Total
RI production for nuclear and solid physics			
	38 h	147 h	185 h
Nuclear chemistry	0	600	600
Radiation biology	58	98	156
Radiation chemistry	306	24	330
Radiation damage of polymer	15	32	47
Radiation damage of semiconductor	0	28	28
Test of radiation detector	346	168	514
Outside users			
Radiochemical analyses	0	236	236
Radiation damage of device for sattelite	0	13	13
Test of single event upset	164	48	212
Proton irradiation on thyristor	0	240	240
Total	927 h	1,634 h	2,561 h
Percentage in total	36.2%	63.8%	100%

Table 3. Distribution of the beam-time among particles acerated.

Particle	(h)	(%)
p	606	23.7
$^3\text{He}^{2+}$	380	14.8
$^4\text{He}^{2+}$	648	25.4
$^{12}\text{C}^{4+}$	29	1.1
$^{14}\text{N}^{4+,5+}$	786	30.7
$^{16}\text{O}^{5+}$	16	0.6
$^{20}\text{Ne}^{6+}$	96	3.7
Total	2,561	100.0

## II-4. Tandetron Operation

T. Kobayashi, H. Sakairi, E. Yagi, and T. Urai

The machine was operated for 184 days during the period from Nov. 1, 1987, to Dec. 31, 1988. The species of accelerated ions were  $^1\text{H}$ ,  $^4\text{He}$ , and  $^{11}\text{B}$ .

After about 7 year-operation without serious trouble at the acceleration tubes and the Cockcroft-Walton circuit, frequent sparkings at accelerating tube occurring in the early summer made the high pressure  $\text{SF}_6$  tank open during July 13 and November 11 for replacement of deteriorated components. They were bleeder resistors to distribute smoothly from the terminal voltage to a ground level, diodes to generate the terminal voltage, and an rf step-up transformer. The other major trouble was the deterioration of a 40 kHz push pull oscillator and the damage of a cesium ion gun due to cracking.

Experimental studies were carried out on following subjects.

- (1) Rutherford backscattering spectroscopy
  - a ) Behavior of Kr atom in Al (Metal Physics Lab.)
  - b ) Lattice location and the disorder of Cu, Fe, or Cr-implanted  $\text{CaF}_2$  (Semiconductors Lab. and

Surface Characterization Center)

- c ) Composition of  $\text{MoS}_2$  irradiated hydrogen plasma films (Plasma Physics Lab.)
- d ) Characterization of  $\text{AlN}_x$  (Surface Characterization Center)
- e ) Crystalline quality evaluation and irradiation effect of a Bi-Sr-Ca-Cu-O system high transition-temperature superconductor (Surface Characterization Center and Surface and Interface Lab.)
- f ) Determination of the crystallographic polarity of c-BN (Surface Characterization Center and Surface and Interface Lab.)
- (2) Nuclear reaction analysis
  - a ) Lattice location of H in Nb-Mo alloys (Metal Physics Lab. and Surface Characterization Center)
  - (3) Particle induced X-ray emission (PIXE)
    - a ) Lattice location of Ga in Ge (Cyclotron Lab.)
    - b ) Basic study of PIXE and its application to medical, environmental, archaeological, and materials science (Inorganic Chemical Physics Lab.)

### III. RESEARCH ACTIVITIES

#### 1. Nuclear Physics

##### 1 . Negative Pion Production in Heavy-Ion Collisions at $E_{\text{lab}}/A=42$ MeV

T. Suzuki, T. Kobayashi, T. Kubo, T. Nakagawa, T. Ichihara,  
M. Fukuda, K. Yoshida, and I. Tanihata

{ NUCLEAR REACTION  $^{12}\text{C}(^{14}\text{N}, \pi^-)$ ,  $E=42A$  MeV; measured inclusive  $\sigma(\pi^-)$ ; deduced inverse slope constant, compared with theory. }

Recently, significant attention<sup>1-5)</sup> has been devoted to the study of neutral pion production in collisions of heavy ions near the absolute threshold of  $25A$  MeV. We report the first inclusive  $\pi^-$  measurement for  $^{14}\text{N} + ^{12}\text{C}$  at  $42A$  MeV incident energy. We believe that the measurement of charged pions provides us better pion kinetic energy and angular resolutions. These data are expected to show the collective effects in nucleus-nucleus collisions.

The pion spectra have been observed to show the exponential shape of which slope parameter decreases with beam energy. An interesting result was observed that the slope of the pion energy spectrum is almost constant below the beam energy of  $60A$  MeV. However the errors are still too large for qualitative discussion. We expect that the systematic measurement of  $\pi^-$  provides better understanding on energy dependence of the slope factor.

The experiment was carried out at RIKEN Ring Cyclotron (RRC) by using a large solid angle ( $\approx 200$  mstr) spectrometer. The experimental setup consists of a rotatable C-type magnet, MWPCs, and scintillation hodoscopes. The time of flight (TOF), the energy-loss ( $\Delta E$ ), and the momentum of emitted particles were measured. A primary beam was led to a Faraday-cup located at 3 m downstream from a target to reduce backgrounds. Particle identification for negative particles in a TOF- $\Delta E$  space is clean as shown in Fig. 1, where positive particles are also overlaid for comparison. The electron backgrounds were removed further by cut in a TOF-

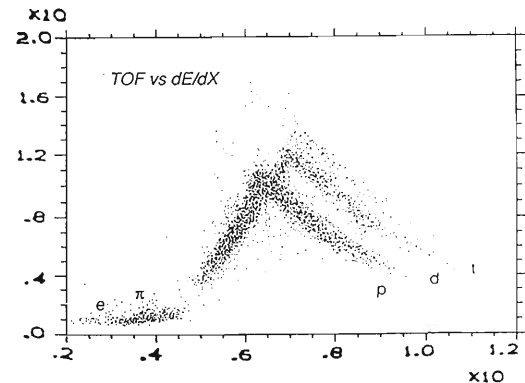


Fig. 1. Plot of time-of flight vs.  $\Delta E$  from  $42A$  MeV  $^{14}\text{N} + \text{C}$  collisions. Time of flight is in terms of TDC channels. One channel corresponds to 25 ps.

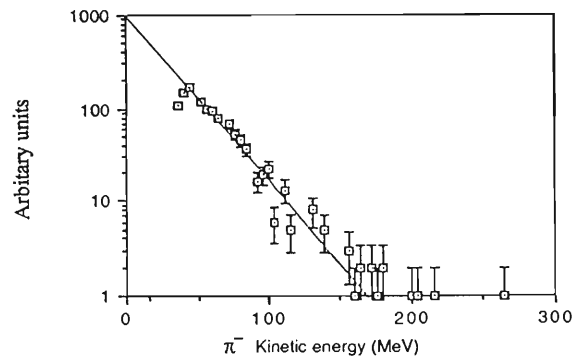


Fig. 2. Pion ( $\pi^-$ ) kinetic energy spectrum in the laboratory frame integrated over  $\theta_\pi = 15^\circ - 25^\circ$ . The straight line represents an exponential with an inverse slope constant of 24.5 MeV.

momentum space. In total, 9,400 pions were accumulated.

Figure 2 shows a pion kinetic energy spectrum obtained in the laboratory frame integrated over  $\theta_\pi=15^\circ\text{--}25^\circ$ . The vertical axis is proportional to  $d\sigma/dT_\pi$ . The error bars show only statistical ones. The solid line is obtained by fitting the measured spectrum for  $T_\pi=40\text{--}150\text{ MeV}$  with the expression:  $d\sigma/dT_\pi=c \exp(-T_\pi/T_0)$ . The preliminary result indicates a remarkably large inverse slope constant of  $T_0=24.5\pm0.9\text{ MeV}$ . The value is consistent with those of  $\pi^0$  at  $48A\text{ MeV}^5)$  for  $^{12}\text{C}+^{12}\text{C}$  and at  $35A\text{ MeV}^4)$  for  $^{14}\text{N}+^{27}\text{Al}$  within error bars.

It was pointed out<sup>4)</sup> that with decreasing beam energy the experimental  $T_0$  values level off at a constant value of  $T_0 \approx 23\text{ MeV}$ . The obtained value agrees with the same trend, which shows clear contrast to that observed at higher beam energies where the inverse slope factors were found to decrease systematically from 27 to 22 MeV in the beam energy of  $84\text{--}60A\text{ MeV}$  as shown in Fig. 3.

The inverse slope constants  $T_0$  of pion kinetic energy spectra calculated within a single nucleon-nucleon collision mechanism are in general much smaller than experimental ones; Refs. 6 and 7 quote  $T_0$  values about half as large as observed at  $E_{\text{lab}}/A=85\text{ MeV}$ . Calculations based on mechanisms such as hot spot models<sup>8)</sup> and thermal models,<sup>9)</sup> which explain integrated production cross sections well for beam energies above  $50A\text{ MeV}$ , do not succeed to explain the trend of the experimental data. To describe pion production at the very low beam energies coherent mechanism is, therefore, necessary. The precise measurement of the source rapidity and the  $p_{\perp}$  (perpendicular momentum) distribution together with the charged multiplicity is expect-

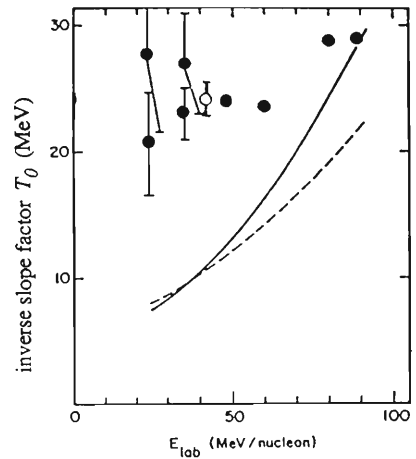


Fig. 3. Experimentally determined slope constants  $T_0$  of pion kinetic energy spectra as a function of beam energy/nucleon. Data (black circle) are taken from Refs. 3–5. Present result is indicated by a white circle. The dashed and solid lines correspond to predictions of Refs. 8 and 9, respectively.

ed to give constraint to these models more qualitatively. Further studies on the beam energy dependence are now in progress.

## References

- 1) H. Heckwolf, *et al.*: *Z. Phys., A*, **315**, 243 (1984).
- 2) P. Braun-Munzinger, *et al.*: *Phys. Rev. Lett.*, **52**, 255 (1984).
- 3) H. Noll, *et al.*: *Phys. Rev. Lett.*, **52**, 1284 (1984).
- 4) J. Stachel, *et al.*: *Phys. Rev. C*, **33**, 1420 (1986).
- 5) E. Grosse: *Nucl. Phys.*, **A447**, 611c (1985).
- 6) C. Guet and M. Prakash: *Nucl. Phys.*, **A488**, 119c (1984).
- 7) R. Shyam and J. Knoll: *Phys. Lett. B*, **136**, 221 (1984).
- 8) R. Shyam and J. Knoll: *Nucl. Phys.*, **A426**, 606 (1984).
- 9) M. Prakash, P. Braun-Munzinger, and J. Stachel: *Phys. Rev. C*, **33**, 937 (1986).

### III-1-2. Search and Identification of New Isotopes

W.P. Liu,\* M. Fukuda, T. Kubo, H. Kumagai, T. Nakagawa,  
 T. Suzuki, M. Yanokura, I. Tanihata, T. Ito,  
 T. Kashiwagi, J. Kikuchi, H. Yamaguchi, T. Doke,  
 H. Murakami, T. Yanagimachi, and N. Hasebe

NUCLEAR REACTIONS  ${}^9\text{Be}({}^{40}\text{Ca}, \text{X})\text{Y}$ ,  $E = 26.0 \text{ MeV}/A$ ,  ${}^{12}\text{C}({}^{64}\text{Zn}, \text{X})\text{Y}$ ,  
 $E = 20.8 \text{ MeV}/A$ ; particle identification; search for new isotopes; measured  
 time of flight, energy loss, total energy and magnetic rigidity; deduced mass  
 number, atomic number, charge state and yield of fragments.

Particle identification is essential for all kinds of experiments in nuclear physics. A novel particle identification technique has been developed, combining the use of a position sensitive silicon detector with a simple magnetic system. The experimental setup includes a magnet system for rigidity ( $B\rho$ ) selection, a PPAC (Parallel Plate Avalanche Counter) for TOF measurement in coincidence with an RF (Radio Frequency) signal, and a  $\Delta E-E$  telescope in which the  $\Delta E$  counter is position sensitive. The detectors were set at the focal plane of the magnet system. This combination provided high efficiency measurements of time of flight, energy loss, total energy, and magnetic rigidity and enabled the determination of the atomic number  $Z$ , charge state  $q$ , and mass  $A$  of produced fragments.

The final  $q$  spectrum is shown in Fig. 1. The resulting resolution  $\Delta q$  was 0.24 in FWHM at  $q=20$ , which can separate nuclei up to  $Z=60$ ; the background was extremely low. The mass spectra of some elements in a  ${}^9\text{Be}({}^{40}\text{Ca}, \text{X})\text{Y}$  reaction are shown in Fig. 2. The magnetic field was set for optimizing the nuclei which  $A/q=1.8$ . The resultant mass resolution  $\Delta A$  was 0.34 in FWHM at  $A=40$ . Therefore, the present system is capable of identification of nuclei of mass numbers up to  $A=100$ .

By using a  ${}^{40}\text{Ca}$  beam, we tried to identify  ${}^{39}\text{Sc}$ . Figure 3 shows the mass spectrum of Sc isotopes and that the number of "would be"  ${}^{39}\text{Sc}$  events was too small to confirm its existence. From the average of 5 runs, the upper limit of the yield ratio was established,  $Y({}^{39}\text{Sc}) / Y({}^{40}\text{Sc}) = 0.02$ .

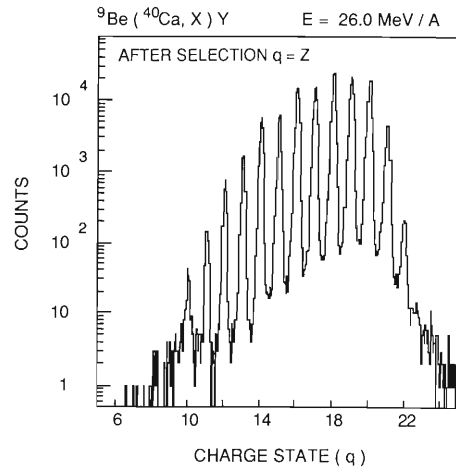


Fig. 1. Charge ( $q$ ) spectrum of the totally stripped charge state, in a  ${}^9\text{Be}({}^{40}\text{Ca}, \text{X})\text{Y}$  experiment,  $A/q=1.8$  magnetic rigidity setting.

This indicates that the life time of  ${}^{39}\text{Sc}$  is much shorter than 130 ns which is the typical flight time of fragments from a target to a detector. This result is consistent with the recent  ${}^{39}\text{Sc}$  mass measurement.<sup>1)</sup>

The search of new isotopes is a basic topic in nuclear studies. The charge radii of an isotope can be deduced by the  $\beta$ -decay half-life of its mirror nuclei, for example. Up to now, the mirror nuclei heavier than  ${}^{59}\text{Zn}$  have not been observed.

On the basis of previous experimental setup and the particle identification technique, we have performed an experiment which aims to search proton-rich new isotopes such as  ${}^{61}\text{Ga}$  and  ${}^{63}\text{Ge}$ . A beam of  ${}^{64}\text{Zn}^{20+}$  with 20.8 MeV/ $A$  was provided by RIKEN Ring Cyclotron at an intensity of 20 enA. The field of a dipole magnet was set to provide the largest acceptance of  ${}^{61}\text{Ga}^{29+}$ , which is the charge state of  ${}^{61}\text{Ga}$  in the highest yield.

\* Permanent address: Institute of Atomic Energy, P.O. Box 275-60, Beijing, China.

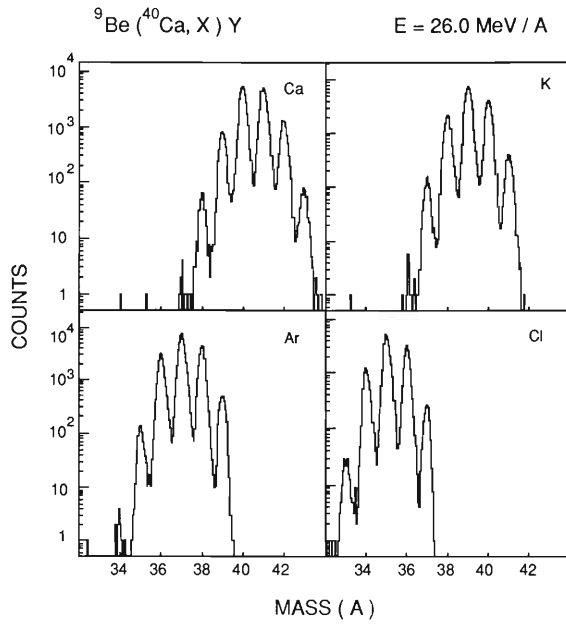


Fig. 2. Mass ( $A$ ) spectra of elements indicated. The conditions are the same as Fig. 1.

The data of totally 30 h have been accumulated.

The searching of new isotope  ${}^{61}\text{Ga}$  and  ${}^{63}\text{Ge}$  provides an effective means to produce mirror

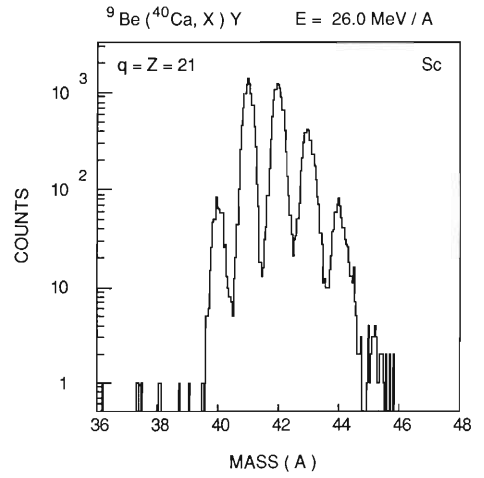


Fig. 3. Mass ( $A$ ) spectrum of Sc isotopes under the same conditions as Fig. 1.

nuclei with  $Z > 30$ . It can be used to study the basic properties of nuclei.

#### Reference

- 1) C.L. Woods, W.N. Catford, L.K. Fifield, and N.A. Orr : *Nucl. Phys.*, **A484**, 145 (1988).

### III-1-3. Nuclear Studies with Secondary Radioactive Beams<sup>1)</sup>

I. Tanihata, K. Sugimoto,\* S. Shimoura, K. Ekuni,\*\*  
T. Kobayashi, N. Takahashi,\*\*\* and T. Shimoda\*\*\*

(nuclear structure, radioactive beam, heavy-ion collisions.)

After the first measurement of interaction cross sections at BEVALAC,<sup>2-4)</sup> it has been recognized that the structure of the nuclei far from stability can be studied by using high-energy beams of radioactive nuclei.

At high energies ( $\geq 400$  MeV/nucleon), the interaction cross sections,  $\sigma_i$ , (the total cross sections for change of proton and/or neutron numbers in the projectile) have been measured for p-shell nuclei by a transmission method. Recent development includes the refinement of the cross sections for neutron drip line nuclei  $^{11}\text{Li}$  and  $^{14}\text{Be}$  and a new measurement for  $^{17}\text{B}$  at 790 MeV/nucleon. Measurements have also been made at 400 MeV/nucleon to verify the method of extracting nuclear radii from the interaction cross sections.

It was shown that the effective root-mean-square ( $r_{\text{rms}}$ ) radii of nucleon distributions can be deduced from  $\sigma_i$  by using a Glauber model calculation.<sup>3,4)</sup> New data at 400 MeV/nucleon provides a mean to verify the method because the nucleon-nucleon cross sections at 400 MeV are very much different from that at 800 MeV. The observed cross section ratio of  $^{11}\text{Li} + \text{C}$  reaction

$$\sigma_i(400)/\sigma_i(800) = 0.91 \pm 0.03$$

is consistent with the Glauber calculation (0.89) employing only the change in nucleon-nucleon cross sections. Therefore, the  $r_{\text{rms}}$  radii determined from  $\sigma_i$  of two different energies are consistent with each other. Figure 1 shows values of the effective  $r_{\text{rms}}$  radii thus obtained up to date.

Now we glance at the radii obtained from the interaction cross sections at 790 MeV/nucleon. Figure 1 shows the  $r_{\text{rms}}$  radii of nucleon distributions as a function of the neutron number ( $N$ ). The radii were determined by assuming the harmonic-oscillator model distribution. The

radii of Li and Be isotopes depend similarly on  $N$ . It is seen that the majority of the  $r_{\text{rms}}$  radii of p-shell nuclei are almost constant (2.3–2.4 fm) except ones close to the neutron drip line. Large increases in the radius from  $^9\text{Li}$  to  $^{11}\text{Li}$ , from  $^{10}\text{Be}$  to  $^{11}\text{Be}$ , from  $^{12}\text{Be}$  to  $^{14}\text{Be}$ , and possibly from  $^{15}\text{B}$  to  $^{17}\text{B}$  are observed. Now it seems common that neutron drip line nuclei have large radius.

The isospin dependence of nuclear radii (for equal mass nuclei) were studied for the first time for isobars of the mass number  $A=6, 7, 8, 9, 11$ , and  $12$ .<sup>4)</sup> A comparison with Hartree-Fock calculations using a Skyrme potential showed that the density dependent force is important for reproducing the increase in radii for nuclei with a large isospin. In general, Skyrme III potential gives the best fit to the data, but it fails to reproduce the radii of  $^{11}\text{Li}$  and  $^{11}\text{Be}$ .

A superior advantage of using radioactive beam is its powerfulness for studying nuclei far from the stability line. Studies of interaction cross sections and fragmentations reveal the interesting behavior in the extremely neutron rich nuclei of He, Li, Be, and B nuclei. Firstly, the

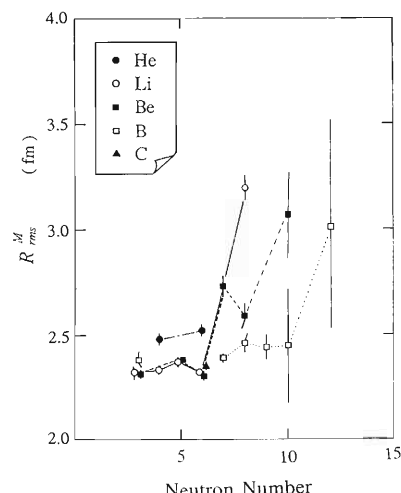


Fig. 1. The  $r_{\text{rms}}$  matter radii of light p-shell nuclei. Nuclear radii are determined from the interaction cross sections for radioactive nuclear beams.

\* Faculty of Science, Osaka University.

\*\* Kyoto University.

\*\*\* Faculty of General Education, Osaka University.

radii of most neutron rich isotopes,  ${}^8\text{He}$ ,  ${}^{11}\text{Li}$ ,  ${}^{14}\text{Be}$ , and  ${}^{17}\text{B}$ , are unusually large. An anomalously large size is also observed for  ${}^{11}\text{B}$ . Secondly, momentum spectra of fragments ( ${}^9\text{Li}$  from  ${}^{11}\text{Li}$  and  ${}^{12}\text{B}$  from  ${}^{14}\text{B}$ ) show extremely narrow component on the top of a wider component which has a width consistent with that observed in fragmentations of stable nuclei.<sup>5)</sup>

Naively, these observations can be understood as follows. In these extremely neutron rich nuclei the separation energies of last two neutrons are very small. The density distribution of such weakly bound neutrons are expected to have a long tail because the asymptotic wave function has a form  $(\exp(-\kappa r)/r)$ , where  $(\hbar\kappa)^2 = 2\mu B$  and  $\mu$  is the reduced mass and  $B$  is the binding energy. On the other hand, the momentum fluctuation of these last neutrons, which is a Fourier transform of the radial wave function,  $F(p) = C/(p^2 + \kappa^2)$ , are very small. Therefore qualitatively, the observed large size and narrow width in the fragment momentum distribution are consistent with the existence of a long tail in the neutron distribution (neutron halo). Because the momentum spread of  ${}^9\text{Li}$  is about a quarter of that of

normal Fermi gas,<sup>5)</sup> it is considered that the decay constant of neutron halo in  ${}^{11}\text{Li}$  is about four times larger than that of normal nuclear surface. However it is difficult to extract the amplitude of the neutron halo because the above discussion is only valid near the surface of a nucleus, and thus not sensitive to the wave function inside the nucleus. Sizes of the cross sections of a narrow and a wide component is expected to include information on the relative density amplitude of the neutron halo.

## References

- 1) published in *Phys. Lett. B*, **206**, 592 (1988) and *Nucl. Phys.*, **A488**, 133c (1988).
- 2) I. Tanihata, et al.: *Phys. Lett. B*, **160**, 380 (1985).
- 3) I. Tanihata, H. Hamagaki, O. Hashimoto, Y. Shida, N. Yoshikawa, K. Sugimoto, O. Yamakawa, T. Kobayashi, and N. Takahashi: *Phys. Rev. Lett.*, **55**, 2676 (1985).
- 4) I. Tanihata, T. Kobayashi, O. Yamakawa, S. Shimoura, K. Ekuni, K. Sugimoto, N. Takahashi, T. Shimoda, and H. Sato: *Phys. Lett. B*, **206**, 592 (1988).
- 5) T. Kobayashi, O. Yamakawa, K. Omata, K. Sugimoto, T. Shimoda, N. Takahashi, and I. Tanihata: *Phys. Rev. Lett.*, **60**, 2599 (1988).

### III-1-4. Projectile Fragmentation of an Extremely Neutron-Rich Nucleus $^{11}\text{Li}$ at 0.79 GeV/nucleon<sup>1)</sup>

T. Kobayashi, O. Yamakawa,\* K. Omata,\*\* K. Sugimoto,\*\*\* and I. Tanihata

(radioactive beam, heavy-ion collision, nuclear structure,  $^{11}\text{Li}$ , neutron halo.)

A Newly developed technique to produce a high quality radioactive nuclear beams<sup>2)</sup> provides a new possibility for the study of nucleon density distribution and the momentum distribution of nucleons in unstable nuclei through their projectile fragmentation. In this report we present the measurements of fragments produced from the projectile fragmentation of an extremely neutron-rich nucleus  $^{11}\text{Li}$  at 0.79 GeV/nucleon incident energy, and then show evidence for the existence of a giant neutron halo in the neutron distribution of the  $^{11}\text{Li}$  nucleus.

Projectile fragmentation was extensively studied by using beams of stable nuclei.<sup>3)</sup> An important finding is the regularity of a momentum distribution of the projectile fragments. It was found that the momentum distribution has a Gaussian shape in the projectile frame, and the width of the Gaussian  $\sigma$  is independent of target mass and beam energy but depend on the mass numbers of a projectile and a fragment in addition to a momentum fluctuation of nucleons inside the nucleus. In other words, internal momentum distribution can be determined from the measurement of projectile fragmentation.<sup>4)</sup>

The transverse momentum distributions of the fragments of  $^{11}\text{Li}$  by a carbon target were measured at 790 MeV/uncleon. Figure 1 presents the transverse momentum distribution of  $^9\text{Li}$ , which shows two-Gaussian structure in which a narrow peak lays on top of the other wider peak. The wider peak has a width  $\sigma_{\text{wide}} = 95 \pm 12 \text{ MeV}/c$  and the other has a narrow width  $\sigma_{\text{narrow}} = 23 \pm 5 \text{ MeV}/c$ . The two-component structure had not been observed in fragmentation of stable nuclei and therefore is a new feature. The narrow peak indicates the existence of nucleons with an extremely small momentum fluctuation. The  $\sigma_{\text{wide}}$  is consistent with the momentum fluctua-

tions of usual nucleons. The momentum width of the projectile fragment is related to the separation energy of last neutrons and thus written as

$$\sigma^2 = u \langle \varepsilon \rangle \frac{A_F (A_B - A_F)}{A_B} \quad (1)$$

where  $u$  is the atomic mass unit and  $\langle \varepsilon \rangle$  is an average separation energy of the removed nucleons. The observed narrow width gives  $\langle \varepsilon \rangle = 0.34 \pm 0.16 \text{ MeV}$  which can be compared with the separation energy of last neutrons:  $\Delta E [(^{10}\text{Li} + n) - (^{11}\text{Li})] = 0.96 \pm 0.1 \text{ MeV}$  and  $\Delta E [(^9\text{Li} + 2n) - (^{11}\text{Li})] = 0.19 \pm 0.10 \text{ MeV}$ . The broad width,

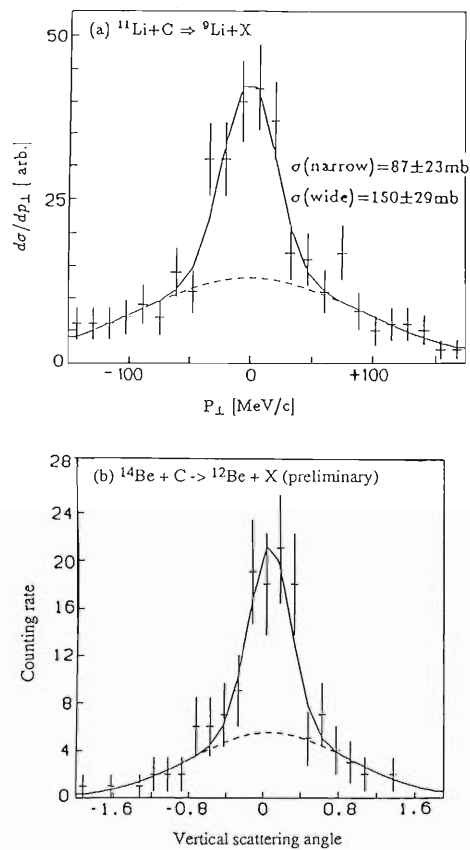


Fig. 1. Spectra of fragments from  $^{11}\text{Li}$  (a) and  $^{14}\text{Be}$  (b). Both spectra show two components which are specific only to the fragmentation of neutron dripline nuclei.

\* National Laboratory for High Energy Physics.

\*\* Institute for Nuclear Study, University of Tokyo.

\*\*\* Faculty of Science, Osaka University.

on the other hand, gives  $\langle \varepsilon \rangle = 6.0 \pm 1.5$  MeV which is roughly consistent with the normal nucleon separation energy. Therefore it is considered that the narrow component is produced by reactions in which weakly bound last two neutrons are removed from  $^{11}\text{Li}$ . The small momentum fluctuation of last two neutron also indicates the existence of a long tail in the neutron density distribution because a decay constant of the wave function on the nuclear surface is a Fourier transform of the momentum distribution. Preliminary data on fragmentation of  $^{14}\text{Be}$  also shows two-Gaussian structure as shown in Fig. 1(b). Therefore  $^{14}\text{Be}$  shows the same characteristics as  $^{11}\text{Li}$  in the fragmentation spectrum as well as the interaction cross sections.<sup>1)</sup>

It is suggestive to discuss the mechanism of producing two components in the fragmentation spectrum. Under the assumption that  $^{11}\text{Li}$  is composed of a core of  $^9\text{Li}$  and two loosely bound neutrons which have an extended tail in their density distribution. When the impact parameter of collision is small and core neutrons are removed, a probability of producing  $^9\text{Li}$  would be very small because loosely bound outer two neutrons are most likely removed simultaneously. Therefore  $^9\text{Li}$  is mostly produced in very peripheral collisions.

If these two neutrons are kicked out simultaneously in a peripheral collision, it is certain that  $^9\text{Li}$  has small momentum fluctuation as discussed before. On the other hand, when only one of them is removed by the collision, the momentum width would be wider. It is due to the

processes involved in the collision; first, the separation energy of one neutron is larger and thus gives wider momentum fluctuation in a p-fragment  $^{10}\text{Li}$ . Then, additional broadening occurs due to the level width of  $^{10}\text{Li}$  and recoils of neutron emission. Therefore, the narrow component is produced only when two neutrons are removed simultaneously from  $^{11}\text{Li}$ .

In a peripheral collision, only a small geometrical overlap occurs of the projectile and the target. Therefore, the simultaneous collision probability of both neutrons with target nucleons is very small if these neutrons are not correlated. A visibly large amount of the cross section of the narrow-component suggests the existence of strong correlation between two outer neutrons. Quantitative discussion on the relative strength is necessary to understand the structure of outer neutrons.

#### References

- 1) published in *Phys. Rev. Lett.*, **60**, 2599 (1988) and *Nucl. Phys.*, **A488**, 133c (1988).
- 2) I. Tanihata: *Hyperfine Interact.*, **21**, 251 (1985); I. Tanihata, H. Hamagaki, O. Hashimoto, S. Nagamiya, Y. Shida, N. Yoshikawa, O. Yamakawa, K. Sugimoto, T. Kobayashi, D.E. Greiner, N. Takahashi, and Y. Nojiri: *Phys. Lett. B*, **160**, 380 (1985); I. Tanihata, H. Hamagaki, O. Hashimoto, Y. Shida, N. Yoshikawa, K. Sugimoto, O. Yamakawa, T. Kobayashi, and N. Takahashi: *Phys. Rev. Lett.*, **55**, 2676 (1985).
- 3) D.E. Greiner, *et al.*: *Phys. Rev. Lett.*, **35**, 152 (1975).
- 4) J. Hüfner and M.C. Nemes: *Phys. Rev. C*, **23**, 2538 (1981).

### III-1-5. Nuclear-Matter Radii of $^7\text{Be}$ and $^7\text{Li}$ and the Astrophysical S-Factors for Radiative Alpha-Capture Reactions

T. Kajino,\* H. Toki,\* K-I. Kubo,\* and I. Tanihata

(nuclear structure, astrophysical reaction, radioactive nuclei.)

The nuclear-matter radii of  $^7\text{Be}$  and  $^7\text{Li}$  measured in high-energy heavy-ion reactions have been calculated and applied to estimate the astrophysical S-factors for the  $^3\text{He}(\alpha, \gamma)^7\text{Be}$  and  $^3\text{H}(\alpha, \gamma)^7\text{Li}$  reactions. The absolute  $S(0)$  values in keV b are constrained to be  $0.36 < S(0) < 0.63$  and  $0.083 < S(0) < 0.15$  for the  $^3\text{He}(\alpha, \gamma)^7\text{Be}$  and  $^3\text{H}(\alpha, \gamma)^7\text{Li}$  reactions, respectively.

A recent experiment<sup>1,2)</sup> of high-energy heavy-ion reactions using exotic-isotope beams provides a new tool for the study of the nuclear structure of light elements He, Li, and Be including several radioactive isotopes. The hadronic matter radii were determined from the measured interaction cross sections in the experiment. The data for unstable  $^7\text{Be}$  and  $^7\text{Li}$  nuclei among them are of particular interest for an application to astrophysics: The formation reactions of these nuclei, *i.e.*,  $^3\text{He}(\alpha, \gamma)^7\text{Be}$  and  $^3\text{H}(\alpha, \gamma)^7\text{Li}$ , are presumed to take one of the keys to resolve the missing solar-neutrino problem<sup>3,4)</sup> and the problem<sup>5,6)</sup> of big-bang production of  $^7\text{Li}$ . Although a number of experiments have been done to measure the reaction cross sections repeatedly, some of them differ appreciably from one another, casting a doubt on the theoretical prediction of the solar neutrino counting rate in the  $^{37}\text{Cl}$  or primordial  $^7\text{Li}$  abundance for which the above two reaction rates are important input parameters. In a recent theoretical study<sup>7)</sup> of these reactions, a very strong correlation was found between the calculated reaction rates and the nuclear sizes of  $^7\text{Be}$  and  $^7\text{Li}$ . The measured matter radii, in particular, of unstable  $^7\text{Be}$  make an independent estimate of the reaction rates by the use of the theoretical correlation between them. The purpose of this report is to constrain the absolute strength of the reaction rates (often expressed as astrophysical S-factors) for the  $^3\text{He}(\alpha, \gamma)^7\text{Be}$  and  $^3\text{H}(\alpha, \gamma)^7\text{Li}$  reactions.

A microscopic cluster model wave function<sup>7)</sup>

was adopted in the present calculation of the matter radii and reaction rates. It was found that almost all existing data on the binding energies, the electromagnetic structures of  $^7\text{Be}$  and  $^7\text{Li}$ , and the scattering amplitudes for alpha + ( $A=3$ ) systems are explained systematically by the use of the modified Hasegawa-Nagata force.<sup>8)</sup>

The experimental data for  $^7\text{Be}$  and  $^7\text{Li}$  show almost identical matter radii within their error bars although the proton and neutron matter radii between the two isobars show appreciable difference as shown in Fig. 1. The theoretical calculation agrees with all these data fairly well. A close comparison between theory and experiment, however, shows different charge dependence from each other.

Performing the calculation of both quantities, S-factors and nuclear sizes, by using many different types of effective interactions, one finds linear correlation between the two observables.

Using the observed RMS matter radius of  $^7\text{Be}$ , we obtain the following constraint on the absolute strength of the astrophysical S-factor:

$$0.36 < S(0) < 0.63 \text{ keV b} \quad (1)$$

This is the first estimate of the S-factor for  $^3\text{He}(\alpha, \gamma)^7\text{Be}$  by using the data of unstable  $^7\text{Be}$ .

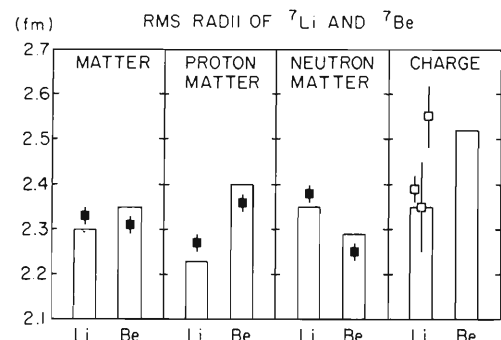


Fig. 1. Comparison of the charge and matter radii of the  $A=7$  nuclear systems between theory and experiments. Experimental values are taken from Ref. 2 (■) and Refs. 9-11 (□).

\* Faculty of Science, Tokyo Metropolitan University.

nucleus. In the estimate we have considered the experimental error of the observed matter radius and a  $\pm 20\%$  uncertainty for the linearity of the theoretical correlation. The present estimate (1) is consistent with the range

$$S(0) = 0.56 \pm 0.03 \text{ keV b} \quad (2)$$

which was determined by extrapolating the S-factors for the  $^3\text{He}(\alpha, \gamma)^7\text{Be}$  reaction observed at higher energies to zero energy, by assuming the energy dependence of the S-factor calculated in the microscopic cluster model.<sup>10)</sup>

As for the  $^3\text{H}(\alpha, \gamma)^7\text{Li}$  reaction, a similar analysis gives a constraint

$$0.083 < S(0) < 0.15 \text{ keV b} \quad (3)$$

This range is consistent with the previous values determined by direct capture gamma-ray experiments; Griffiths' data<sup>11)</sup> extrapolated to zero energy by assuming the energy dependence of the calculated S-factor<sup>10)</sup> lead to  $S(0) = 0.100 \pm 0.025$  keV b<sup>9)</sup> and Schroder's data<sup>12)</sup> with the same theoretical S-factor lead to  $S(0) = 0.134 \pm 0.020$  keV b. Although Schroder, *et al.* have obtained another value  $S(0) = 0.163 \pm 0.024$  keV b. based on another theoretical energy dependence of the S-factor calculated by Williams and Koonin,<sup>13)</sup> the energy dependence referred to proved to be incorrect. The inferred value  $0.162 \pm 0.024$  keV b is out of range of the present study.<sup>6)</sup>

We comment that the primordial  $^7\text{Li}$  abundance calculated in the big-bang model in Ref. 9 is reliable within  $+40\%$  and  $-18\%$  error, if combined with the present constraint<sup>6)</sup> on  $S(0)$  for the  $^3\text{H}(\alpha, \gamma)^7\text{Li}$  reaction.

To summarize, we have calculated the charge,

proton and neutron matter radii of  $^7\text{Be}$  and  $^7\text{Li}$  in a microscopic cluster model. The theoretical matter radii show an interesting difference between  $^7\text{Be}$  and  $^7\text{Li}$  though the observed radii are almost equal to each other. We have also estimated the astrophysical S-factors for the  $^3\text{He}(\alpha, \gamma)^7\text{Be}$  and  $^3\text{H}(\alpha, \gamma)^7\text{Li}$  reactions with the help of the measured matter radii of  $^7\text{Be}$  and  $^7\text{Li}$ . The theoretical relation between the S-factor and the matter radius has been used. The present result strongly constrains the absolute strength of the S-factors which affect the solar neutrino counting rate in  $^{37}\text{Cl}$  and the big-bang nucleosynthesis of  $^7\text{Li}$ .

## References

- 1) I. Tanihata, *et al.*: *Phys. Rev. Lett.*, **55**, 2676 (1985).
- 2) I. Tanihata: Proc. XI Int. Conf. Particles and Nuclei (Kyoto, 1987), to be published in *RIKEN Accel. Facil. Rep.*, RIKEN-RF-NP-59.
- 3) J.N. Bahcall, *et al.*: *Rev. Mod. Phys.*, **54**, 767 (1982).
- 4) R. Davis, Jr., B.T. Cleveland, and J.K. Rowley: Conf. Interactions between Particles and Nuclear Physics (ed. R.E. Mischke), AIP, New York (1984).
- 5) S.M. Austin and C.H. King: *Nature*, **269**, 782 (1977).
- 6) J. Yang, *et al.*: *Astrophys. J.*, **281**, 493 (1984).
- 7) T. Kajino: *Nucl. Phys.*, **A460**, 559 (1986).
- 8) F. Tanabe, A. Tohsaki, and R. Tamagaki: *Prog. Theor. Phys.*, **53**, 677 (1975).
- 9) T. Kajino, H. Toki, and S.M. Austin: *Astrophys. J.*, **319**, 531 (1987).
- 10) T. Kajino and A. Arima: *Phys. Rev. Lett.*, **52**, 739 (1984).
- 11) G.M. Griffiths, *et al.*: *Can. J. Phys.*, **39**, 1397 (1961).
- 12) U. Schroder, *et al.*: *Phys. Lett. B*, **192**, 55 (1987).
- 13) R.D. Williams and S.E. Koonin: *Phys. Rev. C*, **23**, 2773 (1981).

### III-1-6. Angular Momentum Transfer and Spin Alignment in the Reaction $^{40}\text{Ar} + ^{209}\text{Bi}$ at 26 MeV/u

N. Iwasa, K. Ieki, Y. Ando, H. Fujiwara, K. Hata, M. Ishihara,  
S.C. Jeong, S.M. Lee, T. Motobayashi, T. Mizota, H. Murakami,  
T. Murayama, Y. Nagashima, Masahiko Ogiwara, Mitsuhiko Ogiwara,  
S. Okumura, Y.H. Pu, J. Ruan (Gen), S. Shibuya, and S. Shirato

NUCLEAR REACTION  $^{209}\text{Bi} + ^{40}\text{Ar}$ ,  $E(^{40}\text{Ar})/A = 26$  MeV/u;  
measured fission fragment angular distribution, angular  
momentum transfer, spin alignment.

In intermediate heavy-ion reactions, projectile fragmentation is considered as a dominant process. In the present study, we show that multi-nucleon transfer process also contributes to the emission of projectile-like fragments at energy of 26 MeV/u. As is well known in lower energy heavy-ion reactions, large angular momentum transfer and spin alignment accompany with such transfer reactions. We measured fission fragment angular distributions in coincidence with projectile-like fragments to investigate the angular momentum transfer process.

The experimental setup was similar to a previous one.<sup>1)</sup> A 26 MeV/u  $^{40}\text{Ar}$  beam from RIKEN Ring Cyclotron bombarded a self-supporting  $^{209}\text{Bi}$  foil of about  $1 \text{ mg/cm}^2$  in thickness. A counter telescope to detect projectile-like frag-

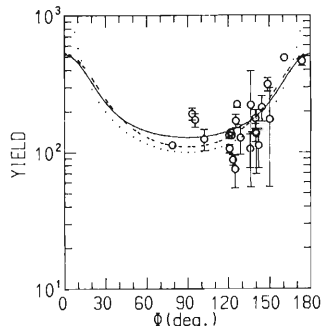


Fig. 1. Angular distribution of fission fragments coincident with projectile-like fragments ( $13 \leq Z \leq 17$ ). The abscissa denotes the angle between the detector and the recoiling direction of the fissile nucleus. Dotted line shows  $1/\sin\phi$  curve. The dashed line shows the case where spin distributes uniformly in the  $y-z$  plane. The solid line shows the case where completely aligned spin component was also included (see text).

ments was located at  $10^\circ$  from the beam axis and at 20 cm from the target. The telescope consisted of three ( $\Delta E-E-E$ ) silicon surface-barrier detectors of  $50, 1,500, 1,500 \mu\text{m}$  in thickness collimated by using an aperture 8 mm wide and 14 mm high. The detection angle was more forward than the previous time and the dynamic range of the counter was set wider so as to measure heavier fragments. Various projectile-like fragments ( $3 \leq Z \leq 18$ ) were observed. Their velocity were 70-80% of that of the beam. Coincident fission fragments were measured with nine thin surface-barrier detectors covering a wide angular region. They were located at 10 cm from the target and collimated by an aperture 7.5 mm in diameter. A sizable fraction of the projectile-like

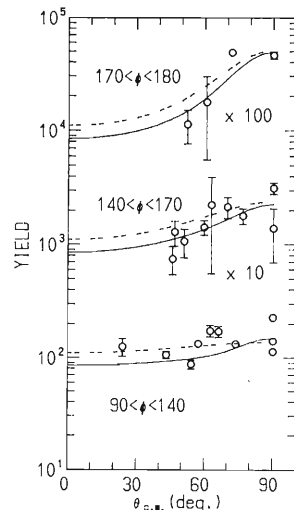


Fig. 2. Out of plane angular distributions of the fission fragments for three  $\phi$  angular ranges. Meanings of the dashed and solid curves are the same as in Fig. 1.

fragments cross section was seen to be coincident with the fission fragments. Angular distributions of the fission fragments were measured at 23 directions both in and out of the reaction plane. The fission fragments were well discriminated from evaporative light particles by the relation between the energy loss in the detector and the time of flight from the target to the detector.

In Figs. 1 and 2, typical angular distributions of fission fragments coincident with projectile-like fragments ( $13 \leq Z \leq 16$ ) are displayed in the rest frame of the recoiling fissile nucleus. The  $z$ -axis and  $x$ -axis are defined as a reaction plane normal and the recoil direction of the fissile nucleus, respectively. As the detection angle dispersed widely both in  $\theta$  and  $\phi$ , the angular distribution is sorted in an angle  $\Phi$  with respect to the  $x$ -axis (Fig. 1). The angular distribution in  $\Phi$  is very asymmetric and strongly peaked in the

backward direction. The angular distribution roughly has a shape of  $1/\sin\Phi$  (dotted curve), which may correspond to the fusion-fission-like process between the remnant of the projectile and the target. Assuming that the spin distributes uniformly in the  $y$ - $z$  plane (dashed curve), we estimated that transferred angular momentum to the target should be larger than  $60 \hbar$ . The angular distribution is almost independent of  $\theta$ , but somewhat deviates from the dashed curve. In Fig. 2, the out-of-plane angular distribution is shown for three angular ranges of  $\phi$ . An 8% addition of a completely aligned spin component to the uniform spin distribution (solid lines in Figs. 1 and 2) gave a little bit better fit.

#### Reference

- 1) K. Ieki, et al.: *RIKEN Accel. Prog. Rep.*, **21**, 9 (1987).

### III-1-7. Multiple Coulomb Excitation of $^{157}\text{Gd}$

M. Oshima, T. Inamura, A. Hashizume, H. Kusakari, M. Sugawara,  
E. Minehara,\* S. Ichikawa,\* and H. Iimura\*

NUCLEAR REACTIONS  $^{157}\text{Gd}(^{58}\text{Ni}, ^{58}\text{Ni}'\gamma)$ ,  $E = 240 \text{ MeV}$ ;  
measured  $E_\gamma$ , nuclear lifetimes; recoil distance method;  
 $B(\text{M}1)$  signature dependence.

In a series of the study of rotational perturbation effects in odd nuclei,<sup>1-4</sup> the nucleus  $^{157}\text{Gd}$  has been multiply Coulomb-excited up to the  $23/2^-$  state. Rotational band members above the  $15/2^-$  state have been established for the first time in  $^{157}\text{Gd}$ .

The experiment was carried out using a Ni beam of 240 MeV obtained from the JAERI tandem accelerator. Targets used were self-supporting metallic  $^{157}\text{Gd}$ , which was 93.3% isotopically enriched: one was about  $30 \text{ mg/cm}^2$ , and the other about  $3 \text{ mg/cm}^2$  in thickness. Deexcitation  $\gamma$  rays were measured with Compton suppressed Ge detectors by using the thick target;  $\gamma$ - $\gamma$  coincidences,  $\gamma$ -ray angular distributions, and nuclear lifetimes were also measured. The nuclear lifetimes were determined by a recoil distance method using the thin target.

As is shown in Fig. 1, energy levels are clearly dependent on the signature  $r$ , which is defined as<sup>5</sup>

$$r = \exp(-i\pi\alpha)$$

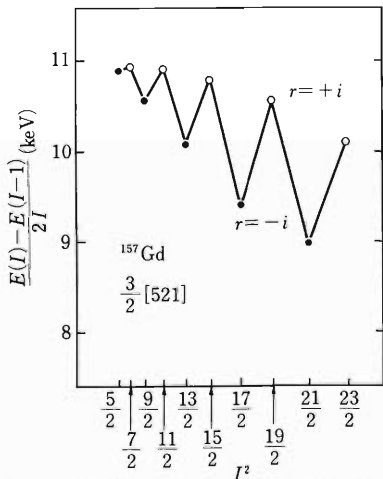


Fig. 1. Energy difference *vs.*  $I^2$  within the  $3/2^-$ -[521] rotational band of  $^{157}\text{Gd}$ . Closed circles denote the signature  $r = -i$ , and open ones the signature  $r = +i$ .

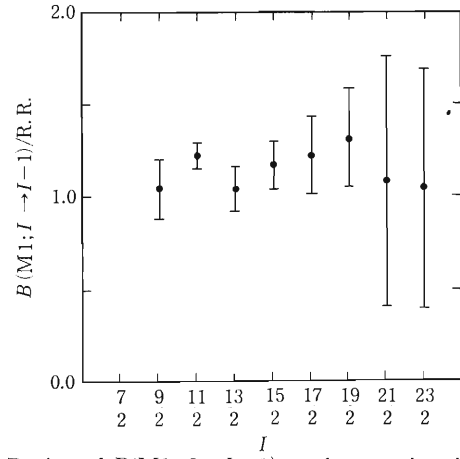


Fig. 2. Ratios of  $B(\text{M}1; I \rightarrow I-1)$  to the rotational values are plotted as a function of spins.

where  $\alpha = -1/2$  for  $I = 1/2, 5/2, 9/2, \dots$ , and  $\alpha = +1/2$  for  $I = 3/2, 7/2, 11/2, \dots$ . On the contrary, reduced M1 transition probabilities,  $B(\text{M}1; I \rightarrow I-1)$ , do not show significant dependence on the signature (see Fig. 2). Usually the latter is much sensitive to the signature, compared to the energy level.

The present result suggests that the configuration mixing strongly affects the signature dependence of  $B(\text{M}1)$  values, because  $B(\text{M}1)$  should be microscopically more sensitive to the wave functions of states concerned than the level energy.

#### References

- 1) M. Oshima, E. Minehara, M. Ishii, T. Inamura, and A. Hashizume: *Nucl. Phys.*, **A436**, 518 (1985).
- 2) E. Minehara, M. Oshima, S. Kikuchi, T. Inamura, A. Hashizume, and H. Kumahora: *Phys. Rev. C*, **35**, 858 (1987).
- 3) M. Oshima, E. Minehara, S. Ichikawa, H. Iimura, T. Inamura, A. Hashizume, H. Kusakari, and S. Iwasaki: *Phys. Rev. C*, **37**, 2578 (1988).
- 4) M. Oshima, E. Minehara, S. Kikuchi, T. Inamura, A. Hashizume, H. Kusakari, and M. Matsuzaki: *Phys. Rev. C*, **39**, 645 (1989).
- 5) M.J.A. de Voigt, J. Dudek, and Z. Szymanski: *Rev. Mod. Phys.*, **55**, 949 (1983).

\* Japan Atomic Energy Research Institute, Tokai.

RIKEN Accel. Prog. Rep. 22 (1988)

### III-1-8. A Candidate for the $K^\pi=4^+$ Double-Gamma Vibrational Band Head in $^{168}\text{Er}$

M. Oshima, T. Inamura, A. Hashizume, H. Kumagai, H. Kusakari,  
M. Sugawara, E. Minehara,\* H. Iimura,\* and S. Ichikawa\*

(NUCLEAR REACTIONS  $^{168}\text{Er}(^{58}\text{Ni}, ^{58}\text{Ni}'\gamma)$ ,  $E=240$  MeV;  
particle- $\gamma$  coincidences; double-gamma vibrational state.)

Whether double-gamma vibrational states exist or not in deformed nuclei is currently the central problem for elucidating the collective excitation of nuclei.<sup>1-4)</sup> Nevertheless, no unambiguous evidence for the double-gamma vibrational states in deformed nuclei have so far been provided experimentally. The present result might be the first observation of  $\gamma$  transitions from the double-gamma vibrational band head ( $I^\pi=4^-_\gamma$ ,  $K^\pi=4^+$ ) to the single-gamma vibrational band members ( $I^\pi=2^+_1$ ,  $3^+_1$ ,  $4^+_1$ ,  $K^\pi=2^+$ ).

$^{168}\text{Er}$  was multiply Coulomb-excited with a  $^{58}\text{Ni}$  beam of 240 MeV obtained from the JAERI tandem accelerator. The target  $^{168}\text{Er}$  was a self-supporting metallic foil of 1.5 mg/cm<sup>2</sup> in thickness (95% isotopically enriched). Deexcitation  $\gamma$  rays were observed with four Ge counters in coincidence with four PPACs (Parallel Plate

Avalanche Counter) which detected recoiled target atoms and scattered projectiles, providing the position signals of detected particles. The Ge counters were placed at  $\pm 45^\circ$  and  $\pm 135^\circ$  to the beam direction, 10 cm from the target. The PPACs were placed symmetrically with respect to the beam, surrounding the target, so that they covered forward as well as backward angles. The size of PPAC was 10 cm  $\times$  10 cm, and the distance between the center of the PPAC window and the target was 7 cm.

The observed  $\gamma$ -ray spectra were corrected for Doppler shifts kinematically by using the position signals of the particles registered. Figure 1 shows the Doppler corrected  $\gamma$ -ray spectrum;  $\gamma$  rays were observed in coincidence with projectiles scattered in the forward direction to see highly excited states with relatively low spins.

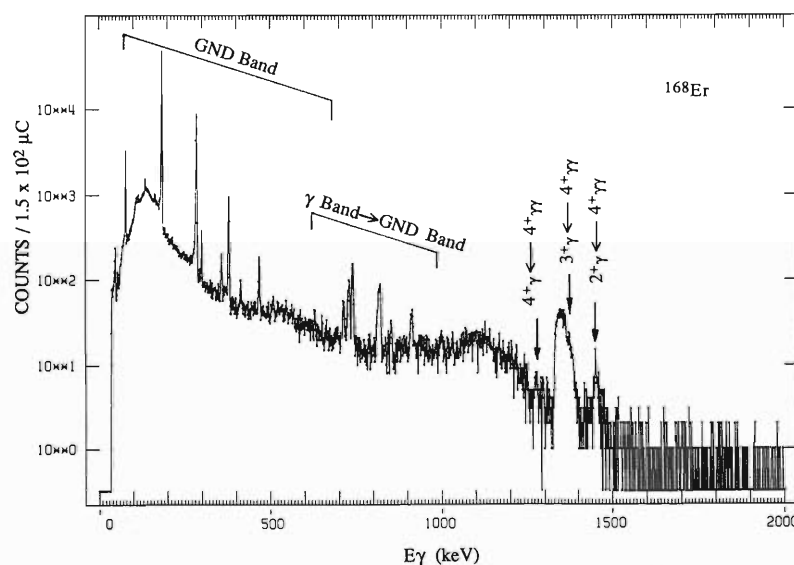


Fig. 1. Doppler corrected  $\gamma$ -ray spectrum observed in coincidence with forwardly scattered projectiles in Coulomb excitation of  $^{168}\text{Er}$ .

\* Japan Atomic Energy Research Institute, Tokai.

In addition to  $\gamma$  rays from the ground-state rotational band and the single-gamma vibrational band,  $\gamma$  rays of interest were observed: 1.452(3), 1.376(6), and 1.276(4) MeV around a giant peak of the  $2^+ \rightarrow 0^+$  (1.4544 MeV) transition in the projectile  $^{58}\text{Ni}$ . If they are of transitions from the double-gamma vibrational band head to the single-gamma vibrational states  $1^\pi = 2_\gamma^+, 3_\gamma^+$ , and  $4_\gamma^+$  respectively, the position of the band head is placed uniquely at 2.272(4) MeV within experimental errors because the energy differences between  $\gamma$  rays coincide with those between the well-established single-gamma vibrational states concerned.<sup>5)</sup> This position is within the theoretical prediction.<sup>1)</sup>

The present result does not support the assumption that the double-gamma vibrational band head should be at 2.056 MeV on the basis of  $(n, \gamma)$  measurements.<sup>5)</sup> Further investigation is under way to confirm the present interpretation.

#### References

- 1) M. Matsuo and K. Matsuyanagi: *Prog. Theor. Phys.*, **74**, 1227 (1985); **76**, 93 (1986); and **78**, 591 (1987).
- 2) N. Yoshinaga, Y. Akiyama, and A. Arima: *Phys. Rev. Lett.*, **56**, 1116 (1986).
- 3) V.G. Soloviev: E4-87-795, Dubna (1987).
- 4) M.K. Jammari and R. Piepenbring: *Nucl. Phys.*, **A487**, 77 (1988).
- 5) V. S. Shirley: *Nucl. Data Sheets*, **53**, 223 (1988).

### III-1-9. Dipole Moment of $^{222}\text{Ra}$ in the Two-Center Configuration

S. Yamaji and N. Yoshinaga

NUCLEAR STRUCTURE    octupole deformation,  
two-center shell model.

The nuclei in the actinide region have characteristic features essentially different from those in other regions: one is strong E1 enhancement and the other is  $^{14}\text{C}$  decay. In order to explain these characteristics, several models such as the octupole deformation model<sup>1)</sup> and the Vibron model<sup>2)</sup> were proposed.

Our motivation is to compare these models and find out which is more suitable to describe the nuclei in this region. We analyzed  $^{222}\text{Ra}$  by using the two-center shell model. In Fig. 1 the defined nuclear shape of  $^{222}\text{Ra}$  is shown. The radii  $R_1$  and  $R_2$  are determined by imposing the conditions that the volume ratio  $(R_1/R_2)^3$  is equal to the mass ratio  $(A_1/A_2)$  and that the total volume is conserved. Here,  $A_1$  and  $A_2$  are the mass numbers of the two fragments.

It is known experimentally that the electric intrinsic dipole moment of  $^{222}\text{Ra}$  is at most  $0.5 e \text{ fm}$ . Therefore, we try to see how large the macroscopic dipole moment  $D_s$  is in our model by using Strutinsky's method.<sup>3)</sup>

First, we calculated the total energy  $E_{\text{tot}}$  as a function of the separation  $z_0$  for several cluster

configurations by the microscopic-macroscopic method.<sup>4)</sup> The set of parameters given on the first row in the Table 1 of Ref. 4 is used in the present calculation.

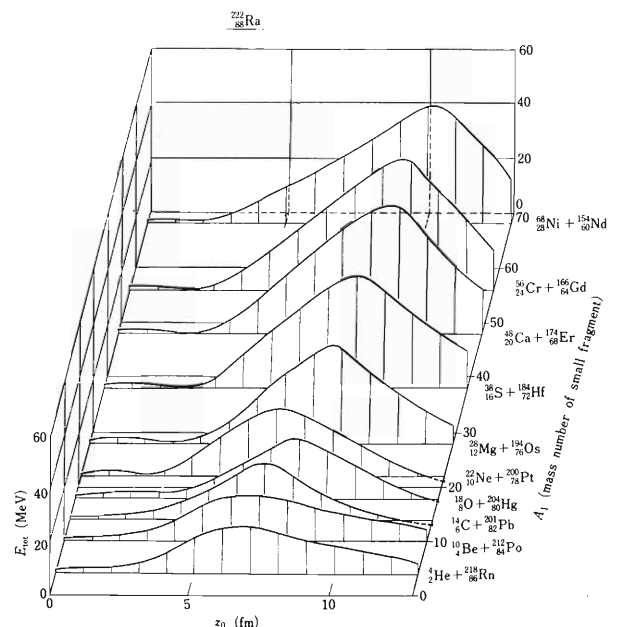


Fig. 2. Total energy  $E_{\text{tot}}$  of  $^{222}\text{Ra}$  as a function of the separation  $z_0$  for various combinations of clusters.

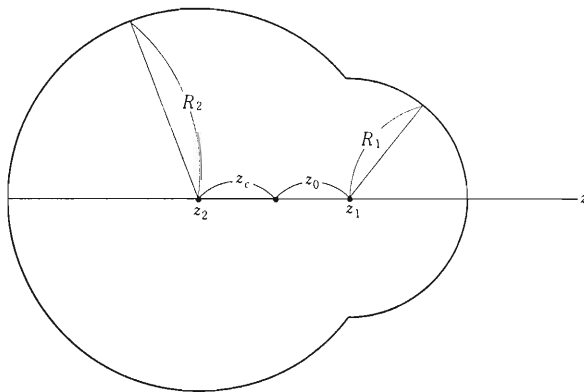


Fig. 1. Nuclear shape.  $z_1$  and  $z_2$  are the centers of two clusters. The separation  $z_0$  is defined by  $z_0 = z_1 - z_2 - z_c$ , where  $z_c$  is the center separation at the configuration where the small cluster just appears on the  $^{222}\text{Ra}$  surface.

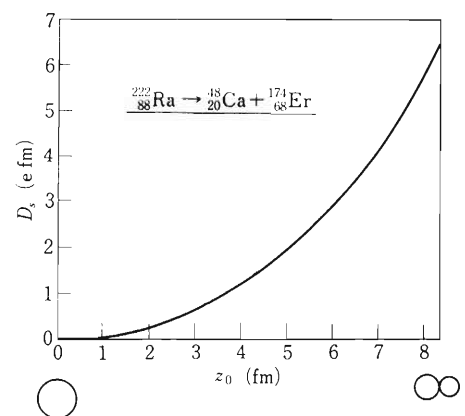


Fig. 3. Macroscopic dipole moment of  $^{222}\text{Ra}$  as a function of  $z_0$  from the configuration of the parent nucleus to the contact configuration.

We have found that the minimum of the total energy exists around  $z_0=2.5$  fm in the  $^{48}_{20}\text{Ca} + ^{174}_{68}\text{Er}$  configuration as shown in Fig. 2. We show the macroscopic dipole moment  $D_s$ <sup>3)</sup> as a function of  $z_0$  for the  $^{48}_{20}\text{Ca} + ^{174}_{68}\text{Er}$  configuration in Fig. 3. The dipole moment of the minimum point ( $D_s=0.46 e \text{ fm}$ ) well reproduces the observed value. The corresponding deformations are  $\beta_2=0.18$ ,  $\beta_3=0.16$ ,  $\beta_4=0.13$ ,  $\beta_5=0.10$ ,  $\beta_6=0.07$ , where  $\beta_2$  and  $\beta_3$  are nearly equal to  $\beta_2=0.12$ ,  $\beta_3=0.11$

obtained by Leander.<sup>1)</sup>

#### References

- 1) G.A. Leander: Proc. Niels Bohr Centenial Conf. on 'Nuclear Structure 1985' (eds. R.A. Broglia, *et al.*) Copenhagen, p. 249 (1985).
- 2) F. Iachello: *Phys. Lett. B*, **160**, 1 (1985).
- 3) V. Strutinsky: *J. Nucl. Energy*, **4**, 523 (1957).
- 4) P. Möller and J.R. Nix: *Nucl. Phys.*, **A361**, 11 (1981).

### III-1-10. Estimation of the Decay Rates of Cluster Emissions in $^{222}\text{Ra}$

S. Yamaji and N. Yoshinaga

[NUCLEAR STRUCTURE radioactive decay.]

Sandulescu, *et al.*<sup>1)</sup> predicted the emission of various heavy clusters from some particular parents such as Ra and Th nuclei on the basis of a very simple calculation of penetrability. In this spirit, Rose, *et al.* and other groups<sup>2)</sup> reported the discovery of  $^{14}\text{C}$  radioactivity; Shi, *et al.*<sup>3)</sup> tried to explain measured branching ratios.

However, in these calculations,<sup>1,3)</sup> a potential barrier was approximated by polynomials without any theoretical foundation. It is very important to study the dependence of the barrier on the deformation in a quantum tunneling calculation. We calculated the barrier as realistically as possible by a microscopic-macroscopic method.<sup>4)</sup> As a deformation parameter, we introduce a center separation  $z_0$  describing the two-center spherical parametrization of the shape shown in Fig. 1. The radii  $R_1$  and  $R_2$  are determined by the following conditions:

a) The volume ratio  $(R_1/R_2)^3$  equals to the mass ratio  $(A_1/A_2)$ , where  $A_1$  and  $A_2$  are the mass numbers of two fragments.

b) The total volume is conserved.

We can calculate the potential barrier  $E_{\text{tot}}(z_0)$  in the configurations of a parent nucleus and the

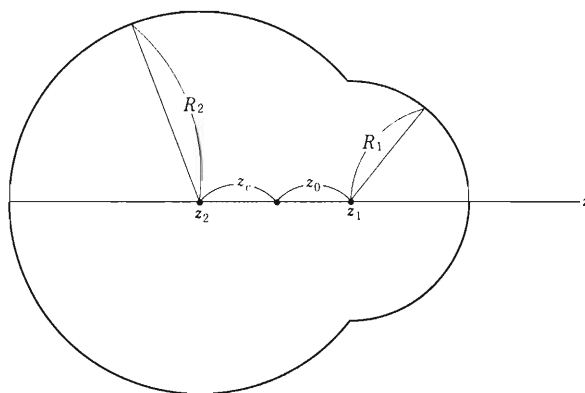


Fig. 1. Nuclear shape.  $z_1$  and  $z_2$  are the centers of two clusters. The separation  $z_0$  is defined by  $z_0 = z_1 - z_2 - z_c$ , where  $z_c$  is the center separation at the configuration where the small cluster just appears on the  $^{222}\text{Ra}$  surface.

well-separated fragments by using the microscopic-macroscopic method.<sup>4)</sup> However, it is difficult to obtain  $E_{\text{tot}}(z_0)$  in the neighbourhood of a touching configuration where there appears a change in charge distribution which comes from difference in the charge-to-mass ratio between the parent nucleus and its fragments. Having obtained no charge distribution in the touching region, we approximate the barrier  $E_{\text{tot}}(z_0)$  by

$$E_{\text{tot}}(z_0) = \frac{1}{2} \left\{ 1 - \tanh \left( \frac{z_0 - z_t}{d} \right) \right\} E_{\text{tot}}^{(\text{P})}(z_0) + \frac{1}{2} \left\{ 1 + \tanh \left( \frac{z_0 - z_t}{d} \right) \right\} E_{\text{tot}}^{(\text{F})}(z_0)$$

Here we introduced two weighting factors of a Woods-Saxon form with a diffuseness parameter  $d$  of  $(1/2)(1 - \tanh((z_0 - z_t)/d))$  and  $(1/2)(1 + \tanh((z_0 - z_t)/d))$ , which are nearly equal to one and zero for  $z_0 \ll z_t$  and zero and one for  $z_0 \gg z_t$ , respectively. We put  $d = 0.5$  fm for the present calculation.  $z_t$  is  $z_0$  when the two fragments are touching at the surfaces. The energy  $E_{\text{tot}}^{(\text{P})}(z_0)$  is the microscopic-macroscopic energy in the configuration of the parent nucleus, and  $E_{\text{tot}}^{(\text{F})}(z_0)$  in the configuration of two fragments. The key quantity to correctly predict the branching ratios in a tunneling calculation is the release energy  $Q$  in disintegration. The  $Q$ -value estimated from the observed ground state masses was used in Refs. 1 and 3, while it is automatically calculated in the present calculation. Therefore, it is very important to confirm if our microscopic shell correction energy  $\Delta E_{\text{shell}}(\text{CAL})$  can reproduce the experimental shell correction energy  $\Delta E_{\text{shell}}(\text{EXP})$ , *i.e.*, the energy difference between the observed mass excess and calculated macroscopic energy. We used a set of parameters given on the first row in the Table 1 of Möller, *et al.*<sup>4)</sup> Since their parameter set was adjusted to reproduce the observed ground state mass of more than one thousand nuclei fairly well, we confirmed good fitting of  $\Delta E_{\text{shell}}(\text{CAL})$  to  $\Delta E_{\text{shell}}(\text{EXP})$  in the configuration of well-separated fragments. For examples,  $\Delta E_{\text{shell}}(\text{CAL})$

$= -13.0$  MeV,  $\Delta E_{\text{shell}}(\text{EXP}) = -12.4$  MeV for  $^{12}\text{C}$  emission,  $\Delta E_{\text{shell}}(\text{CAL}) = -10.8$  MeV,  $\Delta E_{\text{shell}}(\text{EXP}) = -10.0$  MeV for  $^{18}\text{O}$  emission, if we normalize  $\Delta E_{\text{shell}}(\text{CAL}) = \Delta E_{\text{shell}}(\text{EXP}) = -15.8$  MeV for  $^{14}\text{C}$  emission. For  $\alpha$  decay,  $\Delta E_{\text{shell}}(\text{CAL}) = -2.0$  MeV  $> \Delta E_{\text{shell}}(\text{EXP}) = -6.0$  MeV. This discrepancy mainly results from the  $\alpha$ -cluster correlation which was not explicitly taken into account.

The WKB expression for penetrability was evaluated for  $\alpha$  particle and heavy cluster emissions. The effective mass in the disintegration degree of freedom was taken simply as a reduced mass of the fragments.

The branching ratio  $R(X/^{14}\text{C})$  of an X particle to  $^{14}\text{C}$  emission from  $^{222}\text{Ra}$  is given in Table 1. The resulting ratio  $R(\alpha/^{14}\text{C}) \sim 8 \times 10^8$  was found to be in good agreement with the observed ratio of Price, et al.<sup>2)</sup> ( $3 \times 10^9$ ). The inclusion of the  $\alpha$ -correlation energy which makes  $\Delta E_{\text{shell}}(\text{CAL})$  small approaches the calculated ratio  $R(\alpha/^{14}\text{C})$  closer to the observed ratio.

The estimated ratio  $R(^{12}\text{C}/^{14}\text{C})$  seems to suggest the reason why no  $^{12}\text{C}$  emission has been measured.<sup>2)</sup> In order to see this more precisely, we show a potential barrier  $E_{\text{tot}}$  and a shell correction energy  $\Delta E_{\text{shell}}$ . The solid and dashed lines correspond to  $^{14}\text{C}$  and  $^{12}\text{C}$  emissions, respec-

Table 1. Branching ratio  $R(X/^{14}\text{C})$  of  $^{222}\text{Ra}$  decay.

X	$R(X/^{14}\text{C})$	X	$R(X/^{14}\text{C})$
$^4\text{He}$	$9 \times 10^8$	$^{18}\text{O}$	$5 \times 10^{-10}$
$^{10}\text{Be}$	$2 \times 10^{-5}$	$^{22}\text{Ne}$	$3 \times 10^{-22}$
$^{10}\text{C}$	$3 \times 10^{-31}$	$^{28}\text{Mg}$	$6 \times 10^{-36}$
$^{12}\text{C}$	$2 \times 10^{-2}$	$^{38}\text{S}$	$7 \times 10^{-43}$
$^{14}\text{C}$	1	$^{48}\text{Ca}$	$2 \times 10^{-49}$
$^{16}\text{C}$	$6 \times 10^{-10}$	$^{56}\text{Cr}$	$1 \times 10^{-58}$
$^{16}\text{O}$	$3 \times 10^{-9}$	$^{68}\text{Ni}$	$1 \times 10^{-53}$

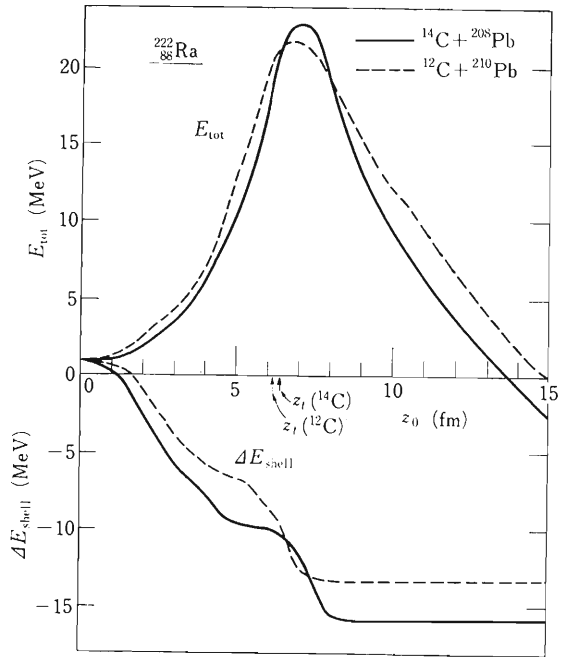


Fig. 2. Potential barrier  $E_{\text{tot}}$  and shell correction energy  $\Delta E_{\text{shell}}$  as a function of deformation  $z_0$  for  $^{14}\text{C}$  and  $^{12}\text{C}$  emissions.

tively. The gain of the release energy or  $\Delta E_{\text{shell}}$  for  $^{14}\text{C}$  compared to  $^{12}\text{C}$  reduces the ratio  $R(^{12}\text{C}/^{14}\text{C})$ . It must also be noticed that  $\Delta E_{\text{shell}}$  is strongly deformation-dependent in the configuration of a parent nucleus, as seen from the lower curves in Fig. 2.

## References

- 1) A. Sandulescu, et al.: Sov. J. Part. Nucl., **11**, 528 (1980); D.N. Poenaru, et al.: J. Phys. G, **10**, L183 (1984).
- 2) H.J. Rose and G.A. Jones: Nature (London), **307**, 245 (1984); S. Gale, et al.: Phys. Rev. Lett., **53**, 759 (1984); P.B. Price, et al.: Phys. Rev. Lett., **54**, 297 (1985).
- 3) Y.J. Shi and W.J. Swiatecki: Phys. Rev. Lett., **54**, 300 (1985).
- 4) P. Möller and J.R. Nix: Nucl. Phys., **A361**, 11 (1981).

### III-1-11. Master Equations in the Microscopic Theory of Nuclear Collective Dynamics

F. Sakata,\* M. Matsuo, T. Marumori,\*\* and Y. Zhuo\*\*\*

$\left[ \begin{array}{l} \text{dissipative collective motion, coupled master equations,} \\ \text{time-dependent Hartree-Fock, selfconsistent collective} \\ \text{coordinate method.} \end{array} \right]$

In such an isolated finite many-body quantal system as the nucleus in which the self-consistent mean field is realized, collective modes of motion (associated with time evolution of the mean field) are highly involved with single-nucleon motion in a strongly selfconsistent way. A microscopic theory<sup>1)</sup> to describe such collective motions has been developed, which employs the time-dependent Hartree-Fock (TDHF) approximation.

We formulate a general framework on the basis of the microscopic theory so that we can not only describe conserved large-amplitude collective motions as well as dissipative ones, but also investigate the mechanism of the transition between the two types of collective motion.

The collective motions is displayed as a dynamical evolution of the ensemble of TDHF state vectors and is also represented as a bundle of the trajectories in a phase space. We introduce a dynamical canonical coordinate (DCC) system: an optimal set of collective (relevant) variables ( $\eta, \eta^*$ ) and non-collective (irrelevant) ones ( $\xi_\alpha, \xi_\alpha^*$ ), the former of which represents a bulk feature (mean trajectory) of the bundle while the latter the fluctuation around the mean trajectory. The DCC system is determined in an extended formulation of the selfconsistent collective coordinate method.<sup>2)</sup> Thus a basic equation for the collective motions is given by the Liouville equation

$$\frac{\partial}{\partial t} \rho(\eta, \eta^*, \xi, \xi^*; t) = -i \mathcal{L} \rho(\eta, \eta^*, \xi, \xi^*; t) \quad (1)$$

where  $\rho(\eta, \eta^*; \xi, \xi^*; t)$  represents the distribution of the bundle of trajectories. The Hamiltonian corresponding to the Liouvillian

$$\mathcal{L} * = i \{ H, * \}_{\text{P.B.}} \quad (2)$$

has generally the following form

$$H = H_{\text{coll}}(\eta, \eta^*) + H_{\text{coupl}}(\eta, \eta^*, \xi, \xi^*) \quad (3)$$

We apply the time-dependent projection operator method of Willis and Picard<sup>3)</sup> to the Liouville equation. This makes it possible to treat not only time evolution of a reduced distribution function  $\rho_\eta(\eta, \eta^*; t) = \text{Tr}_\xi \rho(\eta, \eta^*; \xi, \xi^*; t)$  for the relevant variables but also that of the reduced distribution function  $\rho_\xi(\xi, \xi^*; t) = \text{Tr}_\eta \rho(\eta, \eta^*; \xi, \xi^*; t)$  for the irrelevant variables, without introducing any statistical hypothesis even for the latter. The Liouville equation thus leads to

$$\begin{aligned} \dot{\rho}_\eta(t) &= -i \mathcal{L}_{\text{coll}} \rho_\eta(t) - i \mathcal{L}_\eta(t) \rho_\eta(t) \\ &\quad - \int_0^{t-t_0} d\tau \text{Tr}_\xi \mathcal{L}_\Delta(t) g(t, t-\tau) \\ &\quad \cdot \mathcal{L}_\Delta(t-\tau) \rho_\eta(t-\tau) \rho_\xi(t-\tau) \\ \dot{\rho}_\xi(t) &= -i \mathcal{L}_\xi(t) \rho_\xi(t) - \int_0^{t-t_0} d\tau \text{Tr}_\eta \mathcal{L}_\Delta(t) g(t, t-\tau) \\ &\quad \cdot \mathcal{L}_\Delta(t-\tau) \rho_\eta(t-\tau) \rho_\xi(t-\tau) \end{aligned} \quad (4)$$

where  $\mathcal{L}_{\text{coll}}$  is a Liouvillian for the collective Hamiltonian  $H_{\text{coll}}$ . Coupling Liouvillians  $\mathcal{L}_\eta(t)$ ,  $\mathcal{L}_\xi(t)$  and  $\mathcal{L}_\Delta(t)$  correspond to parts of the coupling Hamiltonian  $H_{\text{coupl}}$ ,

$$H_\eta(t) \equiv \text{Tr}_\xi H_{\text{coupl}} \rho_\xi(t) = \langle H_{\text{coupl}} \rangle_{\xi, t} \quad (5)$$

$$H_\xi(t) \equiv \text{Tr}_\eta H_{\text{coupl}} \rho_\eta(t) = \langle H_{\text{coupl}} \rangle_{\eta, t} \quad (6)$$

$$H_\Delta(t) \equiv H_{\text{coupl}} - \langle H_{\text{coupl}} \rangle_{\eta, t} - \langle H_{\text{coupl}} \rangle_{\xi, t} + \text{Tr}_\eta \text{Tr}_\xi \rho_\eta(t) \rho_\xi(t) H_{\text{coupl}} \quad (7)$$

the first two of which represent the emsemble-averaged effects of the coupling while the last the fluctuation around the average.

The coupled master equations (4) are general and equivalent to the Liouville equation (1). It also allows us to introduce approximation schemes, e.g., the perturbation with respect to the coupling Hamiltonian  $H_{\text{coupl}}$ , or the more sofisticated perturbation with respect to the fluc-

\* Institute for Nuclear Study, University of Tokyo.

\*\* Institute of Physics, University of Tsukuba.

\*\*\* Institute of Atomic Energy, Beijing, China.

tuation of the coupling  $H_\Delta$  where the mean effect of the coupling  $H_n$  and  $H_\xi$  are taken into account in the zero-th order. Thus the coupled master equations (4) provide us with a basis for description of the dissipative behavior of the large-amplitude nuclear collective motions and for investigating their microscopic origins.

### References

- 1) T. Marumori, T. Maskawa, F. Sakata, T. Une, and Y. Hashimoto: Nuclear Collective Dynamics (The 1982 International Summer School of Nuclear Physics, Brasov, Romanis), World Scientific, p. 1 (1983); T. Marumori and F. Sakata: Particles and Nuclei, World Scientific, p. 207 (1986).
- 2) T. Marumori, T. Maskawa, F. Sakata, and A. Kuriyama: *Prog. Theor. Phys.*, **64**, 1294 (1980).
- 3) C.R. Willis and R.H. Picard: *Phys. Rev. A*, **9**, 1343 (1974).

### III-1-12. Dissipative Collective Motion in the Non-Linear Dynamics of the Nuclear Time-Dependent Hartree-Fock Theory

M. Matsuo and F. Sakata\*

(dissipative collective motion, time-dependent Hartree-Fock theory, Liouville equation, fluctuation.)

The time-dependent Hartree-Fock (TDHF) theory for microscopic description of nuclear collective motions incorporates well the non-linear nature that emerges from the strong self-consistency between a large amplitude mean-field motion and single-nucleonic motions. We formulated a general theoretical framework<sup>1)</sup> based on the TDHF theory to describe the collective motions which shows dissipation. In this theory the dissipation is expressed as diffusing behavior associated with the bundle of the trajectories, and this arises from the non-linear time-evolution of the TDHF trajectory.

In order to illustrate that the dissipation due to the non-linearity manifests itself, we perform numerical simulations for the three-level Lipkin model which is a simplification of the nucleus.<sup>2,3)</sup> The TDHF dynamics for the model system is described by only a pair of the relevant (collective) coordinate  $q_1$  and momentum  $p_1$  and another pair of the irrelevant (non-collective) coordinate  $q_2$  and momentum  $p_2$ . We numerically solve the Liouville equation for the distribution function  $\rho(q_1, p_1, q_2, p_2; t)$  which represents the evolution of the bundle of the TDHF trajectory. The distribution function at the initial time is set up so that it associates with high collectivity: the reduced distribution function  $\rho_\eta(q_1, p_1; t=0)$  for the relevant variables is stationary with respect to a collective Hamiltonian ( $\xi_\eta(t=0) \propto \delta(H_{\text{coll}}(q_1, p_1) - E_{\text{coll}})$ ) and the reduced irrelevant distribution  $\rho_\xi(q_2, p_2; t=0)$  has Gaussian distribution. The dynamical behavior varies depending on the initial collective energy  $E_{\text{coll}}$ .

It is indicated what kinds of the collective motions manifest in the model in Fig. 1, which shows typical three examples of the resultant reduced distribution functions  $\rho_\eta(q_1, p_1; t)$  and  $\rho_\xi(q_2, p_2; t)$  after several periods of the collective motion. In the calculation shown in Fig. 1(a), the

collectivity (defined as focusing of the distribution) persists well during the time evolution. This situation, which we call the collective one, represents the conserved collective motion. On the other hand, the collectivity in Fig. 1(c) is almost lost, which represents that no collective motion is expected in this situation. This situation can be called the stochastic one. Figure 1(b) shows the intermediate behavior between these two extremes; the collective motion as a bulk property of the system remains while the collectivity is partially lost. This is just the situation which we can identify as a dissipative collec-

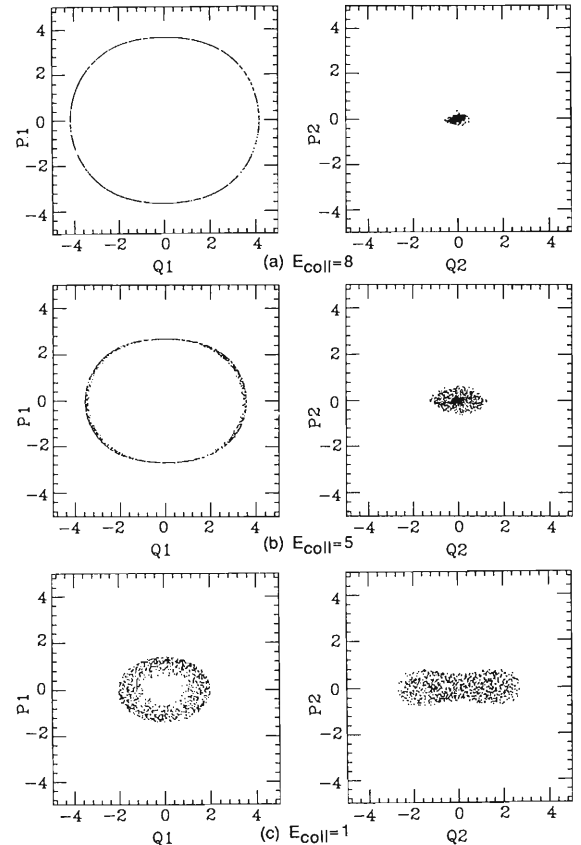


Fig. 1.  $\rho_\eta(q_1, p_1)$  and  $\rho_\xi(q_2, p_2)$  at  $t = 4\tau_{\text{coll}}$ .

\*Institute for Nuclear Study, University of Tokyo.

tive motion.

The coupled master equations which have been proposed in our previous work<sup>1)</sup> give an classification of the coupling between the relevant and the irrelevant degrees of freedom: the mean part of the coupling and the fluctuation part which is not taken into account by an ensemble average over the reduced distribution function. By calculating the distribution function with neglecting the fluctuation part of coupling and comparing it with the Liouville solution, we found that the

dissipative behavior shown in Fig. 1(b) is caused by the fluctuation part of the coupling, which has not been emphasized so far.

#### References

- 1) F. Sakata, M. Matsuo, T. Marumori and Y. Zhuo: This Report, p. 27.
- 2) S. Y. Li, A. Klein and R. M. Dreizler: *J. Math. Phys.*, **11**, 975 (1970).
- 3) K. Muramatsu, F. Sakata, Y. Yamamoto, and T. Marumori: *Prog. Theor. Phys.*, **73**, 380 (1987).

### III-1-13. Microscopic Derivation of Transport Equation in the Time-Dependent Hartree-Fock Theory

M. Matsuo, F. Sakata,\* T. Marumori,\*\* and Y. Zhuo\*\*\*

$\left. \begin{array}{c} \text{dissipative collective motion, Fokker-Planck transport} \\ \text{equation, time-dependent Hartree-Fock theory.} \end{array} \right\}$

We have developed, on the basis of the time-dependent Hartree-Fock (TDHF) description of nuclear many-body dynamics, a general theoretical framework for the large-amplitude collective motions that shows dissipation.<sup>1)</sup> This theory provides us with coupled master equations both for the time-evolution of the collective degrees of freedom and for that of the non-collective ones, and the master equations are formally equivalent to the Liouville equation. On the other hand, many phenomenological theories have described the dissipative collective motions with use of transport equations like the Fokker-Planck equation. We make a connection which links between the microscopic TDHF equation and the phenomenological Fokker-Planck equation.

In the master equations, the coupling  $H_{\text{coupl}}(\eta, \eta^*, \xi, \xi^*)$  between the relevant (collective) variables ( $\eta, \eta^*$ ) and the irrelevant (non-collective) ones ( $\xi, \xi^*$ ) are decomposed into two parts: the mean parts

$$H_\eta(t) \equiv \text{Tr}_\xi H_{\text{coupl}} \rho_\xi(t) = \langle H_{\text{coupl}} \rangle_{\xi, t} \quad (1)$$

$$H_\xi(t) \equiv \text{Tr}_\eta H_{\text{coupl}} \rho_\eta(t) = \langle H_{\text{coupl}} \rangle_{\eta, t} \quad (2)$$

which are the ensemble average over the distribution functions  $\rho_\eta(\eta, \eta^*; t)$  and  $\rho_\xi(\xi, \xi^*; t)$  of the partial system, and the fluctuation part

$$H_\Delta(t) \equiv H_{\text{coupl}} - \langle H_{\text{coupl}} \rangle_{\eta, t} - \langle H_{\text{coupl}} \rangle_{\xi, t} + \text{Tr}_\eta \text{Tr}_\xi \rho_\eta(t) \rho_\xi(t) H_{\text{coupl}} \quad (3)$$

Since the numerical simulations of the Liouville equation for a simply solvable model have revealed that the fluctuation part of the coupling causes the dissipation of the collective motion in a certain situation,<sup>2)</sup> we put emphasis on the effects of the fluctuation part in this analysis.

Perturbation with respect to the fluctuation part up to the second order approximates the

master equations into the following form.

$$\begin{aligned} \dot{\rho}_\eta(t) = & -i\mathcal{L}_{\text{coll}}\rho_\eta(t) - i\mathcal{L}_\eta(t)\rho_\eta(t) \\ & + \int_{-T}^T d\tau [-\sum_{ab} \tilde{\chi}_{ab}(t, t-\tau) \{ A_\eta^a(t, \tilde{A}_\eta^b(t, t-\tau) - \langle A_\eta^b \rangle_{\eta, t-\tau}) \tilde{\rho}_\eta(t, t-\tau) \}_{\text{P.B.}} \\ & + \sum_{ab} \tilde{\Psi}_{ab}(t, t-\tau) \{ A_\eta^a(t, \tilde{A}_\eta^b(t, t-\tau), \tilde{\rho}_\eta(t, t-\tau) \}_{\text{P.B.}}] \end{aligned} \quad (4a)$$

$$\begin{aligned} \dot{\rho}_\xi(t) = & -i\mathcal{L}_\xi(t)\rho_\xi(t) \\ & + \int_0^T d\tau [-\sum_{ab} \tilde{X}_{ab}(t, t-\tau) \{ B_\xi^a(t, \tilde{B}_\xi^b(t, t-\tau) - \langle B_\xi^b \rangle_{\xi, t-\tau}) \tilde{\rho}_\xi(t, t-\tau) \}_{\text{P.B.}} \\ & + \sum_{ab} \tilde{\Psi}_{ab}(t, t-\tau) \{ B_\xi^a(t, \tilde{B}_\xi^b(t, t-\tau), \tilde{\rho}_\xi(t, t-\tau) \}_{\text{P.B.}}] \end{aligned} \quad (4b)$$

where the notation for the coupling Hamiltonian

$$H_{\text{coupl}}(\eta, \eta^*, \xi, \xi^*) = \sum_a A_\eta^a(\eta, \eta^*) B_\xi^a(\xi, \xi^*) \quad (5)$$

is used. The Liouvillians  $\mathcal{L}_\eta$  and  $\mathcal{L}_\xi$  correspond to the mean couplings (1) and (2).

$$\tilde{\chi}_{ab}(t, t-\tau) \equiv -\theta(\tau) \text{Tr}_\xi \{ B_\xi^a(t, \tilde{B}_\xi^b(t, t-\tau)) \cdot \tilde{\rho}_\xi(t, t-\tau) \} \quad (6)$$

and

$$\begin{aligned} \tilde{\Psi}_{ab}(t, t-\tau) \equiv & \theta(\tau) \text{Tr}_\xi B_\xi^a(t, \tilde{B}_\xi^b(t, t-\tau)) \\ & - \langle B_\xi^b \rangle_{\xi, t-\tau} \tilde{\rho}_\xi(t, t-\tau) \end{aligned} \quad (7)$$

correspond to the response and correlation functions in the linear response theory for quasi-equilibrium statistical mechanics.

$$\begin{aligned} \tilde{X}_{ab}(t, t-\tau) \equiv & -\text{Tr}_\eta \{ A_\eta^a(t, \tilde{A}_\eta^b(t, t-\tau)) \cdot \tilde{\rho}_\eta(t, t-\tau) \} \end{aligned} \quad (8)$$

$$\begin{aligned} \tilde{\Psi}_{ab}(t, t-\tau) \equiv & \text{Tr}_\eta A_\eta^a(t, \tilde{A}_\eta^b(t, t-\tau)) \\ & - \langle A_\eta^b \rangle_{\eta, t-\tau} \tilde{\rho}_\eta(t, t-\tau) \end{aligned} \quad (9)$$

are counterparts for the collective variables. Quantities with tilders represent the interaction picture, for example

\* Institute for Nuclear Study, University of Tokyo.

\*\* Institute of Physics, University of Tsukuba.

\*\*\* Institute of Atomic Energy, Beijing, China.

$$\tilde{\rho}_\eta(t, t-\tau) \equiv g_\eta(t, t-\tau) \rho_\eta(t-\tau) \quad (10)$$

The reduced master equations can be solved analytically under the assumption that the time-scale of the relevant (collective) motion  $\tau_{\text{rel}}$  is much larger than that of the irrelevant (non-collective) motion  $\tau_{\text{irrel}}$ . This assumption enables us to solve the master equation (4b) for the irrelevant degrees of freedom with the use of a kind of the adiabatic expansion and leads to the solution for the  $N$ -th moment  $\langle e^{[N]} \rangle_{\xi, i}$  of the irrelevant variables  $(\xi, \xi^*)$ .

$$\langle e^{[N]} \rangle_{\xi, i} = \text{phase} \times e^{\int_{t_0}^t dt' \epsilon^{[N]}(t')} \langle e^{[N]} \rangle_{\xi, i} \quad (11)$$

Here the factor  $\epsilon^{[N]}$  arises from the effect of the fluctuation coupling represented by the last two terms of Eq.(4b) and it is determined by a self-consistency condition. When  $\epsilon^{[N]}$  takes positive value, the excitation of the irrelevant modes increases as the time evolves, and correspondingly the energy dissipates into the irrelevant modes from the relevant degrees of freedom.

In this situation, we can introduce the Markoff approximation for the master equation (4a) for the relevant degrees of freedom. Thus we obtain

$$\begin{aligned} \dot{\rho}_\eta(t) &= \{ H_{\text{coll}}^r(t), \rho_\eta(t) \}_{\text{P.B.}} \\ &+ \sum_{\vec{k}, \vec{l}} M_{\vec{k}, \vec{l}}^{(1)} \frac{d}{dt} \langle A_{\eta}^{\vec{l}}(t) \rangle_{\eta, i} \langle A_{\eta}^{\vec{k}}(t), \\ &\rho_\eta(t) \}_{\text{P.B.}} \end{aligned}$$

$$\begin{aligned} &- \sum_{n=0,1} \sum_{\vec{k}, \vec{l}} M_{\vec{k}, \vec{l}}^{(n)}(t) \{ A_{\eta}^{\vec{k}}(t), (\tilde{A}_{\eta}^{\vec{l}(n)}(t) \\ &- \langle \tilde{A}_{\eta}^{\vec{l}(n)}(t) \rangle_{\eta, i}) \rho_\eta(t) \}_{\text{P.B.}} \\ &+ \sum_{n=0,1} \sum_{\vec{k}, \vec{l}} N_{\vec{k}, \vec{l}}^{(n)}(t) \{ A_{\eta}^{\vec{k}}(t), \\ &\{ \tilde{A}_{\eta}^{\vec{l}(n)}(t), \rho_\eta(t) \}_{\text{P.B.}} \}_{\text{P.B.}} \end{aligned} \quad (12)$$

$$\tilde{A}_{\eta}^{\vec{l}(n)}(t) = \left( \frac{\partial}{\partial \tau} \right)^n \tilde{A}_{\eta}^{\vec{l}}(t, t-\tau) \Big|_{\tau=0} \quad (13)$$

which has formally the same structure as the Fokker-Planck transport equation. Since the Poisson bracket  $\{ , \}_{\text{P.B.}}$  induces the derivative with respect to the relevant variables  $(\eta, \eta^*)$ , the first three terms in the right-hand side represent the drift terms and the last term the diffusion term. The transport coefficients are given by the  $n$ -th moments of the response and correlation functions

$$M_{\vec{k}, \vec{l}}^{(n)} = \int_{-\infty}^{\infty} d\tau \frac{\tau^n}{n!} \tilde{x}_{\vec{k}, \vec{l}}(t, t-\tau) \quad (14)$$

$$N_{\vec{k}, \vec{l}}^{(n)} = \int_{-\infty}^{\infty} d\tau \frac{\tau^n}{n!} \tilde{\Psi}_{\vec{k}, \vec{l}}(t, t-\tau) \quad (15)$$

which can be evaluated by means of the same technique as for the irrelevant master equation (4b).

## References

- 1) F. Sakata, M. Matsuo, T. Marumori, and Y. Zhuo: This Report, p. 27.
- 2) M. Matsuo and F. Sakata: This report, p. 29.

### III-1-14. Average Partial Level Density Including the Effect of Residual Interaction

K. Sato and S. Yoshida

(Level density, Precompound reaction, Realistic)  
one-body spectrum, Random matrix.)

To evaluate the cross section for precompound reactions, the level density  $\rho_m(E)$  with fixed exciton number  $m$  is necessary. Its important role in the theory of precompound reactions has recently been stressed.<sup>1)</sup> Thus, the calculation of the level density in terms of single-particle energies and of two-body interaction matrix elements in a large shell model space is highly necessary. For the calculation, however, the basis must be made sufficiently large and a standard matrix diagonalization method is not feasible.

Therefore, we adopt the precompound theory<sup>2)</sup> based on the Gaussian Distributed Ensemble (GDE), which is the extended ensemble of GOE so as to violate orthogonal invariance and to adopt a chaining hypothesis. The theory gives us a framework to obtain the level density  $\rho_m$  from the solution of saddle point equations which take the second moments of GDE as an input. In the recent papers<sup>3, 4)</sup> we proposed an approximate method of calculating the second moments which characterize the GDE in terms of two-body interaction matrix elements. Taking the second moments as an input, we calculated the level density  $\rho_m(E)$  and the total level density  $\rho(E)$ . The results showed that the residual interaction greatly enhances the level density especially in a low energy region and may improve the agreement with experimental data at thermal neutron resonances. The theory assumed, however, that the one-body part of the Hamiltonian has a degenerate spectrum in every subspace  $m$ , which is not generally realistic.

We have recently proposed a way of including the realistic one-body spectrum<sup>5)</sup> in the calculation of level densities. In the present report we outline the result of such an extension and numerical calculation.

Using the method of generating function and Grassmann integral given in Ref.2 (a slight modification is necessary to include the realistic

one-body spectrum), we obtain the following saddle point equation for  $\tau_m$ :

$$\begin{aligned} \tau_m = & \lambda_m^2 N_m^{-1} \sum_{\mu} (E + i\delta - e_{m\mu} - \tau_m)^{-1} \\ & + \sum_{n(\neq m)} \lambda_{mn}^2 \sqrt{\frac{N_n}{N_m}} \times N_n^{-1} \sum_{\nu} (E + i\delta \\ & - e_{n\nu} - \tau_n)^{-1} \quad (m=2, 4, \dots) \end{aligned} \quad (1)$$

The average partial level density  $\rho_m$  is given by

$$\rho_m = -\frac{1}{\pi} I_m \sum_{\mu} (E + i\delta - e_{m\mu} - \tau_m)^{-1}$$

where  $e_{m\mu}$  is the eigenvalue for the one-body Hamiltonian in class  $m$ , and  $N_m$  is the number of states in class  $m$ . Strength parameters  $\lambda_m^2$  and

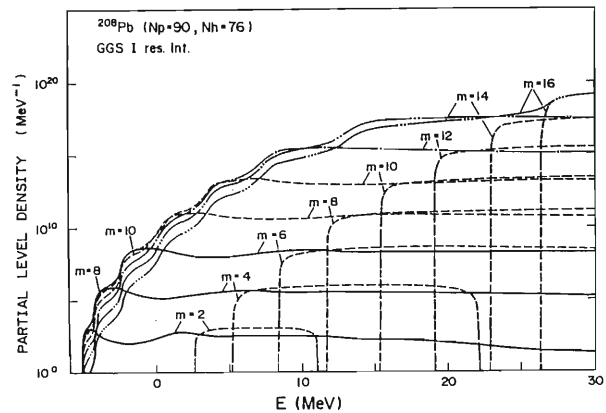


Fig.1. Level densities with fixed exciton number  $m$  for  $^{208}\text{Pb}$ .

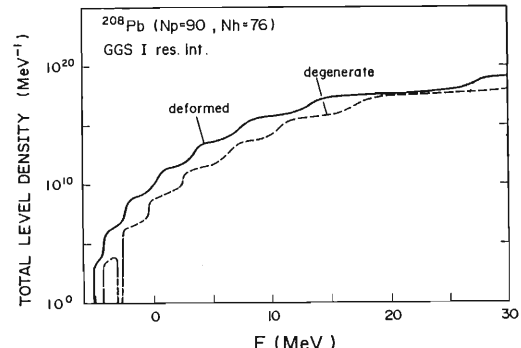


Fig. 2. The total level density for  $^{208}\text{Pb}$ .

$\lambda_{mn}^2$  ( $m \neq n$ ) are given by second moments  $M_{mn}$  from the relations  $\lambda_m^2 = N_m \times M_{mn}$  and  $\lambda_{mn}^2 = \sqrt{N_m N_n} \times M_{mn}$ . Comparing Eq.1 with that for the degenerate spectrum case of Refs.2-4, we see that the present extension requires to replace the propagator  $(E - h_m - \lambda_m)^{-1}$  in the degenerate case by  $N_m^{-1} \times (E + i\delta - e_m \mu - \tau_m)^{-1}$ .

We performed numerical calculation of level densities  $\rho_m(E)$ , which are shown by solid, dashed, and dot-dashed curves in Fig.1. As for a realistic one-body spectrum, we used the one-body level density which was given by Obložinský and Kalbach, and for second moments the same as Ref.3 taking GGS I residual interaction. Figure 2 shows the total level density  $\rho(E) = \sum_m \rho_m(E)$ . The solid curve (deformed) was calculated by using realistic one-body spectrum for  $e_{m\mu}$ , while the dashed curve (degenerate) uses a degenerate one for  $e_{m\mu}$ .

Comparing these two curves, we easily see that a valley, which is not physically observed, does not appear when we include the realistic one-body spectrum. Except for such a drastic change, the overall behavior of the level density remains almost unchanged.

In summary, the previous calculation of the level density is improved by including the realistic one-body spectrum with a fixed exciton number  $m$ .

#### References

- 1) H. Nishioka, H.A. Weidenmüller, and S. Yoshida: *Phys. Lett. B*, **203**, 1 (1988).
- 2) H. Nishioka, J.J.M. Verbaarschot, H.A. Weidenmüller and S. Yoshida: *Ann. Phys.*, **172**, 67 (1986).
- 3) K. Sato and S. Yoshida: *Z. Phys. A*, **327**, 421 (1987).
- 4) K. Sato and S. Yoshida: *Z. Phys. A*, **330**, 265 (1988).
- 5) K. Sato and S. Yoshida: to be published in *Z. Phys. A*.

## III-2. Atomic and Solid-State Physics

### 1. Cross Sections for Radiative Electron Capture Calculated by a Relativistic Impulse Approximation—Formulation

K. Hino and T. Watanabe

The relativistic effect in radiative electron capture (REC) was firstly observed by Spindler, *et al.*<sup>1)</sup> in the bombardments of a target with a light projectile ion. Their observation shows that the radiation pattern of K-REC (REC into a K-shell orbit of a projectile ion) is of a forward-backward symmetry, *i.e.*, the angular distribution of photon emission has a  $\sin^2\theta_L$ -dependence with respect to an angle  $\theta_L$  measured from the incident direction in the laboratory frame. This result is qualitatively understood as the cancellation of the retardation effect of emitted photons by the aberration effect of the emission angle, *i.e.*, by the Lorentz-transformation effect from the moving-frame into the laboratory frame. Anholt, *et al.*<sup>2)</sup> also observed  $\sin^2\theta_L$ -dependence in the case where a  $Xe^{54+}$  ion collides with a Be atom at 197 MeV/u. Hino and Watanabe<sup>3)</sup> theoretically confirmed such behavior of the REC photon angular distributions by employing the relativistic strong-potential Born (SPB) approximation and showed that the angular distribution of photons is slightly enhanced for the backward direction in the case of a 422 MeV/u  $U^{92+}$  colliding on a Be atom because of a strong Coulomb distortion between the ion and the active electron. Furthermore, in contrast to K-REC, L-REC (REC into a projectile L-shell orbit) is asymmetric because the photon retardation corrections do not cancell the aberration effects.<sup>4)</sup>

Aside from the photon angular distributions, the relativistic effects of the REC are revealed from the observations of the linear polarization correlations (linear polarization dependence on emission angle in the laboratory frame) of emitted photons as well.<sup>4)</sup> A polarization vector of a photon induced by collisions with non-relativistic relative velocity always lies on the scattering plane constructed by vectors of the photon momentum and the incident velocity. This polarization vector gets to turn its direction from on the scattering plane to the plane perpendicular to

it with the increase of velocity. Furthermore, the polarization correlation of the photon shows an inversion of its sign at a certain emission angle in the relativistic energy region. This is called a “crossover” feature. According to the Born calculation,<sup>4)</sup> this feature appears in the forward direction relative to 90° when  $v/c > 0.8$  with  $v$  and  $c$  being the relative velocity and the velocity of light, respectively.

An internal conversion process, hereafter, this effect is referred to as the abbreviation of ICP. ICP is herein used to mean the process depicted in the second graph of Fig. 1. The first Feynman diagram shows the conventional REC process. The second diagram indicates the contribution of an intermediate positron. At the first stage, a pair of an electron and a virtual positron is created with an emission of a real photon, then the positron propagates in the intermediate state, and finally a pair of this positron and an initial electron is annihilated into a virtual photon associated with the Coulomb interaction between an active electron and a projectile ion. This

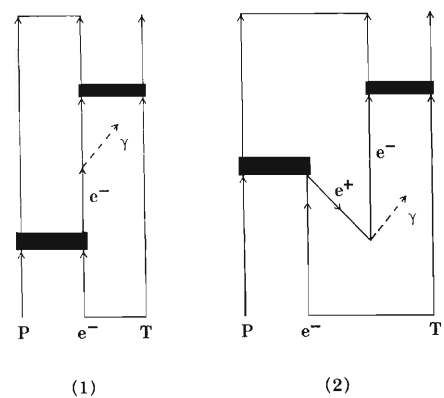


Fig. 1. Feynman diagrams for the relativistic radiative electron capture process. P, T,  $e^-$ , and  $e^+$  stand for a projectile ion, a target nucleus, an electron, and a positron, respectively. A black bold block represents a Coulomb interaction.

effect is expected to become very important with the increase in  $Z_p$ . This is because ICP may be interpreted as follows: The strong electric fields due to the existence of a heavy projectile will induce a vacuum polarization cloud around itself. But the time-variation of the projectile will partially break up the virtual pairs in collisions into the real  $e^+e^-$  pairs.<sup>5)</sup> The electron is converted to a final electron bound on a projectile and, on the other hand, the positron is annihilated with an initial electron. The relativistic effects of K-REC X-ray angular distribution in the case of high  $Z_p$  should not be separated from the influences of ICP.

Here we are going to investigate the K-REC photon angular distributions, the K-REC total cross sections, and linear polarization correlations of emitted photons up to the ultra-relativistic incident energy region by virtue of the relativistic impulse approximation (RIA) including the whole relativistic effects with ICP. We refer to a reason why the impulse approximation (IA), not the SPB approximation<sup>6)</sup> used in our paper previously, is adopted in the present calculations.

The difference between SPB and IA is the presence of the Coulomb off-shell factor in the former (or latter). According to Gorriz, *et al.*,<sup>7)</sup> the non-relativistic REC cross section calculated by the SPB approximation is almost double of that by IA<sup>8)</sup> because of the presence of this off-shell factor. Following the statements by Jakubassa-Amundsen, *et al.*,<sup>9)</sup> the photon angular distribution of REC should be smoothly connected with that of the (two-body) radiative recombination process (RRP) at the on-shell limit, *i.e.*, when the binding energy of a target atom becomes zero. The result of the original SPB approximation does not satisfy this requirements. Jakubassa-Amundsen, *et al.* settled this difficulty temporarily by renormalizing the SPB wave function, in other word, by dividing it by a factor ascribable to this discontinuity between REC and RRP at the on-shell limit so as to satisfy the requirement of the smooth connection. Further, it is found that the discontinuity of REC and RRP is eliminated by incorporating the effect of the asymptotic Coulomb tail with the SPB wave function in accordance with Dollard's idea,<sup>10)</sup> and the resultant REC cross section becomes in agreement with that by IA.<sup>11)</sup> The same statement is applicable to the cross section of the relativistic REC. Therefore, we do not employ the SPB approximation in the present article.

We assume the collision system consists of a

Table 1. Ratios of K-REC total cross sections calculated by using the RIA with including effects of ICP to those by RIA without ICP.

Collision system	Incident velocity $ v $			
	0.70	0.80	0.90	0.99
Ne <sup>10+</sup> -Be	1.006	1.007	1.008	1.009
Xe <sup>54+</sup> -Be	1.21	1.22	1.25	1.32
U <sup>92+</sup> -Be	1.82	1.90	2.02	2.40

projectile ion (P) with the electric charge  $Z_p e$ , a target nucleus (T) with  $Z_T e$ , and an active electron (e) with  $-e$  for simplicity. The transition matrix of the REC is given by

$T^{\text{REC}} = -e \langle \psi_f^{(-)} | \gamma_4 \gamma_\mu A^* \mu | \psi_i^{(+)} \rangle$  (1)

by using notations of Dirac's  $\gamma$  matrices that  $\gamma = -i\beta\alpha$  and  $\gamma_4 = \beta$  with  $\alpha$  and  $\beta$  being the  $\alpha$  and  $\beta$  matrices with respect to an electron. The wave function  $A^* \mu$  of an emitted photon is provided as follows:

$$A^* \mu = (2\pi)^{-3/2} (2\omega)^{-1/2} e_\mu^* e^{-ik \cdot (R + (M_p/M)r_p + (M_t/M)r_t)}$$
 (2)

where  $k$ ,  $\omega$ , and  $e_\mu^*$  are the momentum, the energy, and the polarization vector of an emitted photon, respectively,  $R$  is the position vector of the center of mass of the collisions system, and  $r_p$  and  $r_t$  are the electronic position vector measured from P and T, respectively. Moreover, masses of P, T, and e are defined as  $M_p$ ,  $M_t$ , and  $m$ , respectively, the total mass of the system are given by  $M = M_p + M_t + m$ . The final wave function  $\psi_f^{(-)}$  is provided by the framework of the relativistic impulse approximation. Here we consider the case of extremely asymmetric collision (*i.e.*,  $Z_p \gg Z_t$ ), the initial total wave function  $\psi_i^{(+)}$  of Eq. 1 becomes

$$\psi_i^{(+)} = (1 + G_p^{(+)} V_p) \phi_i$$
 (3)

where  $G_p^{(+)}$  is a relativistic Green function incorporating an effect of a strong potential  $V_p$  between P and e to all orders and provided by

$$G_p^{(+)} = (E - \sum_{N=P,T,e} K_N - V_p + i\eta)^{-1}$$
 (4)

Here,  $K_N$  is a relativistic free Hamiltonian of a particle N and n an infinitesimal real positive value.  $\phi_i$  denotes the initial free wave function.

In order to obtain the differential cross section of the REC photons, we at first calculate it in the moving frame (*i.e.*,  $P_f = 0$ ) and finally Lorentz-transform it into the laboratory frame (*i.e.*,  $P_i = 0$ ). The photon angular distribution in the moving frame reads

$$= (2\pi)^4 |v|^{-1} \sum \int d\omega_M \omega_M^2 \int dq \langle |t^{\text{REC}}|^2 \rangle \delta(\omega_M - \omega_M^{(0)} - \gamma v \cdot q)$$
 (5)

where the summation is taken over all initial states,  $\mathbf{q}$  is the transferred momentum of the electron in REC processes,  $\omega_M^{(0)}$  indicates the peak position of the photon energy  $\omega_M$  in the moving frame and is given by  $\omega_M^{(0)} = m(\gamma\xi_T - \xi_P)$  with  $\gamma = (1 - |v|^2)^{-1/2}$ ,  $\xi_P = [1 - (Z_P\alpha)^2]^{1/2}$ , and  $\xi_T = [1 - (\xi_T\alpha)^2]^{1/2}$  with  $\xi_T$  the optimized  $\xi$ -exponent of an active electron. The summation is taken with respect to  $\xi_T$ -values, i.e., initial states of bound (target) electrons participating in REC. Here  $\theta_M$  is defined as an emission angle of a photon in the moving frame, and  $\Omega_M$  is a solid angle associated with this. The last term in the energy-conserving  $\delta$ -function represents the Doppler broadening effect of the REC photon spectrum. Moreover,  $t^{REC}$  and  $\langle t^{REC2} \rangle$  have been

$$T^{REC} = t^{REC} \delta^{(3)}(K_i + P_i - K_f - k) \quad (6)$$

and

$$\langle |t^{REC}|^2 \rangle = 8^{-1} \sum_{\text{helicities}} |t^{REC}|^2 \quad (7)$$

where we have taken the average with respect to the initial helicities and the summation with respect to the final ones of all three particles, P, T, and e.

Utilizing the Lorentz transformations:

$$\begin{aligned} \sin\theta_M &= \gamma^{-1} \sin\theta_L / (1 - |v| \cos\theta_L) \\ \cos\theta_M &= (\cos\theta_L - |v|) / (1 - |v| \cos\theta_L) \end{aligned} \quad (8)$$

we get the photon angular distribution in the

laboratory frame from moving frame expression:

$$(d\sigma/d\Omega_L) = (1 - v^2) (1 - |v| \cos\theta_L)^{-2} (d\sigma/d\Omega_M) \quad (9)$$

## References

- 1) E. Spindler, H.-D. Betz, and F. Bell: *Phys. Rev. Lett.*, **42**, 832 (1979).
- 2) R. Anholt, S.A. Andriamonje, E. Morenzoni, Ch. Stoller, J.D. Molitoris, W.E. Meyerhof, H. Bowman, J.-S. Xu, Z.-Z. Xu, J.O. Rasmussen, and D.H.H. Hoffmann: *Phys. Rev. Lett.*, **53**, 234 (1984).
- 3) K. Hino and T. Watanabe: *Phys. Rev. A*, **36**, 581 (1987).
- 4) K. Hino and T. Watanabe: *Phys. Rev. A*, **36**, 5862 (1987).
- 5) For instance, G. Soff, J. Reinhardt, B. Müller, and W. Greiner: *Phys. Rev. Lett.*, **38**, 592 (1977); W. Greiner, B. Müller, and J. Rafelski: *Quantum Electrodynamics of Strong Fields*, Springer-Verlag, Heidelberg, p. 366 (1985).
- 6) J. H. Macek and R. Shakeshaft: *Phys. Rev. A*, **22**, 1441 (1980); J. Macek and S. Alston: **26**, 250 (1982); S. Alston: **27**, 2342 (1983).
- 7) M. Gorri, J.S. Briggs, and S. Alston: *J. Phys. B*, **16**, L665 (1983).
- 8) M. Kleber and D.H. Jakubassa: *Nucl. Phys.*, **A252**, 152 (1975).
- 9) D.H. Jakubassa-Amundsen, R. Höppler, and H.-D. Betz: *J. Phys. B*, **17**, 3943 (1984); D.H. Jakubassa-Amundsen: **20**, 325 (1987).
- 10) J.D. Dollard: *J. Math. Phys.*, **5**, 729 (1964).
- 11) K. Hino and T. Watanabe: *Phys. Rev. A*, **39**, 3373.

### III-2-2. Cross Sections for Radiative Electron Capture Calculated by a Relativistic Impulse Approximation—Total and Differential Cross Sections and Linear Polarization

K. Hino and T. Watanabe

The total cross sections for radiative electron capture have been calculated by using relativistic impulse approximation (RIA).<sup>1)</sup> They include all of the relativistic effects explained in the previous report: the relativistic velocity effect, the high  $Z_p$ -effect (projectile charge effect), the spin-orbit coupling, and the internal conversion process of  $e^+e^-$  pair creation and annihilation (ICP) effect, in particular, paying an attention to the last new effect. The K-REC (radiative electron capture into a K-shell orbit of the projectile ion) cross sections for the collision systems of  $Xe^{54+}$ -Be are shown in Fig. 1, in comparison with experiments.<sup>2)</sup> Figure 1 contains two theoretical curves: one is the result by RIA with consideration of ICP, *i.e.*, in accordance with both graphs of Fig. 1 of the previous report,<sup>1)</sup> and the other by RIA irrespective of the ICP effect, *i.e.*, with considering only the first diagram of Fig. 1 of Ref. 1. The differences between two curves indicate the magnitudes of the ICP effect to K-REC. In Table 1, we show the effect of ICP with respect to the electric charges of projectiles as well as velocities.

ICP has small effects on the cross section of the  $Ne^{10+}$ -Be system over all velocity regions. In contrast, the  $U^{92+}$ -Be system is much influenced with ICP, above all, at high impact velocities. At the velocity of 0.99, this effect gives no less than 2.4 times greater contributions than the results without consideration of ICP. ICP is physically interpreted as an effect based on the breakup of virtual  $e^+e^-$  pairs (vacuum polarization cloud around a projectile ion induced by the presence of its strong electric fields) into real pairs due to the projectile motion. Thus we come to a conclusion that as long as a projectile charge is very high, an intermediate positron has nearly the same degree of contributions to the K-REC as that of an associated electron. The velocity-dependence of ICP is less pronounced than expected at the outset. For relativistic heavy ion-atom collisions not to speak of the present REC, in general, it would be improper to neglect

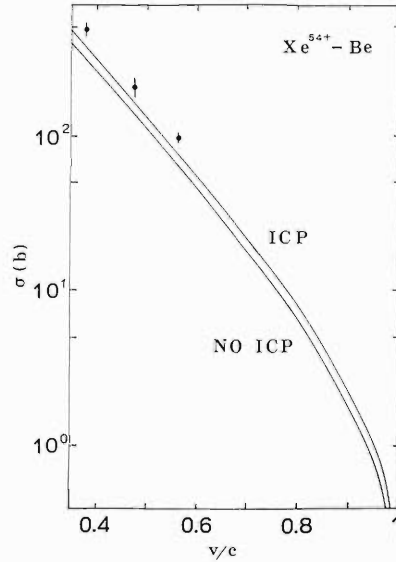


Fig. 1. REC total cross sections for a  $Xe^{54+}$ -Be collision system. ICP and no ICP mean RIA calculations with and without including the internal conversion process, respectively. Experimental values are cited from W.E. Meyerhof, *et al.*<sup>2)</sup>

Table 1. Ratios of the K-REC total cross sections calculated by using RIA with including effects of ICP to those by RIA without ICP.

Collision system	Incident velocity $ v $			
	0.70	0.80	0.90	0.99
$Ne^{10+}$ -Be	1.006	1.007	1.008	1.009
$Xe^{54+}$ -Be	1.21	1.22	1.25	1.32
$U^{92+}$ -Be	1.82	1.90	2.02	2.40

the effects of ICP fully from the beginning as, for example, in the discussion of our proceeding paper.<sup>3)</sup>

We are somewhat concerned with simple velocity dependence of a REC total cross section. In the non-relativistic energy region, as indicated by Briggs and Dettmann,<sup>4)</sup> the cross section is proportional to  $|v|^{-5}$ . It is difficult to deduce

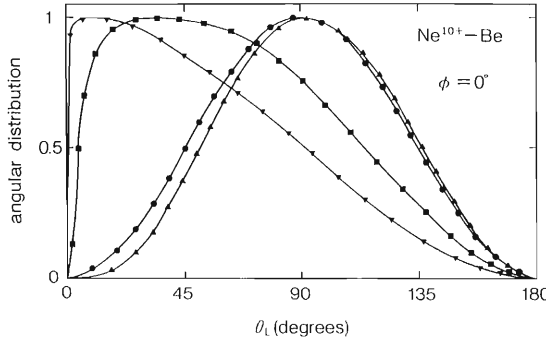


Fig. 2. Normalized photon angular distributions of K-REC induced by collisions of a  $\text{Ne}^{10+}$  ion on a Be atom.  $\phi$  means the polarization angle of an emitted photon. (●), the incident energy 0.1 GeV/u; (▲), 1 GeV/u; (■), 10 GeV/u; (▼), 100 GeV/u, respectively.

such a simple rule from the present RIA method because a total cross section by this method is given numerically and is dependent on terms providing the ICP and the  $Z_p$  effects in complicated manners. Thus, for simplicity, we evaluate simple dependence of the velocity by applying a least-square method to some values calculated at velocities  $|v|$  ranging from 0.1 to 0.8 for a  $\text{Ne}^{10+}$ -Be, from 0.4 to 0.8 for a  $\text{Xe}^{54+}$ -Be and from 0.6 to 0.8 for a  $\text{U}^{92+}$ -Be, respectively. In these velocity regions, logarithmically scaled cross sections show almost straight slopes as in Fig. 1. As a result, a semi-empirical rule is obtained as  $|v|^{-p}$  with  $p$  equal to 4.98, 5.19, and 5.59 for respective collision systems. The slope of a total cross section with respect to ultrarelativistic velocities is steeper than that in the relativistic velocity region considered above.

We show the normalized photon angular distributions  $\sigma_N(\theta_L, \phi)$  at polarization angles  $\phi = 0^\circ$ ,  $45^\circ$ , and  $90^\circ$  for a  $\text{Ne}^{10+}$ -Be system in Fig. 2.

It is possible that the direction of a photon polarization vector  $e$  varies in the relativistic velocity region, while it mostly remains lying on the scattering plane in the non-relativistic velocity region. This nature is reflected by a linear

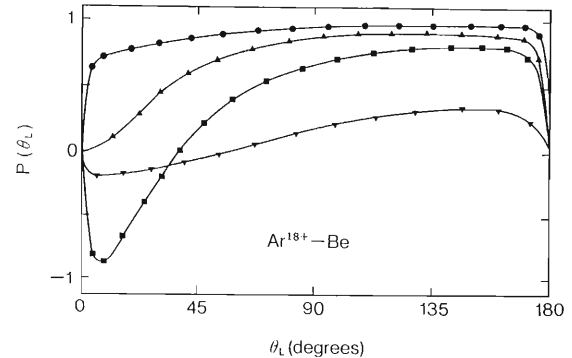


Fig. 3. Linear polarization correlations for K-REC photons induced by collisions of  $\text{Ar}^{18+}$  ions on a Be atom. (●), the incident velocity in the unit of the light velocity 0.7; (▲), 0.8; (■), 0.9; (▼), 0.99, respectively.

polarization correlation function  $P(\theta_L)$  defined by

$$P(\theta_L) = [(d\sigma/d\Omega_L)_{\phi=0^\circ} - (d\sigma/d\Omega_L)_{\phi=90^\circ}] / (d\sigma/d\Omega_L)_{\text{unpol}}$$

where azimuthal angle  $\phi$  is measured from the collision plane around the photon propagation direction.

In Fig. 3, we show the linear polarization correlations of REC photons induced by collisions of  $\text{Ar}^{18+}$  on a Be atom for several relativistic velocities ranging from 0.7 (376 MeV/u) to 0.99 (5.72 GeV/u). For collisions of  $\text{Ar}^{18+}$  on a Be, it is expected that the Born prediction holds true except for the forward and the backward angles. Details will be given elsewhere.<sup>5)</sup>

## References

- 1) K. Hino and T. Watanabe: This Report, p. 35.
- 2) W.E. Meyerhof, R. Anholt, J. Eichler, H. Gould, Ch. Munger, J. Alonso, P. Thieberger, and H.E. Wegner: *Phys. Rev. A*, **32**, 3291 (1985).
- 3) K. Hino and T. Watanabe: *Phys. Rev. A*, **36**, 581 (1987).
- 4) J.S. Briggs and K. Dettmann: *Phys. Rev. Lett.*, **33**, 1123 (1974).
- 5) K. Hino and T. Watanabe: *Phys. Rev.*, **39**, 3373 (1989).

### III-2-3. Circularly Polarized X Ray Emission Due to Radiative Electron Capture

K. Hino and T. Watanabe

We showed that X rays emitted from radiative electron capture (REC) by projectile heavy ions from a usual target, photons are linearly polarized due to the fact that the motion of electrons is confined on the plane parallel to the collision plane.<sup>10</sup> In the nonrelativistic limit, the direction of the electric field vector of X rays is almost parallel to the collision plane because of the confinement electron's motion. When the spins of the target electrons are polarized to a particular direction, the X rays emitted from REC may be circularly polarized. We investigate the property of the X rays due to REC from a spin-polarized target atom.

Let us consider the case where a projectile ion traverses through with a velocity  $\mathbf{v}$  and a photon is emitted to the  $z$  direction with a wave vector  $\mathbf{k}$  and an angle between  $\mathbf{v}$  and  $\mathbf{k}$  of  $\theta_L$  in the laboratory frame as shown in Fig. 1. The angular distribution of the REC photon is given by

$$\frac{d\sigma(\xi, s, s')}{d\Omega_M} = \frac{(2\pi)^4}{v} \sum_{\text{initial electron states}} \int d\omega_M \omega^2 M \times \int d\mathbf{q} |t^{\text{REC}}|^2 \delta(\omega_M - \omega_M^{(0)} - \mathbf{r}\mathbf{v} \cdot \mathbf{q}) \quad (1)$$

in the moving (projectile) frame,<sup>2)</sup> where  $t^{\text{REC}}$  is the  $T$ -matrix of the REC process,  $\xi$  is the Stokes parameter of a photon,<sup>3)</sup>  $\Omega_M$  is the solid angle for emitted photon in the moving frame,  $\mathbf{q}$  is the transferred momentum of the electron in REC, and  $s$  and  $s'$  are the initial and the final spin states of the active electron, respectively. The matrix  $t^{\text{REC}}$  is essentially given by the interaction of charged particles with electromagnetic fields.  $\omega_M$  and  $\omega_M^{(0)}$  are the photon energy and its peak position in the moving frame, respectively. They are given by  $\omega_M^{(0)} = m(\gamma\xi_T - \xi_p)$  with  $\gamma = (1 + |\mathbf{v}|^2)^{-1/2}$ ,  $\xi_p = [1 - (Z_p\alpha)^2]^{1/2}$  and  $\xi_T = [1 - (\xi_T\alpha)^2]^{1/2}$  with  $\xi_T$  the optimized  $\xi$ -exponent of the Slater orbital for the active electron, where  $Z_p$  is the projectile nuclear charge,  $\alpha$  is the fine structure constant, and  $m$  is the electron mass. We use a natural unit system,  $c = \hbar = 1$ , unless otherwise specified.

The transformation from the moving frame (the origin of coordinate system is on the projec-

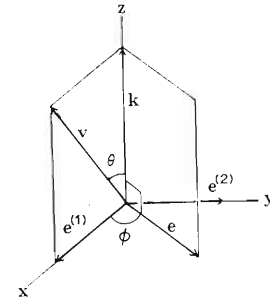


Fig. 1. A coordinate system for vectors  $\mathbf{k}$ ,  $\mathbf{v}$ , and  $\mathbf{e}$ . The plane spanned by  $\mathbf{k}$  and  $\mathbf{v}$  is the scattering plane, and that by  $\mathbf{k}$  and  $\mathbf{e}$  is the polarization plane.

tile nucleus) to the laboratory frame (the origin is on the target nucleus) is given by the Lorentz transformation as

$$\frac{d\sigma(\xi, s, s')}{d\Omega_L} = l(\theta_L)^2 \frac{d\sigma(\xi, s, s')}{d\Omega_M} \quad (2)$$

$$l(\theta_L) = \gamma^{-1}/(1 - v \cos\theta_L) \quad (3)$$

where  $\Omega_L$  is the solid angle for emitted photon in the laboratory frame. The absolute value of the squared  $T$ -matrix is given by

$$|t^{\text{REC}}|^2 = (2\pi)^{-2} \alpha \omega_M^{-1} \rho_{\mu\lambda}^{(\nu)} \cdot \frac{1}{4} \times \text{Tr} |\rho_{\mu}^{(e)}(\mathbf{0}) Q_\mu \rho_{\nu}^{(e)}(-\mathbf{p}) Q_\nu| \quad (4)$$

Here,  $\rho_{\mu\lambda}^{(\nu)}$  is the photon polarization tensor defined by the Stokes parameter  $\xi_i$  as

$$\rho_{\mu\lambda}^{(\nu)} = \sum_{a, b=1}^2 \rho_{ab} e_\mu^{(a)} e_\nu^{(b)} \quad (5)$$

with  $e^{(i)} = (e_\lambda^{(i)}, 0)$  for  $i=1, 2$  and  $\lambda=\mu, \nu$  and with

$$\rho_{ab} = \frac{1}{2} \begin{pmatrix} 1 + \xi_1 & \xi_2 - i\xi_3 \\ \xi_1 + i\xi_3 & 1 - \xi_1 \end{pmatrix} \quad (6)$$

In Eq. 4,  $\rho^{(e)}(\mathbf{q})$  and  $\rho^{(e)}(\mathbf{q}')$  are the initial and final spin densities having momentum  $\mathbf{q}$  and  $\mathbf{q}'$ , respectively, and  $Q_\mu$  and  $\bar{Q}_\nu$  are the matrices for photon emission from an initial momentum state  $\mathbf{k}$  to a final momentum state  $\mathbf{k}'$  and its Hermitian conjugate for  $\nu$  photon emission described in Fig. 2. Here we do not take the internal conversion processes of  $e^+e^-$  pair creation and its annihilation into consideration in the calculation of  $Q_\mu$  and  $\bar{Q}_\nu$ . In the moving frame, the peak momentum of the final spin density lies in zero momentum.

In the case of  $s'=0$ , Eq. 4 can be written in a

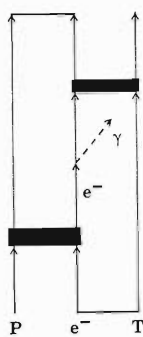


Fig. 2. Feynman diagrams for the relativistic radiative electron capture process. P, T, and  $e^-$  stand for a projectile ion, a target nucleus and an electron, respectively. A black bold block represents a Coulomb interaction.

form of

$$|t^{\text{REC}}|^2 = \frac{(2\pi)^2 \alpha}{v} \omega_M^{(0)} \sum_{i=0}^3 \xi_i s_j K_{ij}(\mathbf{p}, \mathbf{q}) \quad (7)$$

We consider only the case where the final state is not polarized and we set  $s'=0$ . Taking a peaking approximation, we have

$$\frac{d\sigma(\xi_3, s, 0)}{d\Omega_M} = \frac{(2\pi)^2 \alpha}{v} \omega_M^{(0)} \sum_{i=0}^3 \xi_i s_j K_{ij}(\mathbf{p}, \mathbf{q}=0) \quad (8)$$

If we consider circular polarization, we can set  $\epsilon_1 = \epsilon_2 = 0$  and obtain

$$\frac{d\sigma(\xi_3, s, 0)}{d\Omega_M} = \frac{(2\pi)^2 \alpha \omega_M^{(0)}}{v} (K_{00} + \xi_3 \sum_{i=0}^3 s_i K_{3i}) \quad (9)$$

If we define a circularly polarized photon correlation function  $P(\theta_L)$  as

$$\begin{aligned} & \frac{d\sigma(\xi_3, s, 0)}{d\Omega_M} \\ &= \frac{(2\pi)^2 \alpha \omega_M^{(0)}}{v} l(\theta_L) K_{00} (1 + \xi_3 P(\theta_L)) \end{aligned} \quad (10)$$

$P(\theta_L)$  can be written as

$$P(\theta_L) = \frac{\sum s_i K_{3i}}{K_{00}} \quad (11)$$

When we know the initial target spin state, we can set particular values for the parameter  $s_i$ . Calculation of the practical process is now in progress.

## References

- 1) K. Hino and T. Watanabe: *Phys. Rev. A*, **36**, 5362 (1987).
- 2) K. Hino and T. Watanabe: *Phys. Rev. A*, **39**, 3373 (1989).
- 3) L.D. Landau and E.M. Lifshitz: The Classical Theory of Fields, Course of Theoretical Physics, Vol. 2, 4th ed., Pergamon, London, p. 119 (1975); V.B. Beresteskii, E.M. Lifshitz, and L.P. Pitaevskii: Quantum Electrodynamics, Course of Theoretical Physics, Vol. 4, 2nd ed., Pergamon, London, p. 24 (1982).

### III-2-4. Dynamic Electron Correlation in Double Ionization by Charged Particle Impact and Photon Impact

T. Watanabe and L. Vegh\*

After the significant different measurement of the double ionization by anti-proton bombardment on atoms from that by protons,<sup>1,2)</sup> much attention has been attracted to the correlation effect on the occasion of dynamical process caused by charged particle impact, such as electron, positron, proton, anti-proton, and multi-charged ions, as well as photon impact.<sup>3,4)</sup> Firstly we will make a short discussion of this problem and give a short review under the concept of the first order perturbation (Born) theory. Then we are going to refer a new method for the double ionization. It has been recognized that the Born cross sections for excitation and for ionization do depend neither on the sign of projectile charge nor on its mass, if the projectile has the same impact velocity. It is expected to give the same total cross section for single ionization and excitation as well in the high (but non-relativistic) velocity range regardless of projectile particles. For atomic targets, single-ionization cross sections obtained by fast proton and anti-proton projectiles are found to be the same.<sup>1,2)</sup> Let us consider the process of inelastic collision by the impact of a charged particle with a charge  $Z_1 e$  and a velocity  $v$ . The cross section ( $\sigma_{\text{ex}}$  or  $\sigma_{\text{ion}}$ ) for excitation or ionization of the atomic target can be given by the Born approximation as

$$\begin{aligned} \sigma_{\text{ex, ion}} = & \frac{8 \pi Z_1^2 e^4}{v^2 \hbar^2} \int_{K_{\min}}^{K_{\max}} K^{-3} \\ & \times | \langle \psi_n | \sum_j \exp(i \vec{k} \cdot \vec{r}_j) | \psi_0 \rangle |^2 dK \quad (1) \end{aligned}$$

with  $K_{\max} = m(v + v_n)/\hbar$ ,  $K_{\min} = m(v - v_n)/\hbar$ , and  $v_n = \sqrt{2(E - E_n)/M_1}$  where  $m$  is the electron mass,  $M_1$  the mass of projectile ion,  $e$  the electronic charge, and  $\hbar K$  is the momentum difference before and after collisions.  $E$  is the total energy and  $E_n$  is the  $n$ -th eigenenergy. The integrand of Eq. 1 indicates that the differential cross section is also common for various charged projectiles if the integrand is written as a func-

tion of momentum change  $\hbar K$ . However, this point have not been investigated yet.

The ionization by charged particles at the high energy limit is well explained by the Born approximation, Eq. 1. Equation 1 shows the independent characters of the cross sections on the sign of projectile charge and the mass of projectile particles in the same impact velocity in the center-of-mass frame (c. m.) as mentioned above. A difference is found in the angular distribution of ejected electrons. The differential cross section with respect to the angle of an ejected electron is quite different between the sign as well as the mass of projectile particles. The difference appears as result of the interaction between an ejected electron and a projectile particle. It is expected reasonably from the interaction between them.

The cross section for double ionization can be written by the Born approximation, if we extend the method straight-forward by using an independent electron approximation, which is the method that each electron state follows the solution of the Hartree-Fock equation in each step of the electronic transition. Here, we ignore the interaction between electrons during transition. According to the independent electron model scheme, a double ionization process can be classified into two processes, one is single ionization followed by shake-off transition and the other is successive two-step single-ionization. The shake-off is a process of ionization due to the sudden change of an atomic field as a result of first ionization. The scattering amplitude of the second process is considered to be proportional to the square of a projectile charge, but is considered to decrease with the impact velocity at a higher rate than in the shake-off process.

If we take the ratio of the cross section of double ionization to that of single ionization, the ratio should be constant at the high velocity limit when the shake-off process is dominant. The collection of these data indicates that the ratio tends to be constant at the high velocity limit regardless of projectile particles.

Besides the high-velocity limit, the cross sec-

---

\* Institute of Nuclear Research of the Hungarian Academy of Sciences, Debrecen, P.O. Box 51, H-4001, Hungary.

tion ratio  $R_c$  is significantly different depending on the sign of the projectile charge. This is due to the electron-electron interactions in the target systems. If we consider the effective potential range of double ionization, the potential range in the case of positively charged particle impact is reduced because of the large sum potential over the interaction of a projectile particle and electrons, and the interactions between electrons are reduced compared with that of interactions between the projectile and electrons without interactions between electrons. On the contrary, for a negatively charged projectile, the interaction domain is expanded, if we consider the region corresponding to the potential summed over the interaction between the projectile and electrons as well as the interaction between electrons. This feature may explain that the difference in  $R_c$  is in the case of a negative or a positive charged projectile.

If we see the ratio of the cross section of double ionization to that of single ionization and the ratio is found to be independent of a transition mechanism, the ratio is expected to be the same value in photo-ionization. The ratio in photo-ionization,  $R_p$ , is not the same value, but the ratio is larger than that of particle ionization. This unexpected result can be explained by following discussion. In photo-ionization, the ratio  $R_p$  shows the direct correspondence with the shake-off factor and the agreement between experiment and calculation is satisfactory at the present time. For photo-ionization, the theory does well describe the phenomena. For charged particle ionization, however, there are some idealization procedure of the problem in order to make the matter possible to handle. One of the fact which needs idealization is as follows:

A target nucleus is regarded as a simple spectator.

A nucleus itself is in a free state in principle and it can absorb energy even in a small amount during collision.

A dominant difference between the photon case and the particle case is the magnitude of momentum of the initial perturber. The momentum of photon is so small that it can not move nucleus in any significant amount. On the other hand, the momentum of incident particles can give momentum to a nucleus. Considering that the momentum given by the projectile particle can be shared by ejected electrons and the nucleus, the directions of motion of the electron and the nucleus are considered to nearly parallel to each other. This effect may reduce the overlap integral in the second ionization scattering

amplitude by the shake-off process.

For the double ionization process, there have been several theoretical studies, which explain some properties. Characteristic features of the projectile sign dependence come from the difference in the effective interaction potential for this phenomena. The potential should include not only the interactions between a projectile and electrons in a target, but also that between electrons in the target. The summation over respective pairs make the domain of interaction smaller for a positive charge projectile and make it larger in a negative projectile. This is the main process of double ionization by charged particles.

Let us consider the case of a projectile P colliding with a He atom for simplicity. The S matrix for the double ionization can be given by

$$S = \exp \left( \int'_{-\infty} H(t') dt' \right) S_0 \quad (2)$$

where  $H(t)$  is the total Hamiltonian of the system. Usually  $H$  can be taken as the sum of an unperturbed Hamiltonian and a perturbation Hamiltonian. The unperturbed Hamiltonian is taken the Hamiltonian under the initial condition. The electron-electron interaction term  $1/r_{12}$  is involved in the unperturbed one. Here we make a different choice as

$$H_{00} = -\frac{\hbar}{2m} \nabla_1^2 - \frac{\hbar}{2m} \nabla_2^2 - \frac{2e^2}{r_1} - \frac{2e^2}{r_2} \quad (3)$$

$$H'_0 = +\frac{Z_1 e^2}{r_{p1}} + \frac{Z_2 e^2}{r_{p2}} - \frac{e^2}{r_{12}}$$

Noting that  $\psi'_{00}(r_{12}) = \exp(-\alpha r_1 - \alpha r_2)$  is the exact eigenfunction of  $H_{00}$  with  $\alpha=2$ . Because  $H_{00}$  is completely an independent particle Hamiltonian and  $H'_0$  includes the electronic correlation interaction term  $e^2 r_{12}^{-1}$ , we can see only the difference in the effect of dynamic correlation in  $H'_0$ ; the range of interaction  $H'_0$  differs greatly due to the sign of projectile charge, i.e., for negative projectile charge (e.g. anti-proton) the range of interaction  $H'_0$  expands because of the accumulation of same-sign Coulomb potentials and, on the other hands, for positively charged projectiles (e.g. protons) the range shrinks because of the cancellation between different sign Coulomb potentials. If we expand the total target states in terms of an atomic eigen function, S matrix can be given by

$$S = T \cdot \exp \left[ -i \int'_{-\infty} H'_0(t') dt' \right] \cdot \exp(-i \Delta H t) S_0 \quad (4)$$

where  $H = H_{00} - H_0$  and is now a diagonal matrix and  $T$  is the time ordering operator. Further

investigation is now in progress.

#### References

- 1) L.H. Anderson, P. Hvelplund, H. Knudsen, S.P. Møller, K. Elsener, K.-G. Rensfelt, and E. Uggerhøj: *Phys. Rev. Lett.*, **57**, 2147 (1986).
- 2) L.H. Anderson, P. Hvelplund, H. Knudsen, S.P. Møller, A.H. Sørensen, K. Elsener, K.-G. Rensfelt, and E. Uggerhøj: *Phys. Rev. A*, **36**, 3612 (1987).
- 3) J.H. McGuire: Lecture Note in Physics (eds. D. Berényi and G. Hock), Vol. 294, Springer-Verlag, Heidelberg, p. 432 (1988).
- 4) J.H. McGuire: *Nucl. Instrum. Methods A*, **262**, 48 (1987).

### III-2-5. Calculation of Stopping Powers for Energetic Heavy Ions in Solids and Plasmas

S. Karashima, K. Fujima, and T. Watanabe

The stopping powers for fast heavy ions in cold matter and in partially ionized plasmas were calculated over a wide range of temperature and density. A dielectric response function method was used in the calculation.

Detailed analyses of experiments and theories of the energy loss of fast heavy ions in solids and gaseous media have been made. For partially ionized media, the effects of finite temperature on the theories must be taken into account.<sup>1-6</sup> The theoretical treatments of stopping powers are usually based on the approximation that stopping electrons are divided into two parts: those bound to plasma ions and free plasma electrons. The stopping power in ionized media depends on the effective charge and incident energy of projectile ions and on the dielectric polarization of matter.

According to the Brueckner-Senbetu-Metzler (BSM) theory,<sup>5</sup> we formulate the stopping power based on a dielectric function method. Charged particles passing through an ionized medium induce an electric field by polarizing the medium. Consequently, the particles suffer a retarding force from the medium and lose energy. Thus we calculate the electron stopping powers using a polarization response calculation with a collisional dielectric function :

$$\epsilon(\mathbf{k}, \omega) = 1 - \frac{\omega_p^2}{\omega(\omega + i\nu_c) - (kv_e)^2} - \sum_i \frac{\omega_{pi}^2(i)}{i\omega(\omega + i\Gamma_i) - \omega_i^2} \quad (1)$$

where  $\mathbf{k}$  is the wave number vector and  $\omega$  is the frequency. The second term in Eq. 1 represents the contribution of plasma free electrons to the dielectric function. The effect of collisional damping appears through the collision frequency  $\nu_c$ , and  $v_e = (2T_e/m)^{1/2}$  is the electronic thermal velocity, where  $m$  is the electron mass. The third term expresses the contribution of bound electrons. The frequency  $\omega_{pi}(i)$  of the  $i$ -th shell electrons satisfies a relation  $\omega_{pi}^2 = 4\pi Ne^2 n_i / m$ , where  $N$  is the number density of atoms,  $n_i$  the dipole oscillator strength, and  $\Gamma_i$  a phenomenological damping force.

The expression for  $\omega(\mathbf{k}, \omega)$  is complicated

because of the discrete sum which requires information on an atomic shell structure, binding energies, and an electron density. Matter under the extreme conditions of density and temperature can be described by application of the Thomas-Fermi (TF) statistical model. The TF theory normally assumes an ion-sphere approximation; each nucleus is placed at the center of a sphere of a radius  $r_0 = (3/4\pi n_i)^{1/3}$ , where  $n_i$  is the total ion density. The electrostatic potential  $V(r)$  inside the sphere is calculated by solving the Poisson equation:

$$\nabla^2 V(r) = 4\pi e n(r) \quad (2)$$

where  $n(r)$  is the total electron number density including both bound and free electrons. The electron density  $n(r)$  is determined by the formula for a finite temperature :

$$n(r) = \frac{1}{2\pi^2} \left( \frac{2m}{\hbar^2} \right)^{3/2} (k_B T) \cdot I_{\frac{1}{2}} \left( \frac{-\mu + eV(T)}{k_B T} \right) \quad (3)$$

where the Fermi-Dirac distribution function is

$$f(r, p) = \frac{1}{1 + \exp \left( \frac{1}{k_B T} \left[ \frac{p^2}{2m} - eV(r) - \mu \right] \right)} \quad (4)$$

The Fermi integral  $I(x)$  is defined by

$$I_j(x) = \int_0^\infty \frac{y^j dy}{1 + \exp(x+y)} = \int_0^\infty p^j f(r, p) dp \quad (5)$$

The chemical potential  $\mu$  is determined by the requirement that the cell be neutral,  $\int n(r) d^3 r = Z$ :  $Z$  is the atomic number of matter. At zero temperature, Eq. 3 reduces to

$$n(r) = \frac{2}{3} \frac{1}{2\pi^2} \left( \frac{2m}{\hbar^2} \right)^{3/2} [\mu + eV(r)]^{3/2} \quad (6)$$

The potential  $V(r)$  is a self-consistent field, *i.e.*, it must simultaneously satisfy Eqs. 2 and 3. The dimensionless parameter  $x$  is defined by  $r = xbz^{-1/3}$ ,  $b = (3\pi/4)^{2/3} \hbar^2/2me^2$ . For the frequency  $\omega_i$ , we take  $\hbar\omega_i = I(x)$  with  $I(x)$  representing the average over the momentum distributions of the local ionization energy of a bound electron. In the TF approximation,  $I(x)$  is given by

$$I(x) = \hbar \omega_0 \left[ \frac{2}{5} \frac{\phi(x)}{x} - \frac{d\phi(x)}{dx} \Big|_{x=x_0} \right] \quad (7)$$

where  $\omega_0 = (4Z^2/3\pi)^{2/3} (2me^4/\hbar^2)/\hbar^2$ , and  $x_0$  denotes the atom boundary corresponding to  $r_0$ .

The plasma contribution to the dielectric function has the plasma frequency  $\omega_p$ :

$$\omega_p^2 = \frac{4\pi n_e e^2}{m} = \frac{4\pi N (Z - Z_b)}{m} \quad (8)$$

where  $Z_b$  is the average number of bound electrons in a target ion. From these results, Eq. 1 becomes

$$\begin{aligned} \epsilon(\mathbf{k}, \omega) = 1 &- \frac{4\pi Ne^2}{m} \left\{ \frac{(Z - Z_b)}{\omega(\omega + i\nu_c) - (kv_e)^2} \right. \\ &\left. - \int_0^{x_0} \frac{Zx^{1/2} \phi(x)^{3/2} dx}{\omega(\omega + i\Gamma_{x_0}) - [I(x_0)/\hbar]^2} \right\} \end{aligned} \quad (9)$$

For the ionization degree in medium, we use a Saha equation to determine the equilibrium charge states of a target material as a function of temperature and density. We determine the boundary condition for each ion state and calculate the number of electrons bound to the ion and free electrons.

On the assumption that a fast ion with a velocity  $v$  moves on a straight line in the  $x$  direction, the energy loss is given by

$$\begin{aligned} \frac{dE}{dx} = 2 \left( \frac{Z^* e}{2\pi} \right)^2 \int d\mathbf{k} \int_{-\infty}^{\infty} d\omega \delta(\omega - k_x v) \\ \cdot \frac{k}{k^2} \text{Im} \left[ \frac{1}{\epsilon(\mathbf{k}, \omega)} \right] \end{aligned} \quad (10)$$

where  $k^2 = k_x^2 + k_\perp^2$  and  $Z^*$  is the effective charge of the projectile ion.

The numerical calculation of Eq. 10 by using Eq. 9 is still complicated. If the projectile ion velocity  $v$  is large enough,  $v \gg v_e$ , then  $\omega = kv \gg kv_e$ . The dielectric function can be approximated by an expression independent of  $k$ , i.e.,  $\epsilon(\mathbf{k}, \omega) \simeq \epsilon(\omega)$ . In this approximation in Eq. 10, we obtain

$$\frac{dE}{dx} = \frac{(Z^* e)^2}{\pi v^2} \int_0^{\infty} \omega d\omega$$

$$\cdot \ln \left[ \frac{(q_m v)^2 + \omega^2}{\omega^2} \right] \left| \text{Im} \left[ \frac{1}{\epsilon(\omega)} \right] \right| \quad (11)$$

where the cutoff wave number  $q_m$  is necessary to prevent the logarithmic divergence when  $q^2 = k_y^2 + k_z^2 = \infty$ . Most of the contribution to the integral in Eq. 11 is from regions with  $\omega < q_m v$ . The choice of  $q_m$  depends on the Bloch parameter  $\eta = Z^* e^2 / \hbar v$ . This  $\eta$  means the ratio of the minimum impact parameter between the classical and the quantum theory.

The collision frequency  $\nu_c$  directly depends on the states for weakly and strongly coupled plasmas.<sup>7)</sup> A theoretical determination of  $\nu_c$  is a complex problem that calls for the detailed knowledge of interparticle correlations in a coupled plasma. The phenomenological damping force  $\Gamma_i$  in  $\epsilon(\mathbf{k}, \omega)$  is usually very small compared with the binding on resonant frequencies  $\omega_i$ . We here take  $\Gamma_i = 0.03\omega_i$  in the numerical calculation. The effective charge due to the semiempirical formula by Nikolaev-Dmitriev<sup>8)</sup> is used to compare with the results of the BSM theory.

Numerical calculation of the stopping power is in progress for different temperatures and densities in matter and for various kinds of projectile ions and targets.

## References

- 1) E. Nardi, E. Peleg, and Z. Zinamon: *Phys. Fluids*, **21**, 574 (1978).
- 2) T.A. Mehlhorn: *J. Appl. Phys.*, **52**, 6522 (1981).
- 3) J. Meyer-ter-Vehn and N. Metzler: *MPQ*, **48**, 1 (1981).
- 4) G. Maynard and C. Deutch: *Phys. Rev. A*, **126**, 665 (1982).
- 5) K.A. Brueckner, L. Senbetu, and N. Metzler: *Phys. Rev. B*, **25**, 4377 (1982).
- 6) T. Peter and R. Arnold, and J. Meyer-ter-Vehn: *Phys. Rev. Lett.*, **57**, 1859 (1986).
- 7) S. Ichimai: *Plasma Physics*, Benjamin, Tokyo, Chap. 2 (1986).
- 8) V.S. Nikolaev and I.S. Dmitriev: *Phys. Lett. A*, **128**, 277 (1988).

### III-2-6. The Form Factors of the Hydrogenlike Atoms Revisited

I. Shimamura

Bethe<sup>1)</sup> introduced the notion of the form factor and explained its basic significance in collision theory. It is defined as the matrix element of  $\sum_j \exp(i\mathbf{K} \cdot \mathbf{r}_j)$  between a pair of eigenstates;  $\mathbf{K}$  represents the momentum in units of  $\hbar$  transferred from an incident particle to the target system in a collision with the incident particle, and  $\mathbf{r}_j$  is the position vector of the  $j$ th particle in the target system. To be more specific, the matrix element squared determines the probability of the transition between the eigenstates upon momentum transfer  $\hbar\mathbf{K}$  within the first-order perturbation treatment, *i.e.*, the first-Born approximation. The form factors are relevant to interactions with any external agent so long as they are local, and therefore appear in many contexts including collisions with any charged particles or neutrons. Properties of the form factors and related quantities such as the generalized oscillator strengths have been a subject of continued study, both experimental and theoretical, as summarized elsewhere.<sup>2)</sup>

The theoretical study of the form factor naturally began with the atomic hydrogen, for which every eigenfunction is analytically known within the nonrelativistic point-nucleus approximation. In particular, the transition from the ground 1s state to a discrete excited state  $nlm$  is the most fundamental, where  $n$  is the principal quantum number,  $l$  the azimuthal quantum number, and  $m$  the magnetic quantum number. In fact the form factor vanishes if  $m \neq 0$ . For some applications and also for the full understanding of the results, it is appropriate to consider a more general case of the transition from the ground state  $\Psi_{000}(\mathbf{r}; z)$  of a hydrogenlike atom with an effective nuclear charge  $ze$  to a discrete state  $\Psi_{nl0}(\mathbf{r}; z')$  of a hydrogenlike atom with another effective nuclear charge  $z'e$ . Let  $\epsilon_{nl}(K; z, z')$  denote the corresponding form factor  $\langle \Psi_{nl0}(\mathbf{r}; z') | \exp(i\mathbf{K} \cdot \mathbf{r}) | \Psi_{000}(\mathbf{r}; z) \rangle$ .

To derive an analytic expression for  $\epsilon_{nl}(K; z, z')$  one follows Massey and Mohr<sup>3)</sup> using the generating functions of the Laguerre polynomial. However, the crucial page, *i.e.*, page 613, of their paper contains so many errors that it is difficult

to see their precise result.

Bethe's article<sup>4)</sup> in Handbuch der Physik quotes the Massey-Mohr work, and gives an expression for  $\epsilon_{nl}(K; 1, 1)$  as Eq. (52.12). However, the second factor  $2^{2(l+1)}$  of that equation should be  $2^{2l+3}$ .

Furthermore, Eq. (92) of the treatise of Mott and Massey<sup>5)</sup> is meant to be an expression for  $\epsilon_{nl}(K; 1, Z)$  in our notation, but is also incorrect. Equations (7a)-(7e) of Shimamura<sup>6)</sup> are intended to show the most general result for  $\epsilon_{nl}(K; z, z')$ . However,  $z$  and  $z'$  should be interchanged, and the definition of  $x$  has a misprint.

In this way there is confusion even for the simplest case of the transitions from the ground state to discrete states. We have shown some simple methods for proving without explicit calculations that the results in these standard articles are in error, and have derived the correct results. We have also derived an analytic asymptotic formula for  $\epsilon_{nl}(K; z, z')$  as  $K \rightarrow \infty$ .

The hydrogenic states may be defined also in terms of the parabolic coordinates, the parabolic quantum numbers being  $n_1$  and  $n_2$ ; the principal quantum number  $n$  and the magnetic quantum number  $m$  are the same as in those appearing in the treatment in terms of the spherical coordinates.

The form factor for a transition from the ground state to an excited state ( $n, n_1, n_2, m=0$ ) should also be studied for completeness. In principle it should be possible to derive an expression for the form factor  $\epsilon_{nn_1n_2}(K; z, z')$  for this transition by a unitary transformation of  $\epsilon_{nl}(K; z, z')$ . In practice, however, it is much easier to extend the method of Landau and Lifshitz<sup>7)</sup> who calculated  $\epsilon_{nn_1n_2}(K; 1, 1)$ . In this way we have derived an analytic expression for  $\epsilon_{nn_1n_2}(K; z, z')$ .

In many applications the sum of  $|\epsilon_{mn_1n_2}(K; z, z')|^2$  over  $n_1 - n_2$  at a fixed  $n$  is required. We have also calculated this sum analytically. Bethe<sup>4)</sup> and Landau and Lifshitz<sup>7)</sup> give a special case of this expression for  $z = z' = 1$ . This sum is equivalent to the sum of  $|\epsilon_{nl}(K; z, z')|^2$  over  $l$  at a fixed  $n$ . However, we have been unable to derive the same result from the expression for  $\epsilon_{nl}(K; z, z')$ .

Discussion of the form factor is incomplete without mention to those  $\epsilon_{E_l}(K; z, z')$  for the transition to continua  $E$ . Bethe<sup>1)</sup> gives a compact expression for the sum of  $|\epsilon_{E_l}(K; 1, 1)|^2$  over  $l$ . This expression is more general than the counterpart for the bound spectrum in the sense that the analytic continuation of the former should lead to the latter expression.

We are unaware of a convenient expression for individual  $\epsilon_{E_l}(K; z, z')$ . It is difficult to extend the method of Massey and Mohr<sup>3)</sup> to the continuum, and attempts with other methods of evaluation have been so far unsuccessful.

The foregoing exemplifies the surprisingly incomplete knowledge of the form factors for transitions from the ground state. The knowledge concerning transitions from an excited state, either discrete or continuum, is even less satisfactory.

Details of this work will be reported

elsewhere.<sup>8)</sup>

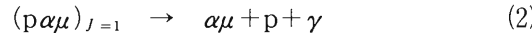
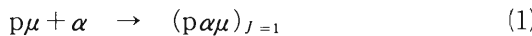
#### References

- 1) H. Bethe: *Ann. Phys.*, **5**, 325 (1930).
- 2) M. Inokuti: *Rev. Mod. Phys.*, **43**, 297 (1971); M. Inokuti, Y. Itikawa, and J.E. Turner: *Rev. Mod. Phys.*, **50**, 23 (1978).
- 3) H.S.W. Massey and C.B.O. Mohr: *Proc. R. Soc. London Ser. A*, **132**, 605 (1931).
- 4) H. Bethe: *Handbuch der Physik* (eds. H. Geiger and K. Scheel), Vol. 24/1, Springer, Berlin, p.273(1933).
- 5) N.F. Mott and H.S.W. Massey: *The Theory of Atomic Collisions*, 3rd ed., Oxford Univ. Press, Oxford (1965) (Japanese translation in four volumes: Translated by K. Takayanagi, Y. Itikawa, and I. Shimamura, Yoshioka Shoten, Kyoto (1975-77)).
- 6) I. Shimamura: *J. Phys. Soc. Jpn.*, **30**, 824 (1971).
- 7) L.D. Landau and E.M. Lifshitz: *Quantum Mechanics*, 3rd ed., Pergamon Press, Oxford, Sect. 148 (1977).
- 8) M. Inokuti, I. Shimamura, and Y. Itikawa: preprint (1988).

### III-2-7. Gamma-Ray Spectrum Due to the De-Excitation of a Muonic Molecule $p\alpha\mu$

S. Hara and T. Ishihara\*

The resonant state of a muonic molecule  $(p\alpha\mu)_{J=1}$  composed of a proton p (or its isotopes deuteron d and triton t), an  $\alpha$  particle  $\alpha$ , and a negative muon  $\mu$  with a total angular momentum  $J = 1$  is related to the muon transfer process



These processes are important since the mesic atoms  $p\mu$  and others contribute to the muon-catalyzed fusion reaction, whereas the final product  $\alpha\mu$  does not. Aristov, *et al.*<sup>1)</sup> and Kravtsov, *et al.*<sup>2)</sup> theoretically investigated the bound state energies of  $(p\alpha\mu)_{J=1}$  (and its isotopes) and the formation rate of  $(p\alpha\mu)_{J=1}$  in process 1. The resonant state  $(p\alpha\mu)_{J=1}$  decays by electric dipole transition into the ground repulsive  $\alpha\mu + p$  state by  $\gamma$ -ray emission (see Fig. 1). The lifetime of  $(p\alpha\mu)_{J=1}$  and the  $\gamma$ -ray spectrum for process 2 are studied by Kravtsov, *et al.*<sup>3)</sup> using the Born-Oppenheimer approximation to the initial resonant and final repulsive states. An experiment is now in progress to measure the  $\gamma$ -ray spectrum for process 2.<sup>4)</sup> Here, we reformulate process 2 and calculate the  $\gamma$ -ray spectra and the lifetime of  $(p\alpha\mu)_{J=1}$  and its isotopes by using an exact expression for the initial resonant state wavefunction.

The total wave function for  $(p\alpha\mu)_{J=1}$  and its isotopes can be written in the following form

$$\Psi^{JM} = \sum_m \Phi^{Jm}(\xi, \eta; R) \left( \frac{2J+1}{8\pi^2} \right)^{1/2} \cdot D_{Mm}^{J*}(\phi, \theta, \varphi) \quad (3)$$

Here  $M$  and  $m$  are the components of the total angular momentum  $J$  along a space fixed  $z$  axis and along an internuclear distance vector  $\mathbf{R}$ , respectively,  $D_{Mm}^{J*}$  the rotation matrix<sup>5)</sup> and  $R = |\mathbf{R}|$ . A set of variables  $\mathbf{r}(\xi, \eta, \varphi)$  represents spheroidal coordinates for the muon,  $\theta$  and  $\phi$  are polar and azimuthal angles for the vector  $\mathbf{R}$  in the space fixed coordinates. The position vector of the muon relative to the mid-point of p and  $\alpha$  is represented by  $\mathbf{r}$ .

We adopt Eq. 3 for the wave function of the initial resonant state and the Born-Oppenheimer approximation for the ground repulsive state. Thus the wave function for the final state, in which the momentum for the relative motion of p and  $\alpha$  is  $k$ , is given by

$$\Psi_{BO}^{JM} = \phi_{1\sigma}(\xi, \eta; R) \frac{X_J(kR)}{R} \left( \frac{2J+1}{8\pi^2} \right)^{1/2} \cdot D_{Mm}^{J*}(\phi, \theta, \varphi) \quad (4)$$

The ground state  $1\sigma$  orbital for  $p\alpha\mu$   $\Phi_{1\sigma}(\xi, \eta; R)$  is determined by the following equation

$$\left[ -\frac{1}{2m} \nabla_r^2 + \frac{2}{R} - \frac{2}{r_{\alpha\mu}} - \frac{1}{r_{p\mu}} - \epsilon_0(R) \right] \Phi_{1\sigma}(\xi, \eta; R) = 0 \quad (5)$$

where  $r_{\alpha\mu}$  and  $r_{p\mu}$  are the distances between  $\alpha$  and  $\mu$ , and p and  $\mu$ , respectively, and

$$1/m = 1/M_\alpha + 1/m_\mu \quad (6)$$

Here  $M_\alpha$  and  $m_\mu$  are the masses of  $\alpha$  and  $\mu$ , respectively. This choice of  $m$  gives the correct dissociation limit for  $p + \alpha\mu$  in the Born-Oppenheimer approximation. The following units are used throughout this paper

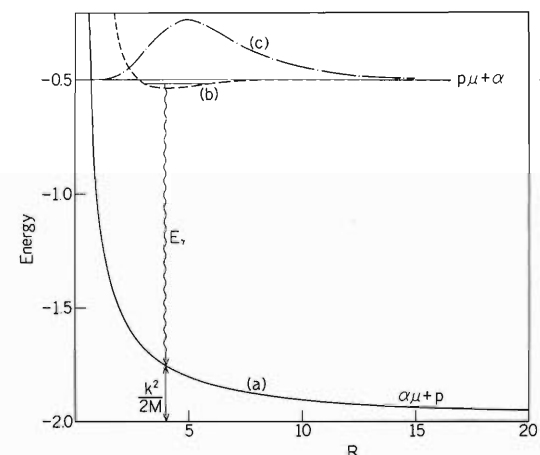


Fig. 1. Schematic diagram for the de-excitation of  $(p\alpha\mu)_{J=1}$  in the units given in Eq. 7. (a), Adiabatic potential energy curve  $\epsilon_0(R)$  for  $\alpha\mu + p$ ; (b), adiabatic potential energy curve for  $p\mu + \alpha$ ; and (c), probability density of the resonant state  $(p\alpha\mu)_{J=1}$ ,  $\int |\Psi^{JM}(\mathbf{r}, \mathbf{R})|^2 d\mathbf{r} 2\pi \sin\theta d\theta$ . The ordinate for curve (c) is arbitrary.

\* Institute of Applied Physics, University of Tsukuba.

$$e = \hbar = m = 1 \quad (7)$$

The radial function  $X_J(kR)$  satisfies the following equation

$$\left[ -\frac{1}{2M} \left\{ \frac{d^2}{dR^2} - \frac{J(J+1)}{R^2} \right\} + \epsilon_0(R) - \frac{1}{2M} k^2 \right] X_J(kR) = 0 \quad (8)$$

with the boundary conditions,

$$X_J(0) = 0 \quad (9)$$

$$X_J(kR) \rightarrow \sin \left[ kR - \frac{J\pi}{2} - \frac{M}{k} \ln(2kR) + \delta_J \right] \quad (10)$$

where  $\delta_J$  is the phase shift including the Coulomb phase. In Eq. 8,

$$1/M = 1/M_p + 1/M_\alpha \quad (11)$$

and  $M_p$  is the proton mass. The momentum  $k$  for the relative motion is determined by

$$E_{p\alpha\mu} - \epsilon_0(\infty) = E_\gamma + \frac{k^2}{2M} \quad (12)$$

where  $E_{p\alpha\mu}$  is the energy of the resonant state, and  $E_\gamma$ , the energy of an emitted photon.

The transition probability per unit time and unit energy, that is, the energy spectrum of  $\gamma$  ray is given by

$$\frac{d\lambda}{dE} = \frac{4}{3} (\alpha E_\gamma)^3 \left( \frac{2M}{\pi k} \right) \sum_{J_f} \sum_{M_f} \sum_{M_i} \frac{1}{(2J_f + 1)} \cdot | \langle \Psi_{BO}^{J,M_i} | \mathbf{d} | \Psi^{J,M_f} \rangle |^2 \quad (13)$$

where bracket denotes volume integral over  $\mathbf{R}$  and  $\mathbf{r}$ ,  $\alpha$  is the fine structure constant, and  $\mathbf{d}$  the dipole moment of  $p\alpha\mu$  with respect to the centre of mass of the system;

$$\mathbf{d} = - \left( 1 + \frac{2m_\mu}{M_{tot}} \right) \mathbf{r} - \frac{1}{M_{tot}} (-3M_p + M_\alpha - m_\mu) \mathbf{R} \quad (14)$$

where

$$M_{tot} = M_p + M_\alpha + m_\mu \quad (15)$$

In Eq. 13, three components of  $\mathbf{d}$  give the same contribution. The space fixed  $z$ -component of  $\mathbf{d}$  can be written in the form

$$d_z = \sum_\lambda D_{0\lambda}^1(\Phi, \theta, \varphi) g_\lambda(\xi, \eta; R) \quad (16)$$

where  $g_\lambda$  are the functions of  $\xi$ ,  $\eta$ , and  $R$ . Substitution of Eqs. 3, 4, and 16 into 13 gives

$$\frac{d\lambda}{dE} = \frac{8M}{3\pi k} (\alpha E_\gamma)^3 \sum_{J_f} \sum_{M_f} \sum_{M_i} | C(J_f J_f; m_f - m_i) A(J_f, m_i) |^2 \quad (17)$$

where

$$A(J_f, m_i) = \int R dR X_{J_f}(kR) (\phi_{1\sigma} | g_{-m_i} | \phi^{J,m_i}) \quad (18)$$

In Eq. 18, the last parenthesis denotes the volume integral over  $\mathbf{r}$  except for an angle  $\varphi$ .

We have calculated the resonant state energies of  $p\alpha\mu$  (and its isotopes)  $E_{p\alpha\mu}$  and the wave function  $\Psi^{J,M_i}$  with  $J_i = 1$ ,  $M_i = 0$  by a variational

Table 1. Energies and lifetimes of the resonant state  $(p\alpha\mu)_{J=1}$  and its isotopes. (a), present ; (b), Refs. 1 and 3 ; (c), Ref. 2.

	Energy (eV)	Lifetime (s)
$p\alpha\mu$		
(a)	-50.02	$5.20 \times 10^{-12}$
(b)	-41.6	$1.8 \times 10^{-12}$
(c)	-43.7	
$d\alpha\mu$		
(a)	-57.84	$5.90 \times 10^{-12}$
(b)	-55.9	$1.9 \times 10^{-12}$
(c)	-57.5	
$t\alpha\mu$		
(a)	-63.53	$6.03 \times 10^{-12}$
(b)	-62.9	$2.1 \times 10^{-12}$
(c)	-63.9	

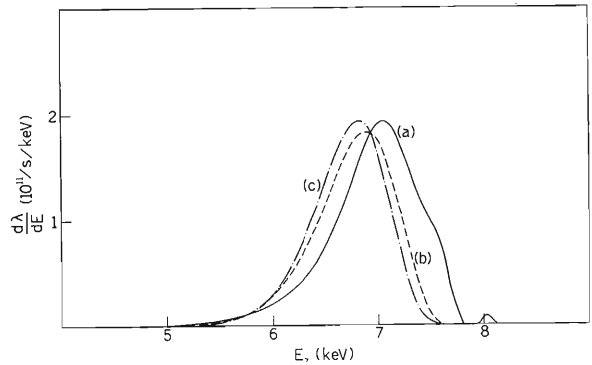


Fig. 2. Gamma-ray spectra due to de-excitation. (a),  $p\alpha\mu \rightarrow \alpha\mu + p$ ; (b),  $d\alpha\mu \rightarrow \alpha\mu + d$ ; and (c),  $t\alpha\mu \rightarrow \alpha\mu + t$ .

method<sup>6,7)</sup> using 300-term trial functions. In Table 1,  $E_{p\alpha\mu}$  are compared with those obtained by using the Born-Oppenheimer approximation.<sup>1,2)</sup> For the final state,  $\Phi_{1\sigma}(\xi, \eta; R)$  and  $\epsilon_0(R)$  were calculated by the method proposed by Bates and Carson.<sup>8)</sup> Equation 8 for  $J = 0$  and 2 were solved numerically to obtain a radial wave function  $X_J(kR)$ . We adopted the following mass constants:  $M_\alpha = 7,294.295 m_e$ ,  $M_p = 1,836.151 m_e$ , deuteron mass  $M_d = 3,670.481 m_e$ , triton mass  $M_t = 5,496.899 m_e$ , and  $m_\mu = 206.769 m_e$ , where  $m_e$  is the electron mass.

The  $\gamma$ -ray spectra are shown in Fig. 2.

The absolute value of intensities in the present calculation is about 3 times smaller than those in the previous one<sup>1)</sup> for all isotopes. The lifetime  $\tau$  of the resonant states

$$\tau = 1 / \int \left( \frac{d\lambda}{dE} \right) dE \quad (19)$$

is also given in Table 1. The values are about 3 times larger than those of previous calculation.<sup>3)</sup>

In our  $p\alpha\mu$  spectrum, there is a small second peak at  $E_\gamma \approx 8$  keV, with a peak height of about 1/22 of the main peak and with a half width of about 0.1 keV.

### References

- 1) Yu A. Aristov, A.V. Kravtsov, N.P. Popov, G.E. Solyakin, N.F. Truskova, and M.P. Faifman: *Sov. J. Nucl. Phys.*, **33**, 564 (1981).
- 2) A.V. Kravtsov, A.I. Mikhailov, and N.P. Popov : *J. Phys. B: At. Mol. Phys.*, **19**, 2579 (1986).
- 3) A.V. Kravtsov, N.P. Popov, G.E. Solyakin, Yu A. Aristov, M.P. Faifman, and N.F. Truskova: *Phys. Lett. A*, **83**, 379 (1981).
- 4) K. Nagamine: private communication; T. Matsuzaki, K. Ishida, K. Nagamine, Y. Hirata, and R. Kadono: *Muon Catalyzed Fusion* **2**, 217 (1988).
- 5) M.E. Rose: Elementary Theory of Angular Momentum, John Wiley & Sons Inc., New York (1957).
- 6) S. Hara, T. Ishihara, and N. Toshima: *J. Phys. Soc. Jpn.*, **55**, 3293 (1986).
- 7) S. Hara, T. Ishihara, and N. Toshima: *Muon Catalyzed Fusion*, **1**, 277 (1987).
- 8) D.R. Bates and T.R. Carson: *Proc. R. Soc. A*, **234**, 207 (1956).

### III-2-8. State Densities and Ionization Equilibrium of Atoms in Dense Plasmas

I. Shimamura and T. Fujimoto\*

Recent developments in experimental studies of dense plasmas have stimulated theoretical efforts to understand spectroscopic properties of atoms and ions in dense plasmas. These efforts include calculations of the energy levels and Stark broadening of bound states in many different models. They range from one-electron central-potential treatment with or without non-spherical perturbation by other particles in the plasma, to many-particle treatment in which electron-electron and electron-ion interactions are explicitly taken into account. Detailed calculations including many kinds of effects, however, are limited to low-lying bound states.

As in the study of ionization equilibrium, one often finds it necessary to know the state density of atoms in a plasma over the whole spectrum from the ground and excited bound states to the entire continuum. This presents a difficult theoretical problem, partly because one has to deal with an infinity of states, and partly because any reasonable model for this problem and associated calculations should be consistent over the whole spectrum.

In the conventional theory of ionization equilibrium in low-density plasmas, Saha's equation is used in which any interactions between particles in the plasma are completely neglected when dealing with electrons in continuum states (with an energy  $E > 0$ ).<sup>19</sup> In other words these electrons are regarded as free electrons that comprise an ideal gas. For the hydrogen plasma this leads to a density of state

$$g_F(E/R) = (E/R)^{1/2} / (2\pi^2 n_e a_0^3) \quad (E > 0) \quad (1)$$

with the Bohr radius  $a_0$ , the Rydberg unit  $R$  ( $= 13.6$  eV), and the number density  $n_e$  of electrons.

On the other hand an electron in a bound state (with  $E < 0$ ) is bound by the Coulomb interaction with a proton. Thus the state density is that of the hydrogen atom, *i.e.*,

$$g_H(E/R) = |E/R|^{-5/2} \quad (E < 0) \quad (2)$$

This state density diverges as  $E$  approaches

zero from below, whereas  $g_F(E/R)$  tends to zero as  $E$  approaches zero from above. This unphysical discontinuity is due to the inconsistency in the treatment in the positive-energy and negative-energy regions.

To derive Saha's equation for low-density high-temperature plasmas in thermal equilibrium, we take into account only low-lying levels in the calculation of the partition function. Thus the singularity in the state density is avoided in this approximation. For high-density plasmas, however, Saha's equation is well known to lead to unreasonable results; more elaborate treatment of the state density across the ionization limit is necessary. In fact the ionization limit for atoms in dense plasmas shifts to the low-energy side, which is known as continuum lowering. It has been theoretically studied in detail especially for a partially ionized hydrogen plasma.

We present here a simple model for the density of states of hydrogen plasmas that is continuous across the ionization limit and that is consistent over the entire energy spectrum; the resultant state density approaches  $g_F(E/R)$  at high  $E$  and coincides with  $g_H(E/R)$  for low-lying bound states. Ionization equilibrium of dense plasmas is also discussed on the basis of this state density.

Consider a hydrogen plasma for which the ion coupling parameter  $\Gamma$ , *i.e.*, the ratio of a representative Coulomb energy  $e^2/r_i$  to the kinetic energy  $k_B T$ , is larger than unity, where  $e$  is the charge of an electron,  $k_B$  is the Boltzmann constant,  $T$  is the electron temperature, and  $r_i = (4\pi n_e/3)^{-1/3}$ . A simple model appropriate for this case is the ion-sphere model that introduces a sphere with a radius  $r_i$  around a proton. The sphere, called an ion sphere, has a volume  $1/n_e$ , and the probability of finding another proton in this sphere should be almost negligible for  $\Gamma > 1$ .

We assume that the density of electronic levels of the hydrogen plasma is approximated by the state density of the hydrogen atom confined in an ion sphere, *i.e.*, the density of levels held by the electron-proton interaction potential  $-e^2/r$  surrounded by an infinitely high potential wall at  $r = r_i$ . This model is probably too crude for the

---

\* Department of Engineering Science, Kyoto University.

calculation of each energy level, and hence, for the calculation of the level shift from a pure hydrogenic energy due to interactions with other particles in the plasma. The interest here, however, is not in the level shift but in the global structure of the level density. The present model should be reasonable for this purpose, though not highly accurate.

We apply the Bohr-Sommerfeld quantization condition, which is known to reproduce exactly both the density  $g_H(E/R)$  of the purely quantal levels of the hydrogen atom and the density  $g_F(E/R)$  of the plane-wave states in a vanishing potential in a finite sphere. We define a dimensionless quantity  $X = (E/R)(r_i/a_0)$ . The density  $g(E/R)$  of states is calculated as

$$\begin{aligned} g(E/R) &= g_H(E/R) G(\alpha) \\ &= (r_i/a_0)^{5/2} |X|^{-5/2} G(\alpha) \end{aligned} \quad (3)$$

with

$$\alpha = X(X+2) \quad (4)$$

where

$$\begin{aligned} G(\alpha) &= \pi^{-1} \left[ \frac{2}{3} \alpha^{3/2} - \sqrt{\alpha(\alpha+1)} \right. \\ &\quad \left. + \ln(\sqrt{2} + \sqrt{\alpha+1}) \right] \\ &\text{for } 0 < X \end{aligned} \quad (5)$$

$$\begin{aligned} G(\alpha) &= \pi^{-1} \left[ -\frac{2}{3}(-\alpha)^{3/2} - \sqrt{-\alpha(\alpha+1)} \right. \\ &\quad \left. + \sin^{-1}\sqrt{-\alpha} \right] \\ &\text{for } -1 \leq X < 0 \end{aligned} \quad (6)$$

$$\begin{aligned} G(\alpha) &= G_{\text{cont}}(\alpha) + G_{\text{bnd}}(\alpha) \\ &\text{for } -2 \leq X < -1 \end{aligned} \quad (7)$$

with

$$\begin{aligned} G_{\text{cont}}(\alpha) &= \pi^{-1} \left[ -\frac{2}{3}(-\alpha)^{3/2} + \sqrt{-\alpha(\alpha+1)} \right. \\ &\quad \left. - \sin^{-1}\sqrt{-\alpha} - \alpha\pi \right] \end{aligned} \quad (8)$$

and

$$G_{\text{bnd}}(\alpha) = \alpha + 1 \quad (9)$$

and

$$G(\alpha) = 1 \quad \text{for } X < -2 \quad (10)$$

The function  $|X|^{-5/2}G(\alpha)$  is plotted in Fig. 1.

The asymptotic form  $(2/3\pi)X^3$  of Eq. 5 for large  $X$  is consistent with Eq. 1 for the free states. This is natural, since a weaker effect of the Coulomb potential is expected for a larger kinetic energy.

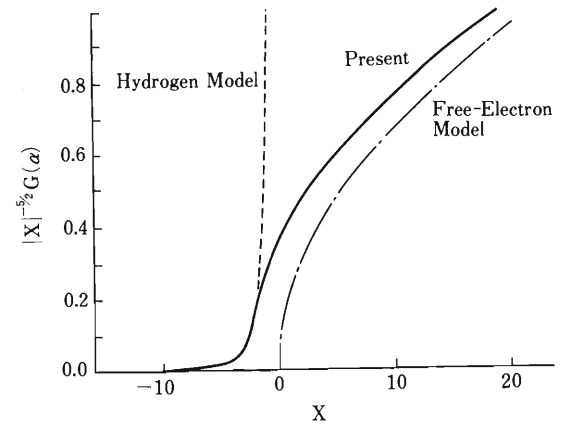


Fig. 1. Reduced density  $|X|^{-5/2}G(\alpha)$  ( $= (r_i/a_0)^{-5/2} \cdot g(E/R)$ ) of electronic states as a function of  $X$  ( $= (E/R)(r_i/a_0)$ ). Also shown are the reduced density of the bound states of the hydrogen atom and that of the free states described by plane waves.

It follows that the above state density is continuous and smooth across  $X = 0$ ,  $-1$ , and  $-2$ , and over the entire spectrum. Also, one finds that the state density is a monotonically increasing function of the energy. The continuum portion of the state density rises linearly from zero at  $X = -2$ .

To study ionization equilibrium we assume that the electrons in the plasma occupy the eigenstates according to the Boltzmann distribution. The integral of this distribution over the continuum gives the number density  $n_i$  of hydrogen ions. The integral, or more accurately, the sum over the bound-state spectrum gives the number density  $n_0$  of neutral hydrogen atoms.

The correction factor on Saha's equation calculated in this way depends both on  $n_e$  and on  $T$ , but only through  $\Gamma$ .

In conclusion, we note that the simple model presented in this paper results in reasonable density of states and ionization equilibrium. Because of its simplicity and of the useful scaling relations, the model should be useful for many future applications.

#### Reference

- 1) W. Ebeling, W.D. Kraeft, and D. Kremp: Theory of Bound States and Ionization Equilibrium in Plasmas and Solids, Akademie-Verlag, Berlin (1976).

### III-2-9. Charge-State Distribution Measurements of 26-MeV/u Ar Ions

Y. Kanai, T. Kambara, T. Mizogawa, A. Hitachi,  
K. Shima, and Y. Awaya

We have estimated mean charges of low-energy (<10 MeV/u) projectile ions in the equilibrium charge-state distribution after passing through a target material by using a semi-empirical formula, where we neglected a shell effect.<sup>1)</sup> For projectile ions with energies of higher than 10 MeV/u, their mean charges are

not easy to estimate. When we do some experiments using RIKEN Ring Cyclotron, such information will be needed. As a first step in the data compilation of equilibrium charge-state distributions of ions in the energy range of RIKEN Ring Cyclotron, we carried out the measurement with 26-MeV/u Ar ions.

Table 1. Charge-state distributions of Ar ions after passing through targets. The incident charge state and energy are 13<sup>+</sup> and 26 MeV/u, respectively. Numbers in parentheses stand for the power of ten. Statistical error is within  $\pm 5\%$  of each value.

Target	Mean charge	Charge state fraction						
		12 <sup>+</sup>	13 <sup>+</sup>	14 <sup>+</sup>	15 <sup>+</sup>	16 <sup>+</sup>	17 <sup>+</sup>	18 <sup>+</sup>
C (10 $\mu\text{g}/\text{cm}^2$ )	13.91	5.4(-5)	3.32(-1)	3.98(-1)	2.02(-1)	6.29(-2)	4.7 (-3)	1.4 (-3)
C (20 $\mu\text{g}/\text{cm}^2$ )	14.62	2.6(-5)	1.19(-1)	3.50(-1)	3.46(-1)	1.64(-1)	1.92(-2)	1.2 (-3)
C (40 $\mu\text{g}/\text{cm}^2$ )	15.33	—	2.11(-2)	1.62(-1)	3.80(-1)	3.49(-1)	8.10(-2)	6.4 (-3)
C (80 $\mu\text{g}/\text{cm}^2$ )	16.83	—	1.44(-4)	4.45(-2)	4.97(-2)	1.78(-1)	6.40(-1)	1.27(-1)
C (173 $\mu\text{g}/\text{cm}^2$ )	17.11	—	—	8.7 (-5)	6.43(-3)	1.34(-1)	5.96(-1)	2.63(-1)
C (600 $\mu\text{g}/\text{cm}^2$ )	17.91	—	—	4 (-7)	4.2 (-6)	1.86(-3)	8.19(-2)	9.16(-1)
C (4.27 mg/cm <sup>2</sup> )	17.98	—	—	—	—	1.24(-4)	2.00(-2)	9.80(-1)
Be (25 $\mu\text{m}$ )	17.97	—	—	—	1.1 (-5)	1.08(-3)	2.90(-2)	9.70(-1)
Be (50 $\mu\text{m}$ )	17.97	—	—	—	1.0 (-5)	9.98(-3)	2.95(-2)	9.65(-1)

Ar<sup>13+</sup> ions of 26-MeV/u were momentum analyzed and passed through target foils (carbon 10  $\mu\text{g}/\text{cm}^2$  - 4.2 mg/cm<sup>2</sup> and beryllium 25 and 50  $\mu\text{m}$  in thickness). The charge-state distributions of Ar ions after passing through the target were measured by a combination of a charge-analyzing magnet and a position-sensitive parallel-plate avalanche counter (PPAC) located just behind the magnet.<sup>2)</sup> Results are summarized in Table 1.

Analysis is now in progress. Using this data, we intend to improve the semi-empirical formula and extend the applicability to projectile ions up to 26-MeV/u.

#### References

- 1) K. Shima, T. Mikumo, and H. Tawara: *At. Data Nucl. Data Tables*, **34**, 147 (1986).
- 2) Y. Awaya, Y. Kanai, T. Kambara, and T. Chiba: This Report, p. 149.

### III-2-10. Multiple Inner-Shell Ionization of Target Atoms by 0.8-26 MeV/u Heavy-Ion Impact

Y. Awaya, T. Kambara, Y. Kanai, T. Mizogawa,  
A. Hitachi, and B. Sulik

Systematics of simultaneous single K and multiple L shell and single L and multiple M shell ionization of target atoms was studied previously by using 4.7-8.2-MeV/u heavy ions accelerated by the cyclotron.<sup>1,2)</sup> K-satellite and hypersatellite X-rays or L-satellite X rays from various target elements were measured by using a step-scanning crystal spectrometer. Projectiles were He, C, N, and O ions. We obtained not only the L-shell ionization probability accompanied by simultaneous K-shell ionization,  $P_L$ , but also the M-shell one accompanied by simultaneous L-shell ionization,  $P_M$ . We also studied the ratio of the double K-shell ionization cross section to the single ionization cross section from the intensity ratio of the  $K\alpha$  hypersatellites to the  $K\alpha$  satellites.

After RIKEN Ring Cyclotron (RRC) started to work, we expanded the previous work to a higher incident energy range. At the same time, we made other measurements at lower energies by using the linear accelerator (RILAC). We used 26-MeV/u N ions from RRC and 0.84-, 1.1-, 1.3-, and 1.6-MeV/u N ions from RILAC as projectiles. Targets were 1-2- $\mu\text{m}$  Ti, Ni, and Cu foils and a piece of Fe wire of 25  $\mu\text{m}$  in diameter for the measurements at RRC and a 2- $\mu\text{m}$  Ti foil for those at RILAC. The K X rays from the targets were measured by using a broad range crystal spectrometer<sup>3)</sup> with a flat crystal and a position-sensitive proportional counter. A crystal of LiF (2 0 0) was used for the measurement of Ti and Fe K X rays and that of LiF (2 2 0) for Ni and Cu K X rays.

A spectrum of the  $Ti K_\alpha$  satellites and hypersatellites and a part of the  $K_\beta$  satellites obtained by 26-MeV/u N-ion impact on the Ti target is shown in Fig. 1, where  $KL^n$  denotes the initial state vacancy configuration. For the 26-MeV/u N-ion impact, a high-level background caused by  $\gamma$  rays induced by nuclear reactions is expected, but the broad-range X-ray crystal spectrometer was found to work sufficiently at this high incident energy.

The experimental values of  $P_L$  obtained from

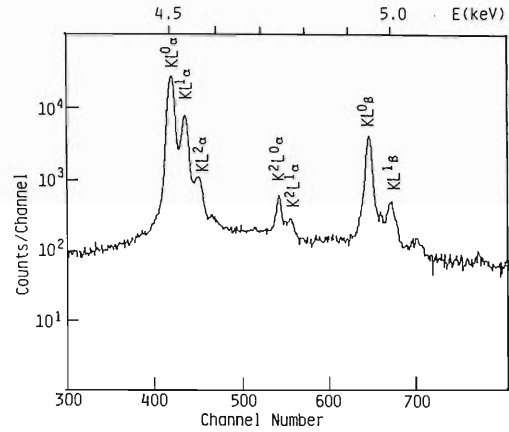


Fig. 1. Spectrum of Ti K X-rays obtained by 26-MeV/u N-ion impact.

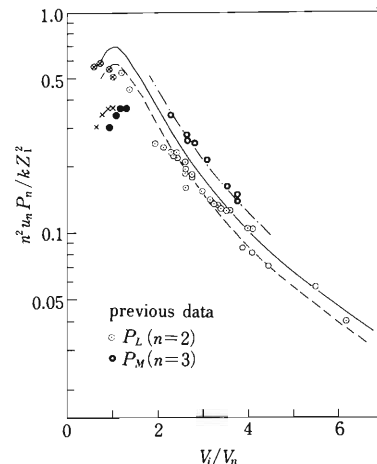


Fig. 2.  $P_L$  values obtained by the present work:  
○, obtained by 26-MeV/u N-ion impact; ●, by 0.84-1.6-MeV/u N-ion impact and  $V_i$  corresponds to incident energy; × and ⊗, explained in the text. Previously obtained  $P_L$  and  $P_M$  values are also shown. Solid curve is the universal BEA one for  $k = \sigma_0 / (2\pi a^2 Ry)$ . Dashed and chain curves are normalized ones.

$K\alpha$  satellites are shown in Fig. 2, where the open circles show those obtained at RRC and closed circles at RILAC together with the previous data.<sup>1,2)</sup> The solid line is the BEA universal curve.<sup>4)</sup> Scaled parameters of  $n^2 u_n P_n / k Z_i^2$  and

$V_1/V_n$  were adopted to fit the theoretical curve to the experimental values of both  $P_L$  and  $P_M$ , where  $n$  is the principal quantum number,  $u_n$  the binding energy of  $n$ -shell electrons ( $n=2$  for L shell and  $n=3$  for M shell),  $u_n$  the binding energy of an  $n$ -orbital electron,  $Z_1$  the nuclear charge of projectile heavy ions,  $V_i$  the velocity of the projectiles and  $V_n$  that of  $n$ -orbital electrons. The constant  $k$  is represented as  $\sigma_0/(2\pi a_0^2 Ry)$ , where  $\sigma_0 = \pi e^4$ ,  $a_0$  is Bohr radius and  $Ry = 13.6$  eV. The energies of the projectiles are taken as the incident ones to estimate  $V_i$  and the value of  $Z_1$  is taken as 7 but we should make some comments on these parameters.

The energy loss of the 26-MeV/u N ions in a target foil is smaller than 0.4 percent of the incident energy and the mean charge of ions in charge equilibrium is almost equal to 7.0+. This means no correction is required for  $V_i$  in the reduced parameter.

On the other hand, the Ti target (2  $\mu$ m) is not thin enough for 0.8-1.5-MeV/u N ions; for example, total energy loss of N ions in the target is about 4 MeV for 1.5-MeV/u (total energy: 21 MeV) incident energy. It may be reasonable to take the incident energy of the projectile to estimate  $V_i$ . The K-shell ionization cross section decreases drastically with decreasing energy of projectile ions in this collision system, whereas the change of L-shell ionization cross section is not so much because the velocity of Ti L electron and that of the projectile is comparable in this collision energy. Since we observed the  $KL^n$  X rays, the production cross section of these X rays depends on mainly by the K-ionization cross section. For the reference, the points are plotted by crosses for the values which correspond to the projectile energy after passing through the half thickness of the target.

Another factor to be considered for low energy impact is the value of  $Z_1$  in the scaled parameter. When we take the mean charge of N ions in charge equilibrium at the energy at the half thickness of the target foil, the corrected experimental data move to the position shown by crosses surrounded by circles. This is the most extreme case and it is difficult to discuss effective  $Z_1$  values for the multiple ionization process.

In the previous study, we found that the universal curve multiplied by a factor of 0.84 fits better to the experimental values of  $P_L$  and that by 1.25 does to the values of  $P_M$ . When we add the  $P_L$

values obtained in the present study at RRC, this becomes more plausible. The broken curve in Fig. 2 is the universal curve multiplied by 0.84 and the chain curve is that by 1.25. This means that the estimated value of the cutoff radius in the calculation is about 10 % smaller for L shell and that for M shell is about 10% larger.

As is seen in Fig. 2, the experimental data obtained by RILAC corrected for the energy loss of the projectiles and charge are fitted well by the universal curve. In order to check the validity of this correction, we are planning re-measurements by using a very thin target where the effect of the energy loss of projectiles is negligible; this will at least make clear the ambiguity of  $V_i$ .

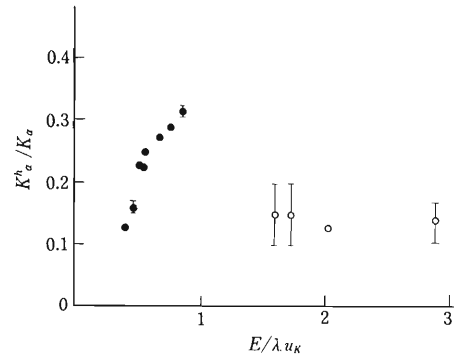


Fig. 3. Intensity ratio of  $K_\alpha$  hypersatellites to hyper-satellites vs.  $E/\lambda u_K$ . ○, present data; ●, previous ones.<sup>1)</sup>

The preliminary results of the intensity ratio of the  $K_\alpha$  hypersatellites to the satellites,  $K^h_\alpha/K_\alpha$  for 26-MeV/u N-ion impact are shown in Fig. 3, with the previous data of N-ion impact.  $E$  is the total incident energy and  $\lambda$  is the projectile mass in electron mass units. It seems that the values of  $K^h_\alpha/K_\alpha$  take a constant value at high energy bombardment, though the data has large uncertainties arising from the estimation of the background. The analysis is in progress.

## References

- 1) Y. Awaya: Electronic and Atomic Collisions, Proc. XI ICPEAC (eds. N. Oda and T. Takayanagi) North Holland Pub. Co., Amsterdam, p. 325 (1979).
- 2) Y. Awaya et al.: *IPCR Cyclotron Prog. Rep.*, **13**, 76 (1979).
- 3) A. Hitachi, H. Kumagai, and Y. Awaya: *Nucl. Instrum. Methods*, **195**, 631 (1982).
- 4) J. H. McGuire and P. Richard: *Phys. Rev. A*, **8**, 1374 (1973).

### III-2-11. Resonant Transfer and Excitation (RTE) in $\text{Ge}^{31+}$ on $\text{H}_2$ Collisions

S. Reusch,\* P. H. Mokler,\* T. Kambara, R. Schuch,\*\* G. Wintermeyer,\*\*\*  
 A. Müller,\*\*\*\* Z. Stachura,\*\*\*\*\* and A. Warczak\*\*\*\*\*

The resonant transfer and excitation (RTE) process is important among the electron transfer processes in collisions between high-velocity highly-charged ions and light atoms. RTE is a collision process in which an electron excitation in the projectile ion and a transfer of a target electron to the projectile occurs simultaneously through an electron-electron interaction. Since the excitation and the transfer are correlated, the energy required for the excitation should match the energy gained by the transfer. Therefore RTE is a resonant process which occurs only at specific collision energies. When a free electron instead of a bound electron in a target atom or molecule is transferred to the projectile, this resonant process is called dielectronic recombination (DR) which is the inverse process of an Auger electron emission. The resonances of RTE and DR are named in accordance with the corresponding Auger processes.

We have investigated the  $\text{KL}n$ -RTE process ( $n = \text{L}, \text{M}, \dots$ ) in collisions between highly charged Ge ions and a  $\text{H}_2$  target at the UNILAC facility of GSI (Gesellschaft für Schwerionenforschung ; Heavy Ion Research Institute) in Darmstadt. An experiment with incident Li-like  $\text{Ge}^{29+}$  ions was reported previously.<sup>1)</sup> In that experiment, the projectile ions were charge-analyzed after the target and those which captured one electron were counted in coincidence with the characteristic X rays of the projectile. The projectile energy was changed between 12 and 18.5 MeV/u to get an excitation function.

When the projectile is a H-like ion, it gets a doubly-excited He-like ion after a  $\text{KL}n$ -RTE

process and it can decay with two K-X-ray photon emissions as shown in Fig. 1. RTE can be observed by coincidence measurements between two K-X-ray photons besides the coincidence measurements between X ray and charge exchange like previous report.<sup>1)</sup> We can get informations about the electronic state of the projectile ions after the RTE process by measuring the energies of the two X-ray photons.

Here we report the measurements of the  $\text{KL}n$  ( $n = \text{L}, \text{M}, \dots$ ) resonances of the RTE process in collision between H-like  $\text{Ge}^{31+}$  ions and a  $\text{H}_2$  target by a two-photon coincidence method.

The experimental set-up is shown in Fig. 2. A  $\text{Ge}^{31+}$ -beam from the UNILAC was collimated and was led to a differentially-pumped gas target at a pressure of about 0.7 mbar. Two Si(Li) detectors placed at 90° to the beam direction and

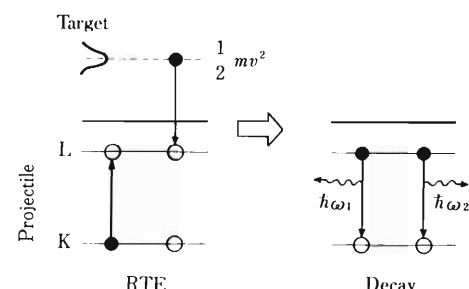


Fig. 1. KLL-RTE process and two-photon decay of the doubly-excited state after RTE in case of a H-like (one-electron) projectile ion shown in the projectile frame.

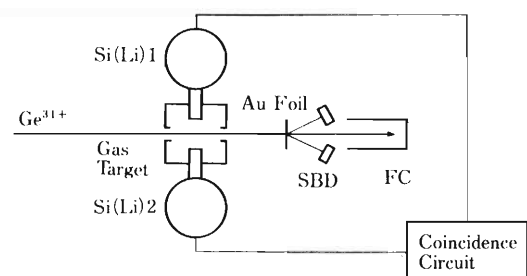


Fig. 2. Experimental set-up.

\* GSI, D-6100 Darmstadt, F. R. Germany.

\*\* AFI Research Institute of Physics, S-10405 Stockholm, Sweden.

\*\*\* Physikalisch Institut, Universität Heidelberg, D-6900 Heidelberg, F. R. Germany.

\*\*\*\* Strahlzentrum, Universität Gießen, D-6300 Gießen, F. R. Germany.

\*\*\*\*\* Institute of Nuclear Physics, 31-342 Kraków, Poland.

\*\*\*\*\* Institute of Physics, Jagiellonski University, 30-059 Kraków, Poland.

opposite each other detected the X rays from the target region. Beam currents were monitored with a Faraday cup. An Au-foil was set before the Faraday cup and scattered Ge-ions were counted with four surface-barrier detectors at a scattering angle of 7.8°. The number of the scattered ions were used for the normalization of the number of incident ions. Events of two-photon detection with the two Si(Li) detectors were accumulated with a coincidence circuit and recorded on magnetic tapes on a PDP 11/45 computer.

Figure 3 shows the correlation between energies of two X rays measured by the two Si(Li) detectors at projectile energies of 13 and 16.5 MeV/u. At both projectile energies, there appears a group of events around  $E_1 = E_2 = 10.5$  keV which corresponds to two  $K_{\alpha}$ -X-ray emissions from doubly-excited  $\text{Ge}^{30+}$  ions. At 16.5 MeV/u, there are two other groups of events around ( $E_1 = 10.5$  keV,  $E_2 = 12$  keV) and ( $E_1 = 12$  keV,  $E_2 = 10.5$  keV) which correspond to one  $K_{\alpha}$  and one  $K_{\beta\gamma}$ -emissions. These events result from radiative decays of  $2lnl'$  states with  $n > 2$  of  $\text{Ge}^{30+}$  ions. Events along a line  $E_1 + E_2 = 10$  keV correspond to the two-photon 2E1 decay of  $1s2s\ ^1S_0$  singly-excited metastable state of  $\text{Ge}^{30+}$  ions.

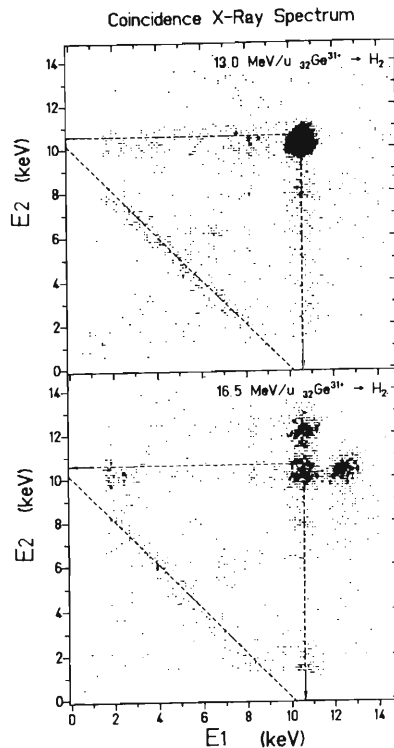


Fig. 3. X-ray energy correlation diagrams at projectile energies of 13 (upper) and 16.5 MeV/u (lower).  $E_1$  and  $E_2$  show the energies of X rays measured by each of the Si(Li) detectors in coincidence.

This state can be produced by the E1 decay of a doubly-excited state like  $2s2p\ ^1P_1$  state. The events along lines of  $E_1 = 10$  keV and  $E_2 = 10$  keV correspond to the detection of a K X-ray from a doubly-excited state to the  $1s2s\ ^1S_0$  state and one of the two photons from the 2E1 transition of the  $1s2s\ ^1S_0$  state.

Figure 4 shows the cross section of two K-X-ray-emission as a function of the projectile energy between 12.1 and 18.8 MeV/u. Dots show the experimental results. Circles are for the total K-X-ray-K-X-ray coincidences and triangles are for  $K_{\alpha}\text{-}K_{\beta\gamma}$  coincidences which are from  $2lnl'$  ( $n > 2$ ) states. Curves show theoretical predictions calculated by folding DR cross sections with the Compton profile of a molecular hydrogen and corrected for the radiative transition probability: Dashed curve shows the total coincidence cross section and dotted curve shows the component of the  $K_{\alpha}\text{-}K_{\beta\gamma}$  coincidence cross section. Arrows show the energies of the DR resonances calculated by a multi-configuration code.<sup>2)</sup>

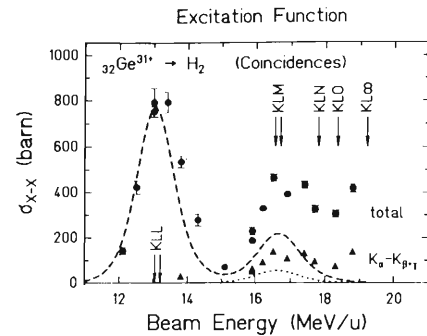


Fig. 4. Cross section of simultaneous double K-X-ray emissions for  $\text{Ge}^{31+}$  on  $\text{H}_2$  collision at projectile energies between 12.1 and 18.8 MeV/u. Dots show the experimental data, curves show theoretical predictions, and arrows show theoretical energies of  $KLn$ -DR resonances.

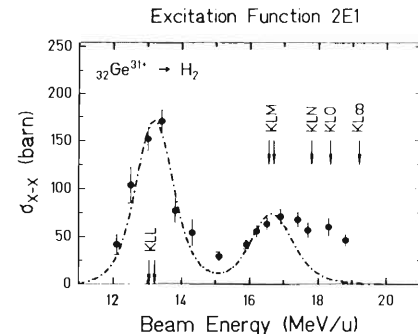


Fig. 5. Cross section of 2E1 photon emission from a metastable  $1s2s\ ^1S_0$  state of  $\text{Ge}^{30+}$  as a function of the beam energy. Descriptions of the dots, curve, and arrows are the same as those in Fig. 4.

The cross section of two K-X-ray emission has a maximum at about 13 MeV/u, a minimum at about 15 MeV/u, and a maximum at about 17 MeV/u. The peak at about 13 MeV/u corresponds to the KLL-RTE processes. In this region the  $K_{\beta\gamma}$  X-rays are not observed. This is expected since the final state of the KLL-RTE processes are  $2l2l'$  which can emit only  $K_\alpha$  X-rays. The agreement between the theory and the experiment is good. The peak at about 17 MeV/u is sum of unresolved  $KLn$ -RTE resonances with  $n > 2$ . In this region, both the  $K_\alpha$ - $K_\alpha$  and  $K_\alpha$ - $K_{\beta\gamma}$  coincidence events are observed. The theoretical prediction is about a half of the experimental data in this region.

Figure 5 shows the cross section of 2E1 photon emissions from the  $^1S_0$ -metastable state as a

function of the projectile energy. Dots show experimental data. The curve shows theoretical prediction, like those in Fig. 4, using the cross sections of DR processes leading to the states from which radiative transitions are allowed to the  $^1S_0$  state. The agreement between the theory and the experiment is good for both KLL and KLM-RTE processes.

#### References

- 1) S. Reusch, Y. Awaya, T. Kambara, D.J. McLaughlin, P. H. Mokler, A. Müller R. Schuch, and M. Schulz: *RIKEN Accel. Prog. Rep.*, **21**, 71 (1987).
- 2) I.P. Grant, B.J. McKenzie, P.H. Norrington, D.F. Mayers, and N.C. Pyper: *Comput. Phys. Commun.*, **21**, 207 (1980).

### III-2-12. Studies on the Continuum X Rays Produced by Heavy-Ion-Atom Collisions

K. Ishii, K. Maeda, Y. Sasa, M. Takami,  
M. Uda, and S. Morita\*

Continuum X rays of radiative electron capture (REC) and molecular orbital X rays (MO) can be produced by heavy-ion/atom collisions. REC X rays are the quanta emitted by the radiative transition of target electrons into a bound orbit of the incident ion. On the other hand, MO X rays are emitted from the molecular orbitals or united atoms in adiabatic collisions between an incident ion and a target atom. The MO process is enhanced when the energy levels of target electrons coincide with those of projectile electrons, especially, a symmetric collision. Anholt has systematically investigated the cross sections for production of MO X rays and has shown that the continuum X rays can be considerably observed even in asymmetric collisions and the production cross sections of these continuum X rays are much larger than the predictions for MO X rays.<sup>1)</sup> Ishii and Morita explained these X rays in terms of the bremsstrahlung produced in ion-atom collisions, namely, atomic bremsstrahlung (AB).<sup>2)</sup>

Since the dipole transition process is predominant in atomic bremsstrahlung, the cross section of AB is almost zero in the case of symmetric collisions and it becomes large for asymmetric collisions. Production of AB is complementary to that of MO. Molecular orbits can be formed in an adiabatic collision process and so, when the incident energy becomes higher, the production cross section of MO X rays decreases. Moreover, the MO X-ray energy cannot exceed the K X-ray energy of the united atom ( $I_{U.K.}$ ). For higher incident energy and in the region of X-rays energy ( $\hbar\omega > I_{U.K.}$ ), the contribution of MO X rays can be neglected and the behavior of AB for symmetric collision is expected to be well studied.

In order to study the behavior of atomic bremsstrahlung in heavy-ion collisions, we bombarded thick targets of C, BeO, NaCl, CaCO<sub>3</sub>, CaF<sub>2</sub>, Al, Si, Ti, Cr, Fe, and Cu with Si<sup>3+</sup> ions (1.435 MeV/

amu). The targets of BeO, NaCl, CaCO<sub>3</sub>, and CaF<sub>2</sub> were coated with carbon in order to avoid electronic charging up at the surface. A polyethylene foil (500μm), Al foils of 140μm or 230μm, or a vanadium metal foil (40μm) was put between the target and the Si(Li) detector.

In Fig. 1, the X-ray yields obtained  $n(Z_p, Z_T, \nu)$  are plotted as a function of target atomic number  $Z_T$  for the normalized X-ray energy  $\nu = 0.7, 1.0, 1.3, 1.5$ , and  $1.8$ .  $n(Z_p, Z_T, \nu)$  is defined by

$$n(Z_p, Z_T, \nu) = \hbar\omega \int N dx \frac{d\sigma^{\text{Brems}}}{d\hbar\omega d\Omega}(\hbar\omega, \theta)$$

where

$$\nu = \hbar\omega / I_{U.K.}, \quad \theta = 135^\circ, \quad \text{and} \quad Z_p = 14.$$

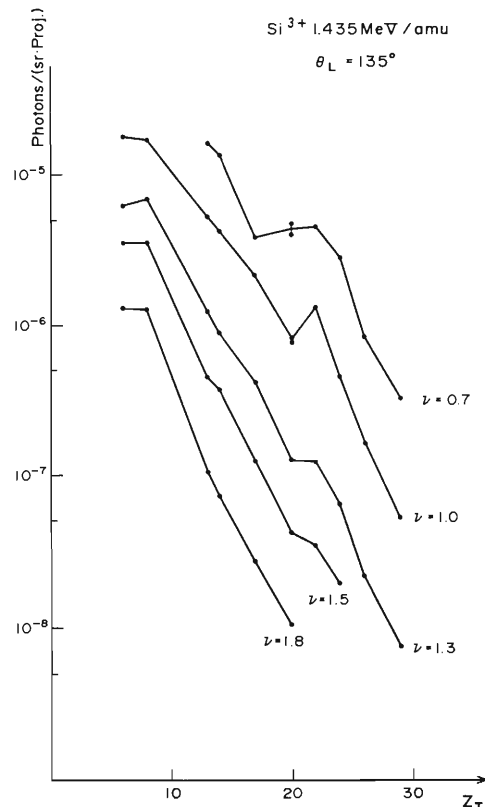


Fig. 1. Target-atom dependence of the continuum X-ray yield produced by 1.435 MeV/amu Si-ion bombardments.

\* Research Center of Ion Beam Technology, Hosei University.

For the target atomic number  $Z_T$  of the compounds, we take the largest one of the component elements. The experimental cross sections decrease monotonously with increase in  $Z_T$  while the theory predicts a minimum at  $Z_T=14$ . We can find that the atomic bremsstrahlung is still effective in the case of symmetric collision. This result leads us to consider that the electrons of projectile and target atom don't occupy each

other a same orbit, and this effect prevents the symmetric collision in a sense of atomic structure. Thus the quanta of dipole transition can be emitted even for  $Z_P = Z_T$ . The theory of AB will be developed on the base of above model.

#### References

- 1) R. Anholt: *Z. Phys. A*, **289**, 41 (1978).
- 2) K. Ishii and S. Morita: *Phys. Rev. A*, **30**, 2278 (1984).

### III-2-13. Target Thickness Dependence of Charge State Fractions of Ar Ions after the Passage through C-Foil, CH<sub>4</sub>, and H<sub>2</sub>

T. Mizogawa, Y. Awaya, T. Kambara, Y. Kanai,  
M. Kase, H. Kumagai, and K. Shima

It is well known that the equilibrium mean charges of fast heavy ions after passing through solid media are larger than those of ions passing through gaseous media.<sup>10</sup> The origin of this "solid effect" is still a problematic issue. To study this problem we have measured the charge-state distributions (CSD) of 50 MeV Ar ions after the passage through carbon foils and gaseous targets, CH<sub>4</sub> and H<sub>2</sub>.

The experimental setup is shown in Fig. 1. The essential points of the experimental procedure are as follows. The 50 MeV Ar ions from RILAC were used. The charge fractions of argon

ions after the passage through the carbon foil ( $2\sim10 \mu\text{g}/\text{cm}^2$ ) or gaseous targets ( $\lesssim 20 \text{ Torr cm}$  for CH<sub>4</sub>,  $\lesssim 50 \text{ Torr cm}$  for H<sub>2</sub>) were measured for two initial charge states (4+ and 12+). After the passage through the foils or a gas cell, the ions entered a charge-analyzing magnet, and were finally detected by a position-sensitive parallel-plate avalanche detector (PPAC). The charge-state distributions were determined from the charge spectra obtained by the PPAC.

In Fig. 2 the charge fractions of Ar ions measured for the CH<sub>4</sub> target are plotted as a function of the target pressure. The results for the C-foil

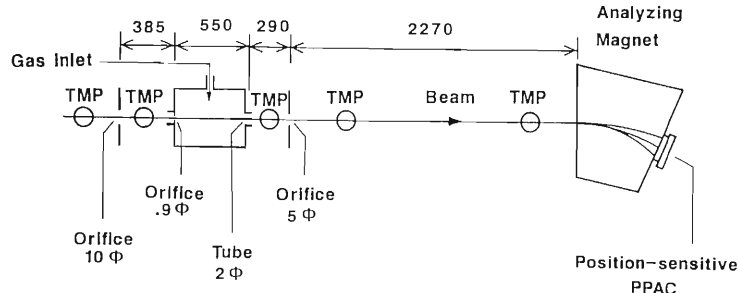


Fig. 1. Experimental setup for Ar-ion charge-state-distribution measurements with gaseous targets. For the solid target measurements the gas cell is replaced by a target holder.

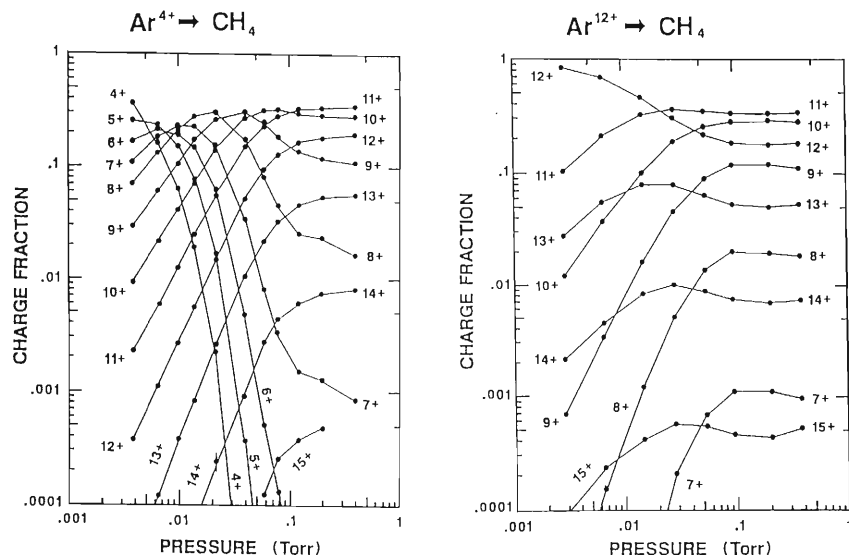


Fig. 2. Target-pressure dependence of charge-state fractions of 50 MeV Ar ions after passage through CH<sub>4</sub>.

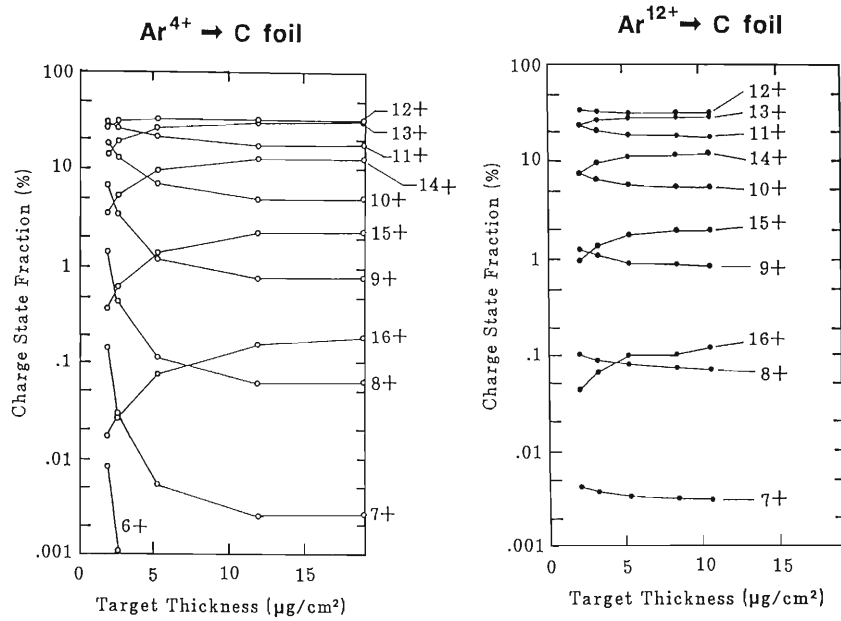


Fig. 3. Target-thickness dependence of charge-state fractions of 50 MeV Ar ions after passage through C foils.

targets are shown in Fig. 3. From these data the mean charges were evaluated and plotted in Fig. 4 as a function of the carbon thickness of the solid target or the CH<sub>4</sub> gas. The mean charges for the solid target change with the carbon thickness more rapidly than those for the gaseous target before reaching the equilibrium values. The equilibrium mean charge for the solid target is +12.33, which is larger than the case of the gaseous target by +1.55.

Our previous measurements of the intensities of K<sub>α</sub> and K<sub>β</sub> satellites of Ar ions passing through C foils<sup>2)</sup> show that the sum  $\bar{n}_L + \bar{n}_M$  of equilibrium average numbers of L-vacancies ( $\bar{n}_L = 4.45 \pm 0.05$ ) and M-vacancies ( $\bar{n}_M = 7.65 \pm 0.25$ ) in K-vacancy bearing ions is  $12.1 \pm 0.3$ . If we assume that these L- and M-vacancy numbers are nearly the same as those for ions without K vacancies, the sum  $\bar{n}_L + \bar{n}_M$  averaged over all Ar ions would be about 12.1, which is in good agreement with the equilibrium mean charge 12.33 for the carbon foil. This assumption is reasonable, because the L- or M-vacancy production is probably independent of the K-vacancy production, and also because the L- or M-shell equilibration time is shorter than the K-vacancy mean life in solid. Then the above agreement means that, if there is no auto-ionization process faster than K-vacancy decay, the solid-gas difference +1.55 should occur inside the solid and/or outside the solid as close to the exit surface as no autoionization processes can take place, because K X-ray emission occurs in such a region. The LLM Coster-Kronig process is energetically for-

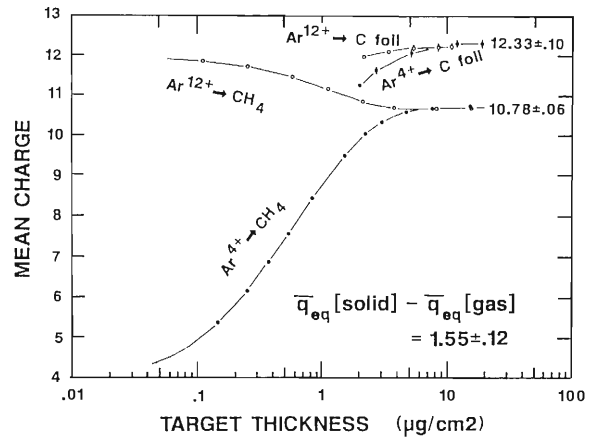


Fig. 4. Target-thickness dependence of the mean charge of 50 MeV Ar ions after passage through C foils or CH<sub>4</sub>.

bidden for multiple L-vacancy bearing states, and the LMM Auger decay may be slower than K-vacancy decay. Therefore the “Betz-Grodzins model,”<sup>11)</sup> which attributes the solid-gas difference in equilibrium mean charge to the fast auto-ionization of excited electrons *outside* the exit surface of solid targets, is considered to be not valid in the present collision system and energy. The difference may be attributed to successive L to M excitation and M to continuum ionization inside the solid.

In this discussion we neglected the existence of four H atoms in a molecule CH<sub>4</sub>. To assess the role of them, we also measured the CSD of Ar ions after passage through H<sub>2</sub> gas. The resulting

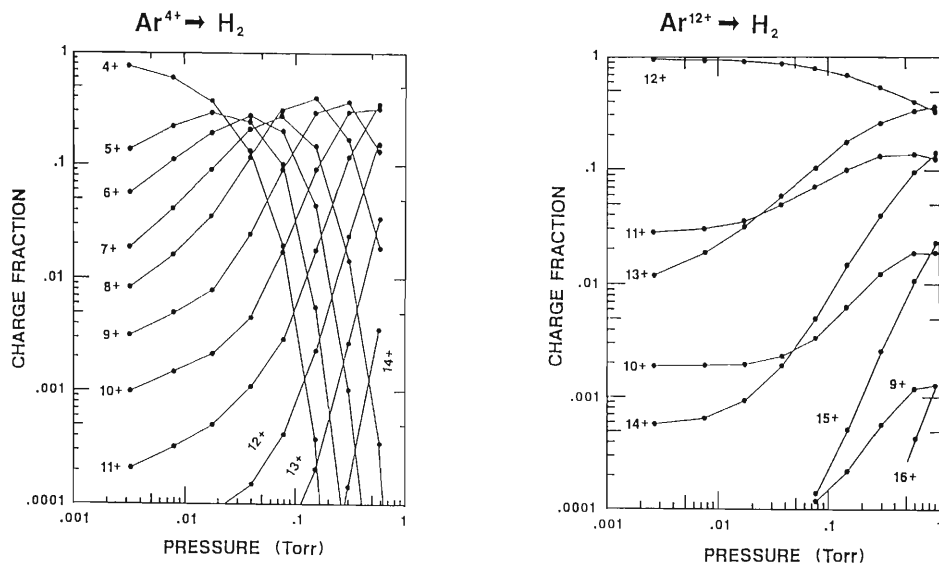


Fig. 5. Target-pressure dependence of charge-state fractions of 50 MeV Ar ions after passage through  $\text{H}_2$ .

CSD and the mean charge of Ar ions are given in Figs. 5 and 6, respectively. The explanation for the horizontal scale of Fig. 6, "equivalent C thickness," will be necessary. In Fig. 4, we used the C thickness in units of  $[\mu\text{g}/\text{cm}^2]$  as a horizontal coordinate, for convenience of the comparison of "solid" and "gas" cases. To compare the results for  $\text{CH}_4$  targets and  $\text{H}_2$  targets, it will be convenient that the same numerical values of the horizontal coordinates of Figs. 4 and 6 give the same H-atom thickness. The "equivalent C thickness" is such a variable which is proportional to the adopted  $\text{H}_2$  pressure.

From these data we can deduce some qualitative conclusions. First, from the thin limit of  $\text{Ar}^{12+}$ -ion data, the electron capture cross section from  $\text{H}_2$  is negligibly small compared with that from  $\text{CH}_4$ . Second, from the thin limit of  $\text{Ar}^{4+}$ -ion data, the electron loss cross section for the  $\text{H}_2$  target is a few tens of percent of that by the  $\text{CH}_4$  target. Therefore, in the charge-equilibration process of Ar ions in the  $\text{CH}_4$  gas, the role of H atom is rather enhancement of electron-loss than electron-gain, provided the simple assumption, *i.e.*, that the charge-changing cross sections for molecule targets are approximately equal to the sum of the cross sections for the constituent independent atoms, is valid. This means that, if "pure carbon gas" is used as charge-stripping

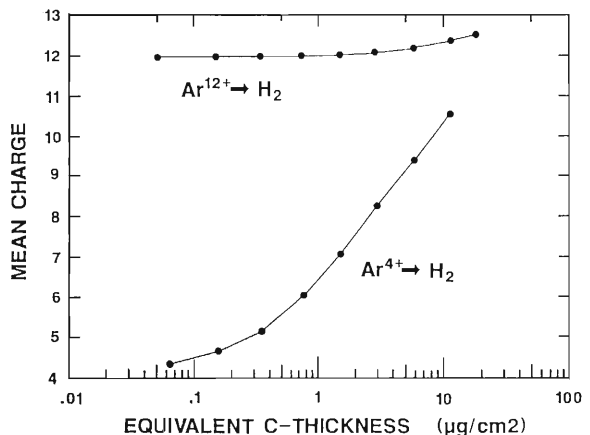


Fig. 6. Target-thickness dependence of the mean charge of 50 MeV Ar ions after passage through  $\text{H}_2$ .

media, the above "solid effect" in the equilibrium mean charge will be further enhanced.

#### References

- 1) H.D. Betz: *Rev. Mod. Phys.*, **44**, 465 (1972).
- 2) T. Mizogawa, Y. Awaya, T. Kambara, Y. Kanai, M. Kase, H. Kumagai, P.H. Mokler, and K. Shima: *RIKEN Accel. Prog. Rep.*, **20**, 53 (1986); T. Mizogawa, Y. Awaya, T. Kambara, Y. Kanai, M. Kase, H. Kumagai, P.H. Mokler, and K. Shima: *Nucl. Instrum. Methods Phys. Res. A*, **262**, 141 (1987).

### III-2-14. Charge Distributions of the Recoil Ions Accompanied with Multiple Ionization of Heavy Projectile Ions

H. Tawara, T. Tonuma, H. Kumagai, and T. Matsuo

Presently it is known that under highly charged, energetic heavy ion impact multiply charged recoil ions are copiously produced, in contrast to structureless particle (electron or proton) impact. In particular, in collisions with heavy ions having inner-shell vacancies, the production of multiply charged recoil ions is significantly enhanced. This is understood qualitatively as well as, to some extent, quantitatively to be due to the (inner-shell) electron transfer from target atoms into projectile vacancies. In fact, Gray, *et al.*<sup>1)</sup> and Kelbch, *et al.*,<sup>2)</sup> for example, have shown that the charge distributions of recoil ions are shifted toward higher charge state with increasing the number of electrons captured into projectile ions.

Taking into account the importance of such transfer ionization where the projectiles capture electrons from target atoms and result in the production of multiply charged recoil ions, Horbatsch<sup>3)</sup> has developed a quantum statistical time-dependent mean-field theory and calculated the cross sections for transfer ionization as well as those for pure ionization over the energy region ranging from 50 keV/amu to 5 MeV/amu for projectiles with the ionic charge of 6, 12, and 20. This calculation suggests that the contribution of electron transfer processes becomes much significant at lower energies, compared with the pure ionization process.

On the other hand, very few experimental and theoretical investigations have been devoted toward understanding the mechanisms of recoil ion production when the ionization of partially ionized projectiles is accompanied simultaneously (loss ionization). Ullrich, *et al.*<sup>4)</sup> have measured the cross sections for multiply charged recoil ions in  $\text{Ne}^{q+}$  ( $q=1, 2, 3$ ) + Ne collisions at relatively low energies (75–360 keV/amu). Their results show that highly charged recoil ions are mainly produced in close collisions, whereas recoil ions with low charge are due to pure multiple ionization under collisions with large impact parameters. In their collision energy region, two neon collision partners tend to form a quasimolecule probably within the L-shell orbit

range of partially ionized neon ions. In fact, the observed charge distributions seem to be similar for both projectile and recoil neon ions and suggest us that the remaining electrons involved in collisions are equally shared between two collision partners.

In the present work, we measure the charge distributions of recoil ions which are produced in collisions of partially ionized ( $\text{Ne}^{q+}$  and  $\text{Ar}^{q+}$ ) projectile ions with Ne atoms with simultaneous ionization in both projectile ions and target atoms. A TOF technique based upon charge-separated projectile-recoil ion coincidence is used.<sup>5)</sup> 1.05 MeV/amu  $\text{Ne}^{2+}$  and  $\text{Ar}^{4+}$  ions are provided from RIKEN linear accelerator (RILAC) and, after passing stripping foils and a switching magnet if necessary, sent into a collision chamber whose pressure is controlled. The projectile charge state after collisions is analyzed with an electrostatic charge separator and finally the projectile ions are detected with a position-sensitive parallel plate avalanche counter. On the other hand, recoil ions are detected with a channeltron detector after flying over about 15 cm from the collision region.

Typical recoil ion charge spectra are shown in Fig. 1. The charge-selected projectile-recoil ion coincidence spectra are accumulated through LIST mode. In Fig. 1 (a) is shown the charge distribution of 1.05 MeV/amu projectile  $\text{Ar}^{q+}$  ions in coincidence with recoil  $\text{Ne}^{i+}$  ions in the incident  $\text{Ar}^{4+}$  ions colliding with Ne atoms. We have found that, at the present collision energy, probabilities of 1–4 electron ionization from projectile  $\text{Ar}^{4+}$  ions resulting into  $\text{Ar}^{5+}$ – $\text{Ar}^{8+}$  ions decreases slowly toward higher ionization stage and is far intense, compared with those for electron capture into projectiles resulting into  $\text{Ar}^{3+}$  ions. The probabilities for further ionization beyond  $q'=8$  are found to be also quite small, compared with those for  $q' \leq 8$ . This is due to a so-called shell effect where the ionization for  $q' > 8$  needs the ionization of 2p shell electrons and, thus, much larger energy transfer to target atoms is necessary.

At the present collision energy, the dominant

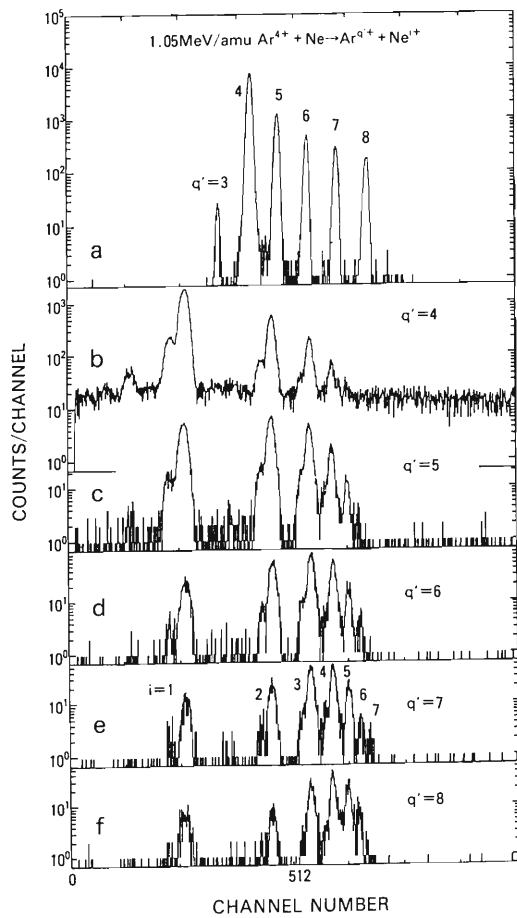


Fig. 1. Observed charge spectra of both projectiles (a) and recoil  $\text{Ne}^{i+}$  ions (b-f) in coincidence with the specified projectile charge  $q'$  in 1.05 MeV/amu  $\text{Ar}^{4+} + \text{Ne}$  collisions.

mechanism of the production of recoil ions with low charge ( $i=1-3$ ) is believed to be pure ionization of target atoms without any change of projectile ion charge where probabilities for multiple ionization decrease drastically with increasing the charge of recoil ions (see Fig. 1 (b)). The collisions accompanying one-electron (single) ionization of projectiles clearly result in relative enhancement of the production of recoil ions with higher charge state (see Fig. 1 (c)), compared with that of lower charge ions. Furthermore, two-, three-, and four-electron ionization of projectiles results in successively higher charge recoil ions (see Fig. 1 (d), (e), and (f)). In fact, for four-electron ionization of projectiles (resulting in  $\text{Ar}^{8+}$ ),  $\text{Ne}^{4+}$  recoil ions are most intense, with a trace of up to  $\text{Ne}^{7+}$  to  $\text{Ne}^{8+}$  ions.

In Fig. 2 are shown the cross sections for the production of recoil  $\text{Ne}^{i+}$  ions estimated from the above data and normalized to the previous values<sup>6)</sup> as a function of the recoil ion charge.

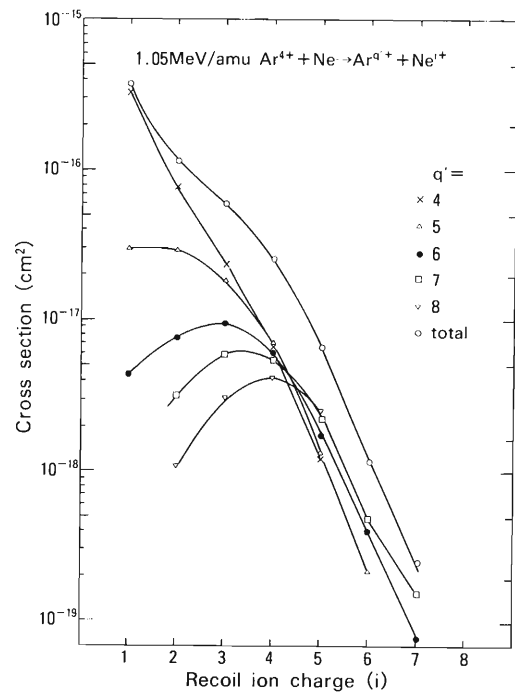


Fig. 2. Partial cross sections for the production of recoil ions with different charge in coincidence with the specified projectile charge after collisions in 1.05 MeV/amu  $\text{Ar}^{4+} + \text{Ne}$  collisions.

This clearly shows that, with increasing the degree of simultaneous ionization of projectiles, the production of recoil ions with higher charge is significantly enhanced.

Similar trends are also seen in  $\text{Ne}^{2+} + \text{Ne}$  collisions (not shown here) where, though absolute cross sections are smaller than those in  $\text{Ar}^{4+}$  collisions as measured in our previous experiments<sup>6)</sup> because of the low projectile  $q$ , three-electron ionization of projectiles (the final projectile charge being  $\text{Ne}^{5+}$ ) results in the production of recoil  $\text{Ne}^{3+}$  ions with the highest probabilities, having weak peaks corresponding to recoiled  $\text{Ne}^{6+}$  to  $\text{Ne}^{7+}$  ions. These results suggest that projectile ions have to penetrate deeper into target atoms when the projectiles are ionized (loss ionization).

Up to now, no theoretical treatment has been reported of multiple ionization of target atoms accompanied with simultaneous ionization of projectiles in collisions of partially ionized projectiles with neutral atoms which can be compared with the present observations. However, the present results can be understood qualitatively as follows: Projectile ions have to come into close collisions with target atoms in order to be highly ionized and, in turn, these close collisions result in higher ionization of target atoms. In particular if the ionization of the inner-shell

electrons would occur, followed by cascading of the inner-shell vacancies toward outer shells, the recoil ions could have much higher charge after collision.

In collisions of partially ionized projectiles, in contrast to collisions involving innershell electron transfer, simultaneous ionization of both collision partners should result in different consequences in their charge distributions. In such cases, both particles should penetrate each other deep enough to be highly ionized and then result in the production of recoil ions with higher charge.

In order to fully understand such a multiple ionization of recoil target atoms, further accumulation is required of experimental data similar to the present work. At the same time, it would be of great help to theoretically investigate related topics such as the impact parameter dependence of multiple ionization processes of target atoms

simultaneously accompanied by projectile ionization or electron capture as well as that in pure ionization without any change of projectile charge.

#### References

- 1) T.J. Gray, C.L. Cocke, and E. Justiniano: *Phys. Rev. A*, **22**, 849 (1980).
- 2) S. Kelbch, J. Ullrich, R. Mann, P. Richard, and H. Schmidt-Böcking: *J. Phys. B*, **18**, 323 (1985).
- 3) M. Horbatsch: *J. Phys. B*, **19**, L193 (1986); M. Horbatsch: *Z. Phys. D*, **1**, 337 (1986); M. Horbatsch and R.M. Dreizler: *Z. Phys. D*, **2**, 183 (1986).
- 4) J. Ullrich, K. Bethge, S. Kelbch, W. Schadt, H. Schmidt-Böcking, and K.E. Stiebing: *J. Phys. B*, **19**, 448 (1986).
- 5) T. Tonuma, T. Matsuo, H. Kumagai, S.H. Be, and H. Tawara: *RIKEN Accel. Prog. Rep.*, **21**, 84 (1987).
- 6) T. Tonuma, T. Matsuo, M. Kase, T. Kambara, H. Kumagai, S.H. Be, I. Kohno, and H. Tawara: *Phys. Rev. A*, **36**, 1941 (1987).

### III-2-15. K-LL Auger Spectra of Nitrogen Projectiles

Y. Kanai, T. Kambara, Y. Awaya, B. Sulik,\*  
N. Stolterfoht,\*\* and Y. Yamazaki

In this report, we present the result from the first measurements on high resolution K Auger electrons from the Be-like nitrogen using the method of zero-degree Auger spectroscopy which has been developed by N. Stolterfoht and coworkers.<sup>1)</sup> By using this method, we can do the high resolution measurement of the ejected electrons from the high velocity projectiles.<sup>1)</sup> Comparing the results of the high resolution measurement with a result of theoretical studies, we can test electron correlation and relativistic interactions in the projectile ions.

This experiment was performed at RILAC. Projectiles of 1.33 MeV/u  $N^{2+}$  were magnetically analyzed and directed into a He gas cell. Emited electrons were analyzed by a zero-degree Auger spectroscopy apparatus which consists of two

consecutive 90° parallel-plate electrostatic analyzers. It had been temporarily transported from the Hahn-Meitner-Institut, Berlin.

Results are shown in Fig. 1. Most of the strong Auger lines in Fig. 1 originate from Be-like initial configurations which were produced by the 'needle ionization (selective inner-shell ionization)' in collisions with He. Most of the prominent Auger peaks were fitted by the Gaussian curve. Energies of the emitted electrons in the projectile rest frame are listed in Table 1. In consideration of the uncertainties of the projectile energy and analyzing voltage of the electron analyzer, absolute values of emitted electron energies were determined with uncertainty of about  $\pm 0.5$  eV. The initial and final states of each Auger electron were determined from the

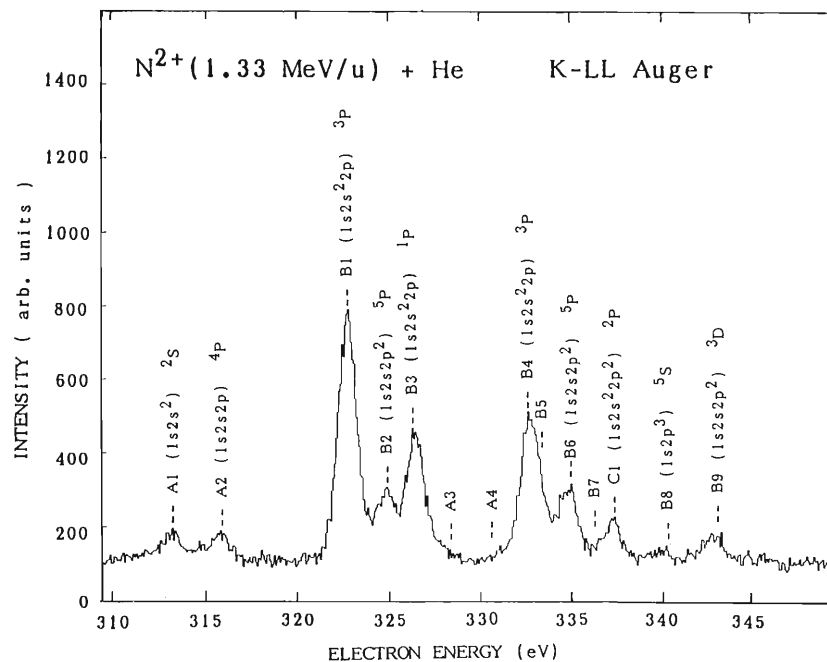


Fig. 1. K Auger spectra from 1.33 MeV/u  $N^{2+}$  projectiles colliding with He atoms. Electron energies have been transformed to the projectile rest frame. Initial configurations are indicated on the peaks.

\* Institute of Nuclear Research of the Hungarian Academy of Sciences (ATOMKI), Debrecen, Hungary.

\*\* Hahn-Meitner-Institut, Berlin, F.R. Germany.

Table 1. Auger transition energies.

	This result (eV)	Initial state		Final state	Theory (eV)
A1	$313.3 \pm 0.5$	$1s2s^2$	$^2S$	$1s^2$	$^1S$ 312.1 <sup>a</sup>
A2	$315.8 \pm 0.5$	$1s2s2p$	$^4P$	$1s^2$	$^1S$ 315.2 <sup>a</sup>
B1	$322.8 \pm 0.5$	$1s2s^22p$	$^3P$	$1s^22p$	$^2P$ 323.36 <sup>b</sup>
B2	$324.9 \pm 0.5$	$1s2s2p^2$	$^5P$	$1s^22p$	$^2P$ 324.76 <sup>b</sup>
B3	$326.6 \pm 0.5$	$1s2s^22p$	$^1P$	$1s^22p$	$^2P$ 326.99 <sup>b</sup>
A3	$328.2 \pm 0.5$	$1s2s2p$	$^2P$	$1s^2$	$^1S$ 328.0 <sup>a</sup>
A4	$331.1 \pm 0.5$	$1s2p^2$	$^2D$	$1s^2$	$^1S$ 331.7 <sup>a</sup>
B4	$332.8 \pm 0.5$	$1s2s^22p$	$^3P$	$1s^22s$	$^2S$ 333.45 <sup>b</sup>
B5	$333.3 \pm 0.5$	$1s2s2p^2$	$^3P$	$1s^22p$	$^2P$ 333.21 <sup>b</sup>
B6	$334.9 \pm 0.5$	$1s2s2p^2$	$^5P$	$1s^22p$	$^2S$ 334.84 <sup>b</sup>
B7	$336.2 \pm 0.5$	$1s2s^22p$	$^1P$	$1s^22s$	$^2S$ 337.08 <sup>b</sup>
C1	$337.4 \pm 0.5$	$1s2s^22p^2$	$^2P$	$1s^22p^2$	$^3P$ —
B8	$340.2 \pm 0.5$	$1s2p^3$	$^5S$	$1s^22p$	$^2P$ 339.88 <sup>b</sup>
B9	$343.2 \pm 0.5$	$1s2s2p^2$	$^3D$	$1s^22s$	$^2S$ 344.41 <sup>b</sup>

a, Ref. 3; b, Ref. 2.

comparison with theories<sup>2,3)</sup> and a systematic study of Auger spectra of oxygen projectiles.<sup>4)</sup>

#### References

- 1) N. Stolterfoht: *Phys. Rep.*, **146**, 315 (1987).
- 2) M.H. Chen: *Phys. Rev. A*, **31**, 1449 (1985).
- 3) R. Mann, F. Folkmann, and H.F. Beyer: *J. Phys. B*, **14**, 1161 (1981).
- 4) R. Bruch, N. Stolterfoht, S. Datz, P.D. Miller, P.L. Pepmiller, Y. Yamazaki, H.F. Krause, J.K. Swenson, K.T. Chung, and B.F. Davis: *Phys. Rev. A*, **35**, 4114 (1987).

### III-2-16. Analysis of the Mg IX 2s3d-2s4f Transition of Beam-Foil Spectra

K. Ando, S. Kohmoto, Y. Awaya, T. Tonuma, and S. Tsurubuchi

Be-like ions have a simple electron configuration, but their energy levels have been known only below the principal quantum number ( $n$ ) of 3. Above  $n=4$ , energies of terms have not fully been analyzed, and the wavelength region around few hundred Angstrom, which occurs mainly from the transitions from  $n=4$  to 3, is blank in wavelength tables. But this wavelength region is important in the experiments on high density plasmas.

The transition array of 2s3d-2s4f has been identified for Be I to F IV, for Al X, and for Si XI. For latter two elements, however, only 3d<sup>3</sup>D-4f<sup>3</sup>F lines have been identified.

A problem in the identification of the singlet transition is that this transition array is overlapped with another transition array of 2p3d-2p4f as shown in theoretical spectra calculated

by the multiconfiguration Dirac-Fock. Also, the 2s4f configuration has a configuration interaction with the 2p3d as described by Edlen.<sup>1)</sup> We analyzed the 2s4f configuration, taking into account the configuration interactions. The lower levels of 2s3d have been already known and their energies were obtained from the Grotorian Diagram of Mg IX.<sup>2)</sup>

Spectra of magnesium ions were measured for the beam energies of 12, 19, and 32 MeV from the RILAC with a 2.2 m grazing incidence spectrometer (McPherson 247) with a grating of 600 grooves/mm. The entrance and exit slit widths were set for sufficient resolution. The wavelengths of spectra were calibrated by using known spectral lines of magnesium ions.

An isoelectronic sequence of the 2s3d-2s4f transition was obtained from the data of C III to

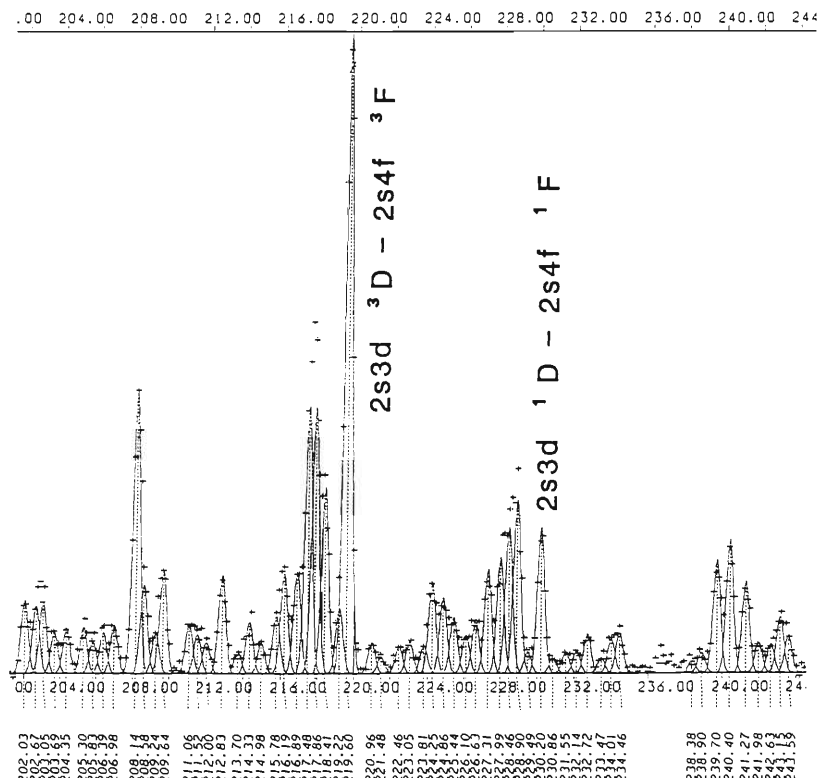


Fig. 1. A spectrum of Mg ions obtained in the beam-foil experiment using 19 MeV, in which newly identified transitions of 2s3d-2s4f are indicated. Numbers appearing in the bottom are uncalibrated wavelengths, which are different about  $-1.5 \text{ \AA}$  from the real wavelength, and the cross marks show the observed intensities.

Table 1. Observed lines of the 2s3d-2s4f transition in Mg IX.

Intensity	Wavelength (Å)	Wavenumber (cm <sup>-1</sup> )	Combination
960	218.45	457,770	2s3d <sup>3</sup> D <sub>1,2,3</sub> - 2s4f <sup>3</sup> F <sub>2,3,4</sub>
170	229.07	436,550	2s3d <sup>1</sup> D <sub>2</sub> - 2s4f <sup>1</sup> F <sub>3</sub>

Table 2. Energy parameters (cm<sup>-1</sup>).

Configuration	Parameter	Fitted value	H-F Value	Fit/H-F
2s4f	$E_{av}$	2,085,141	2,051,485	1.016
	$G^3(2s,4f)$	3,285	4,266	0.770
	$\xi(4f)$	15	15	1.000*
2p3d	$E_{av}$	1,808,032	1,766,807	1.023
	$F^2(2p,3d)$	73,697	68,475	1.076
	$G^1(2p,3d)$	62,654	64,321	0.974
	$G^3(2p,3d)$	32,766	37,352	0.877
	$\xi(2p)$	2,179	2,582	0.844
	$\xi(3d)$	107	107	1.000*
Configuration interaction				
	$R^1(sf, pd)$	-95,502	-50,657	1.885
	$R^2(sf, dp)$	-9,302	-14,435	0.644

\* $\xi(4f)$  and  $\xi(3d)$  were not varied in the least squares fitting, because these values were too small.

F VI, Al X, and Si XI.<sup>2,3)</sup> The wavelength of the triplet transition 2s3d <sup>3</sup>D-2s4f <sup>3</sup>F was estimated from the isoelectronic sequence. From these results, the strong line observed at 218.45 Å was identified as the transition of 2s3d <sup>3</sup>D<sub>1,2,3</sub>-2s4f <sup>3</sup>F<sub>2,3,4</sub>.

After determination of the <sup>3</sup>F levels, the parameters of energy expressions for the 2s4f and 2p3d configurations, which included the configuration interaction mentioned above, were fitted by the least squares method.<sup>4-6)</sup> The parameters used are average energies, Slater direct- and exchange-radial integrals ( $F^k, G^k$ ), spin-orbit interactions ( $\xi$ ) for the 2s4f and 2p3d configuration, respectively, and configuration interaction-radial integrals ( $R^k$ ) between the two configurations. The initial values of these parameters were calculated by using the Hartree-Fock program code of MCHF77.<sup>7)</sup> From the least squares fitting, the energy of the <sup>1</sup>F state are obtained, and the wavelength of the transition of 2s3d <sup>1</sup>D-2s4f <sup>1</sup>F was estimated. An isolated spectral line was found near this estimated wavelength, and was identified as the singlet transition of 2s3d <sup>1</sup>D-2s4f <sup>1</sup>F.

The observed spectrum is shown in Fig. 1, where the identified lines are indicated. The result of identification and classification are given in Table 1.

The parameters are determined from the ob-

served energy levels by means of the least squares fits.<sup>7)</sup> Table 2 shows the fitting values, the Hartree-Fock values, and the ratio of fitted value to Hartree-Fock for each parameter. The designation of energy levels of 2s4f and 2p3d configurations are determined. The standard deviation of fitting energies is 695 cm<sup>-1</sup> for 13 experimental levels of the 2s4f and 2p3d configurations. The differences between the experimental and fitted level energies are small for the levels of 2s4f, but are slightly large for 2p3d, especially for <sup>3</sup>P levels. This suggests that the <sup>3</sup>P levels have a configuration interaction with other configurations.

## References

- 1) B. Edlen: Encyclopedia of Physics, Vol.27, Springer-Verlag, Berlin, p.80 (1964).
- 2) S. Bashkin and J.O. Stoner, Jr.: Atomic Energy Levels and Grotrian Diagrams, Vol. 1, North-Holland Pub. Co., Amsterdam (1975).
- 3) R.L. Kelly: *J. Phys. Chem. Ref. Data*, **16** (Supplement) No. 1, p. 1 (1987).
- 4) R.D. Cowan: *Phys. Rev.*, **163**, 54 (1963).
- 5) R.D. Cowan and D.C. Griffin: *J. Opt. Soc. Am.*, **66**, 1010 (1976).
- 6) R.D. Cowan: The Theory of Atomic Structure and Atomic Spectra, Univ. California Press, California (1981).
- 7) C.F. Fischer: *Comput. Phys. Commun.*, **14**, 145 (1978).

### III-2-17. Impact Parameter Dependence of Ne K-X Ray Emission in 10 MeV $\text{Ne}^{7+}$ on Ne Collisions

T. Kambara, Y. Awaya, Y. Kanai, H. Schmidt-Böcking, and H. Vogt

The excitation mechanism of inner-shell electrons in heavy ion-atom collisions is often described as direct Coulomb or molecular orbital processes which are based on the interaction between the excited electron and the time-dependent nuclear field during the collision. However, in some cases, the interaction between the excited electron and one of the electrons of the collision partner can be important in the excitation process. The electron-electron correlation effect, which is known as resonant excitation and transfer (RTE),<sup>19</sup> is expected to show up in the K-X-ray-emission probability  $P(b, \phi)$  in a specific outgoing charge state, where  $b$  is the impact parameter and  $\phi$  is the angle between the scattering plane and the X-ray emission direction.

In order to investigate the different excitation mechanisms, we have started to measure  $P(b, \phi)$  for different outgoing charge states in Ne-Ne collision systems. At first, we measured the two-dimensional angular dependence of 10 MeV  $\text{Ne}^{7+}$  projectiles colliding with Ne for the outgoing charge states from  $\text{Ne}^{4+}$  to  $\text{Ne}^{7+}$  in coincidence with the Ne K-X rays. In this collision energy, the K-shell excitation is dominated by the  $2p\sigma-2p\pi$  rotational coupling.

The experimental setup is shown in Fig. 1. A  $\text{Ne}^{7+}$  beam from the RILAC was collimated by a pair of slits, passed a Ne gas target, and was charge-state analyzed by a magnetic deflection of  $25^\circ$  and detected by a two-dimensional position-sensitive gas detector (PPAD) with a "wedge and strip" anode 6 m after the target.

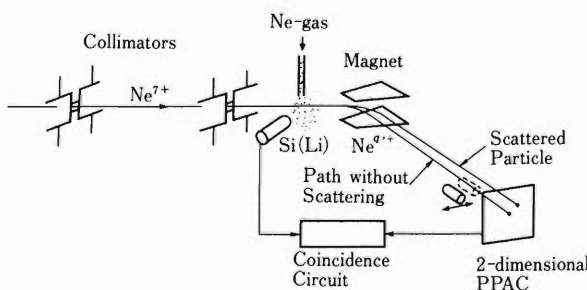


Fig. 1. Experimental setup.

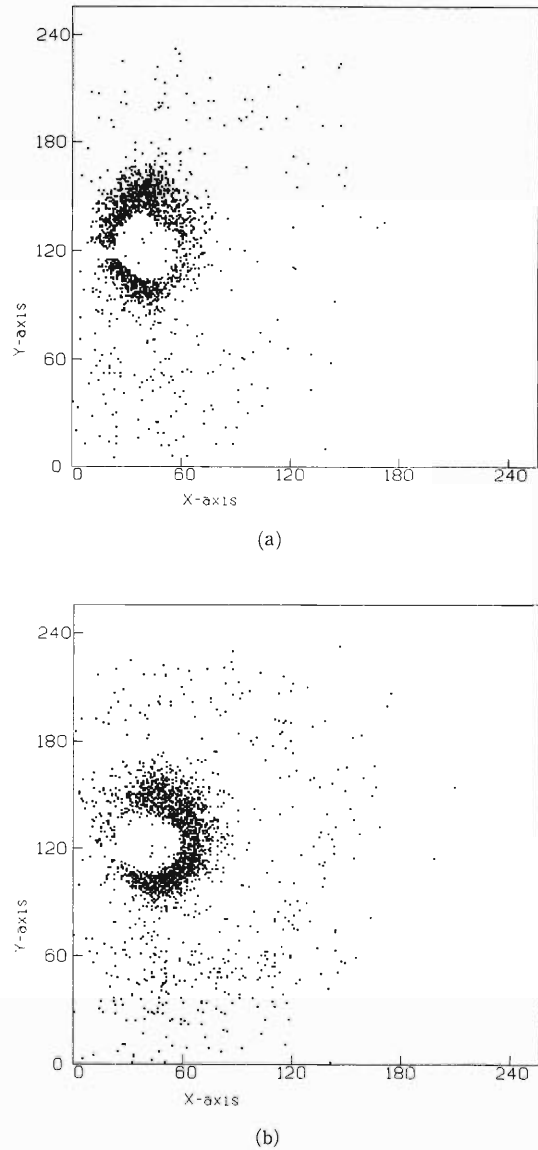


Fig. 2. Examples of position spectra of scattered Ne ions with outgoing charge states of 7+ (a) and 4+ (b) in coincidence with Ne K-X rays. 1 cm corresponds to 40 channels in each direction. Particles with small scattering angles are blocked with a Faraday cup of 12 mm in diameter. A circular blank in each position spectrum is a shadow of the Faraday cup.

The target gas was emitted into a collision region in a evacuated chamber through a thin nozzle. The target density was so small that a single-collision condition was fulfilled. The scattering angle for the separated charge state was determined by the position relative to the beam center. The position resolution is better than 1 mm which corresponds to  $1.6 \times 10^{-4}$  rad of scattering angle  $\theta$ . For measurements of large angle scattering ( $\theta > 10^{-3}$  rad), a Faraday cup with a diameter of 12 mm was inserted in front of the PPAD to block the particles with smaller scattering angle to avoid a too large count rate. The X rays from the target region were measured by a Si(Li) detector mounted at 90° to the beam direction.

Examples of the two-dimensional position spectra of the scattered particles in coincidence with the Ne K-X rays are shown in Fig. 2. The X rays were detected in the direction of the X-axis. The Faraday cup was set in front of the PPAD which made a circular blank in the spectra. The experimental results show a outgoing charge-state dependence of the K-excitation probabilities as a function of the scattering angle. Further analysis is in progress.

#### Reference

- 1) S. Reusch, P.H. Mokler, T. Kambara, R. Schuch, G. Wintermeyer, A. Müller, Z. Stachura, and A. Warczak : This Report, p. 57.

### III-2-18. K Auger Spectra of Doubly-Excited Helium-Like Carbon

H. Sakaue, K. Ohta, T. Inaba,\* Y. Kanai, S. Ohtani, K. Wakiya,  
H. Suzuki, T. Takayanagi, T. Kambara, and Y. Awaya

We started studies of ion-atom collisions by using highly ionized ions from the RIKEN ECRIS (electron cyclotron resonance ion source) which was constructed for the AVF cyclotron. In this report, we present the result of the first measurements of K Auger electrons of doubly-excited He-like carbon using 5.0 keV/u  $^{13}\text{C}^{6+}$  projectiles in collisions with He. The  $^{13}\text{C}^{6+}$  projectiles were made by the ECRIS. Projectiles were analyzed by a 90° analyzing magnet and then collided with target He in a gas cell. Doubly-excited He-like carbon ions were produced by the double-electron capture from target He atoms. Electrons were measured at the observation angle of 0° with respect to the beam direction by an electron spectrometer. It consists of a 90° parallel-plate electrostatic analyzer and a simulated hemispherical electrostatic analyzer; the former was used to steer the electrons out of the ion beam and the latter determines the electron energy resolution. Results are shown in Fig. 1. Under a single-collision condition, we observed Auger electrons whose initial-state configurations were  $(2l\ n'l')$ , where  $l$  and  $l'$  are angular momenta and  $n$  principal quantum number ( $n \geq 3$ ).

When the target pressure was high, we observed spectra like the lower one of Fig. 1. Two groups of peaks below 300 eV correspond to the transitions arising from the Li-like carbon, which were made by double collisions. The spectroscopic studies of K-Auger electrons from the Li-like carbon were made completely by R. Mann.<sup>1)</sup> All peaks below 300 eV can be identified as the same as those reported by R. Mann. The lower group is attributed to the decay of the (1s

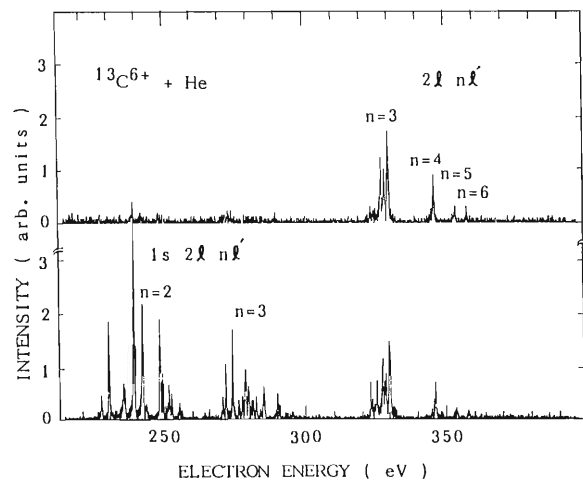


Fig. 1 Auger electron spectra for  $^{13}\text{C}^{6+}$  on He gas. Upper spectrum are under single collision condition. Lower one under double collision condition. Initial state configuration before Auger decay is indicated on each group of peaks. Auger electrons peaks from the  $(2l\ 2l')$  configuration are expected around 270 eV.

$2l\ 2l'$ ) state and upper one to the  $(1s\ 2l\ 3l')$ . Using these peak positions, we calibrated our analyzer.

Under the single-collision condition, we observed spectra like the upper one of Fig. 1. We can identify each group of peaks as shown in the figure. There are two features of this spectrum: (1) no peaks of  $(2l\ 2l')$  configurations (around 270 eV) and (2) peaks of  $(2l\ n'l')$  configurations can be observed in a wide range of  $n$  ( $n \geq 3$ ).

Precise analysis of the results is in progress.

#### Reference

- 1) R. Mann: *Phys. Rev. A*, **35**, 4988 (1987).

\* Institute for Laser Science, University of Electro-Communications.

### III-2-19. Observation of the Velocity Distribution of a Sodium Atomic Beam Irradiated by a Resonant CW Dye Laser

T. Suzuki,\* T. Minowa, and H. Katsuragawa

We have reported two-step photoionization of a sodium atomic beam using cw and pulsed dye lasers.<sup>1)</sup> The dependence of the signal intensity of the two-step photoionization upon the power of the radiation of the cw dye laser suggested that laser cooling of the sodium atomic beam took place. To ascertain this conclusion, we have undertaken to investigate the change in the velocity distribution of a sodium atomic beam irradiated with a resonant laser.

The experimental set up is schematically shown in Fig. 1. The distance between a sodium atomic beam source and an ionization region was 22 cm. Sodium atoms take about 0.2 ms to arrive at the ionization region because the mean velocity of a sodium atomic beam is about  $10^3$  m/s. During this flight time, sodium atoms interact with a counter-propagating resonant cw laser radiation, which has been tuned to the  $3P_{1/2}-3S_{1/2}$  transition of sodium, and are pressed with the radiation toward the beam source.

In the ionization region, sodium atoms were ionized by the radiation of the cw laser and of the pulsed dye laser (wavelength 390 nm). The pulsed dye laser beam was focused with a converging lens (focal length 10 cm). Resultant sodium ions flew freely in a stainless-steel duct

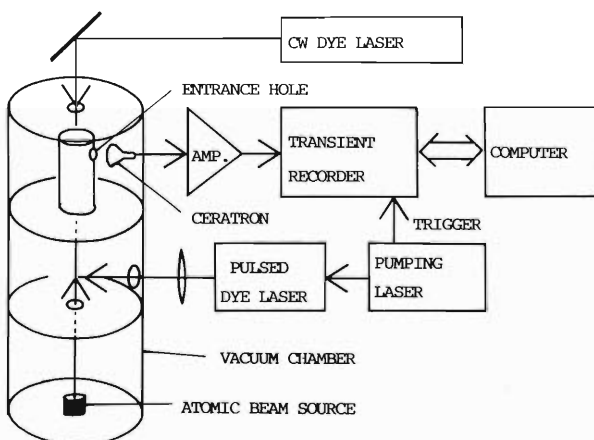


Fig. 1. Schematic diagram of the experimental set up.

(3 cm in diameter). The duct had a hole (5 mm in diameter) at the end, through which ions were pulled out toward a CERATRON detector. The duct shielded the electric field around the detector which was formed by a bias voltage (3.5 kV) to the detector, thus the velocity change of ions having been minimized. Since the distance between the ionization region and the hole was 20 cm, the TOF of sodium ions was estimated at 0.2 ms from the mean velocity of sodium atoms; the estimated value was close to the observed one.

The output signals from the CERATRON detector were fed to a transient recorder triggered with the pulsed dye laser. The time difference between the triggering and the signal acquisition was recorded in a TOF spectrum by a computer. The velocity distribution was obtained from the TOF spectrum and the distance between the ionization region and the entrance hole.

Figure 2 shows the TOF spectra. In Fig. 2 (A)

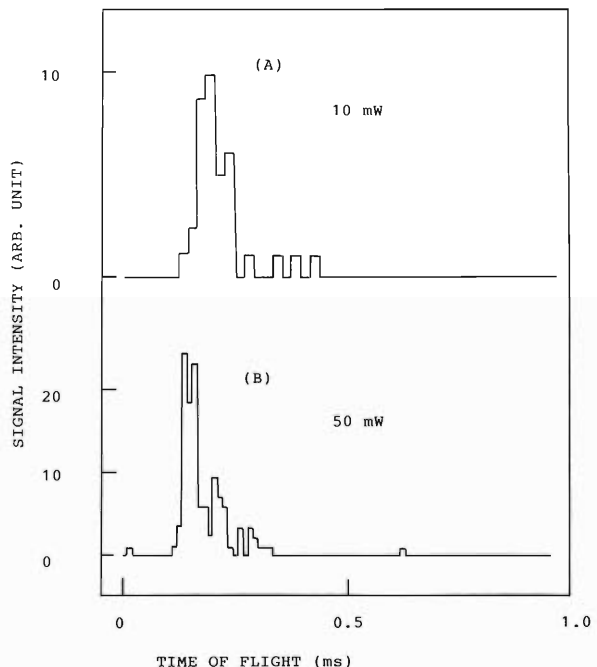


Fig. 2. Time-of-flight spectra. (A) the power of a resonant cw dye laser was kept at 10 mW and (B) at 50 mW.

\* Department of Physics, Faculty of Science, Toho University.

the power of the cw dye laser was kept at 10 mW, and in Fig. 2 (B) at 50 mW. The two spectra show marked differences that the width of the spectrum at 50 mW is narrower than that at 10 mW and that the peak at 50 mW shifts toward the time origin compared with that at 10 mW.

The present results are puzzling to us. The line width of the cw laser was broad; much broader than the Doppler width of the sodium atomic beam. To explain the experimental results we assume that all sodium atoms are under a equal light pressure regardless of their velocities.

In Fig. 3 the calculated result is shown for the change in the velocity distribution (at 800 K); line I is the initial Boltzmann distribution given by

$$f(v) = A \cdot v^2 \cdot \exp(-(v/v_0)^2) \quad (1)$$

where  $A$  is a normalization constant and  $v_0$  is the mean velocity of a sodium atomic beam.

The velocity at the ionization region of a sodium atom under one-dimensional pressure caused by the cw laser is given by

$$v_i = \sqrt{v^2 - 2LP_0/M} \quad (2)$$

where  $v$  is the velocity at the source,  $L$  is the distance between the source and the ionization region (22 cm),  $M$  is the mass of a sodium atom, and  $P_0$  is the light pressure exerted upon sodium atoms under the resonant condition. Substituting  $v_i$  into Eq. 1 and dividing by a expansion factor  $F(v)$ , the velocity distribution at the ionization region is given by

$$g(v_i) = A \cdot (v_i^2 + K) \cdot \exp(-(v_i^2 + K)/v_0^2) / F(v) \quad (3)$$

where  $K$  is  $2LP_0/M$ . The expansion factor

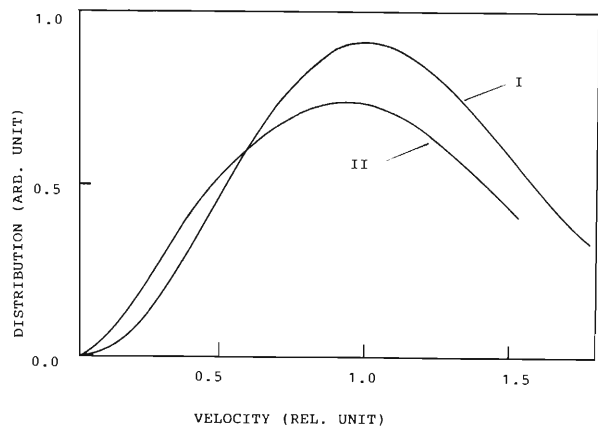


Fig. 3. Velocity distribution of a sodium atomic beam, I, the initial Boltzmann distribution at 800 K, II, a calculated distribution of a sodium atomic beam subjected to a light pressure.

$F(v)$  is obtained by

$$dv_i = F(v) \cdot dv \quad (4)$$

From Eq. 2 we find

$$F(v) = v / \sqrt{v^2 - K} \quad (5)$$

thus we get

$$g(v_i) = A \cdot v_i \sqrt{v_i^2 + K} \cdot \exp(-(v_i^2 + K)/v_0^2) \quad (6)$$

Line II was calculated by Eq. 6 for  $K = 0.36$ . Line II is broader than I, and the peak shifts slightly toward the lower velocities. This results, however, are not in agreement with the present experimental results.

#### Reference

- 1) T. Minowa, H. Katsuragawa, and M. Shimazu: *RIKEN Accel. Prog. Rep.*, **21**, 178 (1987).

### III-2-20. Resonance Ionization Spectroscopy of Lanthanoid Elements

H. Maeda, Y. Mizugai, Y. Matsumoto, A. Suzuki, and M. Takami

In recent years there is much interest in laser application to nuclear physics, in particular in measurements of nuclear spins and multipoles of short-lived nuclei by spectroscopic means.<sup>1)</sup> These physical properties, which provide an important clue for the structural study of nuclei far from stability, manifest themselves as hyperfine structures and isotope shifts in electronic transitions of relevant atoms. For such measurement, resonance ionization spectroscopy is of particular importance since its ultra-high sensitivity is crucial for high resolution hyperfine spectroscopy with a small number of atoms produced by nuclear reactions.

The present work was undertaken with the purpose of supplying spectroscopic data for the laser spectroscopic study of short-lived nuclei provided by RIKEN Ring Cyclotron. Two pulsed dye lasers, pumped by a XeCl excimer laser, were used to ionize target free atoms selectively. The Lanthanoid elements were chosen for the target since all the elements can be ionized resonantly with the two pulsed dye laser beams. As a first stage of such work, ionization spectra were recorded by setting one of the laser frequencies to an intermediate state and scanning the other over auto-ionizing or high Rydberg

states which were subsequently field-ionized. A piece of metal sample was placed in a small Ta crucible and heated up to 1,800 K to form an atomic beam. The atoms were ionized under a 0-4 kV/cm electric field with two laser beams. The produced ions were accelerated and detected with a Ceratron ion detector. The ion current was measured and averaged with a Boxcar Integrator. The laser wavelength was measured by optogalvanic signals in Ne discharge and interference fringes of a solid etalon for interpolation. A schematic diagram of the experimental arrangement is shown in Fig.1.

After preliminary ionization experiments in several metal elements, extensive ionization spectra were recorded for Lu. The relevant energy level diagram is shown in Fig.2. The ground state electronic configuration of Lu is  $4f^{14} 5d6s^2$ . Since the 4f electrons are tightly bound, all the configurations below the ionization energy ( $43,762 \text{ cm}^{-1}$ ) are formed only by excited states of the three  $5d6s^2$  electrons. Nevertheless the electronic level structure of Lu I is very complicated owing to the existence of many terms and interactions among them. As a conse-

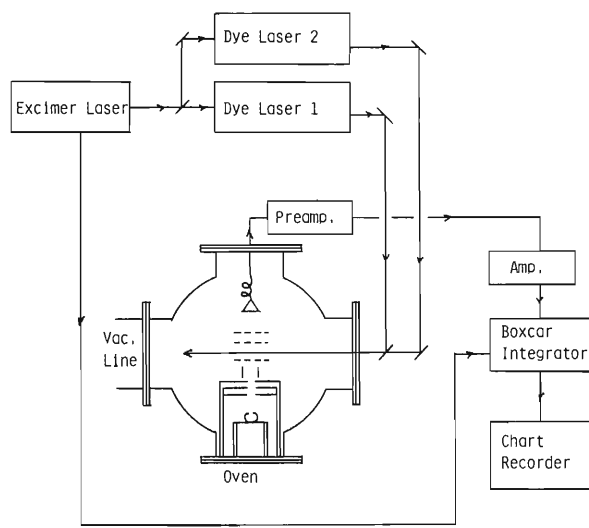


Fig. 1. Schematic diagram for resonance ionization spectroscopy.

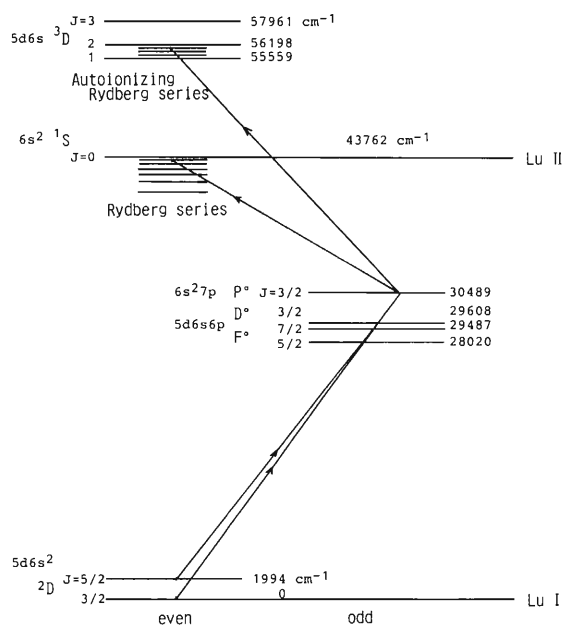


Fig. 2. Energy level diagram of Lu I.

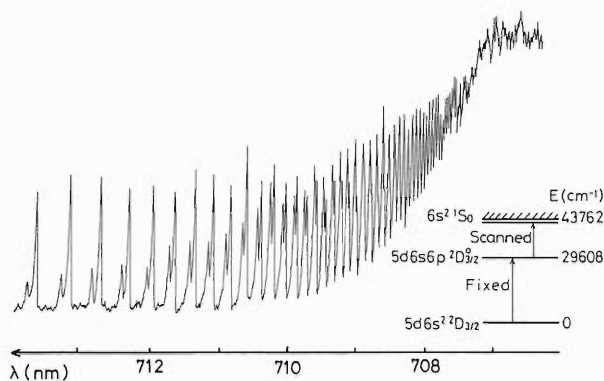


Fig. 3. Rydberg series converging to the first ionization limit of Lu.

quence the energy levels around the first ionization limit is not well analyzed in spite that the lower electronic states are relatively well understood<sup>2)</sup> among Lantanoid elements.

Figure 3 shows a Rydberg series,  $6s^2ns$  and  $6s^2nd$ , converging to the first ionization limit. By changing the intermediate state, three even Rydberg series ( $6s^2ns$ ,  $6s^2nd$ ,  $6s^2ng$ ) were measured. The series show no clear local perturbation and are identified for  $n$  up to 80. Figure 4 shows a forced ionization spectrum under an electric field of 2 kV/cm. Rydberg atoms are very sensitive to an external electric field, which substantially lowers an apparent ionization limit under strong electric field. An interesting feature observed in this spectrum is a very strong signal observed in the forced ionization continuum. Since this signal was observed only when the electric field was strong enough to bring down the ionization limit below this line, we concluded that the signal was due to a doubly-excited odd state which located accidentally among the even Rydberg series, and could be ionized only when it gained oscillator strength by

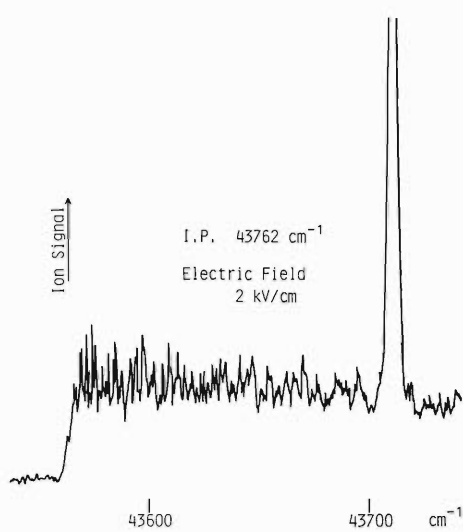


Fig. 4. Forced ionization spectrum of Lu I. The electric field is 2 kV/cm. The intermediate state is the same as in Fig. 3. The ionization limit at zero electric field is  $43762 \text{ cm}^{-1}$ .

Stark mixing with the nearby even Rydberg states. Under a weak electric field, the intensity distribution of the nearby even Rydberg series showed the Fano profile<sup>3)</sup> by the interference of transition matrix elements to the doubly-excited state and the Stark continuum. Similarly autoionizing Rydberg series converging to the  $5d6s$  core excited states were observed. Further analysis and extension of the work to other Lantanoid elements are in progress.

#### References

- 1) See, for example, P. Jaquinot and R. Klapisch: *Rep. Prog. Phys.*, **42**, 773 (1979).
- 2) J.F. Wyart: *Phys. Scr.*, **18**, 87 (1978).
- 3) U. Fano: *Phys. Rev.*, **124**, 1866 (1961).

### III-2-21. Incident Angle Dependence of Al-LVV Auger Spectra for Ar<sup>12+</sup> Impact

A. Koyama, H. Ishikawa, and Y. Sasa

In a previous report,<sup>1)</sup> we showed the  $z_1$ -dependence for energies of Al-LVV Auger peaks for glancing angle incidence of projectiles; with increasing  $z_1$ , the energy of the Auger peak decreased. We also showed that the energy decrease was not due to the Doppler effect of sputtered Al atoms.<sup>1)</sup>

In the present report, we show the incident-angle dependence of the energy of the Al-LVV Auger peak for Ar<sup>12+</sup> impact, and interpret the  $z_1$ - and incident-angle dependence in terms of short-lived decrease in density of valence electrons of Al due to the emission of large amounts of secondary electrons induced by glancing angle incident heavy ion impact.

Experimental conditions are the same as those in the previous report.<sup>1)</sup> Incident energies of Ar<sup>12+</sup> are equal to 1.3 MeV/amu. Electrons are measured at the normal angle to the surface of targets. Al is *in-situ* deposited on polished Mo substrates. The flatness of the target is within the range of 1  $\mu\text{m}$  ups and downs per 1 mm in length. Energies of electrons are measured from 1 to 150 eV.

Figure 1 shows the incident-angle dependence of the energy of Al-LVV Auger peaks for Ar<sup>12+</sup> and electron impact. For the electron impact no dependence on incident-angle can be seen; however, for the Ar<sup>12+</sup> impact a pronounced dependence is seen. For large angle incidence, the energy decrease is rather steep, but almost leveled off as the incidence angles become very small. From extrapolation, we estimate the

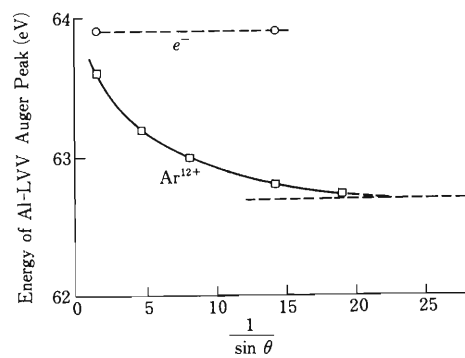


Fig. 1. Incident angle-dependence of energies of Al-LVV Auger peaks for Ar<sup>12+</sup> and electron impact. Incident energy of Ar<sup>12+</sup> corresponds to 1.3 MeV/amu, and that of electrons to 1 keV.

energy of the Auger peak for normal incidence of Ar<sup>12+</sup> to be 63.7 eV, and also that for an extreme glancing angle to be 62.7 eV. In Table 1 the energetical values of Auger peaks for different projectiles are tabulated at an incident angle of 4°, with the estimated values for 90° and 0°, and with differences in these values from that for electron impact,  $\Delta E$ .

Now we discuss the mechanism responsible for the  $z_1$ - and incident angle-dependence; the dependence is caused by the decrease in the density of valence electrons, which will be decreased when a large amount of secondary electrons are emitted, although the lifetime of such density decrease should be short. It is known that the time for relaxation or polarization of valence

Table 1. Energies of Al-LVV Auger peaks for various projectiles for incident angle of 4°, with energetical values at 90° and 0° for Ar<sup>12+</sup> impact estimated from Fig. 1, and with differences in the values from that for electron impact,  $\Delta E$ .

$z_1$	$E_A$ (eV)		Estimated $E_A$ (eV)		$\Delta E$ (eV)		
	$\theta=4^\circ$	$\theta=90^\circ$	$\theta=0^\circ$	$\theta=4^\circ$	$\theta=90^\circ$	$\theta=0^\circ$	
e <sup>-</sup>	63.9						
N <sup>6+</sup>	63.6				0.3		
Ar <sup>12+</sup>	62.8	63.7	62.7	1.1	0.2	1.2	
Xe <sup>9+</sup>	60.9				3.0		

electrons is very short (of the order of plasmon lifetime, nearly  $10^{-16}$  s). It should be noted that the lifetime of the decrease in the density of valence electrons will be longer than that of plasmon damping; the time of real transportation of electron-holes from the surface region is concerned, not the time for polarization of valence electrons.

Energies of Al-LVV Auger electrons are given by

$$E = E_B(L) - E_B(V_1) - E_B(V_2) - C + R, \quad (1)$$

where  $E_B(\nu)$  is the binding energy of  $L$  or valence electrons,  $C$  is the correlation energy of local two electron-holes in an outer shell of the Al lattice atom concerned, and  $R$  is the relaxation energy. It is known that, when there are electron-holes in localized outer shells of the atom concerned together with an inner hole,  $E$  is decreased; energies of satellite lines of Auger electrons are usually lower than that of a diagonal one. The number of holes in the localized outer shell is an important factor to the decrease in  $E$ . However in the case of delocalized outer shells, a density of holes around the lattice atom concerned is important.  $E_B(L)$  and  $E_B(V)$  are increased, and  $R$  is decreased with the increase of the density of valence electron-holes. After all,  $E$  will be decreased with increasing density of the electrons-holes as seen in the usual satellite lines. The density of electron-holes is increased

proportionally with the yields of secondary electrons, that is,  $E$  will be decreased as yields of secondary electrons become high. This is the qualitative explanation for the  $z_1$ -dependence of  $E$ .

Next we discuss the incident-angle dependence of  $E$ .

For very low angle incidence, the length of the region in which electron-holes are produced becomes very large. Thus the components of velocities of the electron-holes effective to the migration of them from the region are those perpendicular to the long axis of the region. On the other hand, for normal incidence, three components are all effective. Therefore the lifetime of the electron holes for small angle incidence  $\tau(g)$  becomes longer than that for normal angle incidence,  $\tau(n)$ . Accordingly the decrease in  $E$  for normal incidence will be less pronounced than that for glancing angle incidence. As the incident angle becomes very low, the lifetime of the electron-holes will become long and nearly  $\tau(g)$ ; that is, saturation will occur. This is the explanation for the incident-angle dependence of  $E$ .

#### Reference

- 1) A. Koyama, H. Ishikawa, and Y. Sasa: *RIKEN Accel. Prog. Rep.*, **21**, 89 (1987); A. Koyama, H. Ishikawa, and Y. Sasa: *Nucl. Instrum. Methods B*, **33**, 308 (1988).

### III-2-22. Excitation of Convoy-Like Electrons by Glancing-Angle Incident Heavy-Ion Impact

A. Koyama, H. Ishikawa, and Y. Sasa

We measured energy spectra of the electrons emitted from a thick Al target for the impact of glancing-angle incident fast heavy ions,  $N^{2+}$ ,  $N^{7+}$ ,  $Ar^{4+}$ , and  $Ar^{12+}$ , with energy corresponding to 1.27 MeV/amu at detection angles from  $1^\circ$  to  $30^\circ$  with respect to the incident beam direction.

The experimental setup is the same as described in a previous report.<sup>1)</sup> The energy analyzer used is an angle resolved one with angle resolution of  $1^\circ$ . Targets are made by *in-situ* vacuum evaporation of Al on Mo or Si substrates with flatness better than  $1 \mu m$  ups and downs per 1 mm length.

Figure 1 shows the energy spectrum of the electrons excited by  $N^{2+}$  incident at an angle of  $0.5^\circ$  and detected at an angle of  $1.5^\circ$  from the surface of the target. For reference the energy spectrum is also shown of usual convoy electrons

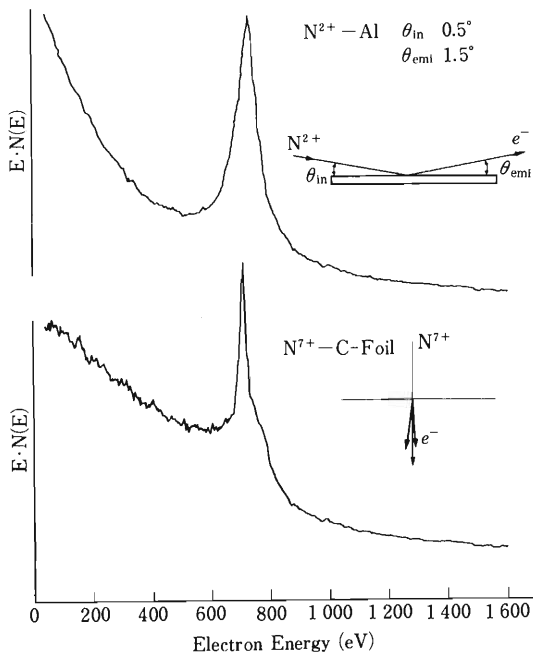


Fig. 1. Energy spectrum of the electrons from Al induced by glancing angle incident  $N^{2+}$  ions, for an incident angle  $0.5^\circ$  and an emission angle  $1.5^\circ$  relative to the surface of the target. For reference a spectrum is also given below for convoy electrons from a C-foil induced by  $N^{7+}$  ions. Energies of projectiles correspond to 1.27 MeV/amu.

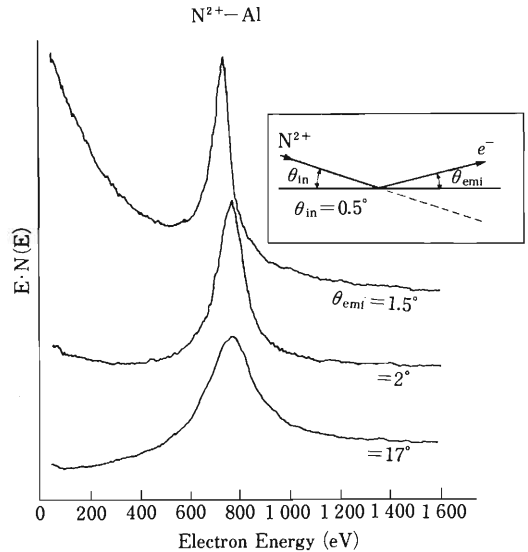


Fig. 2. Energy spectra of the electrons from Al for various emission angles induced by  $N^{2+}$  ions with an incident angle of  $0.5^\circ$ . Each angle is given with respect to the surface of the target.

excited from a C foil for the penetration of  $N^{7+}$ . It is seen that the peak for convoy-like electrons is also very sharp and the energy of the peak is close to that of convoy electrons. Figure 2 shows the energy spectra of electrons induced by  $0.5^\circ$  incident  $N^{2+}$  and detected at various emission angles relative to the beam direction. It is seen that the energy and the width of the peak increase with the emission angle in the angular range shown here (angle is given relative to the beam direction). Figure 3 shows the scattering-angle dependence of the peak energy for various incident angles; (a) for  $N^{2+}$ , (b) for  $N^{7+}$ , (c) for  $Ar^{4+}$ , and (d) for  $Ar^{12+}$ . It is seen that peak energies are given by a function of the scattering angle relative to the beam direction; the peak energy has the same value, only if the scattering angle relative to the beam direction is the same and even if the incident angle or the emission angle relative to the surface of the target is different. For small scattering angles, the peak energies are higher than that expected from usual convoy electrons (the expected value is 692

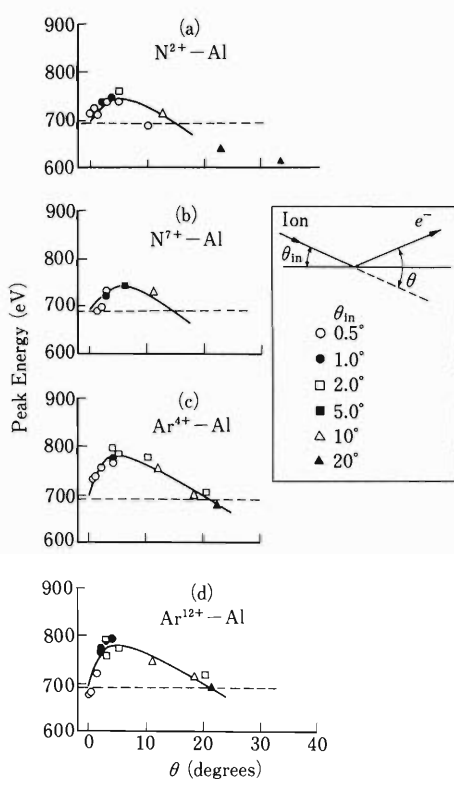


Fig. 3. Emission-angle dependence of peak energies of the electrons induced by projectiles with different incident angles. Incident angles are given with respect to the surface of the target, and emission angles are given with respect to the beam direction.

eV in the present case, and is indicated by the line in Fig. 3). The peak energies are highest at about 5°: 750 eV for  $N^{2+}$  or  $N^{7+}$ , and 800 eV for  $Ar^{4+}$  or  $Ar^{12+}$  ions. They begin to decrease at angles higher than 5°, and become lower than 692 eV at about 13° for N ions, and at about 20° for Ar ions. It should be noted that the scattering-angle dependence of these peak energies is almost the same for  $N^{2+}$  and  $N^{7+}$ , or for  $Ar^{4+}$  and  $Ar^{12+}$ , that is, the peak energies are not dependent on projectiles' charge, but dependent only on atomic number  $z_1$ . This charge independence must be due to the fact that the peak energies are determined only by close collisions, or that they are determined mainly after projectile's charge equilibration.

It is known that for gas targets such an energy increase has not been observed for convoy electrons excited to the direction slightly different from the beam direction. Therefore the prominent energy increase observed here may be due to some kind of solid effect. It may be related to the dynamic surface potential induced by glancing angle incidence of fast high charge projectiles.

#### Reference

- 1) A. Koyama, Y. Sasa, and M. Uda: *RIKEN Accel. Prog. Rep.*, **18**, 86 (1984).

### III-2-23. $^{61}\text{Ni}$ Mössbauer Studies of Heusler Alloys

T. Okada, Y. Kobayashi, M. Katada, H. Sano, M. Iwamoto, and F. Ambe

In spite of many experimentally undesirable nuclear properties,  $^{61}\text{Ni}$  can be a powerful probe in solid-state physics and radiochemistry as a sole Mössbauer nuclide other than  $^{57}\text{Fe}$  in the iron-group transition elements. About twenty years ago, we made the first  $^{61}\text{Ni}$  Mössbauer study of the hyperfine magnetic fields on various Ni-containing oxides with a spinel structure.<sup>1)</sup> This paper reports  $^{61}\text{Ni}$  Mössbauer measurements we started recently on Heusler alloys to elucidate the physical and chemical state of the Ni atoms in these alloys.

A source nuclide  $^{61}\text{Cu}(\rightarrow ^{61}\text{Ni})$  was produced by nuclear reactions,  $^{58}\text{Ni}(\alpha, p)^{61}\text{Cu}$  and  $^{58}\text{Ni}(\alpha, n)^{61}\text{Zn} \rightarrow ^{61}\text{Cu}$ . A thin Ni-V(84-16 at%) alloy plate (18 mm  $\times$  18 mm  $\times$  1 mm) covered with 80  $\mu\text{m}$  Al foil was irradiated for 2 h with 25.5 MeV  $\alpha$ -particles from the cyclotron, and was used as a source without annealing. The experimental procedure of the  $^{61}\text{Ni}$  Mössbauer measurements was reported previously.<sup>1)</sup> Figure 1 shows the decay scheme of  $^{61}\text{Ni}$ . The energy of the  $^{61}\text{Ni}$  Mössbauer  $\gamma$  ray is 67.5 keV. It is necessary to maintain both a source and an absorber at low temperatures because the Mössbauer transition energy is high and the Debye-Waller factors are low. A cryostat, Model HD-700 (Ranger Inc.), was used after slight improve-

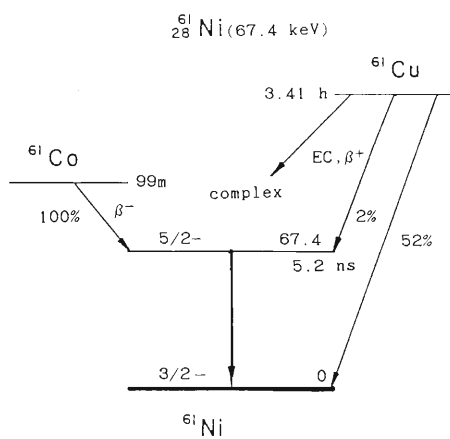


Fig. 1. Decay scheme of  $^{61}\text{Ni}$ .

ment for cooling both source and absorber down to liquid-helium and -nitrogen temperatures.

Heusler alloys are a class of concentrated, ferromagnetic ones of a general composition of  $\text{A}_2\text{BC}$ . The structure is designated as  $\text{L}2_1$ , with A atoms forming a simple cubic matrix and B and C occupying the alternate body centres in the cubic structure.

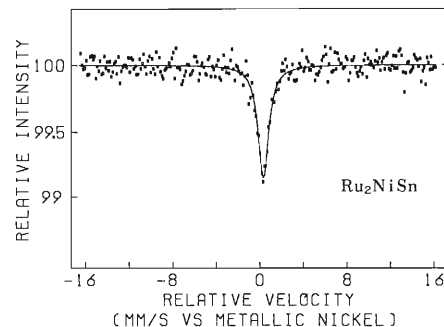


Fig. 2.  $^{61}\text{Ni}$  Mössbauer spectrum of  $\text{Ru}_2\text{NiSn}$  at liquid-nitrogen temperature. The isomer shift is given relative to the Ni metal. The curve is the result of fitting single Lorentzian.

In Fig. 2 is shown the  $^{61}\text{Ni}$  Mössbauer spectrum of  $\text{Ru}_2\text{NiSn}$  above the Curie temperature. This is a case of non-magnetic Ni in the matrix. A typical group of this class of alloys (e.g.  $\text{Ni}_2\text{MnSn}$ ) is known to have magnetic moments localized on the Ni and Mn atoms at the A and B sites. In such a system of  $\text{Ni}_2\text{MnC}$  (C is a typical element of the group III to V in the periodic table), the magnetic moment and the electronic state of the Ni atoms have not been sufficiently elucidated yet. We are studying the physical and chemical properties of the Ni atoms in the system  $\text{Ni}_2\text{MnGe}$  utilizing the hyperfine magnetic field and the isomer shift from the  $^{61}\text{Ni}$  Mössbauer spectra.

#### Reference

- 1) H. Sekizawa, T. Okada, S. Okamoto, and F. Ambe: *J. Phys.*, **32**, C1-326 (1971).

### III-2-24. $^{57}\text{Fe}$ Mössbauer Study on Superconductor Oxides

T. Okada, K. Asai, N. Sakai, Y. Sasa, and T. Yamadaya\*

In spite of a great deal of endeavor of many groups worldwide, the origin of Cooper pairing in high- $T_c$  oxide superconductors still remains unelucidated. A  $\text{YBa}_2\text{Cu}_3\text{O}_{7-y}$  oxide, which is so-called a 1-2-3 compound, has a superconducting critical temperature well above 90 K and so much effort has been devoted to the studies on its chemical and physical properties. Metallic dopants directed at Cu sites in this Cu oxide superconductor are known to systematically alter crystallographic, magnetic, and superconducting properties. To understand these changes, it is crucial to establish the site occupancy and oxygen stoichiometry of the doped materials. Although some microscopic studies on the electronic structures of this material by using hyperfine techniques have been reported by several groups including us,<sup>1-3)</sup> interpretations and conclusions of the experimental results are slightly different among the groups. In this paper, we report the  $^{57}\text{Fe}$  Mössbauer study on the crystallites  $\text{YBa}_2\text{Cu}_{3-x}\text{Fe}_x\text{O}_{7-y}$  ( $x=0.03$ ) aligned along the  $c$  axis by applying a magnetic field. Mössbauer spectra were taken at room temperature with a conventional driving system, and analyzed with a FACOM780.

The preparation of  $\text{YBa}_2\text{Cu}_{3-x}\text{Fe}_x\text{O}_{7-y}$  oxides was described in a previous report.<sup>1)</sup> These oxides obtained with dopant concentrations from  $x=0.03$  up to  $x=0.3$  were found to be of a single phase from X-ray diffraction analysis. We try to elucidate the possible site configuration by establishing for the first time the sign, spatial orientation, and asymmetry parameter  $\eta = (V_{xx} - V_{yy}) / V_{zz}$  of the electric-field-gradient (EFG) tensor. In Mössbauer measurements on single crystals, the ratio of the integrated area in a quadrupole doublet is no longer unity as it is in polycrystalline specimens. This ratio  $I^-/I^+$  changes with the angle  $\theta$  as in Eq. 1 when  $V_{zz} < 0$  and  $\eta = 0$ ,

$$I^- / I^+ = 3(1 + \cos^2\theta) / (2 + 3\sin^2\theta) \quad (1)$$

where  $I^-$  and  $I^+$  are the integrated areas in the low and high energy, respectively, and  $\theta$  is the

angle between the  $\gamma$ -ray direction and the principal axis of EFG. The measurements on single crystal are desired to clarify the site configurations of the Fe ions in the  $\text{YBa}_2\text{Cu}_{3-x}\text{Fe}_x\text{O}_{7-y}$  system. However, there are no single crystals available containing enriched  $^{57}\text{Fe}$  ions. The measurement was made possible by use of oriented crystallites with  $\gamma$  ray transmitted at various tilt angles ( $\phi$ ) relative to the aligned axis ( $c$  axis). The orientation of  $\text{YBa}_2\text{Cu}_3\text{O}_{7-y}$  crystallites along the  $c$  axis using the magnetic field was demonstrated by Farrell, *et al.*<sup>4)</sup> using the same procedure, we have now oriented the  $\text{YBa}_2\text{Cu}_{2.97}\text{Fe}_{0.03}\text{O}_{7-y}$  crystallites and confirmed that they are oriented along the  $c$  axis by means of an X-ray diffraction measurement.

The two X-ray diffraction patterns of  $\text{YBa}_2\text{Cu}_{2.97}\text{Fe}_{0.03}\text{O}_{7-y}$  oxides are shown in Fig. 1. The patterns (A) and (B) were measured on the samples unoriented and oriented along  $c$  axis by applying a magnetic field of 20 kOe, respectively. These patterns were analyzed by utilizing Sasa's method<sup>5)</sup> in order to obtain the orientation degree  $h$  of crystallites. From the pattern (B) in Fig. 1, it is clear that the crystallites are oriented along  $c$  axis, and the  $h$  is obtained to be  $4.0 \times 10^{-2}$ . It

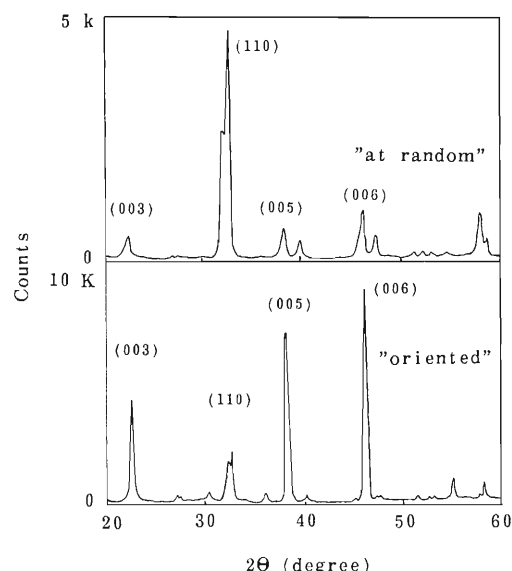


Fig. 1. X-ray powder patterns of  $\text{YBa}_2\text{Cu}_{2.97}\text{Fe}_{0.03}\text{O}_{7-y}$  unoriented (A) and oriented by applying the magnetic field of 20 kOe (B).

\* Faculty of Literature and Science, Yokohama City University.

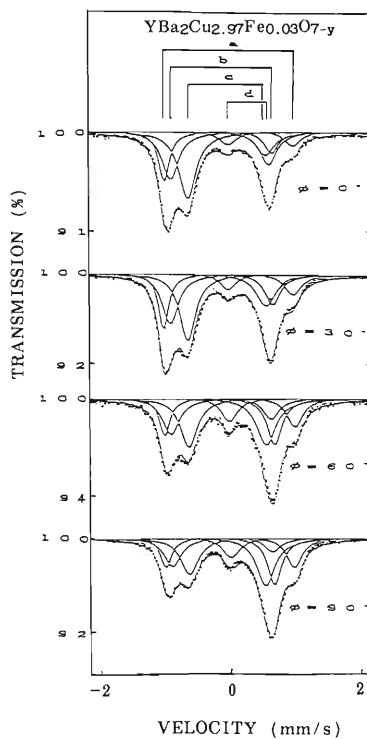


Fig. 2.  $^{57}\text{Fe}$  Mössbauer spectra of the oriented  $\text{YBa}_2\text{Cu}_{2.97}\text{Fe}_{0.03}\text{O}_{7-y}$  measured at room temperature with various tilt angles  $\phi$ .

means that the sample aligned by applying the magnetic field are almost oriented. Figure 2 shows typical Mössbauer spectra of the oriented  $\text{YBa}_2\text{Cu}_{2.97}\text{Fe}_{0.03}\text{O}_{7-y}$  crystallites with various angles  $\phi$  between the  $\gamma$ -ray direction and the  $c$  axis. The spectra of the samples comprise at least four different doublets, a, b, c, and d, with quadrupole splittings of 2.0, 1.6, 1.3, and 0.5 mm/s, respectively. The observed intensity asymmetries  $I^- / I^+$  at the four sites as a func-

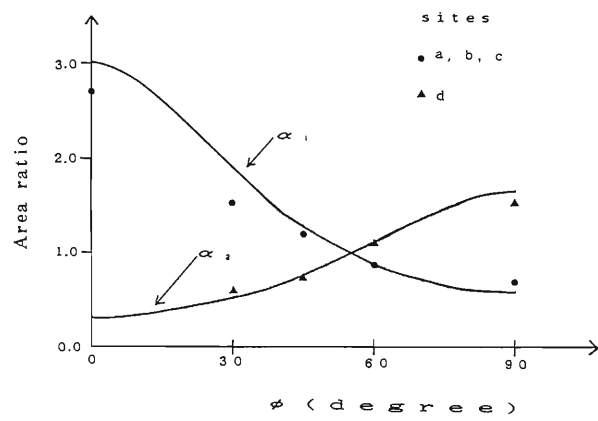


Fig. 3. Observed intensity asymmetries  $I^- / I^+$  at the four sites as a function of the tilt angles  $\phi$ . The upper solid line is obtained from Eq. 1 when  $\theta = \phi$  and  $V_{zz} < 0$ . The lower one is the reversed value of Eq. 1 when  $\theta = \phi$  and  $V_{zz} > 0$ .

tion of the tilt angles are shown in Fig. 3. The values of  $I^- / I^+$  at the a, b, and c sites are nearly on the upper solid line when  $\theta = \phi$  and  $V_{zz} < 0$ . The values of  $I^- / I^+$  at the d sites are on the lower one when  $\theta = \phi$  and  $V_{zz} > 0$ .

These results are being subjected to discussion.

#### References

- 1) T. Okada, N. Sakai, K. Asai, Y. Toba, and T. Yamadaya: *Hyperfine Interact.*, **42**, 1231 (1988).
- 2) D. McDanel, W. Huff, B. Goodman, G. Lemon, D.E. Farrel, and B.S. Chandrasekhar: *Phys. Rev. B*, **38**, 11313 (1988).
- 3) V. Sedykh, S. Nasu, and F.E. Fujita: *Solid State Commun.*, **67**, 1063 (1988).
- 4) D. Farrel, B.S. Chandrasekhar, M.R. McGuire, M.M. Fang, V.G. Kogan, J.R. Clem, and K. Finnemore: *Phys. Rev. B*, **36**, 4025 (1987).
- 5) M.Uda and Y. Sasa: *J. Solid State Chem.*, **46**, 121 (1983).

### III-2-25. Motion of Kr-Bubbles in Krypton-Implanted Aluminum

H. Yamaguchi,\* I. Hashimoto,\* E. Yagi, and M. Iwaki

The random motion of some kinds of inert gas bubbles during isothermal annealing has been observed by several investigators. Willertz and Shewmon studied the motion of the He gas bubbles in Au and Cu foils by measuring the rate of out-diffusion of the bubbles from the foil surface and a change in distance between them during isothermal annealing, and demonstrated that the diffusion rate of the He bubbles in both foils is smaller than that predicted by a surface diffusion model.<sup>1)</sup> The Brownian motion of He bubbles in V during isothermal annealing at 1,223 K was investigated by *in-situ* hot stage transmission electron microscopy (TEM) by Tyler and Goodhew, who concluded that the growth of the bubbles is due to their migration and coalescence.<sup>2)</sup> On the basis of these results, the kinetics of motion is explained in terms of either surface diffusion or ledge nucleation at faceted surfaces, thus suggesting that the migration mechanism of inert gas bubbles seems to be dependent on the materials. In the present study, we investigated which mechanism controls the random motion of Kr bubbles in Al during annealing.

Aluminum foils of about 130  $\mu\text{m}$  in thickness prepared from an ingot of 99.99% purity by rolling were used to prepare single crystals by strain annealing. Thin foil specimens suitable for TEM were prepared by chemical-and electro-lytical-polishing. Kr implantation into the specimens was carried out with 50 keV Kr<sup>+</sup> ions in a vacuum of  $3 \times 10^{-6}$  Torr at room temperature to a fluence of  $10^{16}\text{Kr/cm}^2$  by using a RIKEN low-current implanter. In order to specify the position of Kr bubbles in TEM observation, Au particles were deposited after the implantation as reference points on both top and bottom surfaces of each specimen by a vacuum deposition method.

The specimen was mounted with a Cu mesh and was observed with an electron microscope operating at 100 kV. The specimen was then removed from the specimen holder and annealed in a vacuum capsule together with the Cu mesh

at various fixed temperatures in the range from 573 to 633 K for 10 min. The annealed specimen was observed again to examine the change in relative position of Kr bubbles. Micrographs were taken under the same diffraction condition before and after each annealing using a tilting and rotating specimen stage. They indicated that no growth of Kr bubbles took place during the annealing.

The radii and the centers of about 100 bubbles selected from a micrograph were determined as follows. The image contrast of the bubbles printed on a photographic paper was taken in an image scanner (EPSON, GT-D3000V) as a function of the position, and this information was transferred to a personal computer (PC-9801XL). The values of the radii and the centers of bubbles were obtained accurately after making a minor correction for both magnification and inclination of the specimen by using either three Au particles as mentioned above or large bubbles which did not move during isothermal annealing as reference points. The displacement of a bubble was detected by measuring a distance between centers of the bubble before and after the annealing. The accuracy in the measurement of the distance was estimated at 0.7 nm for a bubble of 2 nm in radius.

Figure 1 shows typical electron micrographs of

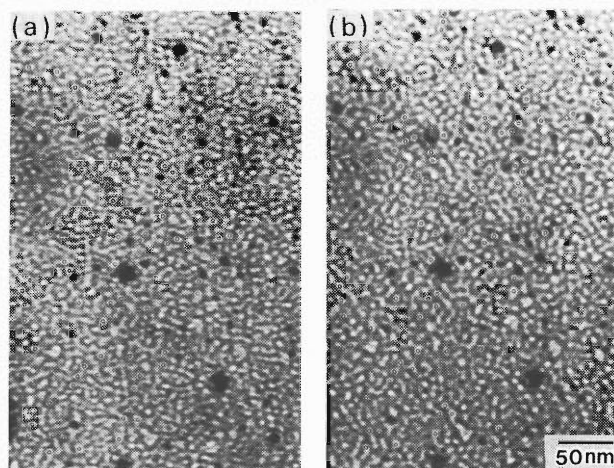


Fig. 1. Typical electron micrographs of Kr bubbles; (a) as-implanted and (b) after annealing at 603 K for 10 min.

\* Department of Physics, Faculty of Science, Science University of Tokyo.

Kr bubbles before (a) and after (b) the annealing at 603 K for 10 min, where white and dark spots correspond to the bubbles and the reference points of gold particles, respectively. The density and the radius of bubbles are estimated at  $8 \times 10^{16}/\text{cm}^3$  and about 2 nm on an average, respectively.

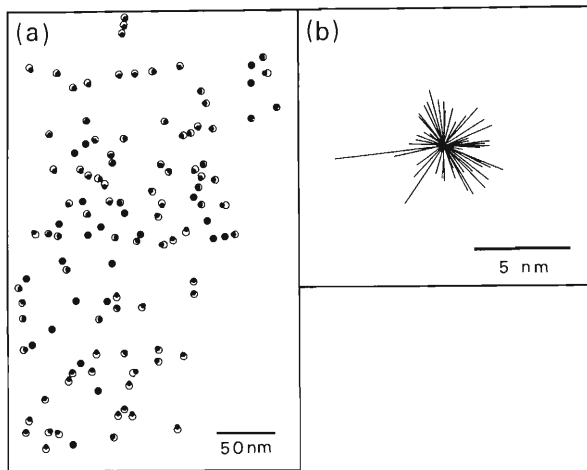


Fig. 2. Behavior of  $^{114}\text{Kr}$  bubbles indicated by small open circles in Fig. 1 on annealing at 603 K for 10 min; (a) the positions of these bubbles before ( $\circ$ ) and after ( $\bullet$ ) annealing, and (b) the radial displacement of these bubbles, in which the magnitude of displacement is shown by the length of lines.

Figure 2 (a) demonstrates the displacement of bubbles before and after annealing. From this result, the distribution of the displacement of these bubbles is shown in Fig. 2 (b), in which the center of each bubble before the annealing is taken as an origin. The result shows that bubbles move in all directions during annealing, in accord with the assumption that bubbles migrate at random.

The radial moving distance of each bubble,  $R$ , during isothermal annealing for a given time  $t$  (Fig. 2(b)) is the distance projected on the horizontal film plane. In such a two-dimensionally projected distribution, the mean square moving distance is given by

$$\langle R^2 \rangle = 4D_B t \quad (1)$$

where  $D_B$  is the diffusion coefficient of bubbles. From the  $\langle R^2 \rangle$  value observed for each bubble,  $D_B$  is calculated. This method has been used by at least other three investigators under isothermal conditions.<sup>1-3)</sup> Figure 3 shows the relation between  $D_B$  and the inverse of annealing temperature  $1/T$  (indicated by  $\circ$ ), together with the diffusion coefficient  $D$  obtained previously from the extraction experiment of Kr in Al (indicated by  $\triangle$ ).<sup>4)</sup> It can be seen that  $\ln D_B$  versus  $1/T$  plot

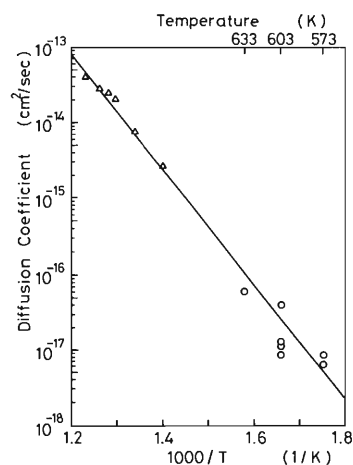


Fig. 3. Diffusion coefficients versus  $1/T$ .

is approximately on an extrapolated line of that obtained from the extraction experiment of Kr atoms.<sup>4)</sup> The activation energy for the motion of Kr bubbles calculated from the plot in Fig. 3 is 1.50 eV, which coincides with that for self-diffusion in Al.<sup>5)</sup> As reported previously, in an as-implanted state of this specimen Kr bubbles are in a solid phase epitaxially aligned with the host Al matrix.<sup>6)</sup> The melting point of solid Kr was estimated at 618 K.<sup>6)</sup> It should be noted that values of both  $D$  and  $D_B$  fell on the same line irrespective of the state of Kr bubbles (solid, liquid, or gas state) (Fig. 3). If the mechanism of the motion of bubbles changes abruptly at some annealing temperature by reflecting the change in their state, the values of  $D_B$  would not be on the extrapolation line of  $D$  versus  $1/T$ . Therefore, we believe that the motion of Kr bubbles in Al is controlled by the volume diffusion of Al atoms over the whole temperature range. This means that the Kr bubbles move at random and reach the surface of the foil specimen to be released. More detailed descriptions are given in Ref. 7.

#### References

- 1) L.E. Willertz and P.G. Shewmon: *Metall. Trans.*, **1**, 2217 (1970).
- 2) S.K. Tyler and P.J. Goodhew: *J. Nucl. Mater.*, **92**, 201 (1980).
- 3) M.E. Gulden: *J. Nucl. Mater.*, **23**, 30 (1967).
- 4) K. Takaishi, T. Kikuchi, K. Furuya, I. Hashimoto, H. Yamaguchi, E. Yagi, and M. Iwaki: *Phys. Status Solidi A*, **95**, 135 (1986).
- 5) T.S. Lundy and J.F. Murdock: *J. Appl. Phys.*, **33**, 1671 (1962).
- 6) I. Hashimoto, H. Yorikawa, H. Mitsuya, H. Yamaguchi, K. Takaishi, T. Kikuchi, K. Furuya, E. Yagi, and M. Iwaki: *J. Nucl. Mater.*, **149**, 69 (1987).
- 7) H. Yamaguchi, I. Hashimoto, H. Mitsuya, K. Nakamura, E. Yagi, and M. Iwaki: *J. Nucl. Mater.*, **161**, 164 (1989).

### III-2-26. Lattice Location Study on Kr Atoms in Aluminium by Means of a Channelling Method

E. Yagi

It has been known that the heavier inert gases (Ar, Kr, and Xe) implanted into various fcc metals precipitate in bubbles into an fcc solid phase epitaxially with a host matrix.<sup>1,2)</sup> The evolution and the annealing behaviour of such precipitates (bubbles) have been investigated mostly by transmission electron microscopy.<sup>3-7)</sup> In the present study the lattice location of Kr atoms implanted into Al crystals at room temperature was investigated by means of a channelling method. The lattice location study in such a fine scale will give information on the bubble nucleation in an early stage of implantation.

Aluminium single crystals of 99.999% purity were chemically and electrolytically polished, and then annealed in a vacuum of  $10^{-6}$  Torr at 823 K for 7 h. Kr<sup>+</sup> implantation was carried out at room temperature at 50 keV at a dose rate of  $3.2 \times 10^{12} \text{ cm}^2/\text{s}$  to two different doses,  $4 \times 10^{14} \text{ cm}^2$  and  $1 \times 10^{15} \text{ cm}^2$ . The channelling angular scan was made with respect to  $\langle 1\ 0\ 0 \rangle$ ,  $\langle 1\ 1\ 0 \rangle$ , and  $\langle 1\ 1\ 1 \rangle$  axes by means of backscattering with a 1.0 MeV He<sup>+</sup> beam accelerated by a tandem accelerator. The beam was collimated to give a divergence of less than 0.076°. The area irradiated was 0.78 mm<sup>2</sup> and the beam current was 1-2 nA. In the angular scan, to minimize the irradiation effect by an analysis-beam, the measurement was started at an incident angle  $\psi$  for the parallel incidence to the channel ( $\psi=0^\circ$ ). For each value of  $\psi$  backscattering yields were accumulated up to the irradiation dose of  $3 \mu\text{C}$  (the  $\langle 1\ 0\ 0 \rangle$  and  $\langle 1\ 1\ 0 \rangle$  channels) or  $3.3 \mu\text{C}$  (the  $\langle 1\ 1\ 1 \rangle$  channel) for the  $4 \times 10^{14} \text{ Kr/cm}^2$  implantation, and  $0.9 \mu\text{C}$  (the  $\langle 1\ 0\ 0 \rangle$  channel) or  $1.2 \mu\text{C}$  (the  $\langle 1\ 1\ 0 \rangle$ , and  $\langle 1\ 1\ 1 \rangle$  channels) for the  $1 \times 10^{15} \text{ Kr/cm}^2$  implantation.

Channelling angular profiles for as-implanted specimens are shown in Fig. 1. As described in previous papers,<sup>8,9)</sup> these results suggest that the Kr atoms are distributed over random (R) sites, substitutional (S) sites, tetrahedral (T) and octahedral (O) sites. The distribution of Kr atoms over these sites was estimated from the fitting of calculated angular profiles to the observed ones. The calculation was performed on a basis of a

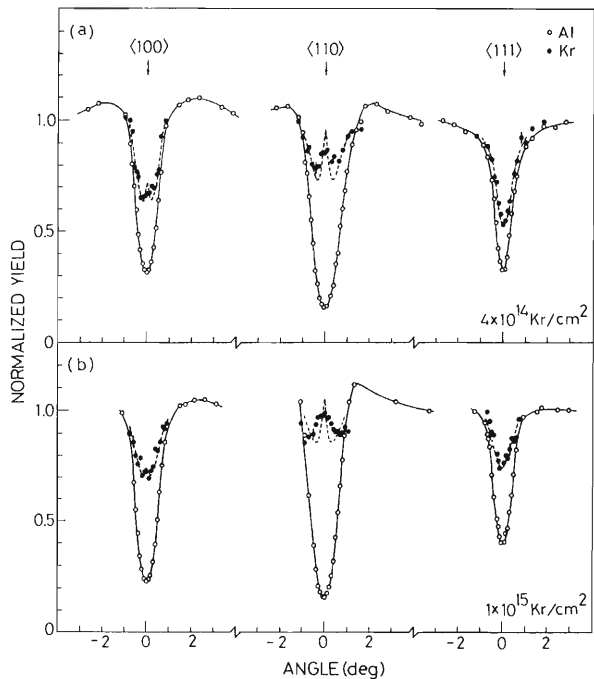


Fig. 1. Channelling angular profiles of backscattering yields of He ions from Al and implanted Kr atoms on the as-implanted specimens for (a)  $4 \times 10^{14} \text{ Kr/cm}^2$  and  $1 \times 10^{15} \text{ Kr/cm}^2$  implantations. The dotted curves are calculated ones for the distribution with (a) 30% of Kr atoms at R-sites, 40% at S-sites, 10% at T-sites and 20% at O-sites, and (b) 57% of Kr atoms at R-sites, 23% at S-sites, 3% at T-sites and 17% at O-sites.

multi-string model.

The observed profiles were well fitted with calculated ones for a distribution with 30-32% of the Kr atoms at R-sites, 40-42% at S-sites, 8-10% at T-sites and 18-20% at O-sites for the  $4 \times 10^{14} \text{ Kr/cm}^2$  implantation, and with 55-57% at R-sites, 23-25% at S-sites, 3-5% at T-sites and 15-17% at O-sites for the  $1 \times 10^{15} \text{ Kr/cm}^2$  implantation. Examples of calculated profiles are indicated by the dotted curves in Fig. 1.

The variation of the distribution with implantation dose is shown in Fig. 2(a) together with the previous result for the  $1 \times 10^{16} \text{ Kr/cm}^2$  implantation, for which Kr atoms precipitate in bubbles into a solid phase (solid bubbles).<sup>7)</sup> The number density of the Kr atoms located at vari-

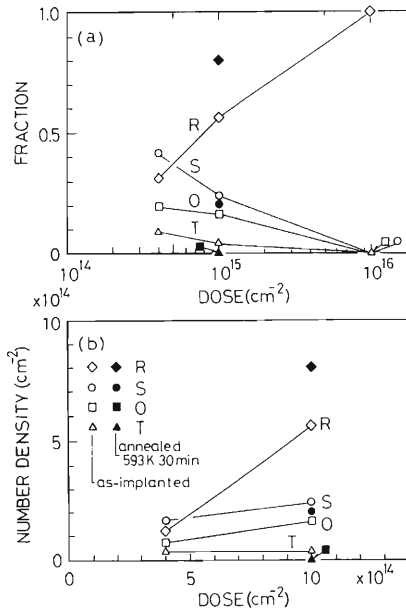


Fig. 2. Dose dependence of the distribution of Kr atoms. (a) The fraction of Kr atoms located at various kinds of sites, and (b) the number density of Kr atoms located at various kinds of sites.

ous kinds of sites were estimated by multiplying the implantation dose by the fraction of occupancy; they are shown in Fig. 2(b).

The irradiation effect on the distribution of Kr atoms was investigated on the  $4 \times 10^{14} \text{ Kr/cm}^2$  implanted specimen (Fig. 3). After having obtained the  $\langle 100 \rangle$  and  $\langle 111 \rangle$  angular profiles shown in Fig. 1(a), measurements were made again around  $\psi = 0^\circ$ , respectively. These results indicate that the fraction of R-site occupancy increased (from 31 to 55% in the case of  $\langle 111 \rangle$  channel) due to the analysis-beam irradiation in the previous measurement run. Therefore, it is concluded that the ion irradiation enhances the fraction of R-site occupancy.

As described in previous papers, the T- and O-site occupancies are considered to be a result of strong interaction between Kr atoms and vacancies introduced during implantation; the Kr atoms trap multiple vacancies and, accordingly, are displaced to T- or O-sites to take configuration similar to trivacancy ( $\text{KrV}_4$ ) or pentavacancy ( $\text{KrV}_6$ ) configuration (Fig. 4).<sup>8,9)</sup> The R-site occupancy is considered to represent the Kr atoms in precipitates.

The dose dependence of the distribution of Kr atoms shown in Fig. 2 is considered to represent the evolution of Kr precipitates (Kr bubbles) under implantation at room temperature. As seen from Fig. 2(b), with increasing dose from  $4 \times 10^{14} \text{ Kr/cm}^2$  to  $1 \times 10^{15} \text{ cm}^{-2}$ , the number density of the T-site occupancy remained approximately un-

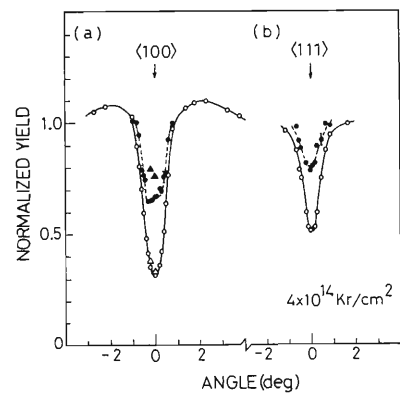


Fig. 3. Effect of ion irradiation on the distribution of Kr atoms in the  $4 \times 10^{14} \text{ Kr/cm}^2$  implanted specimen. (a) Just after having obtained the  $\langle 100 \rangle$  angular profile ( $\circ$ ,  $\bullet$ ) shown in Fig. 1(a), measurements were made again for  $\psi \approx 0^\circ$ . The results are indicated by triangular symbols ( $\triangle$ ,  $\blacktriangle$ ). (b)  $\langle 111 \rangle$  angular profiles obtained one year after the measurements of the  $\langle 111 \rangle$  angular profiles shown in Fig. 1(a), and around specimen area which had been already analyzed. During one year the specimen had been kept in air at room temperature. Full curves and dotted curves were drawn only to guide the eye.

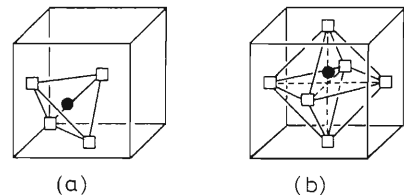


Fig. 4. Proposed vacancy-cluster configurations for (a) a trivacancy and (b) a pentavacancy.<sup>10)</sup> The open squares and closed circles represent vacancies and interstitial atoms, respectively. (The interstitial atom in a pentavacancy is displaced slightly from an O-site.) The closed circles may be considered to represent Kr atoms in the present case.

changed, whereas that of the O-site occupancy became about 2.5 times larger. This behaviour suggests that the Kr-vacancy complexes like  $\text{KrV}_4$  (T-site occupancy) trap still more vacancies introduced under implantation and grow to larger one like  $\text{KrV}_6$  (O-site occupancy). As to the S- and R-site occupancies, the number density of the S-site occupancy increased only by a factor of 1.5, while that of the R-site occupancy (Kr atoms in precipitates) increased more rapidly. As described above, irradiation enhances the fraction of the R-site occupancy, *i.e.*, radiation-enhanced or radiation-induced precipitation. As Kr atoms can move only when they are assisted by mobile vacancies, the implantation-introduced vacancies enhances diffusion of Kr atoms.

From these results it is considered that in the early stage of implantation small Kr-vacancy complexes such as  $\text{KrV}_4$  and  $\text{KrV}_6$  are formed and act as trapping centres for Kr atoms and vacancies. When the implantation is continued, most of the implanted Kr atoms migrate to be trapped by the Kr-vacancy complexes or already existing small precipitates, and the precipitation proceeds; the Kr-vacancy complexes act as nucleation centres for Kr precipitates. More detailed descriptions are given in Ref. 11.

#### References

- 1) A. vom Felde, J. Fink, Th. Müller-Heinzerling, J. Pflüger, B. Scheerer, G. Linker, and D. Kaletta: *Phys. Rev. Lett.*, **53**, 922 (1984).
- 2) C. Templier, C. Jaouen, J.-P. Rivièvre, J. Delafond, and J. Grilhé: *C. R. Acad. Sci. Paris*, **299**, 613 (1984).
- 3) J. H. Evans and D. J. Mazey: *J. Phys. F: Met. Phys.*, **15**, L1 (1985).
- 4) R. C. Birtcher and W. Jäger: *Nucl. Instrum. Methods Phys. Res. B*, **15**, 435 (1986).
- 5) C. Templier, H. Garem, J.-P. Rivièvre, and J. Delafond: *Nucl. Instrum. Methods Phys. Res. B*, **13**, 24 (1986).
- 6) S. E. Donnelly and C. J. Rossouw: *Nucl. Instrum. Methods Phys. Res. B*, **13**, 485 (1986).
- 7) I. Hashimoto, H. Yorikawa, H. Mitsuya, H. Yamaguchi, K. Takaishi, T. Kikuchi, K. Furuya, E. Yagi, and M. Iwaki: *J. Nucl. Mater.*, **149**, 69 (1987).
- 8) E. Yagi: *Phys. Status Solidi A*, **104**, K13 (1987).
- 9) E. Yagi, M. Iwaki, K. Tanaka, I. Hashimoto, and H. Yamaguchi: *Nucl. Instrum. Methods Phys. Res. B*, **33**, 724 (1988).
- 10) G. H. Vineyard: *Discuss. Faraday Soc.*, No. 31, 7 (1961).
- 11) E. Yagi: *Nucl. Instrum. Methods Phys. Res. B*, **39**, 68 (1989).

### III-2-27. Evaluation of Crystalline Quality and Irradiation Effects of a Bi-Sr-Ca-Cu-O System High Transition Temperature Superconductor by Rutherford Backscattering Spectroscopy

T. Kobayashi, S. Takekawa,\* M. Iwaki, H. Sakairi, and M. Aono

The Bi-Sr-Ca-Cu-O system is an attractive superconductor because it is synthesized without any rare earth and virulence elements and  $\text{BiSrCaCu}_2\text{O}_x$  samples were found to have the transition temperature  $T_c$  as high as 105 K. It endures moreover the environmental water. Recently a single crystal of the above system, large enough for physical analyses, become available, which is prepared by a floating zone (FZ) method using infrared heating at the National Institute for Research in Inorganic Materials.

In this paper, Rutherford backscattering spectroscopy (RBS) was applied to this single crystal to study the structural quality by using the sensitivity of RBS to lattice imperfections. The effects of ion bombardment on the structure were also examined by using RBS probe ion itself during the RBS measurement.

The approximate dimensions of a specimen crystal are 5 mm in length, 2 mm in width and 0.03 mm in thickness. Electron probe X-ray analysis determined the composition as  $\text{Bi}_{2.2}\text{Sr}_{1.8}\text{Ca}_{1.0}\text{Cu}_{2.0}\text{O}_x$ . X-ray diffraction analysis

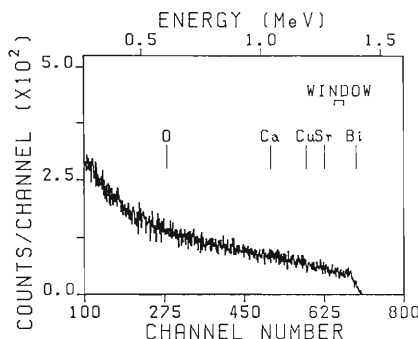


Fig. 1. RBS spectrum of a single crystal of the Bi-Sr-Ca-Cu-O system high  $T_c$  superconductor measured with a 1.5 MeV  ${}^4\text{He}^+$  beam in the  $c$ -axis after  $3.30 \times 10^{15} \text{ He}/\text{cm}^2$  irradiation.

revealed that the largest face of the specimen is parallel to the  $c$ -plane. An electric resistance measurement gave the  $T_c$  value of 91 K. RBS experiments were carried out with a  ${}^4\text{He}^+$  beam accelerated to 1.5 MeV with a Cockcroft-Walton-type tandem accelerator (Tandetron) and collimated to  $0.065^\circ$  in divergence. The diameter of the beam spot on the specimen surface was 1.0 mm, when the current intensity was 0.7 nA and the flux density was  $5.6 \times 10^{11} \text{ He}/\text{cm}^2 \cdot \text{s}$ . The energy of backscattered  ${}^4\text{He}$  particles was analyzed with a surface barrier solid-state detector placed at a scattering angle of  $150^\circ$  at a detecting solid angle of 0.03 sr and with the energy resolution of the detector of 20 keV. The specimen temperature was ambient during RBS experiments.

The RBS spectrum of a  $\text{Bi}_{2.2}\text{Sr}_{1.8}\text{Ca}_{1.0}\text{Cu}_{2.0}\text{O}_x$  crystal, as shown in Fig. 1, was obtained with 1.5MeV  ${}^4\text{He}^+$  ions incident parallel to the  $c$ -axis after  $3.30 \times 10^{15} \text{ He}/\text{cm}^2$  irradiation. Respective energy positions of  ${}^4\text{He}$  ions backscattered by

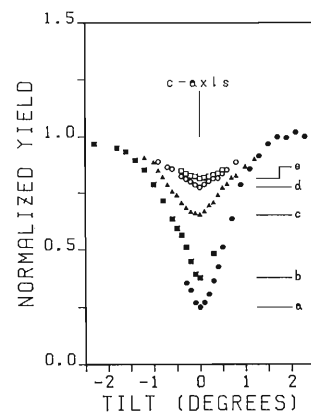


Fig. 2. Angular dependence of the intensity of  ${}^4\text{He}$  particles scattered from bismuth atoms in single crystal of the Bi-Sr-Ca-Cu-O system high  $T_c$  superconductor. The dependence was measured by changing the direction of an incident  ${}^4\text{He}^+$  beam around the  $c$ -axis. Solid circles, solid squares, solid triangles, open circles and open squares represent first, second, third, fourth, and fifth channeling angular scan, respectively.

\* National Institute for Research in Inorganic Materials

Bi, Sr, Cu, Ca, and O atoms on the specimen surface were indicated with lines on the spectrum. A clear rise of the spectrum at the surface was observed only by Bi, which has a larger Rutherford scattering cross section (18.33 barn/sr) than those of Sr(3.81), Cu(2.21), Ca(1.04), and O(0.15).

In Fig. 2 was shown the channeling dip in backscattered  ${}^4\text{He}$  yields, that is, the variation in the yield with the change in the beam incident angle around the  $c$ -axis direction. In this experiment only  ${}^4\text{He}$  ions in a "WINDOW" (shown in Fig.1) were measured. "WINDOW" was limited within a spectrum region where only Bi atoms contribute so that the participation of scattering by other elements was excluded. The counts of each point were accumulated for the exposure of  $2.4 \times 10^{13} \text{ He/cm}^2$ .

The axial half angle  $\psi_{1/2}$  of the dip is calculated out to be  $0.69^\circ$ , but the estimation of the minimum yield  $\chi_{\min}$  is difficult because of its increase with the fluence of  ${}^4\text{He}$ . It is also noted that the specimen was exposed to a dose of  $1.26 \times 10^{15} \text{ He/cm}^2$  during alignment of the crystal axis before the first dip measurements. So the initial value of  $\chi_{\min}$  was roughly estimated at

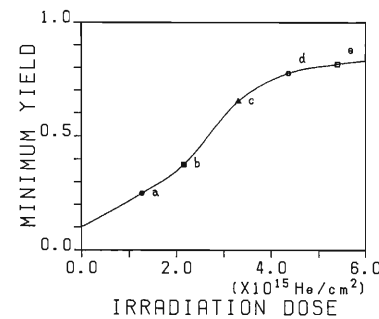


Fig. 3. Plot of Minimum yield  $\chi_{\min}$  vs. irradiation dose for the Bi-Sr-Ca-Cu-O system high  $T_c$  superconductor. The solid line is to guide the reader's eye. The  $\chi_{\min}$  in the initial stage of bombardment estimated at 0.10.

0.10 by extrapolation of an experimental relation of  $\chi_{\min}$  and the fluence as shown in Fig.3. The results indicate that the  $\text{Bi}_2\text{Sr}_2\text{CaCu}_2\text{O}_x$  crystal has a rather high structural quality in the initial stage of bombardment. As the fluence of a He ion beam used for RBS increases, the  $\chi_{\min}$  increases. We thus conclude that a structure disorder is produced by ion bombardment in the Bi-Sr-Ca-Cu-O system high  $T_c$  superconductor by means of the FZ method using infrared heating.

### III-2-28. RBS Investigation of N-Implanted AlN<sub>x</sub> Film Deposited on Silicon

K. Kobayashi, S. Namba, T. Fujihana, T. Kobayashi, and M. Iwaki

Recently aluminium nitride (AlN) is of particular interest because of its large energy gap, good thermal conductivity, and stability up to very high temperature, as well as its chemical inertness.<sup>1)</sup> We investigated by Rutherford back-scattering (RBS) measurements the effects of N-ion implantation on AlN<sub>x</sub> films deposited by an activated reactive evaporation (ARE) method. In a previous report,<sup>2)</sup> we found that the ratio of Al/N in AlN<sub>x</sub> film was dependent on the deposition rate during evaporation by ARE. Two effects of the N-implantation in AlN<sub>x</sub> film were also reported:<sup>3)</sup> (i) N-implantation in AlN<sub>x</sub> ( $x < 1$ ) films causes the formation of (0 0 2) oriented AlN<sub>x</sub> films at room temperature without any thermal annealing, and (ii) the optical transmittance of the AlN<sub>x</sub> ( $x < 1$ ) films is improved.

This report, presents the effect of the incident implantation angle of nitrogen on the composition of the AlN<sub>x</sub> films deposited on silicon. Since the detailed conditions of the deposition of AlN<sub>x</sub> film by the ARE method was previously reported,<sup>3)</sup> key conditions are briefly mentioned here. AlN<sub>x</sub> films of 750 nm in thickness were deposited on Si (1 1 1) by means of ARE in a

nitrogen atmosphere. The base pressure was  $2 \times 10^{-6}$  Torr and the partial pressure of the nitrogen during deposition was  $1 \times 10^{-4}$  Torr by feeding N<sub>2</sub> gas into a chamber. The substrate was water-cooled and no bias voltage was applied between the substrate and the evaporation source.

Nitrogen-implantation into the AlN<sub>x</sub> thin films was performed to the doses ranging from  $5 \times 10^{16}$  to  $5 \times 10^{17}$  N<sup>+</sup>-ions/cm<sup>2</sup> at 80 keV at  $1 \times 10^{-6}$  Torr. For 80-keV implantation, the average projected range calculated by a Lindhard, Scharff and Schiott (LSS) theory was estimated at 180 nm, which was deeper than the interface. Therefore the nitrogen implantation was carried out through the AlN<sub>x</sub> thin films. The beam density was approximately  $2 \mu\text{A}/\text{cm}^2$ , and the temperature of substrates during ion implantation was maintained to be ambient. The incident angle of N<sup>+</sup>-ions was changed from 0° to 45°.

Figure 1 shows RBS random and <1 1 1> aligned spectra before and after the N-implantation to a dose of  $5 \times 10^{17}$  N<sup>+</sup>/cm<sup>2</sup>; the incident angle was 0°. The marking short lines indicate the edges of Al, N, and O at the surface and the edge of Si at the interface.

By comparison of Fig. 1 (a) and Fig. 1 (b), the position of the maximum yield of implanted nitrogen is deeper than the interface between the AlN<sub>x</sub> film and the Si substrate, as predicted from the LSS theory. The distribution of the implanted nitrogen calculated from the difference in the spectra between pre- and post-implantation is of a Gaussian-like shape in the Si substrate. The comparison between aligned and random spectra in Fig. 1 (b) indicates that the Si substrate near the interface would be amorphized by N-implantation. Figure 1 (b) indicates that O-atoms invaded the surface layers of the film after N-implantation, since there was no yield corresponding to the O atoms in the spectra for a pristine film. The O atoms invasion would occur by the following process: the O-atoms in the surface oxide formed by the absorption of contaminations and a consequent segregation induced by the cascade mixing accompanied with N-implantation.

Figure 2 shows RBS spectra for the AlN<sub>x</sub> film

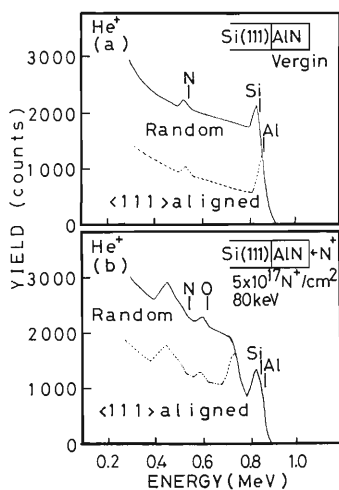


Fig. 1. Rutherford backscattering (RBS) spectra for the AlN<sub>x</sub>-film-deposited Si (1 1 1) before and after N-implantation at an incident angle of 0°. (a), random and <1 1 1> aligned spectra before N-implantation; (b), random and <1 1 1> aligned spectra after N-implantation.

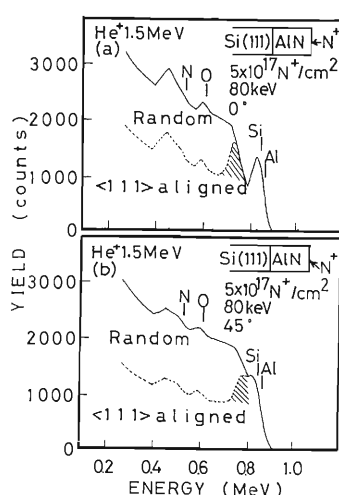


Fig. 2. Rutherford backscattering (RBS) spectra for the  $\text{AlN}_x$  film deposited  $\text{Si} (111)$  after N-ion implantation. (a), random and  $\langle 111 \rangle$  aligned spectra after N-implantation at an incident angle of  $0^\circ$ ; (b), random and  $\langle 111 \rangle$  aligned spectra after N-implantation at an incident angle of  $45^\circ$ .

deposited  $\text{Si} (111)$  after N-ion implantation at two different incident angles. Figure 2 (a) and (b) show random and  $\langle 111 \rangle$  aligned spectra after N-implantation at incident angles of  $0^\circ$  and  $45^\circ$ , respectively.

By comparison of Fig. 2 (a) and Fig. 2 (b), the yield of the N atoms implanted at  $45^\circ$  is found to be smaller than those at  $0^\circ$  at the same doses. The reduction of the yield would result from the following two reasons: one is the removing of extra nitrogen due to nitrogen imping and/or the other is the scattering (reflection) of incident nitrogen at the surface. These two effects of the removing and scattering of incident atoms by

implantation would be dependent on the incident angles.

In comparison with two  $\langle 111 \rangle$  aligned spectra shown in Fig. 2 (a) and (b) in Fig. 2, the shaded peak, which corresponds to the damage of the silicon substrate, was shifted toward the surface with increasing the incident angle from  $0^\circ$  to  $45^\circ$ . This indicates that the amorphous layer near the interface induced by N-implantation at  $45^\circ$  was shallower than those at  $0^\circ$ .

During the investigation of the effects of the incident angles of N-implantation near room temperature on the AlN grain growth by means of X-ray diffraction (XRD), we also obtained the following results.<sup>4)</sup>

(1) The grain growth of AlN took place, even when the incident angles of nitrogen ions were tilted from  $0^\circ$  to  $45^\circ$ .

(2) The  $c$ -axis of the grown AlN grains was normal to the substrate plane, when the incident angles of nitrogen ions were tilted from  $0^\circ$  to  $45^\circ$ .

Futher investigations will be needed for controling the composition and structure of  $\text{AlN}_x$  by N-implantation.

## References

- 1) A. Fathimulla and A. Lakhani: *J. Appl. Phys.*, **54**, 4586 (1983).
- 2) K. Kobayashi, S. Namba, T. Fujihana, Y. Dai, T. Kobayashi, and M. Iwaki: *RIKEN Accel. Prog. Rep.*, **21**, 105 (1987).
- 3) K. Kobayashi, S. Namba, T. Fujihana, T. Kobayashi, Y. Dai, and M. Iwaki: *Appl. Phys. Lett.*, **53**(3), 18 (1988).
- 4) K. Kobayashi, S. Namba, T. Fujihana, Y. Dai, T. Kobayashi, and M. Iwaki: *Nucl. Instrum. Methods Phys. Res. B*, **37/38**, 704 (1989).

### III-2-29. RBS Investigation of N-Implanted Iron

T. Fujihana, Y. Okabe, and M. Iwaki

Over the last decade, N-ion implantation into Fe and steels has been employed in fundamental studies on surface layer modification. In particular, the N-concentration profile as a function of depth is one of the most important subjects for the research on implanted layers, and has been investigated by means of secondary ion mass spectroscopy (SIMS),<sup>1)</sup> Auger electron spectroscopy (AES),<sup>2)</sup> and so on. However, these analyses are accompanied with ion beam sputtering which holds possibility that selective sputtering, cascade mixing, *etc.* would take place, and the sputtering ratio may differ between matrix and implanted layers due to new compound formation by ion implantation. It is important to compare the results of these analyses with those of Rutherford backscattering (RBS) measurement which have no such effects of sputtering.

The present report describes the preliminary results of RBS measurements on the surface compositions of N-implanted Fe-surface layers.

The ion implantation of  $^{14}\text{N}^+$  into Fe plates of 1 mm in thickness with a purity of 99.9% was performed with doses ranging from  $1 \times 10^{17}$  to  $1 \times 10^{18}$  ions/cm<sup>2</sup> at 100 keV at 20°C. The ion beam current density was approximately  $1.0 \mu\text{A}/\text{cm}^2$ . In order to investigate temperature dependence, substrate temperature during implantation with a dose of  $5 \times 10^{17}$  ions/cm<sup>2</sup> was kept at -40, 20, 100, or 200°C by cooling substrate holders with liquid nitrogen or water, or warming them up with a heater. These temperatures were monitored with a pair of alumel-chromel thermocouple fixed on the substrate holders. The pressure in a process chamber during implantation was approximately  $1.5 \times 10^{-4}$  Pa.

The RBS measurement was carried out by using 1.5 MeV  $^4\text{He}^+$  ions with a fluence of  $3 \mu\text{C}$  to estimate the compositions of N-implanted Fe-surface layers. Backscattered particles were detected at an angle of 150 degrees and analyzed with a solid state detector and conventional electronics. The specimens were mounted on a goniometer in a target chamber, where the pressure was below  $5 \times 10^{-4}$  Pa.

Figure 1 shows the RBS spectra for the specimens unimplanted and N-implanted with a dose

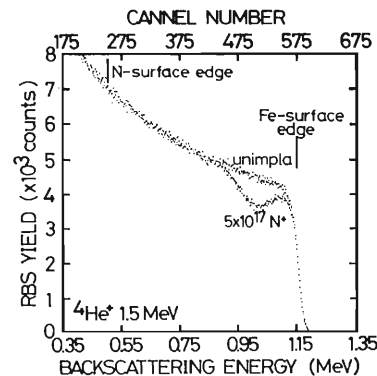


Fig. 1. RBS spectra for unimplanted and N-implanted Fe with a dose of  $5 \times 10^{17}$  ions/cm<sup>2</sup> at 20°C.

of  $5 \times 10^{17}$  ions/cm<sup>2</sup> at 20°C. The leading edge of the Fe surface is at the channel number 574 (located at half-height) and the energy edge of implanted N atoms at the Fe-surface at channel number 250. Comparison of the spectra obtained with the unimplanted specimen and with the N-implanted specimen indicates that the increase in the RBS yield induced by implanted N-atoms can hardly be observed, but the N-depth profile can be expected from the decrease in the yield of the Fe-atoms owing to implanted N atoms.

Figure 2 shows the relationship between tentative N concentrations and backscattering energy as a function of N dose for 20°C implantation. The tentative N concentrations are defined by the ratio of decreasing yields in the N-implanted Fe-surface layers ( $1 - \text{Fe}_i/\text{Fe}_u$ ), which are calculated from RBS spectra, *e.g.*, as shown in Fig. 1. Here  $\text{Fe}_i$  and  $\text{Fe}_u$  are the yields for Fe-atoms of the implanted and of the unimplanted specimens, respectively, at the same backscattering energy. The N doses for (a), (b), (c), and (d) in Fig. 2 are  $1 \times 10^{17}$ ,  $2.5 \times 10^{17}$ ,  $5 \times 10^{17}$ , and  $1 \times 10^{18}$  ions/cm<sup>2</sup>, respectively. The profiles of tentative N concentrations below the dose of  $2.5 \times 10^{17}$  ions/cm<sup>2</sup> are similar to those of the implanted N atoms predicted by the LSS theory,<sup>3)</sup> indicating the Gaussian distribution. When implanted at the dose of  $5 \times 10^{17}$  ions/cm<sup>2</sup>, the specimen shows its maximum N concentration slightly lower than the theoretical value, though the profile shows a

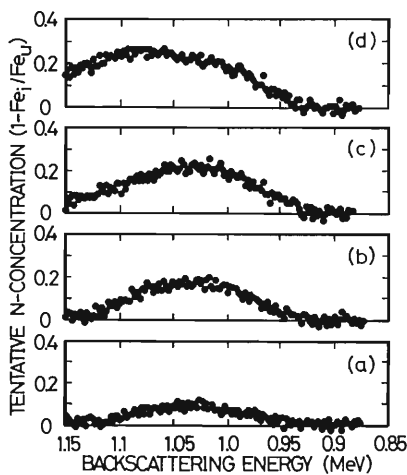


Fig. 2. Profiles of the tentative N concentrations for implanted Fe at 20°C with various doses. (a),  $1 \times 10^{17}$ ; (b),  $2.5 \times 10^{17}$ ; (c),  $5 \times 10^{17}$ ; (d)  $1 \times 10^{18}$ ions/cm<sup>2</sup>. Fe<sub>i</sub> and Fe<sub>u</sub> are the yields for Fe-atoms of the implanted and unimplanted specimens, respectively.

Gaussian distribution. Comparison of (c) and (d) indicates that the maximum N concentration at  $1 \times 10^{18}$ ions/cm<sup>2</sup> does not exceed the one at  $5 \times 10^{17}$ ions/cm<sup>2</sup>, and implanted N atoms migrate towards the Fe surface. The saturation of N-concentration in Fe during implantation, the maximum of which is approximately 30 at%, was previously obtained by our AES measurements.<sup>2)</sup> The saturation phenomena like this are also reported for the N implantation into Al,<sup>4)</sup> Ti,<sup>2)</sup> and Cr,<sup>2)</sup> and in each case the maximum N concentration is approximately 50 at%. If no migration of N atoms occur and the N distribution is caused due to sputtering during implantation, the maximum N concentration in Fe would be almost identical to the one in Cr because the mass, atomic number, and density of Fe are nearly the same as those of Cr. These results indicate that the migration of N atoms causes the change of N distribution from a Gaussian type to an error-functional type in accordance with the increase in N dose.

Figure 3 shows the profiles of the tentative N concentration for N-implanted specimens at a dose of  $5 \times 10^{17}$ ions/cm<sup>2</sup> as a function of substrate temperature during implantation. The substrate

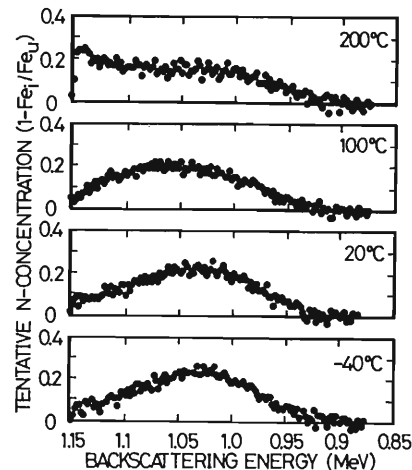


Fig. 3. Profiles of the tentative N concentrations for implanted at a dose of  $5 \times 10^{17}$ ions/cm<sup>2</sup> with various substrate temperatures during implantation. Fe<sub>i</sub> and Fe<sub>u</sub> are the yields for the implanted and unimplanted specimens, respectively.

temperatures during implantation are indicated in the figure. The Gaussian-distribution is observed for the implantation below 100°C. The profile for 200°C implantation is quite different from others and shows an error-functional distribution. The result suggests that the migration of N atoms is enhanced in the implantation at 200°C, as shown for the specimen with a dose of  $1 \times 10^{18}$  ions/cm<sup>2</sup> in Fig. 2.

From these results, we conclude that in the high-dose N-implantation into Fe, the migration of N-atoms occurs towards the Fe-surface even during 20°C implantation and is enhanced at higher temperatures, and consequently, the depth profile of the implanted N atoms has an error-functional distribution.

#### References

- 1) M. Iwaki, T. Fujihana, and K. Okitaka: *Mater. Sci. Eng.*, **69**, 211 (1985).
- 2) T. Fujihana, Y. Okabe, and M. Iwaki: Proc. Int. Conf. Surface Modification of Metals by Ion Beams, Riva Del Garda, Italy, 1988, to be published.
- 3) J. Lindhard, M. Scharff, and H. E. Schiøtt: *K. Dan. Vidensk. Selsk. Mat.-Fys. Medd.*, **33** (14), 1 (1963).
- 4) S. Ohira and M. Iwaki: *Mater. Sci. Eng.*, **90**, 143 (1987).

### III-2-30. Hydrogen Trapping by Solute Atoms in Nb-Mo Alloys as Observed by a Channelling Method

E. Yagi, T. Kobayashi, and T. Matsumoto\*

The enhancement of the terminal solubility for hydrogen (TSH) in group V<sub>a</sub> metals (V, Nb, and Ta) on alloying with metal solute atoms has been reported for various alloying elements.<sup>1,2)</sup> For the mechanism of this enhancement a trapping model has been proposed.<sup>1-3)</sup> On the other hand, it has also been reported that no evidence for trapping was observed,<sup>4)</sup> and it has been suggested that the enhancement is explained only on the basis of the concept of macroscopic thermodynamics.<sup>5)</sup> To elucidate the mechanism of this enhancement, the lattice location of hydrogen has been investigated by a channelling method using a nuclear reaction  $^{1\text{H}}(^{11}\text{B}, \alpha)\alpha\alpha$ ,<sup>6-8)</sup> on the Nb alloys containing undersized Mo atoms.<sup>9)</sup>

In a previous study on Nb-3at%Mo alloys the following conclusion was deduced.<sup>9)</sup> In a Nb-3at%Mo-2at%H alloy all hydrogen atoms are trapped by Mo atoms at room temperature and located at sites displaced from tetrahedral (T) sites by about 0.6 Å towards the Mo atoms (trapped sites). In a Nb-3at%-5at%H alloy some fraction of hydrogen atoms are located at the trapped sites and the rest are at T-sites at room temperature, while at 373 K they are detrapped and enter T-sites. These results give direct evidence for the existence of attractive interaction between substitutional solute atoms and hydrogen in Nb-3at%Mo alloys and strongly support the trapping model for the enhancement of the TSH in Nb by alloying with Mo atoms in the low concentration region of Mo solute atoms.

In the present study, experiments were extended to the alloy containing higher concentration of Mo atoms (~10at%). The experiments were performed at room temperature with a 2.03 MeV  $^{11}\text{B}^{2+}$  beam on a Nb-10at%Mo-6at%H alloy, and channelling angular profiles of backscattered  $^{11}\text{B}$  and emitted  $\alpha$  particles were obtained for  $\langle 1\ 0\ 0 \rangle$ ,  $\langle 1\ 1\ 0 \rangle$  and  $\{1\ 0\ 0\}$  channels. The results are shown in Fig. 1.

These  $\alpha$ -angular profiles are very similar to those for the Nb-3at%-5at%H alloy. For exam-

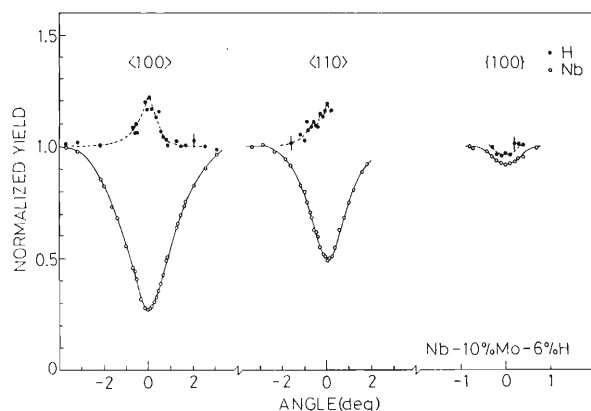


Fig. 1. Channelling angular profiles of  $\alpha$  particle and backscattered  $^{11}\text{B}$  yields obtained at room temperature for Nb-10at%Mo-6at%H alloy. The full curves and the dashed curves were drawn to guide the eye.

ple, for the  $\langle 110 \rangle$  channel small subpeaks were observed at  $0^\circ$ ,  $-0.35^\circ$ , and  $-0.6^\circ$  in both alloys. These results indicate that some fraction of hydrogen atoms are located at trapped sites and the rest are at T-sites, because the subpeaks at  $0^\circ$  and  $-0.35^\circ$  are attributed to the T-site occupancy,<sup>10)</sup> and at  $-0.6^\circ$  to the trapped site occupancy.<sup>9)</sup> The trapping efficiency,  $f$ , the number of H atoms trapped by one Mo atom, was roughly estimated at 0.67-1.0 for the Nb-3at% Mo-5at%H alloy,<sup>9)</sup> and at 0.25-0.35 for the Nb-10at%Mo-6at%H alloy. The decrease in the trapping efficiency with increasing Mo concentration is considered to be a result that the effect of strain due to undersized Mo atoms does not become strongly localized with increasing Mo concentration. Experiments on more concentrated alloys are in progress.

#### References

- 1) J. F. Miller and D. G. Westlake: Proc. 2nd JIM Int. Symp. Hydrogen in Metals, *Suppl. Trans. Jpn. Inst. Metals*, **21**, 153 (1980).
- 2) T. Matsumoto, Y. Sasaki, and M. Hihara: *J. Phys. Chem. Solids*, **36**, 215 (1975).
- 3) T. Matsumoto: *J. Phys. Soc. Jpn.*, **42**, 1583 (1977).
- 4) D. T. Peterson and S. O. Nelson: *Metall. Trans.*, **16A**, 367 (1985).

\* National Research Institute for Metals.

- 5) W. A. Oates and T. B. Flanagan: *Acta Metall.*, **33**, 693 (1985).
- 6) E. Yagi, T. Kobayashi, S. Nakamura, Y. Fukai, and K. Watanabe: *J. Phys. Soc. Jpn.*, **52**, 3441 (1983).
- 7) E. Yagi, T. Kobayashi, S. Nakamura, Y. Fukai, and K. Watanabe: *Phys. Rev. B*, **31**, 1640 (1985).
- 8) E. Yagi, T. Kobayashi, S. Nakamura, F. Kano, K. Watanabe, Y. Fukai, and S. Koike: *Phys. Rev. B*, **33**, 5121 (1986).
- 9) E. Yagi, S. Nakamura, F. Kano, T. Kobayashi, K. Watanabe, Y. Fukai, and T. Matsumoto: *Phys. Rev. B*, **39**, 57 (1989).
- 10) E. Yagi, S. Nakamura, T. Kobayashi, K. Watanabe, and Y. Fukai: *J. Phys. Soc. Jpn.*, **54**, 1855 (1985).

### III-2-31. Radiation Damage in Ion-Implanted $\text{CaF}_2$ Observed by Channeling

K. Aono, M. Iwaki, and S. Namba

In our previous reports,<sup>1,2)</sup> we have presented the results on the radiation damage and depth profiles of Eu in Eu-implanted  $\text{CaF}_2$  investigated by an RBS-channeling method using the TANDDETRO. These results indicate that the 100 keV Eu-implantation does not produce severe radiation damage. In the ion implantation into  $\text{CaF}_2$  studied with various ions ( $\text{Cr}^+$ ,  $\text{Fe}^+$ ,  $\text{Cu}^+$ , and  $\text{Eu}^+$ ), we found that the color of luminescence emitted from  $\text{CaF}_2$  during ion-implantation varies as a function of the implantation-dose. In addition, the originally colorless and transparent properties of  $\text{CaF}_2$  wafers did not change even after a considerable ion implantation to a dose of  $10^{16}$  ions/ $\text{cm}^2$ ; these phenomena may be caused by the alternations in ion-states depending on the dose.

In the present study, the radiation damage of Cr-implanted  $\text{CaF}_2$  was investigated by the same method as that used in the Eu implantation. Chromium, iron, copper, and europium ions of 100 keV were implanted into colorless and transparent single crystalline  $\text{CaF}_2$  wafers with doses of  $10^{13}$ – $10^{16}/\text{cm}^2$ . The channeling measurement was carried out by using 1.5 MeV  $\text{He}^+$ , and backscattered particles were detected at an angle of  $150^\circ$ . With Eu, the heaviest of these ions, the color of luminescence emitted from  $\text{CaF}_2$  during Eu-implantation changed sensitively with dose. It is known that in the early stage of ion implantation, both ionic states of  $\text{Eu}^{2+}$  and  $\text{Eu}^{3+}$  are dominant and at the high dose implantation  $\text{Eu}^{3+}$  is dominant.<sup>2)</sup> The  $\langle 1\ 1\ 1 \rangle$  channeling measurements show that there is a little difference in the minimum yield of the backscattering between fluences of  $10^{13}$  and  $10^{16}/\text{cm}^2$ . These results can be explained in terms of the stability of the ionic states in the  $\text{CaF}_2$  matrix. As the stress in the implanted layers becomes high with increasing dose, the  $\text{Eu}^{3+}$  state will be more stable than the

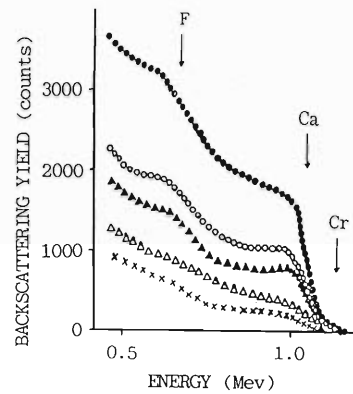


Fig.1. Random (●) and  $\langle 1\ 1\ 1 \rangle$  aligned (○) spectra obtained for Cr-implanted  $\text{CaF}_2$  with  $1 \times 10^{16}$   $\text{Cr}/\text{cm}^2$ , and  $\langle 1\ 1\ 1 \rangle$  aligned spectra for  $\text{CaF}_2$  implanted with  $1 \times 10^{15}$   $\text{Cr}/\text{cm}^2$  (▲),  $1 \times 10^{14}$   $\text{Cr}/\text{cm}^2$  (△), and  $1 \times 10^{13}$   $\text{Cr}/\text{cm}^2$  (×).

$\text{Eu}^{2+}$  state, the ionic radius of which (1.12 Å) is larger than that of the former (0.98 Å). However, in the case of Cr that is the lightest ion in the above-mentioned ions, the change in color of the luminescence as a function of the implantation-dose was not so significant as was the case of Eu, and the channeling measurement shows a difference in the minimum yield between fluences of  $10^{13}$  and  $10^{16}/\text{cm}^2$ , as shown in Fig.1. Since the ionic radius of Cr ion is smaller than that of  $\text{Ca}^{2+}$  (0.99 Å), the stress of compression in the Cr-implanted layers may increase slowly with increasing Cr-dose. Further investigations are needed for more accurate explanation of these phenomena.

#### References

- 1) K. Aono, M. Iwaki, and S. Namba: *RIKEN Accel. Prog. Rep.*, **20**, 79 (1986).
- 2) K. Aono, M. Iwaki, and S. Namba: *Nucl. Instrum. Methods Phys. Res. B*, **32**, 321 (1988).

### III-2-32. PIXE-Channeling Analysis of Ga in the Ge Epitaxial Layer on a Si Substrate

K. Tanaka and E. Yagi

RBS-channeling is an effective tool for investigating lattice location of impurity atoms; however, detection of a light element in a heavy matrix is difficult by RBS. Thus, the application of RBS-channeling has been limited to the analysis of a heavy element in a light matrix. On the other hand, PIXE can be applied to the analysis of elements in any combinations of hosts and

impurities, and the impact parameter of K-shell excitation which is in the order of  $10^{-2}$  Å is smaller than the Thomas-Fermi screening radius.<sup>1,2)</sup> In the present study, therefore, we used the PIXE-channeling method together with an RBS-channeling method to investigate the lattice location of Ga atoms doped in the Ge epitaxial layer on a Si(100) substrate.

Ge layers were grown on a Si(100) substrate by using a molecular beam epitaxy method and by a two-step procedure in order to reduce the lattice mismatch between Ge and Si.<sup>3)</sup> In this work the growth temperature of the first layer was kept at 300°C and that of the second layer at 550°C. The thickness of the first layer was 2,000 Å and that of the second layer was 7,000 Å. Ga was evaporated simultaneously with the second Ge layer growth so that the Ga atoms were distributed homogeneously in the depth of

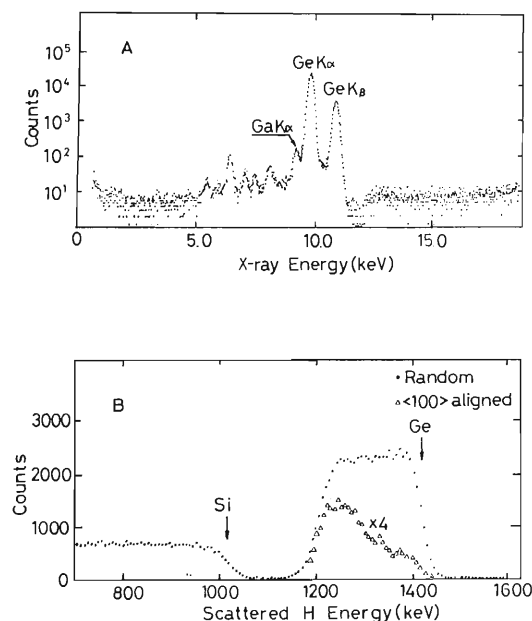


Fig. 1. Energy spectra of X rays and backscattered protons for a Ga-doped Ge layer on a Si substrate. (A) PIXE spectrum with polyester film of 1 mm in thickness; (B) RBS spectrum.

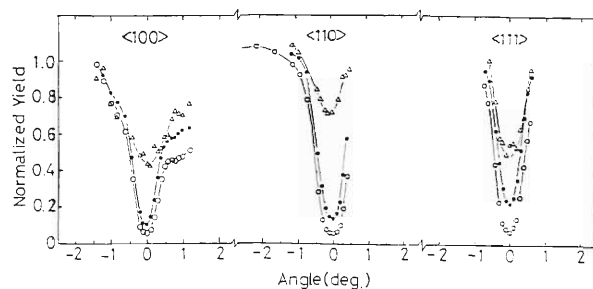


Fig. 2. Channeling angular profiles of protons (○), Ge X-rays (●) and Ga X-rays (△) yields for a Ga-doped Ge layer on a Si substrate.

Table 1. Values of  $\psi_{1/2}$ - and  $\chi_{\min}$ - for backscattered protons, Ge K $\alpha$  X-rays and Ga K $\alpha$  X-rays through the <100>, <110>, and <111> axes.

	Ga X-ray (K $\alpha$ )	Ge X-ray (K $\alpha$ )	B.S. (Whole Ge layer)	B.S. (Near surface)	B.S. (Ge/Si interface)
<100>	$\psi_{1/2}$	0.75	0.45	0.50	0.38
	$\chi_{\min}$	0.42	0.10	0.06	0.16
<110>	$\psi_{1/2}$	0.43	0.45	0.50	0.45
	$\chi_{\min}$	0.61	0.13	0.05	0.18
<111>	$\psi_{1/2}$	0.45	0.38	0.45	0.39
	$\chi_{\min}$	0.50	0.22	0.07	0.31

4,000 Å below the surface. The concentration of a Ga was  $1 \times 10^{18}$  atoms/cm<sup>3</sup>. Channeling analysis was carried out with a 1.5 MeV proton beam. The beam diameter was 1 mm and the beam divergence was less than 0.07°; the current was approximately 10 nA. The characteristic X-rays emitted from the sample were detected with a Si(Li) detector which has a sensitive area of 30 mm<sup>2</sup> and a 3 mm depletion depth, viewed the sample at 135° to the beam direction. The distance between the sample surface and the detector was 90 mm. An X-ray detector has a Be window of 7.5 μm in thickness. We used an additional polyester film of 1 mm in thickness to reduce Si X-rays from the substrate of the sample and avoid pulse pile-up effects. Scattering protons were detected with a surface barrier solid-state detector at a scattering angle of 155°. Figure 1 shows typical spectra of PIXE and of the backscattered protons for <1 0 0> aligned and random incidences. A notable peak observed in the spectra for the <1 0 0> aligned case arises from the dislocations at the Ge/Si interface. In order to investigate the lattice location of Ga atoms, we performed channeling angular scans through <1 0 0>, <1 1 0>, and <1 1 1> axes. Figure 2 shows the angular scans for the backscattered protons, Ge K $\alpha$  X-rays, and Ga K $\alpha$  X-rays. The backscattering proton signals accepted for the

angular scans correspond to a thickness of 1,200 Å below the surface. The half-width of a channeling dip at a level halfway between the minimum and random level ( $\phi_{1/2}$ ) and the normalized minimum yield ( $\chi_{\min}$ ) for each angular scans are summarized in Table 1. Also performed were angular scans for the backscattering proton signals corresponding to a thickness of 1,200 Å near the Ge/Si interface and the whole Ge layer. Their  $\phi_{1/2}$ -values and  $\chi_{\min}$ -values are summarized in Table 1. The angular scan curve for Ge K $\alpha$  X-ray agrees with that for the whole Ge layer. The <1 0 0>, <1 1 0>, and <1 1 1> Ga K $\alpha$  X-rays angular profiles exhibit clear dips. We concluded that 50% of Ga atoms are located at substitutional sites and 50% at random sites. We confirmed that the PIXE method can be applied to ion-channeling analysis of the Ga lattice location in a Ge layer.

#### References

- 1) L. Feldman, J. Mayer, and S. Picraux: Materials Analysis by Ion Channeling, Academic Press, New York (1982).
- 2) J. Chemin, I. Mitchell, and F. Saris: *J. Appl. Phys.*, **45**, 532 (1974).
- 3) Y. Fukuda and Y. Kohama: *J. Cryst. Growth*, **81**, 451 (1987).

### III-2-33. Chemical Erosion of Molybdenum Disulphide ( $\text{MoS}_2$ ) by Hydrogen Plasma

K. Yano, Y. Sakamoto, H. Oyama, M. Yanokura,  
H. Kokai, S. Itoh,\* and A. Miyahara \*\*

Molybdenum disulphide is widely utilized, as a suitable lubricant in an ultrahigh vacuum. We need application of  $\text{MoS}_2$  in fusion devices; in reality, screw systems with  $\text{MoS}_2$  lubricant are utilized to drive the graphite blades in an ALT-II pumped limiter in a TEXTOR device. Under hydrogen plasma irradiation, however, this lubricant would be deteriorated by erosion of sulphur through a chemical reaction:  $\text{MoS}_2 + 4\text{H} \rightarrow 2\text{H}_2\text{S} + \text{Mo}$ . Dimigen and others have reported that the content of sulphur in  $\text{MoS}_x$  is an essential factor for the tribological properties of this lubricant.<sup>1)</sup> Thus it is necessary to have data on the chemical erosion of  $\text{MoS}_2$  by irradiation of  $\text{H}^+$  and/or  $\text{H}^0$  flux from a hydrogen plasma as a part of tribological studies of  $\text{MoS}_2$ .

The present erosion experiment has been carried out using hydrogen plasma produced by means of an electron cyclotron resonance (ECR) discharge. The ECR-2 device used in this experiment has been described in Ref.2. Throughout experiments, plasma conditions were as follows:  $\text{H}_2$  gas pressure,  $4 \times 10^{-2}$  Pa; microwave frequency, 2.45 GHz; power, 200 W in CW; electron density,  $n_e = 2.7 \times 10^{10} \text{ cm}^{-3}$ ; and electron temperature,  $T_e = 10 \text{ eV}$ .

Thin ( $1\mu\text{m}$ )  $\text{MoS}_2$  were deposited on SUS 304 stainless steel substrates by sputtering. The samples were irradiated at two positions for (1) hybrid irradiation (ions+neutrals) and (2) irradiation of the Franck-Condon neutrals only. The sample temperature was monitored with a thermocouple. Chemical erosion of  $\text{MoS}_2$  was investigated mainly by Auger Electron Spectroscopy (AES). The stoichiometry of the  $\text{MoS}_2$  film examined by AES was found to be  $\text{Mo} : \text{S} = 1 : 2$ . Before plasma irradiation, a sample was heated up to  $350^\circ\text{C}$  in vacuum and no change in the stoichiometry was verified by AES.

The hybrid irradiation was carried out by varying the bias voltage from 0 to  $-300$  volts with respect to the potential of the grounded

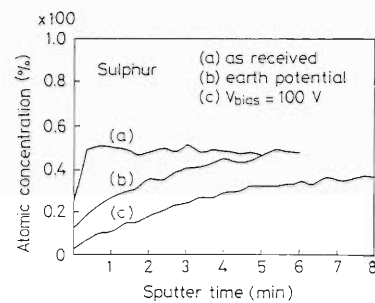


Fig. 1. Depth profiles of sulphur after hybrid irradiation with hydrogen ions of 30 eV (earth potential) and 100 eV, along with "as received." The sputter rate is *ca.* 10 nm/min.

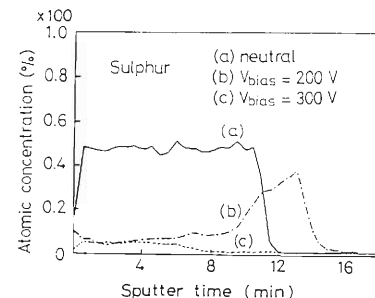


Fig. 2. Depth profiles of sulphur after hybrid irradiation with hydrogen ions of 200 eV and 300 eV, along with neutral atom irradiation. The sputter rate is *ca.* 100 nm/min.

chamber. The zero bias voltage gives the sample  $-30 \text{ V}$  with respect to the plasma due to the positive space potential of the plasma. Figure 1 shows the depth profiles of sulphur for "as received," zero bias voltage ( $-30 \text{ V}$ ), and  $-100 \text{ V}$ , and Fig. 2 for  $-200 \text{ V}$ ,  $-300 \text{ V}$ , and neutral irradiation. The sputter rate is  $10 \text{ nm/min}$  and  $100 \text{ nm/min}$  in the cases of Fig. 1 and Fig. 2, respectively. Molybdenum was not depleted by irradiation. A prominent decrease in sulphur near the surface is noticed even for the zero bias voltage. Ions of an energy above  $200 \text{ eV}$  cause a virtually complete loss of sulphur from a  $\text{MoS}_2$  film. Unfortunately, at  $-200 \text{ V}$  and  $-300 \text{ V}$ , films were partially cracked and exfoliated due

\* Toshiba Corporation.

\*\* IPP Nagoya, Nagoya University.

to thermal stress. The ion fluence was evaluated to be  $2 \times 10^{20} \text{ cm}^{-2}$  in this irradiation from current measurement.

In the case of the Franck-Condon neutral irradiation, sulphur was eroded near the surface (50 nm) only. The neutral atom fluence in this irradiation was estimated at  $1 \times 10^{20} \text{ atoms cm}^{-2}$  from plasma parameter measurement. The neutral atoms have the energy of about 5 eV because their origin is the Franck-Condon dissociation. The experiment shows that the sulphur atoms of MoS<sub>2</sub> are removed by hydrogen ions and atoms. On the basis of the depth profile on the erosion of sulphur shown in Fig. 1, the depleted thickness can be estimated at 50 nm, under the assumption that the sulphur atoms in the thickness corresponding to sputter time of 5 minutes are

removed by ions of 100 eV. The mass density of MoS<sub>2</sub> ( $4.8 \text{ g cm}^{-3}$ ) gives a mean atomic distance of 0.57 nm. Thus the total number of sulphur atoms in the thickness of 50 nm per cm<sup>2</sup> is about  $1.4 \times 10^{18}$ . Therefore, the erosion efficiency by ions of 100 eV is about  $10^{-2}$  sulphur atoms/hydrogen ion. The measurement of the amount of the retained hydrogen by the ERD was tried, but was not successful because of the large amount of hydrogen contained in the MoS<sub>2</sub> specimen itself.

#### References

- 1) H.Dimigen, H.Huebsch, and P.Willich: *Thin Solid Films*, **129**, 79 (1985).
- 2) K.Yano, H.Oyama, Y.Sakamoto, and M.Yanokura: *RIKEN Accel. Prog. Rep.*, **21**, 114 (1987).

### III-2-34. Charge Collection Measurements for the Study on Single Event Upset

Y. Shimano

Single event upset in semiconductor memories has increasingly been concerned when integrated circuits are scaled down in size.<sup>1)</sup> The upset is known to be caused by a rapid drift current termed "funneling." Because of the interest in predicting the single event upset rate in the space environment, we performed charge collection measurements for N ions incident on p<sup>+</sup>-n junctions in n-Si and on n<sup>+</sup>-p junctions in p-Si.

In this experiment we used 76.1 MeV <sup>14</sup>N-ions from the cyclotron. We exposed four kinds of samples to these ions: two p-Si samples with NA (the acceptor concentration) =  $1 \times 10^{15}/\text{cm}^2$  and  $5 \times 10^{15}/\text{cm}^2$ , two n-Si samples with ND (the donor concentration) =  $1 \times 10^{15}/\text{cm}^2$  and  $5 \times 10^{15}/\text{cm}^2$ . These samples were large-area diodes ( $1,000\mu\text{m} \times 1,000\mu\text{m}$ ), and were reverse biased. Figure 1 schematically shows our experimental apparatus. The signal was integrated with a wide-bandwidth GaAs amplifier and transmitted to a pulse-shape digitizer. Figure 2 shows the amplifier circuit. The samples were mounted at incident angles  $\theta = 0, 30,$  and  $60^\circ$  to a beam, and the applied bias was varied  $V_b = 5, 10,$  and  $16$  volts.

Figure 3 presents the experimental results with a peak value of the pulse acquired by the pulse-shape digitizer as a function of the effective depletion-layer length, which was varied according to NA (or ND),  $\theta$ , and  $V_b$ . The peak value in mV is expected to be equivalent to the total charge collected through the funneling process. Thus, as shown in Fig. 3, the total charge is reasonably proportional to the effective depletion layer length. However, the total charge is apparently greater than the charge ionized by N ions within the depletion layer. Therefore the effective funnel length  $W_f$ , which is termed in place of the effective depletion-layer length  $W_d$ , would be expressed by

$$W_f = \beta \times W_d \quad (1)$$

where  $\beta$  is the constant, but will change with a junction type (n<sup>+</sup>-p or p<sup>+</sup>-n) and incident particle, and its energy or LET. For example,  $\beta=2.65$  for 76.1 MeV N ion and an n<sup>+</sup>-p junction.

Aiming to investigate the  $\beta$  value for high-

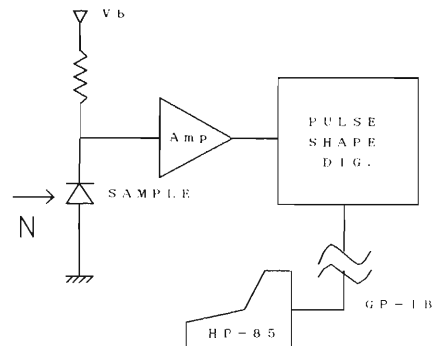


Fig. 1. Experimental apparatus.

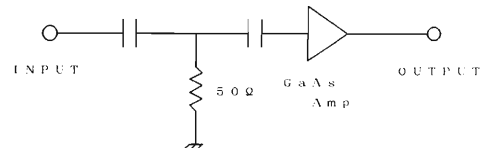


Fig. 2. Amplifier circuit.

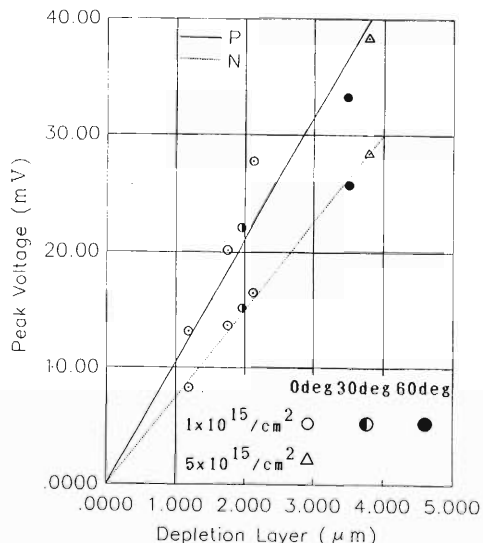


Fig. 3. Depletion layer-peak voltage (<sup>14</sup>N (76.1 MeV) irradiation).

LET particles abundant in the cosmic rays, such as Fe and Ni, we will continue similar experiments on heavier particles.

#### Reference

- 1) T. R. Oldman and F. B. McLean: *IEEE Trans., NS-30*, 4493 (1983).

### III-2-35. Correlation of Particle-Induced Displacement Damage in Si and GaAs

N. Hayashi, H. Watanabe, I. Sakamoto, K. Kuriyama,\*  
H. Kawahara,\* and I. Kohno

The total energy imparted in nonionizing collisions by recoil atoms in silicon was calculated as a function of proton energy by various authors.<sup>1)</sup> The calculation has been extended also to cover the proton-induced displacement damage in gallium arsenide.<sup>2)</sup> Summers, *et al.*<sup>3)</sup> compared their calculations with experimental results on the proton-bombarded silicon bipolar transistors, and they found a good correlation in their systematic study of displacement damage factors.

In this study resistivity and Hall mobility measurements in ion irradiated bulk silicon have been made with changing incident proton energy. We have also measured photoconductivity in gallium arsenide at low temperatures and found, for the first time to our knowledge, that the measurement is sensitive to the induced displacement damage. Furthermore, the correlation of the displacement damages produced by protons and neutrons respectively has been studied to make clear how cascade structures affect formation of stable defects.

The energy spectrum and spatial directions of primary knock-on atoms (PKAs) depend on the type and energy of the incident particles. Because of the different PKA spectra, it is expected that the final damage would differ when different incident particles are used and result in different property changes (damage factors) such as carrier removal and mobility degradation. A main point in the irradiation experiments, therefore, is whether it is possible to establish a correlation of device degradation for various incident particles.

Proton irradiation was performed with the cyclotron. The proton energies of 6, 9, and 15 MeV were selected to give mean ranges over the specimen thickness of 100–350  $\mu\text{m}$ . The neutron irradiation was carried out within a standard neutron field with an energy of 14 MeV at Electrotechnical Laboratory. The resistivity and Hall mobility were measured in the van der Pauw geometry of square-shaped Si specimens.

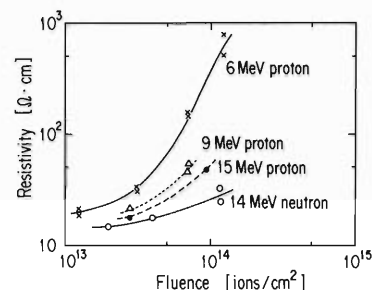


Fig. 1. Resistivity *vs.* proton and neutron fluence for n-type silicon samples.

The photoconductance in semi-insulating GaAs was measured at a temperature range of 80–300 K from the photoexcitation of a light-emitting diode with a peak wavelength of 940 nm at an intensity of 640 mW.<sup>4)</sup>

Figure 1 shows a typical result of the resistivity change in irradiated n-type Si. The resistance apparently increases with increasing proton fluence and it also depends on whether the projectiles are neutrons or protons. The resistivity change results mainly from the carrier removal due to induced defects and can be analyzed in terms of a damage factor,  $K_r$ . The rate of resistivity change is thus expressed as

$$(R - R_0)/R = K_r \times \phi$$

where  $R_0$  is the initial resistivity, and  $R$  is that after exposure to a fluence of  $\phi$  particles/cm<sup>2</sup>.

It was reported that the displacement damage by protons of MeV energies is mainly due to elastic scattering by the coulomb field of a nucleus (Rutherford scattering) and that the damage factor is directly proportional to the total number of initially produced defects.<sup>3)</sup> It is, therefore, expected that  $K_r$  will decrease monotonically with increasing proton energy. The result in Fig. 1 is consistent with the consideration and also with previously reported results.<sup>3)</sup>

Figure 2 shows the temperature dependence of the photoconductance in proton and neutron irradiated GaAs; two types of the specimens were used, *i.e.*, In-doped GaAs with an etch pit density (EPD) of  $10/\text{cm}^2$  and undoped GaAs with an EPD of  $10^5/\text{cm}^2$ . It should be noted that the

\* Hosei University, Koganei.

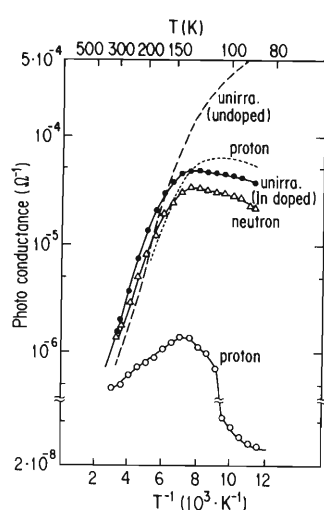


Fig. 2. Temperature dependence of photoconductance in In doped (solid lines) and undoped (broken line) GaAs before and after irradiation. The fluences were  $3 \times 10^{13} \text{ cm}^{-2}$  for 15 MeV proton and  $5 \times 10^{12} \text{ cm}^{-2}$  for 14 MeV neutron. No change was observed in undoped GaAs after neutron irradiation.

quenching phenomenon observed around 100–150 K is enhanced with proton irradiation. The enhancement is prominent for a nearly dislocation-free In-doped GaAs. Therefore, the results indicate that the irradiation-induced defects assist the transition from a midgap electron trap state ( $\text{EL}2^0$ ) to its metastable state ( $\text{EL}2^*$ ).

Figures 1 and 2 apparently indicate that the correlation of displacement damage for neutron and proton irradiations is similar in Si and GaAs. The present results suggest that the irradiation effects induced by nonionizing elastic collisions are independent of the PKA spectrum and not affected by defect cascades. Thus, the damage factor is expected to be less by a factor of about 5–3 in neutron irradiation than in proton irradiation; the correlation is confirmed by a further experiment of neutron irradiation to GaAs. It is remarkable that we detected the effect of neutron irradiation with such a low fluence as less than  $10^{13} \text{ n/cm}^2$ .

#### References

- 1) For example, E.A. Burke: *IEEE Trans. Nucl. Sci.*, **NS33**, 1276 (1986).
- 2) E.A. Burke: *IEEE Trans. Nucl. Sci.*, **NS34**, 1220 (1987).
- 3) G.P. Summers, E.A. Burke, C.J. Dale, E.A. Wolicki, P.W. Marshal, and M.A. Gehlhausen: *IEEE Trans. Nucl. Sci.*, **NS34**, 1134 (1987).
- 4) K. Kuriyama, H. Kawahara, M. Satoh, and T. Kawakubo: *Appl. Phys. Lett.*, **53**, 1074 (1988).

### III-3. Radiochemistry and Nuclear Chemistry

#### 1. Study on Incorporation of Carbon, Boron, and Oxygen in LEC-GaAs Using Charged Particle Activation

Y. Itoh, Y. Kadota, H. Fukushima, N. Nonaka,  
K. Tachi, and T. Nozaki

Carbon, boron, and oxygen are the most important residual impurities in undoped gallium arsenide (GaAs) single crystals grown by the liquid-encapsulated Czochralski (LEC) method.<sup>1)</sup> These impurities are inevitably introduced, since the ingot is grown from a GaAs melt covered with a  $B_2O_3$  encapsulant in a pyrolytic boron nitride crucible sustained in a graphite heater. The behavior of these impurities during crystal growth and their effects on the electrical properties of a semi-insulating LEC GaAs matrix remain obscure, primarily because of the deficiency of the reliable methods for the analysis at ppb levels. We have reported the determination of carbon and boron in LEC-GaAs by means of deuteron activation analysis with the simultaneous  $^{12}C(d, n)^{13}N$  and  $^{nat}B(d, xn)^{11}C$  reactions.<sup>2,3)</sup> We used this method to obtain the calibration factor in IR spectrometry of carbon in GaAs.<sup>4)</sup> For boron analysis, secondary ion mass spectroscopy has been used. Commercial LEC-GaAs sam-

ples were reported to contain  $10^{16}$  to  $10^{18}$  B atoms  $\cdot cm^{-3}$  and  $10^{15}$  C atoms  $\cdot cm^{-3}$ , respectively.<sup>5)</sup> As for oxygen in GaAs, little has ever been studied though its determination by the  $^{16}O(^3He, p)^{18}F$  reaction has been reported.<sup>6,7)</sup> As samples for the study on the behavior of C, B, and O in the crystal growth, four ingots were grown under different atmospheric conditions especially on the introduction of C and O from the ambient atmosphere into the crystal. Carbon is found to be introduced to the crystal as CO formed from the graphite heater.

Table 1 shows the concentrations of C, B, and O in eight samples cut from the top and bottom positions of four ingots grown in three different ambiances (Ar, Ar+1%  $O_2$ , and Ar+1% CO).

The following four results are summarized from Table 1.

(i) The addition of 1 % of  $O_2$  or CO to the ambient argon resulted in notable elevation (as much as a factor of 35;  $1.8 \times 10^{16}$  at  $\cdot cm^{-3}$ ) of the

Table 1. Concentrations of carbon, boron, and oxygen in GaAs crystals grown in Different ambiances.

Sample No.	Atmosphere*	Solid fraction**	Impurity concentration atoms $cm^{-3}$		
			Carbon ( $\times 10^{15}$ )	Boron ( $\times 10^{16}$ )	Oxygen ( $\times 10^{15}$ )
A	Ar	0.17	0.93	2.5	1.9
		0.64	0.51	1.9	3.4
B	Ar+1% $O_2$	0.14	16	3.6	1.8
		0.76	18	3.4	3.0
C	Ar+1% CO	0.1	6.4	1.7	3.1
		0.77	6.4	1.5	4.3
D	Ar+1% CO	0.17	6.0	2.8	5.7
		0.78	6.1	1.9	5.2

\* Initiation time of  $O_2$  or CO addition to Ar: B and C, initiation of crystal pulling (seeding to the melt); D, initiation of heating.

\*\* The two different values for each sample correspond to the top and bottom of the ingot.

C concentration, a very slight increase in the O content, and no clear effect on the B concentration.

(ii) Carbon is regarded as being introduced to the melt as CO formed by the reaction of additional O<sub>2</sub> and the graphite heater because the carbon concentration of Sample B was much higher than that of Sample C (2C+O<sub>2</sub>↔2CO).

(iii) The correlations between the concentration of each impurity and the solidified fraction were: (a) for C, no clear dependence (nearly constant for the most part); (b) for B, a slight decrease with the solidified fraction; and (c) for O, an increase with the solidified fraction.

(iv) Different from C and O in silicon,<sup>8)</sup> no clear correlation was observed between their concentrations in GaAs and the CO content of the ambient atmosphere during crystal growth.

Further studies with more variety of samples are in progress, to obtain clearer information about the behavior of C, B, and O in the crystal

growth and their effects on electronical properties of GaAs.

#### References

- 1) L.B. Ta, H.M. Hobgood, A. Rehatgi, and R.N. Thomas: *J. Appl. Phys.*, **53**, 5771 (1982).
- 2) T. Nozaki, Y. Itoh, Y. Ohkubo, T. Kimura, and H. Fukushima: *Jpn. J. Appl. Phys.*, **24**, L801 (1985).
- 3) Y. Itoh, Y. Kadota, T. Nozaki, H. Fukushima, and K. Takeda: *Jpn. J. Appl. Phys.*, **28**, 210 (1989).
- 4) Y. Kadota, K. Sakai, T. Nozaki, Y. Itoh, and Y. Ohkubo: *Semi-Insulating III-V Materials*, Ohmusha, Tokyo, p. 201 (1986).
- 5) L.C. Wei, G. Blondiaux, A. Glovagnoli, M. Valladon, and J.L. De: *Nucl. Instrum. Methods B*, **24/25**, 999 (1987).
- 6) T. Nozaki: *J. Radioanal. Chem.*, **72**, 527 (1982).
- 7) H. Fukushima, T. Kimura, H. Hamaguchi, T. Nozaki, Y. Itoh, and Y. Ohkubo: *J. Radioanal. Nucl. Chem. Artic.*, **112**, 415 (1987).
- 8) Y. Endo, Y. Yatsurugi, Y. Terai, and T. Nozaki: *J. Electrochem. Soc.*, **126**, 1422 (1979).

### III-3-2. Profiling of Light Elements in the Surface Layer of Solid by Means of the Elastic Recoil Detection

Q. Qiu, E. Arai,\* M Aratani, M. Yanokura, and R. Imura

Using a 50-MeV  $\text{Ar}^{4+}$  beam from the RILAC an ERD experiment has been performed to profile the depth distributions of light elements implanted into silicon wafers. Two points were aimed to be clarified: 1) the quality of profiling data extracted from the ERD measurements and 2) the choice of absorber foils placed in front of an elastic recoil detector to cut off disturbing heavy ions such as projectiles scattered by a target.

The geometry of measurement was chosen for this experiment as follows: the target is inclined by  $30^\circ$  in respect to the beam axis. Scattered and recoiled particles were registered with two surface-barrier detectors placed at  $52^\circ$  and  $37^\circ$ , respectively. The distance between the beam spot and the detector surfaces was 13 cm. A 20- $\mu\text{m}$  aluminium foil was placed in front of the detector for recoiled particles. The beam spot was 1.5 mm in diameter. The electric current of beam was of the order of 10 nA. The vacuum in the scattering chamber was  $1 \times 10^{-5}$  Torr.

Helium samples were prepared by implanting ions into silicon wafers, where two accelerating energies of 20 keV and 45 keV were chosen considering the helium depth distribution and the energy spectrum expected at the ERD measurements. The dose values of implanted helium were  $3 \times 10^{15}$  atoms  $\text{cm}^{-2}$  and  $5 \times 10^{15}$  atoms  $\text{cm}^{-2}$ .

Lithium samples were prepared by evaporating LiF onto silicon wafers because we have technical difficulties generating Li ions at the implantation laboratory. In order to simulate a Li-implanted sample, the LiF was covered with a thin aluminium layer. We made several variations of samples to investigate the deterioration of depth resolution due to atomic collision of recoiled Li in the sample and in the absorber foil: 1) substrates covered only with a 35-nm LiF layer, 2) the LiF layer was sandwiched with the substrate and a 60-nm aluminium layer, 3) samples with three layers with a sequence of LiF-AL-LiF-substrate, and so on.

Figure 1 shows, from top to bottom, the spec-

tra of particles recoiled from a blank silicon wafer, a LiF-evaporated silicon wafer, and two He-implanted silicon wafers. Around 100 channel each spectrum has a sharp peak from surface hydrogen of adsorbed moisture and/or hydrocarbon from the vacuum system. The broad rise of counts below the hydrogen peak is supposed to be caused by scattered projectiles which pass through the absorber foil.

Figure 1b) shows the experimental result with a LiF sample of variation 1. It is well demonstrated that the two stable isotopes of lithium were separated. Recoiled atoms of fluorine were not observed. The depth distribution of Li was assumed to have a box form with a depth of 35 nm.

When we measured the ERD spectra of hydrogen and helium implanted into the Si-wafers using an 8-MeV  $^{16}\text{O}$  beam from the Tokyo Institute of Technology Tandem, the leak of scattered particles through an absorber foil has caused a background below the surface hydrogen peak. Because the aluminium absorber foil was theoretically thick enough to stop 8-MeV  $^{16}\text{O}$  ions, we thought that the aluminium foil had inhomogeneity in the thickness. The aluminium foil was replaced by a Havar foil. Good results have been obtained in reducing background and also in improving energy resolution.

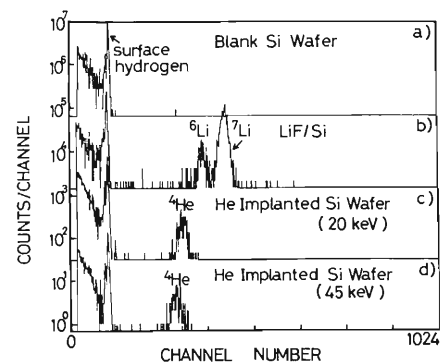


Fig. 1. ERD spectra. Samples are: from top to bottom, a blank silicon wafer, a LiF-evaporated silicon wafer and two He-implanted silicon wafers.

\* Research Laboratory for Nuclear Reactors, Tokyo Institute of Technology.

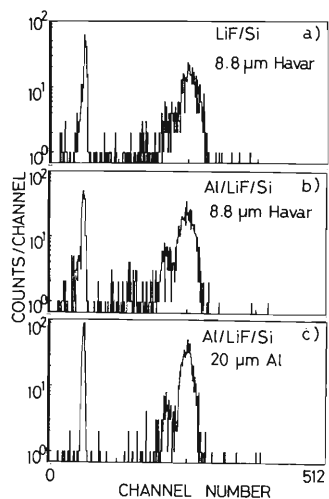


Fig. 2. Comparison of ERD spectra observed using a Havar-foil absorber with those using an Al-foil absorber. a) Spectrum of recoiled Li atoms from the same sample as that for the measurements shown in Fig. 1b). b) and c) spectra of particles recoiled from an Al-LiF-Si samples, where an 8.8- $\mu\text{m}$  Havar foil and a 20- $\mu\text{m}$  aluminium foil are used as an absorber of projectiles, respectively.

Considering the range of scattered particles, we mounted an 8.8- $\mu\text{m}$  thick Havar foil. The Havar foil consists of Co (42.5%), Cr (20%), Ni (13%), W (2.8%), Mo (2%), Mn (1.6%), and Fe (rest). Figure 2 shows the experimental results: Fig. 2a) represents the spectrum of recoiled Li atoms from the same sample as that for the measurements shown in Fig. 1b). The separation between the two isotopes of Li became poorer. Spectra of particles recoiled from an Al-LiF-Si sample are shown in Figs. 2b) and 2c), where an 8.8- $\mu\text{m}$  Havar foil and a 20- $\mu\text{m}$  aliminium foil are used as absorber of projectiles, respectively. It is obvious that the aliminium foil is better than the Havar foil for ERD measurements using a 50-MeV Ar beam. Although the uniformity in thickness is an important factor for absorber foils, larger straggling in the high- $Z$  absorber is more serious in this energy range.

### III-3-3. Depth Profiling of Light and Heavy Elements—Application to the Study on the Compositions of Anodic Oxide Films on Titanium—

K. Tachi, M. Aratani, T. Kato, M. Yanokura,  
T. Sato,\* and M. Otsuka\*

When elastic recoil detection analysis (ERDA) is performed with heavy ions such as an argon ion, it is possible to obtain the depth profiles of light elements such as oxygen, carbon and hydrogen atoms in a specimen by using suitable absorbers.<sup>1)</sup> Moreover, simultaneous performance of Rutherford forward scattering spectroscopy (RFS) makes it possible to get the depth profiles of heavy elements in the specimen. Thus the information can be obtained on the composition in complicated specimens.

Titanium anodic oxide film of less than 1  $\mu\text{m}$  in thickness is a kind of interference film which produces various colors and has a high dielectric constant. Therefore, the titanium anodic oxide film is a promising material for color production<sup>2)</sup> and for condensers.<sup>3)</sup>

Using a 50 MeV  $\text{Ar}^{4+}$ -ion beam from RILAC, we performed the simultaneous analysis of ERDA and RFS in order to investigate the composition of titanium anodic oxide films prepared at various electrolysis voltages in a phosphoric acid solution (5 wt.%).

A scattering chamber (75 cm in diameter) located at the RILAC A-1 beam line was used. At the center of the chamber, the specimens were set up at an angle of 30° to the incident beam. Two surface-barrier semiconductor detectors (SSD) were arranged at an angle of 33° (SSD-1) and at 48° (SSD-2) to the incident beam. In front of SSD-1, an aluminium foil was set up to detect only light elements (H and O). The thicknesses were 10  $\mu\text{m}$  for specimens No. 1 to 5 and 5  $\mu\text{m}$  for specimens Nos. 6 and 7. The spot size of an incident ion beam was 2 mm × 2 mm on the specimen.

Figure 1 shows a typical current-voltage curve for titanium oxidized anodically in a 5 wt.% phosphoric acid solution. The change in the composition in the oxide films were investigated at the points where the remarkable changes in current appeared with increase of the electrolysis voltage. The titanium plates with a purity of

99.86% were used for specimen. Conditions for anodic oxidation of specimens, ratios of oxygen to titanium, and the possible structure in oxide films for each specimen are shown in Table 1.

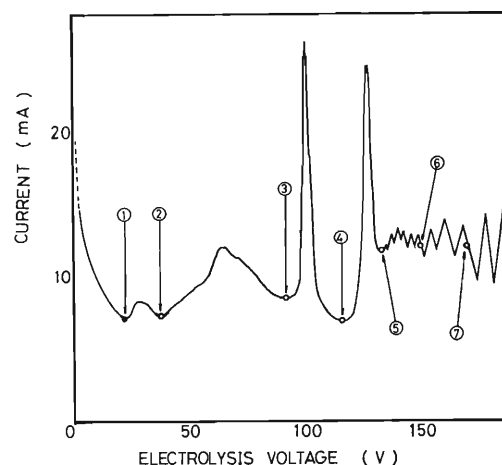


Fig. 1. Voltage-current curve for titanium with a purity of 99.86% oxidized anodically in a 5 wt.% phosphoric acid solution. Specimens are identified by numbers.

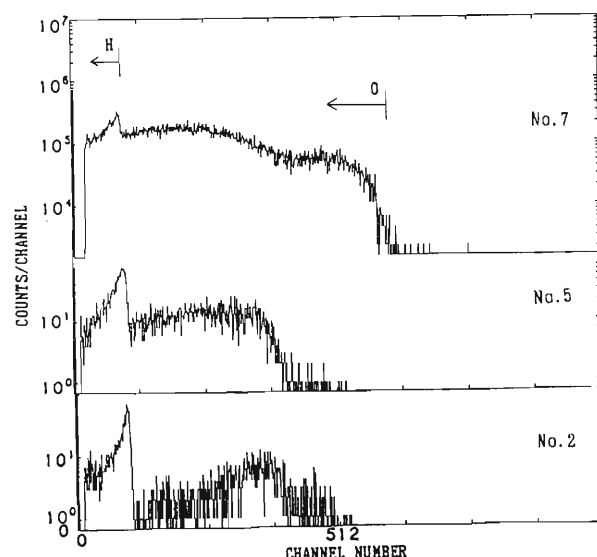


Fig. 2. Depth profiles of oxygen and hydrogen in the oxide films of the specimens of Nos. 2, 5, and 7. The peaks at far right-hand sides indicate the surfaces of specimens.

\* Department of Metallurgy, Shibaura Institute of Technology.

Table 1. Electrolysis conditions and analytical results of specimens.

No.	Electrolysis voltage (V)	Oxide film thickness (nm)	Ratio of Ti and O	Constitution of oxide film
1	23	95	1 : 0.57	TiO, Ti
2	38	106	1 : 0.77	TiO, Ti
3	91	151	1 : 1.19	Ti <sub>2</sub> O <sub>3</sub> -TiO
4	118	177	1 : 1.48	Ti <sub>2</sub> O <sub>3</sub> -TiO
5	133	190	1 : 1.62	Ti <sub>2</sub> O <sub>3</sub>
6	150	313	1 : 1.83	Ti <sub>2</sub> O <sub>3</sub> -TiO <sub>2</sub>
7	170	335	1 : 2.03	Ti <sub>2</sub> O <sub>3</sub> -TiO <sub>2</sub>

\* Each specimen is prepared from 99.86% Ti in H<sub>3</sub>PO<sub>4</sub> (5wt.%).

Figure 2 shows the oxygen and hydrogen spectra obtained for the specimens Nos. 2, 5, and 7 with SSD-1, in which the peak width of oxygen indicates the thickness of the oxide film, and the ratio of titanium and oxygen in the oxide film is determined from the peak height of oxygen.

These results indicate that the thickness of the oxide film became thicker with the increase in the electrolysis voltage. Moreover, the composition of the film was varied from TiO to Ti<sub>2</sub>O<sub>3</sub>, and finally to TiO<sub>2</sub>.

For the specimens Nos. 1 and 2, the thicknesses of the oxide films were estimated to be about 100 nm, and the structures are considered to be mixtures of Ti and TiO. For the specimens Nos. 3, 4, and 5, the thicknesses were more than 150 nm. In the specimens Nos. 3 and 4, the compositions of the oxide films were considered to be Ti<sub>2</sub>O<sub>3</sub> near the surface and TiO at a deep part, while a uniform Ti<sub>2</sub>O<sub>3</sub> composition was found in

the specimen No. 5. However, there were the surface and substrate oxide layers in the oxide film of the specimen No. 5, and the thickness of the surface oxide layer was estimated as about 55 nm. For higher electrolysis voltages, the oxide in the specimen Nos. 6 and 7 grew to thicker beyond 300 nm. On the other hand the surface oxide layers became thinner and the substrate oxide layers were varied to TiO<sub>2</sub>. This result proves that the substrate oxide layer is preferably varied to TiO<sub>2</sub> at an electrolysis voltage beyond a critical value.

#### References

- 1) H. Nagai, S. Hayashi, M. Aratani, T. Nozaki, M. Yanokura, T. Kohno, O. Kuboi, and Y. Yatsurugi: *Nucl. Instrum. Methods B*, **28**, 59 (1987).
- 2) T. Onaka and S. Ito: Proc. 78th Conf. Metal Finishing Soc. Jpn., p. 192 (1988).
- 3) A. Miyata and M. Koyama: *Rep. IPCR*, **37**, 290 (1961).

RIKEN Accel. Prog. Rep. 22 (1988)

### III-3-4. Behavior of a Releasing Agent Coated on a Heated Substrate as Studied by Heavy-Ion Rutherford Scattering

I. Sugai, M. Aratani, T. Kato,\* H. Kato, and M. Yanokura

Recent high-resolution measurements in nuclear physics require target as pure and uniform as possible and self supporting foils of less than hundreds of micrograms per square centimeter in thickness.<sup>1)</sup>

Self-supporting foils were prepared by following processes. A releasing agent coated by evaporation between a deposited layer and a substrate was dissolved in water, and the deposited layer was separated and floated on water, and then picked up on a target frame. The foils deposited on a substrate at high temperature are well known to have improved lifetime and durability against heavy-ion bombardment. The releasing agent coated on the substrate plays very important roles to release the deposited layer. The foils on the releasing agent, however, are not separated easily from the substrate in almost cases.

In order to investigate why the layer deposited at high temperature can not be separated smoothly from the releasing agent on the substrate, we applied the heavy-ion Rutherford scattering method both at backward (Rutherford backscattering; RBS) and at forward angles. A preliminary measurement was presented previously.<sup>2)</sup>

We used  $\text{NiCl}_2$  as a releasing agent. The quartz plate was used as a substrate instead of conventional soda glass<sup>2)</sup> because it gave rise to Na component into releasing agent. The substrates were vacuum-deposited with  $\text{NiCl}_2$  of  $100 \mu\text{g}/\text{cm}^2$  in thickness and were heated to  $250^\circ\text{C}$ ,  $320^\circ\text{C}$ , and  $400^\circ\text{C}$ . The thickness of  $\text{NiCl}_2$  was monitored with a crystal thickness gauge during vacuum deposition, and weighed with an electron ultra microbalance in dry  $\text{N}_2$  gas in order to keep  $\text{NiCl}_2$  unhydrinous.

The sample were bombarded with a 50 MeV  $\text{Ar}^{4+}$  beam from RILAC at an intensity of about 20 nA. Surface-barrier silicon detectors were set at angles of  $35^\circ$ ,  $50^\circ$ , and  $155^\circ$  in a scattering chamber of 1 m in diameter to measure recoiled

light elements and to monitor argon ions scattered from the samples.

The lifetime of carbon foils were found to be independent of the substrate in the temperature range investigated up to  $430^\circ\text{C}$ , but the lifetimes of the foils of elements other than carbon were improved by the heat treatment.

Figure 1 shows the spectra of the  $\text{NiCl}_2$  layer treated by heating. The upper and lower spectra were obtained with the samples heated to  $400^\circ\text{C}$  and  $250^\circ\text{C}$ , respectively. The amount of the Ni

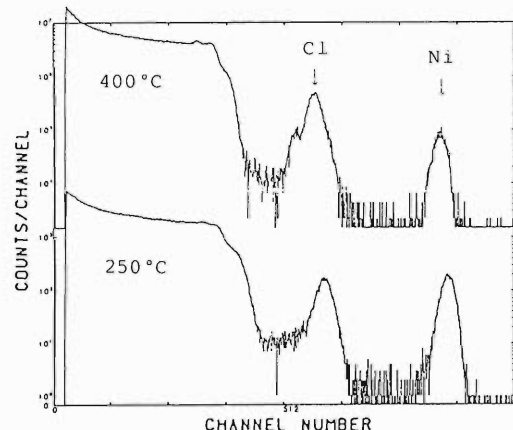


Fig. 1. Spectra of the particles scattered and recoiled from  $\text{NiCl}_2$  at  $E(\text{Ar}^{4+}) = 50 \text{ MeV}$  and  $Q_{\text{lab}} = 50^\circ$ .

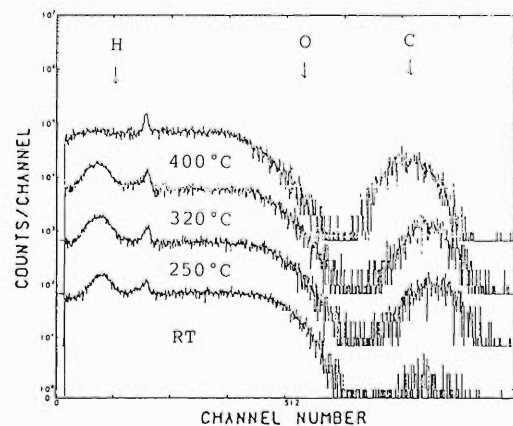


Fig. 2. Spectra of recoiled impurities of hydrogen, carbon, and oxygen from  $\text{NiCl}_2$  on the  $\text{SiO}_2$  substrate at  $E(\text{Ar}^{4+}) = 50 \text{ MeV}$  and  $Q_{\text{lab}} = 35^\circ$ .

\* Present address: Toyo Seikan Company, Ibaraki, Osaka.

layer on the substrate heated at 400°C pronouncedly decreased compared with that heated at 250°C. A Cl layer is seen as two peaks in Fig. 1. The low energy-side peak of Cl layer is due to some Cl component which invaded into the substrate.

Figure 2 shows the spectra of light-element impurities from the  $\text{NiCl}_2$  layer and  $\text{SiO}_2$  substrate. Peaks of hydrogen, oxygen, and carbon are also observed. Hydrogen and carbon come from impurities contaminated, and oxygen is mainly from the substrate  $\text{SiO}_2$ . The two peaks of hydrogen in Fig. 2 indicate surface hydrogen in a sharp shape and internal hydrogen in a broad shape. The peak due to internal hydrogen disappears at 400°C.

In conclusion, at a high temperature of 400°C the Ni layer decreases and the Cl layer invades

into the  $\text{SiO}_2$  substrate. Namely, the releasing agent seems to decrease at 400°C by sublimation and invade into the substrate. As a result, separation ability of the foil is reduced. Thus, we found the mechanism of reduction of separation ability of the foil after the heat treatment at high temperature. The heat treatment is effective to improve the strength of foils; the heat treatment is necessary for the preparation of self-supporting targets. A farther investigation, however, for releasing agents is also necessary for it.

#### References

- 1) S. Takeuchi, C. Kobayashi, Y. Satoh, T. Yoshida, E. Takekoshi, and M. Maruyama: *Nucl. Instrum. Methods*, **158**, 333 (1979).
- 2) I. Sugai, H. Kato, M. Aratani, M. Yanokura, and T. Nozaki: *RIKEN Accel. Prog. Rep.*, **20**, 103 (1986).

### III-3-5. Cross-Check of He Profiles by ERDA Method with $^{16}\text{O}$ and $^{40}\text{Ar}$ Beams

K. Kurimoto, H. Hashimoto, M. Nakajima, M. Ogawa, and M. Aratani

We investigate the hydrogen retention in stainless steel pre-irradiated with helium ions in order to study plasma-wall interactions for fusion energy. We have found that the hydrogen profiles are very close to the range distributions of helium atoms as predicted from theories.<sup>1-3)</sup> We have initiated measurements of helium depth profiles by means of Elastic Recoil Detection Analysis (ERDA).<sup>4)</sup> We have performed cross-checks of He profiling with two different beams, *i.e.*, an 8 MeV  $^{16}\text{O}$  beam and a 50 MeV  $^{40}\text{Ar}$  beam.

Two specimens of stainless steel were irradiated with 10 keV helium ions to fluences of  $2 \times$  and  $4 \times 10^{17}\text{He}/\text{cm}^2$ . These fluences correspond to those below and above the critical fluence, which induces blistering. The third specimen was implanted with 10 keV molecular hydrogen ions subsequent to helium pre-irradiation with a fluence of  $4 \times 10^{17}\text{He}/\text{cm}^2$ . The range of helium is 50 nm on the basis of the calculation using the TRIM86<sup>5)</sup> code. The  $^{16}\text{O}$  beam of 8 MeV was generated by the 1.6 MV tandem pelletron at Tokyo Institute of Technology. The  $^{40}\text{Ar}$  beam of 50 MeV was provided by RILAC. In order to make a comparison simple, we adopted the same

geometrical configuration in ERDA. The incident angle of the beams with respect to the target surface was 15° and an outgoing angle of recoiled atoms was also 15° with the scattering angle of 30°. This geometry was chosen to optimize the depth resolution with an  $^{16}\text{O}$  beam. The geometry was also close to the optimum condition of the depth resolution with an  $^{40}\text{Ar}$  beam.

Figure 1 shows the ERDA spectra measured with an  $^{16}\text{O}$  beam for three specimens. The right-hand peaks correspond to the helium profiles and the left-hand ones to the hydrogen profiles. If we ignore the energy dependence of the stopping power as the first order approximation, peak shapes give depth profiles. We observed the change in the helium profiles depending on the irradiation conditions. The depth resolution was estimated as an order of 10 nm, because the Figs. 1(B) and 1(C) indicate double peaks. The maximum probing depth was about 120 nm due to overlapping with hydrogen signals.

Figure 2 shows the ERDA spectra taken with an  $^{40}\text{Ar}$  beam. The spectra indicate exactly the same trends as those with the  $^{16}\text{O}$  beam. Figures. 2(B) and 2(C) also show the double peaks in the

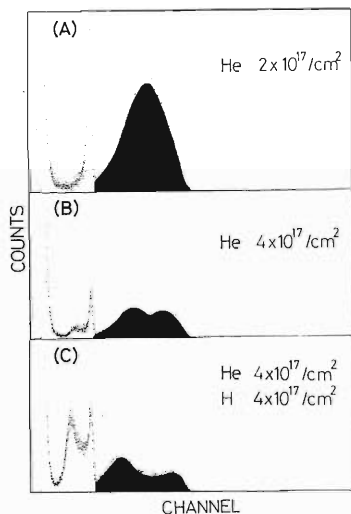


Fig. 1. ERDA spectra measured with an 8 MeV  $^{16}\text{O}$  beam for stainless steel irradiated to fluences of (A)  $2 \times 10^{17}\text{He}/\text{cm}^2$ , (B)  $4 \times 10^{17}\text{He}/\text{cm}^2$ , and (C)  $4 \times 10^{17}\text{He}/\text{cm}^2$  and  $4 \times 10^{17}\text{H}/\text{cm}^2$ .

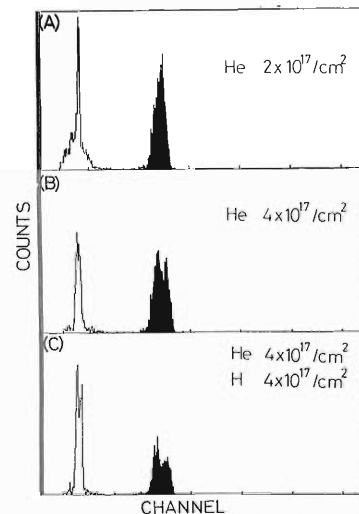


Fig. 2. ERDA spectra measured with a 50 MeV  $^{40}\text{Ar}$  beam for stainless steel irradiated to fluences of (A)  $2 \times 10^{17}\text{He}/\text{cm}^2$ , (B)  $4 \times 10^{17}\text{He}/\text{cm}^2$ , and (C)  $4 \times 10^{17}\text{He}/\text{cm}^2$  and  $4 \times 10^{17}\text{H}/\text{cm}^2$ .

helium distributions. The depth resolution with an  ${}^{40}\text{Ar}$  beam is lower than that with a  ${}^{16}\text{O}$  beam by a factor of two to three. The maximum probing depth with the  ${}^{40}\text{Ar}$  is about 400 nm, which is three times larger than that with the  ${}^{16}\text{O}$  beam. For a 50 MeV  ${}^{40}\text{Ar}$  beam, the depth resolution was strongly affected by the energy spread of the incident beam. This is because the beam-energy spread is no more negligible compared with the straggling of stopping power and the detector resolution.

#### References

- 1) M. Ogawa, K. Saneyoshi, Y. Takagi, A. Shirota, and Y. Suzawa: *J. Nucl. Mater.*, **149**, 247 (1987).
- 2) M. Ogawa, K. Saneyoshi and T. Harada: *Nucl. Instrum. Methods B*, **33**, 768 (1988).
- 3) M. Ogawa, K. Saneyoshi, T. Harada, and K. Imai: *Fusion Technol.*, **14**, 719 (1988).
- 4) A. Turos and O. Meyer: *Nucl. Instrum. Methods B*, **4**, 92 (1984).
- 5) J. F. Ziegler, J. P. Biersack, and U. Littmark: *The Stopping and Range of Ions in Solids*, Pergamon, New York (1985).

### III-3-6. Application of PIXE Analysis to Materials Sciences (I)

Y. Sasa, K. Maeda, and M. Uda

Particle induced X-ray emission (PIXE) spectroscopy has been applied to the analysis of trace element concentrations in the specimens from such various fields as bio-medical,<sup>1-3)</sup> environmental,<sup>1,4)</sup> archaeological,<sup>1,5)</sup> and geological sciences.<sup>1,6)</sup> This method is excellent notably in the quantitative measurements of heavier elements included in the matrix composed of low atomic number elements. These merits are expected to be effectively utilized in the field of materials science as well. We have attempted to develop a simple and convenient data-processing procedure suited for the PIXE analysis of industrial materials. As a first step, trace element distributions on the industrial Al thin foils ( $\sim 15 \mu\text{m}$  in thickness) were studied.

In this study, three Al foils supplied by different companies were used as test targets, and an NBS Al alloy (SRM 1241a) and six Al sheets ( $\sim 0.1 \text{ mm}$ ) containing known amounts of variable impurities were adopted as the reference materials. The chemical compositions of the reference Al sheets were determined by ordinary chemical analysis: atomic absorption, inductively coupled plasma atomic emission, and color-

imetric analysis. The composition of the Al alloy was guaranteed by NBS. Target materials were irradiated with 1.6 MeV  $\text{H}^+$  ions obtained from the tandemron. The spot size of the ion beam focused on the targets was 3 mm in diameter and the beam intensities were regulated to be about 50 nA on the targets. X Rays emitted from the targets were measured with a Si(Li) semiconductor detector through a  $7.5 \mu\text{m}$  Be window. High-energy X rays generated from trace amounts of elements were detected through a polyethylene absorber ( $92 \text{ mg/cm}^2$  in thickness) placed between the target and the detector in order to press down the pile-up phenomenon in the detector. Signals from the detector were stored in a multichannel pulse height analyzer, and then processed on a microcomputer and recorded on magnetic disks.

Figure 1 shows a typical PIXE spectrum obtained from an industrial Al thin foil. The integrated intensity of the characteristic X-ray peak for each component ( $P_{ob}$ ) was obtained from the observed spectra after subtraction of background and corrections for escape peaks, pile-up peaks, and peak overlappings.<sup>2,3)</sup> To determine the absolute concentration of minor and trace elements, the intensity of continuous X rays ( $B_{con}$ ) was employed as a normalizing parameter<sup>2,3)</sup> in place of other parameters, such as the total amount of the incident ions and that of the backscattered ions, both of which are conventionally used for normalization. This is because, under the present experimental conditions, most of the continuous X rays are emitted from the matrices of the target materials due to secondary electron bremsstrahlung and atomic bremsstrahlung.<sup>7,8)</sup> The intensity of the continuous X rays was estimated from the background intensity around 4 keV where neither escape peaks nor the exponential tails of the characteristic X-ray peaks were detected. Here the contribution from a step-like low-energy tail was subtracted from the observed background intensity. The normalized X-ray peak intensities ( $P_{ob}/B_{con}$ ) were then converted into concentrations ( $C_{px}$ ) by means of the theoretically calculated X-ray yields ( $Y_{cal}$ ) and the conversion factor ( $k$ )

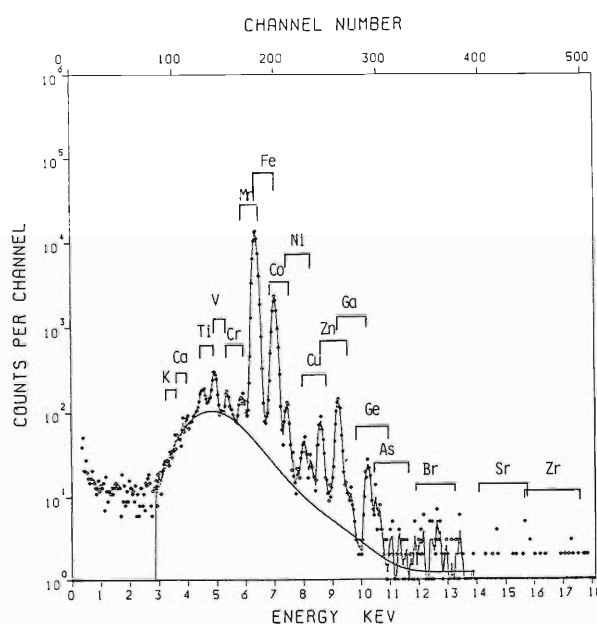


Fig. 1. PIXE spectrum obtained from an industrial Al thin foil; a  $92 \text{ mg/cm}^2$  polyethylene absorber was used.

estimated from the PIXE spectra of seven reference materials of known chemical compositions.

The conversion factor was determined by the following procedure. The relationship between the concentration measured by the chemical methods  $C_{\text{CA}}$  and the normalized peak intensity divided by the theoretical X-ray yield  $N_{\text{px}}$  ( $= (P_{\text{ob}}/B_{\text{con}})/Y_{\text{cal}}$ ) is illustrated in Fig. 2 for the reference materials. Here,  $Y_{\text{cal}}$  was calculated by a computer program 'PIXAN'<sup>9)</sup> using the ionization cross section of elements  $\sigma$ , the stopping powers  $S$ , absorption of X rays by an Al matrix, and the experimental conditions including a beam-target-detector geometry.

Figure 2 indicates that the data points for Fe, Cu, Zn, and Ga are fitted on the same line with a gradient of 1.0 over a wide range of concentration. This feature gives evidence that the amounts of the continuous X rays generated from a target itself correctly give the conversion factor of PIXE intensities into chemical concentrations. That is, in PIXE analysis the element

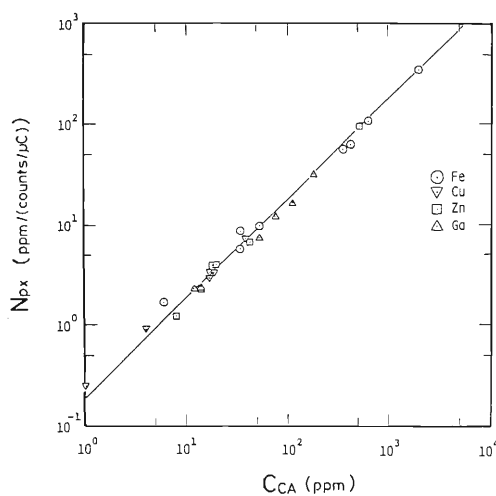


Fig. 2. Correlation of chemical contents  $C_{\text{CA}}$  and normalized PIXE intensities divided by the theoretical X-ray yield  $N_{\text{px}}$  ( $N_{\text{px}} = (P_{\text{ob}}/B_{\text{con}})/Y_{\text{cal}}$ ).

concentrations can be determined by

$$C_{\text{px}} = kN_{\text{px}} \quad (1)$$

The conversion factor  $k$  for the Al matrix system was evaluated here to be 0.165 (counts/ $\mu\text{C}$ ) from the intersect of the ordinate of Fig. 2. With use of this factor, the contents of Fe, Cu, Zn, and Ga in the Al foil, whose PIXE spectrum is shown in Fig. 1, were estimated as 4700, 190, 60, and 140 ppm, respectively.

This study demonstrated that the continuous X-ray background can be successfully used as a normalizing parameter for the quantitative trace analysis, and that the conversion factor evaluated on one element can be applied to any other elements in a series of samples of similar matrices.

## References

- 1) S.A.E. Johansson and T.B. Johansson: *Nucl. Instrum. Methods*, **137**, 473 (1976); 1a) Proc. 1st Int. Conf. PIXE and Its Analytical Applications, *Nucl. Instrum. Methods*, **142** (1977); 1b) Proc. 2nd Int. Conf. PIXE and Its Analytical Applications, *Nucl. Instrum. Methods*, **181** (1981); 1c) Proc. 3rd Int. Conf. PIXE and Its Analytical Applications, *Nucl. Instrum. Methods B*, **3** (1984); 1d) Proc. 4th Int. Conf. PIXE and Its Analytical Applications, *Nucl. Instrum. Methods B*, **22** (1987).
- 2) M. Uda, K. Maeda, Y. Sasa, H. Kusuyama, and Y. Yokode: *Nucl. Instrum. Methods B*, **22**, 184 (1987).
- 3) K. Maeda, Y. Yokode, Y. Sasa, H. Kusuyama, and M. Uda: *Nucl. Instrum. Methods B*, **22**, 188 (1987).
- 4) K. Maeda, Y. Sasa, M. Maeda, and M. Uda: *Nucl. Instrum. Methods B*, **22**, 456 (1987).
- 5) Y. Sasa, M. Maeda, and M. Uda: *Nucl. Instrum. Methods B*, **22**, 426 (1987).
- 6) H. Yabuki, A. Okada, S. Yabuki, K. Maeda, Y. Sasa, and M. Uda: *RIKEN Accel. Prog. Rep.*, **19**, 119 (1985).
- 7) K. Ishii, S. Morita, and H. Tawara: *Phys. Rev. A*, **30**, 2278 (1984).
- 8) K. Ishii and S. Morita: *Phys. Rev. A*, **33**, 3018 (1986).
- 9) E. Clayton: PIXAN: The Lucas Heights PIXE Analysis Computer Package, AAEC/M113, Australian Atomic Energy Commission (1986).

### III-3-7. Multielement Analysis of Human Spermatozoa by PIXE

K. Maeda, Y. Sasa, H. Kusuyama, K. Yoshida,\* and M. Uda

Much attention has been paid to the elementary compositions in biological organisms in order to obtain information for the elucidation of the mechanisms and diagnosis of diseases. PIXE (particle induced X-ray emission) spectroscopy has a great potential for such an investigation, because of its ability to analyze multiple elements simultaneously with high sensitivity without tedious chemical pre-treatments. We have continued a study on the application of PIXE to medical science.<sup>1-4)</sup> We have used this method for analysis of human spermatozoa, expecting the understanding of the roles of trace elements in fertilization.

Seventeen semen samples were taken from ten patients who were afflicted with infertility. Later, three of these patients have proved to be normal. A part of each semen sample was used for determination of the bio-medical qualities of

semen, such as a spermatozoon density (/ml), a motility of spermatozoa in semen (% motile cells), and a concentration of transferrin (a kind of protein which serves as a carrier of iron) in semen ( $\mu\text{g}/\text{ml}$ ). Spermatozoa were separated from seminal plasma by centrifugation and washed three times with distilled and deionized water. The washed spermatozoa were deposited on  $0.5 \mu\text{m}$ -thick Microfilm ( $(\text{H}_9\text{C}_5\text{O}_3)_n$ ), dried in a vacuum desiccator, and used as targets for the PIXE analysis. The thickness and the area of the target samples were  $0.3\text{-}3\text{mg}/\text{cm}^2$  and  $0.1\text{-}0.4 \text{mm}^2$ , respectively.

A beam of  $1.6 \text{ MeV H}^+$  ions obtained from the tandemron was used as an excitation source. The beam was regulated to a  $3 \text{ mm}$  diameter spot on the target by mean of a graphite collimator. X rays emitted from the target were detected with a Si(Li) detector through an X-ray absorber

Table 1. Semen qualities and concentrations of elements contained in human spermatozoa.

Patient	Semen quality				Concentration of element in spermatozoa (ppm in dry weight)														
	Volume (ml)	Density ( $\times 10^6/\text{ml}$ )	Motility (%)	Transferrin ( $\mu\text{g}/\text{ml}$ )	P	S	Cl	K	Ca	Fe	Zn	Ti	V	Cr	Mn	Ni	Cu	Se	Br
†KI	3.2	88	80	—	9,690	3,800	2,490	6,340	1,960	19	2,170	< 3	3	4	< 2	4	6	6	7
†TA	2.4	74	70	—	25,700	7,680	1,580	2,110	1,300	56	860	< 3	< 3	3	3	< 2	4	3	< 2
†SH	2.0	51	50	80	20,100	6,580	2,920	2,600	1,230	54	1,630	< 10	< 10	11	8	5	13	< 7	< 7
†SH	1.2	77	70	78	20,100	7,150	2,900	3,370	1,030	50	1,700	3	3	3	5	4	9	3	14
KO	3.0	70	70	27	21,700	7,520	1,740	3,750	1,040	58	1,330	10	4	5	4	< 5	9	< 5	< 6
WA	3.8	120	60	37	24,300	6,700	2,610	3,880	1,040	68	1,130	6	< 3	5	6	4	7	7	3
HO	3.8	90	60	41	16,000	4,940	5,920	3,430	1,710	39	1,370	2	3	< 2	4	4	3	< 4	8
YO	2.0	22	20	23	12,600	1,650	910	810	6,950	13	1,100	< 3	4	2	6	4	< 3	< 3	4
YO	2.2	32	20	25	17,000	4,110	1,310	1,980	4,690	32	1,130	< 3	3	3	3	< 2	2	3	3
YO	2.0	60	50	23	8,320	2,090	3,740	3,180	2,430	20	790	< 4	3	3	< 3	3	3	< 4	5
IS	2.4	20	20	60	12,700	8,320	730	3,780	3,680	121	3,840	8	4	6	8	8	18	9	18
IS	1.8	22	10	70	17,700	10,700	1,210	4,100	2,160	82	2,810	7	< 4	9	4	6	13	7	11
KU	4.6	1.2	0	27	6,670	6,780	3,220	3,580	1,250	16	2,090	< 9	< 8	< 7	< 9	< 10	< 9	< 27	< 10
KU	4.0	0.77	40	25	10,300	6,040	5,920	6,460	2,240	40	2,900	5	8	6	7	4	14	< 6	15
SI	1.3	0.30	20	160	10,200	3,270	6,680	3,300	1,110	14	850	2	< 2	2	2	5	8	< 2	9
SI	1.8	6.0	30	133	10,100	3,140	4,820	4,560	1,240	48	560	< 4	4	6	2	17	27	< 3	13
KA	3.0	38	0	30	15,000	4,540	3,300	3,210	2,870	27	1,990	< 4	< 3	3	4	4	5	3	4

† normal.

\* Saitama Medical Center, Saitama Medical School.

made of  $1.5 \mu\text{m}$  thick polypropylene or  $0.5 \text{ mm}$  thick polyethylene film. The details of the data processing procedure were described elsewhere.<sup>1,2)</sup>

The results are summarized in Table 1 together with the semen qualities. The concentrations of the elements in the samples were estimated by comparison with a calibration curve

obtained from the reference samples with known compositions.<sup>1,2)</sup> To determine the absolute concentrations, the intensity ratios of the characteristic X-ray peaks to the background continuum<sup>1)</sup> were adapted. Here the intensities of the continuous X rays were integrated over the energy range from 4 to 10 keV to get better statistics.

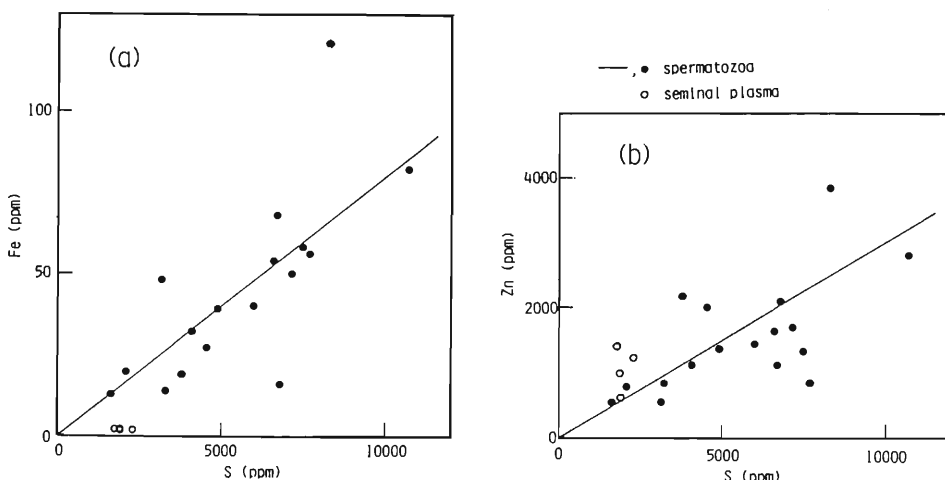


Fig. 1. Concentrations of iron (a) and zinc (b) as a function of that of sulfur: ●, the observed data on spermatozoa; ○, the observed data on seminal plasma (estimated from the PIXE spectra reported in Ref. 4). Straight lines show the average concentration ratios (Fe/S and Zn/S) obtained from the observed data on spermatozoa.

As shown in Fig. 1 (a), a linear relationship was clearly recognized between the sulfur content and the iron content of the spermatozoa, although strong correlations could not yet be found between the semen qualities and element concentrations in the spermatozoa. Zinc also seemed to move along with sulfur (see Fig. 1 (b)). These results suggest that the human spermatozoa contain proteins containing a large amounts of Fe-S and Zn-S components.

The work concerning trace elements in semen and seminal plasma has been reported in many papers. However, there is little information on the trace elements in spermatozoa. This may be partly due to the fact that trace-element analysis by analytical techniques commercially available requires large amounts of samples. PIXE needs very small amounts of samples ( $10^{-9}\text{--}10^{-16} \text{ g}$ ). In

addition, by use of this method, it is possible to detect fugacious elements such as sulfur, chlorine and bromine together with other elements simultaneously. Thus, as can be seen from the examples presented here, PIXE is a promising tool for investigating the mechanism of fertilization.

#### References

- 1) M. Uda, K. Maeda, Y. Sasa, H. Kusuyama, and Y. Yokode: *Nucl. Instrum. Methods B*, **22**, 184 (1987).
- 2) K. Maeda, Y. Yokode, Y. Sasa, H. Kusuyama, and M. Uda: *Nucl. Instrum. Methods B*, **22**, 188 (1987).
- 3) H. Kusuyama, K. Okada, T. Kawai, K. Maeda, Y. Sasa, and M. Uda: *Trace Met. Metab.* (in Japanese), **16**, 51 (1988).
- 4) K. Maeda, Y. Sasa, H. Kusuyama, K. Yoshida, M. Maeda, and M. Uda: *RIKEN Accel. Prog. Rep.*, **17**, 127 (1987).

### III-3-8. Mössbauer Emission Spectroscopy of $^{57}\text{Fe}$ Arising from $^{57}\text{Mn}$

Y. Watanabe, M. Nakada, K. Endo, Y. Kobayashi, H. Nakahara,\* H. Sano,\*  
 K. Kubo, K. Mishima, Y. Sakai, T. Tominaga, T. Okada, K. Asai,  
 N. Sakai, I. Kohno, M. Iwamoto, and F. Ambe

Mössbauer emission spectroscopy offers unique information concerning extremely dilute defect atoms in solid. Literature contains a large number of emission spectra of  $^{57}\text{Fe}$  produced by the EC decay of  $^{57}\text{Co}$  in various matrices. Little attention has been paid, however, to another source nuclide of  $^{57}\text{Fe}$ ,  $^{57}\text{Mn}$ .<sup>1)</sup> The short-lived nuclide (1.45 m) undergoes  $\beta$ -decay, about 80% of it decaying directly to the 14.4 keV Mössbauer level of  $^{57}\text{Fe}$ . EC decay is well-known to result in appreciable damage around the decaying atom due to the Auger process following it. In the case of  $\beta$ -decay, on the other hand, the aftereffects are usually not serious and often an increase in the oxidation number by one is induced. Manganese can take oxidation states up to 7+ in ordinary solid state chemistry, which is not observed in cobalt. It is expected from these facts that an unusually high-valent iron species could be detected after decay of  $^{57}\text{Mn}$  in an appropriate matrix. So far as we know, there have been no investigations with such an object in view. In search of such possibilities, we intend to use a  $^{57}\text{Mn}^{n+}$  beam, which will shortly be

available from the ring cyclotron.

This year, we started a series of preparatory experiments using the  $^{54}\text{Cr}(\alpha, p)^{57}\text{Mn}$  reaction by means of the 160 cm cyclotron. A target transportation system for this purpose was designed and constructed as described in a separated paper of this volume.<sup>2)</sup> It was installed in a 1 m diameter scattering chamber at the #1 beam course of the cyclotron. We have successfully observed the emission spectrum of  $^{57}\text{Mn}$  produced in  $^{54}\text{Cr}$  metal and  $^{54}\text{Cr}_2\text{O}_3$  with the target transport system, a piezoelectric bimorph transducer developed by one of the authors (N. S.),<sup>3)</sup> and a Si(Li) detector. Experiments on other chromium compounds are in progress.

#### References

- 1) R. S. Preston and B. J. Zabransky: *Phys. Lett. A*, **55**, 179 (1975).
- 2) Y. Ikegami, K. Nishi, Y. Watanabe, K. Endo, K. Kubo, M. Iwamoto, and F. Ambe: This Report, p. 152.
- 3) N. Sakai, F. Ambe, and K. Asai: *RIKEN Accel. Prog. Rep.*, **21**, 92 (1987).

---

\* Faculty of Science, Tokyo Metropolitan University.

### III-3-9. $^{99}\text{Ru}$ Mössbauer Spectroscopic Studies of Heusler Alloys

Y. Kobayashi, M. Katada, H. Sano,\* T. Okada,  
K. Asai, M. Iwamoto, and F. Ambe

In this period,  $^{99}\text{Ru}$  Mössbauer spectroscopy was applied to a series of ordered Heusler alloys. They are a ternary system consisting of ruthenium, iron, and silicon with a chemical formula  $\text{Ru}_x\text{Fe}_{3-x}\text{Si}$ , so that the ruthenium atoms in this system are considered to substitute iron atoms of a collinear ferromagnet  $\text{Fe}_3\text{Si}$ .<sup>1)</sup> It is expected that the application of  $^{99}\text{Ru}$  Mössbauer spectroscopy is very significant for the elucidation of the complex magnetic behavior of this system.

Powdered Fe (99.999%), Ru (99.99%), and Si (over 99.99%) were mixed in an appropriate proportion, pressed into a pellet, and then melted into an ingot in an argon-arc furnace. The powder X-ray diffraction patterns of annealed samples showed that they are essentially in a single phase with a cubic  $\text{L}2_1$  Heusler structure. Mössbauer spectra of  $^{99}\text{Ru}$  were measured with  $^{99}\text{Rh}$  in Ru metal by means of a conventional spectrometer. The source nuclide,  $^{99}\text{Rh}$  ( $T_{1/2}=15.0$  d), was produced by irradiating a target of 97% enriched  $^{99}\text{Ru}$  metal powder covered with an 80  $\mu\text{m}$  Al foil with 12 MeV protons accelerated by the cyclotron.<sup>2)</sup>

The Heusler structure has four kinds of lattice sites designated as A, B, C, and D (Fig. 1). In a typical compound  $\text{Fe}_3\text{Si}$ , Fe atoms occupy the A, C, and B sites, A and C being equivalent to each other.

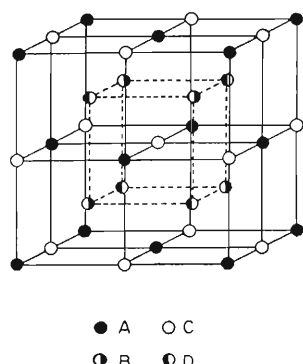


Fig. 1. Unit cell of the Heusler structure.

The  $^{99}\text{Ru}$ -Mössbauer spectrum of  $\text{RuFe}_2\text{Si}$  observed at 5 K, shown in Fig. 2, has a hyperfine structure with little asymmetry; this means that the origin of the hyperfine splittings is only magnetic. The observed spectrum could be hardly analyzed with one set of magnetically split 18 lines and satisfactory fitting required two such sets. The hyperfine magnetic fields at  $^{99}\text{Ru}$  for these two components are 290 and 215 kOe, respectively, and the intensity ratio of the former to the latter is about 1.8. Each of these two components is considered to correspond to Ru [A,C] or Ru [B].

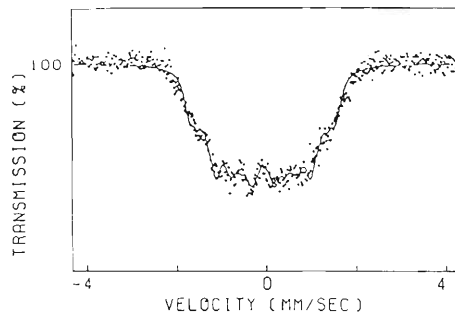


Fig. 2.  $^{99}\text{Ru}$  Mössbauer spectrum of  $\text{RuFe}_2\text{Si}$  at 5 K. The isomer shift is given against the Ru metal at the same temperature.

The origin of  $H_{hf}$  at  $^{99}\text{Ru}$  in  $\text{RuFe}_2\text{Si}$  is ascribed to the neighboring Fe atoms, if Ru atoms are postulated not to have large magnetic moments as in usual alloys. In a first-near-neighbor (1nn) model,<sup>3)</sup> it is further assumed that the dominant part of  $H_{hf}$  at  $^{99}\text{Ru}$  originates from 1nn Fe atoms and their contribution is proportional to the product of their number and magnetic moment. If we take the values for  $\text{Fe}_3\text{Si}$ , 1.35 and 2.2  $\mu_B$ , as the magnetic moments of Fe [A,C] and Fe [B] respectively, the Mössbauer component with a larger  $H_{hf}$  is assigned to Ru [B] and that with the smaller  $H_{hf}$  to Ru [A,C]. It is because the Ru [B] has as 1nn four A and four C sites both occupied by Fe atoms and Ru [A,C] has as 1nn four B and four D sites, only the former of which are occupied by Fe atoms. If we adopt this model, the present  $^{99}\text{Ru}$ -Mössbauer study is con-

\* Faculty of Science, Tokyo Metropolitan University.

cluded to show that Ru occupy both [A,C] and [B] sites, but the latter preferentially.

More detailed discussion will be described elsewhere along with the results of  $^{57}\text{Fe}$  Mössbauer spectroscopy and magnetization measurement.

#### References

- 1) V.S. Patil, R.G. Pillay, A.K. Grover, P.N. Tandon, and H.G. Devare: *Solid State Commun.*, **48**, 945 (1983).
- 2) Y. Kobayashi, M. Katada, H. Sano, T. Okada, K. Asai, N. Sakai, S. Ambe, and F. Ambe: *Hyperfine Interact.*, **41**, 487 (1988).
- 3) V.A. Niculescu, T.J. Burch, and J.I. Budnick: *J. Magn. Magn. Mater.*, **39**, 223 (1983).

### III-3-10. Mössbauer Study of Organic Ruthenium Clusters

Y. Kobayashi, M. Katada, H. Sano,\* T. Chihara,  
H. Yamazaki, T. Okada, and F. Ambe

Organic metal clusters exhibit interesting properties characteristic of both mononuclear metal complexes and metals. Application of Mössbauer spectroscopy to such compounds is very attractive, since it provides useful information concerning the electronic state of metals which is inaccessible by other spectroscopic methods. Quite recently, we started a  $^{99}\text{Ru}$  Mössbauer study on a series of organic ruthenium clusters. This report describes the preliminary result on the first sample of our study,  $[\text{PPN}] [\text{Ru}_{10}\text{C}(\text{CO})_{24}]$  ( $\text{PPN}=(\text{PPh}_3)_2\text{N}$ ).

The preparative method of the cluster and its characterization by other techniques will be reported elsewhere.<sup>1)</sup> Its Mössbauer spectrum was measured at 5 K using  $^{99}\text{Rh}$  ( $T=15.0$  d) produced by the cyclotron. The details of the measurement were essentially the same as described in our previous paper.<sup>2)</sup>

The spectrum given in Fig. 1 is constituted apparently with a single line, but computer analysis revealed the existence of a certain structure. The curve drawn in Fig. 1 is the result of tentative fitting by assuming only one kind of ruthenium atoms with a unique electric quad-

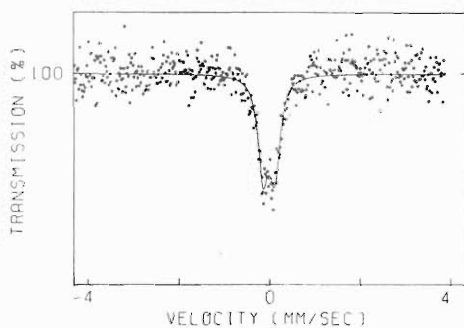


Fig. 1.  $^{99}\text{Ru}$  Mössbauer spectrum of  $[\text{PPN}] [\text{Ru}_{10}\text{C}(\text{CO})_{24}]$  ( $\text{PPN}=(\text{PPh}_3)_2\text{N}$ ) at 5 K. The isomer shift is given relative to metallic ruthenium.

rupole field. More detailed analysis and interpretation will be given in the next volume of this progress report along with the experimental results on other clusters.

#### References

- 1) T. Chihara, R. Komoto, K. Kobayashi, H. Yamazaki, and Y. Matsuura: *Inorg. Chem.*, **28**, 964 (1989).
- 2) Y. Kobayashi, M. Katada, H. Sano, T. Okada, K. Asai, N. Sakai, S. Ambe, and F. Ambe: *Hyperfine Interact.*, **41**, 487 (1988).

\* Faculty of Science, Tokyo Metropolitan University.

### III-3-11. $\gamma$ -Rays Perturbed Angular Correlation of $^{111m}\text{Cd}$ in CdO, $\text{Cd}(\text{OH})_2$ , and $\alpha\text{-Fe(2 at.\% Cd)}_2\text{O}_3$

Y. Ohkubo, S. Ambe, T. Okada, F. Ambe,  
K. Asai, Y. Kawase,\* and S. Uehara\*

Perturbed angular correlations (PAC) were measured for the  $^{111}\text{Cd}$   $5/2^+$  level ( $t_{1/2}=85$  ns) mostly by using  $^{111}\text{In}$  ( $t_{1/2}=2.8$  days), which decays by electron capture (EC) to the excited states of  $^{111}\text{Cd}$ . It is well known, however, that for insulators  $^{111}\text{In}$ -PAC is strongly influenced by the excited electronic states produced by EC and the subsequent Auger process. This phenomenon, so-called aftereffects of EC, is generally thought to be undesirable in applying PAC to solid state physics or chemistry because the hyperfine frequencies are widely spread usually to the extent that no anisotropy can be observed. We aim to apply PAC to solid state physics and chemistry by using short-lived  $^{111m}\text{Cd}$  ( $t_{1/2}=48.6$  min), which decays by isomeric transition and thus is free from the aftereffects accompanying EC. We are establishing a radiochemical procedure to separate no-carrier-added  $^{111m}\text{Cd}$  from an  $\alpha$ -irradiated palladium target. In the present preparatory work,  $^{111m}\text{Cd}$  with a carrier was produced by neutron irradiation and PAC of  $^{111m}\text{Cd}$  in CdO,  $\text{Cd}(\text{OH})_2$  and  $\alpha\text{-Fe(2 at.\% Cd)}_2\text{O}_3$  were measured.

It is expected from the crystal form of each compound that i) there is no extranuclear perturbation in CdO, ii)  $^{111m}\text{Cd}$  in  $\text{Cd}(\text{OH})_2$  feels an axially symmetric electric field gradient and iii)  $^{111m}\text{Cd}$  in  $\alpha\text{-Fe(2 at.\% Cd)}_2\text{O}_3$  feels both an axially symmetric electric field gradient and a hyperfine magnetic field at room temperature and only an axially symmetric electric field gradient above the Néel point  $\cong 960$  K. The measurements on the first two compounds were intended to check the whole experimental procedure and apparatus. Our main interest was in the measurement on the third sample.

The above compounds containing about 0.5 mg of isotopically enriched (94 %)  $^{110}\text{Cd}$  were irradiated for 5 min at a thermal neutron fluence of  $1.93 \times 10^{13} \text{ s}^{-1}\text{cm}^{-2}$  in the Kyoto University reactor. A PAC spectrometer with a four  $\text{BaF}_2$  ( $1.5 \text{ in} \phi \times 1 \text{ in}$ ) detector arrangement consisted

of specially designed digital modules and commercially available analog modules, and was connected to a personal computer. The coincidence counts for detector combinations of 90 and 180 degrees were measured simultaneously as a function of delay time between the emissions of the 151 and 245 keV  $\gamma$ -rays. Total measurement time for each experiment was about 1 hour.

The measured time-differential PAC (TD-PAC) spectra  $A_{22}G_{22}(t)$  are shown in Fig. 1. For CdO, no significant perturbation was observed, as expected from its crystal form,  $A_{22}G_{22}(t=0)=A_{22} \cong 0.1$  (Fig. 1(a)). For  $\text{Cd}(\text{OH})_2$ , the perturbation characteristic of an axially sym-

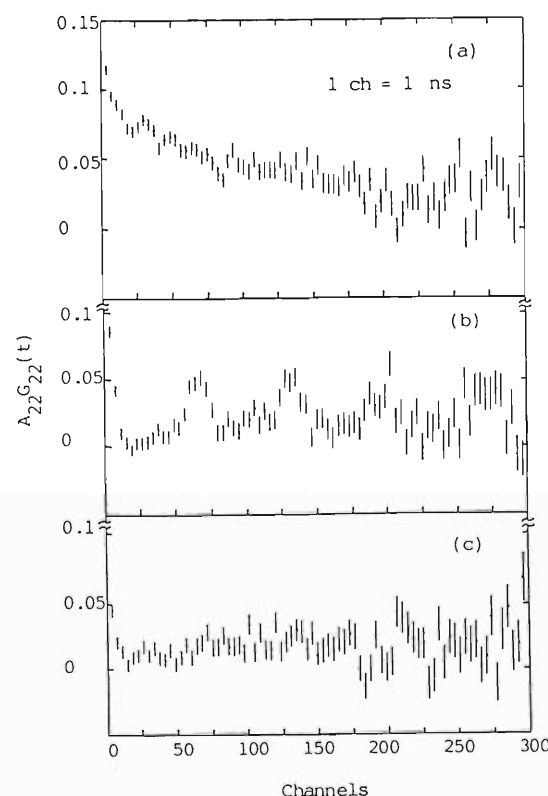


Fig. 1. TDPAC spectra of  $^{111}\text{Cd}$  ( $5/2^+$ ) in CdO (a) and  $\text{Cd}(\text{OH})_2$  (b) measured at room temperature, and  $\alpha\text{-Fe(2 at.\% Cd)}_2\text{O}_3$  (c) at 1,023 K.

\* Research Reactor Institute, Kyoto University, Osaka.

metric electric field gradient was observed. The frequency was about 70 ns, which is in conformity with the value reported by another group,<sup>1)</sup> but the amplitude we observed was about a half of the value of the group (Fig.1(b)). For  $\alpha$ -Fe(2 at.% Cd)<sub>2</sub>O<sub>3</sub>, measurements were made at room temperature and at 1,023 K. Identical TDPAC spectra were obtained at both temperatures. The latter temperature was chosen to be higher than the Néel point  $\cong$  960 K, above which only axially symmetric electric field gradient is expected to cause perturbation. However, almost no anisotropy was observed in the spectra, irrespective of annealing done after the neutron irradiation (Fig.1(c)). The observation indicates that <sup>111m</sup>Cd was not in the regular site of iron in the matrix. This is in striking contrast to

the result on  $\alpha$ -Fe(<sup>111</sup>In)<sub>2</sub>O<sub>3</sub> obtained by using no-carrier-added <sup>111</sup>In.<sup>2-4)</sup>

We plan to study further on no-carrier-added <sup>111m</sup>Cd embeded in  $\alpha$ -Fe<sub>2</sub>O<sub>3</sub> and other various compounds, using the <sup>nat</sup>Pd( $\alpha$ ,xn)<sup>111m</sup>Cd reaction and a radiochemical method for separating <sup>111m</sup>Cd from palladium irradiated at the cyclotron.

#### References

- 1) R.S. Raghavan, P. Raghavan, and J.M. Friedt: *Phys. Rev. Lett.*, **30**, 10 (1973).
- 2) K. Asai, F. Ambe, S. Ambe and H. Sekizawa: *J. Phys. Soc. Jpn.*, **53**, 4109 (1984).
- 3) F. Ambe, K. Asai, S. Ambe, T. Okada, and H. Sekizawa: *Hyperfine Interact.*, **29**, 1197 (1986).
- 4) K. Asai, F. Ambe, S. Ambe, T. Okada, and H. Sekizawa: *Hyperfine Interact.*, **34**, 277 (1987).

### III-3-12. Preparation of No-Carrier-Added $^{111m}\text{Cd}$ for the Measurement of $\gamma\text{-}\gamma$ Perturbed Angular Correlation

S. Ambe, Y. Ohkubo, M. Iwamoto, and F. Ambe

Commercially available  $^{111}\text{In}$  is one of the most convenient source nuclides for  $\gamma\text{-}\gamma$  perturbed angular correlation (PAC) studies. This nuclide, however, is known to give rise, in insulators, to the smearing-out of PAC patterns due to the aftereffects of its EC decay to  $^{111}\text{Cd}$ , providing little information on the electronic state of  $^{111}\text{Cd}$ .<sup>1,2)</sup> On the other hand,  $^{111m}\text{Cd}$  (half-life: 48.6 min), another  $^{111}\text{Cd}$ -PAC source nuclide, undergoing isomeric transition causes no serious after-effects. The nuclide is produced by the  $^{110}\text{Cd}(n,\gamma)^{111m}\text{Cd}$  reaction in a reactor, but is not obtained in a state free from non-radioactive cadmium. In this study we have established a procedure of preparing no-carrier-added  $^{111m}\text{Cd}$  by using the cyclotron, that is, by the  $\text{Pd}(\alpha,xn)^{111m}\text{Cd}$  reaction. The pH dependence of adsorption of divalent Cd\* ion onto  $\alpha\text{-Fe}_2\text{O}_3$  and its coprecipitation behavior with ferric hydroxide were also investigated for the PAC studies on the adsorption structure of  $^{111}\text{Cd}^{2+}$  on the  $\alpha\text{-Fe}_2\text{O}_3$  surface and the defect structure of  $^{111}\text{Cd}_{2+}$  in the bulk  $\alpha\text{-Fe}_2\text{O}_3$ .

Pd foils (8  $\mu\text{m}$ ) were irradiated with 40 MeV  $\alpha$  particles accelerated in the cyclotron. Since  $\alpha$  irradiation produces  $^{107}\text{Cd}$  (half-life: 6.5 h) along with  $^{111m}\text{Cd}$ , we used both nuclides as tracers; thus, we refer  $^{111m}\text{Cd}$  and  $^{107}\text{Cd}$  to as Cd\*.

The Pd target was heated in a quartz tube with a glass cold finger under a rotary pump vacuum (8–11 Pa). The sublimation yield of Cd\* was determined in order to find the optimal temperature for expelling Cd\* from the target by measuring the  $\gamma$  rays from Cd\* with a Ge detector installed under a furnace. Stepwise elevation of heating temperature showed that marked sublimation of Cd\* starts at around 1,000°C. Above 1,050°C Pd was markedly sublimated. We, therefore, adopted 1,050°C as the temperature for routine sublimation. We found that at 1,050°C more than 90% of Cd\* was sublimated in 60 min and trapped on the cold finger.

Most of the Cd\* deposited on the cold finger with a minute amount of metallic Pd was dissolved in hot 1 : 1 nitric acid in 5 min. Palladium and radioactive Ag produced by the ( $\alpha$ , pxn)

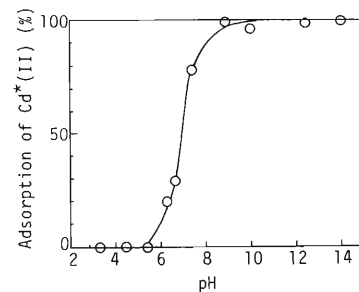


Fig. 1. Adsorption of no-carrier-added divalent Cd\* onto  $\alpha\text{-Fe}_2\text{O}_3$  from a  $0.5 \text{ mol} \cdot \text{dm}^{-3}$   $\text{NaNO}_3$  solution.

reactions were sublimated and dissolved together with Cd\* and completely eliminated by 0.01% dithizone- $\text{CCl}_4$  extraction after the solution was mixed with a dil. NaOH solution to be pH 2.0.

In the adsorption experiment, 30 mg  $\alpha\text{-Fe}_2\text{O}_3$  powder was added to a  $15 \text{ cm}^3$  Cd\* tracer solution and the suspension was shaken for 1 h at room temperature. Adsorption of divalent Cd\* onto  $\alpha\text{-Fe}_2\text{O}_3$  was observed above pH 6.5, increasing with pH to be virtually 100% above pH 9 (Fig. 1). The adsorption curve is typical of hydrolyzable metal ions. Irrespective of the different pH of adsorption, no thermal dissociation of the adsorbed Cd\* from  $\alpha\text{-Fe}_2\text{O}_3$  was detected on heating at 600°C for 20 min in air.

After addition of the Cd\* tracer to a  $40 \text{ cm}^3$  ferric nitrate solution ( $0.02 \text{ mol} \cdot \text{dm}^{-3}$ ), the Cd\* ions were coprecipitated with ferric hydroxide by adding NaOH or  $\text{NH}_4\text{OH}$ . More than 60% of Cd\* was coprecipitated, but about a half of Cd\* was lost when the sample was heated at 800°C for 30 min in air.

The  $^{111m}\text{Cd}$  on the surface and in the bulk of  $\alpha\text{-Fe}_2\text{O}_3$  will be subjected to PAC measurement in the near future.

#### References

- 1) P. Lehmann and J. Miller: *J. Phys. Radium*, **17**, 526 (1956).
- 2) H. Haas and D.A. Shirley: *J. Chem. Phys.*, **58**, 3339 (1973).

### III-4. Radiation Chemistry and Radiation Biology

#### 1. High-Density Excitation by Heavy Ion: Techniques and Measurement of the Fast Emission Decay of BaF<sub>2</sub> Single Crystal

K. Kimura, T. Suzuki, K. Watanabe, K. Uehara, and H. Kumagai

Ions of energies lower than few eV/amu may induce many particular elementary processes in condensed matter, *e.g.*, charge transfer, collective excitations, wake-field, and compton-electron effect. These processes may conceal possibilities to give rise to characteristic radiation effects to matter, though such effects have not yet been found. However, a principal part of radiation effect in condensed matter is considered to be high density excitations, because primarily collisional events, as well as processes aforementioned, lead to excited states of an outermost shell *via* electron cation recombination and cascading internal conversion. The maximum energy-deposition by heavy ion amounts to as large as thousands electron volt per Angstrom at an ion track termination. This may imply that only excited states are contained in a track termination. Therefore, it may be possible that the concentration of excited states exceeds that of the ground state near the track termination, and hence more than two excited states can collide in their lifetimes. Our previous work shows that short-lived free excitons of few ps in alkali halides collide with each other to give an LET-dependent ratio of yields between self-trapped excitons.<sup>1)</sup> Thus, the decay modes of excited states are in general different from those of spontaneous ones, and lifetimes are shortened with density. Decay measurement is one of the methods to investigate the effect of high-density excitation by heavy ions. For this aim, we developed equipment for subnanosecond emission-decay measurement which can operate not only without any improvement of an accelerator but also operate using radio isotopes as an irradiation source.<sup>2)</sup> The equipment was applied to a single crystal of BaF<sub>2</sub>, which has recently attracted special interest, because of its extraordinarily fast emission decay at 2,200 Å.<sup>3)</sup>

We adopted a single-ion hitting and single-photon counting technique developed previous-

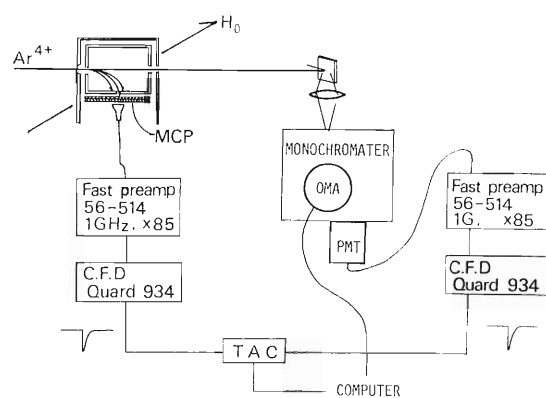


Fig. 1. A block diagram of the detectors and circuit. A cryostat was set as described in Refs. 3, 7, and 12.  $H_0$  stand for the static magnetic field; MCP, a multi-channel plate; TAC, a time-to-amplitude converter; CFD, a constant fraction discriminator; OMA, a optical multi-channel analyzer.

ly,<sup>1)</sup> and improved detectors for ions and photons at same time. As shown in Fig. 1, an incident ion passes through orifices of two coaxial copper-cylinders before hitting a target. A thin carbon foil of 10 micro g/cm<sup>2</sup> is attached on the entrance orifice (0.5 mm in diameter) of the outer cylinder. Secondary electrons emitted from the carbon foil were accelerated to 2 keV between the outer and the inner cylinders, bent by 90 degree by a magnetic field, monochromatized by cut off with an orifice (1 mm in diameter), and excited MCP. This system was termed FASD (fast secondary-electron detector). Other timing pulses were generated by single photon detection using a photomultiplier (MCP-installed Hamamatsu R1564u of a rise time of 220 ps).

As shown in Fig. 2, a time integrated spectrum shows only one broad peak at about 3,100 Å, but no prominent peak at 2,200 Å, in contrast with the case of electron and photon irradiation.<sup>4,5)</sup> A shoulder could be recognized near 2,200 Å at most by a plot of the rises near time 0. Thus, a

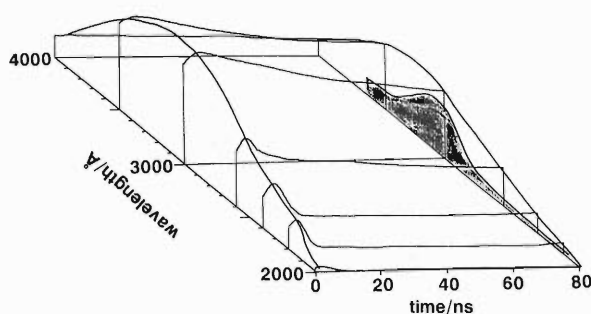


Fig. 2. Time resolved spectra of N-ion irradiated  $\text{BaF}_2$  at room temperature. Time integrated spectrum measured by a monochromator and OMA is also superposed at 80 ns.

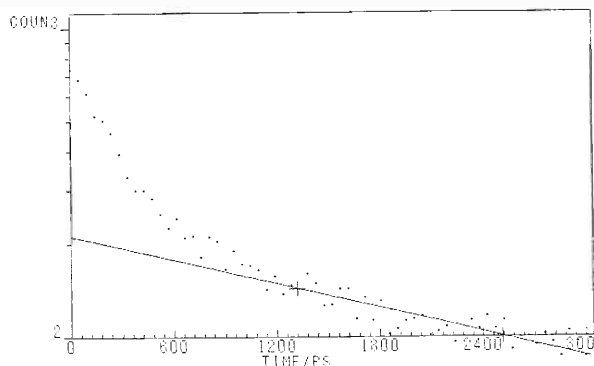


Fig. 3. Logarithmic plot of emission decay of  $\text{BaF}_2$  2,200 Å emission; a straight line is the best fit of the slow component.

fast decay component at 2,200 Å is suppressed in intensity with ion irradiation and also possibly broadened.

A logarithmic plot of the fast decay at 2,200 Å, Fig. 3, shows that the decay consists of two exponentials of half lifetimes of  $250 \pm 50$  ps and  $32 \pm 0.7$  ns. The slow component is considered due to the stray of 3,100 Å emission because resulting from the use of a band-path interference filter at 2,000 Å.

The emission at 2,200 Å was suppressed by lowering temperature and disappeared at 4.2 K in contrast with alkali halides. Similar temperature dependence was observed for the intensity of the 3,100 Å peak. Relative intensities to that at room temperature were about 0 at 4.2 K, 0.2 at 97 K, 0.29 at 142 K, 0.34 at 188 K, and 0.67 at

233 K.

The emission at the 2,200 Å peak is explained to originate in a crossover transition from valence electron of  $\text{F}^{-2p}$  to an inner shell vacancy of  $\text{Ba}^{2+5p}$ .<sup>3,5)</sup> The present results, the linear and fast decay, may support this model. The lifetimes for X irradiation<sup>4)</sup> and electron irradiations,<sup>5)</sup> however, are reported to be 600 ps and 880 ps, respectively. It is an important problem to be resolved whether this discrepancy between the electron or X-ray and heavy-ion irradiation is due to LET or caused by poor resolution. The LET dependent suppression of the 2,200 Å emission is also curious, which cannot be explained on the basis of simple density effect such that a density of  $\text{F}^{-2p}$  electrons is lowered considerably because of high density excitation by heavy ions, because the suppression was at maximum for alpha particles whose LET is considerably lower than that of Ar ion. In addition, no significant difference was recognized between 5 and 10 MeV/amu alpha-irradiations despite the latter's larger delta ray effect and lower LET. The result seems to suggest that an increase in LET increases radiative processes in a crossing manner to quenching processes. Also, the result that the temperature dependence is rather reverse to the case of alkali halides means that formation mechanisms of free and self-trapped excitons are completely different from those in alkali halides. Details are discussed in Ref. 1. The formation mechanisms of excitons along with the LET effect aforementioned is an interesting problem to be solved.

#### References

- 1) K. Kimura, Y. Matsuyama, and H. Kumagai: *Int. Radiat. Chem. Phys.*, in press.
- 2) K. Kimura and M. Imamura: *Phys. Lett. A*, **67**, 159 (1978); K. Kimura, K. Mochizuki, T. Fujisawa, and M. Imamura: *Phys. Lett. A*, **78**, 108 (1980).
- 3) Yu.M. Aleksandrov, V.N. Makhov, P.A. Rodnyi, T.I. Syreishchikova, and M.N. Yakimenko: *Sov. Phys. Solid State*, **26**, 1734 (1984).
- 4) M. Laval, M. Moszynski, R. Allemand, E. Cormoreche, P. Guinet, R. Odoru, and J. Vacher: *Nucl. Instrum. Methods Phys. Res.*, **206**, 169 (1983).
- 5) S. Kubota, M. Suzuki, Jian-zhi Ruan, F. Shiraishi, and Y. Takami: *Nucl. Instrum. Methods Phys. Res., A*, **242**, 291 (1986).

### III-4-2. LET Dependence of Cellulose Triacetate Film Dosimeter Response for Ion Beams

H. Sunaga, R. Tanaka,\* K. Yoshida,\* and I. Kohno

A commercial cellulose triacetate (CTA) film dosimeter FTR-125 has been widely used in radiation processing using electron beams and gamma rays. We examined if the dosimeter is applicable conveniently to ion beams.

In a previous report<sup>1)</sup> on the characteristics of CTA film dosimeter for proton beams, we found that the value of  $\Delta OD$  (difference in optical densities at 280 nm) per unit dose measured with 5 MeV protons, was smaller those with 8 and 15 MeV protons, suggesting LET dependence.

To study the LET dependence of CTA film dosimeter in the high LET region, we measured the dose response for ion beams with different LET, *i.e.*, 30-MeV helium, 80-MeV carbon, and 80-MeV nitrogen ions.

A CTA film of 125  $\mu\text{m}$  in thickness and 8 mm in width was mounted on a cylindrical holder of a rotation type irradiation apparatus for uniform irradiation.<sup>1)</sup> The apparatus was set at the No. 2 course of the cyclotron. All samples were exposed in vacuum.

The ion fluence was evaluated from the ratio of a total charge impinging on the sample holder to an effective irradiation area. The dose absorbed in a CTA sample was estimated from the mass stopping power of the sample by a

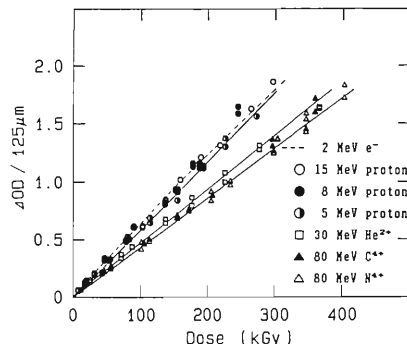


Fig. 1. Relation between absorbed dose and the  $\Delta OD$ 's in CTA samples irradiated with various ions, in comparison with the results obtained with 2 MeV electrons and 5, 8, and 15 MeV protons.

computer program OSCAR. We took the values of mass stopping power of 214, 2,120, and 3,260  $\text{MeVg}^{-1}\text{cm}^2$  for 30-MeV He ions, 80-MeV C ions, and 80-MeV N ions, respectively.

Figure 1 shows the relations between the absorbed dose and the  $\Delta OD$ 's in CTA samples irradiated with various ions, in comparison with the result obtained with 2 MeV-electrons and 5, 8, and 15 MeV protons. The  $K$ -value (defined by  $\Delta OD/10 \text{ kGy}$ ) decreases with increasing LET, and linear dose dependence was observed for heavy-ion beams with LET higher than that of the proton beams.

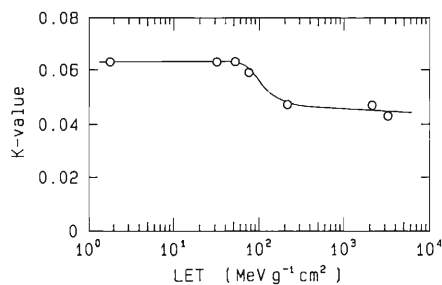


Fig. 2. Dependence of the  $K$ -value ( $\Delta OD/10 \text{ kGy}$ ) on the initial LET for the various ions and 2 MeV electrons.

Figure 2 illustrates the dependence of the  $K$ -value on the initial LET for various ions and electrons, showing that the  $K$ -value decreases remarkable with increasing LET in the region of  $50\text{-}200 \text{ MeVg}^{-1}\text{cm}^2$  and that the rate of decrease becomes low at higher LET's.

For practical ion beam dosimetry using CTA dosimeter, further dosimetry characterization will be necessary for dependence of the dose response on effective LET, the useful ranges of absorbed dose and LET, and the dosimetry uncertainty.

#### Reference

- 1) H. Sunaga, T. Agematsu, R. Tanaka, K. Yoshida, and I. Kohno: *RIKEN Accel. Prog. Rep.*, **21**, 141 (1987).

\* Takasaki Radiation Chemistry Research Establishment, JAERI.

### III-4-3. Proton Irradiation Effects on Mechanical Properties of Aromatic Polymers

T. Sasuga, S. Kawanishi,\* M. Nishii, T. Seguchi,\* and I. Kohno

For evaluation or selection of polymer materials used in space as the components and equipments of artificial satellites, knowledge about the radiation damage induced by high energy ions is needed. Primary experimental results on proton irradiation effects were described in the previous report,<sup>1)</sup> in which the changes in mechanical properties of a variety of aliphatic polymers were studied and compared with those obtained by electron irradiation. The radiolysis yields of organic liquids are known to alter by linear energy transfer (LET),<sup>2,3)</sup> while small or no LET effects were observed on the aliphatic polymers between 8 MeV proton and 2 MeV electron irradiation even though protons have LET 30 times larger than that of electrons. Our experimental results<sup>1)</sup> suggest that (1) there is no significant difference in crosslinking/chain scissions ratio, or (2) the differences in the chemical reactions in micro domains are not directly reflected on mechanical properties.

In the present study, we carried with four aromatic polymer films different in structures from those used in the previous study<sup>1)</sup> and compared with the results of electron irradiation. The polymers used were polyethylene-terephthalate (PET), polyethersulfone (PES), bisphenol A based polyarylsulfone (U-PS), and polyarylester (U-polymer). These polymers were obtained in a film form with 100 μm in thickness. The chemical structures are shown in Fig. 1.

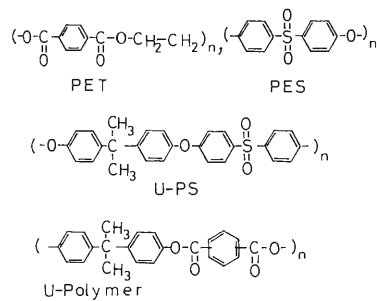


Fig. 1. Chemical structures of polymers used.

Proton irradiation was performed with a beam of 8 MeV accelerated with the cyclotron in the specially constructed chamber reported previously.<sup>1)</sup> The fluence rate was about 13 nC/(cm<sup>2</sup>s). Electron irradiation was carried out under a helium gas flow with a 2 MeV electron beam obtained from an accelerator at JAERI Takasaki. The electron fluence rate was 1.07 μC/(cm<sup>2</sup>s). Irradiation effects were evaluated by tensile tests at a cross head speed of 200 nm/min at 25°C for the specimens cut into an ASTM D-1822 type dumbbell.

The absorbed dose  $D$  (kGy) for protons was calculated from the relation:

$$D = S \times Q$$

where  $S$  (MeV cm<sup>2</sup>/g) is the mass collision stopping power and  $Q$  (μC/cm<sup>2</sup>) is the fluence. The stopping powers were calculated by Bethe's equation as listed in Table 1. The absorbed dose ( $D_e$ ) in the electron irradiation was measured by use of a cellulose-triacetate (CTA) film dosimeter and was corrected for the stopping powers of each polymer for 2 MeV electrons.

Table 1. Stopping powers of the polymers for 8 MeV protons and 2 MeV electrons.

Polymer	Stopping power (MeV · cm <sup>2</sup> /g)	
	for protons	for electrons
PES	48.9	1.78
U-PS	49.6	1.78
U-polymer	50.4	1.78
PET	50.1	1.78

Figure 2 shows the variations in the tensile strength and elongation at break as a function of proton and electron doses for PET. In proton irradiation, the decrement of the tensile strength with dose is less and the decrement of elongation with dose is rather larger than those for electron irradiation. The polymer chain of PET is composed of aromatic and aliphatic units. The result for PET indicates that LET of radiation affects change in mechanical properties.

The result for U-PS, which is composed of only

\* Takasaki Radiation Chemistry Research Establishment, JAERI.

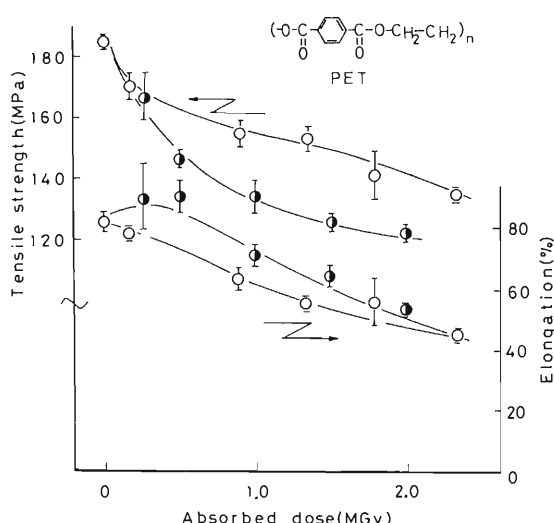


Fig. 2. Tensile properties as a function of dose for PET films irradiated with 8 MeV protons ( $\circ$ ) and 2 MeV electrons ( $\bullet$ ).

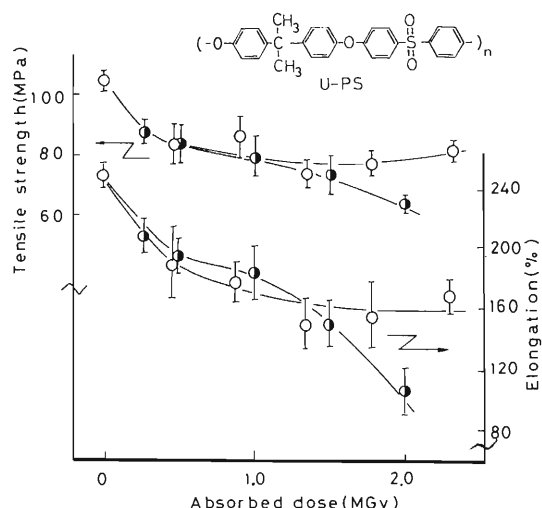


Fig. 3. Tensile properties as a function of dose for U-PS films irradiated with 8 MeV protons ( $\circ$ ) and 2 MeV electrons ( $\bullet$ ).

aromatic units, is shown in Fig. 3. The dose dependence for the two tensile parameters is almost the same up to 1 MGy in proton and electron irradiation, but above 1 MGy the decreasing rates of the strength and elongation per dose in proton irradiation become less than those in the electron irradiation, indicating that the radiation effects decrease with increasing LET. The same results also were obtained in PES and U-polymer. From the results of aliphatic polymer<sup>1)</sup> and PET, the LET effect seems

to increase with increasing aromaticity.

Figure 4 shows the gel fraction of U-PS as a function of dose. In electron irradiation, no gel is formed, but in proton irradiation the gel content increases with dose. This finding shows that crosslinking takes place in proton irradiation. The smaller decrement of the strength and elongation in proton irradiation than in electron irradiation would be caused by increase in the probability of crosslinking.

In general, radiation effects in a condensed phase with high LET irradiation is characterized by high density excitation and high probability of recombination in the supr.<sup>2,3)</sup> The results in Figs. 2 to 4 could be interpreted in terms of the increase in the probability of bimolecular recombination of excited molecules, like in benzene. However, this model fails to interpret the experimental results for aliphatic polymers; the other mechanism also has to be taken into account for the interpretation of the LET effects on polymeric materials.

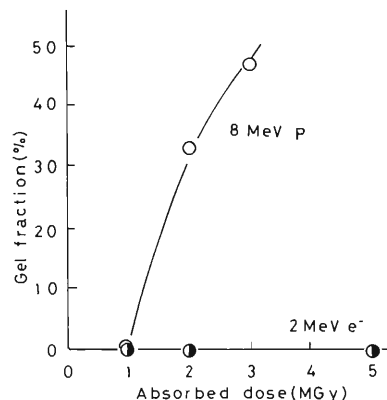


Fig. 4. Gel fraction as a function of dose of U-PS films irradiated with 8 MeV protons ( $\circ$ ) and 2 MeV electrons ( $\bullet$ ).

## References

- 1) T. Sasuga, S. Kawanishi, T. Seguchi, and I. Kohno: *RIKEN Accel. Prog. Rep.*, **21**, 139 (1987).
  - 2) J.W.T. Spinks and R.J. Woods: An Introduction to Radiation Chemistry, John Wiley, New York, p. 368 (1964).
  - 3) P. Ausloos (Ed.): Fundamental Process in Radiation Chemistry, International Publishers, New York, p. 482 (1968).

### III-4-4. An Irradiation System for Biological Samples and Dosimetry at RIKEN Ring Cyclotron

I. Kaneko, T. Kosaka, T. Kanai, Y. Yamada, Y. Ikegami, T. Watanabe, S. Watanabe, K. Nakano, K. Eguchi-Kasai, T. Katayama, F. Yatagai, T. Takahashi, and K. Hatanaka

In a previous paper,<sup>1)</sup> design and construction of an irradiation system for biological samples were described. In the present paper, a preliminary test of the system and the methods of dosimetry at RIKEN Ring Cyclotron facility are presented.

The beam port for biological research is composed of an apparatus for making a homogeneous

irradiation field and a beam monitoring system. To make an irradiation field equal to the size of a culture dish of 35 mm in diameter, a wobbler scanning magnet was constructed. The energy of an Ar ion beam used in the present experiment was  $\sim 26$  MeV/u. The beam was allowed to pass through a quadrupole-triplet magnet and focussed either on a sample dish

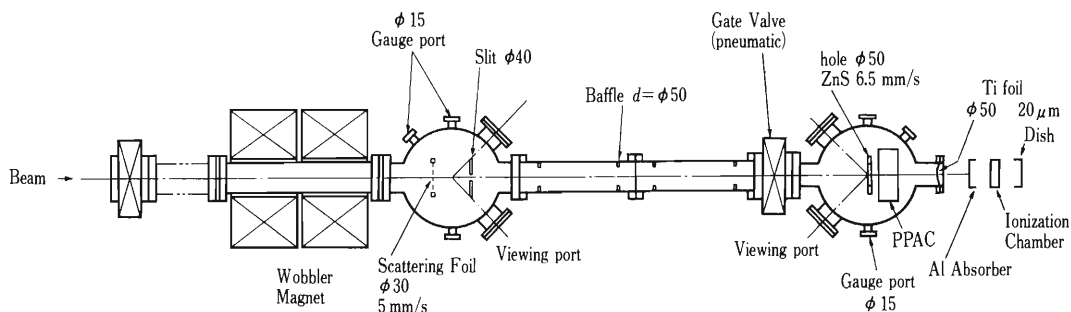


Fig. 1. Schematic diagram of the beam port for biological research.

containing a sample or on a zinc sulfide monitor (Fig. 1). The beam was focused by monitoring a beam profile on the ZnS monitor with a television camera. A beam passing through a vertical and a horizontal magnetic fields of the wobbler magnet produced a bright circle on the ZnS monitor because of the circular motion of the beam due to the sinusoidal magnetic fields (Fig. 2). In homogeneous irradiation, a gold scattering foil of  $34 \mu\text{m}$  in thickness was inserted immediately after the wobbler magnet. The beam showed a gaussian profile and, by its circular motion, gave a nearly homogeneous irradiation field when a flight path length was  $\sim 2$  m. The beam monitoring system is composed of a parallel-plate avalanche counter (PPAC) and an ionization chamber. The PPAC was used for both beam profile monitoring and measurement of the beam intensity.<sup>2)</sup> The beam profile displayed every 5 s on a CRT of a minicomputer was found nearly homogeneous in some cases; further improvement is required for constant

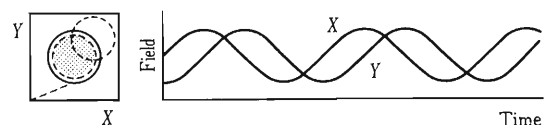


Fig. 2. Time-dependent magnetic field of the wobbler magnet and the circular motion of a beam.

homogeneity. A mechanical device for exchanging Al absorbers of various thicknesses and an ionization chamber were set outside the irradiation window located at the end of the vacuum window (a  $20 \mu\text{m}$  Ti foil). The ionization chamber made of two parallel aluminized Mylar films of  $4 \mu\text{m}$  in thickness, which were fixed 2 mm apart, was filled with atmospheric air.

The irradiation chamber was constructed from materials which are not toxic to cell growth and can be sterilized to prevent biological contaminations. Nine samples in culture dishes were set on an aluminum holder, and each sample was successively irradiated according to the preset num-

ber of counts of the PPAC. The temperature of the chamber are controllable at 30–37°C for the optimal growth conditions. To investigate the synergistic action of hyperthermia and radiation, the temperature of the chamber is adjustable in the range of 37–45°C within  $\pm 0.05^\circ\text{C}$ . The damage of high molecular-weight molecules such as nucleic acids and protein in the cell and their repair process can be investigated below 4°C to prevent repair during exposure by blowing air at a desired temperature into the irradiation chamber; the air should contain 5% CO<sub>2</sub> to maintain desired pH in a culture medium. For the measurement of the oxygen enhancement ratio and for the test in hypoxic radiosensitizers, N<sub>2</sub> gas containing 5% CO<sub>2</sub>, instead of air, should be used.

Comparing the beam intensities measured with

the PPAC and with a CR-39 track detector in the dish of the sample, we found that the number density of etch pits observed on the CR-39 track detector was in agreement with the number of counts of the PPAC within  $\sim 10\%$ . The Bragg curve was successfully observed by inserting Al absorbers of different thicknesses with the ionization chamber whose current was normalized to the PPAC counting rate.

#### References

- 1) I. Kaneko, K. Eguchi, T. Takahashi, and K. Nakano: *Sci. Papers I. P. C. R.*, **79**, 60 (1985).
- 2) H. Kumagai, Y. Yamada, N. Tajima, T. Kosaka, K. Nakano, F. Yatagai, and T. Takahashi: This Report, p. 135.

### III-4-5. Parallel Plate Avalanche Counter for Dosimetry in the RIKEN Ring Cyclotron Biology Facility

H. Kumagai, Y. Yamada, N. Tajima, T. Kosaka,  
K. Nakano, F. Yatagai, and T. Takahashi

A position-sensitive parallel-plate avalanche counter (PPAC) was designed and constructed for dosimetry in RIKEN Ring Cyclotron biology facility. As shown in a separate paper<sup>1)</sup> in this volume, homogeneous irradiation of Ar ions was attempted by using a wobbler magnet and a scattering foil, but beam homogeneity over the area of a biological sample was not easily attainable. PPAC is expected to be useful to obtain information on the homogeneity as well as on the precise flux of the beam on a sample.

#### (1) Construction of PPAC

PPAC is suitable for counting very high rates since the pulse width of its output is of several nanoseconds. It is also suitable for detecting heavy ions of several tens of MeV/u, because output signals are sufficiently large but energy loss is negligibly small, when the ions traverse through the PPAC. As shown in Fig. 1, the PPAC is composed essentially from a central anode foil and two outer foils with sensitive areas of  $50 \times 50 \text{ mm}^2$ . The anode is made of  $2 \mu\text{m}$  mylar foil, both sides of which were deposited with gold to  $40 \mu\text{g}/\text{cm}^2$  in thickness. The cathodes are made of  $2 \mu\text{m}$  mylar foils, one side of which was deposited with gold to  $80 \mu\text{g}/\text{cm}^2$  in thickness,

using a mask with ten stripes. Ten gold stripes of  $4.5 \text{ mm}$  in widths, each having intervals of  $0.5 \text{ mm}$ , were formed as cathodes on the foil to get position information of the  $x$  or  $y$  axis. The distance between the cathode and the anode was  $3 \text{ mm}$  and the anode bias of  $600 \text{ V}$  was applied when  $26 \text{ MeV/u}$  Ar ions were used. Isobutane of about 6 torr was used as a counter gas.

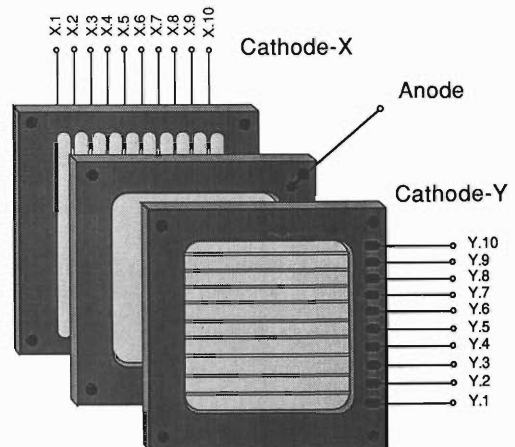


Fig. 1. Schematic view of two-dimensional PPAC.

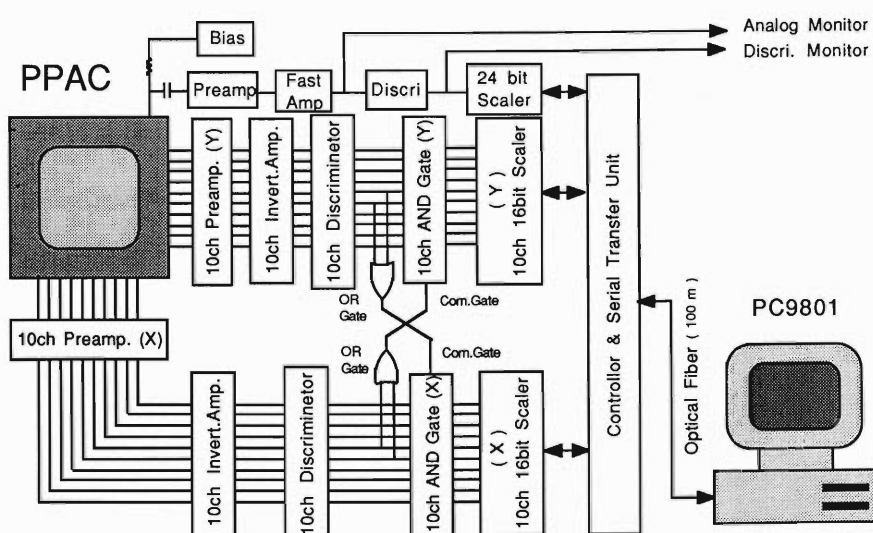


Fig. 2. Block diagram of the electronics of the beam profile monitor.

### (2) Beam profile monitor

The block diagram of electronics for a beam profile monitor is shown in Fig. 2. The output pulses of the anode were amplified 100 times with a preamplifier and a fast main amplifier. After discrimination of noise signals, the anode pulses are converted to fast NIM signals and counted with a 24 bit scaler. The total counts of the anode signals were used to estimate doses. The output pulses from the  $x$  or  $y$  cathode are amplified 100 times with a preamplifier and an inverting amplifier, and are converted to fast NIM signals with a discriminator. The signals from the  $x$  axis are counted with a 10 channel scaler for the  $x$  axis ( $x$ -scaler), when the  $x$  signal coincides with a signal from the Y5 or Y6 cathode (Fig. 1). Thus, the position information along the  $x$  axis (50 mm long and 10 mm wide) is available from the number of counts of the 10 channel  $x$ -scaler. The position information along the  $y$  axis is also available from a 10 channel scaler for the  $y$  axis, because the signals from the  $y$  axis are counted with a  $y$ -scaler, when the  $y$  signal coincides with a signal from X5 or X6 cathodes (Fig. 1). The beam profiles for the  $x$  and  $y$  axis are displayed on a CRT of minicomputer PC9801.

### (3) Linearity between the counting rate of PPAC and the beam intensity

To obtain a dose from the counting rate of anode signals of PPAC, it is necessary to confirm the linearity of the relation between a counting rate and a beam intensity. In 1985, we confirmed the linearity up to  $2 \times 10^6$  cps by using He ions from RILAC,<sup>2)</sup> however, sufficient accuracy was not obtained because beam intensity was measured with a Faraday cup. In the present work, we have examined the relation between the counting rate of PPAC and an ion current from an ionization chamber. The ionization chamber is made of two parallel aluminized myler films of 4  $\mu\text{m}$  in thickness fixed 2 mm apart, and is filled with 1 atm air. Figure 3 shows the relation

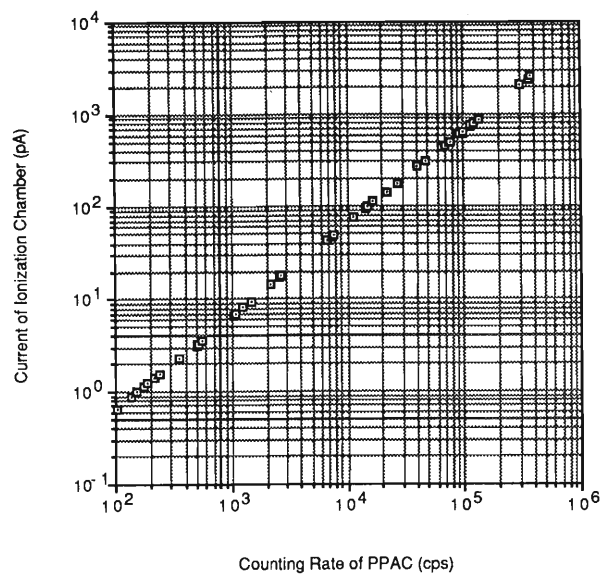


Fig. 3. Relation between the counting rate of PPAC and the current of the ionization chamber.

between the counting rates of PPAC and ionization currents from the ionization chamber for 26 MeV/u Ar ions. We found that good linearity is held in the range from  $10^2$  to  $4 \times 10^5$  cps within  $\pm 3\%$  errors. Electric charge produced by an Ar ion, when it passed through the ionization chamber, was found to be  $6.49 \times 10^{-15}$  C/particle, which is in rough agreement with a calculated result, *i.e.*,  $7 \times 10^{-15}$  C/particle. The calculation is based on  $W = 35$  eV and  $S = 6.0$  MeV/(mg/cm<sup>2</sup>), where  $W$  and  $S$  are the  $W$ -value and the stopping power in air, respectively, for 25 MeV/u Ar ion.

### References

- 1) I. Kaneko, T. Kosaka, T. Kanai, Y. Yamada, Y. Ikegami, T. Watanabe, S. Watanabe, K. Nakano, K. Eguchi-Kasai, T. Katayama, F. Yatagai, T. Takahashi, and K. Hatanaka: This Report, p. 133.
- 2) H. Kumagai, T. Takahashi, T. Kubo, and M. Ishihara: *Ioniz. Radiat.*, **12** (3), 38 (1986).

### III-4-6. Combined Effect of *cis*-Diamminedichloroplatinum and Heavy Ions on Mammalian Cells *In Vitro*

M. Suzuki, S. Yamashita, K. Nakano, and I. Kaneko

Many experiments were carried out on the combined effect of X-rays and *cis*-dichlorodiammineplatinum (CDDP) on mammalian cells *in vitro* as summarized below. (1) The synergism which reduced the extrapolation number of a survival curve was found from the treatment with CDDP within two hours after X-ray irradiation.<sup>1)</sup> (2) CDDP plays a role as a radiosensitizer for hypoxic cells.<sup>2,3)</sup> (3) The recovery from sublethal damage (SLDR) and from potentially lethal damage (PLDR) was inhibited by CDDP treatment.<sup>3,4)</sup> These results prompted us to carry out studies of the combination effects of CDDP and heavy ions in relation to the cancer radiotherapy using heavy ions.

Chinese hamster V79 cells were cultured in Eagle's minimum essential medium supplemented with 10% fetal bovine serum in a 5% CO<sub>2</sub> incubator at 37°C. The cells were inoculated onto cover glasses of 22 mm in diameter attached to plastic dishes of 35 mm in diameter with silicon grease at a concentration of 1×10<sup>4</sup> cells per dish. After 15 h incubation, cells were irradiated to various doses with heavy ions (95 MeV nitrogen ion or 22 MeV helium ion) from the cyclotron. Before irradiation, cells were added with CDDP of 5 µg/ml and kept for one hour at 37°C. After CDDP treatment and irradiation, the cells were trypsinized and seeded onto 60 mm plastic dishes. Cultures were incubated for 7 days in a CO<sub>2</sub> incubator at 37°C to form colonies. The colonies were fixed, stained, and then counted. We assessed the combined effect by calculating the surviving fraction (S. F.) given by

$$S. F. = \frac{\text{the number of colony counted} \atop \text{(treated with radiation & CDDP)}}{\text{the number of colony counted} \atop \text{(treated with CDDP)}}$$

Figure 1 shows the cytotoxicity of CDDP on V79 cells treated with various concentrations of CDDP at 37°C for one hour. The results indicate that the survival curve has an initial shoulder at low concentrations of CDDP and at high concentration ( $\geq 5 \mu\text{m}/\text{ml}$ ) becomes exponential.

Figure 2 (a and b) shows the combined effect of He ion and CDDP. The synergism was found in

both cases of the CDDP treatment before and after irradiation. In the case of the CDDP treatment before He-ion irradiation, an extrapolation number (*n* value) was 3.5 and the *D*<sub>0</sub> value (*D*<sub>0</sub>) was determined from the straight portion of the survival curve as the dose required to reduce the number of surviving cells to 37% was 0.75 Gy (Fig. 2a). The *n* value is the same, but the *D*<sub>0</sub> value is 0.68 times smaller than that of untreated case (*D*<sub>0</sub>=1.1 Gy). The results indicate that radiosensitivity becomes high by treating with CDDP before He-ion irradiation. In the case of the CDDP treatment after He-ion irradiation, the *n* value is 1.0 and the *D*<sub>0</sub> value is 0.90 Gy (Fig. 2b). The initial shoulder of the survival curve vanishes to be the same as that in the untreated case (*n*=3.5; Fig. 2b), indicating that SLDR is inhibited by the treatment with CDDP after He-ion irradiation.

Figure 3 (a and b) shows the combined effect of N ion and CDDP. The results indicate that the synergism is found in both cases of the CDDP treatment before and after irradiation. The *D*<sub>0</sub>

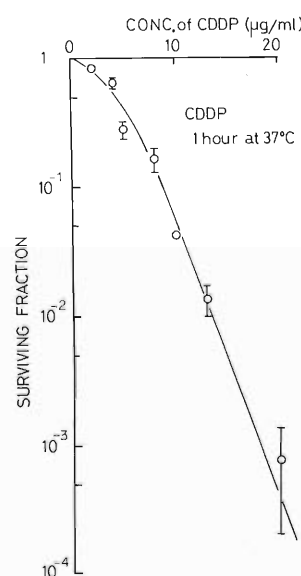


Fig. 1. Dose response curve of V-79 cells exposed to CDDP for 1 h at 37°C. Results are presented as the means  $\pm$  S.F. of three independent experiments.

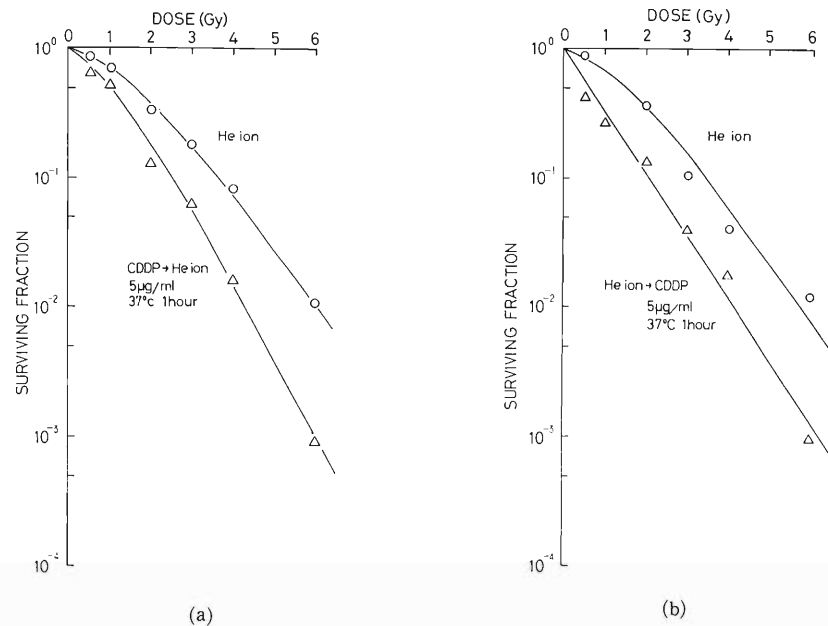


Fig. 2. Combined effect of CDDP and He-ion irradiation. (a), treated with CDDP of 5  $\mu\text{g}/\text{ml}$  for 1 h at 37°C ( $\triangle$ ) 2 h before irradiation; (b), treated with CDDP of 5  $\mu\text{g}/\text{ml}$  for 1 h at 37°C ( $\triangle$ ) 3 h after irradiation;  $\circ$ , CDDP untreated.

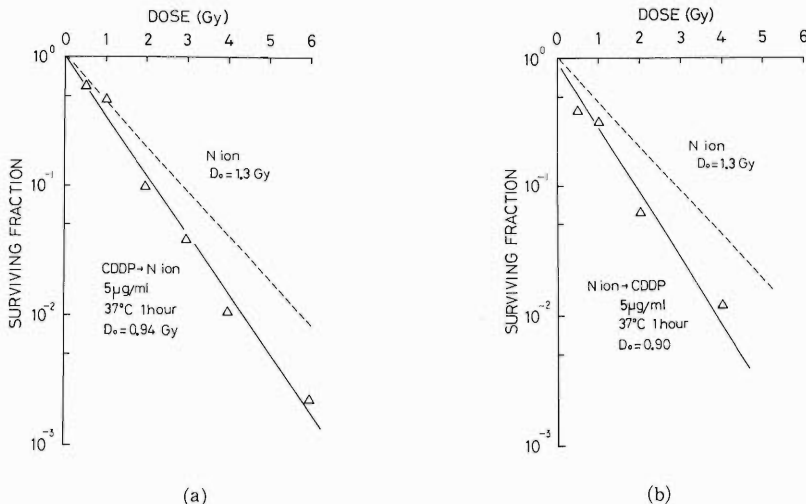


Fig. 3. Combined effect of CDDP and N-ion irradiation. (a), treated with CDDP of 5  $\mu\text{g}/\text{ml}$  for 1 h at 37°C ( $\triangle$ ) 4 h before irradiation; (b), treated with CDDP of 5  $\mu\text{g}/\text{ml}$  for 1 h at 37°C ( $\triangle$ ) 3 h after irradiation; Dashed line, CDDP untreated.

values of the CDDP treatment before and after irradiation are 0.94 Gy and 0.90 Gy, respectively. On the other hand, the  $D_0$  value is 1.3 Gy in the case of the CDDP untreatment. Therefore, the radiosensitivity becomes 1.4 times high compared with the case of combination of CDDP and N ion.

The combination effect of CDDP and heavy ions was found to be dependent on the type of radiation synergism which alters the  $D_0$  value

without the alteration of the  $n$  value.

#### References

- 1) S. Momiki, Y. Yamaguchi, and T. Miyamoto: *J. Jpn. Soc. Cancer Ther.*, **22**, 2352 (1987).
- 2) I. J. Stratford, C. Williamson, and G. E. Adams: *Br. J. Cancer*, **41**, 517 (1980).
- 3) P. Carde and F. Lavel: *Int. J. Radiat. Oncol. Biol. Phys.*, **7**, 929 (1981).
- 4) A. Dritschilo, A. J. Piro, and A. D. Kelman: *Int. J. Radiat. Oncol. Biol. Phys.*, **5**, 1345 (1979).

### III-4-7. Dependence of the Strand Breakage in DNA on Radiation Quality

I. Kaneko, T. Kosaka, K. Nakano, K.F. Barverstock, and C. McCintyre

Energy transfer along DNA molecules following the deposition of ionizing energy has been postulated to be a possibly influential mechanism in radiobiology. The existence of such processes has not yet been unequivocally demonstrated. With a view to testing for such processes a dry DNA/salt film matrix has been adopted which optimises those mechanisms which follow ionizing energy that is directly deposited in the DNA. A technique for assessing the full distribution of the broken fragments of irradiated DNA has also been developed using the electron microscope imaging technique. In experiments carried out so far these two techniques together have demonstrated that following irradiation with cobalt 60  $\gamma$ -rays abnormal distributions of fragment lengths are obtained. There are two main proposals to account for these observations namely, a) that the track structure of the radiation and the geometric distribution of the DNA molecules in the target film interact in such a way as to generate abnormal distribution or b) that energy transfer processes within the DNA are operating and that the sites of damage are not necessarily the sites of energy deposition. Either hypothesis would have considerable implications for the understanding of radio-biological mechanisms.<sup>11</sup>

In investigating further the two hypotheses the most favoured variable is radiation quality. For this reason a series of experiments involving a range of charged particles of different masses and velocities is proposed. The most interesting qualities lie in the range of energies from 0-10 MeV/amu and ions of up to 40 atomic mass units. Such radiations are best obtained from various variable energy cyclotrons. Within these limits a wide variation in the spatial distribution of ionizing events can be obtained. Track structure models are available and would enable a detailed interpretation of the results in terms of clearly defined physical parameters.

A further variable which has been found to be interesting is the size of the DNA molecule. Currently available techniques enable us to manufacture molecules, both linear and circular, in range of lengths from submicron to the order

of tens of microns. A further variable is the water content of the DNA film which can be controlled by manipulating the relative humidity of the environment in which the film is contained.

Experiments of this kind are important in radiobiology since the implicit assumption of many models used to extrapolate over the variables of dose, dose rate and radiation quality rely on the assumption that damage occurs in cells at the sites of energy deposition. Such models are of importance for radio-biological protection and to our understanding of the mechanisms of radiation induced cancer.

In these experiments we have used a supercoiled plasmid DNA (pSVL plasmid, Pharmacia Co.) with salt to ratios of 0.2 : 1, 1 : 1, and 10 : 1 by weight. Isolation of the DNA was carried out, as described in the NACS Application Manual published by BRL, to achieve a preparation containing a high proportion of supercoiled molecules. Prior to irradiation DNA was ethanol precipitated and resuspended in the appropriate strength NaCl solution free from contaminating enzymes. This solution was dried down under controlled humidity to form a dry DNA salt film matrix.

DNA samples mounted on thin glass cover slips were attached to the bases of plastic petri dishes designed to fit standard irradiation holders. These vessels were flushed with air at room temperature and relative humidity of 75%. Irradiations using 5.5 MeV/u and 1.75 MeV/u  $\alpha$ -particles, 26 MeV/u Argon ions, and  $^{60}\text{Co}$   $\gamma$ -rays were carried out. Dose rates in the range of 30 to 80 Gy/min were employed.

Each sample was dissolved overnight in 75  $\mu\text{l}$  of 1.0 M NTEB (1 M NaCl in 10 mM tris (pH 7.6) and 1 mM EDTA). The preparations were analyzed by gel electrophoresis on a 0.8% agarose gel in the presence of ethidium bromide. Polaroid photographs were scanned on a densitometer and the proportions of the different forms of DNA is determined by measuring the area under each peak with a SEESCAN image analyzer.

Irradiation of samples at the three salt/DNA ratios with 5.5 MeV/u  $\alpha$ -particles indicated considerable cross-linking of DNA at the two lower

ratios. Neary, *et al.*<sup>2)</sup> noted that some cross-linking in their analysis and this is probably due to the low salt to DNA ratio used. In earlier experiments with  $\gamma$ -rays we have observed no marked influence on the frequency of strand breakage of salt concentration and the relative absence of cross-linking at ratios of 10 : 1 has the advantage of improving the reliability of the analysis.

Single strand breaks were measured using electrophoresis to determine the loss of the supercoiled form of the plasmid and the efficiency of breakage for the three qualities of radiation are given in Table 1. These results are not keeping in data of other investigator who showed that single strand breaks increased with increasing LET.<sup>2)</sup> To determine single strand breaks Neary, *et al.* denatured the DNA in alkali and measured the distribution of lengths of single strands using boundary analysis. The loss of supercoiled plasmid as measured by electrophoresis should prove more reliable although it will not record alkali labile breaks. Direct comparison with the results of Christensen, *et al.*<sup>3)</sup> is complicated due to the fact that these irradiations were not of the track

Table 1. Measurement of DNA single strand breaks induced by different radiation sources.

Radiation	LET(keV/ $\mu$ m)	ssb/dalton/Gy
$\gamma$ -rays	low	5.5 $\pm$ 0.5
$\alpha$ -particles	36	6.9 $\pm$ 0.7
$\alpha$ -particles	77	9.0 $\pm$ 2.0
Argon-ions	600	11.1 $\pm$ 2.0

segment type but for total absorption of the beam.

Our research is on the way along this line. We should confirm the present results by using other ions of different masses and velocities and by using the results of DNA double strand break analysis in the near future.

#### References

- 1) K.F. Baverstock, and R.B. Cundall: *Radiat. Phys. Chem.*, **32**, 553 (1980).
- 2) G.J. Neary, V.J. Horgan, D.A. Bance, and A. Stretch: *Int. J. Radiat. Biol.*, **22**, 525 (1972).
- 3) R.C. Christensen, C.A. Tobias, and W.D. Taylor: *Int. J. Radiat. Biol.*, **22**, 457 (1972).

### III-4-8. *In Vitro* Cell Transformation and Mutation by Heavy Ions

M. Watanabe, K. Suzuki, M. Suzuki, T. Kosaka,  
K. Nakano, and I. Kaneko

Carcinogenesis and mutagenesis are two of the most important biological effects of ionizing radiation. With the progress in cell culture techniques, studies on the dose-response relationship and the mechanism(s) of radiation-induced cell transformation and mutation become possible.

Within the last few years, the transformation and the mutation of cells by ionizing radiation have been studied by many investigators. Most quantitative data, however, have been obtained for low-LET radiation, and a limited amount of information is available for high-LET ions.<sup>1-3)</sup> In general, high-LET radiation has been found to be more effective in producing cell transformation<sup>1,2)</sup> and mutation<sup>1,3)</sup> than  $\gamma$  or X rays. Because on the potential applications of heavy-ion radiation in cancer therapy, there is a need for information on the carcinogenic and mutagenic effects of heavy ions. We have initiated transformation and mutation experiments to estimate the carcinogenic and mutagenic potential of normal tissue exposed to high-LET heavy ions.

In the present study we have two aims in collecting fundamental data for cancer radiotherapy by high-LET radiations. One is to find quantitative dose-response relationships for the induction of *in vitro* cell transformation that can be used in the estimation on the carcinogenic potential of the normal tissue. The other is to assess the RBE and its LET dependence.

We used diploid golden hamster embryo cells (GHE) from 13- or 14-day-old embryos as previously reported.<sup>3,4)</sup> The GHE cells were cultured in Eagle's minimum essential medium supplemented with 10% fetal bovine serum in a 5% CO<sub>2</sub> incubator at 37°C. The cells cultured on 22-mm cover glasses at a cell concentration of  $3 \times 10^5$  were irradiated to various doses of heavy ions or  $\gamma$  rays. After exposed to radiation, the cells were trypsinized into single cells and plated into 60-mm dishes at a density that gave about 70 survivors. Transformed colonies were identified as morphologically altered colonies which were densely stacked and had a criss-cross pattern as described previously.<sup>5,6)</sup> Colonies containing

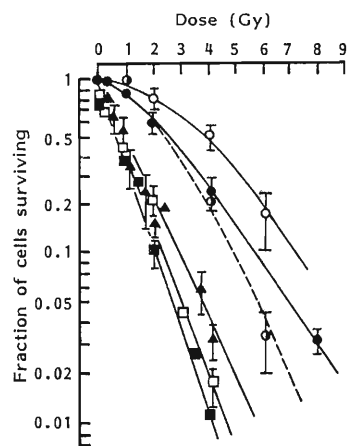


Fig. 1. Survival curves of GHE cells by  $^{60}\text{Co}$   $\gamma$  rays (●),  $^{137}\text{Cs}$   $\gamma$  rays (○), N ions (3.1 MeV/u, 530 keV/ $\mu\text{m}$ ) (▲), He ions (4.2 MeV/u, 36 keV/ $\mu\text{m}$ ), He ions with a 100- $\mu\text{m}$  Al absorber (1.7 MeV/u, 77 keV/ $\mu\text{m}$ ) (□), and X rays (182 kVp) (○).

more than 50 cells were counted as survivors and the frequency of transformants was expressed as the ratio of their number of morphologically transformed colonies to the total number of colonies survived.

Figure 1 shows the survival curves of the GHE cells following exposure to heavy ions,  $\gamma$  rays and X rays. The results indicate that the heavy ions are more effective than X rays and  $\gamma$  rays for cell killing. For N-ion and He-ion beams, the cell survivals exponentially decreased as the dose is increased. On the contrary, the survival curves for X rays and  $\gamma$  rays have a small initial shoulder at the low dose regions up to 1 Gy, but over 1 Gy they have an exponential damping. The RBE relative to  $^{60}\text{Co}$   $\gamma$  rays at the  $D_0$  value is about 2.3 for a N-ion beam (530 keV/ $\mu\text{m}$ ), 3.0 for a He-ion beam without absorber (36 keV/ $\mu\text{m}$ ), and 3.0 for a He-ion beam with a 100- $\mu\text{m}$  Al absorber (77 keV/ $\mu\text{m}$ ). Figure 2 shows that cell transformation of GHE cells after exposure to various radiations. The results indicate that the heavy ions are much more effective than  $\gamma$  rays in producing *in vitro* cell transformation. The transformation frequency per surviving cells for

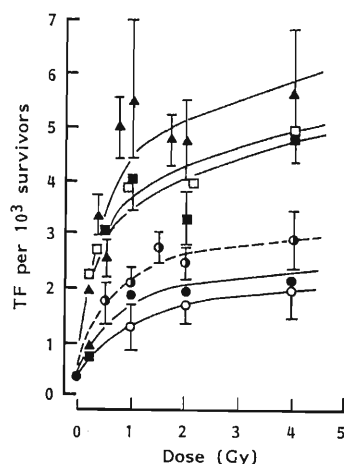


Fig. 2. Dose-response curves for cell transformation of GHE cells by  ${}^{60}\text{Co} \gamma$  rays (●),  ${}^{137}\text{Cs} \gamma$  rays (○), N ions (3.1 MeV/u, 530 keV/ $\mu\text{m}$ ) (▲), He ions (4.2 MeV/u, 36 keV/ $\mu\text{m}$ ) (■), He ions with a 100- $\mu\text{m}$  Al absorber (1.7 MeV/u, 77 keV/ $\mu\text{m}$ ) (□), and X rays (182 kVp) (○).

N-ion and He-ion beams, and  $\gamma$  rays appears to be steeply linear up to 1 Gy and over 1 Gy shows a constant level or a slight increase. The frequency for a constant level is about 2.5 times higher for a N-ion beam and about 2 times higher for a He-ion beam than  $\gamma$  rays. When the RBE is determined as the transformation frequency per surviving cell at the same frequency level up to 1 Gy, the RBE relative to  ${}^{60}\text{Co} \gamma$  rays is about 3.3 for N ions, 2.4 for He ions without an absorber, and 3.3 for He ions with a 100- $\mu\text{m}$  Al absorber.

6-Thioguanine (6TG) was used to study the mutation induction in GHE cells by various radiations. A part of irradiated GHE cells were seeded at a low density and incubated for 8 days before selecting for mutants with 6-TG medium as previously reported.<sup>7)</sup> The results are given in Fig. 3. X rays increased the number of mutants per 10<sup>6</sup> viable cells curvilinearly with an increase in dose. Heavy ions appear to be highly effective in producing mutation at lower doses up to 1 Gy, as compared with  $\gamma$  rays. The frequency of 6TG mutants, however, decreased drastically at higher dose than 1 Gy. The RBE value, which was determined by taking the mutation frequency per viable cell induced by an X-ray dose given 37% survival as a reference point, was about 3.9 for He ions (4.2 MeV/u, 36 keV/ $\mu\text{m}$ ), 3.8 for He ions with a 100- $\mu\text{m}$  Al filter (1.7 MeV/u, 77 keV/ $\mu\text{m}$ ), and 4.9 for N ions (3.1 MeV/u, 530 keV/ $\mu\text{m}$ ), respectively. A comparison of the RBE's for mutation induction and for cell killing at a 37% survival level indicates that, compares to X rays, heavy ions can produce more mutation

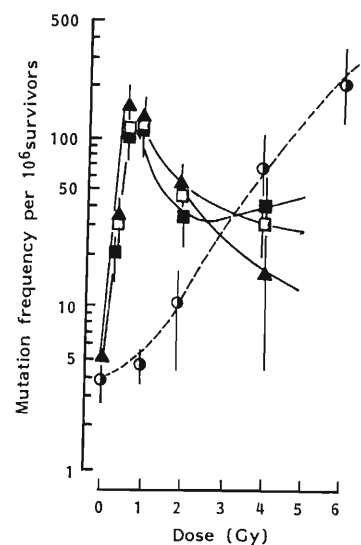


Fig. 3. Dose-response curves for mutation at HGPRT locus of GHE cells by N ions (3.1 MeV/u, 530 keV/ $\mu\text{m}$ ) (▲), He ions (4.2 MeV/u, 36 keV/ $\mu\text{m}$ ) (■), He ions with a 100- $\mu\text{m}$  Al absorber (1.7 MeV/u, 77 keV/ $\mu\text{m}$ ) (□), and X rays (182 kVp) (○).

lesions than lethal injures.

Because heavy ions has been known to damage DNA, we examined the chromosome aberrations immediately after irradiation. The efficiency of induction of every type of aberration, including chromatid gaps, breaks, and translocations, was less in cell exposed to heavy ions than those to X ray and  $\gamma$  rays. Some investigators reported that the number of the initially induced DNA strand breaks resulting from exposure to high LET radiations was smaller than those from X rays and  $\gamma$  rays.<sup>8,9)</sup> Our data of chromosome analysis are comparable to there results. Low LET radiations required more than four times chromosomal aberrations for the induction of the same biological effects.

The results indicate that the heavy ions are more effective for the induction of transformation and mutation than X rays and  $\gamma$  rays. The studies on the mutation and cell transformation with heavy ions give us a great insight into the molecular mechanisms of cell transformation. We plan to continue the studies on chromosomal and DNA lesions induced by heavy ions and hope that these studies provide information on the nature of molecular structure alterations in DNA which are related to oncogenesis and mutagenesis.

#### References

- 1) T.C. Yang, L.M. Craise, M. Mei, and C.A. Tobias: *Radiat. Res.*, **104**, S177 (1985).
- 2) C. Borek, E.J. Hall, and H.H. Rossi: *Cancer Res.*, **38**,

- 2997 (1978).
- 3) R. Cox, J. Thacker, D.J. Goodhead, and R.J. Munson: *Nature*, **267**, 425 (1977).
  - 4) T.C.H. Yang, F.Q.H. Ngo, J. Howard, and C.A. Tobias: Biological and Medical Research with Accelerated Heavy Ions at the BABALAC, Lawrence Berkeley Lab., Univ. Calif., p. 149 (1980).
  - 5) M. Watanabe, M. Horikawa, and O. Nikaido: *Radiat. Res.*, **98**, 274 (1984).
  - 6) M. Watanabe, N. Suzuki, S. Sawada, and O. Nikaido: *Carcinogenesis*, **5**, 1293 (1984).
  - 7) M. Watanabe, V.M. Maher, and J.J. McCormick: *Mutat. Res.*, **146**, 285 (1985).
  - 8) K. Sakai, S. Suzuki, N. Nakamura, and S. Okada: *Radiat. Res.*, **110**, 311 (1987).
  - 9) K. Eguchi, T. Inada, M. Yaguchi, S. Sato, and I. Kaneko: *Int. J. Radiat. Biol.*, **52**, 115 (1987).

## III-5. Instrumentation

### 1. Network in the RIKEN Accelerator Facility

T. Ichihara, T. Wada, and T. Inamura

In the year of 1988, the environment of the networks around the RIKEN Accelerator Facility has been improved; here we describe its outlines.

#### (1) Local area network

An ethernet cable is stretched all over RIKEN Ring Cyclotron building to connect VAX computers and terminal servers. Currently 6 DECnet nodes, 5 terminal servers, and 3 TCP/IP nodes are connected to the Ethernet in RIKEN Ring Cyclotron buildings.

In the Spring of 1988, ethernet cables were stretched over the main research building and the linac building. Figure 1 shows the current ethernet cable routing in RIKEN. One segment of Ethernet consists of a 500 m coaxial cable. Segments of Ethernet are connected with each other by "data link bridge" or "buffered repeater." While data link bridge repeats only the ethernet packets which cross over the segments, buffered repeater repeats all the ethernet packet. Optical-fiber cables are used to connect the ethernet of the accelerator facility and main research build-

ing.

In the accelerator facility, DECnet is the main protocol of Ethernet. Local Area Transport (LAT) protocol is also used for terminal servers. In a VAX-8350 computer, CMU/TEK TCP/IP software is installed on the VAX/VMS operating system to communicate to TCP/IP nodes in the main research building.

#### (2) Terminal connection to the host computers via digital PBX

In the spring of 1988, the PBX of RIKEN was replaced by new one. The new PBX (FETEX 3700) supports not only analog communication lines, but also digital data transfer lines. Many host computers in RIKEN are connected to the digital PBX by digital Access Units (DAU) or by Digital Network Interfaces (DNI). Figure 2 shows the digital PBX and host computer connections. In the accelerator facility 12 DAU's are connected to a FACOM M380 computer, 11 DAU's are connected to VAX computers, and 1 DAU is connected to M60 computers for accelerator control.

In order to access host computers connected to the PBX, digital telephones with RS232C ports are placed in each room. Usually a personal computer (Macintosh, PC9801 etc.) is connected to the RS-232C Port of a digital telephone at 9, 600 bps and can be used as a terminal of the host computer. Host computers can be selected by "ATD × × ×" command. There is also an analog modem pool to access these digital lines of the PBX from the "public telephone line + modem" from outside of the RIKEN.

One of the most convenient features of this digital telephone is that a digital port (RS-232C) and an analog port (voice) can be used independently at the same time. When someone is using a RS232C port of the digital telephone to connect to the host computer, he can also call a person by the same telephone with voice.

#### (3) Wide area network

(a) HEPNET In the end of 1988, the DECnet link of the RIKEN accelerator facility was con-

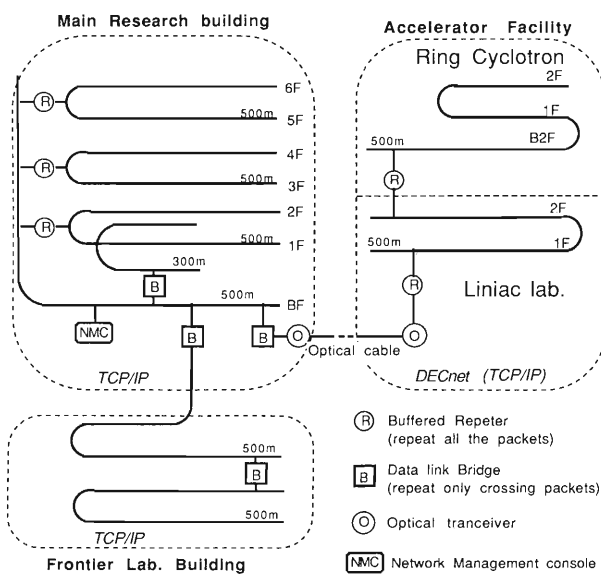
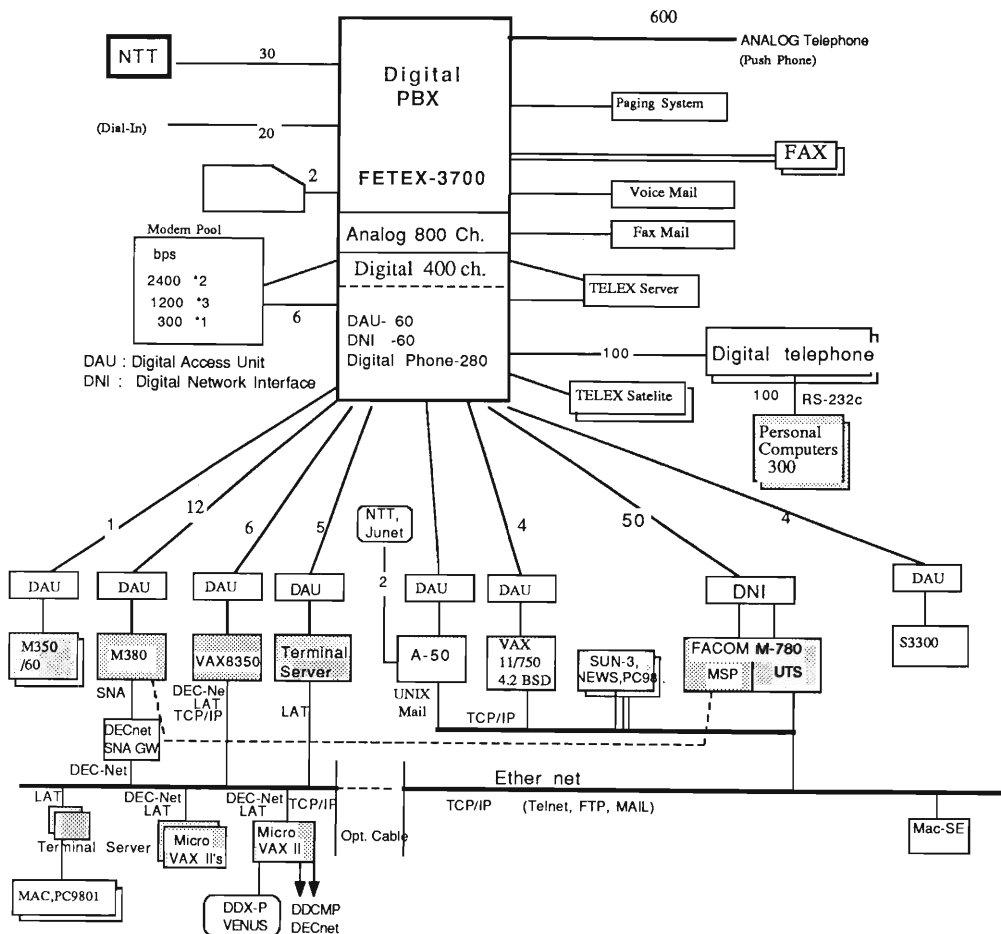


Fig. 1. Ethernet cable routing at RIKEN.

Riken PBX LAN



X.25 (VENUS-P) DTE Address of Micro VAX II  
4 401-4384118

DAU Telephone number list

7711	9600 bps 3ch	FACOM M-380 MSP
7712	9600 bps 3ch	FACOM M-380 MSP
7713	4800 bps 2ch	FACOM M-380 MSP
7721	9600 bps 5ch	VAX-8350 VMS
7731	Auto 4ch	VAX Terminal servers

Any computer connected to the digital PBX (FETEX 3700) can be accessed from the Digital telephone with RS232C port.

Telephone (voice) and digital data link by RS232C port can be used at the same time.

(8-bit, no-parity, Full-duplex, xon-xoff flow cont.)

Fig. 2. Digital PBX of RIKEN.

nected to the world-wide High Energy Physics Network (HEPNET) via National Laboratory of High Energy Physics (KEK) at Tsukuba. For this link, NTT DDX-P (X. 25) is used till March 1989. From April 1989, it is replaced by a leased digital line of NTT at 9,600 bps. At the same time, a DECnet link to the University of Tokyo will also start the operation using a leased digital line of NTT at 9,600 bps.

A Micro VAX 3600 computer at RIKEN in Komagome and a VAX11/730 computer of Tokyo Institute of Technology are connected to the RIKEN accelerator facility with DECnet at 9,600 bps using a 3.4 kHz-band leased analog line

of NTT and modems.

The DECnet node names and address are as follows:

RIKEN::	(40.950)	Micro VAX II
RIK835::	(40.951)	VAX 8350
RIKSNA::	(40.952)	DECnet/SNA
		Gateway
RIKMOV1::	(40.953)	Micro VAX II for experiment
RIKMOV2::	(40.954)	Micro VAX II for experiment
RIKVS1::	(40.955)	VAX Station II/GPX
RIKSOR::	(40.956)	Micro VAX 3600

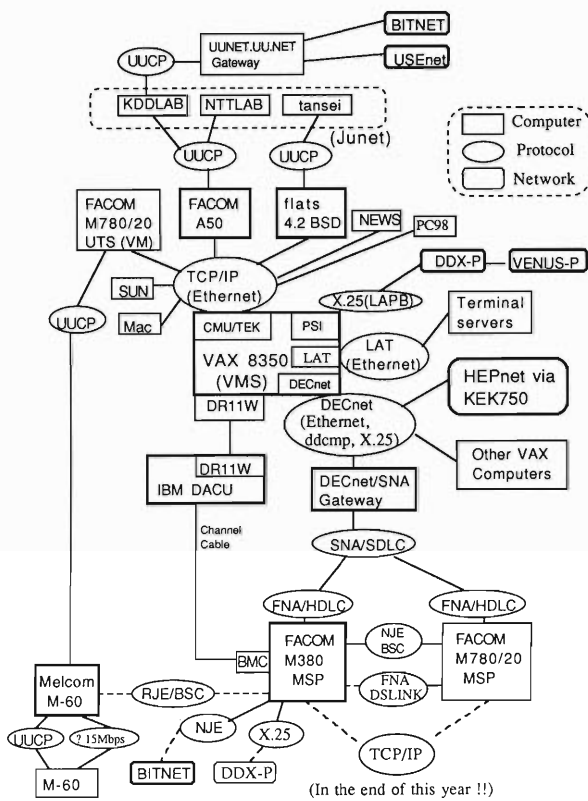


Fig. 3. Network between different computers at RIKEN Accelerator Facility.

RIKTIT:: (40.957) VAX11/730 at Tokyo Inst. of Tech.  
 RIKMV3:: (40.958) Micro VAX II for experiment (linac)

(b) Junet Some VAX's in the Accelerator Facility is connected to a domestic computer network between research facilities, Junet, via FACOM A50 Gateway computers. Figure 3 shows the network between different computers at RIKEN Accelerator Facilities and also Junet connection. The node name of Junet and TCP/IP address are as follows:

RIKMV. RIKEN. JUNET  
 (192.48.138.151) RIKEN::  
 RIK835. RIKEN. JUNET  
 (192.48.138.152) RIK835::

### III-5-2. Large Scattering Chamber at RIKEN Ring Cyclotron Facility

T. Nakagawa, I. Tanihata, and S.M. Lee

For the study of reaction mechanisms in intermediate-energy heavy-ion collisions ( $20 < E < 100$  MeV/A), a large scattering chamber will be installed in the target room E2. A schematic drawing of the scattering chamber is shown in Fig. 1. Its diameter and length are 2.95 m and 4.8 m, respectively. To satisfy various needs in experiments, three different target positions (P1, P2, and P3) are provided, and three movable detector arms are controlled independently at each target position. In order to extend the flight path near the scattering angle of 90 degrees, a

small chamber may be attached at the side of the large scattering chamber (see Fig. 1). The maximum flight paths are 3 m at forward angles and 2.5 m at 90 degrees.

The vacuum system consists of a rotary pump (15,000 l/min), a mechanical booster pump (100,000 l/min) and two cryogenic pumps (16,000 l/s). A vacuum of  $5 \times 10^{-6}$  torr is achieved within 1 h from 1 atm with this system. For routine operation,  $P = 1 \times 10^{-6}$  torr is expected.

A design of detector systems is in progress to facilitate measurements of reaction products in the large scattering chamber:

- 1) A large Frish-grid type ionization chamber;
- 2) A large two dimensional position sensitive Parallel Plate Avalanche Counter (PPAC);
- 3) A PPAC and a Channel Plate Detector (CPD); and
- 4) A large size solid state detector.

The large Frish-grid type ionization chamber will be used as a  $\Delta E-E$  counter telescope for charge identification. The PPAC and the CPD will be used as a time pick off detector for a Time of Flight telescope. A  $4\pi$  counter for measurement of light particles and  $\gamma$  rays can also be placed in the large scattering chamber.

The great advantage of the large scattering chamber is its capability of a long flight path. This capability provides a possibility for studying reaction mechanisms of heavy ions in the energy region supplied by RIKEN Ring Cyclotron.

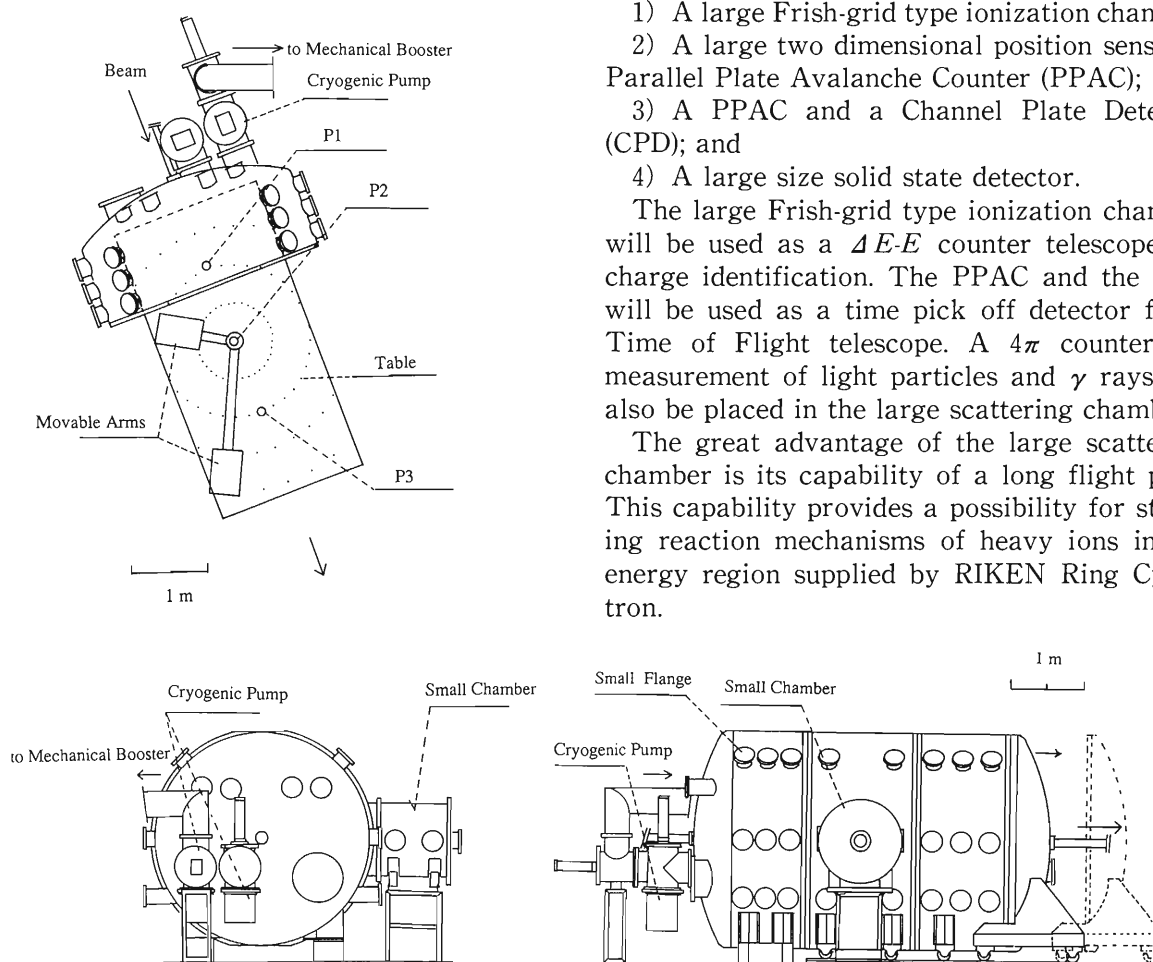


Fig. 1. Schematic drawing of large scattering chamber.

### III-5-3. RIKEN Swinger-Spectrometer System

H. Ohnuma, K. Hatanaka, S. Hayakawa, T. Ichihara, M. Ishihara, S. Kato, T. Kubo, S. Kubono, K. Maeda, T. Nakamura, H. Orihara, H. Shimizu, H. Toyokawa, Y. Yano, M. Yasue, H. Yoshida, and S. Wakasa

RIKEN swinger-spectrometer system<sup>1)</sup> is at its final stage of designing. The system has been ordered from The Japan Steel Works, Ltd., and the construction has started. Major components will be delivered in summer 1989. Field measurements will start shortly afterwards, and final installation and adjustment will be completed by the end of 1989.

There have been several changes in the design from the Progress Report last year, although the basic concepts remain unchanged. Parameters of magnets are summarized in Tables 1 and 2. The twister is now a quadrupole septet instead of a quadrupole triplet. This ensures an exact rota-

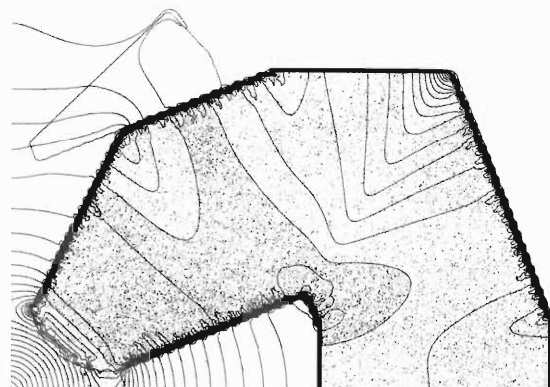


Fig. 1. Cross section and the field distribution of the first quadrupole magnet of the spectrometer.

Table 1. Parameters of swinger magnets.

	WD1	WQ1/WQ2	WD2
Central orbit radius (m)	2.3		2.3
Deflection angle (deg)	60		150
Maximum field (T or T/m)	1.51	15	1.51
Pole gap or bore radius (cm)	6	3.5	6
Weight (t)	4.5	0.18	11
Maximum power consumption (kW)	94	2.9	168

Table 2. Parameters of spectrometer magnets.

	PQ1	PQ2	PD1	PQ3	PD2
Central orbit radius (m)			2.4		2.4
Deflection angle (deg)			60		120
Maximum field (T or T/m)	7.7	4.0	1.5	3.3	1.5
Pole gap or bore radius (cm)	13.5	18.5	20	13.75	10
Weight (t)	15.8	8.5	102	1.9	82
Maximum power consumption (kW)	76	79	204	30	199

tion of the shape of the object and the beam divergence at the object.<sup>2)</sup> The quadrupole triplet of the swinger has been replaced by a quadrupole doublet to save space and reduce the weight of the swinger. The distance between the two dipoles of the spectrometer has been extended due to the space problem.

Each magnet has also been modified after repeated field calculations. Shapes of the yokes, shims, coil windings, field chams, etc. of the dipole magnets have been carefully adjusted to optimize the field distribution at various excitations. The first quadrupole magnet of the spectrometer, which is of a split type in order to realize large acceptance and small angle measurements as reported previously,<sup>1)</sup> has a cross section shown in Fig. 1.

The mechanical design of the support structure of the swinger magnet is in progress. Vacuum chambers, detector boxes and a scattering chamber are also being designed.

#### References

- 1) H. Ohnuma, et al.: RIKEN Accel. Prog. Rep., **21**, 164 (1987).
- 2) S. Kato: Nucl. Instrum. Methods A, **254**, 487 (1987).

### III-5-4. Facilities for Atomic Physics at RIKEN Ring Cyclotron

Y. Awaya, Y. Kanai, T. Kambara, and T. Chiba

We have constructed a beam line with equipments which are mainly dedicated to the study of atomic collisions in the E2-experimental room at RIKEN Ring Cyclotron. The beam line was designed so that we can get a vacuum better than  $10^{-8}$  Torr, if necessary, that is, CF seals or metal O-rings are used when required. In order to reduced the background radiation as low as possible, there are no slits or baffles in the experimental room. A charge stripper setup is installed in the cyclotron vault to provide different charge-state projectile ions. The equipments which are installed on the beam line are as follows (also shown in Fig. 1).

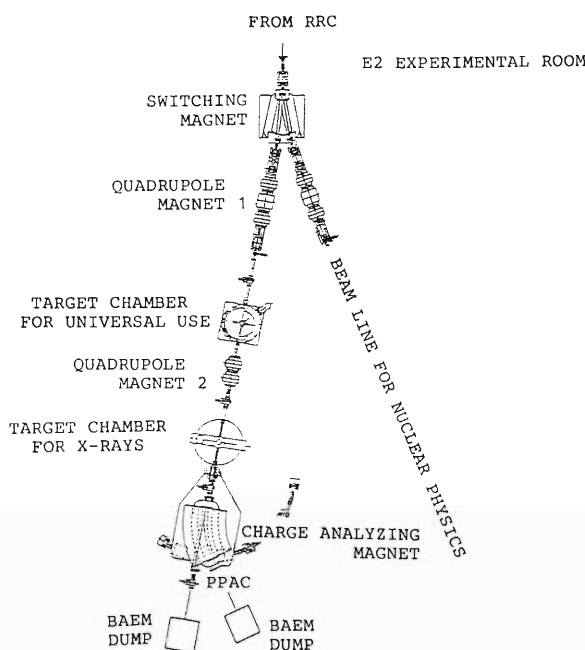


Fig. 1. Experimental setup for atomic physics in the E2-experimental room. The position of the target chamber for measurement of angular distribution of X rays and the quadrupole magnet 2 will be changed in the near future.

#### (1) Target chamber for universal use

The size of the chamber is 100 cm in diameter  $\times$  50 cm in depth. Inside the chamber, the wall is covered with a  $\mu$ -metal shield. There are a turn table, two arms and a target holder in the chamber and they are controlled from the counting room.

#### (2) Target chamber for measurement of angular distribution of X rays

The size of the chamber is 30 cm in diameter. The window is opened from  $25^\circ$  to  $155^\circ$  with respect to the beam for the measurement of X rays and is covered with a sheet of 25  $\mu\text{m}$  Mylar film. There are a target holder inside the chamber and two turn arms outside which rotate around the target holder carrying a Si(Li) or Ge detector with a liquid nitrogen Dewar vessel. The target holder and two arms are controlled from the control room.

#### (3) Charge state analyzer (broad range)

The specification of the charge analyzing magnet is as follows:

radius	250 cm
maximum field	15,000 Gauss
deflection angle	35 degree
gap of the pole pieces	71 mm

The magnet can be rotated from  $0^\circ$  to  $60^\circ$  respect to the beam direction. A position sensitive parallel plate avalanche counter or a solid state detector is used for the detection of the ions.

Another facility for atomic physics has been constructed in the ion source vault of the AVF cyclotron. When the AVF cyclotron is not working, ions from the ECR ion source<sup>1)</sup> are available for the study of the atomic physics.<sup>2)</sup>

#### References

- 1) K. Hatanaka and H. Nonaka: *RIKEN Accel. Prog. Rep.*, **21**, 212 (1987).
- 2) H. Sakaue, *et al.*: This Report, p. 74.

### III-5-5. Falling-Ball Irradiation System and the Hot Laboratory

M. Yanokura, Y. Ohkubo, S. Ambe, M. Iwamoto, and F. Ambe

The falling-ball irradiation system and the hot laboratory notified in the preceding volume of this report<sup>1)</sup> were constructed and tested with success. This report describes some details of both facilities.

The schematic view of the whole arrangement of the irradiation system is shown in Fig. 1. The irradiation chamber is installed near the end of

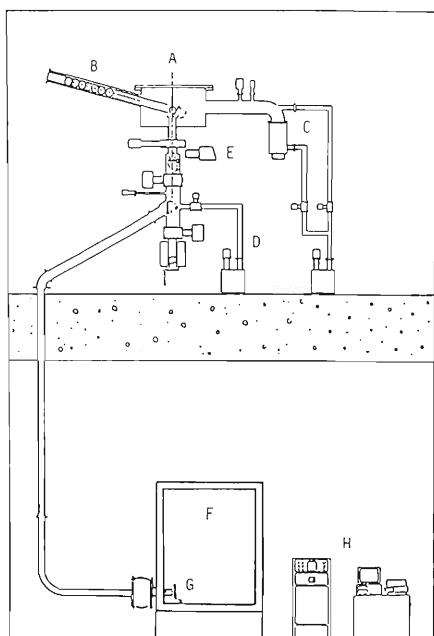


Fig. 1. The whole layout of the 'falling ball' irradiation system. A: irradiation chamber, B: stand-by holder tube for the balls, C: vacuum system for the chamber, D: vacuum system for the transport tube, E: radiation monitor (ionization chamber), F: hood, G: end station for the ball, H: control system.

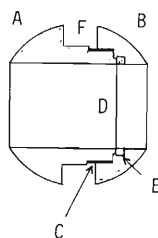


Fig. 2. The 'falling ball.' A, B: The separable two parts of the ball, C: screw groove, D: target foil, E: suppression ring, F: groove for guide.

the oblique beam line in the E3 irradiation room. The transport tube for the 'falling ball' passes through the floor of the room down into a hood in the hot laboratory downstairs. The chamber and the transport tube can be evacuated to  $1 \times 10^{-5}$  and  $1 \times 10^{-1}$  Pa, respectively.

Target foil is mounted in a 'falling ball' as shown in Fig. 2. The ball with a diameter of 42 mm is made of aluminum and has a piercing cylindrical hole for a beam and also a groove for guide. The diameter of the hole for the beam can be as large as 22 mm.

Several balls can be set at the same time in the stand-by holder tube connected to the chamber. A quartz plate for beam monitoring is mounted on the first 'falling ball.' After evacuation of the chamber, the balls can be transferred one by one to the irradiation position of the chamber, the direction of the target against the beam being kept proper by the groove on the ball and rails in the chamber.

After irradiation, the ball is transported down to a radiation monitoring station under the

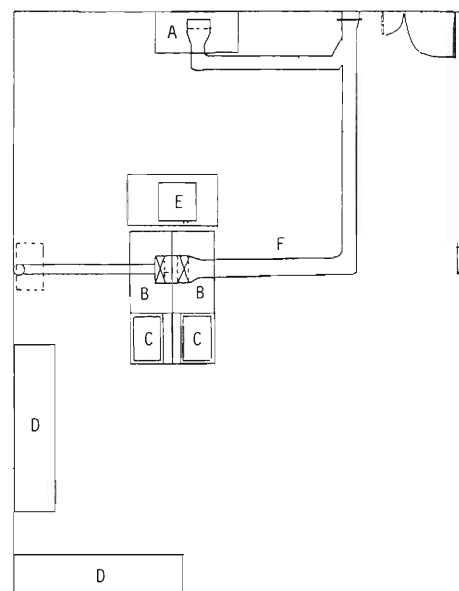


Fig. 3. The layout of the hot laboratory. A: hood for the end station of the 'falling ball,' B: hood for chemical work, C: hot sink, D: work bench, E: tank for liquid waste, F: duct for exhaust.

chamber. If the radiation level is confirmed to be appropriate for handling in the hot laboratory, the ball is further rolled down through the tube to the hot laboratory. After passing through a deceleration device, the ball stops at the end station in a hood. The gate valve near the end of the transport tube is then closed, the terminal lid of the tube is open, and the ball with the irradiated target is taken out. Thus, the target can be ready for physical and chemical studies within one minute after the end of irradiation. Whole the procedure can be controlled from the control station installed in the hot laboratory. If a vessel with a vacuum-tight valve is attached at the end of the transport tube, an irradiated target can be sealed in the vessel directly and can be transported

to other controlled areas safely.

In Fig. 3 is given the layout of the hot laboratory. There are three hoods, one for the end station of the 'falling ball' and the other two for chemical studies. The laboratory is also equipped with workbenches, hot sinks, and so on. It is, however, considered to be used only for experiments using relatively short-lived radioisotopes. Long-lived isotopes are to be handled in the radioisotope experiment facility in the cyclotron building.

#### Reference

- 1) M. Yanokura, Y. Ohkubo, S. Ambe, and F. Ambe: *RIKEN Accel. Prog. Rep.*, **21**, 163 (1987).

### III-5-6. Target Transportation System for a One-Meter Diameter Scattering Chamber

Y. Ikegami, K. Nishi, Y. Watanabe, K. Endo,  
K. Kubo, M. Iwamoto, and F. Ambe

A target transportation system was designed and constructed for the Mössbauer spectroscopy of  $^{57}\text{Fe}$  using a short-lived source nuclide,  $^{57}\text{Mn}$  (1.45 m). It is installed in a one-meter diameter scattering chamber at the #1 course of the cyclotron.

The plane view of the system is shown in Fig. 1. The target (A) is irradiated at the center of the chamber with a cyclotron beam. After irradiation the target is transported to a side window of the chamber for Mössbauer measurement by means of a motor (B) and a drive wire (C). The

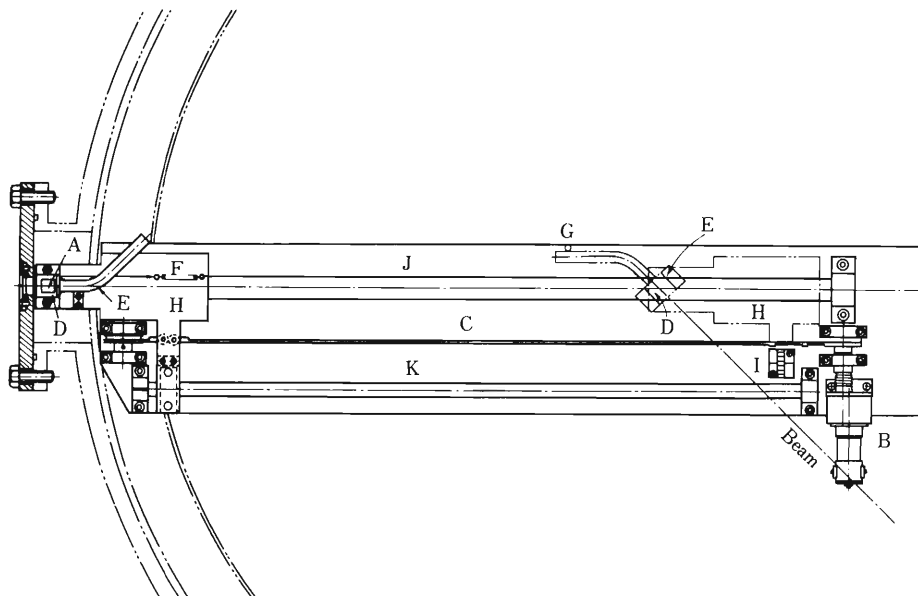


Fig. 1. Plane view of the target transportation system. A, Target; B, motor; C, drive wire; D, target holder; E, target rotator; F, spring; G, pole; H, moving rack; I, limit switch; J, main rail; and K, subrail.

time required for the transportation is about 10 s. When the measurement is finished, the target is moved back to the center of the chamber for further irradiation. The cycle of irradiation and measurement can be repeated infinitely, the time of both steps being selectable to be from 1 to 999 s from the control room of the cyclotron.

The target is mounted on a holder (D) slanted at an angle of 45° against the beam. The holder is set on a rotator (E) with a long bent tail. It can rotate around its central axis, but is strained in the clock-wise direction with a spring (F). So long as the target is in the center of the chamber, that is, in the position for irradiation, the target faces the direction of the beam, the rotation of the rotator being hindered by a pole (G). When

the rotator moves toward the window with its rack (H), the tail of the rotator is released from the pole and the target turns to face the window. In Fig. 1 are shown the target assembly in both irradiation and measurement positions.

The system has been successfully utilized for  $^{57}\text{Fe}$  Mössbauer spectroscopy with a  $^{57}\text{Mn}$  source.<sup>1)</sup> It is also expected to be useful for  $\gamma$ -ray spectroscopy of nuclides with a half-life exceeding several seconds, since the  $\gamma$ -ray background is considerably reduced in comparison with the usual on-line experiments.

#### Reference

- 1) Y. Watanabe, *et al.*: This Report, p. 121.

### III-5-7. Test of a Superconducting Secondary Beam Transport System with Large Solid Angle (SLΩ)

K. Ishida, T. Matsuzaki, K. Nagamine, H. Kitazawa,  
Y. Miyake, and E. Torikai

A new type of beam transport system for light charged particles (Superconducting Large  $\Omega$  beam course; SLΩ) was constructed at E7B course of RIKEN Ring Cyclotron (RRC). It makes use of the focusing property of an axially-symmetric magnetic field. This type of focusing system is featured by its ability to accept the charged particles emitted in a large solid angle with good momentum selection. The main purpose of this beam channel is to collect secondary particles as many as possible. The principle and the design of the system have already been reported.<sup>1)</sup> The apparatus consists of three superconducting coils, where the current of each coil ( $I_1$ ,  $I_2$ , and  $I_3$ , respectively, from the target) can be adjusted independently. The coil is of an air-core design without an iron return yoke. This type of coil was chosen because the field is precisely calculable and proportional to the current. This means that an envelope of the beam trajectory can always be fixed irrespectively to the momentum by only scaling the current. Otherwise, the slit system would become very complicated. But this coil caused a nonnegligible fringing field to the primary beam, and correc-

tion had to be done as shown later.

Here, we report a test experiment performed by using a completed SLΩ system. Before an in-beam experiment, the system was tested by using a  $^{106}\text{Ru}$   $\beta$  source, which was set at the target position, and the currents  $I_2$  and  $I_3$  were tuned for each value of  $I_1$  to obtain the maximum number of  $\beta$  rays at a counter placed at the focusing point. The results are shown in Fig. 1. The determined values of  $I_2$  and  $I_3$  agree very well with those calculated by a ray tracing program. But the measured collection efficiency was estimated to be smaller than the designed value by a factor of 4. The difference may come from, for example, mis-alignment of slits, mis-alignment of source position, blocking by a screw slit and slit supports, etc. Precise estimation of the beam loss is now in progress to make necessary modifications.

The system was tested by using a  $^{14}\text{N}$  beam of 42 MeV/u from RRC. First, the deflection of a primary beam by the fringing field was corrected by two deflecting magnets placed before and after the production target. For each excitation of the coils, the deflection magnets were adjusted

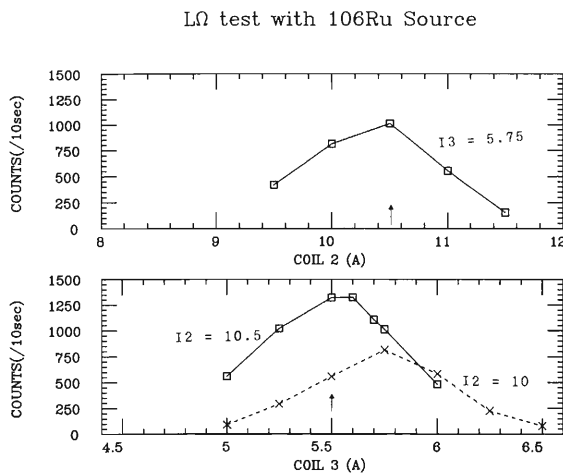


Fig. 1. Number of collected  $\beta$  rays from  $^{106}\text{Ru}$  source as a function of  $I_2$  (above) and  $I_3$  (below).  $I_1$  was fixed to 10 A so that the particles with 2 MeV/c momentum go through. The dotted line corresponds to the case when the  $I_2$  is a little off tune. The arrows show the design value.

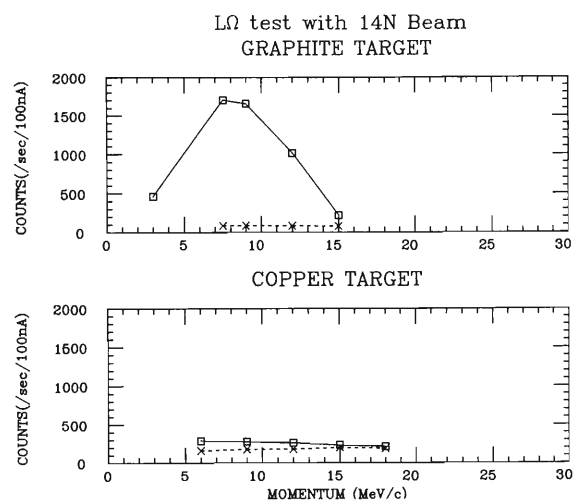


Fig. 2. Positron momentum distribution measured by SLΩ, when a beam of  $^{14}\text{N}$  with 42 MeV/u hits a graphite target (above) or a copper target (below). The dotted lines correspond to the case when the target is out.

so that the primary beam hits the center of a target and goes into a beam dump.

Next, the coil currents were tuned to collect the positrons produced in a target. The tuning was carried out for various momenta of positrons. The positrons were detected with a pair of plastic scintillation counters. The number of positrons detected is shown in Fig. 2 as a function of the positron momentum for a graphite target and for a copper target. The number of positrons has a peak around 7.5 MeV/c for the graphite target. The number is much smaller for the copper target. This may indicate that the source of positrons are mainly due to radioactive nuclei produced in the reaction.

Finally, we tuned the system to 27 MeV/c in order to get surface muons from the copper target. The surface muons are expected to be produced when the pions produced in heavy-ion reactions stop and decay in the skin of the target material. The muon was identified by using a stack of three scintillation counters. The muon comes through the first thin counter and stops in the second counter. The muon then decays with a lifetime of 2.2  $\mu$ s and emits a positron. The positron hits the counter 3 with a 50% probability. Thus coincident signals from counters 1 and 2 followed by those from counters 2 and 3 with a few microsecond delay is a typical muon signal. The data obtained in a three-hour run show about 20 events above a random coincidence level as in Fig. 3. This number is not much different from our estimation; 30 muons were

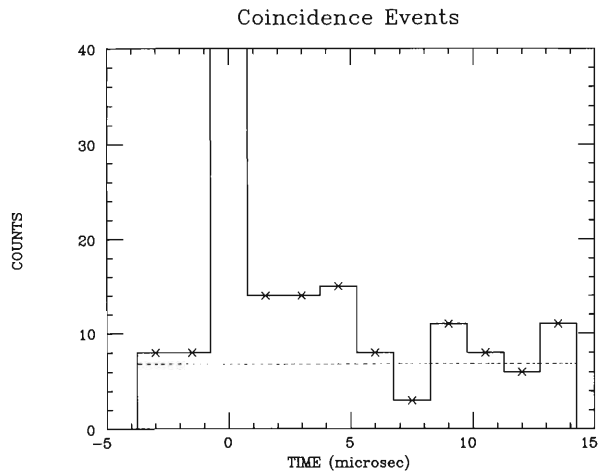


Fig. 3. Time difference between 2·3 signal and 1·2 signal, when a beam of  $^{14}\text{N}$  with 42 MeV/u hits a copper target. The dotted line corresponds to the random coincidence level determined from each counting rate. The number around time zero is 19, 700 and is mainly due to penetrating particles. Time resolution was below 0.1  $\mu$ s and far less than the time bin represented.

expected from the cross section of 400 nb for pion production and collection efficiencies estimated by Monte-Carlo calculation. We can expect more muons when the energy of the beam becomes higher with the operation of the AVF injector cyclotron.

#### Reference

- 1) K. Ishida, T. Matsuzaki, and K. Nagamine: *RIKEN Accel. Prog. Rep.*, **21**, 172 (1987).

### III-5-8. Construction of a New Type of Low Energy Radioisotope Beam Channel "SLOW" for Surface Studies

T. Matsuzaki, K. Ishida, and K. Nagamine

We have constructed a low energy radioisotope beam line "SLOW" in the E7 experimental area of RIKEN Ring Cyclotron (RRC). The SLOW beam line will be utilized for the study of emission mechanisms of various low energetic radioactive atoms from characterized surfaces and also for the extraction of useful radioisotope ions for surface-physics studies.

Heavy-ion beams from RRC are injected into various targets and produce many kinds of radioisotope atoms by nuclear reactions. The produced atoms are moderated in targets and reach to the target surfaces by thermal diffusion. At the target surface, a part of the atoms could evaporate into vacuum and could be ionized through various mechanisms based on the surface physics. By observing emitted ions with an

aid of the SLOW beam line, we can investigate emission mechanisms of various atoms from the target surface.

In Fig. 1, the layout of the SLOW beam line is shown. The details about the beam line design is described in Ref. 1. All beam line components are electrostatic lenses with no magnetic field. In this manner, the ions with an equal charge state and a different mass can be transported and focussed under the same beam line conditions. The SLOW beam line is composed of a SOA lens,<sup>2)</sup> five sets of electrostatic quadrupole lens, a troidal-shaped electrostatic bend, an X-Y electrostatic deflector and three sets of slit. At the end of the beam line, there is located a multichannel plate in order to detect the transported particles. The mass identification of the particles will be performed by

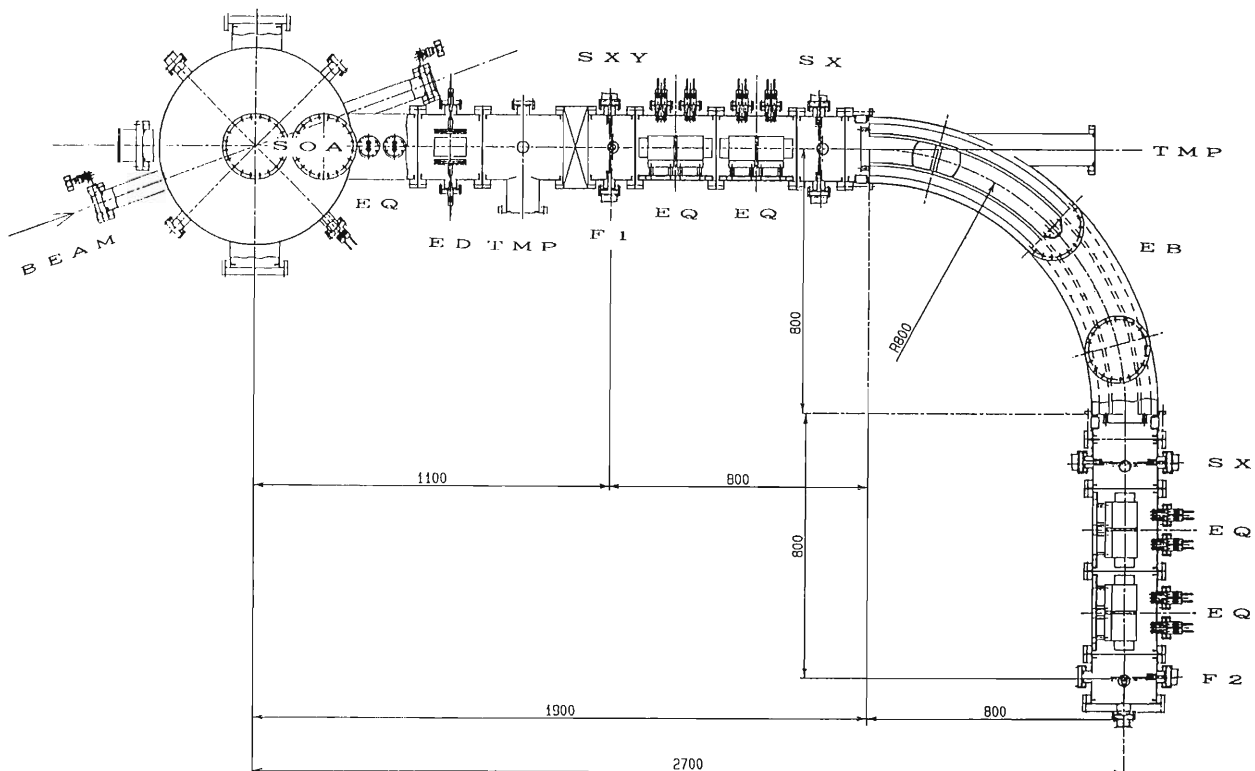


Fig. 1. Layout of the "SLOW" beam channel. The targets are placed at the center of a large high vacuum chamber. The heavy-ion beams are injected into the target by 70 degree. The beam line components are SOA lens (SOA), electrostatic quadrupole lens (EQ), electrostatic bend (EB), electrostatic deflector (ED), slit (SXY, SX), and turbo molecular pump (TMP). F1 and F2 are first and second focussing points, respectively.

measuring the time of flight through the beam line path, where the second electrode voltage of SOA lens is rectangularly pulsed to define a time zero of the flight time.

The high voltages are supplied to 32 electrodes of the beam line components through five voltage dividers. The voltage divider has a main regulated voltage supply (10 kV, 10 mA, stability;  $10^{-4}/\text{h}$ ) and eight independent outputs. The high voltage upto  $\pm 5$  kV was easily applied to the terminals of electrostatic quadropole lenses. For other components, the voltage of up to  $\pm 10$  kV is sustainable. The applied voltage can be remotely controlled from the data taking room of RRC.

A DC regulated power supply (500 A, 16 V, stability;  $10^{-4}/\text{h}$ ) was installed to heat up the target metal. Also, we installed an AC power supply (20 A, 100 V) for an electron filament in order to investigate an optical property of SLOW beam line by using emitted thermal electrons. For the pulsed voltage applying to the second electrode of SOA lens, a pulse generator was equipped, which produces pulses with a rising time of  $<20$  ns, widths from 100 ns to 100  $\mu\text{s}$ , amplitudes from 0 to 400 V, and repetition rates from 0 to 1 kHz. The above three modules were installed into one shielding box and were electrically floating to change independently their ground potential up to  $\pm 10$  kV. The magnetic shield to the SLOW beam line is now being designed, which is essential to transport thermal electrons. The E7 experimental area is located just beside the RRC accelerator and just below the AVF injector, and the stray magnetic field was measured to be high.

The vacuum space of beam line was evacuated by two sets of turbo moleculer pump (300 l/s). At a head of the SLOW beam line, there is a large high vacuum chamber evacuated with a cryopump (1,500 l/s), the inside vacuum of which is aimed to reach as high as  $10^{-10}$  torr after outgassing by baking.

A preliminary evacuation test without baking proved that the attainable vacuum of the chamber was  $1.2 \times 10^{-8}$  torr after evacuation for two days. The setup of a baking heater is now being preparing, including a temperature control system.

Above the large chamber, we put an additional chamber equipped with an argon-ion gun, a LEED/AUGER spectrometer, and an electric quadrupole mass spectrometer. The argon-ion

gun (5 kV, 30 mA) is to make ion etching on the metal surface. By employing the LEED/AUGER spectrometer (120 deg type), the LEED patterns for metal surfaces give us crystallographic information and an Auger electron spectrum is used to analyze the components existing on metal surfaces. An electric quadrupole mass spectrometer is utilized to analyze the residual gas component of the vacuum; this analysis is essential to control the metal surface.

A primary beam transpotation test to E7 was performed. A beam spot of 2 mm in diameter was obtained at the target position of the SLOW beam line, and no induced discharge phenomena by primary beams was observed at every electrode of the SLOW beam line component.

In the experiments using the SLOW beam line to investigate an emission mechanism of ions from the characterized metal surface, a variety of emitted ions and their yields will be observed by changing experimental conditions, *i.e.*, target materials, surface temperature, surface treatment, coating materials, crystallographic axis, target thickness, incoming heavy ions beams and energy. The superior point of this method is that various atoms generate inside the target and are emitted from the surface after thermal diffusion; this method is quite different from the cases of an ion scattering or an ion implantation method.

In addition to metal targets, we will try ionic crystals and rare-gas solids, having large band-gap energies. In the positron studies, it was observed that energetic positrons implanted into various ionic crystal surfaces were re-emitted with maximum kinetic energies (about 14.7 eV for LiF) near the band-gap energy.<sup>3)</sup> This new surface mechanism is considered to occur also for various atoms. We will begin to prepare a rare-gas solid target.

As described in Ref.1,  ${}^6\text{He}$  and  ${}^8\text{He}$  beams will be a powerful probe to many fields. The initial design of an ionization device, yield estimation, and optical calculation for a microbeam line are now in progress.

## References

- 1) T. Matsuzaki, K. Ishida, and K. Nagamine: *RIKEN Accel. Prog. Rep.*, **21**, 170 (1987).
- 2) K.F. Canter, P.G. Coleman, T.C. Griffith, and G.R. Heyland: *J. Phys. B*, **5**, L167 (1972).
- 3) A.P. Mills, Jr. and W.S. Crane: *Phys. Rev. Lett.*, **53**, 2165 (1984).

### III-5-9. Performance of the Stop Detector for Time-of-Flight (T.O.F) System

T. Mizota, T. Nakagawa, K. Yuasa-Nakagawa, H. Fujiwara,  
M. Ogihara, Y.H. Pu, and S.M. Lee

In heavy-ion reactions it is often necessary to use a time of flight telescope to determine the mass and energy of the reaction products. Several authors reported the good time resolution (150 ps) achieved for heavy ions for the channel plate detector (CPD)<sup>1-4</sup> they used. In order to obtain a better mass resolution with a large solid angle, we have developed a CPD which provides a good time resolution and a large effective area, simultaneously.

A schematic drawing of the detector is shown in Fig. 1. Incident ions pass through a thin foil which consists of Au ( $20\mu\text{g}/\text{cm}^2$ ) evaporated on formvar foil ( $10\mu\text{g}/\text{cm}^2$ ). Secondary electrons are accelerated by the potential difference between the foil and the acceleration grid. The electrostatic field between two grids placed at 45 deg to the ion path deflects the electrons 90 deg towards the micro channel plate (MCP) which has a sensitive area of  $1,380 \text{ mm}^2$ . The main drawback with these designs is such that the grid can introduce spurious peaks in energy spectra,

particularly when elastic yields are very large. In order to minimize this effect, we used thin wires (Au-W wires of  $10\mu\text{m}$  in diameter with a 1 mm space) for the grid. The overall transparency is about 97%.

The performance of the CPD was studied with 5.5 MeV  $\alpha$  particles and various ions produced by a 12 UD tandem accelerator at the University of Tsukuba. The ions were elastically scattered by an  $80\mu\text{g}/\text{cm}^2$   $^{197}\text{Au}$  target and detected with a T.O.F system, which was placed at an angle of 8 deg. The T.O.F system for these test experiments consisted of CPD as a start detector and a totally depleted silicon surface barrier detector (SBD:  $100 \text{ mm}^2$   $100\mu\text{m}$  thick) as a stop one. The flight path was about 20 cm. The signal from the CPD was fed directly into a constant fraction discriminator (ORTEC 943). The timing signal from the SBD was first amplified with a fast preamplifier (IV 48 developed by the electronics department of Hahn-Meitner-Institute).

Figure 2 shows the overall time resolution for 85 MeV  $^{16}\text{O}$  as a function of the acceleration voltage between the foil and the acceleration grid. It is shown that the time resolution is about 100 ps for  $V_{\text{acc}} > 0.5$  kV and becomes bad with decreasing the  $V_{\text{acc}}$  below 0.5 kV. This is due to the transit time spread of the secondary electrons emitted from the foil. The time resolution and the detection efficiency for various ions are listed in Table 1. The time resolution for  $^{35}\text{Cl}$  are rather worse than that for  $^{16}\text{O}$ . This is due to the

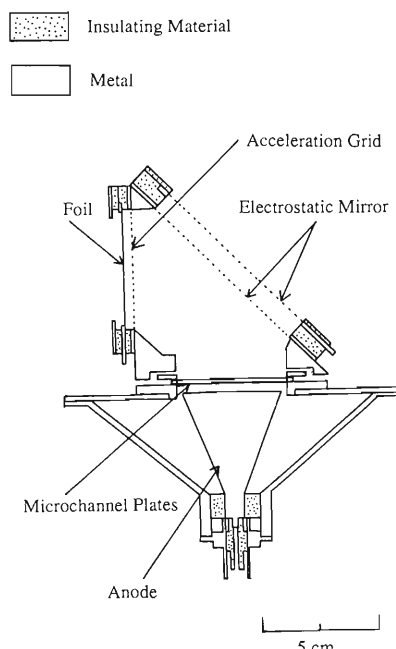


Fig. 1. Schematic drawing of the mirror type channel plate detector.

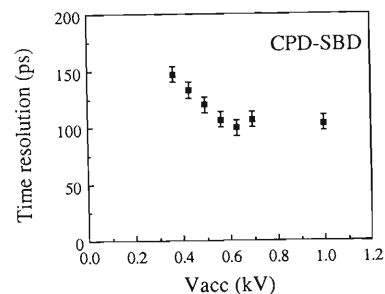


Fig. 2. An overall time resolution as a function of  $V_{\text{acc}}$ .

Table 1. Overall time resolution of the CPD-SBD system for various ions.

Ion	Energy (MeV)	Time resolution (ps) (FWHM)
$\alpha$	5.5	167
$^{16}\text{O}$	85	100
$^{35}\text{Cl}$	105	128

effects of the plasma discharge in the SBD<sup>5,6)</sup> and the energy straggling of  $^{35}\text{Cl}$  ion in the foil.

### References

- 1) W. Startecki, A.M. Steffanini, S. Lunardi, and C. Signorini: *Nucl. Instrum. Methods*, **193**, 499 (1982).
- 2) J. Girard and M. Bolore: *Nucl. Instrum. Methods*, **140**, 279 (1977).
- 3) F. Busch, W. Pfeffer, B. Kohlmeyer, D. Schull, and F. Puhlhöfer: *Nucl. Instrum. Methods*, **171**, 71 (1980).
- 4) T. Nakagawa and W. Bohne: *Nucl. Instrum. Methods A*, **271**, 526 (1988).
- 5) M. Moszynski and B. Bengston: *Nucl. Instrum. Methods*, **91**, 73 (1971).
- 6) T. Nakagawa and K. Yuasa-Nakagawa: *Jpn. J. Appl. Phys.*, **29**, 498 (1989).

### III-5-10. Timing Property of New Type Time Pick-Up Detector

T. Nakagawa, K. Yuasa-Nakagawa, and I. Tanihata

In heavy-ion reactions a measurement of time-of-flight is commonly used to determine the mass and the energy of a reaction product. For measurement of the flight time, various kinds of timing detectors are used, for example thin film scintillators,<sup>1)</sup> thin  $\Delta E$  solid state detectors,<sup>2)</sup> and an electron multiplier with a thin film secondary electron emission foil. In order to minimize energy straggling and energy loss of particles, a detector with a least amount of material is usually desired. For this reason, the last method become more and more popular recently. One setup of this kind is to use a micro-channel plate (MCP) as an electron multiplier (EM), which is called a channel plate detector (CPD). Several authors have reported the good time resolution ( $\leq 150$ ps) for heavy ions<sup>3-5)</sup> by using this detector. However the MCP needs a clean high vacuum ( $\leq 10^{-6}$  Torr) to prevent breakdown. Therefore it is not suitable for use under the conditions where a good vacuum is difficult to maintain. The large scattering chamber at RIKEN Ring Cyclotron (RRC) Facility meets one of such condition.

Another common method uses a plastic scintillator which is optically coupled to a photomultiplier tube.<sup>6,7)</sup> However, because it is very sensitive to a magnetic field, we can not use it in a strong magnetic field without shielding. In addition the scintillator is not very compact (length: 20-30 cm) and needs high voltage up to 10-17kV.

In the present paper we report a new-type time pick-up detector which has a thin foil and a proximity mesh type electron multiplier; presently a developed detector can be operated in a poor vacuum ( $\sim 10^{-4}$  Torr). Therefore, this time pick-up detector is quite suitable for use in the large scattering chamber at RRC.

Experiments were carried out at Tandem Accelerator Center, University of Tsukuba. Figure 1 shows a schematic drawing of the detector and the experimental set up. Ions pass through a thin foil made of  $20 \mu\text{g}/\text{cm}^2$  Al evaporated on Mylar. Electrons emitted from the foil are accelerated by the electric field between the foil and a grid which is made of a 97% transparent electroformed mesh. The electrons then run

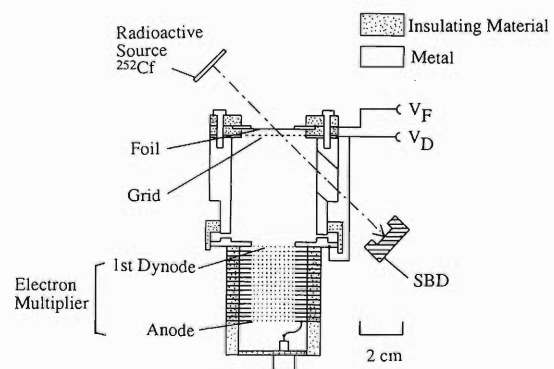


Fig. 1. Sectional view of the time pick-up detector.

through the field free region and strike the first dynode of an Electron Multiplier (EM) (R2362 Hamamatsu photonics). An electron is multiplied up to  $10^6$  in the EM. The R2362 EM which has 23 proximity mesh dynodes is very compact (max. length is about 6 cm) compared with other Photo Multiplier Tube (PMT) and has a high immunity to magnetic fields.

Fission fragments and 6 MeV  $\alpha$  particles of a  $^{252}\text{Cf}$  fission source impinge on the thin film at an incidence of 45 degrees. They are then stopped in a standard silicon surface barrier detector (SBD,  $100 \text{ mm}^2$  and  $150 \mu\text{m}$  thick). The flight path is 7cm. A timing signal is derived from the SBD through a fast preamplifier (IV 48 developed in Hahn-Meitner-Institute). The signal was then fed into a constant fraction discriminator (CFD, TNNEREC 454). The anode signal of EM was amplified with a Timing Filter Amplifier (TFA, ORTEC 474) and fed into another CFD. The vacuum of the test chamber was kept to be about  $10^{-4}$  Torr.

The electric potential applied to the first dynode of the EM and the grid was  $-3.5$  kV. The electric potential of the anode was 0 V. The rise time of an output signal was about 2.5 ns. The typical pulse height for 6 MeV  $\alpha$  particles was about 20 mV. The following components are contributed to affect the time resolution.

- 1) Variation in transit time of electrons between the foil and the first dynode due to a different initial velocities of electrons:  $\delta_D$
- 2) Transit time spread of electrons in EM:  $\delta_E$

### 3) Time resolution of SBD: $\delta_{\text{SBD}}$

In order to investigate the contribution of  $\delta_b$ , we have varied the voltage applied to the foil ( $V_F$ ). In Fig. 2, closed circles show the overall time resolution for 6 MeV  $\alpha$  particles as a function of  $V_{\text{acc}} (= V_F - V_D)$ . The time resolution of SBD for 6 MeV  $\alpha$  particles and fission fragments was below 100 ps.<sup>8-10)</sup> The observed time resolution is almost independent of  $V_{\text{acc}}$  within experimental errors. These results show that the contribution of  $\delta_b$  and  $\delta_{\text{SBD}}$  is significantly small compared with the total time resolution and that the time resolution of  $550 \pm 50$  ps for 6 MeV  $\alpha$  particles is mainly due to the transit time spread of electrons in EM.

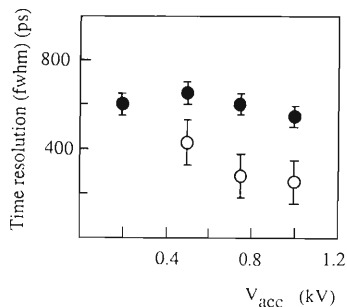


Fig. 2. Time resolution of the time pick-up detector as a function of  $V_{\text{acc}}$ . Closed and open squares represent the time resolution of the time pick-up detector for 6 MeV  $\alpha$  particle and fission fragments, respectively.

In order to evaluate the time resolution of the time pick-up detector for fission fragments, we subtracted the contribution of mass and kinetic energy distribution<sup>11)</sup> from the total time resolution. In Fig. 2, the open circles show the time resolution of fission fragments (lighter partner) as a function of  $V_{\text{acc}}$ . The time resolution is improved better with increasing  $V_{\text{acc}}$  and the time resolution remains constant when  $V_{\text{acc}}$  reaches 1 kV. It is therefore considered that the contribution of  $\delta_b$  become negligible for  $V_{\text{acc}}$  larger than 1 kV. The  $\delta_b$  contribute up to about 300 ps for  $V_{\text{acc}}$  less than 1 kV.

Figure 3 shows the time resolution of the time pick-up detector as a function of the number of emitted electrons from the foil, which is evaluated from the experimental results reported in Refs. 12 and 13. The time resolution is better for increasing number of emitted electrons, and can be explained from a simple formula in Ref. 14.

$$\delta_E^2 = (1 + \varepsilon_A^2(1 - 1/R)^2) \delta_h^2 / R$$

where  $R$  is the average number of electrons emitted from the thin film,  $\delta_h^2$  the variance of the transit time of a current pulse by a single elec-

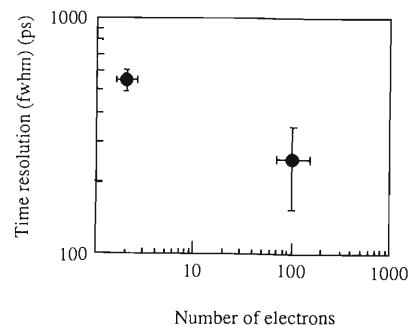


Fig. 3. Total time resolution as a function of the number of emitted electrons from a thin foil.

tron, and  $\varepsilon_A^2$  the relative variance of the multiplier gain  $A$ :

$$\varepsilon_A^2 = \delta_A^2 / A^2$$

If the large number of electrons are emitted, the  $\delta_E^2$  is proportional inversely to  $R$ .

The detection efficiency of the time pick-up detector for 6 MeV  $\alpha$  particles and fission fragments are 85% and 100%, respectively. At the vacuum pressure of  $10^{-4}$  Torr, the detector was sufficiently stable for a long term (about 10 h).

We designed, built, and tested a thin foil time pick-up detector using an electron multiplier. A time resolution of  $550 \pm 50$  ps and  $250 \pm 100$  ps was obtained for 6 MeV  $\alpha$  particles and fission fragments (lighter partner) from a  $^{252}\text{Cf}$  source with the efficiency of 85 and 100%, respectively. The resolution of the time pick-up detector is mainly determined by the transit time spread of electrons in an electron multiplier when a high acceleration voltage ( $>1$  kV) between a foil and an acceleration grid is applied. If we use an electron multiplier which has better time resolution, we will obtain a better time resolution. The time pick-up detector which is described in this paper is suitable for the measurement of time of flight of heavy ions in a poor vacuum.

### References

- 1) C.K. Gelbke, K.D. Hildenbrand, and R. Bock: *Nucl. Instrum. Methods*, **95**, 397 (1971).
- 2) H. Pleyer, B. Kohlmayer, W.F.W. Schneider, and R. Bock: *Nucl. Instrum. Methods*, **96**, 263 (1971).
- 3) W. Starzecki, M.A. Steffanini, S. Lunardi, and C. Signorini: *Nucl. Instrum. Methods*, **193**, 499 (1982).
- 4) J.D. Bowman and R.H. Heffner: *Nucl. Instrum. Methods*, **148**, 503 (1978).
- 5) T. Nakagawa and W. Bohne: *Nucl. Instrum. Methods A*, **271**, 523 (1988).
- 6) E. Dietz, R. Bass, R. Reiter, V. Reidland, and B. Habert: *Nucl. Instrum. Methods*, **97**, 581 (1971).
- 7) W.F.W. Schneider, B. Kohlmeyer, and R. Bock: *Nucl. Instrum. Methods*, **95**, 397 (1971).
- 8) T. Nakagawa and K. Yuasa-Nakagawa: *Jpn. J. Appl.*

- Phys.*, **28**, 498 (1989).
- 9) M. Moszynski and B. Bengston: *Nucl. Instrum. Methods*, **91**, 73 (1971).
  - 10) H. Henschel, H. Hipp, A. Kohnle, and F. Gonnaenwein: *Nucl. Instrum. Methods*, **161**, 331 (1979).
  - 11) W.H. Schmit, J.H. Neiler, and F.J. Walter: *Phys. Rev.*, **141**, 1146 (1966).
  - 12) K.E. Pferdekamper and H.G. Clerc: *Z. Phys. A*, **275**, 223 (1975).
  - 13) J. Girard and M. Bolore: *Nucl. Instrum. Methods*, **140**, 279 (1977).
  - 14) F. de la Barre: *Nucl. Instrum. Methods*, **102**, 77 (1972).

### III-5-11. Timing Properties of a Time-of-Flight Detector

T. Nakagawa and K. Yuasa-Nakagawa

We have studied the influence of a plasma effect on the time resolution of a silicon surface barrier detector. The time resolutions were measured by changing an electric field strength, the size of a detector, and the resistivity of a material. The very good timing properties of a silicon surface barrier detector (SBD) for charged particles are utilized by time of flight measurements in nuclear reactions.<sup>1-3)</sup> However, from many experimental investigations, it is well known that a timing signal obtained from a SBD may not represent the correct time arrival of an ion in the detector, as it usually is too late (Plasma Delay Time (PDT)).<sup>4,5)</sup> Recently the time resolutions of SBD were studied by Mozynski and Bengston.<sup>6)</sup> They have reported that the dependence of the time resolution of SBD on an electric field strength and interpreted it in terms of plasma discharge, but not studied for the various conditions of the SBD. The purpose of the present experiment is, therefore, to survey the plasma effect under the various conditions. From present measurement we discuss a relation between PDT and the time resolution of SBD.

The experimental setup is shown schematically in Fig. 1. It consists of a CPD as a start detector and a SBD as a stop detector. The flight path between the CPD and SBD is  $70 \pm 0.5$  mm. The CPD consists of an electron-emitting foil and two channel plates (25 mm in diameter) with a central hole (6 mm in diameter) and without any grid.<sup>7)</sup> A secondary emitting foil, two channel plates and an electron-collecting anode are mounted on the common axis and placed perpendicular to the ion path. In order to enhance the electron emission, magnesium oxide ( $15 \mu\text{g}/\text{cm}^2$ ) is evaporated onto a formvar foil ( $10 \mu\text{g}/\text{cm}^2$ ).

The timing signals from the SBD were first amplified by a fast preamplifier (IV 69B) and a fast amplifier (IV 64) with a rise time of less than 0.8 ns (both developed at the Hahn-Meitner Institute). These signals were fed into a constant fractional discriminator (CFD, ORTEC 943). The signals from the CPD were fed directly into the CFD. Throughout the measurements, the time range of the time-to-amplitude converter (TAC) was set at 50 ns. In order to test the plasma delay

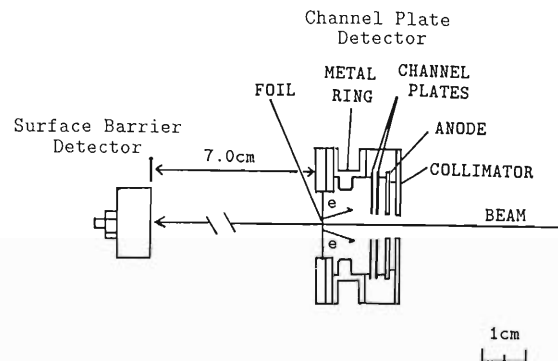


Fig. 1. Schematic drawing of the channel plate detector with a central hole.

time and the time resolution of SBD, we used the 8.78 MeV alpha particles of a ThC' source.

In order to test the dependence of plasma delay time on the properties of SBDs, we used two different SBDs (Det. 1:  $S = 300 \text{ mm}^2$ ,  $T = 179 \mu\text{m}$ ,  $\rho = 2,300 \Omega\text{cm}$   $C \sim 180 \text{ pF}$ ,  $V_N = 180$  volt, and Det. 2:  $S = 50 \text{ mm}^2$ ,  $T = 500 \mu\text{m}$ ,  $\rho = 6,100 \Omega\text{cm}$   $C \sim 11.5 \text{ pF}$ ,  $V_N = 170$  volt), where  $S$ ,  $T$ ,  $\rho$ ,  $C$ , and  $V_N$  are the area, thickness, resistivity, capacitance and recommended bias voltage of the SBD, respectively. The time-zero calibration was performed by varying the field strength  $F$ . As early as 1966, Meyer proposed the linear dependence of the plasma time on an inverse field. Neidel and Henschel showed that this holds as well for the plasma delay, and that by extrapolation to infinity of a high field strength ( $1/F \rightarrow 0$ ), the plasma delay vanishes.<sup>4)</sup> The plasma delays of two detectors are shown in Fig. 2 as a function of  $1/F_{\text{eff}}$ , which is given

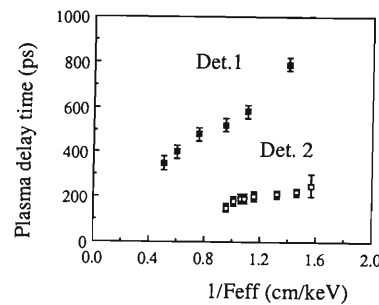


Fig. 2. Plasma delay time as a function of  $F_{\text{eff}}$ .

$F_{\text{eff}} = (d - x) / \mu\tau$ , where  $d = (2\tau\mu V)^{1/2}$  is the depletion depth at a given bias voltage  $V$ ,  $\mu = 1,481 \text{ cm}^2\text{V}^{-1}\text{s}^{-1}$  is the constant electron mobility and  $\tau = \rho \times 10^{-12} \text{ s}$  with the resistivity of a material  $\rho (\Omega\text{cm})$ ;  $x$  is taken at the charge centroid of the ionization track produced by a charged particle. The charge centroid for 8.78 MeV alpha particles can be estimated at 2/3 of the range calculated by Ref. 8. The plasma delay time of Det. 2 is quite small (about 200 ps). The difference between the two detectors is mainly due to the effect of capacitance.<sup>5)</sup>

Figure 3 shows the overall time resolution of a T.O.F. detector which consists of a CPD and SBD (Det. 2) as a function of bias voltages. The overall time resolution ( $\sigma_{\text{total}}$ ) was determined by the following components: time resolution of CPD ( $\sigma_{\text{cpd}}$ ), contribution of noise to the time resolution ( $\sigma_{\text{noise}}$ ) and intrinsic time resolution of SBD ( $\sigma_{\text{SBD}}$ ). Then,  $\sigma_{\text{total}}$  is given by

$$\sigma_{\text{total}}^2 = \sigma_{\text{SBD}}^2 + \sigma_{\text{noise}}^2 + \sigma_{\text{cpd}}^2 \quad (1)$$

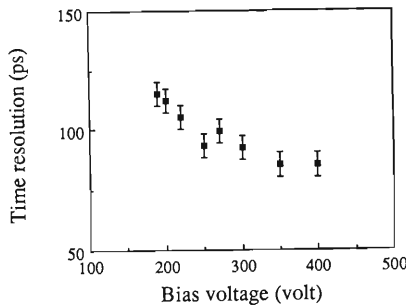


Fig. 3. Overall time resolution of the T.O.F. detector as a function of detector bias.

To determine the noise contribution, we used a pulser at a fixed amplitude. In this way, the time resolution was obtained as 50 ps. In order to investigate the time resolution of CPD, two identical CPDs were used as a start and stop detector. The overall time resolution was about  $80 \pm 5$  ps. Owing to the basic symmetry of the experimental device, we could obtain the time resolution of each CPD by dividing the previous width by  $\sqrt{2}$ . Thus, we obtained the time resolution of 56 ps for 8.78 MeV alpha particles.

Figure 4 shows the  $\sigma_{\text{SBD}}$  ( $\sigma_{\text{SBD}}^2 = \sigma_{\text{total}}^2 - \sigma_{\text{cpd}}^2 - \sigma_{\text{noise}}^2$ ) as a function of  $1/F_{\text{eff}}$ . The intrinsic time resolution of SBD decreases with increasing  $F_{\text{eff}}$ . This tendency is also seen for the plasma delay time. The time resolution of Det. 2 is smaller than that of Det. 1 at the same  $F_{\text{eff}}$ . This is due to

the property of SBD. The time resolution of SBD corresponds to about 20% of the plasma delay time within the experimental error.

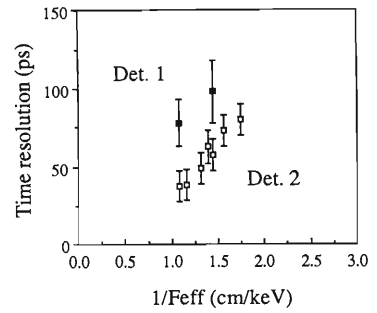


Fig. 4. Intrinsic time resolution of SBD as a function of  $F_{\text{eff}}$ .

We obtained the best time resolution of 80 ps for 8.78 MeV alpha particles using a simple detector system which consisted of a small capacitance surface barrier detector and a channel plate detector with a central hole. We found that the plasma delay time is strongly dependent on the detector properties such as the resistivity and capacitance described in Ref. 5. The time resolution of the surface barrier detector for 8.78 MeV alpha particles is also strongly affected by the electric field strength and the properties of the SBD. The time resolution is about 20% of the PDT. In order to get a good time resolution using the surface barrier detector, it is better to have a small capacitance with low resistivity and overbiasing.

## References

- 1) W. Strazeci, A.M. Steffanini, S. Lunardi, and C. Signorini: *Nucl. Instrum. Methods*, **193**, 499 (1982).
- 2) E.C. Pollaco, J.C. Jacmart, Y. Blumenfeld, Ph. Chomaz, N. Frascaria, J.P. Garron, and J.C. Poynette: *Nucl. Instrum. Methods*, **225**, 51 (1984).
- 3) A.M. Zebelman, W.G. Meyer, K. Kalbach, A.M. Poskanzer, R.G. Sexto, G. Gabor, and D.A. Landis: *Nucl. Instrum. Methods*, **141**, 439 (1977).
- 4) H.-O. Neidel, H. Henschel, H. Geissel, and Y. Laichter: *Nucl. Instrum. Methods*, **212**, 299 (1983) and references therein.
- 5) W. Bohne, W. Galster, K. Grabisch, and H. Morgenstern: *Nucl. Instrum. Methods A*, **240**, 145 (1985).
- 6) M. Moszynski and B. Bengtson: *Nucl. Instrum. Methods*, **91**, 73 (1971).
- 7) T. Nakagawa and W. Bohne: *Nucl. Instrum. Methods A*, **271**, 71, 523 (1988).
- 8) L.C. Northcliff and R.C. Schilling: *Nucl. Data Tables*, **7** (1979).

### III-5-12. Compact and Gridless Channel Plate Start Detector

T. Nakagawa and W. Bohne\*

Mass identification in heavy ion reactions is often performed by using the time of flight method. A start detector as thin as possible is required to avoid energy loss and straggling of particles. For many years arrangements of secondary electron emitting foils and a micro channel plate (MCP) have been used successfully. The majority of these electrons have low energies and are ejected in all directions from very thin foil when the ion path through the foil and they have to be transported isochronously to a channel plate. In several constructions this is achieved by placing an acceleration grid directly behind the foil.<sup>1-3)</sup> All detectors of this type have serious disadvantage that ions are stopped or energically degraded and scattered by the inhomogeneous material of the grid. Taking this problem into account, we have chosen and tested a system where the ion path through a central hole in the MCP and anode similar to the ones developed by Oed, *et al.*<sup>4)</sup> To avoid any inhomogeneous material in the beam path, however, we do the electron transport without a wire between the foil and MCP.

Figure 1 shows a schematic drawing of the detector design. A secondary electron emitting foil, two MCP's with a central hole (6 mm in diameter) and an electron collecting anode also with central hole (5.9 mm in diameter) are mounted on a common axis and placed perpendicularly into the ion path. All parts are made of metal or ceramics to exclude any plastic material near channel plate. In order to enhance electron emission, magnesium oxide ( $15 \mu\text{g}/\text{cm}^2$ ) is evaporated on a formvar foil ( $10 \mu\text{g}/\text{cm}^2$ ). The secondary electrons from this foil are accelerated toward the channel plates by the potential deference between the foil and the front surface of the first channel plate ( $V_F = -3.9 \text{ kV}$ ,  $V_{CP} = -2.8 \text{ kV}$ ). A potential ring is placed between the foil and the channel plates to increase the vertical velocity component of electrons ( $V_R = 0 \text{ V}$ ). Its voltage was chosen to optimize the electron collection on the channel-plate ring. Furthermore

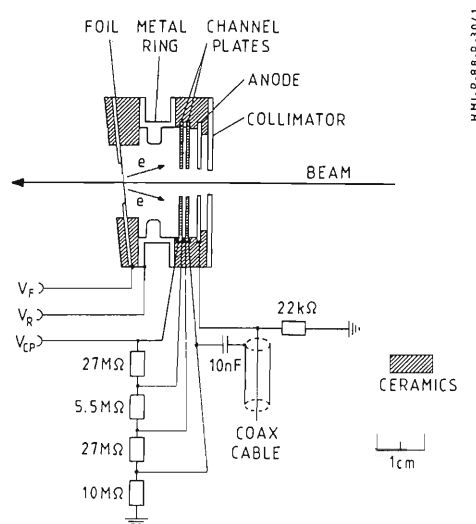


Fig. 1. Schematic drawing of the coaxial timing detector.

the foil is not mounted parallel to the channel plate surface but with a small angle of approximately 6 deg. This help to disturb a little bit the symmetric electric field between foil and channel plate to reduce the fraction of the central part of the beam spot from which no effective electron collection is possible. All test measurements are performed together with a standard surface-barrier detector (SBD) as a stop detector. For radioactive sources we used a  $500 \mu\text{m}$  thick SBD of  $50 \text{ mm}^2$  at 10 cm behind the CPD. In experiments with a beam from a heavy ion accelerator VICKSI, a time-of-flight spectrometer consists of the same CPD at 35 cm from the target and a  $100 \text{ mm}^2$  large SBD of  $150 \mu\text{m}$  in thickness; the flight path between both detectors was 90 cm.

The experiment with radioactive source was done in Hahn-Meitner-Institut. Most of the test measurements were carried out with a collimated ThC'α-source. The electric potential applied to each channel plate was always 1.1 kV. The maximum detection efficiency for α-particles was 50% with a time resolution of 90 ps. For fission fragments of  $^{252}\text{Cf}$ , the detection efficiency was always 100%. In an experiment with 840 MeV and 710 MeV  $^{32}\text{S}$  beams from the VICKSI accelerator, elastically scattered at a thin foil

\* Hahn-Meitner-Institut-P Berlin, D-1000 39, Postfach 390128, F.R. Germany.

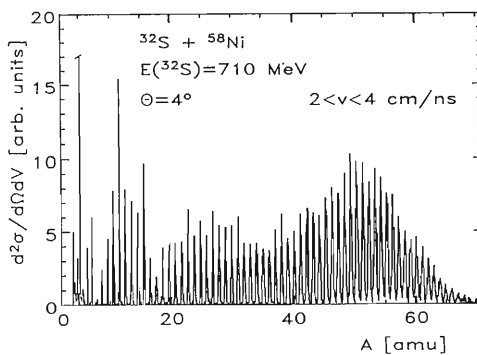


Fig. 2. Mass spectrum of the fusion evaporation reaction of  $^{32}\text{S} + ^{58}\text{Ni}$  for a velocity window between 2 and 4 cm/ns at  $\theta_{\text{lab}} = 4$  deg.

(200  $\mu\text{g}/\text{cm}^2$ ) gold target, we achieved a total time resolution of 60 ps with an efficiency of 70%. The time resolution is not collected for velocity variations due to the energy-loss straggling in the target and formvar foil. If the signals from the channel plate anode are not fed directly

into a constant fraction discriminator, but are amplified by a very fast preamplifier with a rise time of 95 ps and a gain of 10 dB (IV 70, developed by the Hahn-Meitner-Institut) efficiencies of almost 100% for  $^{32}\text{S}$  ions and 90% for  $\alpha$  particles are possible, virtually without any deterioration of the time resolution. Figure 2 shows a part of a typical mass spectrum of the fusion-evaporation reaction measured with a flight path of 1.1 m. The detection efficiency was about 100%.

#### References

- 1) W. Startecki, A.M. Steffanini, S. Lunardi, and C. Signorini: *Nucl. Instrum. Methods*, **193**, 499 (1982).
- 2) J. Girard and M. Bolore: *Nucl. Instrum. Methods*, **140**, 279 (1977).
- 3) F. Busch, W. Pfeffer, B. Kohlmeyer, D. Schull, and F. Puhlhöfer: *Nucl. Instrum. Methods*, **171**, 71 (1980).
- 4) A. Oed, G. Barreau, F. Gonnenwein, P. Perrin, C. Ristori, and P. Geltenbrot: *Nucl. Instrum. Methods*, **179**, 265 (1981).

### III-5-13. A Position Sensitive Ionization Chamber

Y.H. Pu, T. Nakagawa, K. Yuasa-Nakagawa, T. Mizota,  
H. Fujiwara, M. Ogihara, and S.M. Lee

For last years, a large ionization chamber for identifying charge number of reaction products has become widely used in heavy-ion physics.<sup>1-3)</sup> This chamber can be built in a large dimension, and the energy and energy loss resolutions achieved with them are comparable to that of solid state detectors. In order to obtain a large solid angle and information on scattering angles of reaction products, we constructed and tested a compact and large area position-sensitive  $\Delta E$ - $E$  counter telescope which consists of an ionization chamber as a  $\Delta E$  counter and a large area solid state detector as a  $E$  counter (effective area 2,000 mm<sup>2</sup>).

Figure 1 shows a schematic drawing of the

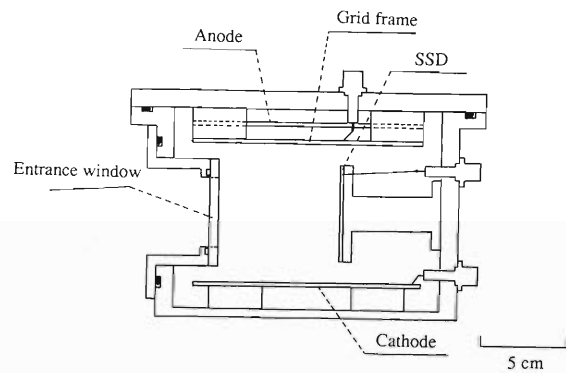


Fig. 1. Schematic drawing of a position sensitive ionization chamber.

Table 1. Energy-loss resolution for various ions.

	Ion energy (MeV)	Gas pressure (Torr)	Energy-loss (keV)	Energy loss resolution (keV, FWHM)
$\alpha$	5.5	20	520	54 (10.3%)
		30	840	82 ( 9.7%)
$^{28}\text{Si}$	90.0	30	1130	435 ( 4.0%)

ionization chamber. The distance between a frisch grid and an anode is 2 cm. The distance between the grid and the cathode is 8 cm. The frisch grid consists of Au-W wires of 50  $\mu\text{m}$  in diameter at a distance of 1 mm. The shield inefficiency<sup>4)</sup> for positive ions, which exist between the grid and the cathode, by this grid is about 2%. According to the experiment conditions, the effective length of the  $\Delta E$  counter can

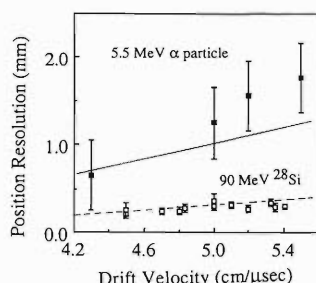


Fig. 2. Position resolution as a function of the drift velocity of electrons between a grid and a cathode at 30 Torr.

be changed from 0 to 10 cm. In order to minimize the effect of energy straggling and energy loss in an entrance foil, we used a thin foil (45  $\mu\text{g}/\text{cm}^2$ ) supported by a mesh grid. The  $E$  counter is a large area ion-implantation solid state detec-

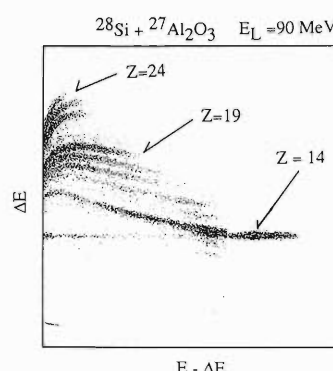


Fig. 3. Energy loss ( $\Delta E$ ) vs. energy ( $E - \Delta E$ ) for heavy residues produced by bombarding a target  $^{27}\text{Al}_2\text{O}_3$  with 90 MeV  $^{28}\text{Si}$ . Particles are detected at 10 deg. Isobutane of 30 Torr was used as a counter gas.

tor ( $4.5 \times 4.5 \text{ cm}^2$ ) made by HAMAMATSU Photonics. The performance of the  $\Delta E-E$  telescopes was studied with 5.5 MeV  $\alpha$  particles and  $^{28}\text{Si}$  beams produced by the 12 MV UD tandem accelerator in University of Tsukuba. The ions are elastically scattered by a  $100 \mu\text{g}/\text{cm}^2$   $^{197}\text{Au}$  target and detected in an ionization chamber placed at an angle of 10deg.

The energy-loss resolutions for 5.5 MeV alpha particles and 90 MeV  $^{28}\text{Si}$  ions are listed in Table 1. These values are comparable to an empirical formula of energy straggling in the isobutane gas.<sup>1)</sup>

The position of incident particles is given from the drift time of electrons between the path of the incident particle and the frisch grid. Figure 2 shows the position resolution as a function of the drift velocity of electrons between the cathode and the frisch grid. The position resolution was improved with decreasing the drift velocity. The

full and dashed lines correspond to the time resolution of 16 ns and 5.6 ns, respectively. The best position resolution of 0.25 mm for  $^{28}\text{Si}$  ( $E_L = 90 \text{ MeV}$ ) has been obtained at 30 Torr.

Figure 3 shows a two-dimensional nuclear charge  $Z$  spectrum for the reaction products of 90 MeV  $^{28}\text{Si} + \text{Al}_2\text{O}_3$ .

#### References

- 1) K. Kusterer, J. Betz, H.L. Harney, B. Heck, Liu Ken Pao, and F. Porto: *Nucl. Instrum. Methods*, **177**, 485 (1980).
- 2) J. Pochodzella, R. Butsch, B. Heck, G. Hlauatsh, A. Miczaika, H.J. Rabe, and G. Rosner: *Nucl. Instrum. Methods A*, **234**, 97 (1985).
- 3) K.D. Schilling, P. Gippner, W. Seidel, F. Stary, E. Will, K. Heidel, S.M. Lukyanov, Yu.E. Penionzhkevich, V.S. Salametin, H. Sodan, and G.G. Chubarian: *Nucl. Instrum. Methods A*, **257**, 197 (1987).
- 4) I. Ogawa: Radioisotope (ed. F. Yamazaki), Kyouritsu Shuppan, Tokyo, p. 135 (1973) (in Japanese).

### III-5-14. Performances of a Two-Dimensional Position-Sensitive Silicon Detector with a Large Effective Area

K. Munakata, T. Kohno, T. Imai, A. Yoneda, T. Doke, J. Kikuchi,  
H. Murakami, T. Yanagimachi, N. Hasebe, and K. Nagata

For the observation of the elemental and isotopic compositions of cosmic-ray heavy particles by a  $\Delta E-E$  telescope, a two-dimensional position sensitive detector (PSD) with a large effective area plays an essential role in realizing a large acceptance angle of a telescope.<sup>1)</sup> Recently, new large PSDs (62 mm  $\times$  62 mm) have been developed in collaboration with Hamamatsu Photonics Company and exposed to cyclotron beams. In this report, we briefly summarize the characteristics of the new PSD.

The PSD is a silicon solid-state detector of an ion-implanted type of 400  $\mu\text{m}$  in thickness and junction capacitance of 500 pF. The position of an ion on PSD is reproduced by taking a linear combination of four signals from electrodes at the corners of an ion-implanted anode, where the surface resistivity and the line resistivities of the strips at the four sides are formed.<sup>2)</sup> The energy deposited in PSD is also reproduced by taking a sum of these four signals. To test the characteristics of the PSD, we used a N beam with 85 MeV. In front of PSD, we placed a 2 mm thick aluminium collimator with 0.5 mm  $\phi$  holes on 13  $\times$  13 lattice points at 5 mm intervals. A main beam was scattered with a 1  $\mu\text{m}$  Au foil target, and a detector system was set at a 30° scattering angle.

Pulse height signals from PSD are amplified and recorded on a micro-computer through a CAMAC system. Three different pulse shaping time constants of 3, 6, and 10  $\mu\text{s}$  were tested.

An example of position data is shown in Fig. 1(a), where each spot represents N ion passed through a hole on a collimator located in front of PSD. In Fig. 1(b), we plot the displacement vectors of each spot from the center of each hole on the collimator. The distortion of a two-dimensional pattern clearly increases near the edge of a 62 mm  $\times$  62 mm PSD. This distortion mainly arises from non-linearity of ADC around the pedestal. When a simple linear conversion from the ADC-channel to energy is assumed regardless this non-linearity, the small signals from the electrodes far from ion track are overestimated. Owing to this overestimation, reproduced positions are shifted to the inside of PSD. We confirmed that this distortion can be markedly suppressed by using non-linear conversion from the ADC channel to energy. It is also noteworthy that this distortion can be easily reformed by regulating the position of ions based on the displacement vectors in Fig. 1(b). In the following analysis, we eliminated the distortion in this manner.

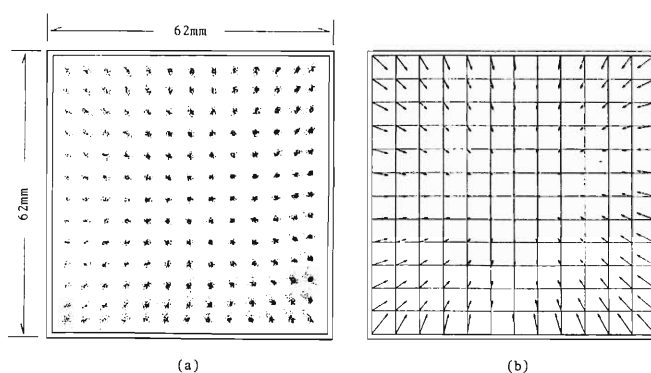


Fig. 1. Distortion in the two-dimensional pattern for 85 MeV N ions. The pulse shaping time is 6  $\mu\text{s}$ . In front of 62 mm  $\times$  62 mm PSD, a multi-slit collimator with 13  $\times$  13 holes of 0.5 mm  $\phi$  is located. a, Position data for 85 MeV N ions; b, Displacement vectors of each spot in (a) from the center of each hole on collimator. This pattern is essentially unchanged for other shaping times.

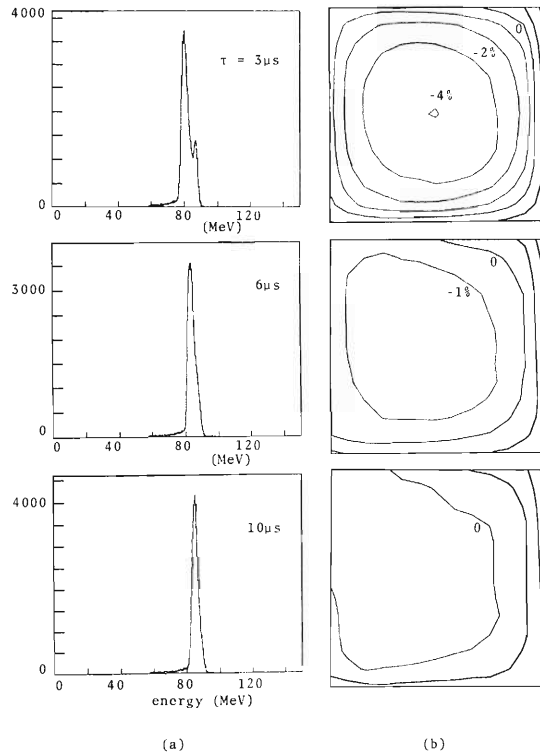


Fig. 2. Spectra and spatial distributions of energy loss on PSD. Three shaping times of 10, 6, and 3  $\mu\text{s}$  are tested. a, Energy spectra for three shaping times; b, The equal energy loss contours on PSD for three shaping times. These contours are derived from average energy losses of ions passing through each hole on the collimator. The numbers attached to contour lines represent the difference in energy loss from 85 MeV in percentage.

Figure 2(a) shows the energy spectra of N ions in PSD for three shaping time constants of 10, 6, and 3  $\mu\text{s}$ . It is obviously seen that the main peak of Fig. 2(a) shifts toward lower energies with decreasing shaping time constant. This is due to the fact that the time necessary to collect the whole charge deposited on PSD varies with the ion position on PSD. To show this more clearly, we plot in Fig. 2(b) the equal energy loss contours on PSD. The numbers attached to contour lines represent the deviation from 85 MeV in percentage. It is clear that the charge deposited on the

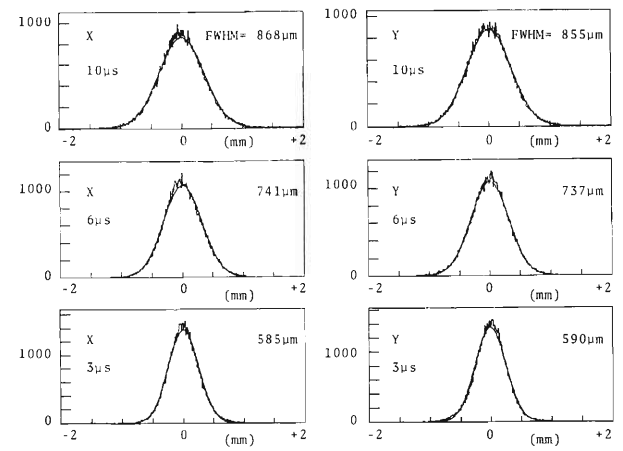


Fig. 3. The position resolutions in  $x$  and  $y$  coordinates for three shaping timer of 10, 6, and 3  $\mu\text{s}$ . Plotted are histograms of difference between reproduced coordinate of ion and that of the center of hole passed by the ion. The FWHMs of these histograms are calculated by fitting the Gaussian distribution and indicated.

position closer to the edge of PSD is more effectively collected for each shaping time and the average distribution of collected charge becomes more uniform with increasing shaping time.

The  $x$  and  $y$  position resolutions of PSD are shown in Fig. 3, where plotted are the histograms of difference between reproduced coordinate of each ion and that of the center of the hole on collimator passed by the ion; the FWHM of each histogram is indicated. The position resolution is clearly improved with decreasing shaping time and, at 3  $\mu\text{s}$ , the FWHM becomes comparable to the radius of the hole on the collimator (0.5 mm  $\phi$ ). This is due to the fact that the fluctuation arising from a low frequency noise such as a thermal noise is considerably suppressed for such shorter shaping time.

#### References

- 1) T. Kohno: *Space Sci. Rev.* (1989), in press.
- 2) T. Doke, J. Kikuchi, H. Yamaguchi, S. Yamaguchi, and K. Yamamura: *Nucl. Instrum. Methods A*, **261**, 605 (1987).

### III-5-15. Calibration of Si-Detector Telescopes for Heavy-Ion Measurements in Space

N. Hasebe, T. Doke, T. Kashiwagi, J. Kikuchi, T. Kubo,  
 W.P. Liu, H. Murakami, A. Nakamoto, K. Nishijima,  
 T. Suzuki, I. Tanihata, T. Yanagimachi, and M. Yanokura

Silicon detector telescopes with extremely large geometric factors will be boarded in the GEOTAIL satellite scheduled to be launched in 1992 to observe elemental and isotropic compositions of solar energetic particles with  $2 \leq Z \leq 30$  in a wide energy region from 3 MeV/n to 210 MeV/n. The telescopes consist of several layers of Si-detectors, of which top two layers are newly developed position-sensitive silicon detectors (PSSDs). The PSSDs provide two-dimensional position information so that an accurate measurement of a path length can be obtained in each layer. The PSSDs also measure the energy losses with the following Si-detectors. The use of the PSSDs as  $dE$ -detector enable us to realize the large geometric factor of the telescope.

To achieve an excellent mass resolution and a wide aperture in the telescope, a good position-resolution, a position-linearity, and uniformity of the detector thickness must be attained.

In previous experiments using nitrogen beams from the cyclotron, the characteristics of the PSSDs such as position linearity and position resolution were measured and excellent linearity and resolution as well as those expected from the theoretical estimation were obtained.<sup>1-5)</sup> Experiments made in FY 1988 were focused on the uniformity of detector thickness which is crucial to identify isotopes of ions.

In the present experiments, two kinds of PSSDs were tested by using Ar, Ca, and Zn beams from RIKEN Ring Cyclotron. One (hereafter referred to as PSSD1) is 30 mm × 30 mm in size and 100  $\mu\text{m}$  in thickness. The other (hereafter PSSD2) has four sensitive segments, that is, one silicon wafer is divided into four segments, because a thin detector has an extremely large capacitance. The size of each segment is 13 mm × 13 mm and its thickness is 50  $\mu\text{m}$ .

In addition to these  $dE$ - and  $E$ -signals, the TOF and  $B \times r$  formation were obtained from other experimental setup (PPAC) used at the

same time. From these information, the charge state,  $Q$ , and the mass,  $A$ , of the ions were simultaneously determined and accurate isotope separation was achieved consequently.

#### Experiment-1:

The telescope consists of PSSD1 as a  $dE$ -detector, a thick  $E$ -detector, and an anti-coincidence detector. The beam energy of Ar and Ca used in the experiment was 26 MeV/n. The charge distribution of reaction fragments obtained by Ca beam is shown in Fig. 1. The charge resolution is estimated to be about 0.15 charge unit in rms. From the energy loss measurement, the non-uniformity of the thickness (thickness variation) was estimated to be  $\pm 2.5 \mu\text{m}$  when expressed in peak to peak value. In the restricted region smaller than 10% of the whole area, the thickness variation is less than 1.3  $\mu\text{m}$ , which agrees with the result obtained by the Cu-beam experiment performed in FY1987.

#### Experiment-2:

The telescope consists of PSSD2 as  $dE$ -detector, a 400  $\mu\text{m}$  thick PSSD as  $E$ -detector, and an anti-coincidence detector. The beam energy of Zn used in the experiment was also 26 MeV/n.

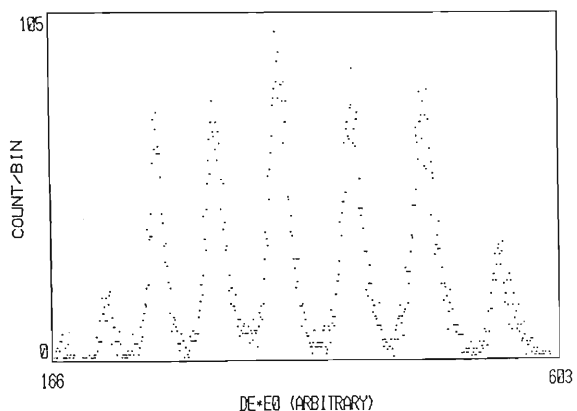


Fig. 1. Nuclear charge histogram obtained by Experiment-1. A Ca-beam is bombarded to a Be-target and various fragments produced are shown. The charge resolution is about 0.15 charge unit in rms.

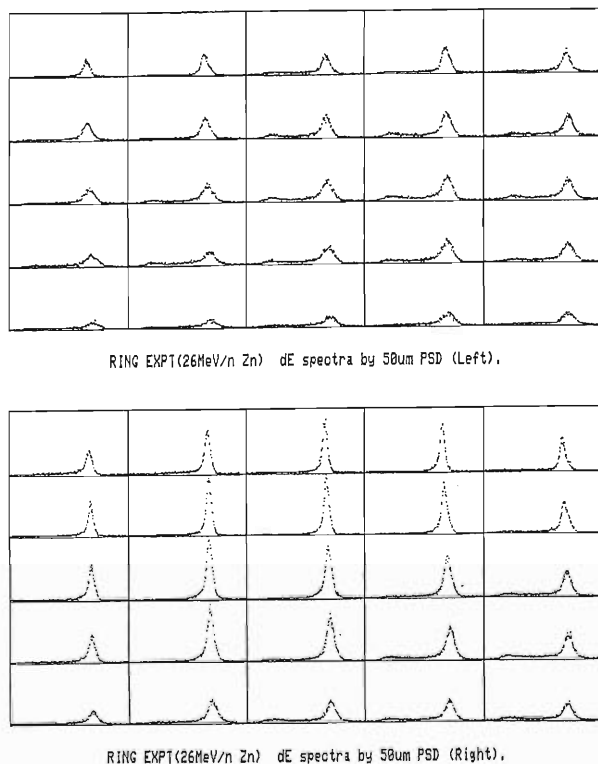


Fig. 2. Energy loss distribution of Zn-ions of 26 MeV/n in PSSD with the thickness of 50  $\mu\text{m}$ . The PSSD has four position-sensitive segments. These show the thickness variation of each segment of the detector.

Table 1. Variation in the detector thickness of PSSD expressed in peak to peak.

Beam	Energy (MeV/n)	PSSD		
		Thickness ( $\mu\text{m}$ )	Variation ( $\mu\text{m}$ )	
Zn	26	Sg-1 50	1.8	
		Sg-2 50	1.7	
Ca/Ar	26	100	2.5	
		100	1.3	
N	5/6	Sg-1 25.2	1.1	
		Sg-2 25.3	0.8	
		Sg-3 24.4	0.7	
N	5	Sg-1 50.1	0.9	
		Sg-2 50.4	0.8	
		Sg-3 49.4	1.0	

PSSDs with 25 and 50  $\mu\text{m}$  in thickness have four segments in each wafer.

Two among four sensitive segments of PSSD2 were tested. Energy loss distributions of Zn ions for PSSD2 are shown in Fig. 2. The variation of peak position of the distributions corresponds to the thickness variation of the detector. The non-uniformity of the thickness was  $\pm 1.8 \mu\text{m}$  in peak to peak value and the difference in average thickness between two segments was less than 0.2%. This result is not in consistent with that obtained with a nitrogen beam of 70 MeV in FY1988.

The results of both experiments summarized in Table 1 indicate that there exists the non-uniformity of the detector thickness of 1-2  $\mu\text{m}$  for the second models of the PSSDs. The value (peak to peak) must be reduced to be less than 1  $\mu\text{m}$  as the goal. The non-uniformity in detector thickness obtained in the present experiment seems to be caused by the non-uniformity in the lapping and/or etching processes in fabrication of Si-detectors.

In the first model of the PSSD, there was a large position deformation of the imaging pattern as reported in 1986.<sup>1)</sup> In the second model of the PSSD, the position linearity has been greatly improved by a new approach in which the four corners of the resistive electrodes are connected with low resistive strip lines. In the second model, uniform thickness to identify their iron-group isotopes has not yet sufficiently been attained though the excellent position performance has been achieved.<sup>5)</sup> In the next stage of the PSSD-development, we are planning to make PSSDs paying a special attention to the lapping and etching processes in the detector fabrication.

#### References

- 1) T. Doke, et al.: *RIKEN Accel. Prog. Rep.*, **20**, 122 (1986).
- 2) T. Kohno, et al.: *RIKEN Accel. Prog. Rep.*, **21**, 152 (1987).
- 3) T. Doke, J. Kikuchi, H. Yamaguchi, S. Yamaguchi, and K. Yamamura: *Nucl. Instrum. Methods A*, **261**, 605 (1987).
- 4) N. Hasebe, Y. Ezawa, H. Yoshii, and T. Yanagimachi: *Jpn. J. Appl. Phys.*, **27**, 816 (1988).
- 5) T. Yanagimachi, et al.: *Nucl. Instrum. Methods* (1989), in press.

### III-5-16. Measurements of Some Characteristics of Thin Position-Sensitive Silicon Detectors

K. Nagata, T. Doke, J. Kikuchi, K. Nishijima, T. Kashiwagi,  
 T. Kohno, T. Imai, K. Munakata, A. Nakamoto,  
 H. Murakami, T. Yanagimachi, and N. Hasebe

To observe elemental and isotopic compositions of solar flare particles, silicon detector telescopes with extremely large geometric factors are planned to be used in the GEOTAIL mission scheduled to be launched in 1992. To realize such telescopes, the development of position-sensitive silicon detectors (PSSDs) with a good position linearity and resolution were required. Recently we succeeded in developing of new PSSDs which meet such requirements. However, the PSSDs were planned to be used as  $\Delta E$ -detectors, too. To achieve an excellent mass resolution, the non-uniformity of the detector thickness must be kept less than  $\pm 1\%$  for thin PSSDs to be used as MI-sensors. In this experiment, we investigated the non-uniformity in

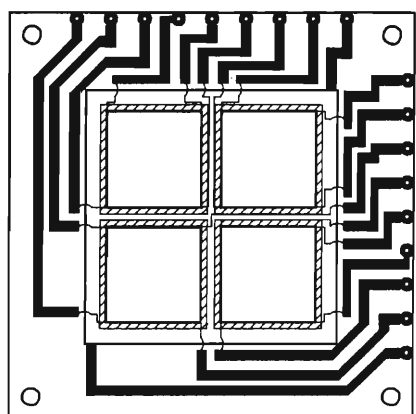
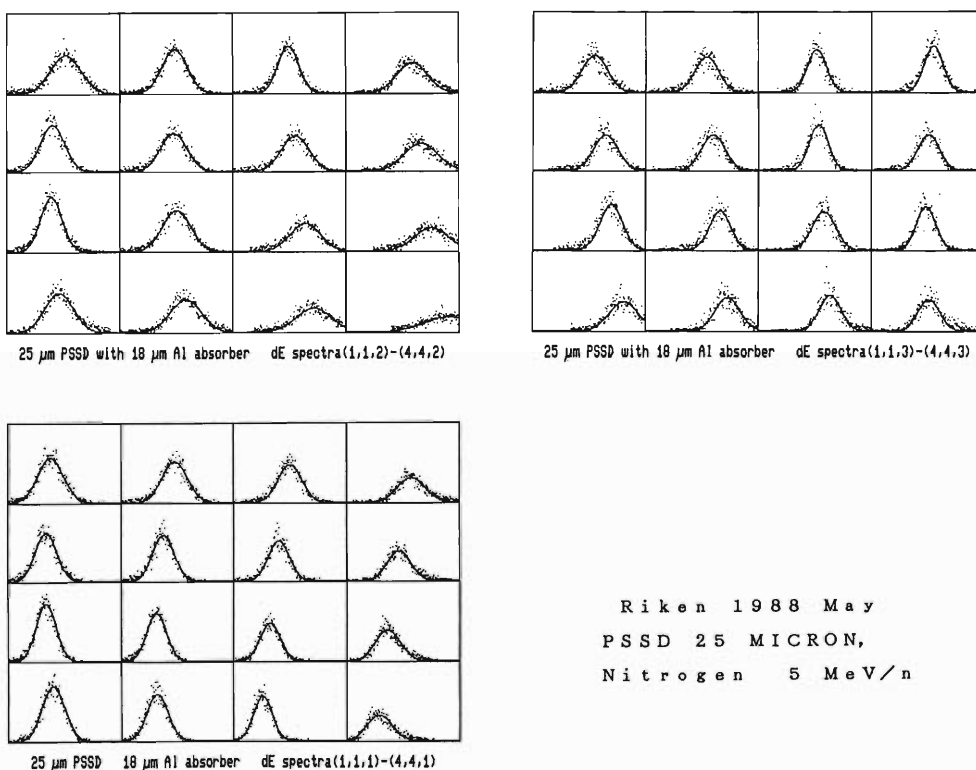


Fig. 1. Schematic view of a position-sensitive silicon detector (PSSD).



R i k e n   1 9 8 8   M a y  
 P S S D   2 5   M I C R O N ,  
 N i t r o g e n   5   M e V / n

Fig. 2. Pulse height distributions of energy losses measured by an 84 MeV nitrogen beam for a 25  $\mu\text{m}$  thick PSSD.

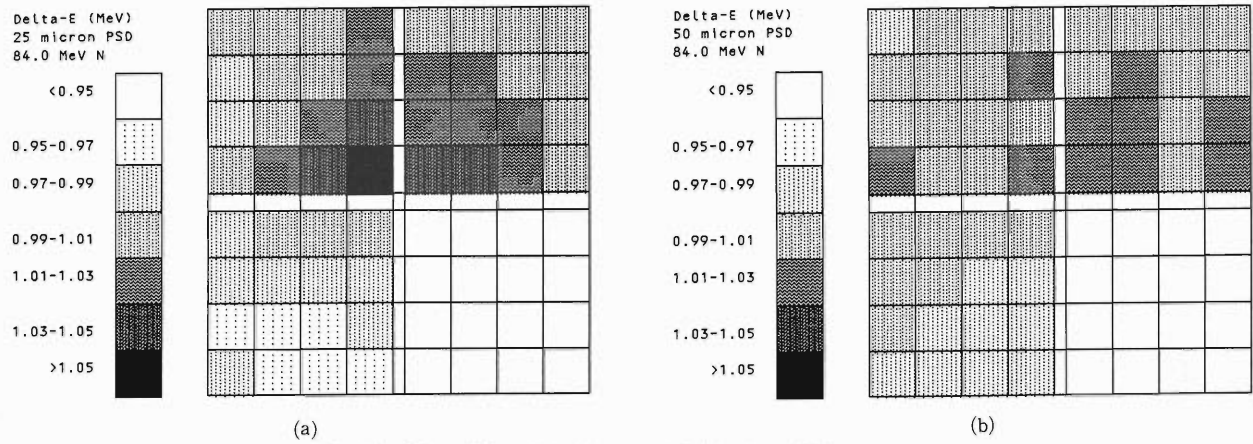


Fig. 3. Two-dimensional maps of detector thicknesses.  
(a), a  $25 \mu\text{m}$  thick PSSD; (b), a  $50 \mu\text{m}$  thick PSSD.

detector thickness for two kinds of PSSDs with different thicknesses by measuring the energy losses of 70 MeV and 84 MeV nitrogen beams. The PSSDs tested are rectangular type detectors and each detector is divided into four segments as shown in Fig. 1, because a thin detector has an extremely large capacitance. The size of the segments and their thickness for tested PSSDs are shown in the following.

Thickness ( $\mu\text{m}$ )	Size ( $\text{mm} \times \text{mm}$ )
25	$13 \times 13$
50	$22 \times 22$

The segment has four point-electrodes at each corner. The position signals are obtained from the arithmetic calculations of four pulse heights from the point electrodes.<sup>1,2)</sup> On the other hand, the energy loss signals are obtained from the back side electrode, that is, the opposit side to the position sensitive surface. The residual energy after passing through PSSD is measured with a 0.3 or 0.4 mm thick position sensitive detector. A typical distribution of the energy losses in three segments of a  $25 \mu\text{m}$  thick PSSD is shown in Fig. 2. The energy loss spectra in the fourth segment were not measured because of a lack of signal cables from the scattering chamber. Each segment is divided into 16 areas, and by using position information for incident parti-

cles from PSSD, we obtained an energy loss spectrum for each area. Figure 2 shows the result. However, these are not raw data, but the spectrum in each area shows only their neighbourhood of the peak. The difference in the peak position gives the average detector thickness in the area. Thus, we can draw the 2-dimensional map of detector thicknesses.

Figure 3 (a) shows thus obtained two dimensional map of the detector thickness in a  $25 \mu\text{m}$  thick PSSD, and Fig. 3 (b) shows that in a  $50 \mu\text{m}$  thick PSSD. In these maps, we assume that the average thickness in all three segments (48 areas) is unity. These results show that the thickness in the  $25 \mu\text{m}$  thick PSSD ranges from 0.95 to 1.05 and that in the  $50 \mu\text{m}$  thick PSSD from 0.97 to 1.03. On the other hand, our final goal on the thickness uniformity is 0.99-1.01. Thus, the above results are still worse than expected.

#### References

- 1) T. Doke, J. Kikuchi, H. Yamaguchi, S. Yamaguchi, and K. Yamamura: *Nucl. Instrum. Methods A*, **261**, 605 (1987).
- 2) T. Yanagimachi, T. Doke, N. Hasebe, T. Imai, T. Kashiwagi, J. Kikuchi, T. Kohno, W.P. Liu, K. Munakata, T. Motobayashi, H. Murakami, K. Nagata, A. Nakamoto, and H. Yamaguchi: *Nucl. Instrum. Methods A*, **275**, 307 (1989).

### III-5-17. Test of a Si Two-Dimensional Position-Sensitive Detector for Unbound Particle Measurements

M. Ogiwara, K. Ieki, Y. Ando, N. Iwasa, and H. Murakami

In detection of unbound particles emitted in medium-energy heavy-ion reactions, accurate measurement of the relative momenta between decaying particles is important. The energy and position of the particles should be determined precisely and the charge and mass of the particles should be identified correctly. A large area detector array of  $\Delta E$ - $E$  counter telescopes of Si solid-state detectors (SSD's) is most useful<sup>1)</sup> because of their good detection efficiency. Two dimensional position sensitive detectors (PSD's) can be used as  $\Delta E$  counters. Recently, a very good position resolution and a position linearity are reported<sup>2)</sup> for such large area PSD's with line resistance at four sides. For correlation experiments, however, PSD's with line resistance are not suitable because a good time resolution of the detector is also required to avoid accidental coincidence. We, therefore, tested another type of PSD, made by Hamamatsu Photonics, with electrodes at four corners. The PSD is of an ion-implanted type with a sensitive area of 45 mm × 45 mm and 300  $\mu\text{m}$  in thickness. The PSD and an E counter with the same area and 2,000  $\mu\text{m}$  in thickness constitute a counter telescope.

The test was performed with a 45 MeV  $^4\text{He}$  beam and a 84 MeV  $^{14}\text{N}$  beam from the cyclotron. Elastically scattered particles with a 4  $\mu\text{m}$  Au foil target were collimated by a 1 mm brass plate with 5 × 5 holes of 0.7 mm<sup>2</sup> and detected with the counter telescope located at 25° from the beam axis and 30 cm from the target. Adjacent holes in the vertical and horizontal directions have a 10 mm distance.

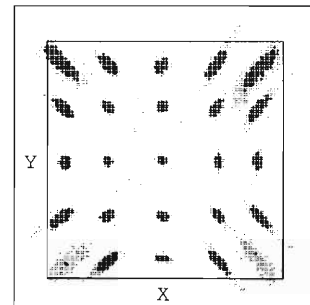
Since the charge collection of the electrodes is known to be rather slow and position dependent<sup>2)</sup> in large detectors, we studied the ballistic deficit by changing the shaping time constant  $\tau$  of a shaping amplifier to be 0.5, 1, 2, 3, and 6  $\mu\text{s}$ . For cases of insufficient charge collection, peak splitting was observed in the energy spectra obtained by summing the outputs of the four electrodes. We found that ballistic deficit is negligible for the data with  $\tau=3 \mu\text{s}$ , which is far shorter than the case of PSD's with line resistance.

The incident position of the particles can be

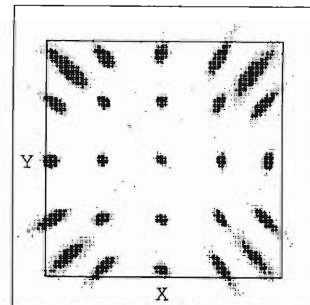
calculated from the charge signals from the four electrodes. Using a simple formula like (1) or (2) of Ref. 2, we observed a large distortion of the position. We propose, therefore, following formulas. The origin of the coordinate (0,0) is set at the center of the detector. Four charge signals  $Q_i$  ( $i=1, 2, 3, 4$ ) are from the electrodes located at (1, 1), (-1, 1), (-1, -1), and (1, -1), respectively. The position ( $X, Y$ ) can be expressed by

$$\begin{aligned} X &= \frac{2A}{1 + \sqrt{1 - 2(A^2 + B^2)}} \\ Y &= \frac{2B}{1 + \sqrt{1 - 2(A^2 + B^2)}} \\ A &= (-S_1 + S_2 + S_3 - S_4)/C \\ B &= (-S_1 - S_2 + S_3 + S_4)/C \\ C &= S_1 + S_2 + S_3 + S_4 \\ S_i &= \exp\left(\frac{p}{Q_i}/\sum_{j=1}^4 \frac{1}{Q_j}\right) \end{aligned} \quad (a)$$

or



(a)



(b)

Fig. 1. Position calculated from (a) or (b) for  $^{14}\text{N}$  particle. Inner squares denote the boundary of the sensitive area. In (a), the parameter  $p$  is set to be 13.78; in (b), the parameter  $n$  is 0.545. The shaping time constant is 3  $\mu\text{s}$ .

$$S_i = Q_i^{-\frac{2}{n}} \quad (b)$$

where  $p$  and  $n$  are parameters.

In derivation of these formulas, we assumed that the charge  $Q$  collected on each electrode depends on the distance,  $d$ , between the incident position and the electrode. When the reflection of a charge wave at the side of the detector is taken into account, the dependence of  $Q$  on  $d$  is well simulated by (a)  $Q \approx p'/\log(d/a)$ , or (b)  $Q \approx d^{-n}$ . In Fig. 1, examples of the position data are shown for the cases (a) and (b). In both cases, position images are fairly well reproduced except for those near the corners. Note that the position linearity is still good at the side of the

sensitive area, which is an important region for the correlation experiments. The position resolution is as small as the collimator hole size at the center position, but becomes large for the position near the corner. It also depends on  $\tau$  and becomes better for smaller shaping time constants.

#### References

- 1) T. Motobayashi, S. Satoh, H. Murakami, H. Sakai, and M. Ishihara: *RIKEN Accel. Prog. Rep.*, **20**, 125 (1986).
- 2) T. Kohno, et al.: *RIKEN Accel. Prog. Rep.*, **21**, 152 (1987).

### III-5-18. Resonance Ionization Spectroscopy of a Fe Atomic Beam Generated by a Spark Discharge Method

M. Otsuki,\* T. Minowa, H. Katsuragawa, and T. Inamura

For resonance ionization spectroscopy (RIS), a powerful tool is urgently required for generation of neutral atoms. We have reported RIS of atoms generated by a laser ablation method.<sup>1)</sup> Although the laser ablation method is one of the most powerful tools for generation of neutral atoms, this method has some demerit: A difficulty in fine control of the generation rate of atoms and fine-dust creation which reduces sensitivity.

For metals a spark discharge method is better substitution for the laser ablation method because of its simplicity and low cost. Prior to applying the spark discharge method to an atomic beam source, we have carried out RIS of Al and Fe atoms generated by the spark discharge method in order to investigate generation rate.<sup>2)</sup> In the present study, we have found much less fine-dust creation, which improved the detection sensitivity of the apparatus. As a next step, we have applied the method to a Fe atomic beam source.

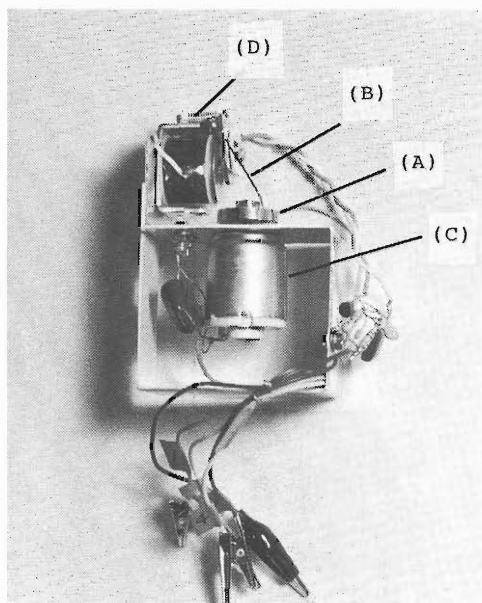


Fig. 1. A device for generation of an Fe atomic beam by a spark discharge method. (A), (B), (C), and (D) denote a steel rotor, a steel wire, a dc motor, and a magnetic coil, respectively.

\* Department of Physics, Faculty of Science, Toho University.

Figure 1 shows a photograph of the device for production of a Fe atomic beam. Spark discharge was produced by contact of a steel rotor (A) and a steel wire (B). The rotor was driven by a dc motor (C). The wire was forced to touch the rotor by using a magnetic coil (D) switching of which was controlled by a computer. The repetition rate of contact was set at 4 Hz. The rotor and the wire were connected to the positive and the negative poles of a charged capacitor (1,500  $\mu$ F, 15 V). We employed a rotation mechanism because a rotating metal hardly welded with another piece of metal in contact.

Spark discharge was efficiently produced in a high vacuum ( $10^{-6}$  Torr) chamber. It is well known that discharge hardly occurs at such low pressures. The reason why spark discharge occurred so efficiently is as follows: In the first

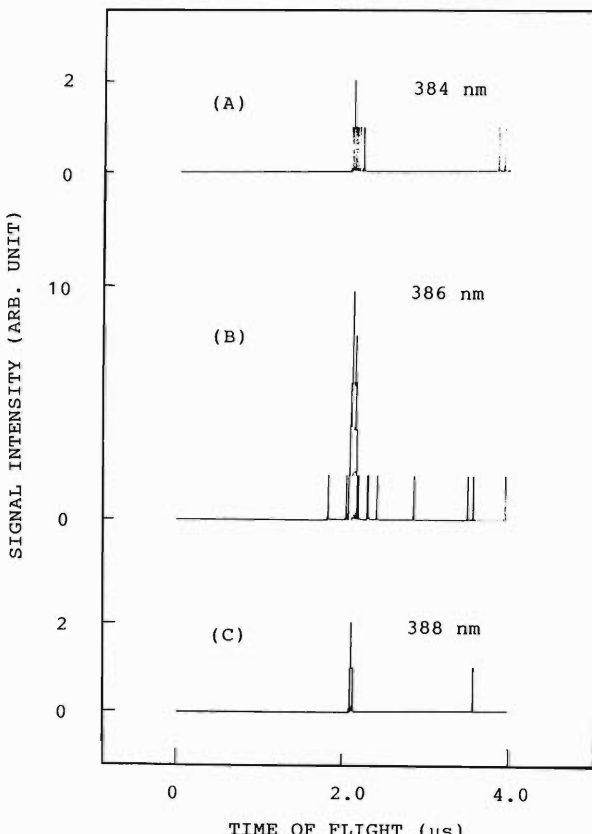


Fig. 2. Observed time-of-flight spectra for Fe.

contact of the two metals they melt and vaporize due to joule heating caused by a high peak current through the contact point. The vapor becomes a seed for a spark discharge. The ions and electrons produced by the spark discharge increase the temperature of the metal surface to generate further vapor. The ions and electrons emit light by recombination, which is clearly seen.

Except for the device for spark discharge, the experimental setup was the same as that described in Ref. 1. The neutral atoms existed only during a few milliseconds after the discharges, so that we optimized the delay time for triggering of a pulsed laser and kept it under a computer control. The ions and electrons generated by the resonance ionization were detected by two CER-ATRON detectors, and recorded as a time-of-flight (TOF) spectrum. In Fig. 2 an example of a TOF spectrum of Fe ions is shown: (B) the pulsed dye laser was tuned to the  $a^5D_4-z^5D_4$  transition of Fe (386.0 nm); (A) and (C) the laser was detuned by 2 nm.

The observed TOF (about 2  $\mu$ s) was close to a calculated value and the intensity of the peak became most intense under the resonance condition. Therefore we were convinced that the peak in Fig. 2 was due to Fe ions caused by resonance ionization.

The total count of Fe ions in the TOF spectrum was about 30. The time to observe the spectrum was 220 s. The repetition rate of the pulsed dye laser was 4 Hz. Therefore the counting rate for Fe ions was  $3 \times 10^{-2}$  per laser shot.

The volume of the ionization region was estimated at  $10^{-4} \text{ cm}^{-3}$ . If all Fe atoms in the ionization region were ionized and detected, the density of the Fe atomic beam in the region was  $3 \times 10^2 \text{ cm}^{-3}$ . The solid angle of the ionization area looked from the spark discharge was about  $10^{-7} \text{ sr}$ . Thus a generation rate of  $3 \times 10^9$  per discharge was obtained; in this case the shorter duration time of the laser pulse (10 ns) than that of the discharge (longer than microsecond) was not taken into account. We concluded, therefore, that more than  $3 \times 10^9$  atoms were generated at every discharge. Emission of Fe atoms by heating due to spark discharge lasted during about few milliseconds. Hence the generation rate of  $10^{12}/\text{s}$  was obtained. By thermal heating, the generation rate of Fe atoms can be obtained at a temperature slightly about the melting point of Fe (1,800 K). The apparatus for spark discharge is much simpler than that for heating thermally to such a high temperature and is able to vaporize even tungsten (melting point 3,300 K).

In the present study we have demonstrated the usefulness of the spark discharge method as a neutral atomic beam source. For RIS of metal samples this method will be most advantageous for its simplicity and low cost.

#### References

- 1) T. Minowa, H. Katsuragawa, and M. Shimazu: *RIKEN Accel. Prog. Rep.*, **21**, 178 (1987).
- 2) T. Hoshino, M. Otsuki, T. Minowa, H. Katsuragawa, and T. Inamura: This Report, p. 178.

### III-5-19. Resonance Ionization Spectroscopy of Neutral Atoms Generated by a Spark Discharge Method

T. Hoshino,\* M. Otsuki,\*\* T. Minowa, H. Katsuragawa, and T. Inamura

We reported resonance ionization spectroscopy (RIS) of neutral atoms generated by a laser ablation method.<sup>1)</sup> The laser ablation method is one of the most powerful tool for generation of neutral atoms because it is capable of vaporizing all the matter. This method is based on highly nonlinear phenomena caused by an intense electro-magnetic field, so that the fine control of the phenomena is difficult. This may lead to a low signal-to-noise ratio because the generation of neutral atoms by the method shows higher order dependence upon the field intensity. Another disadvantage of the method is that a lot of fine dust is produced because the laser ablation is essentially a micro-size explosion. The dust scatters light, which causes the emission of photoelectrons and reduce signal-to-noise ratios, and pollutes a detector to reduce its sensitivity.

For metals a spark discharge method is a better substitution for the laser ablation method because of its simplicity and low cost. We successfully carried out RIS of Fe and Al atoms generated by the spark discharge method and checked the generation of much less fine dust than in the laser ablation method, thus having improved sensitivity.

The schematic diagram of the experimental setup is shown in Fig. 1. Spark discharges were

performed by contact of a pair of metals connected to the plus and the negative poles of a charged capacitor (capacitance 4,500  $\mu\text{F}$  and applied voltage 10 V), respectively. The contact was mechanically done between a star-shaped plate rotated by a motor and a strip of the same metal (5 cm long and 1 cm wide); the repetition rate was about 2 Hz.

Resonance ionization of neutral atoms were allowed to take place in a proportional counter by focusing radiation from a resonant pulsed dye laser. Ionization signals were detected by a stainless-steel wire biased at 1 kV and by using the multiplying action of argon.

The discharge chamber was spatially separated from the proportional counter by connecting with a Teflon tube, into which argon was supplied to transport neutral atoms generated in the discharge chamber to the proportional chamber. The flux of argon gas was about 10  $\text{cm}^3/\text{s}$ . Because argon gas contained a small amount of oxygen, the number of neutral atoms decreased due to oxidation. The density of the neutral atoms at the ionization region could, therefore, be controlled by the flux of argon gas.

Except for the discharge method, the experimental setup was similar to that described in Ref.

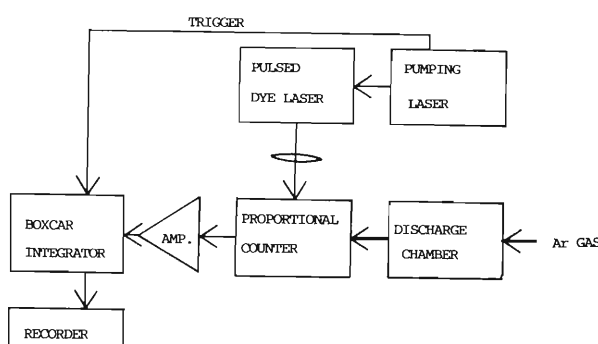


Fig. 1. Block diagram of the experimental setup.

\* Department of Applied Physics, School of Science and Engineering, Waseda University.

\*\* Department of Physics, Faculty of Science, Toho University.

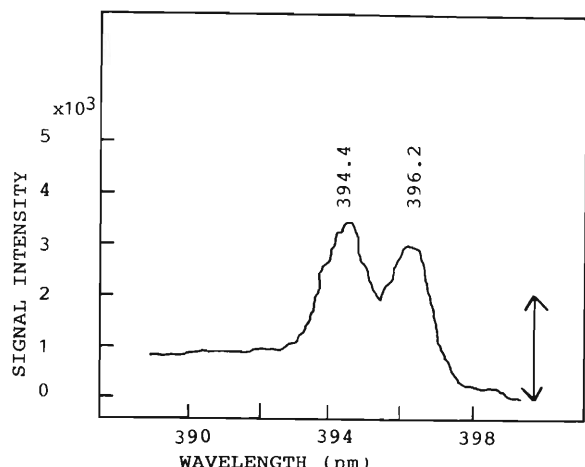


Fig. 2. A resonance ionization spectrum observed for Al. The signal intensity is shown in electron number generated by resonance ionization.

1. Ionization signals were amplified, averaged by a boxcar integrator, and recorded against the wavelength of the radiation from the pulsed dye laser.

Spectra observed were shown in Fig. 2. The peak I and II are due to resonance of the radiation from the pulsed dye laser with the  $4S_{1/2}^-3P_{3/2}$  and the  $4S_{1/2}^-3P_{1/2}$  transition, respectively. We measured the multiplying gain of the proportional counter by detecting  $\alpha$  rays ( $^{241}\text{Am}$ ) and  $\gamma$  rays ( $^{55}\text{Fe}$ ). According to the measurement the signal intensity corresponding to  $2 \times 10^3$  elec-

trons that exist before electron-multiplication is indicated by an arrow. We succeeded in observing the spectra of Al whose peak intensity corresponds to  $2 \times 10^2$  electrons. This sensitivity is much better than that achieved by the laser ablation method. The discharge method can be applied to all metals with high conductivities.

#### Reference

- 1) M. Otsuki, T. Minowa, H. Katsuragawa, M. Shimazu, and T. Inamura: *RIKEN Accel. Prog. Rep.*, **21**, 176 (1987).

### III-5-20. Resonance Ionization Spectroscopy with a Sputtering Atomic Beam Source

M. Koizumi, T. Inamura, Y. Matsumoto, T. Murayama,  
M. Takami, H. Katsuragawa, and I. Sugai

Resonance ionization spectroscopy (RIS) makes it possible to detect a single atom with high selectivity of elements.<sup>1)</sup> Here we describe the performance of a detector system for the RIS chamber equipped with an ion gun to produce neutral atoms.<sup>2)</sup> Although the sputtering of atoms with an ion gun is powerful especially for refractory elements, it is absolutely necessary to remove stray ions and electrons produced by sputtering ions in measurements of resonance ionization.

In order to remove these background ions and electrons, wire meshes were placed between two pin holes as shown in Fig. 1. Pairs of ion and electron produced by the resonance ionization of neutral atoms are detected with a pair of ceratrons. An electric field between the two ceratrons drives ions and electrons oppositely to the detectors. The electrons give prompt signals and the time difference between collected ions and electrons depends on the mass of ions, the electric field, and the distance between the detectors.<sup>3)</sup>

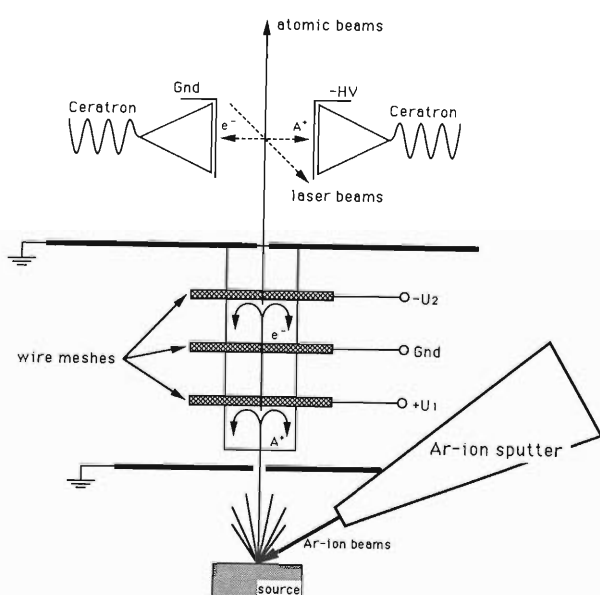
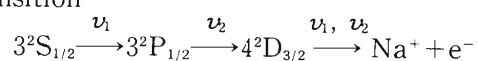


Fig. 1. Schematic diagram of resonance ionization spectroscopy with a sputtering atomic beam source.

First, we carried out a test experiment on sodium atoms with a thermal atomic beam source, which were resonantly ionized *via* the transition



where  $\nu_1$  and  $\nu_2$  correspond to wavelengths  $\lambda_1 = 589.5930 \text{ nm}$  and  $\lambda_2 = 568.267 \text{ nm}$ , respectively.<sup>4)</sup> A first photon tuned to  $\lambda_1$  (laser 1) was obtained from a cw-dye laser pumped by an Ar-ion laser, and a second photon tuned to  $\lambda_2$  (laser 2) from a pulsed dye-laser pumped by a copper-vapor laser. The two photon beams crossed the atomic beams at right angles. Laser 1 with a power of about 1.4 mW was focused on a 2-mm diameter spot in sodium beams; and laser 2 with a 6-kHz repetition rate and a 20-ns pulse width on about 1 mm in diameter in the interaction region at a power of about 35 mW. The distance and potential difference between two ceratrons was 40 mm and 4.5 kV, respectively.

A time spectrum observed with a time-to-amplitude converter is shown in Fig. 2. There are two peaks: The left-hand-side peak is a prompt peak due to the background signals; the right-hand-side one is a delayed peak produced by resonantly ionized sodium atoms ( $^{23}\text{Na}^+$ ). The distance between the left- and right-hand-side peaks is about 346 ns, which is nearly equal to the value estimated by taking into account a cone shape of the ceratron like a trumpet's head with a depth of about 10 mm. The time resolution

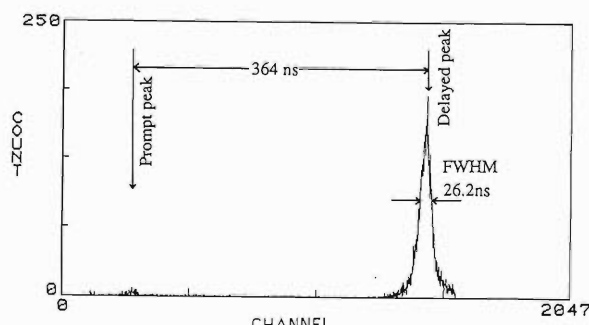


Fig. 2. Time-of-flight spectrum of resonantly ionized Na atoms.

(FWHM) observed was 26.2 ns.

Measurement with the Ar-ion gun is in progress on Na atoms for reference, and we proceed to investigate refractory elements such as Mo, Hf, Os, Ta, and W by the method of Ar-ion beam sputtering.

Academic Press, Orlando (1987).

- 2) T. Murayama, M. Takami, Y. Matsumoto, and T. Inamura: *RIKEN Accel. Prog. Rep.*, **21**, 174 (1987).
- 3) T. Minowa, H. Katsuragawa, K. Nishiyama, T. Inamura, and M. Shimazu: *J. Appl. Phys.*, **61**, 436 (1987).
- 4) S. Mayo, T.B. Lucatorto, and G.G. Luther: *Anal. Chem.*, **54**, 553 (1982).

#### References

- 1) V.S. Letokhov: *Laser Photoionization Spectroscopy*,

### III-5-21. A Radiation-Detected Optical Pumping System for the Achievement of Nuclear Orientation in Solids

S. Matsuki, K. Shimomura, M. Koizumi, T. Murayama, and T. Inamura

Oriented samples of nuclei are of considerable utility in solid-state, nuclear, and particle physics. Especially in nuclear physics, the achievement of significant nuclear orientation is crucial for the precise measurement of nuclear magnetic and quadrupole moments of unstable nuclei. Among various methods in use for orienting nuclei, optical pumping is a relatively simple and still quite efficient method for getting significant nuclear orientation. The development of a technique for orienting nuclei in solids by optical pumping is highly desirable, since the method does not require either sub-Kelvin temperature or high magnetic field as opposed to the case of thermal equilibration methods.

We have developed a new technique for orienting unstable nuclei with the optical pumping in solids and for detecting the degree of orientation by a sensitive measurement of the  $\beta$ -decay asymmetry and/or the  $\gamma$ -rays anisotropy from oriented nuclei ( $\beta(\gamma)$ -RADOPS;  $\beta$ -rays ( $\gamma$ -rays) Radiation-Detected Optical Pumping in Solids). With this technique, we achieved nuclear polarization of up to about 4% in  $\text{SrF}_2$  crystal.<sup>11</sup>

In order to apply the method further to the study of nuclei far from the stability line, we now are developing an experimental system for the  $\beta(\gamma)$ -RADOPS system at RIKEN. The apparatus

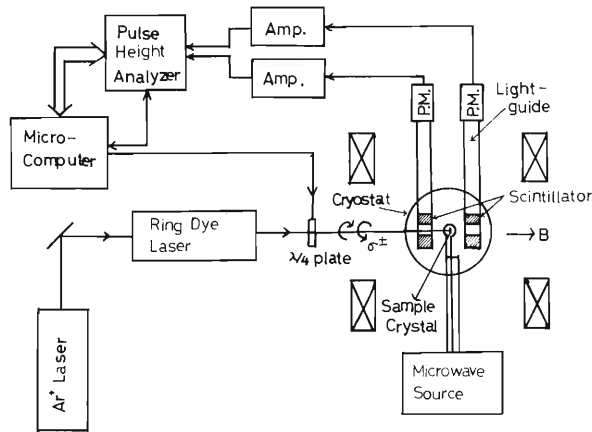


Fig. 1. Schematic diagram of the present experimental  $\beta(\gamma)$ -RADOPS system for the achievement of nuclear orientations.

system is schematically shown in Fig. 1. The unstable nuclei produced in heavy-ion reactions are mass-separated with the isotope separator GARIS-IGISOL system, or the recoil-ion separator RIPS system in RIKEN Ring Cyclotron facility, and are then implanted into a sample crystal, such as  $\text{CaF}_2$  and  $\text{GaAlAs}$  which is cooled down to 77 K to 1.7 K in a cryostat. The implanted atoms are then optically pumped with a circularly polarized laser beam at an appropriate wavelength, thus achieving nuclear as well as electron orientations. The degree of nuclear orientations is measured by detecting the asymmetry of emitted  $\beta$  rays and/or the anisotropy of emitted  $\gamma$  rays in the angular distributions following the decay of the unstable nucleus.

The experimental setup of the detecting system is schematically shown in Fig. 2. The  $\beta$  rays are detected with a counter telescope of plastic

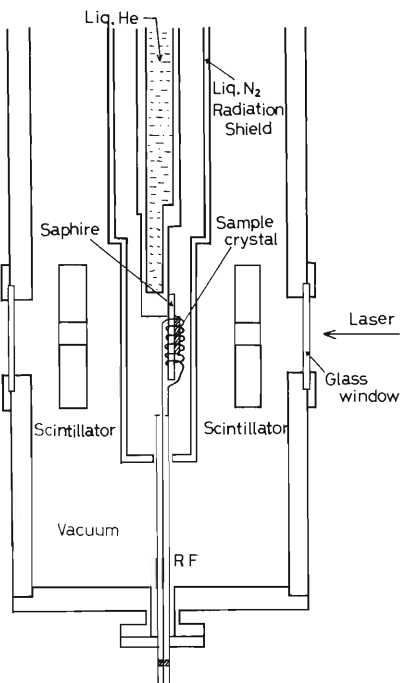


Fig. 2. Schematic detail of the detecting system of the present  $\beta(\gamma)$ -RADOPS experiments. An RF system is applied to measure radiation-detected magnetic resonance for the precise measurement of magnetic moments.

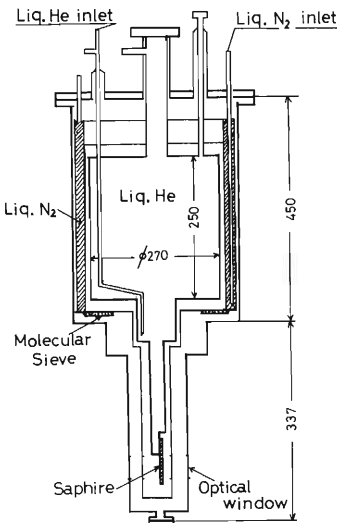


Fig. 3. Schematic structure of the liquid He cryostat system in the present  $\beta(\gamma)$ -RADOPS experiments.

scintillators and/or a solid-state counter system in the sample chamber set parallel to the laser beam. The  $\gamma$  rays are detected outside the cham-

ber with Ge(Li) detectors. An electromagnet with a variable pole gap, into which a liquid He cryostat system is inserted, produces a magnetic field of up to 3.0 kG at a gap width of 15 cm. The magnetic field is uniform to less than 1 G at 3 kG within the area of 1 cm<sup>3</sup> at the center of the pole gap.

The liquid-He cryostat system is shown in Fig. 3. About 15 l of liquid He can be contained in the cryostat, thus enabling to maintain sample crystal at low temperature for more than 20 hours even under laser irradiation for optical pumping.

This system can be utilized for both off-line and on-line experiments. A few unstable nuclei with lifetimes longer than 1 day will be firstly investigated off-line, then the on-line research of light nuclei with shorter lifetime will be followed.

#### Reference

- 1) K. Shimomura, S. Matsuki, S. Uemura, T. Kohmoto, Y. Fukuda, and T. Hashi: Proc. Int. Conf. Quantum Electronics, Tokyo, Jul., p. 298 (1988).

### III-5-22. An Attempt for a Local Loop Network Using an MC6854 ADLC

J. Fujita

RIKEN Ring Cyclotron is a computer controlled accelerator.<sup>1)</sup> A CIM-DIM microcomputer network<sup>2)</sup> interfaces between the computer system and electric instruments and machines along the accelerator. A CIM module is connected to max. 12 DIMs in a star configuration. This type of network has a disadvantage of complication and overlapping of network wirings. A loop configuration gets rid of the annoyance and expands the number of nodes.

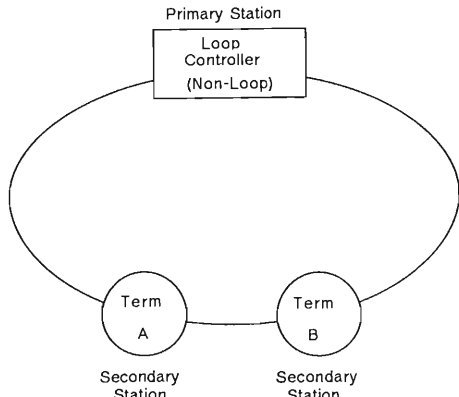


Fig. 1. Loop configuration.

The loop configuration we studied is composed of three stations, a primary station and two secondary stations as shown in Fig. 1. Three stations have the same circuit arrangement shown in Fig. 2 except for a switching circuit of a synchronous clock in the primary and repeater logics in each secondary. Three chips form the core of the loop network function. A microprocessor MC68B00 is chosen because of its availability of hardware and software, and pin-compatibility with other two chips. An Advanced Data Link Controller (ADLC), MC68B54, provides data link capability. Incorporation of a Direct Memory Access Controller (DMAC), MC68B44, with ADLC allows to transfer large data with high speed on the loop. The loop is always under control of the primary. The ADLC in the primary operates in a non-loop full-duplex mode. The ADLCs in the secondaries operate in a loop mode, monitoring up-loop data on their receiver data input. The ADLC transmits and receives bit-oriented data in a format called a

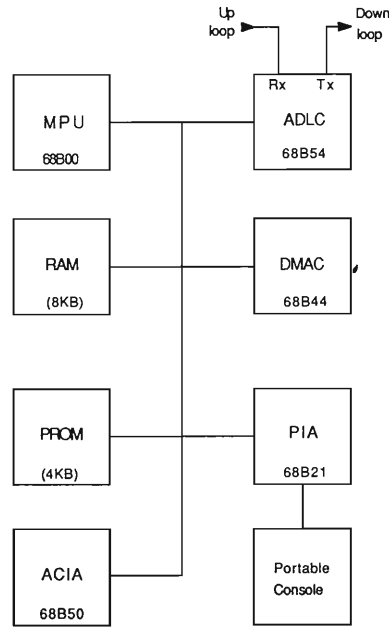


Fig. 2. Block diagram of the station.

frame. All frames start with an opening flag and end with a closing flag. Between both flags, a frame contains an address field, a control field, an information field and a frame check sequence (FCS) field. The primary station provides serial data and a synchronous clock to the receiver section of the secondaries through two twisted pair cables. Each secondary is in series and adds one bit delay to the loop data.

The loop is set to a mark idling state by initialization of the system. The synchronous clock rate in the state is 230 kbps. The primary sends a message of length of three bytes on the loop. The first byte is an address of a delivered secondary station and permits up to 256 different addresses. The second is a command or a response to the secondary. The last shows the length of the data record. When the secondaries receive the frame, they interrupt present work and compare the received address with their own. The stations of a different address return to a paused sequence. The fitted station decodes the next control field and answers to the primary with an "Acknowledge" frame. It has the length of three bytes in the same format as the message from the pri-

mary. If the content of the control field includes transfer of block data, the two stations change the state to a DMA mode and the synchronous clock is accelerated to 1.84 Mbps by the primary. That is, in a DMA mode, data are transferred at a rate eight times faster than 0.23 Mbps in the idling state. At the end of DMA transfer, the primary sets the clock to be a slow rate again and the loop network comes back to the idling state. A programmable frequency divider IC SN74LS292 on the primary board serves to switch the clock. The IC divides 7.37 MHz quartz controlled oscillating frequency to 1/4 or 1/32. The clock rate of the microprocessor is 1.84 MHz, which is the same rate as a synchronous clock at a DMA mode. The ADLC has 32-bit shift registers in RxD input and TxD output to relieve some of software constraints. Exchange of the 3-byte message in an idling state is based on the feature. The message over 3-byte tends to generate an error of receiver overrun in the present system.

A gate logic on the secondary board repeats up-loop data to down-loop station as shown in Fig. 3. If a Loop On-line Control (LOC) signal of ADLC holds a high level, up-loop data moves down-loop via gate A. The station gets out the loop. If the LOC is low, up-loop data moves

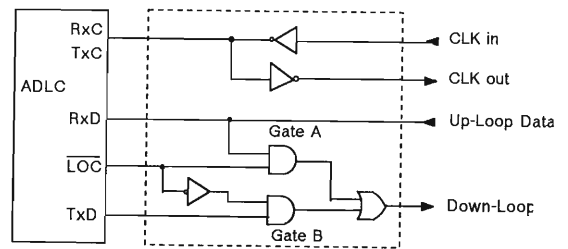


Fig. 3. Repeater logic.

down-loop via an ADLC receiver-transmitter plus gate B. The station gets in the loop. The synchronous clock moves down-loop with the same phase through two inverters.

Short twisted pair cables are used to connect the stations in the test system; communication between remote stations is feasible by replacing of the cables with optical fibers and by changing I/O parts.

#### References

- 1) T. Wada, H. Takebe, J. Fujita, T. Kanbara, and H. Kamitsubo: *RIKEN Accel. Prog. Rep.*, **20**, 170 (1986).
- 2) N. Nagase, H. Takebe, T. Wada, and K. Shimizu: 11th Int. Conf. Cyclotron and Their Applications, Tokyo, Oct. (1986).

### III-5-23. Spectral Analysis with a Graphic Terminal

M. Yasue and T. Wada

A program which was originally coded by T. Wada was modified so that one can handle spectral data displayed on graphic terminal by conversing with a super-mini computer S-3500 through a keyboard or a touch-pen. Also improved were several points such as 1) easiness of handing, 2) analysis speed, 3) versatile curves for a continuum background in spectra and, 4) availability of spectral data with several types of 8, 16, 20, 24, and 32 bits/channel. Instructions to use the program are described in Ref. 1.

With the aid of a peak fitting procedure, the cross sections for high-spin states lying above the thresholds of particle decay can be obtained, providing interesting shell structures of the unbound high-spin states in light nuclei.<sup>2,3)</sup>

#### References

- 1) M. Yasue and T. Wada: *INS-Rep.*, No. 670, 1 (1988).
- 2) R.J. Peterson, *et al.*: *Phys. Rev. C*, 38, 1130 (1988).
- 3) M. Yasue, *et al.*: to be published in *Phys. Rev. C*.

## IV. NUCLEAR DATA

### 1. Status Report of the Nuclear Data Group

A. Hashizume, Y. Tendow, Y. Ohkubo, K. Kitao, and K. Sueki

In this period four items have been continued as the last work.<sup>1)</sup> They are (1) the compilation of charged particle induced reaction cross section data,<sup>2)</sup> (2) the evaluation of cross section data for charged particle induced reactions, (3) the mass-chain evaluation of nuclear structure data, and (4) the compilation of the nuclear references taken from the reports published in Japan. For the first item, we cooperated with Nuclear Data Section in International Atomic Energy Agency (IAEA) and other nuclear data centers. The second was started from the recommendation of the IAEA meeting held in Tokyo in 1987.<sup>3)</sup> The third is concerned with the world wide mass-chain evaluation work of nuclear structure for the implement of the Evaluated Nuclear Structure Data File (ENSDF). We cooperated with a nuclear data group in Japan Atomic Energy Research Institute. The fourth is connected to the RNDF (References of the Nuclear Data File). NNDC (National Nuclear Data Center) in Brookhaven National Laboratory compiles the references and publishes as The Recent References for nuclear structures and reactions. We owe the covering the reports published in Japan.

(1) The work for the compilation of new EXFOR (Exchange Format for Experimental Data) files of nuclear reaction cross sections has been continued. The reactions in which we mainly interested are those whose products are utilized for mediobiological applications. The cross sections of the reactions producing the following isotopes have been compiled in the EXFOR file. The isotopes are <sup>11</sup>C, <sup>13</sup>N, <sup>15</sup>O, <sup>18</sup>F, <sup>28</sup>Mg, <sup>52</sup>Fe, <sup>67</sup>Ga, <sup>68</sup>Ge, <sup>68</sup>Ga, <sup>74</sup>As, <sup>77</sup>Br, <sup>82</sup>Br, <sup>77</sup>Kr, <sup>81</sup>Rb, <sup>82m</sup>Rb, <sup>111</sup>In, <sup>123</sup>Xe, <sup>127</sup>Xe, <sup>123</sup>I, <sup>124</sup>I, and <sup>125</sup>I nuclei.<sup>1)</sup> We have also compiled the reaction cross-sections for various combinations of incident particles and target nuclei described in the reports in which the above primarily interested reactions were investigated. The effort was made in this period to complete the collection of these data and to make figures of cross section data for publication, and the situation of cross sections

producing positron emitters <sup>11</sup>C, <sup>13</sup>N, <sup>15</sup>O, and <sup>18</sup>F were studied.<sup>4-6)</sup>

The number and kind of nuclides for medical use are increasing; there are 65 radioisotopes permitted legally for pharmaceutical applications. However more than 50 nuclides are also proposed for medical use and the production methods have been studied.

The compilation of the integrated nuclear reaction cross-section data originated in Japan in the EXFOR files is continued. The main sources of recent data are annual reports published by universities and institutes having accelerator facilities.

(2) As explained in the last status report,<sup>7)</sup> it is important to make clear the present status and to propose standard cross sections for monitor reactions. We are examining the details of collected data on the <sup>12</sup>C(p, pn)<sup>11</sup>C, <sup>27</sup>Al(p, 2pn)<sup>24</sup>Na, <sup>63</sup>Cu(p, 2n)<sup>62</sup>Zn, and <sup>65</sup>Cu(p, n)<sup>65</sup>Zn reactions.

A new version of a computer code ALICE to search parameters and to calculate nuclear reaction cross sections in compound and precompound processes is being used. By using this code, the comparison between the experimental results and the those from the exciton model can be made. The parameter search of the code was carried out for the several reactions. The center host computer used for the calculation is a FACOM 780/10.

(3) For the mass chain evaluation of nuclear structure data, a new editor for treating the nuclear structure data file was completed for a computer PC-9801. The evaluation work on the nuclear structure of the  $A=177$  mass chain has been continued.

(4) The recent reference files published periodically by Brookhaven National Laboratory should cover all references in the field of nuclear physics. The references of annual reports and quartary reports published in Japan were compiled and preparing to sent to the BNL Data Center. In connection with this work, all reference files of Nuclear Data Sheets were received.

## References

- 1) A. Hashizume, Y. Tendow, Y. Ohkubo, K. Sueki, K. Kitao, and T. Nozaki: *RIKEN Accel. Prog. Rep.*, **20**, 152(1986).
- 2) A. Hashizume: Invited talk and Proc. Int. Conf. Nuclear Data for Science and Technology, Mito, May (1988).
- 3) Report on the 8th IAEA Consultants Meeting of the Nuclear Reaction Data Centers, INDC(NDS)-178. Oct.(1985).
- 4) Y. Ohkubo, A. Hashizume, Y. Tendow, and K. Kitao: This Report, p. 189.
- 5) A. Hashizume, Y. Ohkubo, Y. Tendow, and K. Kitao: This Report, p. 191.
- 6) Y. Tendow, A. Hashizume, Y. Ohkubo, and K. Kitao: This Report, p. 194.
- 7) A. Hashizume, Y. Tendow, Y. Ohkubo, K. Kitao, K. Sueki, and T. Nozaki: *RIKEN Accel. Prog. Rep.*, **21**, 185(1987).

## IV-2. On the Cross Sections for the $^{12}\text{C}(\text{p}, \text{pn})^{11}\text{C}$ Reaction

Y. Ohkubo, A. Hashizume, Y. Tendow, and K. Kitao

A single nucleon removal reaction is an important reaction for studies of both nuclear structure and reaction mechanism itself. The  $^{12}\text{C}(\text{x}, \text{xn})^{11}\text{C}$  reaction was studied for the above

Table 1. List of the total cross sections for the  $^{12}\text{C}(\text{p}, \text{pn})^{11}\text{C}$  reaction.

First author	Place	Ref.	Target (mg/cm <sup>2</sup> )*	Beam energy (MeV)**	Detector	Errors and comment
R.L. Aamodt	(Berkeley)	1)	5-mil, 0.010-in. polystyrene	340,32	GM	stacked foils at 340 MeV
J.M. Cassels	(Harwell)	2)	1,750, naphthalene	142	internal, NaI	5%, ionization chamber
N.M. Hintz	(Harvard)	3)	0.005-in. polystyrene	100	GM	stacked foils, energy range from threshold to 100 MeV, normalized the relative excitation function to the absolute values of Ref. 1 at 32 and 110 MeV
W.E. Crandall	(Berkeley)	4)	1-15 mil polystyrene	170-350	ppc	+5, -4% at 350 MeV, stacked foils, beam energy degrader, Faraday cup
A.H. Rosenfeld	(Chicago)	5)	4, polyethylene	461	ppc	3%, ionization chamber
Iu.D. Prokoshkin	(USSR)	6)	graphite	150-660	ppc	2-4%, thermal battery, normalized relative cross sections to the value of Ref. 4 at 350 MeV
J.B. Cumming	(Brookhaven)	7)	1-in. polystyrene- based plastic scint.	2,3 GeV	internal	3.5% at 2 GeV, 3.8% at 3 GeV 3-element scint. counter telescope
A.B. Whitehead	(McGill)	8)	10, polythene	42	NaI	5%
N. Horwitz	(Berkeley)	9)	3, plastic scint.	3, 4.5, 6 GeV	internal	5.4% at 3 GeV, 6.1% at 4.5 GeV, 5.4% at 6 GeV, emulsion
V. Parikh	(Liverpool)	10)	540, graphite	383	GM	2.9-3.6%, beam energy degrader covering energy range down to 288 MeV, Faraday cup
K. Goebel	(CERN)	11)	300, polythene	591	GM	5.0%, 20-plate secondary emission chamber
J.B. Cumming	(Brookhaven)	12)	1-in. polystyrene- based plastic scint.	28 GeV	internal	4.6%, 4 types of combination with emulsions and plastic scint.
J.B. Cumming	(Brookhaven)	13)	10, polythene	51	NaI	3.0-3.4%, stacked foils with beam energy degrader covering energy range down to 21 MeV, Faraday cup
D.F. Measday	(Harvard)	14)	1.4-mm polystyrene	160	NaI	2.9-3.5%, beam energy degrader covering energy down to 51 MeV, Faraday cup
P.T. Andrews	(Liverpool)	15)	50, 250, 375, and 625, polystyrene	385	internal, NaI	1.6%, Faraday cup
K.R. Hogstrom	(Los Alamos)	16)	181 and 354, plastic scint.	800	internal, NaI	3.1% based solely on the uncertainty in ion chamber, ion chamber
S.B. Kaufman	(Argonne)	17)	310, plastic scint.	300 GeV	internal, NaI	6.5%, scint. counter telescope

\* If unit is not given, thickness is represented by mg/cm<sup>2</sup>.

\*\* If unit is not given, beam energy is represented by MeV.

purposes and also for monitoring beam intensities because of the convenience of measuring  $^{11}\text{C}$  activities. The cross sections of the  $^{12}\text{C}(\text{p}, \text{pn})^{11}\text{C}$  reaction were measured in the energy range from threshold (18.5 MeV) to 300 GeV by numerous investigators. Listed in Table 1 are representative authors who measured cross sec-

tions of this reaction, target thicknesses, primary beam energies, detector employed, errors, methods for beam intensity determination and so on. Table 1 does not include all the data published on the reaction. The data of several experiments up to 300 GeV of incident energies are plotted in Fig. 1.

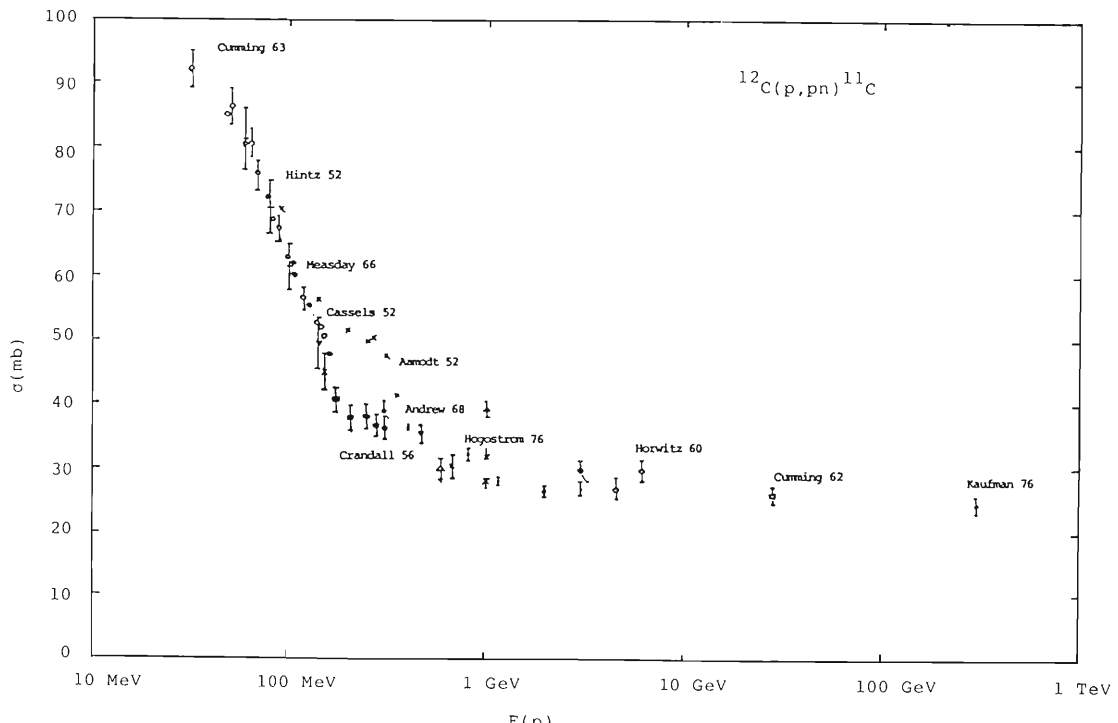


Fig. 1. Excitation function for the  $^{12}\text{C}(\text{p}, \text{pn})^{11}\text{C}$  reaction.

The results of Aamodt, *et al.*<sup>1)</sup> were shown to be in error owing to absorber effects,<sup>4)</sup> counter efficiency<sup>5)</sup> and gas loss from thin plastic target foils.<sup>18,19)</sup> The value at 385 MeV of Andrews, *et al.*<sup>15)</sup> is greater than the value measured by Parikh.<sup>10)</sup> Andrews, *et al.* made a comment that the uniformity of graphite targets employed by Parikh and the difficulties associated with the calibrated Geiger counter technique could have led to errors of the magnitude of Parikh.

## References

- 1) R.L. Aamodt, V. Peterson, and R. Phillips: *Phys. Rev.*, **88**, 739 (1952).
- 2) J.M. Cassels, T.G. Pickavance, and G.H. Stafford: *Proc. Phys. Soc. A*, **214**, 262 (1952).
- 3) N.M. Hintz and N.F. Ramsey: *Phys. Rev.*, **88**, 19 (1952).
- 4) W.E. Crandall, G.P. Millburn, R.V. Pyle, and W. Birnbaum: *Phys. Rev.*, **101**, 329 (1956).
- 5) A.H. Rosenfeld, R.A. Swanson, and S.D. Warshaw: *Phys. Rev.*, **103**, 413 (1956).
- 6) Yu.D. Prokoshkin and A.A. Tiapkin: *JETP (Sov. Phys.)*, **5**, 148 (1957).
- 7) J.B. Cumming, G. Friedlander, and C.E. Swartz: *Phys. Rev.*, **111**, 1386 (1958).
- 8) A.B. Whitehead and J.S. Foster: *Can. J. Phys.*, **36**, 1276 (1958).
- 9) N. Horwitz and J.J. Murray: *Phys. Rev.*, **117**, 1361 (1960).
- 10) V. Parikh: *Nucl. Phys.*, **18**, 628 (1960).
- 11) K. Goebel, D. Harting, J.C. Kluyver, A. Kusumegi, and H. Schultes: *Nucl. Phys.*, **24**, 28 (1961).
- 12) J.B. Cumming, G. Friedlander, and S. Katcoff: *Phys. Rev.*, **125**, 2078 (1962).
- 13) J.B. Cumming: *Nucl. Phys.*, **49**, 417 (1963).
- 14) D.F. Measday: *Nucl. Phys.*, **78**, 476 (1966).
- 15) P.T. Andrews, P.G. Butler, A. Christy, A.N. James, P. Kirkby, B.G. Lowe, and B.W. Renwick: *Nucl. Phys.*, **A109**, 689 (1968).
- 16) K.R. Hogstrom: *Phys. Rev. C*, **14**, 753 (1976).
- 17) S.B. Kaufman, M.W. Weisfield, B.D. Wilkins, D. Henderson, and E.P. Steinberg: *Phys. Rev. C*, **13**, 253 (1976).
- 18) H. Fuchs and K. Linderberger: *Nucl. Instrum. Methods*, **7**, 219 (1960).
- 19) J.B. Cumming, G. Friedlander, J. Hudis, and A.M. Poskanzer: *Phys. Rev. Lett.*, **6**, 484 (1961).

### IV-3. The Nuclear Data for $^{13}\text{N}$ Production

A. Hashizume, Y. Ohkubo, Y. Tendow, and K. Kitao

Nitrogen-13 is used in the studies on metabolic fate of nitrogen-containing biomolecules in biological systems at tracer levels with an extremely high sensitivity. The  $^{16}\text{O}(\text{p}, \alpha)^{13}\text{N}$  reaction is commonly employed to produce a radiomedical nuclei  $^{13}\text{N}$ . Gas targets can be cryogenically transferred to a vial containing activated charcoal. Other reaction cross sections studied by light incident particles are listed in Table 1. Besides the reaction listed in Table 1, the neutron stripping reactions induced by heavy-ion  $^{14}\text{N}$  have been studied for ten kinds of targets.<sup>1-3)</sup>

Excitation functions of the  $^{12}\text{C}(\text{p}, \gamma)^{13}\text{N}$ ,<sup>4,5)</sup>  $^{13}\text{C}(\text{p}, \text{n})^{13}\text{N}$ ,<sup>6)</sup>  $^{14}\text{N}(\text{p}, \text{pn})^{13}\text{N}$ ,<sup>7)</sup>  $^{12}\text{C}(\text{d}, \text{n})^{13}\text{N}$ ,<sup>8)</sup> and  $^{13}\text{C}(\text{He}^3, \text{pn})^{13}\text{N}$ <sup>9)</sup> are shown in Figs. 1, 2, 3, 4, and 5. For  $(\text{p}, \gamma)$  reaction cross sections, Hall<sup>4)</sup> and Lamb<sup>5)</sup> studied in a high energy region and Cohen<sup>10)</sup> for incident energies of 5 and 11 MeV. As shown in these figures, the resonance is observed in  $(\text{p}, \text{n})$  and  $(\text{d}, \text{n})$  reactions. In obtaining their cross sections, neutrons were directly measured. The target thickness of the  $^{13}\text{C}$  in  $(\text{p}, \text{n})$  reaction was 24.8  $\mu\text{g}/\text{cm}^2$  and those of  $^{12}\text{C}$  in  $(\text{d}, \text{n})$  reaction were 80 and 92  $\mu\text{g}/\text{cm}^2$ . Incident

protons or deuterons were accelerated with a Van de Graaff generator. The overall accuracy of the cross section values reported is within  $\pm 3\%$  for the  $(\text{d}, \text{n})$  reaction.

Figure 6 shows the excitation function of  $^{16}\text{O}(\text{p}, \alpha)^{13}\text{N}$ . The cross sections were first reported by Whitehead and Foster<sup>11)</sup> followed by Furukawa,<sup>12)</sup> Hill<sup>13)</sup> observed several resonances from a high resolution measurement. McCamis,<sup>14)</sup> Vero,<sup>15)</sup> Gruhle,<sup>16)</sup> and Sajjad<sup>7)</sup> also studied the cross sections of  $^{17}\text{O}(\text{p}, \alpha)$ .

The excitation function reported by Gruhle (indicated by a line in Fig. 6) has statistical errors of about 2% in the high energy region and about 15% in the low energy region. The absolute values have errors of about 9%. Nitrogen-13 could also be produced by  $(\text{p}, \text{pt})$  or  $(\text{p}, \text{dd})$  reactions; however, these reactions have not yet studied in a wide range of incident energies. There is a report only at 50 MeV.<sup>17)</sup>

The  $^{16}\text{O}(\text{p}, \alpha)^{13}\text{N}$  reaction has also been subjected to the attention of astrophysicists in connection with the oxygen burning in stellar regions.

Table 1. Reactions for  $^{13}\text{N}$  production by light particles.

Reaction	Range of particle energy (MeV)	Particle energy at maximum cross section (MeV)	Maximum cross section	Reference
$^{12}\text{C}(\text{p}, \gamma)^{13}\text{N}$	5, 11 80-127	5	2.5 mb	4), 10)
$^{12}\text{C}(\text{d}, \text{n})^{13}\text{N}$	1.5-4.5	2.3	200	8)
$^{13}\text{C}(\text{p}, \text{n})^{13}\text{N}$	3.2-5.3	5	90	6)
$^{13}\text{C}(\text{He}^3, \text{pn})^{13}\text{N} +$ $^{13}\text{C}(\text{He}^3, \text{d})^{13}\text{N}$	4.5-24	13	135	9)
$^{14}\text{N}(\text{p}, \text{pn})^{13}\text{N}$	12.6-29.8	20	32	7)
$^{16}\text{O}(\text{p}, \alpha)^{13}\text{N}$	6.8-17.8	8	120	7), 11), 12), 13) 14), 15), 16)
$^{16}\text{O}(\text{p}, \text{pt})^{13}\text{N}$	50	—	21 (at 50 MeV)	17)
$^{16}\text{O}(\text{p}, \text{dd})^{13}\text{N}$	50	—	12 (at 50 MeV)	17)

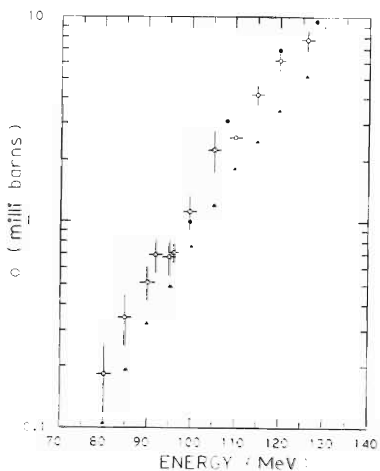


Fig. 1. Excitation function of  $^{12}\text{C}(\text{p},\gamma)^{13}\text{N}$ . From Refs. 4 and 5. The results of calculation by using Breit-Wigner's formula are cited in Ref. 5. These values are plotted by black triangles in the figure.

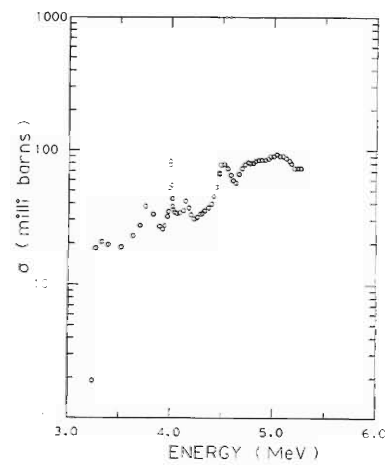


Fig. 2. Excitation function of  $^{13}\text{C}(\text{p},\text{n})^{13}\text{N}$ . From Ref. 6.

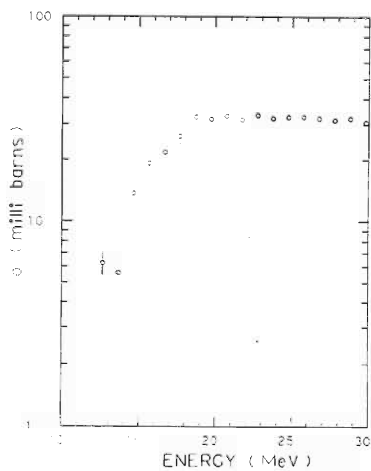


Fig. 3. Excitation function of  $^{14}\text{N}(\text{p},\text{pn})^{13}\text{N}$ . From Ref. 7.

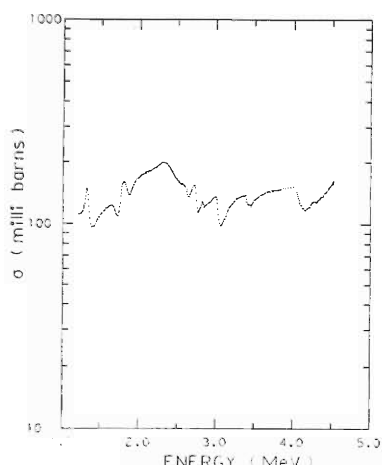


Fig. 4. Excitation function of  $^{12}\text{C}(\text{d},\text{n})^{13}\text{N}$ . From Ref. 8

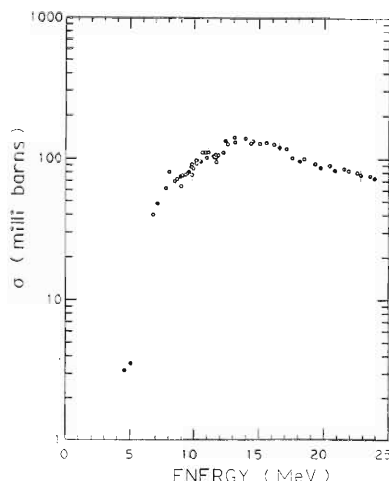


Fig. 5. Excitation function of  $^{13}\text{C}({}^3\text{He}, \text{pn}+\text{d})^{13}\text{N}$ . From Ref. 9.

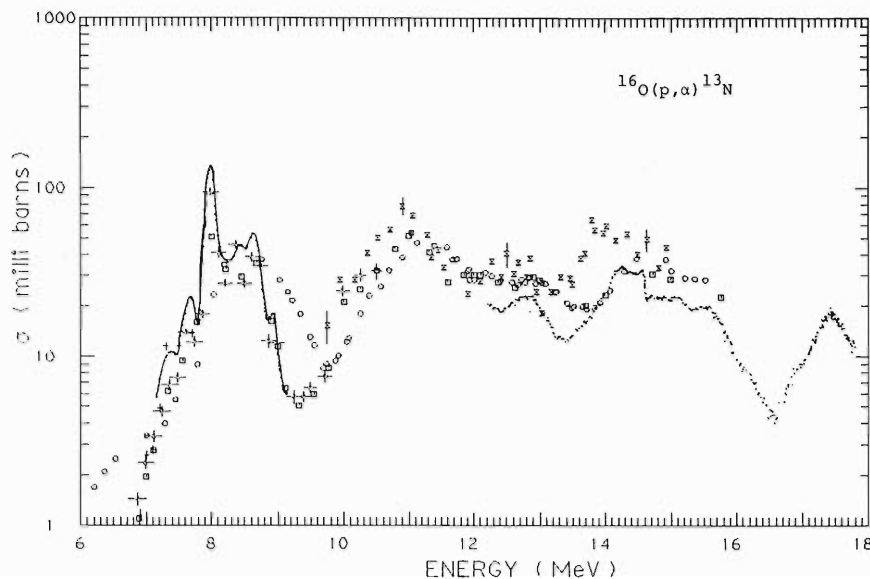


Fig. 6. Excitation function of  $^{16}\text{O}(\text{p},\alpha)^{13}\text{N}$ . From Refs. 11, 12, 13, 14, 15, and 16.

## References

- 1) M.L. Halbert, T.H. Handley, J.J. Pinajian, W.H. Webb, and A. Zucker: *Phys. Rev.*, **106**, 251 (1957).
- 2) J.G. Couch and J.A. McIntyre: *Phys. Rev.*, **152**, 883 (1966).
- 3) R.M. Gaedke, K.S. Toth, and I.R. Williams: *Phys. Rev.*, **141**, 996 (1966).
- 4) R.N. Hall and W.A. Fowler: *Phys. Rev.*, **77**, 197 (1950).
- 5) W.A.S. Lamb and R.E. Hester: *Phys. Rev.*, **107**, 550 (1957).
- 6) J.H. Gibbons and R.L. Macklin: *Phys. Rev.*, **114**, 571 (1959).
- 7) M. Sajjad, R.M. Lambrecht, and A.P. Wolf: *Radiochem. Acta*, **39**, 165 (1986).
- 8) R.J. Jaszcak, R.L. Macklin, and J.H. Gibbons: *Phys. Rev.*, **181**, 1428 (1969).
- 9) D.R.F. Cochran and J.D. Knight: *Phys. Rev.*, **128**, 1281 (1962).
- 10) B.L. Cohen: *Phys. Rev.*, **100**, 206 (1955).
- 11) A.B. Whitehead and S. Foster: *Can. J. Phys.*, **36**, 1276 (1958).
- 12) M. Furukawa, Y. Ishizaki, Y. Nakano, T. Nozaki, Y. Saji, and S. Tanaka: *J. Phys. Soc. Jpn.*, **15**, 2167 (1960).
- 13) H.A. Hill, E.L. Haas, and D.B. Knudsen: *Phys. Rev.*, **123**, 1301 (1961).
- 14) R.H. McCamis, G.A. Moss, and J.M. Cameron: *Can. J. Phys.*, **51**, 1689 (1973).
- 15) A.V. Vero and A.J. Howard: *Nucl. Phys.*, **A210**, 60 (1973).
- 16) W. Gruhle and B. Kober: *Nucl. Phys.*, **A286**, 523 (1977).
- 17) A.I. Vdovin, I.G. Golikov, M.N. Jikov, I.I. Lojakov, and V.I. Ostroumov: *Izv. Akad. Nauk.*, **43**, 148 (1979).

#### IV-4. Excitation Function Data for $^{15}\text{O}$ Production

Y. Tendow, A. Hashizume, Y. Ohkubo, and K. Kitao

Radioisotope  $^{15}\text{O}$  is widely used in a variety of applications. Because of its short halflife ( $T_{1/2} = 2.04$  min) and pure  $\beta^+$  emission ( $E = 1.74$  MeV),  $^{15}\text{O}$  is an especially suitable radiotracer for life science and biomedical applications.  $^{15}\text{O}$  is also used for the activation analysis of nitrogen by the  $^{14}\text{N}(\text{d}, \text{n})^{15}\text{O}$  reaction.  $^{15}\text{O}$  isotope is produced *via* several nuclear reactions. The excitation function data for these reactions are very important to estimate the final yields of  $^{15}\text{O}$ . Nevertheless, only an insufficient number of works on the cross section measurements have appeared in the literature. The possible reactions to produce  $^{15}\text{O}$  isotope are  $^{14}\text{N}(\text{d}, \text{n})^{15}\text{O}$ ,  $^{15}\text{N}(\text{p}, \text{n})^{15}\text{O}$ ,  $^{16}\text{O}(\text{p}, \text{pn})^{15}\text{O}$ ,  $^{14}\text{N}(\text{He}^3, \text{d})^{15}\text{O}$  and  $^{12}\text{C}(\alpha, \text{n})^{15}\text{O}$ .

Among these reactions,  $^{14}\text{N}(\text{d}, \text{n})^{15}\text{O}$  seems to be useful when high specific activity or carrier-free products are required. Wholleben and Schuster<sup>2)</sup> measured the cross sections for deuterons of 0.5 and 3.2 MeV. They used a thick-target yield method on boron nitride targets. Ruiz and Wolf<sup>1)</sup> studied the reaction on nitrogen gas targets with deuterons of 0.6–14.35 MeV by using a saturation method. Excitation curves obtained in the two studies show very similar shapes, but the

absolute values of Wholleben are systematically 1.4 times greater than those of Ruiz. The curves are shown in Fig. 1 up to about 5.7 MeV. Ruiz's data above that energy are not shown here in the figure but they slowly decrease until up to 14.35 MeV. The cross sections published by Newson<sup>4)</sup> as early as in 1937 are an order of magnitude lower than the data published there after. Retz-Schmidt and Weil<sup>3)</sup> measured the excitation function for the same reaction to the  $^{15}\text{O}$  ground state only.

In the case of  $^{15}\text{N}(\text{p}, \text{n})^{15}\text{O}$  reaction, it is necessary to employ an enriched  $^{15}\text{N}_2$  gas target. Barnett<sup>7)</sup> measured the relative total cross section in the range of 3.78–12 MeV and the absolute cross sections at 5.52, 5.68, and 5.75 MeV. The excitation curve had many resonance peaks and a maximum of  $\sim 300$  mb at around 6.4 MeV. Sajjad, *et al.*<sup>5)</sup> measured the cross section in the range of 3.72–16.58 MeV. The shape of their excitation curve was very similar to Barnett's but absolute values were systematically smaller. Sajjad<sup>5)</sup> asserted that the discrepancy might be due to incorrect measurements of the absolute detector efficiency in Barnett's work.<sup>7)</sup>

The cross sections for  $^{16}\text{O}(\text{p}, \text{pn})^{15}\text{O}$  on beryl-

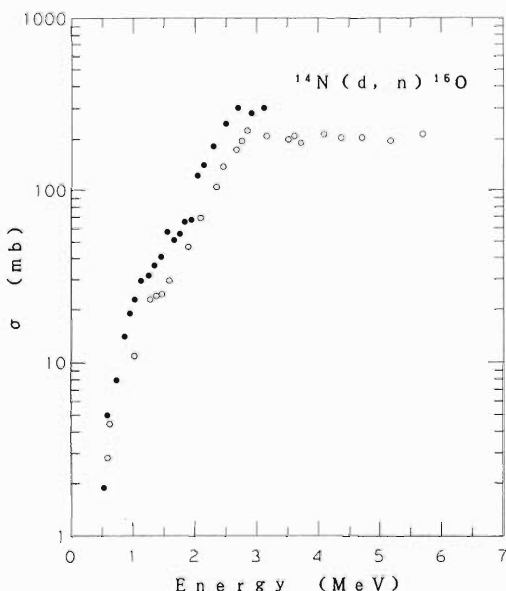


Fig. 1. Excitation curves for  $^{14}\text{N}(\text{d}, \text{n})^{15}\text{O}$  by  $\circ$  Ruiz<sup>1)</sup> and  $\bullet$  Wohlleben.<sup>2)</sup>

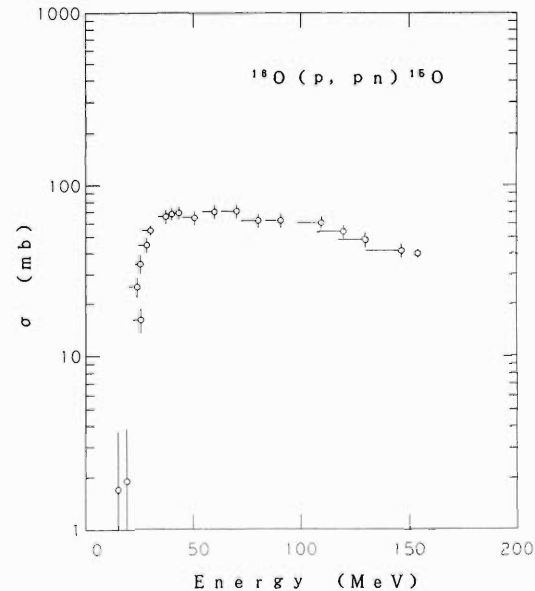


Fig. 2. Excitation curve for  $^{16}\text{O}(\text{p}, \text{pn})^{15}\text{O}$  by Valentin.<sup>8)</sup>

Table 1. Excitation functions for  $^{15}\text{O}$  production.

Reaction	Energy (MeV)	$\sigma_{\max}$ (mb at MeV)	Reference
$^{14}\text{N}(\text{d}, \text{n})$	0.6 - 14.35	220 (at 2.8)	1)
$^{14}\text{N}(\text{d}, \text{n})$	0.5 - 3.2	300 (at 2.8)	2)
$^{15}\text{N}(\text{p}, \text{n})$	3.72 - 16.58	142 (at 6.41)	5)
$^{15}\text{N}(\text{p}, \text{n})$	5.53 - 9.26	207 (at 6.31)	6)
$^{15}\text{N}(\text{p}, \text{n})$	3.8 - 12	resonance peaks	7)
$^{16}\text{O}(\text{p}, \text{pn})$	30 - 155	70 (at 50)	8)
$^{16}\text{O}(\text{He}^3, \alpha)$	2.9 - 8.9	169 (at 6.6)	9)
$^{12}\text{C}(\alpha, \text{n})$	11.35 - 22.65	resonance peaks	10)

lum oxide targets were measured by Valentin<sup>8)</sup> for protons of 30-155 MeV, the excitation curve is shown in Fig. 2.

Hahn, et al.<sup>9)</sup> measured the cross sections for the  $^{16}\text{O}(\text{He}^3, \alpha)$  reaction using Mylar-foil targets at a beam energy range of 2.9 to 8.9 MeV. The maximum value was 169 mb at 6.6 MeV beam energy.

The cross sections for  $^{12}\text{C}(\alpha, \text{n})^{15}\text{O}$  were measured by Black, et al.<sup>10)</sup> by using an activation method from the threshold at 11.345 MeV up to 22.65 MeV. The excitation curve shows a complex resonance structure varying from 5 to 25 mb.

A brief summary for the cross section data published to date are given in Table 1.

### References

- 1) H. Vera Ruiz and A.P. Wolf: *Radiochim. Acta*, **24**, 65 (1977).
- 2) Von K. Wohlleben and E. Schuster: *Radiochim. Acta*, **12**, 75 (1969).
- 3) T. Retz-Schmidt and J.L. Weil: *Phys. Rev.*, **119**, 1079 (1960).
- 4) H.W. Newson: *Phys. Rev.*, **51**, 620 (1937).
- 5) M. Sajjad, R.M. Lambrecht, and A.P. Wolf: *Radiochim. Acta*, **36**, 159 (1984).
- 6) K. Murphy, R.C. Byrd, P.P. Guss, C.E. Floyd, and R.L. Walter: *Nucl. Phys.*, **A355**, 1 (1981).
- 7) A.R. Barnett: *Nucl. Phys.*, **A120**, 342 (1968).
- 8) L. Valentin: *Nucl. Phys.*, **62**, 81 (1965).
- 9) R.K. Hahn and E. Ricci: *Phys. Rev.*, **128**, 650 (1966).
- 10) J.L. Black, H.M. Kuan, W. Gruhle, M. Suffert, and G.L. Latshaw: *Nucl. Phys.*, **A115**, 683 (1968).

## V. DEVELOPMENT OF ACCELERATOR FACILITIES

### 1. Ion Accelerator Development

#### 1. Performance of New Grid Bypass Capacitors of the Final RF Amplifier for RIKEN Ring Cyclotron

K. Ogiwara, S. Kohara, Y. Kumata,\* Y. Taniguchi,\*\* and T. Fujisawa

The maximum output power of the final amplifier was intended to be 300 kW in a frequency range of 20 to 45 MHz, but at the frequency around 40 MHz, it has been limited to 160 kW because of the second harmonic (80 MHz) resonance between the screen and control grids of the final tube, SIEMENSE RS2042SK, used in grounded grid. To promote the resonant frequency higher than 90 MHz, we designed new

bypass capacitors based on a model test.<sup>1)</sup>

Figure 1 shows the cross-sectional view of the new bypass capacitors ( $C_{g1}=15,000$ ,  $C_{g2}=15,000$  pF), which consist of cylindrical capacitors made of 50  $\mu$ m Kapton film coated with copper on both side and disk capacitors whose insulator are Kapton sheets (125  $\mu$ m). The cylindrical capacitor is a part newly added to reduce circuit inductance governing the resonance frequency.

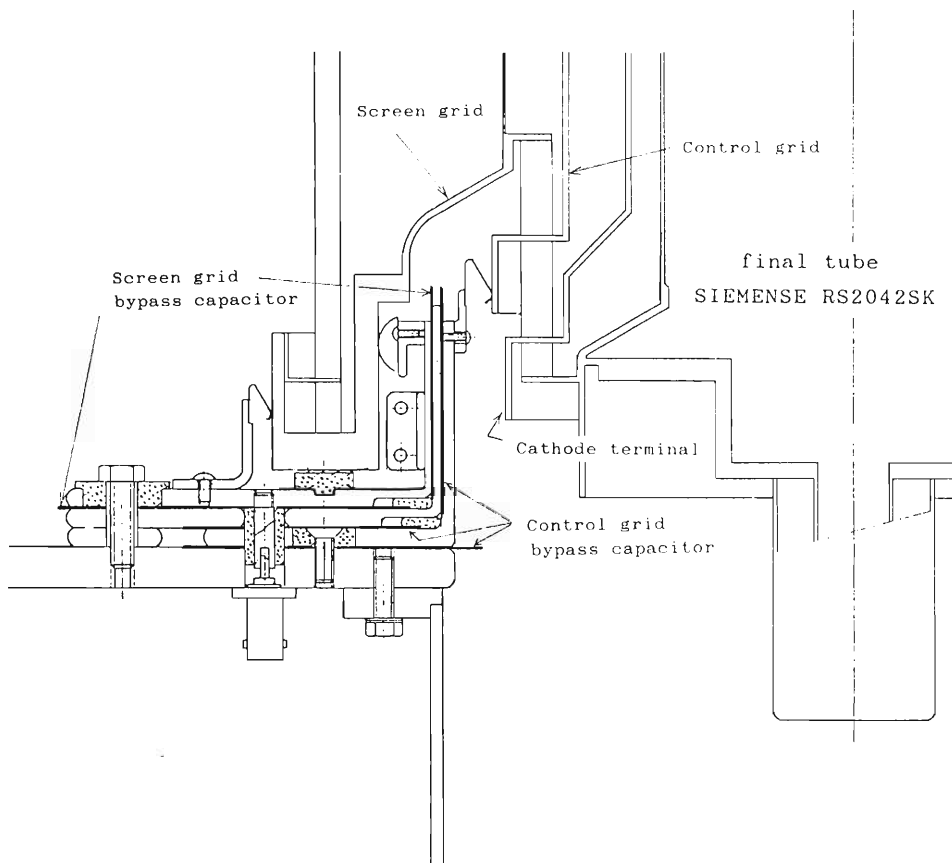


Fig. 1. Cross-sectional view of new bypass capacitors.

\* Sumitomo Heavy Industries, Ltd.

\*\* Denki Kogyo, Ltd.

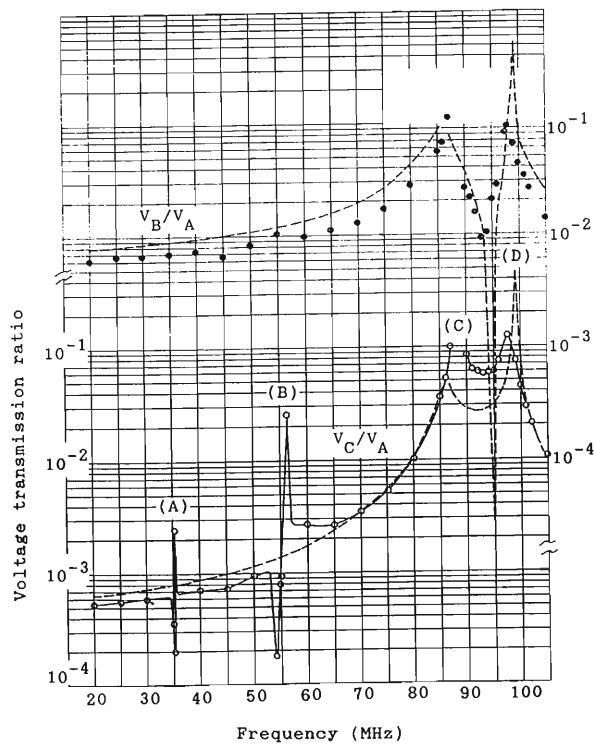


Fig. 2. Frequency dependence of the voltage transmission ratios from the plate terminal of the final tube to the screen and control grid bypass capacitors. Dotted lines show the values calculated by the equivalent circuit shown in Fig. 3. A: resonance of tuning frequency 35 MHz, B: resonance of cathode circuit, C: resonance of the cylindrical earth for measurement, and D: G1-G2 resonance.  $V_A$ ,  $V_B$ , and  $V_C$  refer to Fig. 3.

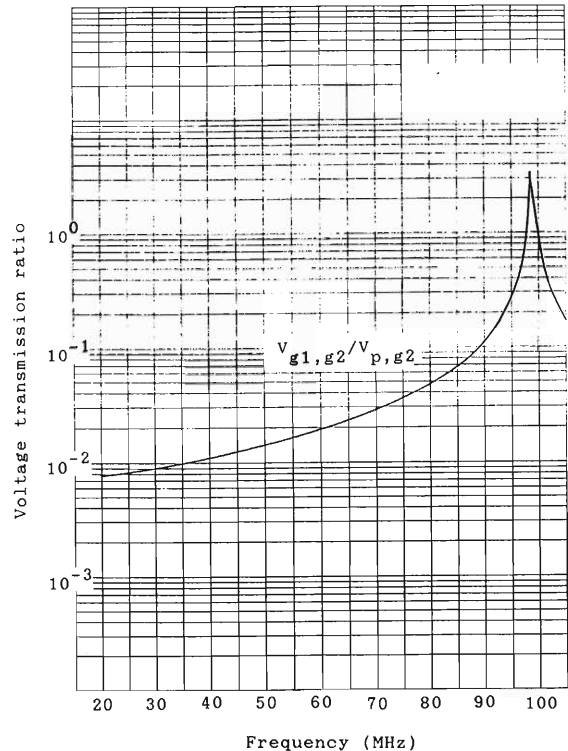


Fig. 4. Calculated voltage transmission ratios of the plate to the screen and control grid.

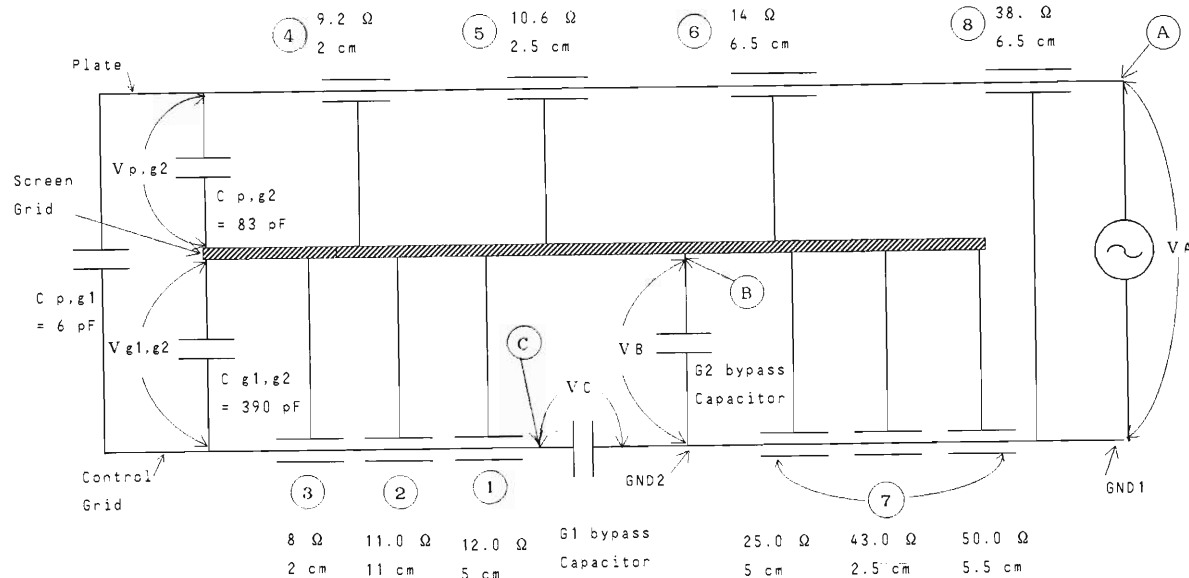


Fig. 3. Equivalent circuit of the bypass capacitors and the final tube including the attachment for measurement. The letters A, B, and C, and the numbers 1-8 correspond to those in Fig. 1 of Ref. 1.

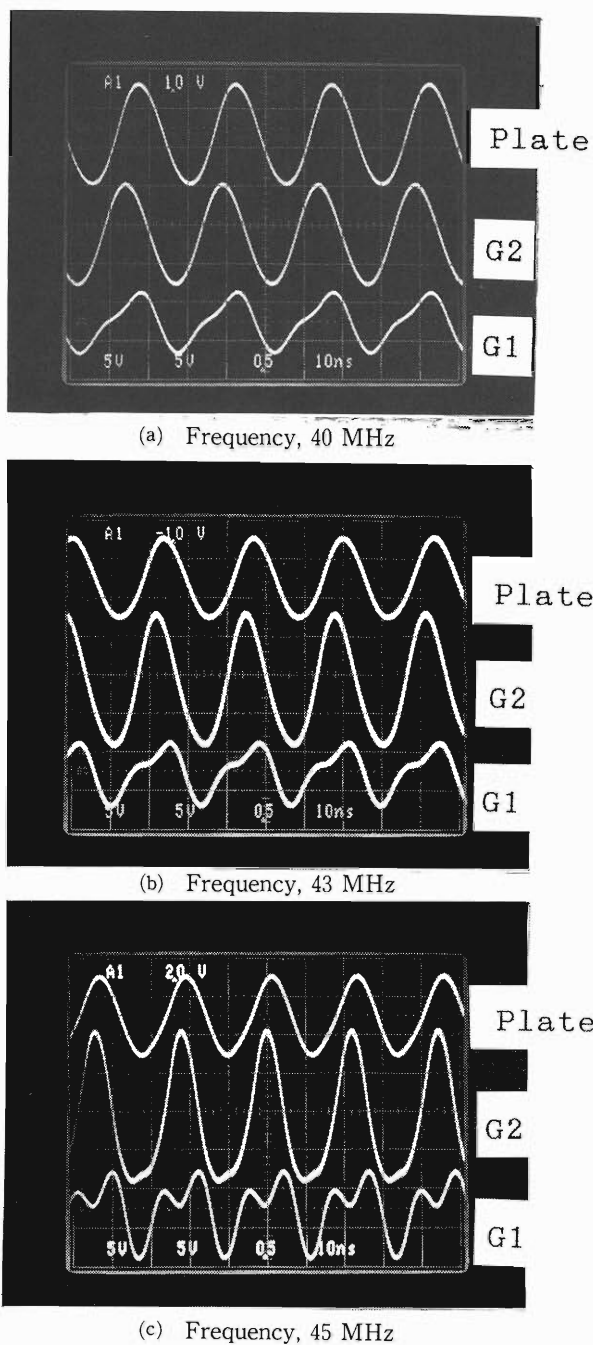


Fig. 5. Typical wave form of the RF voltages on power test.

The voltage transmission ratios from the plate terminal to the screen and control grid bypass capacitors were measured by the same method as represented in Ref. 1.

Figure 2 shows the measured ratios and the calculated result of the equivalent circuit shown in Fig 3. An undesirable  $G_1$ - $G_2$  resonance is promoted to 97.5 MHz, which is good agreement with the calculation. Several resonances appeared in this measurement are explained in the figure caption. To estimate voltages appeared at active area inside the tube, the calculation on the equivalent circuit is also carried out. The results are shown in Fig 4.

The power test was carried out in the frequency range of 40 to 45 MHz at intervals of 1 MHz, and the RF voltages were measured for the plate, screen grid ( $V_B$ ), and control grid ( $V_C$ ). Figure 5 shows the typical wave forms of the RF voltage in the power test.

This improvement of bypass capacitors makes the operation of the RF amplifier system stable in the whole frequency range.

#### Reference

- 1) T. Fujisawa, S. Kohara, M. Saito, and Y. Chiba: *RIKEN Accel. Prog. Rep.*, **21**, 203 (1987).

RIKEN Accel. Prog. Rep. **22** (1988)

### V-1-2. Present Status of the Vacuum System for RIKEN Ring Cyclotron

K. Ikegami, S. Nakajima, and S.H. Be

The vacuum system of RIKEN Ring Cyclotron<sup>1)</sup> has been smoothly operated without serious trouble since the cyclotron was put into operation at the beginning of October 1986. Little water leakage ( $\sim 10^{-4}$  Pa m<sup>3</sup>/s) occurred at two locations in the vacuum chamber during the period: one at a joint of the cooling pipe for the upper movable box of the north side RF resonator and one at the bottom wall of copper-clad stainless steel in the south side RF resonator. In spite of the water leakage, the pressure in the vacuum chamber was held at less than  $10^{-5}$  Pa.

The degassing of fourteen cryopumps was done once a month in average. After used for 15,000 h, adsorbers of the compressors for the cryopumps were replaced with new ones in August this year. Figure 1 shows a typical evacuation curve of the chamber for the cyclotron. The chamber was evacuated from atmospheric pressure by two sets of rotary pumps (4,700 l/min) and mechanical booster pump (2,600 m<sup>3</sup>/h). After pumping for 20 min to  $10^2$  Pa, the pumping system was switched to four turbomolecular pumps (5,000 l/s). When the pressure became below  $10^{-2}$  Pa, fourteen cryopumps which have a cooling down time of 150 min were switched on. Below  $2 \times 10^{-5}$  Pa, turbomolecular pumps were switched off and evacuation was continued by using only the cryopumps. After evacuation for 24 h, the pressure was reduced below  $10^{-5}$  Pa; after evacuation for 100 h, the pressure reached below was  $10^{-6}$  Pa.

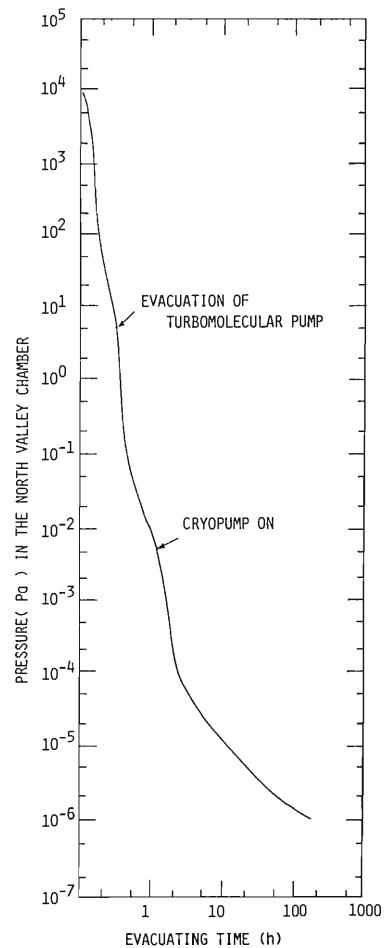


Fig. 1. Evacuation curve of the vacuum chamber for RIKEN Ring Cyclotron.

#### Reference

- 1) K. Ikegami, S. Nakajima, S. H. Be, I. Takeshita, Y. Oikawa, and S. Motonaga: *RIKEN Accel. Prog. Rep.*, **17**, 156 (1983).

### V-1-3. Present Status of the Control System for RIKEN Ring Cyclotron

H. Takebe, M. Kase, I. Yokoyama, M. Nagase, and S. Takahashi\*

Experimental halls of E4, E5, and E6 of the ring cyclotron building were completed by the end of January 1989. The third part of the beam transport system and AVF cyclotron will be installed by the end of this fiscal year. The control system is going to be arranged for these devices.

Figure 1 shows the computer network of the RILAC and RRC control system, and the present system of the CAMAC loop for the SSC-control computer (M350/60-#3).<sup>1)</sup> The program-development computer (M350/60-#1) has a remote tty port from the d-PBX.<sup>\*\*</sup> This d-PBX system can be used for local device control or a program

test. The program-development computer is connected to a FACOM M780/UTS (UNIX) through a "Unix to Unix Communication Path" (UUCP, 9600 bps). A source file backup and hi-speed calculation are done in this M780/UTS system. A load module program, compiled in computer #1, can be run in SSC-control computer. So that, a library file is copied between them. Most of the test programs and experimental user programs are run in a unix operating system with a remote tty terminal. Touch panel programs and some programs, which are required a hi-speed execution or forked by an interrupt, are copied to a real time system (OS60) of the same computer and are run.

CAMAC crate-#5 was moved into the ion source room from the control room and is used for the ion source and the AVF injection beam transport system. CAMAC crate-#7# is newly equipped in an E-power supply room and connected to the magnets power supplies and a beam diagnostic system of the E4, E5, and E6 experimental halls. For the AVF cyclotron, magnet power supplies, a high voltage supply, an RF system, vacuum system, and buncher systems will be controlled by the CIM/DIM system. Some CIM's in CAMAC crate-#6 are also equipped newly for the AVF control devices in a D-power supply room. The length of the plastic fiber

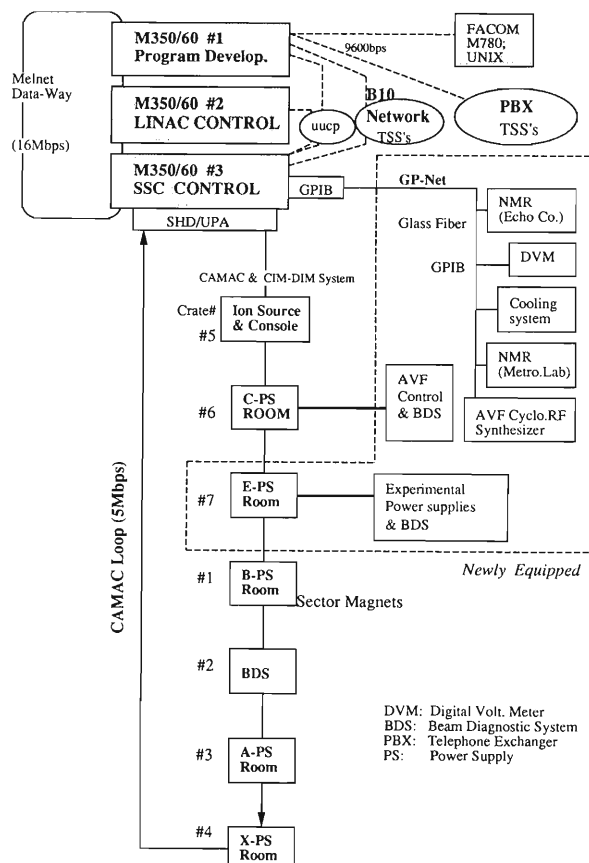


Fig. 1. Block diagram of the computer network and CAMAC loop for RIKEN Ring Cyclotron.

Table 1. DIM and CIM number of the RRC control system.

System	Name	DIM	CIM	DAC
RRC	Magnets	56	9	284
	RF	2	1	
	Vacuum	1		
	Cooling	1		
	Buncher	1		
	RIPS/Spectr.	4		10
	Magnets	10	1	70
	RF	2		
	Vacuum	1		
	Bunchers	2		
Beam diagnostics		65	7	
Total		145	18	364

\* Mitsubishi Electric Co., Ltd.

\*\* Digital Phone Private Branch Exchanger (Fujitsu; FETEX-3700).

cables used between CIMs and DIMs is limited to 30m. Those optical fibers which exceed this length are equipped with an opt-opt amplifier or are changed to glass fiber cables (Dupont Co., Ltd.). Table 1 shows DIM and CIM numbers of the RRC control system. After installation of the AVF cyclotron, the total number of the DIM will be 145 and the total DAC number of the power supplies is 364. A GP-IB interface of SSC Control computer is expanded by using an optical interface (GP-NET; Network Supply Co. and Dupont glass fiber Cable) into a B-Power supply (B-PS) room and the 2nd stage of the AVF room, for DVM for the magnet current monitoring and an RF synthesizer control for the AVF.

A new touch panel system (Mitsubishi Electric. Co.; DP610R) is equipped to the program-development computer and being tested. As seen in a Fig. 2, a 20-inch color graphic display and a photo-sensed touch panel (Carol Touch Co. Ltd.) are controlled by a small computer (Digital Computer Co. Ltd.; DP-610VT) which has 224 kB segment memory, keyboard, digitizer, and 3.5 inch floppy disk. This DP-610VT computer is connected to the M350/60 computer with a 9,600 bps RS-232C interface. Graphic patterns are created in this small computer with a digitizer

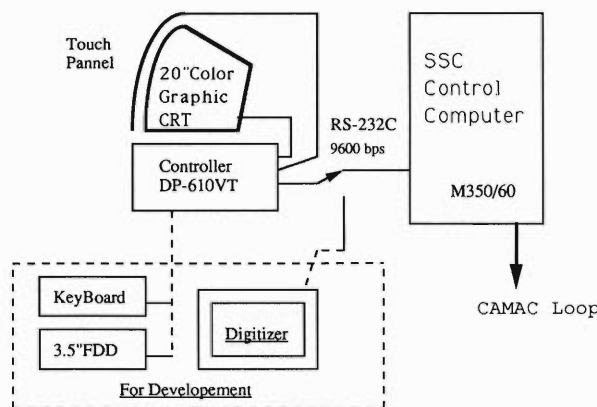


Fig. 2. New touch panel system using a small computer (DP610VT).

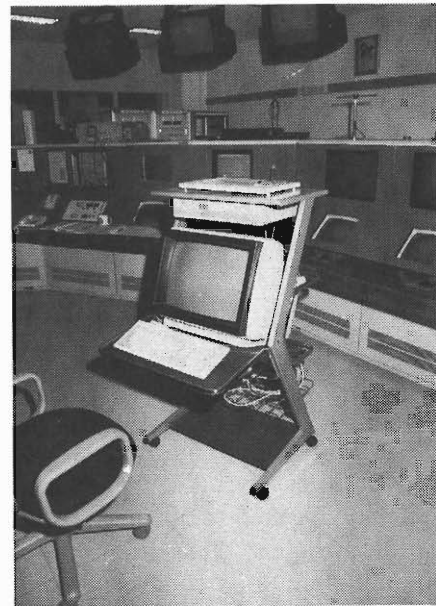


Fig. 3. New touch panel setup with a portable caster rack.

and stored in a segment memory, so that high-speed paging of patterns is performed with communication of a short information (tag number). The setup is portable as seen from Fig. 3 with a castered rack. There is no compatibility in the interface protocols between the present VT241 touch panel system and the new DP-610VT system.

A target beam current or rate meter outputs are monitored with a personal computer (NEC; PC9801)'s ADC circuits and displayed through a CATV system.<sup>2)</sup> A high-resolution color graphic display signal (RGB) of the PC9801 is converted to a NTSC video composite signal by using a newly developed video converter (Central Engineering Co.; PVC-400).

#### References

- 1) T. Wada, H. Takebe, J. Fujita, and H. Kamitsubo: *RIKEN Accel. Prog. Rep.*, **20**, 170 (1986).
- 2) H. Takebe, S. Fujita, R. Abe, H. Akagi, T. Wada, and T. Inamura: *RIKEN Accel. Prog. Rep.*, **21**, 207 (1987).

#### V-1-4. Status of Construction of the Injector AVF Cyclotron

A. Goto, K. Hatanaka, K. Ikegami, T. Kageyama, M. Kase, S. Kohara,  
M. Nagase, M. Saito, H. Takebe, Y. Yano, and Y. Kumata\*

The construction of the injector AVF cyclotron started in April 1987. After completion of a cyclotron magnet, magnetic fields were measured in April 1988 at Sumitomo Heavy Industries, Ltd. (SHI); the results were generally as good as expected. From the beginning of May to the end of November 1988, other parts of the cyclotron including a vacuum chamber, an rf system, a main probe, a deflector, and a magnetic channel were preliminarily assembled at SHI. Almost all the problems found in a series of tests in leak, operation, and rf were solved during this period.

The installation of the cyclotron in the RIKEN cyclotron vault started at the beginning of December 1988; the assembling is in progress without significant delay for completion by the end of March 1989. Figure 1 shows a photograph of the cyclotron at the cyclotron vault as of January 1989 as viewed from the downstream of the extraction beam line. Commissioning of the

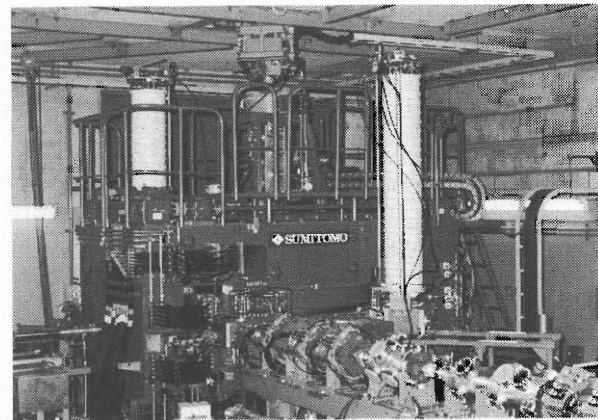


Fig. 1. Photograph of the cyclotron at the cyclotron vault as of January 1989 as viewed from the downstream of the extraction beam line.

cyclotron will start at the beginning of April 1989. The first beam planned is  $^{14}\text{N}^{5+}$  of 7 MeV/u. Upon coupling with RRC, the energy will go up to 135 MeV/u.

---

\* Sumitomo Heavy Industries, Ltd. (SHI).

### V-1-5. Magnetic Field Measurement of the Injector AVF Cyclotron

A. Goto, H. Takebe, T. Kageyama, N. Nakanishi,  
T. Tachikawa,\* and Y. Kumata\*

The magnet system of the injector AVF cyclotron has following characteristics. The magnet is of an H-type with four spiral sectors. A pole diameter is chosen to be 1,730 mm by taking account of the extraction radius of 714 mm, which is determined from the matching condition to RIKEN Ring Cyclotron (RRC). A pair of plugs made of iron to produce a central field bump are set at a corner of the central holes through an upper and a lower yoke. To compensate the reduction in the magnetic field near the extraction radius at high excitation levels, an iron shim is attached to the side of the outermost part of each sector. Nine pairs of circular trim coils are wound on the sectors and four pairs of harmonic coils are placed in the extraction region of valley sections. Maximum currents of a main coil, trim coils, and harmonic coils are 1,000 A, 360 A, and 120 A, respectively.

Magnetic field measurement was made at the factory of the company in April 1988. After determining the most appropriate field setting procedure, maps of base field and trim field were measured. Base field maps were measured for eleven levels of main coil currents. Trim field maps were measured for the maximum current of each trim coil at each level of six main coil currents, after confirming for a few trim coils that the distribution is proportional to the trim coil current. The azimuthal range of the map was 90° at intervals of 1.8° and the radial ranges were 1,200 mm for a base field and 800 mm for a trim field at interavals of 20 mm. The measurement of 360° maps was made at radial intervals of 100 mm to check the first harmonic component. Magnetic field distributions were also measured in the area through which an extracted beam passes and inside the hole of a yoke through which a beam from the ion source is injected.

Figure 1 shows the excitation procedure of main coil current for field setting optimized in the measurement. (For this setting procedure, the reproducibility of field distribution was better than  $2 \times 10^{-4}$ .) The excitation characteristics is

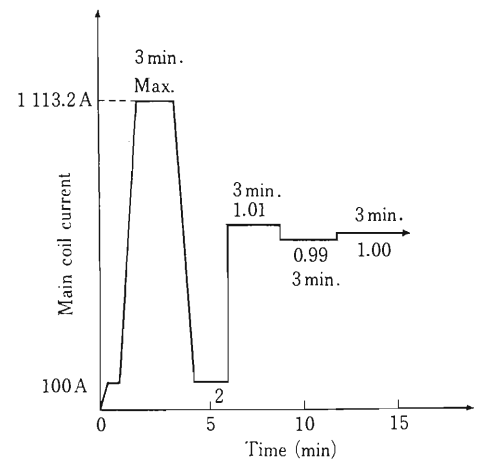


Fig. 1. Excitation procedure of main coil current for field setting.

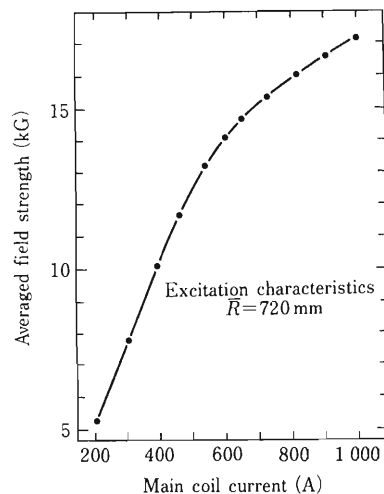


Fig. 2. Excitation characteristics of the cyclotron magnet.

given in Fig. 2. An average field of 17 kG, which is the designed maximum value required, was obtained at a main coil current of 970 A. The radial distributions of a base field and a trim field are shown in Fig. 3 and Fig. 4 (a) and (b), respectively. Bumps due to the plugs and the iron shim are seen in Fig. 3, in particular, at low levels. The excitation characteristics as well as the flutter and the betatron frequencies ( $\nu_r$ ,  $\nu_z$ ) are in accordance with the design. An un-

\* Sumitomo Heavy Industries, Ltd. (SHI)

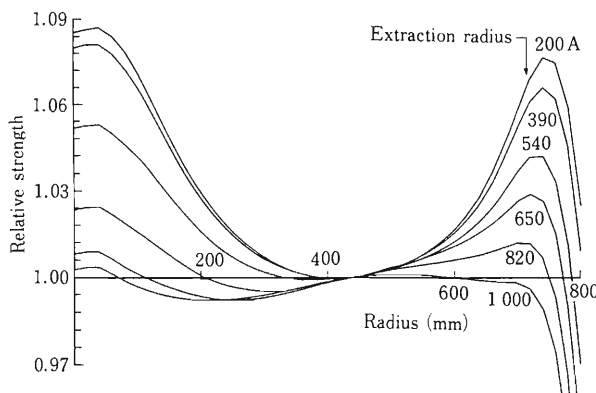


Fig. 3. Radial distributions of a base field at six excitation levels.

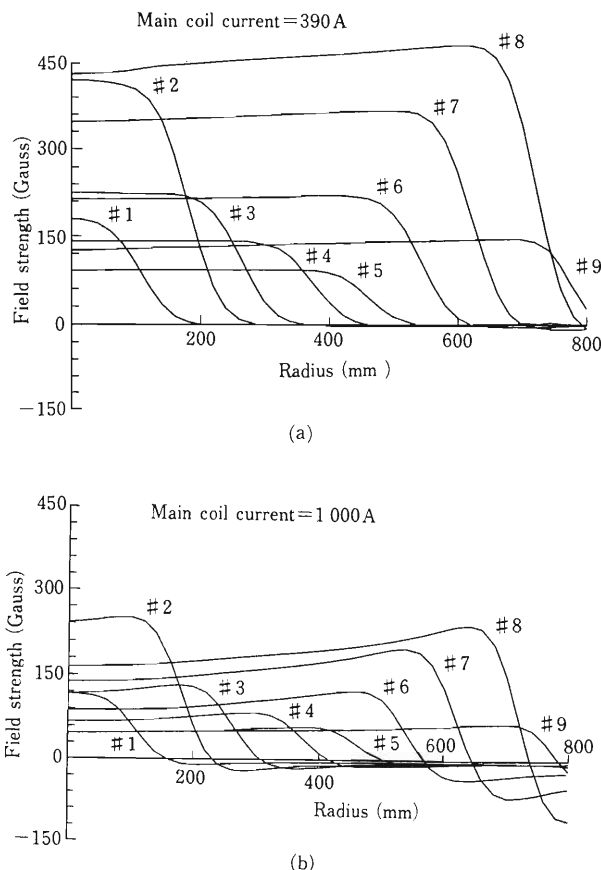


Fig. 4. Radial distributions of a trim field for nine trim coils (a) at a main coil current of 390 A, and (b) at 1,000 A.

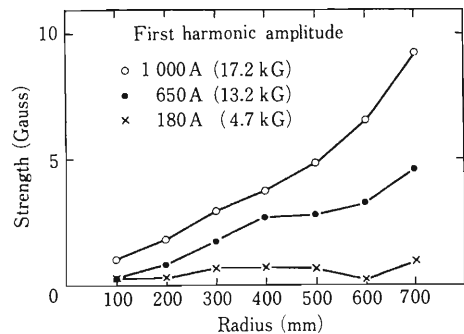


Fig. 5. Radial distributions of the first harmonic field at several excitation levels.

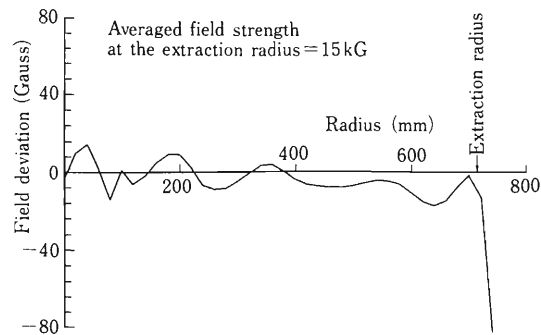


Fig. 6. Difference between the ideal isochronous field distribution and that predicted for 7 MeV/u  $^{14}\text{N}^{5+}$  ion.

expected first harmonic field appeared at higher excitation levels as shown in Fig. 5. The direction of this field lay nearly along one of the sector-center line. We found, however, from the computer simulation that this occurrence is tolerable and the designed extraction energy can be obtained.

The data base of average fields along equilibrium orbits, which will be used to produce an isochronous field, was deduced from the results of the measurement. In order to check the predictability of the method, the field distributions calculated by using the data base for the 7 MeV/u  $^{14}\text{N}^{5+}$  ion, which is expected to be the first beam, was excited and measured over the range of 360°. Figure 6 shows the difference between the ideal isochronous field distribution and the measured one. The result indicates that the prediction is satisfactory for the initial setting of an isochronous field distribution.

### V-1-6. Design of the Central Region of the Injector AVF Cyclotron

A. Goto

The injector AVF cyclotron is a type 750 PV of Sumitomo Heavy Industries, Ltd. (SHI), modified so as to be used as an injector for RIKEN Ring Cyclotron (RRC). One of the most significant changes from the 750 PV is the central region of the cyclotron. To design this region, a computer program has been developed that simulates a beam orbit, the acceptance of the cyclotron, and so on. Principal requirements are 1) a beam

should be accelerated on a well-centered orbit, 2) the acceptances of the cyclotron in  $(r, r')$  and  $(z, z')$  phase spaces should be as large as possible, and 3) the phase of a beam can be cut effectively with a phase defining slit. The optimal combination of the shape of a central field bump and the configuration of a central electrode of the rf resonator were searched to meet these requirements.

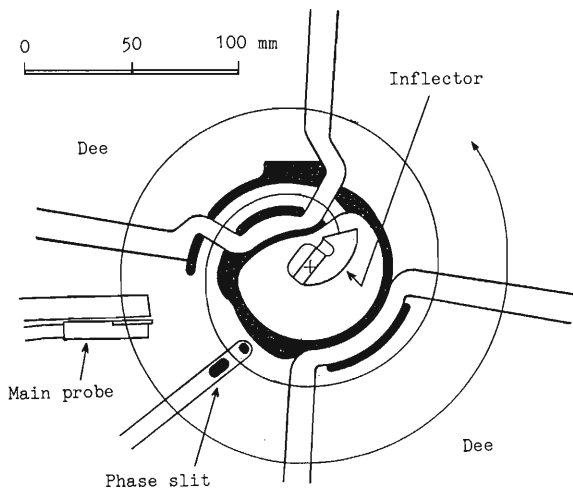


Fig. 1. Designed layout of the central region of the cyclotron.

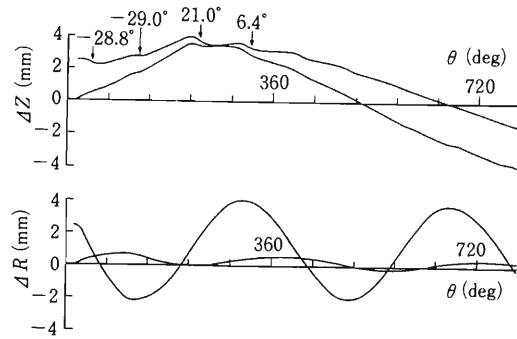


Fig. 2. Motions of two particles in both horizontal and vertical directions for the first two revolutions. The two particles are orthogonal to each other lying on either horizontal or vertical phase ellipse whose area is  $\pi \times 2.5 \text{ mm} \times 40 \text{ mrad}$ . Arrows and values indicate the positions of the first four gaps and the rf phases when the particles pass through the gaps.

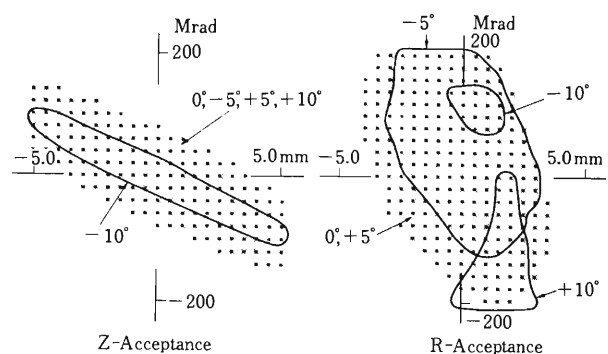


Fig. 3. Acceptances of the cyclotron in both horizontal and vertical directions for various injection phases.

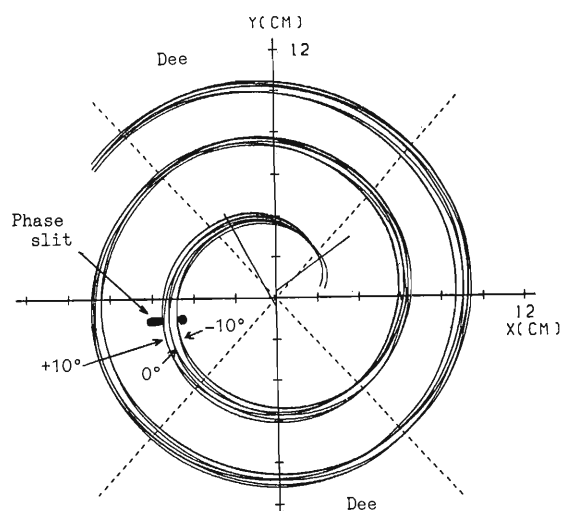


Fig. 4. Dependence of trajectories for the first few revolutions on the injection phase. Trajectories with the injection phases of  $0^\circ$  and  $\pm 10^\circ$  are simulated, each consisting of three particles: the central particle and two particles orthogonal to each other lying on the phase ellipse whose area is  $\pi \times 2.5 \text{ mm} \times 40 \text{ mrad}$ .

The layout of the central region thus determined is shown in Fig. 1. The peak of the central field bump is 1 %. Drift-tube-like pillars, which form a rectangular aperture, are placed at the first two gaps. The nose part of the electrode is remountable for maintenance or repair. Figure 2 shows the motions of selected two particles in both horizontal and vertical directions for the first two revolutions. Acceptances of the cyclotron in both directions are shown in Fig. 3 for various injection phases. This figure indicates that calculated acceptances within the injection phases of  $\pm 5^\circ$  or more cover an expected beam emittance of about  $100 \pi \text{ mm} \cdot \text{mrad}$  from the

ECR source. (Note that the gap of the inflector is 5 mm.) Here the definitions of acceptance are given by that, up to a radius of 20 cm, particles should lie within the distance of  $\pm 5 \text{ mm}$  and  $\pm 10 \text{ mm}$  from the central particle in the horizontal and the vertical directions, respectively. A movable phase defining slit is set in the first turn inside the dummy dee. The computer simulation indicates that the slit is very effective because at this place not only a beam spreads radially according to phase but also it shrinks with respect to the radial emittance as shown in Fig. 4.

### V-1-7. Calculation of the Extraction Orbit for the Injector AVF Cyclotron

T. Kageyama and A. Goto

The beam extraction system for the injector AVF cyclotron consists of an electrostatic deflector and a magnetic channel which peel off a beam from the last acceleration orbit, and a gradient corrector which focuses the beam hori-

zontally. The gradient corrector is of a passive type. The layout of the system is shown in Fig. 1, together with some other main components of the cyclotron.

To determine a beam trajectory in this system, we chose a 7 MeV/u  $^{14}\text{N}^{5+}$  ion as a reference particle. The initial beam parameters at the entrance of the deflector were obtained by tracing a group of particles from the exit of an inflector (the injection point) with a program code AVF4. Emittances at the exit of the inflector were assumed to be  $\pi \times 2.5 \text{ mm} \times 40 \text{ mrad}$ ,  $\pi \times 2.5 \text{ mm} \times 40 \text{ mard}$ , and  $\pi \times 6^\circ \times 1\%$ , in a horizontal, a vertical, and a longitudinal directions, respectively. A program code AVFEXT was used to calculate the extraction orbit from the entrance of the deflector up to the extraction hole of the vacuum chamber (at the point A in Fig. 1). In AVFEXT the fields of the deflector and the magnetic channel, and the field gradient of the gradient corrector were superimposed on the field distribution produced by the main coil and trim coils.

Figure 2 shows a beam separation between the extraction orbit and the last internal orbit for  $^{14}\text{N}^{5+}$  ions of 7 MeV/u. In general, the extraction orbit varies with the excitation level of the magnet, because the shape of fringe field distribution changes with the excitation level. To see the difference, we calculated extraction orbits for several fringe field distributions, *i.e.* for several excitation levels. Figure 3 shows examples of the dependence of extraction orbit on the main coil current. Deviations from the reference orbit at a main coil current of 685 A (corresponding to 7 MeV/u  $^{14}\text{N}^{5+}$ ) are shown for main coil currents of 200 and 1,000 A. As can be seen from Fig. 3, the beam position changes as long as about 8 mm at the entrance of the gradient corrector in order to transport a beam into the center of the hole at point A.

Beam sizes along the extraction orbit were also calculated by using AVFEXT. Figure 4 shows the change in the beam sizes in the horizontal and vertical directions for 7 MeV/u  $^{14}\text{N}^{5+}$  ions. A horizontal focusing and a vertical defocusing with the gradient corrector can be

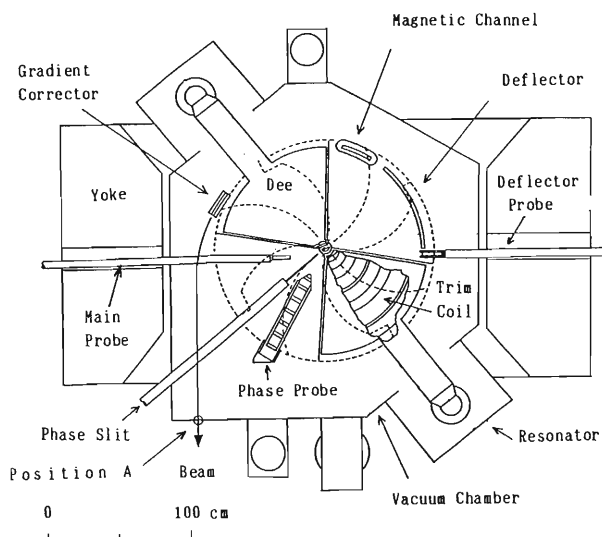


Fig. 1. Layout of the extraction system in the AVF cyclotron.

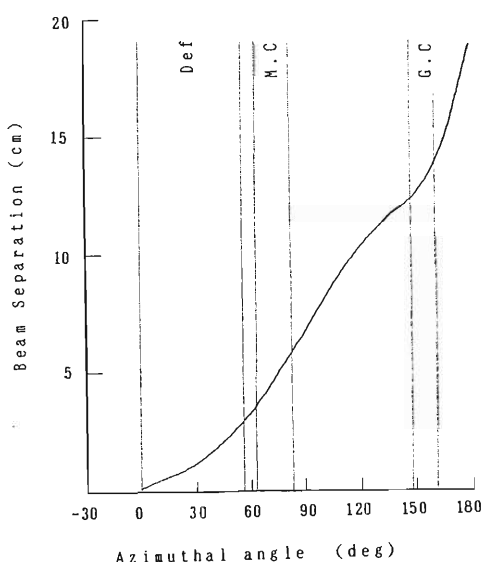


Fig. 2. Beam separation between the extraction orbit and the last internal orbit for 7 MeV/u  $^{14}\text{N}^{5+}$  ions as a function of the azimuthal angle in the AVF cyclotron. Def., deflector; M. C., magnetic channel; G. C., gradient corrector.

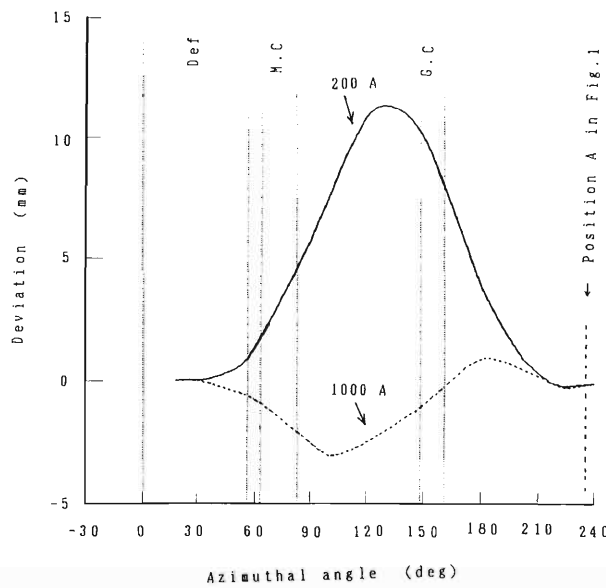


Fig. 3. Dependence of the extraction orbit on the excitation level of the magnet. Deviations from the reference orbit ( $^{14}\text{N}^{5+}$  ion of 7 MeV/u; the main coil current is 685 A) for main coil currents of 200 and 1,000 A.

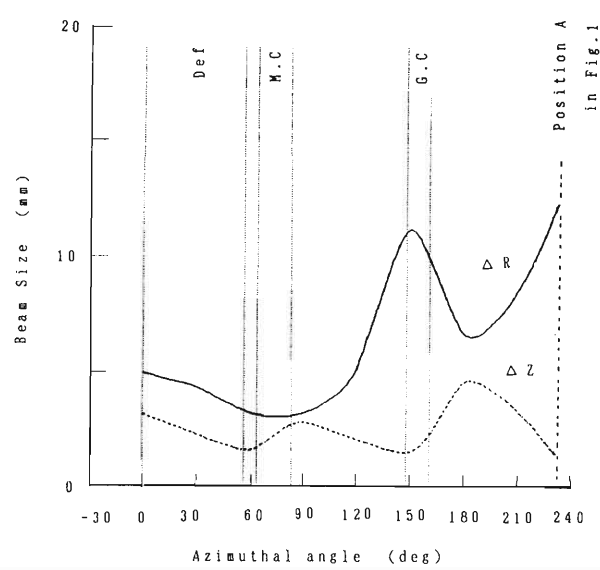


Fig. 4. Beam sizes calculated along the extraction orbit in both horizontal ( $\Delta R$ ) and vertical ( $\Delta Z$ ) directions.  $^{14}\text{N}^{5+}$  ion of 7 MeV/u was taken as an example.

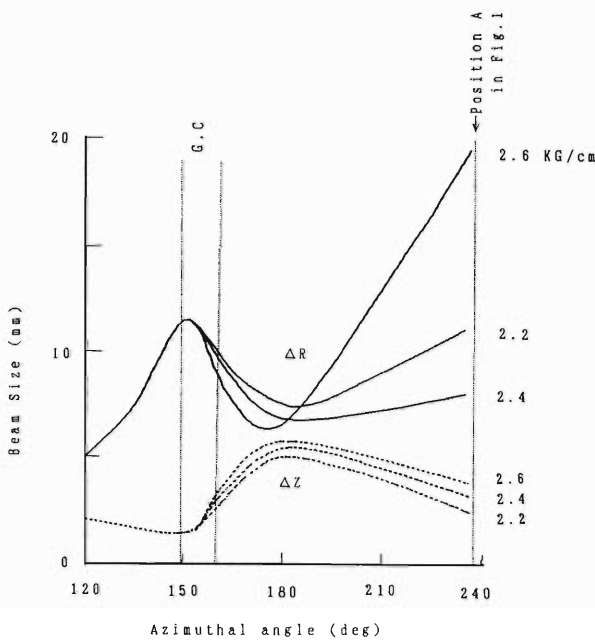


Fig. 5. Dependence of the beam sizes in the horizontal ( $\Delta R$ ) and the vertical ( $\Delta Z$ ) directions on the strength of field gradient of the gradient corrector for 7 MeV/u  $^{14}\text{N}^{5+}$  ions (the main coil current is 685 A).

seen from Fig. 4. To see the effect of the gradient

Table 1. Calculated horizontal beam sizes at the exit hole of the vacuum chamber (position A in Fig. 1) for various excitation levels of the magnet.

Main coil (A)	Field gradient inside G. C. (kG/cm)	Beam size (mm)
200	0.9	9
390	1.6	19
540	2.0	17
685	2.2	11
820	2.3	18
1,000	2.4	18

corrector, the beam sizes after the gradient corrector were calculated for several field gradients. The beam size in the horizontal direction was found to be strongly dependent on the strength as shown in Fig. 5. Table 1 gives the calculated horizontal beam sizes at point A for several excitation levels of the magnet. In the calculation the measured values were used for the strength of field gradient of the gradient corrector. The results show that the beam size can be kept rather small with this gradient corrector of a passive type at all excitation levels despite the sensitivity on the strength.

RIKEN Accel. Prog. Rep. 22 (1988)

### V-1-8. Measurement of the Characteristics of a Resonator of the Injector AVF Cyclotron

S. Kohara, A. Goto, and Y. Kumata\*

The electrical characteristics of a resonator of the injector AVF cyclotron for RIKEN Ring Cyclotron (RRC) were measured with a low-level signal at Sumitomo Heavy Industries, Ltd. in September 1988. The cyclotron<sup>†</sup> has two resonators,<sup>††</sup> which are of the coaxial quarter-wave-length type with a dee angle of 83°. A cross sectional view of the resonator is shown in Fig. 1. The frequency range is from 12 to 23 MHz. A shorting plate is used for coarse tuning and a

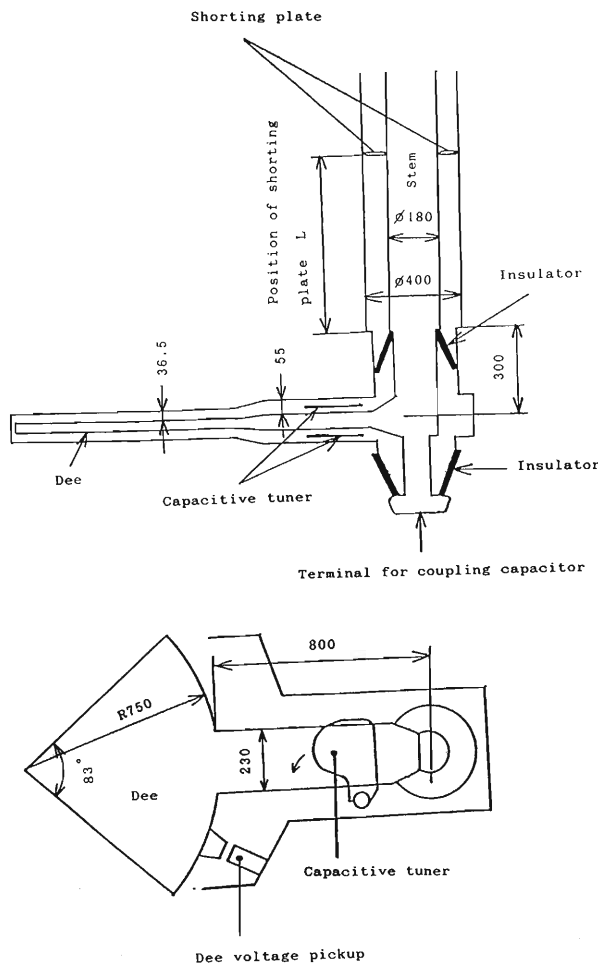


Fig. 1. Cross sectional view of the resonator.

\* Sumitomo Heavy Industries, Ltd. (SHI).

<sup>†</sup> This cyclotron is based on the SHI model 750 PV and modified to meet the requirement as an injector.

<sup>††</sup> SHI patent.

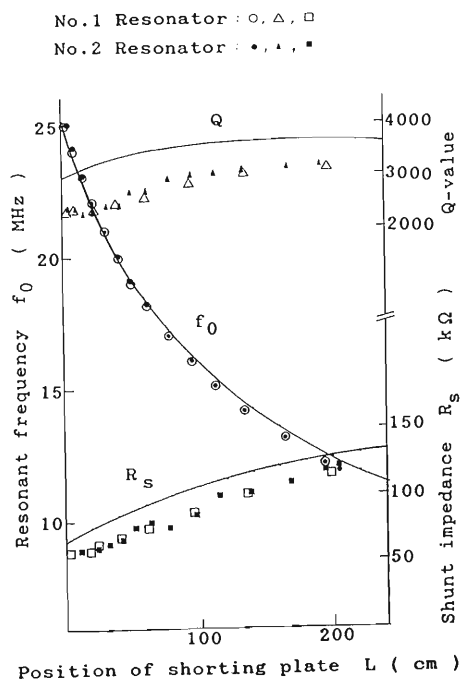


Fig. 2. Resonant frequencies,  $Q$ -values, and shunt impedances measured as a function of the position of the shorting plate. Solid lines are the calculations based on a transmission line approximation.

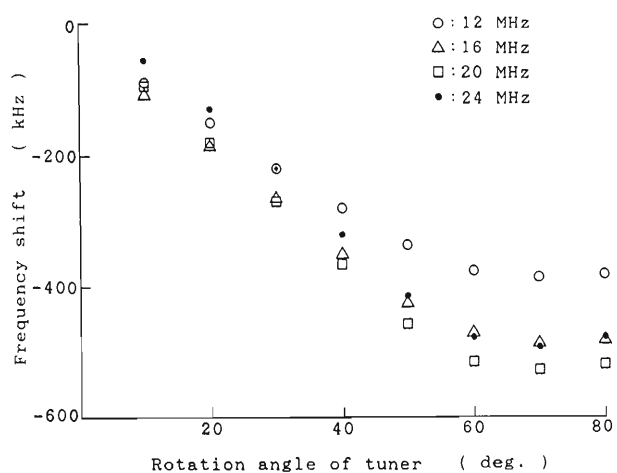


Fig. 3. Frequency shift of the capacitive tuner.

capacitive tuner for automatic fine tuning. The driving speed of the shorting plate is 32 cm/min. The contact fingers of the shorting plate are pressed with a pneumatic pressure of 5 kg/cm<sup>2</sup>. The rotation angle of a capacitive tuner is 90°. Ceramics insulators are used for support of a stem and a dee as well as for a vacuum seal.

Resonant frequencies, *Q*-values, and shunt impedances measured as a function of position of the shorting plate are shown in Fig. 2 for two resonators. No significant differences were seen

between the characteristics of the two resonators. The measurements were reproduced well by calculation based on a transmission line approximation as shown in Fig. 2. The traveling length of the shorting plate is 1.8 m for the required frequency range. Frequency shifts as a function of rotation angle of the capacitive tuner were measured and are shown in Fig. 3. Frequency coverage of the tuner is wide enough to compensate a frequency shift due to heat in normal operation.

### V-1-9. Power Test of the RF System for the Injector AVF Cyclotron

S. Kohara, M. Nagase, M. Saito, T. Kageyama,  
A. Goto, T. Fujisawa, and Y. Kumata\*

The RF amplifier system of the injector AVF cyclotron for RIKEN Ring Cyclotron (RRC) was preliminarily assembled at Sumitomo Heavy Industries, Ltd. (SHI) in October 1988. The excitation test of the resonator was also carried out there; the characteristics of the resonator had been measured beforehand.<sup>1)</sup> The power amplifier system consists of a solid-state wide-band amplifier (500W) and a grounded-cathode tetrode amplifier (EIMAC 4CW50,000E). An all-pass network is adopted in the input circuit of the tube.

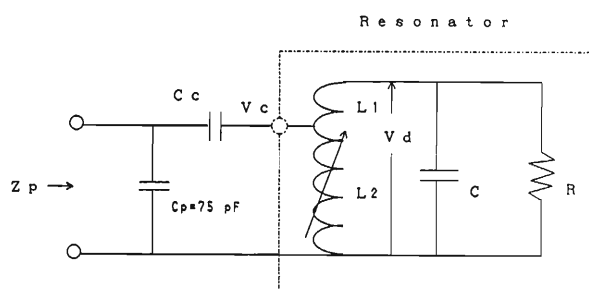


Fig. 1. Load circuit of the tube.

The specifications of the amplifier system were presented previously.<sup>2)</sup>

Figure 1 shows the equivalent circuit of the plate load of the tube (see Fig. 1 in Ref. 1). The amplifier is capacitively coupled<sup>†</sup> to the resonator with a coupling capacitor ( $C_c$ ). The output capacitance ( $C_p$ ) of the tube was measured to be 75 pF. The load impedances ( $Z_p$ ) of the tube and the ratios ( $V_c/V_d$ ) of the voltage at the coupling position ( $V_c$ ) to the dee voltage ( $V_d$ ) are shown in Fig. 2. The ratio decreases as the frequency increases because the inductance ( $L_2$ ) decreases as the frequency increases. The load impedance thus becomes very low at high frequencies.

The results of the power test for several frequencies are shown in Table 1. Required accelerating voltages were obtained in a frequency range from 12 to 22 MHz. At 23 MHz, however, the required accelerating voltage could not be obtained with the wide-band amplifier whose maximum output power is 500 W. This is because the load impedance is too low at this frequency.

Table 1. Measured results of operational conditions of the amplifier. RF voltages are peak values.

Frequency (MHz)	Pre-amplifier output power (W)	Screen grid current (mA)	Final amplifier			
			Plate current (A)	RF control grid voltage (V)	RF plate voltage (kV)	Accelerating voltage (kV)
12	270	5	1.2	120	7.8	41
13	310	10	1.6	140	7.6	43
14	340	20	1.8	140	7.0	45
15	370	20	2.0	160	6.7	48
16	450	30	2.5	160	6.6	50
18	300	5	2.2	150	4.0	36
20	310	2	2.4	150	2.8	32
22	460	0	3.1	180	2.4	33
23	480	0	3.0	160	1.7	28

DC plate voltage : 10kV

DC screen voltage : 1,200V

DC control voltage : -300V

\* Sumitomo Heavy Industries, Ltd. (SHI).

† SHI patent pending.

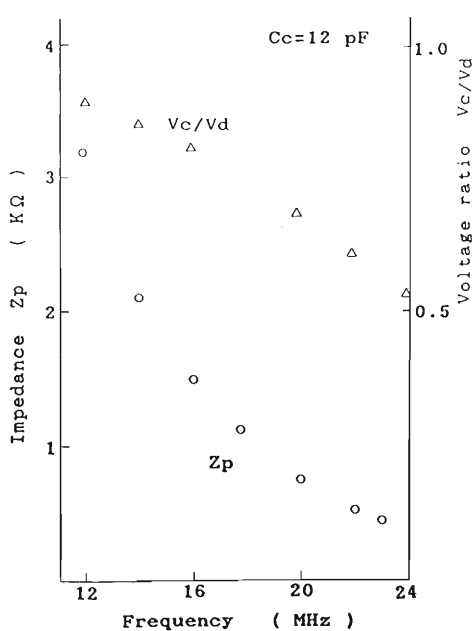


Fig. 2. Load impedances of the tube and the ratios of the voltage at a coupling position to the dee voltage.

In the above measurement a fixed capacitor of 12 pF was used for the coupling capacitance. This value was low to some extent for high frequencies. It is desirable to use a variable capacitor in order to get good impedance matching between the amplifier and the resonator. However, because a variable capacitor initially installed had been broken in the excitation test, the fixed capacitor was used tentatively. The coupling capacitor is planned to be replaced from 12 to 16 pF to get the required accelerating voltage at 23 MHz as well in the power test that will be carried out at RIKEN in the spring of 1989.

#### References

- 1) S. Kohara, A. Goto, and Y. Kumata: This Report, p. 209.
- 2) S. Kohara, M. Nagase, M. Saito, T. Kageyama, A. Goto, and T. Fujisawa: *RIKEN Accel. Prog. Rep.*, **21**, 214 (1987).

RIKEN Accel. Prog. Rep. 22 (1988)

### V-1-10. Beam Buncher in the Injection Beam Line for the Injector AVF Cyclotron

K. Ikegami and A. Goto

A beam buncher has been developed for efficient bunching of D.C. beams from the ion source. The buncher is to be placed in the injection beam line at 2 m upstream from the inflector set in the center of the median plane of the AVF cyclotron. The buncher consists of two parallel mesh plates forming a single accelerating gap, and is excited by an RF voltage with a sawtooth-like waveform. The sawtooth-like wave calculated by combining RF sine waves with the first three higher harmonics is shown in Fig. 1. The combined RF voltage  $V_b$  is given by  $V_b = V_0 (\sin \omega_0 t + 1/3 \sin 2\omega_0 t + 1/9 \sin 3\omega_0 t)$ . Figure 2 shows a block diagram of the buncher circuit. A fundamental frequency range is 12-24 MHz. Required peak-to-peak amplitudes of fundamental, second harmonic, and third harmonic frequencies are

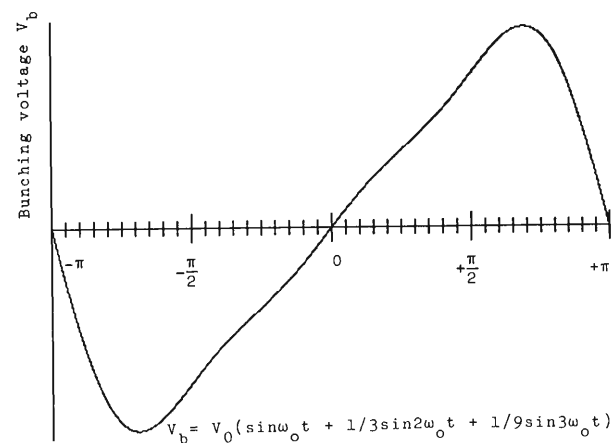


Fig. 1. Sawtooth-like waveform calculated by combining RF sine waves with fundamental ( $\omega_0$ ), second harmonic ( $2\omega_0$ ), and third harmonic ( $3\omega_0$ ) frequencies.

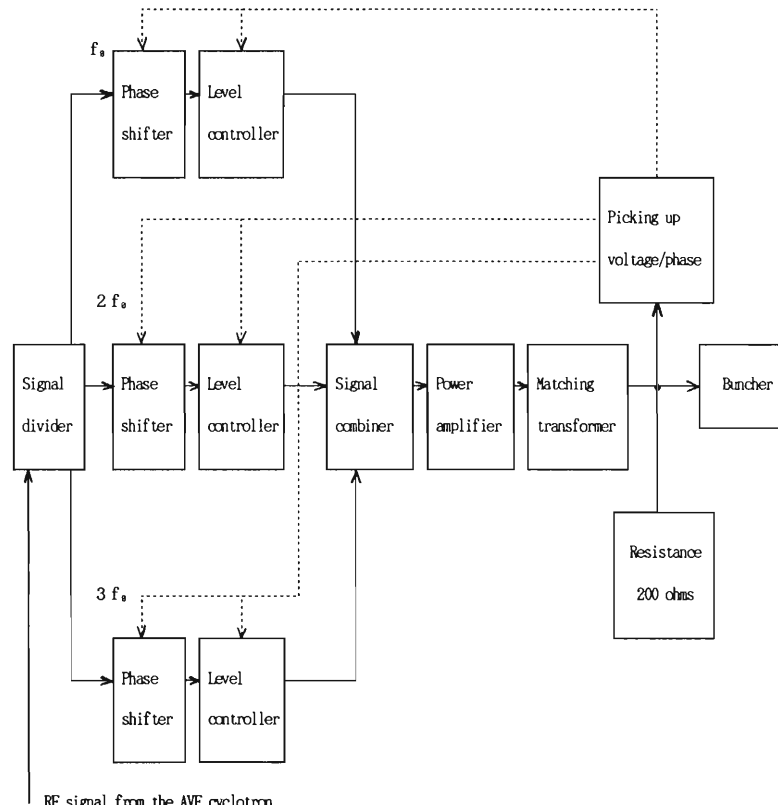


Fig. 2. Block diagram of the buncher circuit.

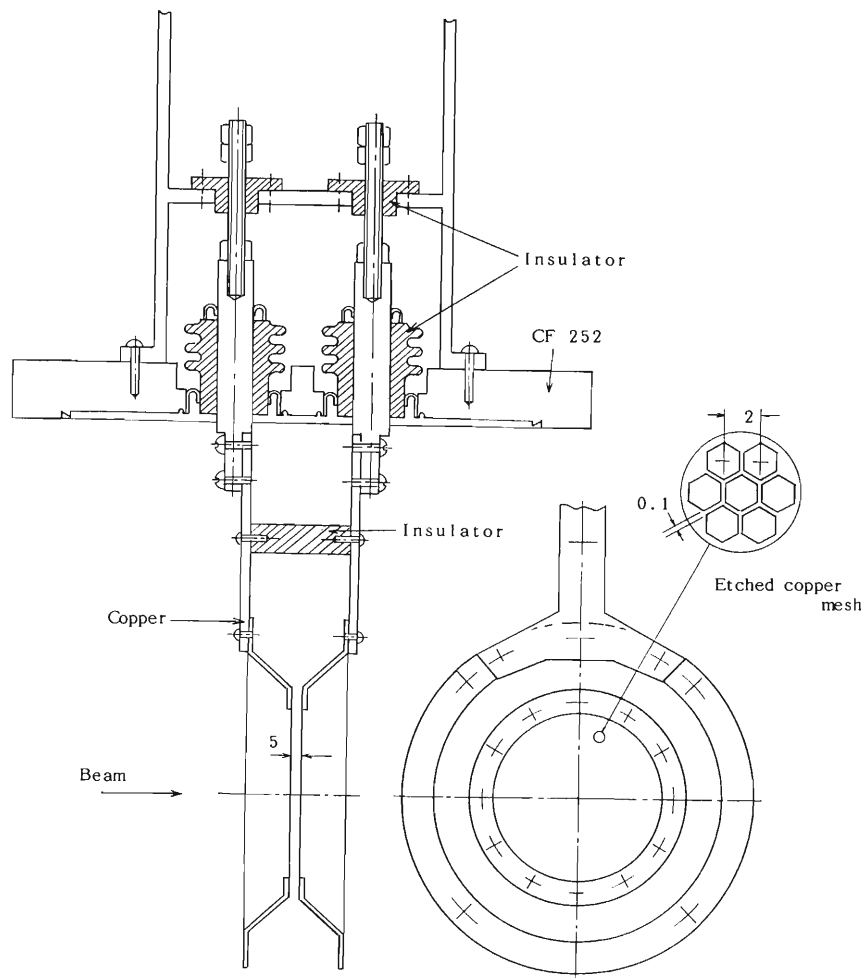


Fig. 3. Schematic drawing of the electrodes of the beam buncher along the beam axis.

750V, 450V, and 150V at the maximum, respectively. The stabilities of the voltage and the phase should be within less than  $\pm 1 \times 10^{-3}$  and  $\pm 0.5^\circ$ , respectively. The combined RF voltage is applied through a matching transformer to one of the two electrodes to which a resistance of  $200\Omega$  is connected in parallel. A combination of the matching transformer and the resistance of  $200\Omega$  is used to decrease the combined RF power as low as possible. The maximum required RF power is 500 W. Figure 3 shows a schematic

drawing of the electrodes of the beam buncher along the beam axis. Two electrodes with tortoise shell (hexagon)-shaped mesh are made of etched copper plates and are insulated with ceramics. The size of the hexagon is 2 mm. Both width and thickness of the mesh are 0.1 mm. The gap between two electrodes is 5 mm and the diameter of the mesh section is 60 mm. The beam transmission of the mesh is estimated at more than 83 % ( $0.91 \times 0.91$ ).

### V-1-11. Model Study of the Beam Rebuncher for the Injector AVF Cyclotron and RIKEN Ring Cyclotron

A. Goto, M. Saito, S. Kohara, and R. Abe\*

A beam rebuncher was designed for use in the beam transport line between the injector AVF cyclotron and RIKEN Ring Cyclotron (RRC). The design concept is almost the same as that of the beam rebuncher used in the beam transport line between RILAC and RRC.<sup>1)</sup> A fourth harmonic mode with respect to the rf frequency of the AVF cyclotron was adopted to help reduce the maximum required voltage and the length of gap separation. (Note that the rf frequency of RRC is twice that of the AVF cyclotron.) A multi-gap system was also adopted for further reduction of required voltage. The characteristics of the beam rebuncher thus determined by taking ion-optical calculations into account are as follows:

Frequency range	48-90 MHz
Harmonics	4
Number of gaps	3
Maximum peak voltage per gap	40 kV
Width of each gap	25 mm
Separation of gaps	280 mm
Aperture of beam transmission	40 mm

A 1/3-scale model of the beam rebuncher was constructed, and its electrical characteristics were measured. Figure 1 shows the schematic

drawing of the model.

The resonator is of a shielded Lecher-wires type with two stems. At the end of each stem a drift tube is mounted, which forms three gaps. The resonant frequency is adjusted with a shorting plate and a pair of capacitive frequency tuners. The rf power is fed into the resonator through a  $50 \Omega$  coaxial feeder line coupled with the resonator by a tunable capacitive coupler.

Measurement was performed for a few combinations of positions of the capacitive frequency tuner ( $d$ ) and the shorting plate ( $s$ ), whose definitions are given in Fig. 1. Figure 2(a) gives resonant frequencies,  $Q$  values, and shunt impedances against  $s$  for  $d=95$  mm (max.); Fig. 2(b) is the same as Fig. 2(a) except for  $d=10$  mm. In these figures the results and the values of  $s$  and  $d$  are converted for use in the actual scale by multiplying a scale factor. The shunt impedance was obtained with a perturbation method using a dielectric ceramic bead. Calculations with a transmission line approximation are compared to the data for three values of capacitances produced by the drift tubes and the frequency tuners.

By taking the above results into account, the

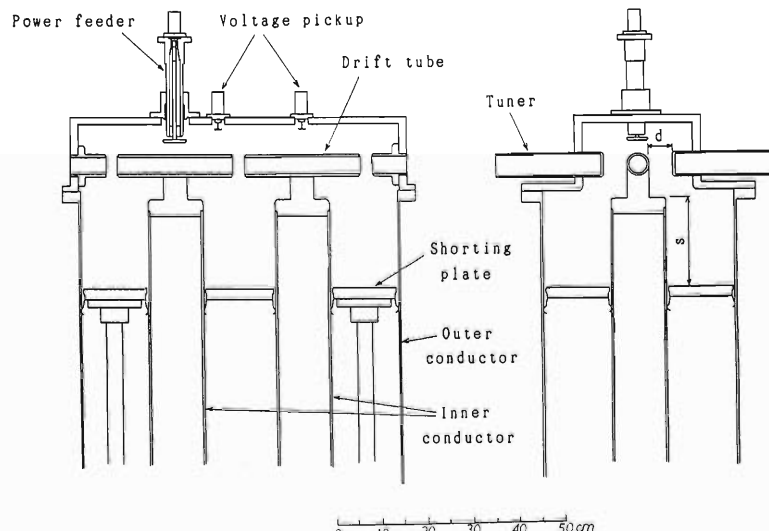


Fig. 1. Schematic drawing of the model rebuncher.

\* Sumijyu Accelerator Service, Ltd.

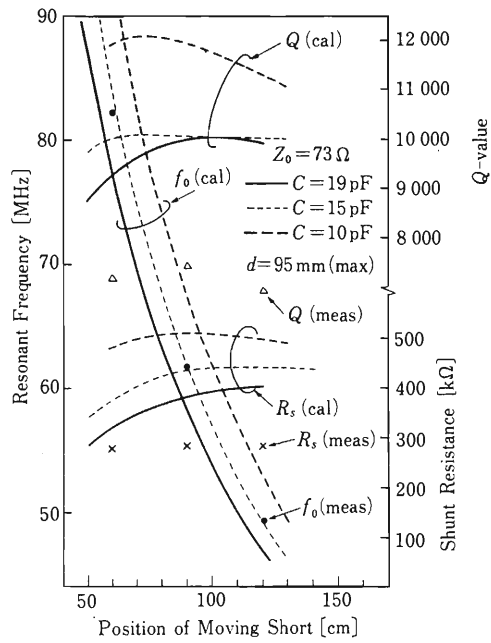


Fig. 2(a). Measurements of resonant frequencies,  $Q$  values, and shunt impedances against the position of the movable shorting plate for  $d=95$  mm (max.). Calculations using a transmission line approximation are also shown for comparison for three values of capacitances produced by the drift tubes and the frequency tuners.

design of actual beam rebuncher has been fixed. The length of a stem ( $s$ ) was chosen to be 90 cm and the maximum power of a power amplifier to be 3 kW. The outer tube of the shielded Lecher-wires part has been decided to be a cylinder rather than a racetrack shape because of easiness of fabrication. The beam rebuncher system

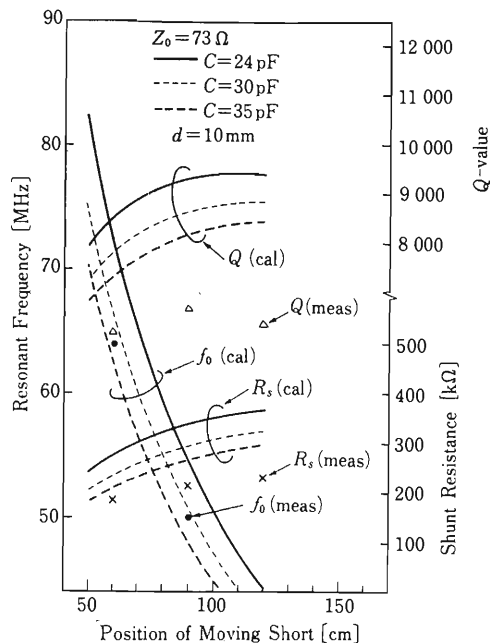


Fig. 2(b). The same as Fig. 2(a) except for  $d=10$  mm.

is scheduled to be completed by the end of March 1989.

#### Reference

- 1) A. Goto, T. Fujisawa, and I. Takeshita: *RIKEN Accel. Prog. Rep.*, **18**, 184 (1984).

RIKEN Accel. Prog. Rep. 22 (1988)

## V-1-12. Rotational Beam Scanner

M. Kase, I. Yokoyama, and M. Saito

A rotational beam scanner was made and installed in a momentum analysing section of the beam line from the injector linac (RILAC) to RIKEN Ring Cyclotron (RRC). With this scanner, one-dimensional beam profiles can be measured continuously. For a well-tunned beam, the scanner can work as a monitor for a beam energy and its spread as well as a relative beam intensity.

Figure 1 shows a schematic diagram of the rotational beam scanner. The detection part is a tungsten straight wire of 0.5 mm in diameter and 40 mm in length, supported at its one end with a rotational ceramic arm. The wire moves on a circle of 60 mm in diameter around a rotation rod which is perpendicular to the beam axis. As a result, the wire scans a beam twice every turn in different directions. The rod is introduced out of a vacuum chamber through a magnetic-fluid vacuum seal, and there connected to three components. The first one is a dc motor, which can drive the scanner over 60-1,200 rpm through gears.

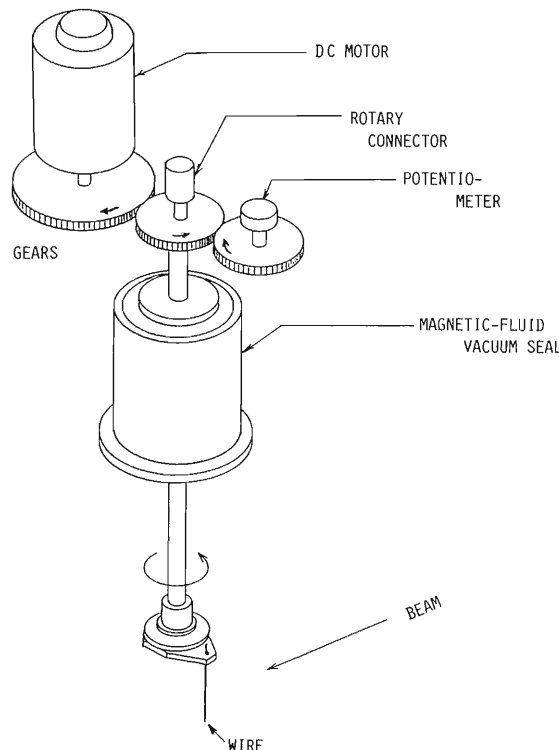


Fig. 1. Schematic view of the rotational beam scanner.

The second is a potentiometer, which generates a voltage signal approximately proportional to sine of a rotational angle of the rod. It gives a distance of wire from the beam axis after some calculations. The third components, a mercury-type rotary connector, is combined directly to the rod, permitting an electric connection between a rotated signal line from the wire and a fixed BNC connector with a low noise level. These mechanical components were selected in view that they can stand for a long-term and continuous use without any maintenance.

Electronics is shown in Fig. 2. The position signal becomes  $-10$  to  $10$  V through an amplifier, AMP1. The current signal from the wire is converted to a voltage signal ( $-10$  to  $0$  V) with a gain-controllable amplifier, AMP2. These two signals, after passing through sample holders, are fed to analog inputs of DIM (Device Interface Module<sup>1)</sup>). Turning on/off of a motor power supply, gain-control of AMP2, and a trigger to the sample holder are done by DIM with digital I/O ports. DIM samples the two analog signal periodically (typically every 2 ms), stored these data in a 2 kB memory, and, after a memory becomes full, transfer the data to a host computer (Mitsubishi M60 for RILAC control). DIM repeats these processes every few seconds.

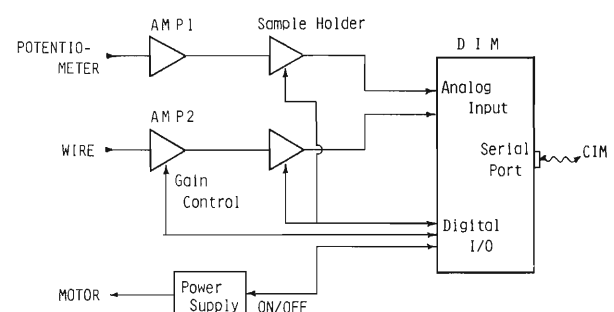


Fig. 2. Electronics for the rotational beam scanner.

Figure 3(a) and (b) show a set of typical raw data obtained in one measurement. Because of a time variation in beam intensity, for obtaining a reliable beam profile, it is necessary to scan a beam several times during one measurement, and

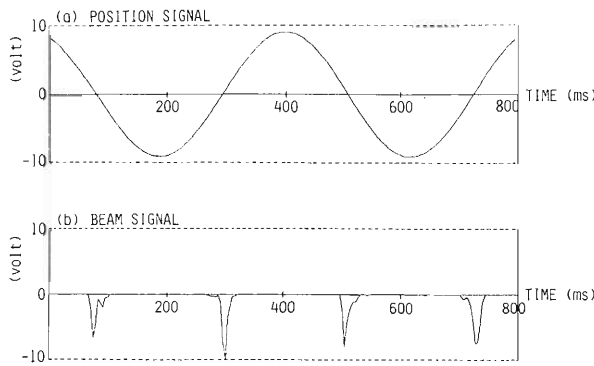


Fig. 3. Data for position (a) and beam signal (b), which are taken by DIM.

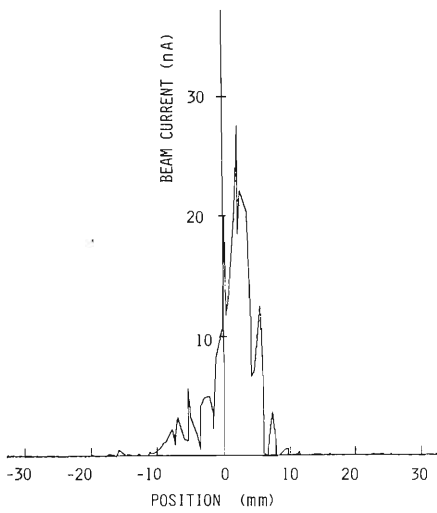


Fig. 4. Beam profile obtained from the data in Fig. 3.

to convert these data into a beam profile. Thus obtained profile are shown in Fig. 4. The computer shows a beam profile on a colour graphic display of the operational console and also immediately calculates an averaged beam position, a

beam width, and the area of the distribution.

Since the beam scanner is installed at a momentum analysing section of the beam transport line, after a beam is tuned, the beam position gives a relative beam energy from RILAC; a position shift of 1 mm corresponding to an energy variation of about 0.1%. The beam width gives a rough idea about an energy spread in the same way. If a noise effect is subtracted from the area of the beam profile, the area should be proportional to the beam intensity. Once calibration is done with a Faraday cup at the same position for each kind of beam, it can also work as a beam intensity monitor. These measurements can be made down to a 1 nA beam (in case of Ar beam, for example) with fairly good accuracy.

For an efficient operation of RRC, it is required to keep the injector as stable as possible. For monitoring the stability, this beam scanner will be very helpful. Since the averaged fraction of a beam interrupted by the wire is less than 0.6%, the continuous measurement is possible. The latest data are immediately transferred to a main computer of RRC via a local area network between computers. At a operational console of RRC, one can see the variation in energy, its spread, and intensity of a beam from RILAC, when necessary.

We plan to use this scanner on every stage of accelerator, that is, at exits of ion sources and the new injector (AVF cyclotron) and also at the exit of RRC itself, and to construct a beam stabilizing system for the whole accelerator using these scanners.

#### Reference

- 1) M. Kase and I. Yokoyama: *RIKEN Accel. Prog. Rep.*, **21**, 201 (1987).

RIKEN Accel. Prog. Rep. **22** (1988)

### V-1-13. Status of the RIKEN Electron Cyclotron Resonance Ion Source (ECRIS) for an Injector AVF Cyclotron

K. Hatanaka, H. Nonaka, E. Ikezawa, and W. Yokota

An ECR ion source for an AVF-ring cyclotron complex has been constructed. The source, assembled and pumped down on April 8, 1988, is used to produce highly charged ions for relatively heavy elements (up to Ca). The first plasma was ignited on April 11, and an Ar<sup>8+</sup> beam was successfully analyzed with the intensity of 15  $\mu$ A on April 13. The source has been operated mainly with gaseous elements since then. Through further half a year development, the beam from the source will be axially injected into the AVF cyclotron.

The design of the RIKEN-ECRIS was discussed elsewhere.<sup>1,2)</sup> The source consists of two stages: the first stage, 6 cm in diameter and 25 cm

long, is used for plasma filamentation and the second stage, 10 cm in diameter and 52 cm long, for production of highly charged ions. It is provided with three gas feeding lines: two at the first stage and another at the second stage for gas mixing.

After some improvements, the source has intensively operated since June 20. Up to now, ions are produced for nine kinds of gaseous elements. The present source performance is summarized in Table 1. These currents represent the "typical best" results from the source with a natural isotopic abundance. In the table 1, maximum energies attained with the AVF-ring cyclotron complex are listed for ions which can be

Table 1. Ions from RIKEN ECRIS.

	<sup>12</sup> C	<sup>14</sup> N	<sup>16</sup> O	<sup>19</sup> F	<sup>20</sup> Ne	<sup>32</sup> S	<sup>40</sup> Ar	<sup>84</sup> Kr	<sup>129</sup> Xe
Charge state	CO <sub>2</sub> +He	N <sub>2</sub> +He	O <sub>2</sub> +He	CHF <sub>3</sub> +He	Ne+He	SF <sub>6</sub> +O <sub>2</sub>	Ar+O <sub>2</sub>	Kr+O <sub>2</sub>	Xe+O <sub>2</sub>
1									
2	85	300	180						
3	*	230	225	45	110				
4	56◎	155	*	46	115				
5	12	110◎	120◎	33	*	11			
6		24	125	*	95	*	52		
7			20	18◎	50◎	24	72		
8				*	35	*	95		
9				0.05	1.1	16◎	87		
10						*	*	20	
11						2.4	30○	23	
12						*	10	*	
13						0.025	2.2	27	4.8
14							0.5	25	5.0
15								15	5.0
16								5.3	*
17								2.5	5.0
18								*	5.5
19								1.6	5.5
20								0.6	5.2
21								*	
22								0.1	

Currents in e  $\mu$ A.

13 kV extraction voltage (10 kV for Xe).

Final beam energy at the ring cyclotron is 135 MeV/u (◎), 110 MeV/u (○), 95 MeV/u (○).

accelerated by the injector AVF cyclotron. For all elements, gases are fed only to the first stage. Gas flow rates are not measured directly, but are controlled by monitoring the pressure of the first stage. Usually, the pressure is  $4 \times 10^{-5}$ ,  $3 \times 10^{-6}$ , and  $2 \times 10^{-7}$  Torr at the first, second, and extraction stage, respectively. Typical RF powers of 50 W and 800 W are fed to the first and second

stage, respectively. The extraction voltage is 13 kV except for Xe (10 kV). Figure 1 shows a schematic drawing of the charge analyzing system. Openings of SLITS 1 and 2 are 20 mm in full width for lighter elements up to Ar. They are reduced to 10 and 2 mm for Kr and Xe, respectively, in order to resolve adjacent peaks. Figure 2 shows a typical spectrum obtained with Xe.

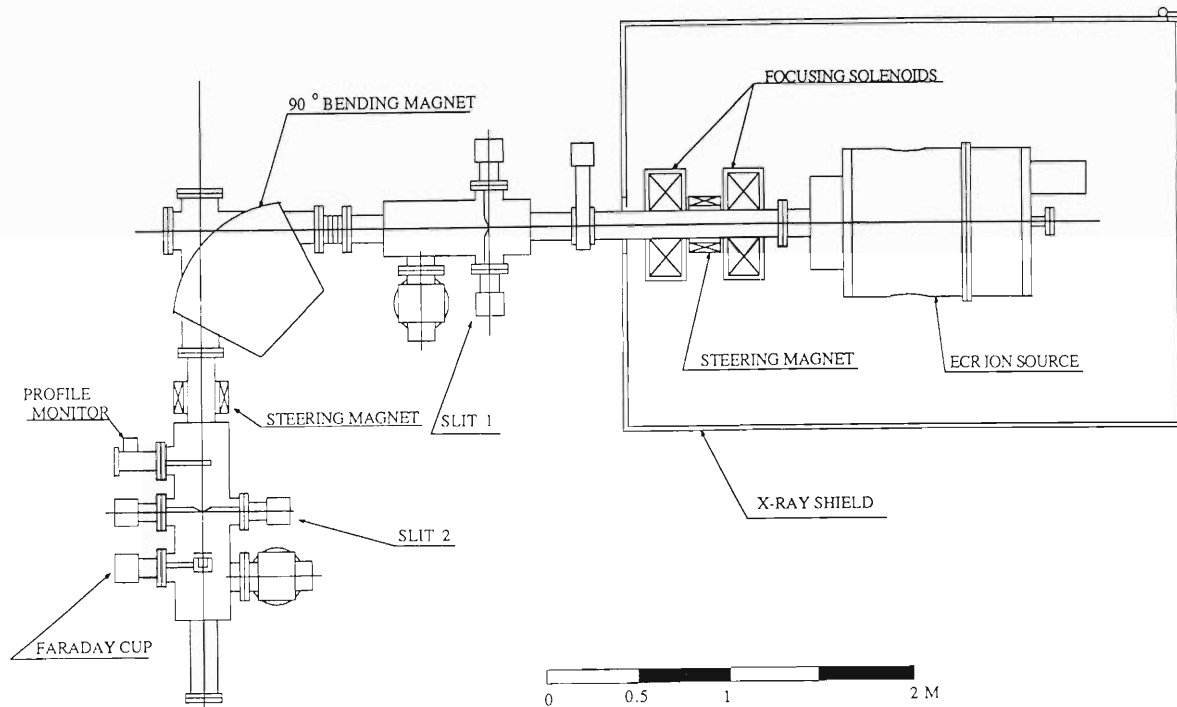


Fig. 1. Schematic drawing of the charge analyzing system.

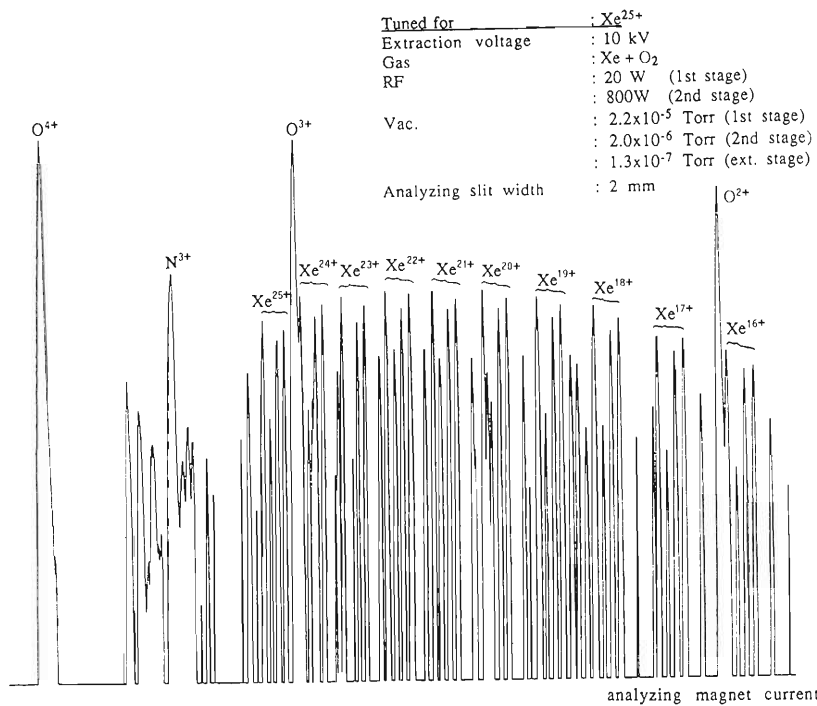


Fig. 2. Charge state spectrum with Xe.

Table 2. Gas mixing effect.

CS.	Gas	<sup>12</sup> C			<sup>20</sup> Ne	
		CH <sub>4</sub> +O <sub>2</sub>	CO <sub>2</sub> +O <sub>2</sub>	CO <sub>2</sub> +He	Ne+O <sub>2</sub>	Ne+He
2	41	85	85			
3	*	*	*	110	110	
4	6.3	37	56	115	115	
5	0.3	2.3	12	*	*	
6				63	95	
7				24	50	
8				14	35	
9				0.3	1.1	

Table 2 summarizes the performance with different combinations of gases for C and Ne. It can be seen that helium is a better support gas for Ne than oxygen. For the carbon beam, CO<sub>2</sub> gas gives better performance than CH<sub>4</sub> gas. A similar result is obtained with a PIG source. From the beam size measured at the SLIT 2, the emittance of the beam from the source is estimated to be less than  $100\pi$  mm•mrad, which is smaller than that assumed in the design of the beam transport system.

A low temperature oven for solid elements was constructed and preliminary tests have been performed with magnesium. Oxygen gas was fed

to the first stage for plasma filamentation, and magnesium vapor was introduced to the second stage. A <sup>24</sup>Mg<sup>7+</sup> beam was obtained with the intensity of 3  $\mu$ A. Further improvements are required to extract more intense beam from the source.

#### References

- 1) K. Hatanaka, H. Nonaka, and H. Kamitsubo: Proc. Int. Conf. ECR Ion Sources and Their Applications, p. 353 (1987).
- 2) K. Hatanaka and H. Nonaka: *RIKEN Accel. Prog. Rep.*, **21**, 212 (1987).

### V-1-14. Basic Study of a Polarized $^3\text{He}$ Ion Source by Laser Optical Pumping. I

T. Fujisawa, A. Minoh, Y. Taniguchi, S. Ishii,  
K. Hatanaka, and Y. Oshiro\*

Despite a polarized  $^3\text{He}$ -ion beam is very useful to study nuclear physics, no extensive development of the source has been made since the first polarized beam was accelerated in 1968,<sup>1)</sup> and only three ion sources are at work in the world.<sup>1-3)</sup> Recently, a new method was developed to produce polarized  $^3\text{He}$  by laser optical pumping<sup>4)</sup> and ECR ion sources deliver high intensity beams of high charge state heavy ions very stably. We study a new polarized  $^3\text{He}$  ion

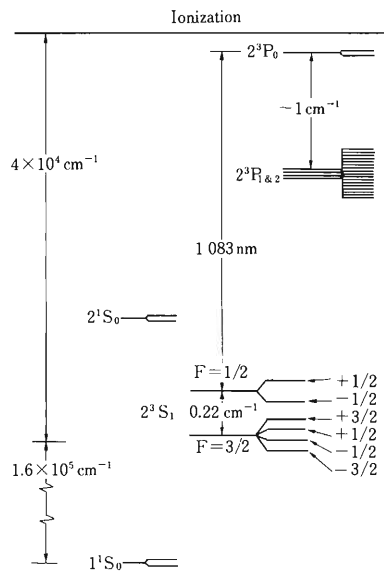


Fig. 1. Energy levels of  $^3\text{He}$  atom in an external magnetic field. See Ref. 5.

source consisting of a laser system and an ECR ionizer. The procedure of the optical pumping has been known<sup>1,5)</sup> but no powerful light source had been available. Figure 1 shows energy levels of  $^3\text{He}$  atom in an external magnetic field. The  $2^3\text{S}_1$  metastable state has a long lifetime (4,000 s) and the  $2\text{P}$  state spontaneously decays to the  $2\text{S}$  state by emitting the light (1,083 nm). Thus the  $2\text{S}$  state atom and a  $^3\text{He}$  nucleus can be polarized if the  $2\text{S}$  state atom is excited to the  $2\text{P}$  state in a magnetic field by absorbing the circularly polarized light which travels along the magnetic field, because the  $z$ -component of spin of the circularly polarized light is 1 or -1 corresponding to its polarization. Figure 2 shows a block diagram of the polarized  $^3\text{He}$  ion source proposed. The 1,083 nm linearly polarized light is produced from a LNA crystal excited with an Ar laser (514 nm) and polarized circularly by a quarter wavelength plate. In the RF discharge region where a weak magnetic field is supplied, the ground states of  $^3\text{He}$  are excited to the  $2\text{S}$  triplet states by an RF electro-magnetic field, and the  $2\text{S}$  states are excited to the  $2\text{P}$  states by circularly polarized light. The polarization of the  $2\text{S}$  state transfers to the ground state. The polarized atoms are transported into the ionization region and ionized by an RF field (28 GHz, 1 kW) in a static magnetic field (about 1 Tesla) strong enough to

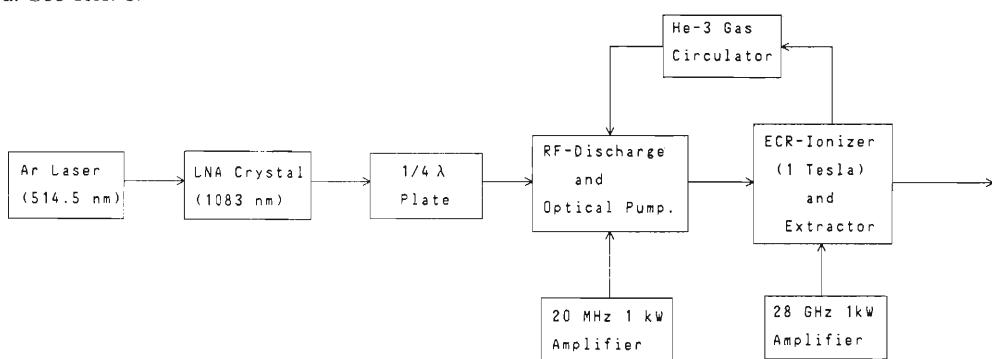


Fig. 2. Block diagram of a polarized  $^3\text{He}$  ion source by laser optical pumping.

\* Institute for Nuclear Study, University of Tokyo.

hold the nuclear polarization. The study of the discharge system is described in the present report and the development of the laser system in a separate one of this progress report.<sup>6)</sup>

The 2S metastable states are created by several method, for example, by RF discharge, DC discharge, or charge exchange reactions of atoms. We tried to create the 2S state by RF discharge with the dissociator of the atomic

beam type polarized ion source (INS-PIS) installed on the cyclotron of the Institute for Nuclear Study of the University of Tokyo, which is shown in Fig. 3. The dissociator tube is made of Pyrex and the aperture of the exit channel is 2.2 mm. In this study,  $^4\text{He}$  gas is used for economical reason. The gas was excited by a 20 MHz RF electro-magnetic field and flew into the ionizer through the sextupole magnet whose field converges only He atoms whose spin components are +1. Consequently, the intensity of the He beam in the ionizer becomes higher when sextupole field is supplied than that when not supplied if a significant amount of 2S state atoms are created. The  $\text{He}^+$  ion beam is extracted by 8 kV DC voltage and separated from other ions with a bending magnet next to the ionizer. We measured the difference of the beam intensities between when the sextupole field was supplied and when not supplied but we detected no difference. We consider several reasons why the difference was not detected.

1. Impurities in the He gas quenched the 2S state created in the tube.
2. The 2S state atoms spontaneously decay to the ground state by collision with the wall of the dissociator tube.
3. The 2S state atoms decay to the ground state by collision with other He atoms.
4. A substantial amount of 2S state atoms are not produced in the tube.

We have examined these issues. First, the He gas was passed through a liquid nitrogen trap to remove impurities, but no current difference was observed. Second, we used the dissociator tube with an aperture of 8 mm in diameter to extract He atoms without colliding on the wall of the aperture. The RF discharge was carried out at gas pressures of 0.01 Torr to 1 Torr, but no difference in the current intensity was observed. Finally, we measured RF power dependence of the light of transition from the 2P state to 2S state, which is shown in Fig. 4. The light intensity increases as the RF power increases, and doesn't depend on the pressure in the tube. It seems that the RF power is not enough to create an appreciable amount of the 2S states. The quenching of the 2S states due to He-He collision is, however, most probable because the RF power of 400 W is enough to dissociate a large amount of  $\text{H}_2$  molecules under the same condition. If it is the case, the  $^3\text{He}$  nucleus can be polarized by laser optical pumping. A DC discharge method will be examined to find out the best way to produce the 2S state.

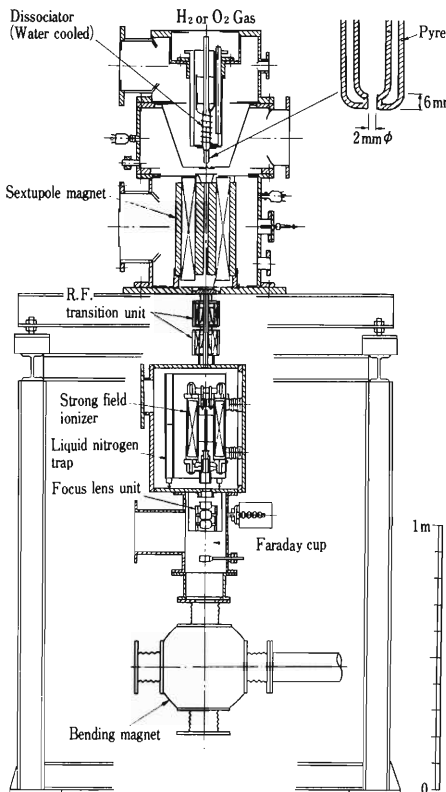


Fig. 3. Atomic beam type polarized proton and deuteron ion source at INS of the Univ. of Tokyo.

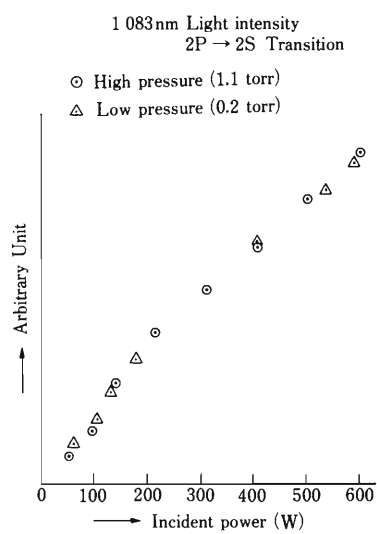


Fig. 4. Intensity of 1,083 nm light from a dissociator tube.

## References

- 1) S.D. Baker, E.B. Carter, D.O. Findley, L.L. Hatfeld, G.C. Phillips, N.D. Stockwell, and G.K. Waltters: *Phys. Rev. Lett.*, **20**, 738 (1968).
- 2) R.J. Slobodrian, C. Rioux, J. Giroux, and R. Roy: *A. I.P. Conf. Proc.*, No. 131, 8 (1985).
- 3) W.E. Burcham, O. Karban, S. Oh, and W.B. Powell: *Nucl. Instrum. Methods*, **116**, 2 (1974).
- 4) F. Laloe, P.J. Nacher, M. Leduc, and L.D. Schearer: *A.I.P. Conf. Proc.*, No. 131, p. 45 (1985).
- 5) F.D. Colegrove, L.D. Schearer, and G.K. Walters: *Phys. Rev.*, **132**, 2561 (1963).
- 6) A. Minoh, T. Fujisawa, Y. Taniguchi, S. Ishii, and K. Hatanaka: This Report, p. 225.

### V-1-15. Basic Study of a Polarized ${}^3\text{He}$ Ion Source by Laser Optical Pumping. II

A. Minoh, T. Fujisawa, Y. Taniguchi, S. Ishii, and K. Hatanaka

We study the production of nuclear-polarized  ${}^3\text{He}$  atoms for an accelerator ion source by a laser optical pumping method. A stable laser system for the optical pumping of  ${}^3\text{He}$  2S-2P transition of 1,083 nm has not been established in the world. A color-center laser using  $\text{F}_2^+$  centers in NaF was employed by Nacher, *et al.*<sup>1)</sup> However it should be operated at liquid-nitrogen temperature and its colored crystal should be replaced periodically. The YAG laser is a very excellent and technically established laser system, but the wavelength of laser line is slightly shorter than 1,083 nm. Recent development of

solid-state lasers provide us with more convenient laser materials. Nd<sup>3+</sup> ion ( ${}^4\text{F}_{3/2} \rightarrow {}^4\text{I}_{11/2}$  transition) in proper host crystal can be laser action in the 1  $\mu\text{m}$  infrared region.<sup>2)</sup> Two materials with a laser line at 1,083 nm have been known; one of them is yttrium aluminum perovskite (YAP)<sup>3)</sup> and another is lanthanum neodymium hexaaluminate (LNA).<sup>4)</sup>

At the start of the design and development of a laser system for  ${}^3\text{He}$  optical pumping, we measured the fluorescence yield of the YAP laser rod excited with a GaAlAs diode laser of 800 nm (Sony Co. Ltd. SLD-301V) and an Ar<sup>+</sup> laser of

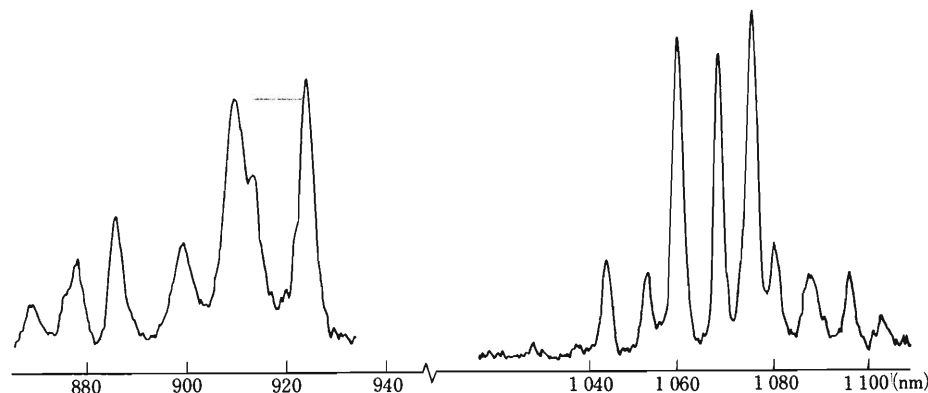


Fig. 1. Fluorescence spectrum of Nd<sup>3+</sup>: YAP excited with the diode laser. The spectral response of photomultiplier R-318 is not corrected.

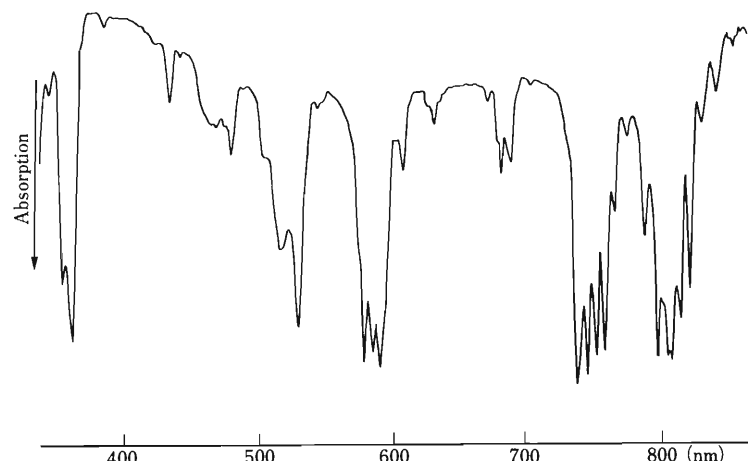


Fig. 2. Absorption spectrum for Nd<sup>3+</sup>: YAP.

514.5 nm (NEC GLS-3200). The YAP rod is cylindrical, 2 mm in diameter and 12 mm in length. A beam from the diode laser was collimated with collected lenses and longitudinally focused into the YAP rod. The emitted fluorescence was analyzed with a 50-cm grating spectrometer and detected with a photomultiplier (Hamamatsu Photonix R318).

The observed fluorescence spectrum shown in Fig. 1 exhibits two strong transition. One is a group from 900 to 930 nm and another is the group from 1,050 to 1,100 nm. The intensity of the fluorescence peaks around 910 nm excited with the Ar<sup>+</sup> laser was four times larger than that with the diode laser. The power of a focused Ar<sup>+</sup> laser beam on the YAP rod was found to be 3.5 mW with a SCIENTIC Model-361 power meter. The total output power of the diode laser is known to be 70 mW from the laser operation current and the internal monitor photodiode.

An unpolarized absorption spectrum of Nd<sup>3+</sup>: YAP measured with a spectrophotometer (HITACHI 320) is shown in Fig. 2, which shows that the absorption coefficient at 514.5 nm is the same as that at 800 nm, and the quantum efficiency of fluorescence from Nd<sup>3+</sup>: YAP is not

varied appreciably by changing the excitation wavelength from 514.5 nm to 800 nm. Thus, we conclude that the power focused on the YAP rod was only a very small fraction of the total output power from the diode laser. Since the diode laser output beam had an asymmetric and large divergence angle, the collimation lenses were not capable of transferring the diode laser output beam into the YAP rod.

The laser 1,083 nm output power strongly depend on the power and characters of the pumping laser beam. The results indicate that the Ar<sup>+</sup> laser is excellent for a pumping laser. When the diode laser is used as a pumping laser, a beam collimation system is indispensable to obtain the same qualities as the Ar<sup>+</sup> laser.

#### References

- 1) P.J. Nacher, M. Leduc, G. Trencé, and F. Laloe: *J. Phys. Lett.*, **43**, L-525 (1982).
- 2) Kh. S. Bagdasarov, A.A. Kaminskii, and G.I. Rogov: *Sov. Phys. Dokl.*, **14**, 346 (1969).
- 3) G.A. Massey and J.M. Yarborough: *Appl. Phys. Lett.*, **18**, 576 (1971).
- 4) L.D. Schearer, M. Leduc, D. Vivien, A.M. Lejus, and J. Thery: *IEEE J. Quantum Electron.*, **QE-22**, 713 (1986).

## V-2. Synchrotron Radiation Source Development

### 1. A Preliminary Design of the 8 GeV Chasman-Green Lattice

R. Nagaoka, H. Tanaka, K. Yoshida, K. Tsumaki, and M. Hara

A lattice design for the light-source storage ring is presented. Following our previous work on the 6 GeV Chasman-Green (CG) lattice,<sup>1)</sup> we reinvestigated the CG lattice by increasing the energy from 6 to 8 GeV. Keeping the main performance of the machine the same as in the 6 GeV case, we confined ourselves to design a machine smaller than 1,500 m in circumference: The increase of energy would be preferable to the "users," but it generally results in having a larger ring since the emittance is proportional to the square of energy:  $\epsilon_x \propto E^2 \cdot \theta^3$ , where  $E$  is the beam energy and  $\theta$  is the bending angle. A simple scaling from the 6 GeV result causes the number of cells to shift from 36 of the 6 GeV ring up to nearly 44 to preserve the same emittance value ( $\sim 8$  nmrad). Considering the beam dynamics in a low-emittance machine to be quite sensitive to the symmetry of the ring, we chose the nearest "good" number, 48, as the number of cells. The minimum achievable emittance then becomes  $\sim 1.7$  nmrad. Associated with the change of energy, the strength of dipole field is lowered from 0.8 to 0.6 T to lighten the load of the rf system. A rough estimate gives 25% reduction in the accelerating power.

The basic magnet arrangement of the lattice is unaltered: 2 dipoles (rectangular type), 10 quadrupoles, and 7 sextupoles in a single cell. The length of a free straight section is taken to be 6.5 m. In the present study, quadrupole and sextupole fields are limited to the following values to ensure the technical validity of  $10^{-4}$  order precision of the field strength:  $|dB_y/ds| \leq 16$  T/m, and  $|d^2B_y/ds^2| \leq 300$  T/m<sup>2</sup>, respectively. These threshold values are expected to be raised in future. Since the field strength basically scales linearly with energy, some of the magnets are designed to be thicker. In particular, the focusing quadrupole in the triplet has 110 cm in thickness to allow the low beta mode (see below). Also, spacing are taken care of to install chromaticity correcting sextupoles thicker than the previous

Table 1. Major parameters of the 8 GeV Chasman-Green lattice considered in this study.

	Parameter list of the 8 GeV CG lattice		
	High beta mode	Hybrid mode	
	type A	type B	
Natural emittance (horizontal) [nm · rad]	7.4	4.9	7.5
Betatron tune			
Horizontal	40.22	51.75	45.22
Vertical	17.16	19.82	15.16
Natural chromaticity			
Horizontal	-69.8	-126.1	-86.4
Vertical	-34.1	-42.6	-33.4
Horizontal beta at straight section [m]	20.37	23.11	32.67
		1.13	4.08

value of 40 cm. Spacing on both sides of dipoles are kept longer than a meter (113 cm) to accomodate the bump magnet for the injection and crotches of the vacuum system. The resulting cell length is 30.8 m and the circumference is 1,478.4 m.

In addition to the "high beta" mode studied for the 6 GeV ring, the so-called "hybrid" mode is designed and examined in the present study. The hybrid mode, which is also employed by the ESRF for their 6 GeV CG lattice,<sup>2)</sup> is an optics in which the horizontal betatron function at the straight section is alternatively varied from high ( $\sim 20$  m) to low ( $\sim 1$  m). Undulators will be installed at high beta sections, while wigglers and rf cavities will be placed at low beta sections. In the hybrid mode, the 48-cell ring possesses the superperiodicity of 24 at the maximum. We present here, three optics considered in the given

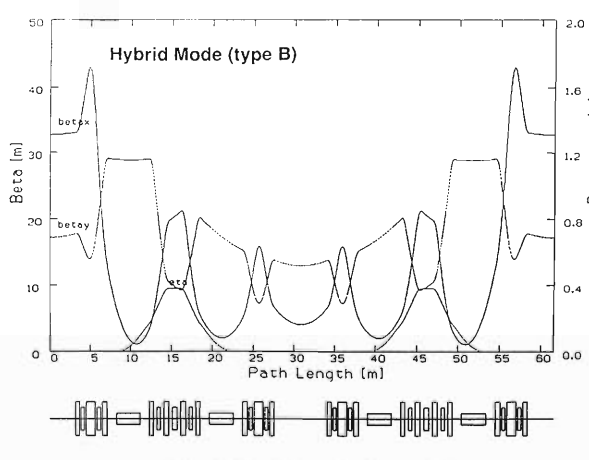
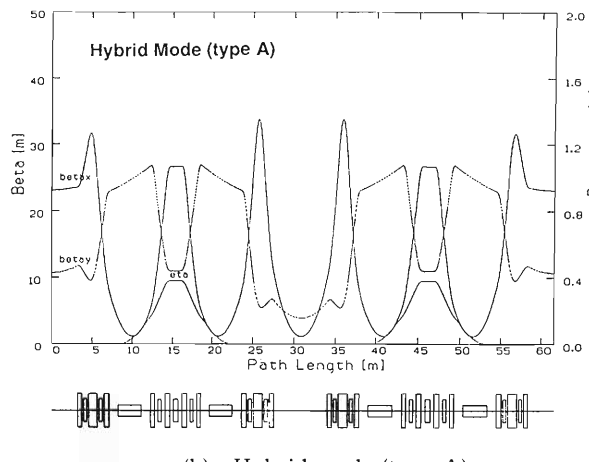
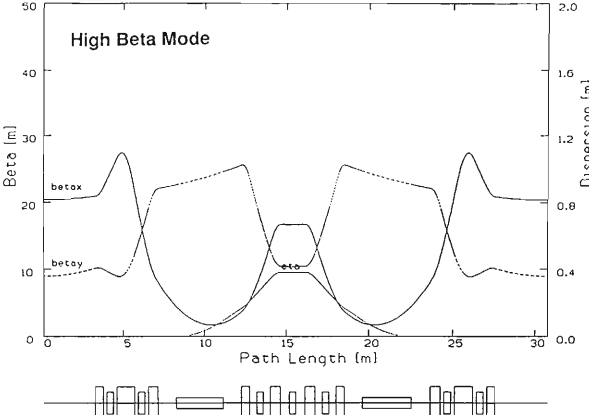


Fig. 1. Betatron and dispersion functions over a super-periodic cell.

magnet arrangement: One high beta mode and two hybrid modes. The optics functions are displayed in Fig. 1, and major parameters are listed in Table 1. In all three optics, working points are selected so that tunes per superperiodic cell stay away from 1st- and 3rd-order resonances of the sextupoles, and total tunes of the ring avoid

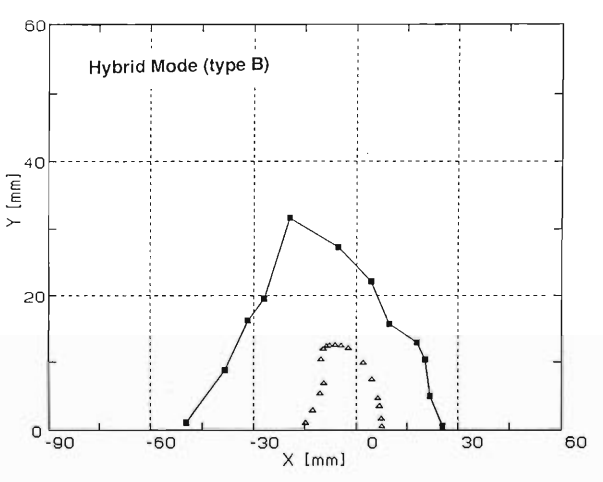
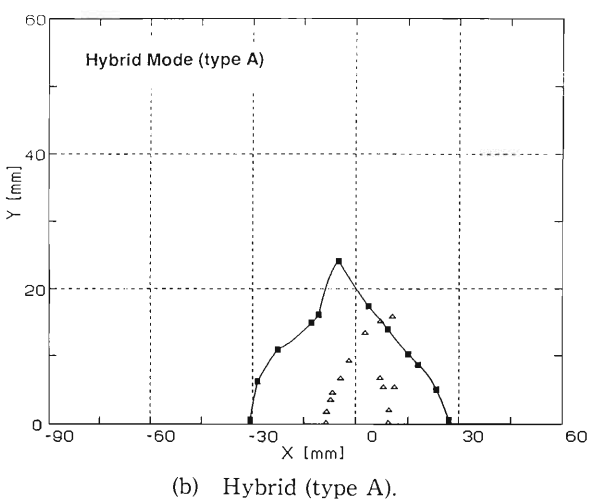
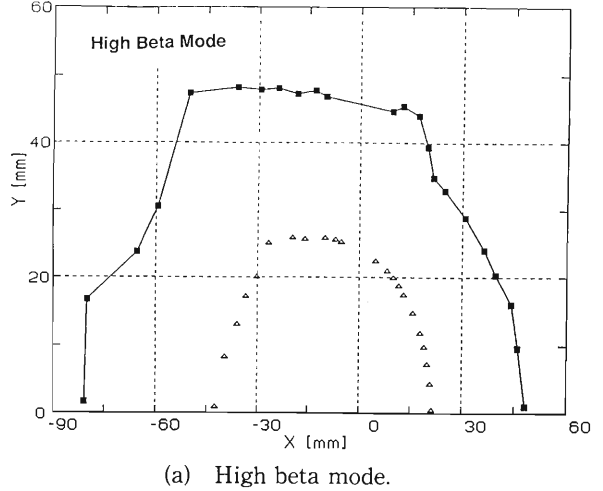


Fig. 2. Dynamic aperture of the ideal lattice. Triangles indicate the dynamic aperture without harmonic correction, and dark squares represent the dynamic aperture with correction.

nearby non-structural low-order resonances. Type A of the hybrid mode, which more or less resembles the optics of the ESRF, is rather strongly focused and has a local mirror symme-

try at the midst of an achromatic arc. Type B is a much more detuned optics in which the horizontal tune per superperiodic cell is intentionally lowered below 2 to reduce the influence of the strong integer resonance driven by the sextupoles.

As in the 6 GeV CG lattice, two “harmonic” sextupoles are placed on each side of an arc to enlarge the otherwise insufficiently small dynamic aperture. Harmonic sextupoles are optimized by using the computer code CATS.<sup>3)</sup> The resultant dynamic aperture of an ideal machine is shown in Fig. 2 for the three optics. Although the dynamic apertures of the hybrid modes are calculated at the high beta section as well, they are found to be smaller, especially in type A, than that of the high beta optics. Indeed, despite the use of four families of harmonic sextupoles in the hybrid modes, the optimization was not as effective and transparent as in the high beta case. We found that large amplitude motions in the hybrid optics are apt to be affected by higher-order resonances of the sextupoles (6th order in the case of type A), which is presumably due to the reduction of the symmetry.<sup>4)</sup> Tune shifts with amplitude and with momentum deviation are shown in Figs. 3 and 4, respectively, for type A.

Tracking with various errors in the ring as well as the correction of closed-orbit distortion (COD) is done by using RACETRACK.<sup>5)</sup> Table 2 lists the kinds of errors included. The COD correction is done with 8 monitors and 6 horizontal (vertical) correctors in a cell. Figure 5 illustrates the magnitude of the dynamic aperture as a function of residual COD in the ring. One finds

Table 2. Kinds of errors included in the tracking calculation and in the COD correction.

Distribution: Gaussian

(A) Dipole:		
—Field error $\Delta B/B$ :	$5 \times 10^{-4}$	(dipole)
—Tilt error $\Delta \theta$ :	0.5 mrad	(dipole)
(B) Quadrupole:		
—Field error $\Delta B'/B'$ :	$5 \times 10^{-4}$	(normal quad)
—Misalignment error:	0.2 mm	(dipole)
—Tilt error $\Delta \theta$ :	0.5 mrad	(skew quad)
(C) Sextupole:		
—Field error $\Delta B''/B''$ :	$5 \times 10^{-4}$	(normal sext.)
—Misalignment error:	0.2 mm	(dipole)
—Tilt error $\Delta \theta$ :	0.5 mrad	(normal quad) (skew quad) (skew sext.)

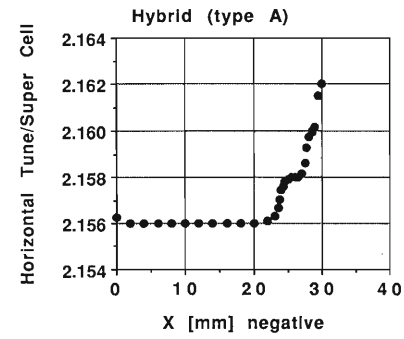


Fig. 3. Amplitude dependence of the betatron tune. Calculation is performed for the hybrid mode (type A) measuring the tune shift per superperiodic cell.

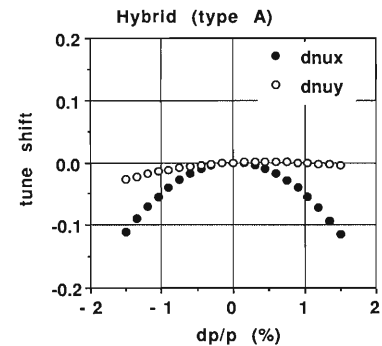


Fig. 4. Momentum dependence of the betatron tunes after chromaticity correction. Filled circles denote horizontal, and open circles represent vertical tune shifts. Calculation is performed for the hybrid mode (type A).

that the dynamic aperture cannot be fully restored even in the limit of zero rms of COD. The optimization of the correction system and the tracking calculation in view of beam injection

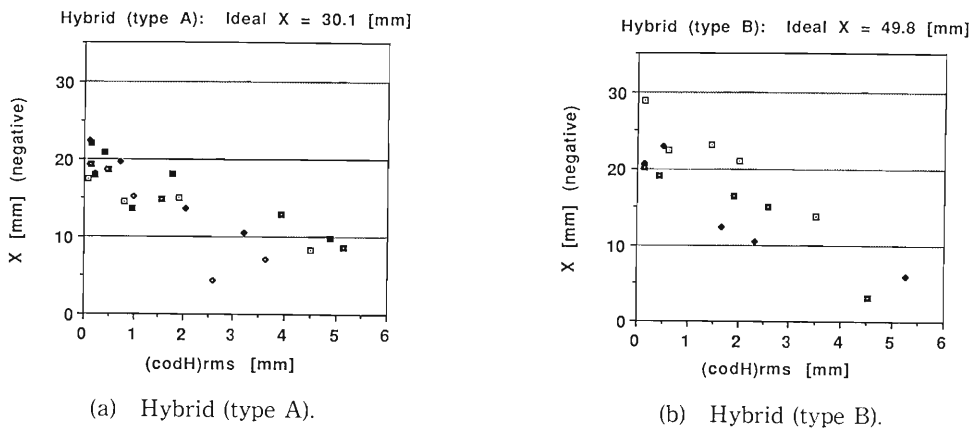


Fig. 5. Dependence of the dynamic aperture on the magnitude of residual COD. The dynamic aperture is calculated at 1% coupling for several rings with errors (different random seeds).

are currently carried out.

We have designed the 8 GeV CG lattice composed of 48 cells and examined their properties. In brief, we found that there do exist many good low-emittance optics with moderate focusing in both high beta and hybrid modes, owing to the smallness of the bending angle  $\theta$ . We have noticed, however, that the smallness of  $\theta$  is not advantageous in having a large dynamic aperture: The suppressed dispersion function in the arc brings about stronger sextupoles for the chromaticity correction leading to the enhancement of the unwanted resonances. We actually checked this trend by designing rings composed of fewer cells. A geometrical problem of spacing

between each photon beam line may also be serious with a too small  $\theta$ . With these positive and negative aspects of the 48 cell ring, further investigation is yet to be done to obtain the optimal 8 GeV light source storage ring.

#### References

- 1) H. Tanaka, R. Nagaoka, and M. Hara: *RIKEN Accel. Prog. Rep.*, **21**, 225 (1987).
- 2) The Red Book Draft B, ESRF (1987).
- 3) R. Nagaoka, H. Tanaka, K. Yoshida, K. Tsumaki, and M. Hara: This Report, p. 248.
- 4) R. Nagaoka, K. Yoshida, H. Tanaka, K. Tsumaki, and M. Hara: This Report, p. 242.
- 5) A. Wrulich: DESY Rep., 84-026 (1984).

## V-2-2. Correction of the Closed Orbit Distortion (COD) for an 8 GeV Storage Ring (1)

H. Tanaka, R. Nagaoka, K. Tsumaki, K. Yoshida, and M. Hara

The COD correction is crucial for a low-emittance storage ring which is very sensitive for electromagnetic errors. The COD at a sextupole magnet makes a circulating particle feel an additional quadrupole component corresponding to its amplitude, inducing a tuneshift at every sextupole around the ring. That is, the COD breaks a local phase advance among the sextupoles arranged well along the ring to suppress the resonance driving terms induced by themselves. The COD also distorts the workpoint that has been carefully optimized to avoid the fatal resonances, and a beam stay clear region is markedly reduced consequently. To minimize these breaks and to recover the wide beam stay clear region, the COD should be corrected around the ring as precisely as possible. In the literature, a COD correction system of a 48 cell-8 GeV Chasman Green (CG) lattice<sup>1)</sup> has been investigated.

In Table 1, a condition of random errors is shown. The value for each error represents the variance ( $\sigma$ ) of a special Gaussian distribution truncated at  $2\sigma$ .

To simulate a COD correction, we use "RACETRACK"<sup>2)</sup> in which two kinds of correction methods are prepared: "Local Bump"<sup>3)</sup> (LB) and "Most Effective Corrector"<sup>4)</sup> (MEC) methods. The MEC and the LB can be iteratively used with arbitrary combination. In addition, a concept of dipole random error scaling was adopted to make a simulation easy. The final error condition (scale factor=1) can be approached step-

Table 1. Condition of random errors.

...Bending magnet field error ( $dB/B$ )	$5.0 \times 10^{-4}$
...Bending magnet tilt error	$5.0 \times 10^{-4}$ rad
...Misalignment at Q magnet	$2.0 \times 10^{-4}$ m
...Q magnet gradient error ( $dB'/B'$ )	$5.0 \times 10^{-4}$
...Q magnet tilt error	$5.0 \times 10^{-4}$ rad
...Misalignment at sextupole magnet	$2.0 \times 10^{-4}$ m
...Sextupole magnet tilt error	$5.0 \times 10^{-4}$ rad
...Sextupole magnet gradient error ( $dB''/B''$ )	$5.0 \times 10^{-4}$

wise by taking serial scale factors like 0.3, 0.5, 0.7, and 1.0. A maximum corrector strength was limited to 2 mrad and a minimum phase advance for the LB between two correctors was defined 0.075 in the horizontal plane and 0.050 in the vertical plane.

Following six parameters were used to estimate a system performance: a maximum corrector strength, a convergence of COD, the recovery ratio of a dynamic aperture, a final residual COD value, a number of elements in the correction system, and the influences on the design of hardware. In respect of a dynamic aperture, the dynamic aperture at the low X-Y coupling (0.01) was used. The effects of difference among COD correction schemes on the parameters were also considered.

The COD correction system has so many degrees of freedom that we can not treat all

Table 2. Case study list of investigation of the COD correction system.

Case	Arrangement		Number of machines	Number of monitors	Number of correctors	
	Monitor <sup>1)</sup>	Corrector <sup>1)</sup>			Horizontal	Vertical
1	at sextupole	B	7	336 (7/cell)	288 (6/cell)	288 (6/cell)
2	at quadrupole	B	5	480 (10/cell)	288 (6/cell)	288 (6/cell)
3	at quadrupole	A	5	480 (10/cell)	432 (9/cell)	432 (9/cell)
4	at sextupole	A	5	336 (7/cell)	432 (9/cell)	432 (9/cell)
5	at sextupole	A	5	336 (7/cell)	432 (9/cell)	432 (9/cell)
6	at sextupole	C	6	336 (7/cell)	144 (3/cell)	192 (4/cell)

1) See Fig. 1.

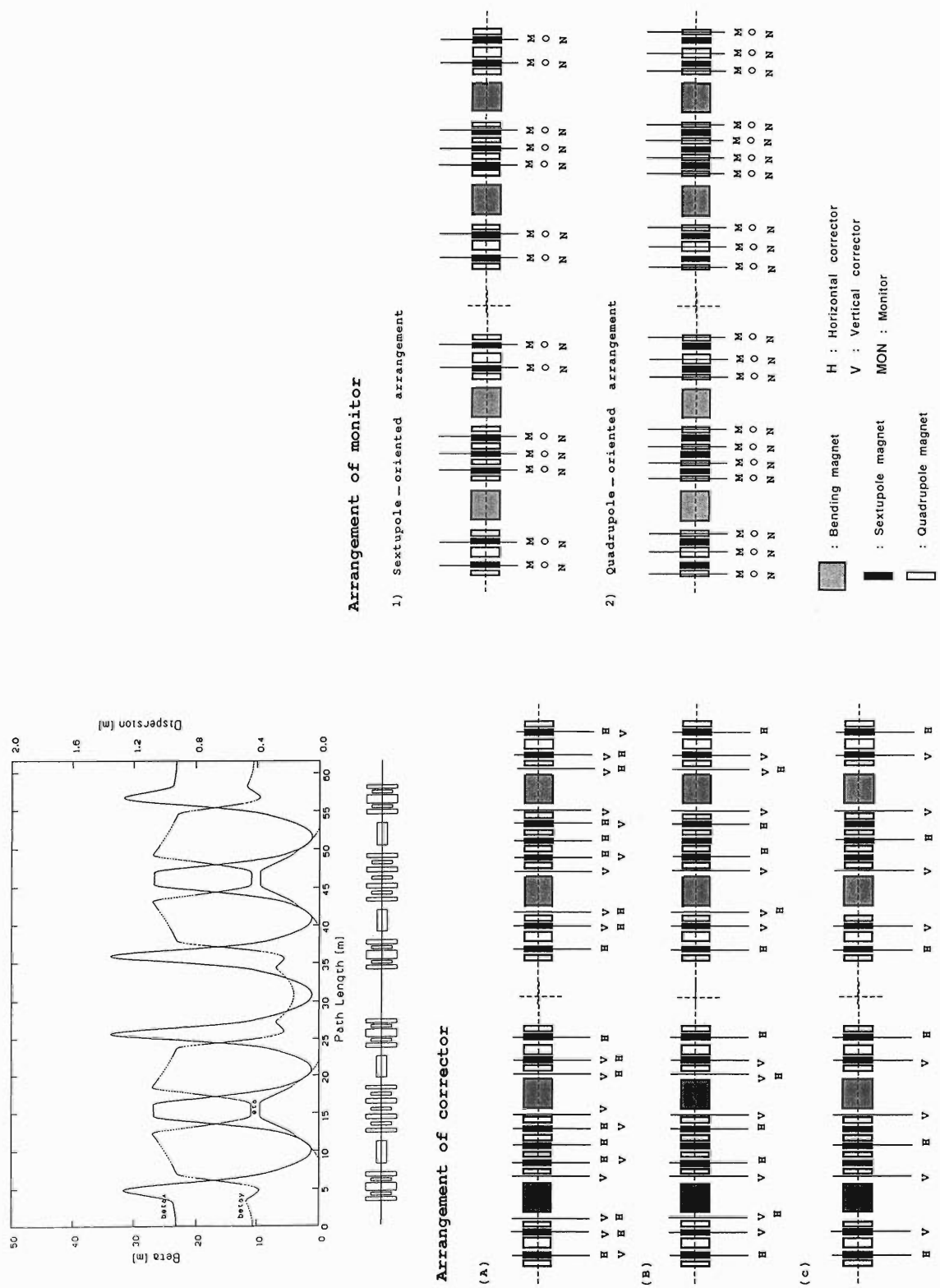


Fig. 1. Arrangement of monitors and correctors.

parameters simultaneously. We intentionally divide the investigation into two parts: one is arrangement of monitors and the other is that of correctors. All case studies are listed in Table 2, and all arrangements of monitors and correctors are shown in Fig. 1.

The arrangement of monitors is categorized into two: one is based on the correction of misalignment of the quadrupoles which mainly cause COD, and the other is based on the correction of the tuneshift induced by the sextupoles. Two arrangements were compared with each other under two conditions: the same corrector arrangement (Case 1 and Case 2 in Table 2) and the same ratio of the number of monitors and correctors (Case 1 and Case 3 in Table 2). In these comparisons, no appreciable difference was found for a maximum corrector strength, a convergence of COD, the recovery ratio of a dynamic aperture, and a final residual COD value. This result is due partly to the fact that the sextupoles are located very closely to the quadrupoles in a CG lattice and both arrangements give almost the same COD pattern at the sextupoles through the COD correction. In respect of monitors, sextupole-oriented arrangement has less number of monitors than quadrupole-oriented one. The less number of monitors makes simpler design of a vacuum chamber because of their setting needs high accuracy. Therefore, sextupole-oriented arrangement has advantages in designing hardware. As a result, we found that the sextupole-oriented arrangement is better than the quadrupole-oriented one; this result is always right in a CG lattice under the assumption that the sextupole optimization (including location of the sextupoles) is not so different among all candidates for CG lattices.

The arrangement of correctors was investigated on the basis of sextupole-oriented arrangement of monitors with three kinds of arrangement of correctors shown in Fig. 1; as the case studies, Case 1, Case 4, and Case 6 in Table 2.

The calculation results are shown in Figs. 2 and 3. A difference appears in the convergence of COD and the maximum corrector strength. The maximum corrector strength increases with increasing number of correctors. The convergence of COD is improved with increasing number of correctors and seems to be leveled off when the number of correctors exceeds those in Case 1. This result will be explained as follows. The increase (or decrease) in the number of correctors means the increase (or decrease) in the degree of freedom for the correction; therefore, a

proper increase (or decrease) leads to quick (or slow) convergency of the COD and the small (or large) final residual COD value. An excessive increase (or decrease), on the other hand, reduces (or promotes) the phase advance among correctors and leads to not only quick (very slow) convergency and the small (or large) final residual COD value but also a strong (weak) corrector strength especially on the LB method adopted in "RACETRACK." The convergence of COD represents how easy COD can be corrected. In addition, since every sextupole includes only one kind of corrector (horizontal or vertical), Case 1 and Case 6 have an advantage in designing a sex-

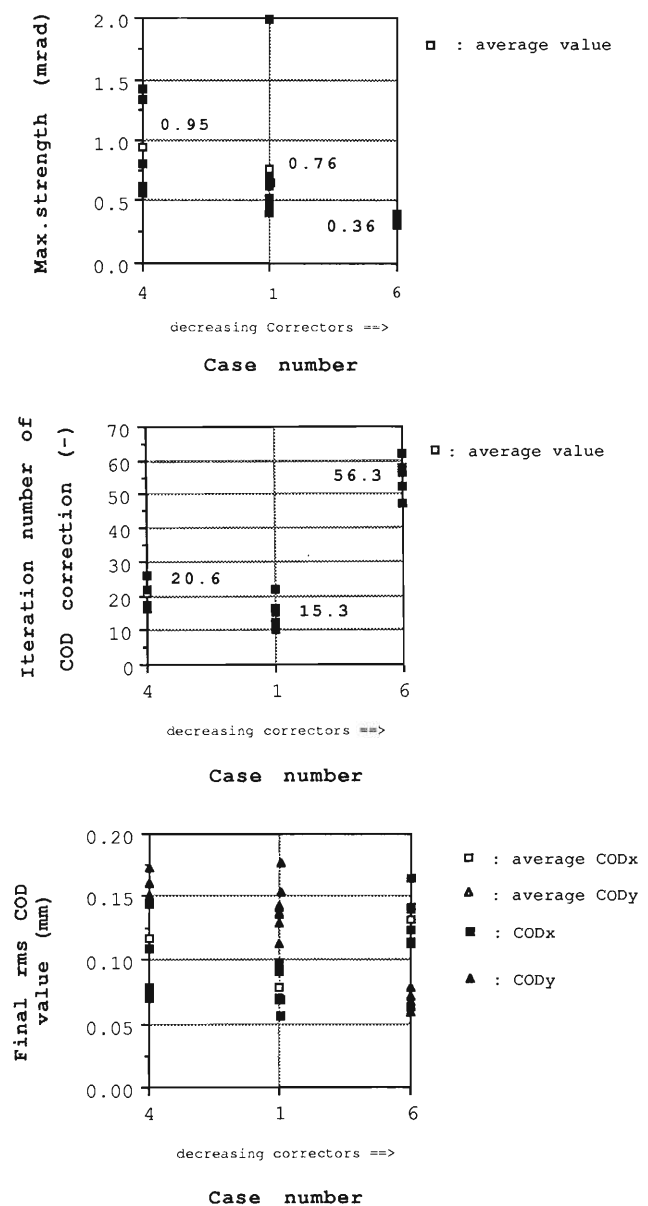


Fig. 2. Dependence of the corrector arrangement on the maximum corrector strength (upper diagram), the COD convergence (middle diagram), and the final residual COD value (lower diagram).

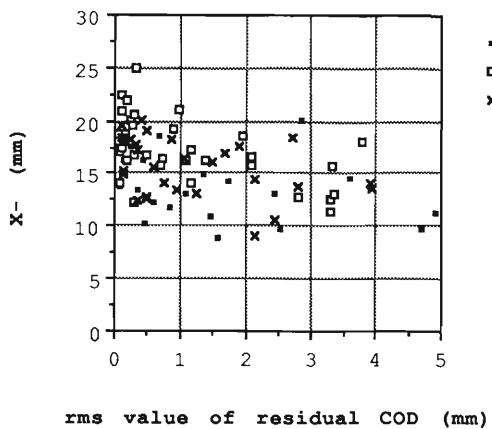


Fig. 3. Dependence of the dynamic aperture behavior on the corrector arrangement.  $X-$  represents the dynamic aperture of a tracking initial phase = 180 deg. Tracking condition, turn no. = 500 at the center of high  $\beta$  straight section;  $X-Y$  coupling factor = 0.01.

tupole. Thus, Case 1 is found to be the best, because Case 4 has a fatal disadvantage in designing a sextupole and Case 6 also has a fatal disadvantage in the COD convergence. The final performance of the COD correction system is:

the recovery ratio of a dynamic aperture is

50–70%; and

a final residual COD value is  $< 0.2$  mm.

An important result is that the number of correctors more than 6 per cell in each plain is not effective for the COD correction. We can avoid installing two kinds of correctors in one sextupole and this is much preferable to design of a sextupole.

On the basis of the present study, a further investigation of the arrangement of monitors and correctors should be carried out with more random seeds (more number of machines) and with more kinds of arrangements. We hope to optimize not only the correction system for the global COD but also the correction system for the local COD at the long straight section in more detail in the near future.

#### References

- 1) R. Nagaoka, H. Tanaka, K. Yoshida, K. Tsumaki, and M. Hara: This Report, p. 227.
- 2) A. Wrulich: DESY Rep., 84-026 (1984).
- 3) H. Fukuma: KEK Accel. Semin.-OHO'88, III-3 (1988).
- 4) E. Gianfelice and R. Giannini: CERN/PS, 85-42 (LEA) (1985).

### V-2-3. Correction of the Closed Orbit Distortion (COD) for an 8 GeV Storage Ring (2)

H. Tanaka, R. Nagaoka, K. Yoshida, K. Tsumaki, and M. Hara

For the arrangement preliminarily optimized in the previous COD correction,<sup>1)</sup> following two detail investigations were performed:

- (1) Effects of a monitor and a corrector error to the performance of the COD correction system.
- (2) Effects of adjustment of a workpoint to the recovery of a dynamic aperture.

The calculation was executed with "RACETRACK"<sup>2)</sup>.

A monitor error results from a misalignment of a monitor and inaccuracy of a monitor detection signal. It can be regarded a kind of displacement error at a monitor. Effects of a monitor error were investigated with five values between

0.1 mm and 0.5 mm, which are the same order of the tolerance of the Advanced Light Source Project in Lawrence Berkeley Laboratory.<sup>3)</sup>

The calculation result of the final residual COD value is shown as a function of a monitor error in Fig. 1. The final residual COD simply increases with increasing the value of a monitor error and is beyond 0.2 mm at 0.3 mm error. Figure 2 shows the correlation between a dynamic aperture and a monitor error. Within smaller errors than 0.3 mm, the change in the dynamic aperture is slight, but between 0.3 and 0.4 mm, it becomes irregular and large. We can find the monitor error beyond 0.3 mm, the dy-

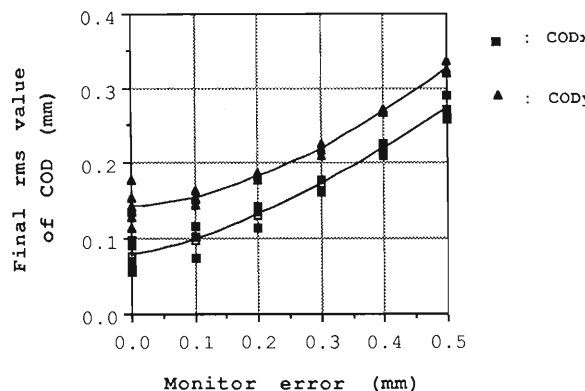


Fig. 1. Dependence of a final residual COD on a monitor error.

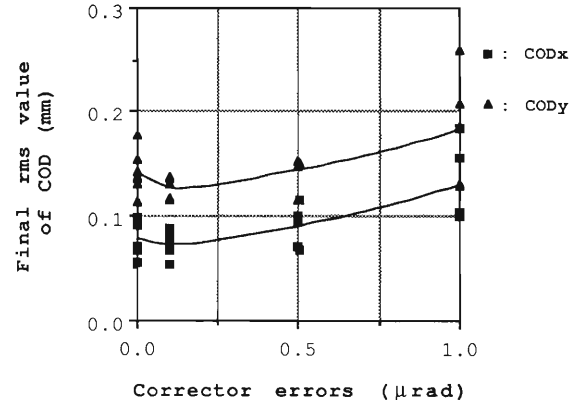


Fig. 3. Dependence of a final residual COD on a corrector error.

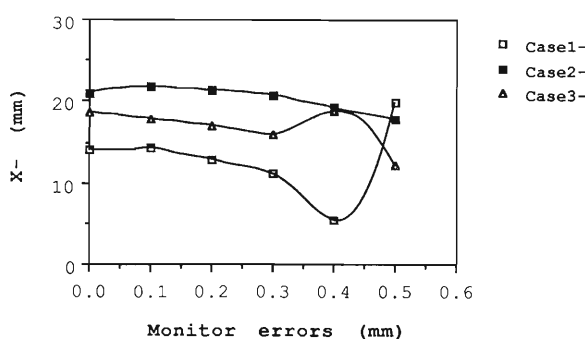


Fig. 2. Correlation between a dynamic aperture and a monitor error.  $X^-$  represents the dynamic aperture of a tracking initial phase=180 deg. Tracking condition: The tracking turn number is 500. The calculating point is at the center of a high  $\beta$  straight section and  $X-Y$  coupling is 0.01.

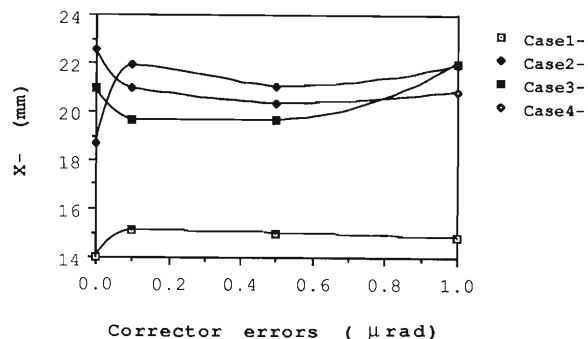


Fig. 4. Correlation between a dynamic aperture and a corrector error.  $X^-$  represents the dynamic aperture of tracking initial phase=180 deg. Tracking condition: The tracking turn number is 500. The calculating point is at the center of high  $\beta$  straight section and  $X-Y$  coupling is 0.01.

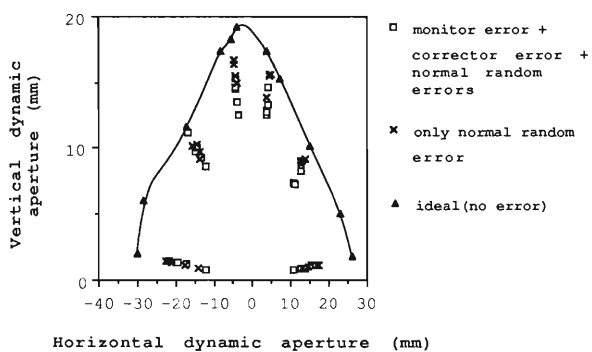


Fig. 5. Comparison of dynamic apertures for three cases. Tracking condition: The tracking turn number is 500. The calculating point is at the center of high  $\beta$  straight section.

namic aperture is no longer anticipated. Therefore, taking some allowance, we adopted 0.2 mm as the *tentative* tolerance of the monitor error.

A *corrector error* results from the defects in a power supply and in a magnet. It can be regarded as a kind of field error at a corrector. On the design of a magnet, we may suppose about 0.01% of errors of a full range (1-2 mrad). Effects of a corrector error were investigated with the three values (0.1, 0.5, and 1.0  $\mu$ rad).

The final residual COD value calculated as a function of a corrector error (Fig. 3) is almost constant within errors smaller than 0.5  $\mu$ rad, and beyond 0.5  $\mu$ rad its scattering and average value become large. The correlation between a dynamic aperture and a corrector error is shown in Fig. 4. The dynamic aperture is almost constant within errors smaller than 1.0  $\mu$ rad. Considering that the scattering of the final residual COD value becomes large at the corrector error of 1.0  $\mu$ rad and taking some allowance, we adopted 0.5  $\mu$ rad as the *tentative* tolerance of the

Table 1. Comparison of dynamic aperture to find the level of the COD correction. Tracking condition: The tracking turn number is 500. The calculating point is at the center of high  $\beta$  straight section.

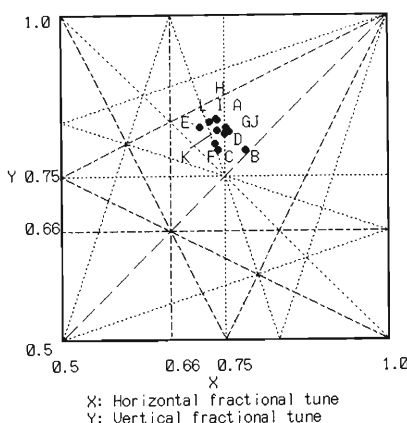
Random seed	Dynamic aperture (mm)			Case 3 Case 2
	Case 1 ( $X, Y$ )	Case 2 ( $X, Y$ )	Case 3 ( $X, Y$ )	
<i>X-Y coupling</i> =0.01, Initial phase=0.0 (deg), Ideal dynamic aperture (-26.22, 1.79)				
1	(19.57, 1.36)	(17.93, 1.11)	(17.38, 1.10)	0.97
2	(21.29, 1.48)	(17.31, 1.05)	(14.70, 0.96)	0.85
3	(19.65, 1.34)	(16.85, 1.16)	(17.33, 1.19)	1.03
4	(21.37, 1.45)	(13.72, 0.95)	(12.84, 0.86)	0.94
<i>X-Y coupling</i> =0.01, Initial phase=180 (deg), Ideal dynamic aperture (-30.13, 2.05)				
1	(21.76, 1.51)	(20.82, 1.39)	(22.54, 1.42)	1.08
2	(22.93, 1.59)	(21.29, 1.30)	(17.43, 1.14)	0.82
3	(23.63, 1.62)	(20.36, 1.40)	(18.70, 1.29)	0.92
4	(20.98, 1.42)	(15.58, 1.07)	(14.01, 0.94)	0.90

Case 1: the only quadrupole gradient error.

Case 2: the gradient error + the sextupole misalignment error.

Case 3: normal random errors with the COD correction.

$X, Y$  represent horizontal, vertical dynamic aperture.



<i>X-Y</i> Coupling=0.01, Initial phase=0.0 (deg.)		
	Ideal dynamic aperture (26.22, 1.79)	Ideal fractional tune (0.749958, 0.819906)
Case	Dynamic aperture (mm)	Fractional tune
A	( $X, Y$ ) (19.57, 1.36)	( $N_x, N_y$ ) (0.751511, 0.824432)
B	(17.93, 1.11)	(0.782490, 0.790325)
C	(17.38, 1.10)	(0.739174, 0.790349)
D	(21.29, 1.48)	(0.749591, 0.815654)
E	(17.31, 1.05)	(0.711696, 0.824438)
F	(14.70, 0.96)	(0.735046, 0.800265)
G	(19.65, 1.34)	(0.751660, 0.818021)
H	(16.85, 1.16)	(0.738237, 0.836594)
I	(17.33, 1.19)	(0.737156, 0.837636)
J	(21.37, 1.45)	(0.756371, 0.818884)
K	(13.72, 0.95)	(0.738814, 0.819629)
L	(12.84, 0.86)	(0.726100, 0.834027)

Fig. 6. For 12 kinds of practical rings where the COD is corrected, the tunes are plotted in the left diagram and the tunes and the dynamic apertures are listed in the right table.

corrector error.

Assuming a monitor error and a sextupole misalignment are independent of each other, we calculated a dynamic aperture for the ring including the normal random errors,<sup>1)</sup> the monitor error of 0.2 mm, and the corrector error of 0.5  $\mu$ rad corresponding to the tolerance. Figure 5 shows the calculation result together with other two cases; the case including the only normal random errors and no error (the ideal case), indicating that the dynamic aperture is largely reduced at a low  $X-Y$  coupling compared with that at a high  $X-Y$  coupling and that, at worst, the dynamic aperture of a  $X-Y$  coupling of 0.01 is reduced to one third of the ideal one, about 10 mm. Compared with the case including only normal random errors, the reduction is few dozens percent larger.

To improve the recovery ratio of the dynamic aperture, we investigated its behavior in detail. For the following three cases, dynamic apertures were calculated to investigate the level of the COD correction. Case 1 includes only the quadrupole gradient error ( $COD=0.0$ ), Case 2 includes the gradient error and the sextupole misalignment error ( $COD=0.0$ ), and Case 3 includes the normal random errors and the COD correction. The dynamic aperture reduction in Case 1 and Case 2 represents the contributions of phase advance breaks, which can not be compensated by the COD correction. Table 1 compares the dynamic apertures among three cases. The dynamic aperture in Case 1 is reduced to two third of the ideal one. The dynamic aperture of Case 2 is reduced to one second of the ideal one, which almost corresponds to the dynamic aper-

ture of Case 3. This means that the dynamic aperture is no longer improved by the COD correction. We can find that the level of the COD correction achieving the final residual COD of 0.1-0.20 mm has already been sufficient.

To investigate correlation between a global tuneshift and the reduction in the dynamic aperture, the dynamic apertures were plotted on a tune-diagram as shown in Fig. 6, which suggests that the reduction in the dynamic aperture does not greatly depend on the workpoint, because the ring whose workpoint is nearest to the third integer resonance has a large dynamic aperture. To confirm this suggestion, the workpoints were recovered to the ideal point by the COD correction and the dynamic aperture was calculated for seven rings; Table 2 shows results. In half of the rings, the reduction of dynamic aperture is improved by adjusting the workpoint. In remaining half, on the contrary, the dynamic aperture is more reduced by adjustment. These results indicate that the reduction in the dynamic aperture does not correlate closely with the shift of the workpoint. It is also expected that the breaks of the local phase advance is dominant in the reduction in the dynamic aperture.

Since the improvement in the COD correction and the recovery of the workpoint are not effective to enlarge the dynamic aperture, all we can do is to take the following two, if necessary, for the stable operation, a dynamic aperture larger than what we can get now. One is to protect the ring from all kinds of errors more severely; this means that the tolerance of each error should be reduced and probably leads to the difficulty in alignment and in hardware design. The other is to find an optics more tough to errors, which probably gives rise to a large emittance.

With respect to the tolerance of a monitor and a corrector error, extensive case studies should be performed to determine the tolerance, and will be tried at the next step.

The minimum required dynamic aperture should be analyzed from the viewpoint of the injection efficiency for the ring including the practical errors with the COD correction as soon as possible. The proper feedback must be taken into the design of a storage ring lattice.

## References

- 1) H. Tanaka, R. Nagaoka, K. Tsumaki, K. Yoshida, and M. Hara: This Report, p. 231.
- 2) A. Wrulich: DESY Rep., 84-026 (1984).
- 3) 1-2 GeV synchrotron Radiation Source Conceptual Design Report—July 1986, PUB-5172 Rev., LBL.

Table 2. Effect of the adjustment of a workpoint on the recovery of a dynamic aperture.

Dynamic aperture (mm) ( $X, Y$ )		
Case before correction	After correction	Effect
B (17.93, 1.11)	(15.59, 1.03)	—
E (17.31, 1.05)	(18.16, 1.14)	+
H (16.85, 1.16)	(15.20, 1.05)	—
K (13.72, 0.95)	(17.93, 1.23)	+
F (14.70, 0.96)	(17.62, 1.18)	+
I (17.33, 1.19)	(16.76, 1.12)	—
L (12.84, 0.86)	(8.71, 0.59)	—

Effect+ means that the tune adjustment is effective.

Effect— means that the tune adjustment is ineffective.

## V-2-4. Effect of Insertion Devices on Beam Dynamics of 8 GeV Light Source Storage Rings

R. Nagaoka, K. Yoshida, H. Tanaka, K. Tsumaki, and M. Hara

The study of the effect of insertion devices (IDs) on revolving particles is very important in designing light-source dedicated storage rings. Anticipated effects of the insertion devices are: Breakdown of the original symmetry, distortion of linear optics, and introduction of nonlinear forces that may lead particles to additional resonances. The purpose of the present study is to estimate the degree of influence in storage rings operated at an energy region of 8 GeV. In particular, we work with three types of lattice: Chasman-Green (CG), Triple Bend Achromat (TBA), and Quadruple Bend Achromat (QBA) to examine the dependence of the effect on the lattice structure. Numerical calculation relies for the most part on the extended version of the computer code RACETRACK, which is motivated to include the effect of IDs in particle tracking.<sup>1)</sup>

Our analysis initiates from the following analytical expressions of a magnetic field which is known to be a good approximation for the actual distribution inside IDs:<sup>2)</sup>

$$B_x = k_x/k_y \cdot B_0 \sinh k_x X \cdot \sinh k_y Y \cdot \cosh k Z \quad (1)$$

$$B_y = B_0 \cosh k_x X \cdot \cosh k_y Y \cdot \cos k Z \quad (2)$$

$$B_z = -k/k_y B_0 \cosh k_x X \cdot \sinh k_y Y \cdot \sin k Z \quad (3)$$

with

$$k_x^2 + k_y^2 = k^2 = (2\pi/\lambda)^2 \quad (4)$$

$(X, Y, Z)$  is the fixed frame of reference with  $Z$  as the longitudinal coordinate. The peak field and the period length of an ID are given by  $B_0$  and  $\lambda$ , respectively. The above formulas, which keep only the fundamental harmonic of the field variation in the  $Z$ -direction, satisfy the Maxwell equations. Damping of the field in the  $X$ -direction can be expressed by the replacement  $k_x \rightarrow ik$ .

To find how the field distribution of Eq. 1 affects the betatron motion, equations of motion in terms of the conventional coordinate system  $(x_\beta, y_\beta, s)$  must be derived. This is done in Ref. 3 in the Hamiltonian formalism by assuming  $1 \ll k\rho$  ( $\rho$ : Radius of curvature in the peak field  $B_0$ ) and by partially averaging the Hamiltonian over the period length:

$$\begin{aligned} x'' &= -k_x(2k^2\rho^2)(k_x x + k_x^3 x^3/6 + k_x k_y^2 x y^2/2) \\ &\quad - \cos ks/\rho \cdot (k_x^2 x^2 + k_y^2 y^2)/2 \\ &\quad - y' y k \sin ks/\rho \end{aligned} \quad (5)$$

Table 1. Parameter list of the undulator and the wiggler employed in this study.

		Undulator	Wiggler
Field parameter	$K$	1.0	25.2
Peak field	$B_0$ (T)	0.357	1.5
Period length	$\lambda$ (cm)	3	18
No. of period	$N_p$	166	12
Total length	$L$ (m)	4.98	2.16
Radius of curvature in the peak field	$\rho$ (m)	74.7	17.78
Vertical wave number	$k_y$ (1/m)	$2.05 \times 10^2$	34.23
Horizontal wave number		$k_x = 0.2 k_y$	$k_x = 0.2 k_y$
Amplitude of the equilibrium orbit	$\rho/(k\rho)^2$ ( $\mu\text{m}$ )	0.3	46.1
Photon energy	$\epsilon$ (keV)	13.5 <sup>†</sup>	64.0

<sup>†</sup> First harmonic

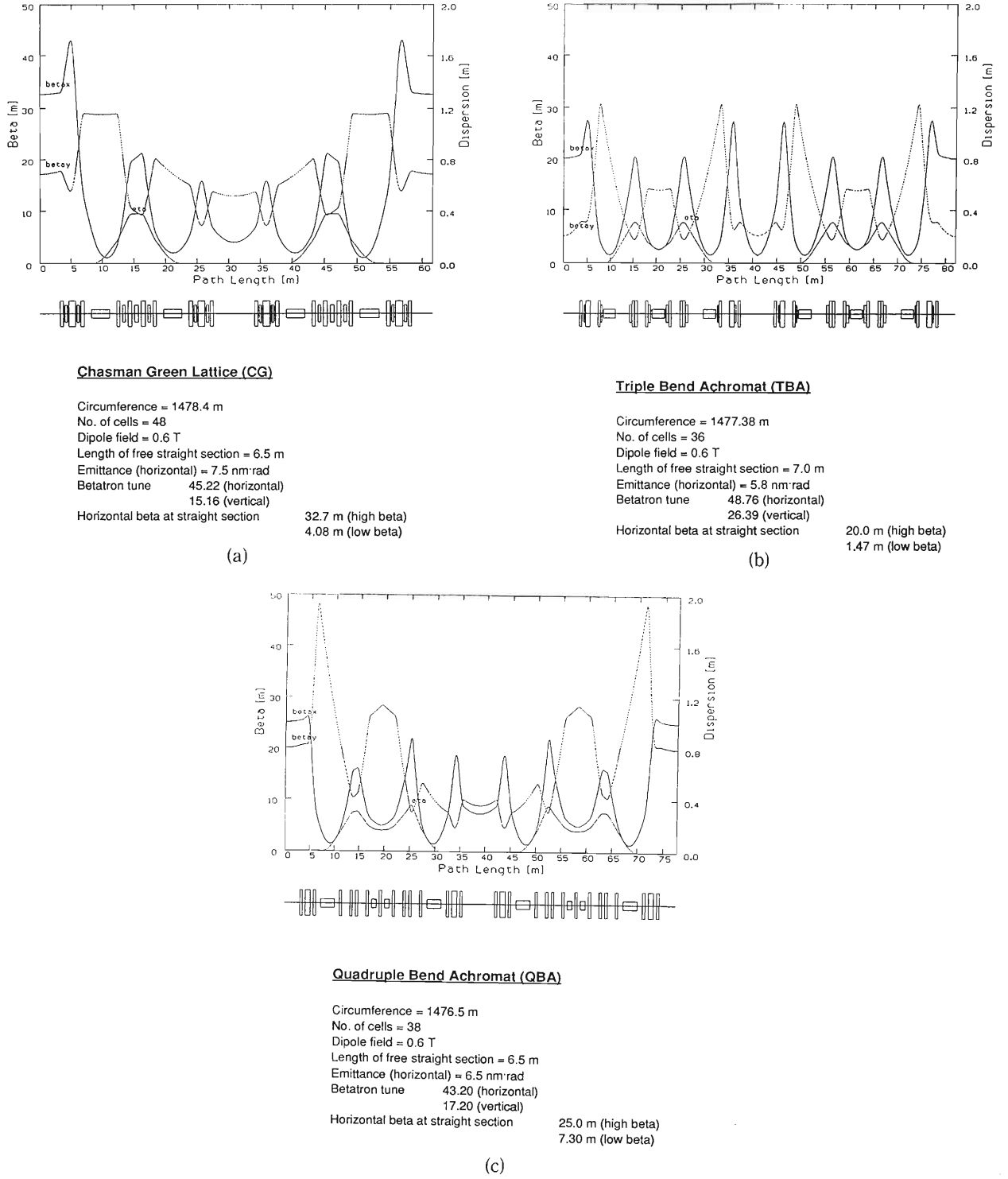


Fig. 1. Optics functions and the major parameters for (a) CG, (b) TBA, and (c) QBA lattice.

$$\begin{aligned} y'' &= -k_y(2k^2\rho^2)(k_y y + k_y^3 y^3/6 + k_y k_x^2 y x^2/2) \\ &\quad + \cos ks/\rho \cdot k_x^2 xy + x' y k \sin ks/\rho \end{aligned} \quad (6)$$

In Eqs. 5 and 6, terms up to third order are retained and we have dropped the subscript  $\beta$ . We notice first that, in situations where  $k_x = ik$  and  $|k| \ll |k_y|$ , the linear effect of ID is equivalent to that of a “pseudo” quadrupole

which is weakly defocusing in the  $x$  direction, and focusing in the  $y$  direction. The weak defocusing in the  $x$  direction can be interpreted as a result of cancellation between the focusing effect of a dipole and the defocusing effect of a magnetic edge. Major nonlinear forces come from the octupole-like components as well as from the sextupole-like components that vary

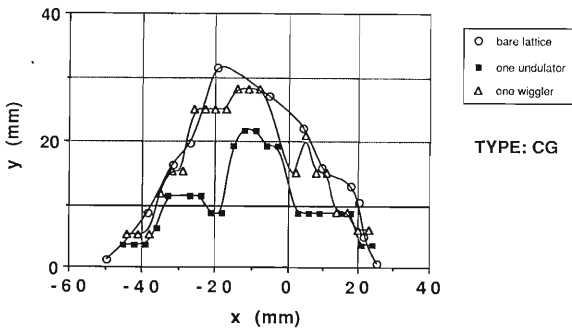


Fig. 2. Effect of one ID on the dynamic aperture of the CG lattice. White circles: Bare lattice. Dark squares: One undulator. White triangles: One wiggler.

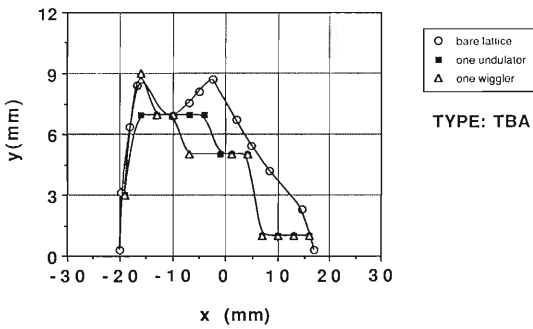


Fig. 3. The same as Fig. 2 for the TBA lattice.

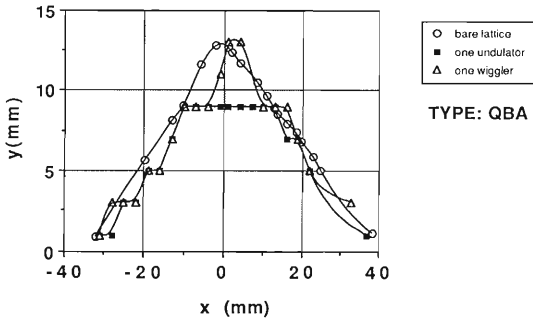


Fig. 4. The same as Fig. 2 for the QBA lattice.

with the position  $s$ . These forces may seriously reduce the dynamic aperture of low-emittance rings in which strong sextupoles are usually optimized to enlarge the dynamic aperture.<sup>4)</sup>

Table 1 lists the parameters of an undulator and a wiggler employed in this study. The optics functions and the major parameters characterizing the ring are shown in Fig. 1 for the three lattice. In all three lattice, the “hybrid” mode is chosen in which high beta sections are for the undulators and low beta sections are for the wigglers.<sup>5)</sup>

The degree of linear optics distortion with one

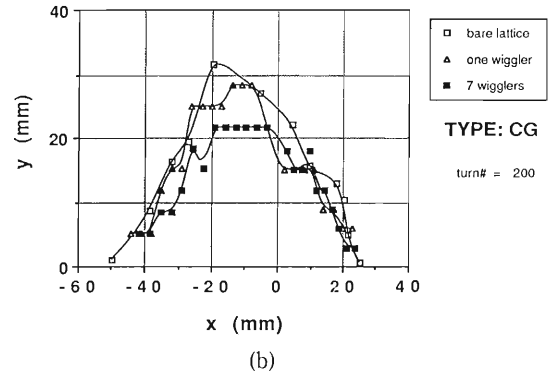
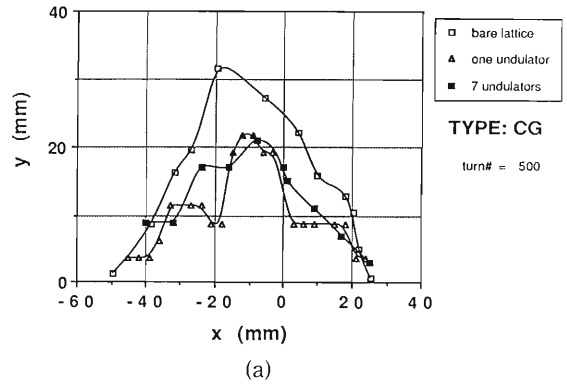


Fig. 5. Dependence of the dynamic aperture on the numbers of IDs included. (a) Undulators. (b) Wigglers. CG lattice is chosen as an example.

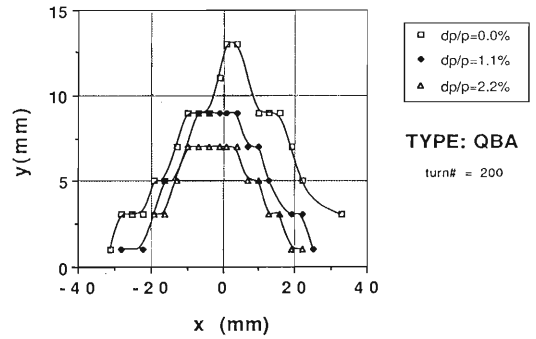


Fig. 6. Momentum dependence of the dynamic aperture with one wiggler. QBA lattice is chosen as an example.

ID in the ring is calculated to be as follows in case of CG lattice: (i) With one undulator,  $\Delta \nu_x = 4.6 \times 10^{-5}$ ,  $\Delta \nu_y = 5.8 \times 10^{-4}$ ,  $\Delta \beta_x/\beta_x = -2.9 \times 10^{-4}$ , and  $\Delta \beta_y/\beta_y = -4.4 \times 10^{-3}$ , (ii) with one wiggler,  $\Delta \nu_x = 4.3 \times 10^{-5}$ ,  $\Delta \nu_y = 3.4 \times 10^{-3}$ ,  $\Delta \beta_x/\beta_x = -2.4 \times 10^{-4}$ , and  $\Delta \beta_y/\beta_y = -2.5 \times 10^{-2}$ . The magnitude of distortion is roughly the same as to the remaining two lattice as well. We find a reasonable result that the distortion is more pronounced with a wiggler due to a smaller  $\rho$ . The degree of distortion by a single ID being nevertheless small, restoration of the optics is done locally by matching betatron functions to their original

values at the midst of an achromatic arc and matching their derivatives to zeros at the center of IDs. By this way, linear optics is unaffected in the cells without IDs. Quadrupole triplets on both side of ID are used for this readjustment. Two quadrupoles are used for the betatron matching, and the remaining one is adjusted to keep the tune shifts minimal. Numerical changes required for quadrupole strength are mostly within few percent and small.

Effects of nonlinear fields on the dynamic apertures are examined in Figs. 2–6. The tracking calculation with IDs is performed in RACE-TRACK by dividing ID into small pieces thereby incorporating the nonlinear forces as kicks according to Eqs. 5 and 6, up to fourth order in amplitudes. What can be noticed from the figures are: (i) Reduction in the dynamic aperture is more pronounced with an undulator than a wiggler. This is plausible since, as seen in Eqs. 5 and 6, the nonlinearity is enhanced with larger wave numbers; this is the case with an undulator that has a much shorter period length. (ii) Observed nonlinear effect is more or less the same for all three lattice considered. (iii) There is no marked dependence on the number of IDs included (see Fig. 5). (iv) With one wiggler in the QBA lattice, the dynamic aperture decreases monotonically with the momentum deviation (see

Fig. 6).

For all these findings, the reduction in the dynamic aperture turned out to be not as large as expected. This fortunate aspect should be attributed primarily to the largeness of the radius of curvature in the 8 GeV machine compared with those of the rings operated at lower energies. Note that the dynamic aperture reduction mostly in the  $y$  direction is due to the assumed relation  $|\kappa| \ll |k_y|$ . We also mention that the linear optics restoration described above does not help, in general, to improve the reduced dynamic aperture: Dynamic aperture may turn out smaller with the restoration. We wish to extend our analysis in future by working with a more realistic field distribution, and in addition, by taking various possible imperfections of the machine into account to examine the validity of our present conclusion.

#### References

- 1) L. Tosi and A. Wrulich: ST/M-88/12 (1988).
- 2) K. Halbach: Workshop on Magnetic Errors, Brookhaven, New York (1986).
- 3) L. Smith: ESG Technical Note-24 (1986).
- 4) R. Nagaoka, H. Tanaka, and M. Hara: *RIKEN Accel. Prog. Rep.*, **21**, 228 (1987).
- 5) R. Nagaoka, H. Tanaka, K. Yoshida, K. Tsumaki, and M. Hara: This Report, p. 227.

## V-2-5. Nonlinear Dynamics with Sextupoles

R. Nagaoka, K. Yoshida, H. Tanaka, K. Tsumaki, and M. Hara

Large amplitude betatron motions of the electrons circulating in low-emittance storage rings are greatly influenced by the nonlinear sextupole fields needed for chromaticity correction. In most cases the resulting dynamic aperture is not adequately large, for instance, to allow the off-axis beam injection. To improve the stability, one needs to elucidate the dynamics of the motion close to the dynamic aperture. An analysis is made taking a Triple Bend Achromat (TBA) lattice as an example (Fig. 1), in which two families of chromaticity correcting sextupoles are located in the dispersive section. The dynamic aperture obtained from tracking calculation<sup>1)</sup> is shown in Fig. 2.

The Hamiltonian describing the motion is given by

$$\begin{aligned} H = & \nu_x I_x + \nu_y I_y + (2I_x)^{3/2} \sum_{jm} A_{jm} \cos Q_{jm} \\ & - 3(2I_x)^{1/2} 2I_y \sum_m [2B_{lm} \cos Q_{lm} + B_{+m} \cos Q_{+m} \\ & + B_{-m} \cos Q_{-m}] \end{aligned} \quad (1)$$

with

$$\begin{aligned} Q_{jm} &= j\phi_x - m\theta \quad (j=1, 3) \\ Q_{\pm m} &= \phi_x \pm 2\phi_y - m\theta \end{aligned} \quad (2)$$

Action and angle variables are denoted by  $I_u$  and  $\phi_u$ , respectively, and  $\nu_u$  is the betatron tune per cell ( $u=x, y$ ). Third and fourth terms on the right-hand side of Eq. 1 express the sextupole

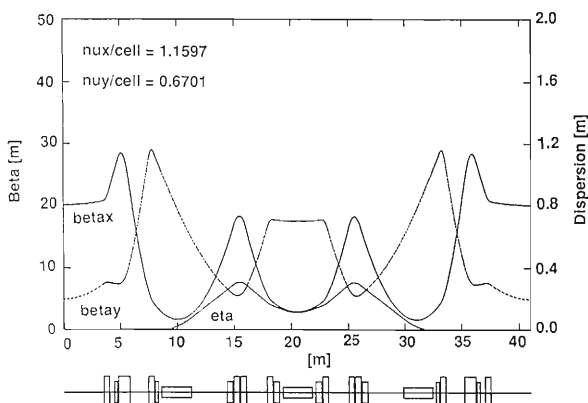


Fig. 1. Betatron and dispersion functions over the Triple Bend Achromat (TBA) cell employed in this study.

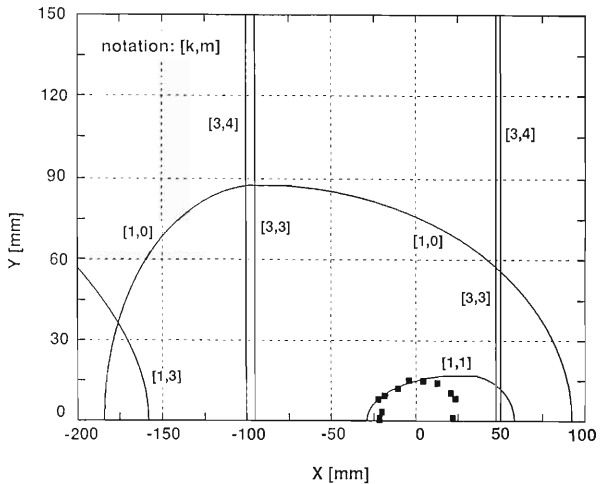


Fig. 2. Prediction of the dynamic aperture in the single resonance approximation for lowest-order (1st and 3rd) sextupolar resonances. Dark squares indicate the actual dynamic aperture of the lattice obtained from the tracking calculation.

potential expanded into harmonics ( $-\infty < m < +\infty$ ).<sup>2)</sup> Time dependence of the system is indicated by the variable  $\theta = 2\pi s/C$  ( $s$ : longitudinal displacement,  $C$ : cell length). Coefficients  $A_{jm}$ ,  $B_{lm}$ , and  $B_{\pm m}$  depend linearly on the strength of sextupoles, and are also dependent on the position of the sextupoles. From Eq. 2, one finds that the resonances occur at  $\nu_x = \text{integer}$  (1st order), and  $3\nu_x = \text{integer}$ ,  $\nu_x \pm 2\nu_y = \text{integer}$  (3rd order).

In case we pick up particular harmonics in Eq. 1 and consider the effect of a single resonance, we can transform the system to the rotating frame to obtain the approximate static stability boundaries.<sup>3)</sup> In Refs. 2 and 4,  $m=1$  boundaries are compared with the tracking results in the Chasman-Green (CG) lattice and are found to agree remarkably well. This means that the stability in the CG lattice, without the harmonic correction, is strongly limited by the integer resonance  $\nu_x = 1$ . Generalization of the procedure is done in Fig. 2, where stability boundaries are depicted for a number of  $m$ 's close to  $\nu_x = 1.1597$ . Although boundaries shown tend to reproduce more or less the actual dynamic aperture, one cannot conclude from this that the dynamics is

determined by any one of these resonances as in the CG lattice. The figure implies the simultaneous contribution of several harmonics.

To look into more details, we observe, in Fig. 3, the phase space behavior at 1% coupling, which is obtained from the tracking calculation. The outer curve and the islands appearing further out are close to the stability limit. The number of islands and the shape of the inner closed curve suggest the excitation of 7th-order resonance. Furthermore, correspondent amplitude-dependent tune is found to be very close to  $1+1/7$ .

It first seemed to us rather unlikely to suppose a resonance of such high order (7th) to be induced by sextupoles. However, if we follow the perturbation theory, we find that, in principle, sextupoles can excite resonances of arbitrary order.<sup>5)</sup> In the following we shall confine ourselves to the one-dimensional case for simplicity and also because we are mainly interested in the horizontal dynamics.

The canonical perturbation theory developed by Poincare and von Zeipel (PZ) defines a transformation of canonical variables from  $(\phi_x, I_x)$  to  $(\psi_x, J_x)$  with the generating function.<sup>6)</sup>

$$S(\phi_x, J_x; \theta) = J_x \cdot \phi_x + \varepsilon S_1 + \varepsilon^2 S_2 + \varepsilon^3 S_3 + \dots \quad (3)$$

where  $\varepsilon$  is a parameter representing the strength of the perturbation (sextupole strength). The idea is to define the function form of  $S_k$  ( $k = 1, 2, \dots$ ) at each order of  $\varepsilon$  so that the action  $J_x$  in the new system becomes an invariant up to that order. When the theory is applied to our problem, we find that following orders of resonance are possible at each order of  $\varepsilon$ :

$$\begin{aligned} \varepsilon^1: & 1, 3 \\ \varepsilon^2: & 2, 4, 6 \\ \varepsilon^3: & 1, 3, 5, 7, 9 \\ \varepsilon^4: & 2, 4, 6, 8, 10, 12 \end{aligned}$$

To see if the observed features of the phase space close to the stability limit can be explained in terms of the 7th-order resonance, we performed a perturbation calculation according to the PZ theory up to  $O(\varepsilon^3)$ . The new Hamiltonian is derived as

$$\begin{aligned} H(\phi_x, J_x; \theta) = & v_x J_x + C_{11} J_x^2 \\ & + 3 \sqrt{2} J_x^{5/2} \sum_{\Lambda M} D_{\Lambda M} \\ & \cdot \cos(\Lambda \phi_x - M \theta), \end{aligned} \quad (4)$$

where  $C_{11}$  is the coefficient describing the second-order tune shift with amplitude,<sup>4)</sup>  $\Lambda$  takes the values 1, 3, 5, 7, and 9, and  $-\infty < M < +\infty$ .

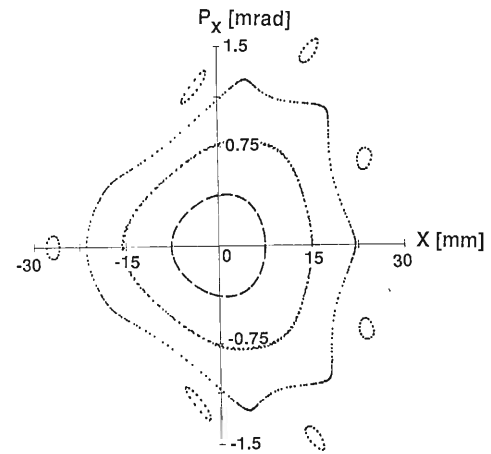


Fig. 3. Phase space obtained from the tracking calculation.

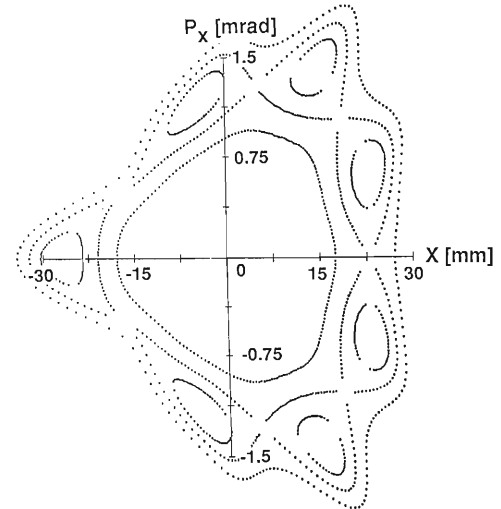


Fig. 4. Phase space obtained analytically from the perturbation calculation of Poincare-von Zeipel (PZ).

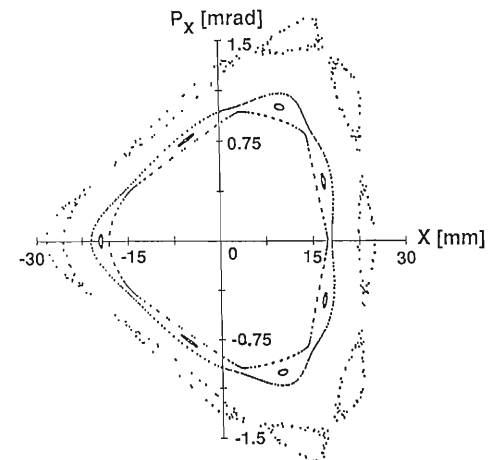


Fig. 5. Phase space obtained from the fictitious tracking using the computer code HRMTRC.

Coefficient  $D_{\Lambda M}$  is composed of triple summation over coefficients  $A_{jm}$ . Here we are interested in the combination  $(\Lambda, M)=(7, 8)$ . In the numerical calculation, convergence for  $D_{78}$  was achieved at  $|m| \approx 90$ . By performing the single resonance approximation in  $O(\epsilon^3)$  and by further transforming the system into the rotating frame, we obtain the analytical phase space behavior, which is shown in Fig. 4. The agreement with the tracking result (Fig. 3) is quite impressive. We found, in particular, that harmonics with the index  $[j, m]=[1, 0], [1, 1], [3, 3]$ , and  $[3, 4]$  have the major contribution to  $D_{78}$ . We notice an interesting relation that these harmonics indeed correspond to the boundaries of the single resonances surrounding the dynamic aperture in Fig. 2.

Knowing that the dynamics is determined only by few harmonics, we tentatively performed a fictitious tracking with a computer code HRMTRC<sup>7)</sup> in which the sextupole field is composed only of the selected harmonics. Figure 5 shows the resultant phase space including above four components. The agreement with the “real” tracking result is less impressive than that of the perturbative approach, but as expected, one can still identify the occurrence of the 7th-order resonance. The discrepancy is due to the remaining contribution of the background harmonics to the amplitude-dependent tune, which is missing in Fig. 5. On the contrary, the remarkable agreement of the perturbative approach with the exact tracking in phase space structure implies that most of the amplitude dependence of the tune fortunately comes from the second-order effect which is rigorously incorporated in the perturbation calculation using the closed formula. Note also the excitation of 8th-order resonance with a larger  $J_x$  in Fig. 5 which is absent in the real tracking. We find this excitation to be reasonable, however, considering how the four harmonics enter the terms of  $O(\epsilon^4)$  to induce 8th-order

resonance with  $M=9$ .

In the present study, we have shown, taking the TBA lattice as an example, that in low-emittance rings, the dynamics of betatron motion close to the dynamic aperture can be subject to higher-order resonances of the sextupoles. Situation differs with the other lattice, of course, depending on the details of their structure, but we have encountered with many in which one can observe the effect of higher-order resonances.<sup>8)</sup>

When one attempts to enlarge the dynamic aperture, following considerations might be of some help: ( i ) Proper choice of the tunes. One should also have in mind the possibility of higher-order sextupolar resonances. ( ii ) Suppression of the harmonics that would otherwise enhance the second-order tune shift with amplitude or limit the stability via first- and third-order resonances (see Fig. 2). ( iii ) Observation of the phase space and the amplitude dependence of the tune to check the contribution of the higher-order effect. If it is notable, one way is to identify the harmonics that are responsible to it and to try to perform the same steps as in ( ii ).

## References

- 1) R. Nagaoka, H. Tanaka, K. Yoshida, K. Tsumaki, and M. Hara: This Report, p. 248.
- 2) E.A. Crosbie: ANL-HEP-CP-87-21 (1987).
- 3) E. Courant, R. Ruth, and W. Weng: SLAC PUB-3415 (1984).
- 4) R. Nagaoka, H. Tanaka, and M. Hara: *RIKEN Accel. Prog. Rep.*, **21**, 228 (1987).
- 5) S. Ohnuma: Proc. US-Japan Semin. High Energy Accelerator Science, p. 114 (1973).
- 6) A.J. Lichtenberg and M.A. Lieberman: Applied Mathematical Science, Vol. 38, Springer-Verlag, p. 71, (1983).
- 7) R. Nagaoka, K. Yoshida, H. Tanaka, K. Tsumaki, and M. Hara: This Report, p. 245.
- 8) R. Nagaoka, H. Tanaka, K. Yoshida, K. Tsumaki, and M. Hara: This Report, p. 227.

## V-2-6. Particle Tracking in Harmonic Expanded Sextupole Fields

R. Nagaoka, K. Yoshida, H. Tanaka, K. Tsumaki, and M. Hara

In designing a lattice for a low-emittance storage ring, optimization of intentionally included sextupole fields is of great importance in achieving a large dynamic aperture of transverse motions.<sup>1-3)</sup> The procedure usually taken is to expand the sextupole fields into harmonics and by somehow identifying the particular harmonics that limit the stability, try to suppress them either by introducing additional sextupoles in the lattice, or by modifying the optics of the lattice. Apart from the problem of whether or not one can successfully eliminate them, the first task is therefore to find out the harmonics that are most responsible to the dynamic aperture. In certain optics, one simply finds that the second-order amplitude-dependent tune shift is dominated by just one harmonic and that this harmonic also determines the dynamics of large amplitude motions. It is possible, in such a case, to step forward to make a theoretical analysis of the system using the single resonance approximation to predict the phase space structure and the stability limit.<sup>1,2)</sup>

Generally, however, it is not the case. There are several harmonics that simultaneously influence the dynamics and they are not necessarily identified from the second-order tune shifts. For this reason, we have developed a computer code "HRMTRC," for an attempt to extract the net effect on beam dynamics brought about by the certain selected harmonics, by performing the following "fictitious" particle tracking. Namely, a tracking in which the field is composed only of specified harmonics. Below is shown the brief scheme as well as some results of the application using HRMTRC.

We initiate from the Hamiltonian expressed in terms of action and angle variables, with the sextupole potential expanded into harmonics. (See Eq. 1 and below of Ref. 4 for the explicit form as well as for the meaning of the notations.) Using the relations

$$z = \sqrt{2}I_z \cdot \cos\phi_z, \quad p_z = -\sqrt{2}I_z \cdot \sin\phi_z, \quad (1)$$

$$(z = x, y)$$

we then rewrite the Hamiltonian in terms of  $x$ ,  $p_x$ ,  $y$ , and  $p_y$ :

$$H = \frac{p_x^2}{2\mu_x} + \frac{p_y^2}{2\mu_y} + V(x, p_x, y, p_y; \theta) \quad (2)$$

where

$$\begin{aligned} V(x, p_x, y, p_y; \theta) &= \frac{x^2}{2\mu_x} + \frac{y^2}{2\mu_y} + a(\theta)x^3 + b(\theta)xy^2 \\ &\quad + c(\theta)x^2p_x + d(\theta)y^2p_x + e(\theta)xp_y + f(\theta)xp_x^2 \\ &\quad + g(\theta)xp_y^2 + h(\theta)yp_xp_y + i(\theta)p_x^3 + j(\theta)p_xp_y^2 \end{aligned} \quad (3)$$

and  $\mu_z = v_z^{-1}$  ( $z = x, y$ ). Ten coefficients  $a(\theta)$ - $j(\theta)$  are given by the infinite sum of products of the harmonics  $A_{jm}$ ,  $B_{lm}$ , and  $B_{\pm m}$ ,<sup>2)</sup> and the sinusoidal functions. The first three coefficients read, for example,

$$\begin{aligned} a(\theta) &= +\sum_m (A_{3m} + A_{lm}) \cos m\theta \\ b(\theta) &= -3\sum_m (2B_{lm} + B_{+m} + B_{-m}) \cos m\theta \\ c(\theta) &= -3\sum_m (A_{3m} + A_{lm}/3) \sin m\theta \end{aligned} \quad (4)$$

Remaining coefficients have similar expressions. Out of the infinite sum over  $m$ , our aim is to keep only of those selected ones. This requires us to carry out a numerical integration at every point in the ring since the effects of harmonics are, by themselves, distributed everywhere. On the other hand, it is well known that non-symplectic numerical integration of the canonical equations may lead one to spurious damping or excitation of the system. With our present Hamiltonian, however, the potential is fully nonlinear in momenta, and in addition, the problem is two-dimensional (see Eq. 3). Canonical integration therefore becomes non-trivial in this case and we shall content ourselves with a method which is accurate only to the lowest order in the integration step:

For a system with the Hamiltonian

$$H = p^2/(2\mu) + V(x, p; t) \quad (5)$$

this approach defines a mapping to the new coordinate system  $(x_1, p_1)$  with the generating function

$$F_3(x_1, p, t) = -x_1p + G(x_1, p, t) \quad (6)$$

Suppose  $x = x_0$ , and  $p = p_0$  at time  $t = t_0$ . With  $h$ ,

the integration step, one chooses  $G(x_1, p, t)$  at  $t = t_0 + h$  to be

$$G(x_1, p, t) = -[p^2/(2\mu) + V(x_1, p, t_0)] \cdot h \quad (7)$$

The resultant canonical relations are

$$x = x_1 + p/\mu \cdot h + V_p(x_1, p, t_0)h, \quad (8)$$

$$p_1 = p + V_{x1}(x_1, p, t_0)h, \quad (9)$$

$$H_1 = V_{x1}(x_1, p, t_0)[p/\mu + V_p(x_1, p, t_0) + V_t(x_1, p, t_0)]h, \quad (10)$$

where the subscripts denote partial derivatives. It should be stressed that, with the above transformation, the new Hamiltonian  $H_1$  has become of  $O(h^1)$ . Since  $x_1 = x_0$  and  $p_1 = p_0$  at  $t = t_0$  as seen from Eqs. 8 and 9, it follows that

$$x_1(t) = x_0 + O(h^2) \quad (11)$$

$$p_1(t) = p_0 + O(h^2) \quad (12)$$

One therefore obtains  $x(t)$  and  $p(t)$  from Eqs. 8 and 9 within the accuracy of  $O(h^1)$  by replacing  $x_1$  and  $p_1$  by  $x_0$  and  $p_0$ , respectively. Note however that when the potential is momentum dependent, Eq. 9 generally cannot be solved analytically for  $p$ . Indeed, in our problem coupled equations for  $p_x$  and  $p_y$  must be solved numerically using, for example, Newton's method. A trial has been made, in analogy with the techniques found in Ref. 5, to develop an integration scheme which is accurate to higher orders in  $h$ , but since it inevitably involves several steps solving the coupled

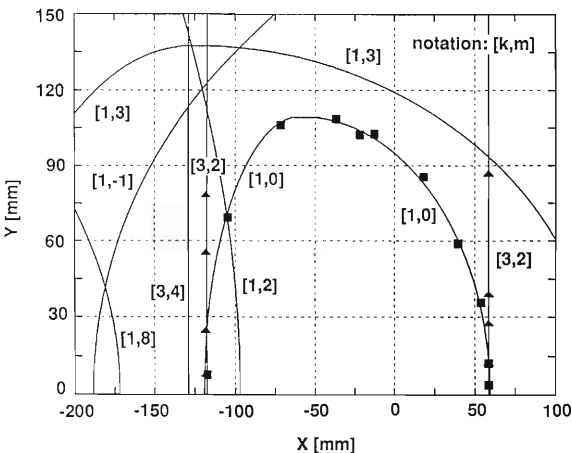


Fig. 1. Comparison of the dynamic apertures between the HRMTRC results (dark squares and dark triangles) and the theoretical predictions in the single resonance approximation (solid lines). Dark squares: Single effect of the harmonics  $[k, m] = [1, 0]$  (1st-order resonance). Dark triangles: Single effect of the harmonics  $[k, m] = [3, 2]$  (3rd-order resonance).

equations for the momenta, we thought it better to use the lowest-order formulas and take  $h$  to be sufficiently small.

Input data for HRMTRC are the same as for the program DYNAM.<sup>3)</sup> Strength, location, and betatron phase of the sextupoles. Prior to tracking, ten coefficients  $a(\theta) - j(\theta)$  are prepared at every integration point in the ring, taking account only of the specified harmonics. Division of  $\theta$ , namely, the integration step size  $h$  is determined from the convergence of the integration as well as from the degree of agreement with the result of DYNAM when all the harmonics are added up. It turned out that with the lattice considered so far, an accuracy of  $\sim 1\%$  is obtained when the longitudinal increment is taken to be as small as 1.5 mm. This amounts to the division of the ring into  $\sim 20,000$  pieces in case of single cell tracking which is permissible

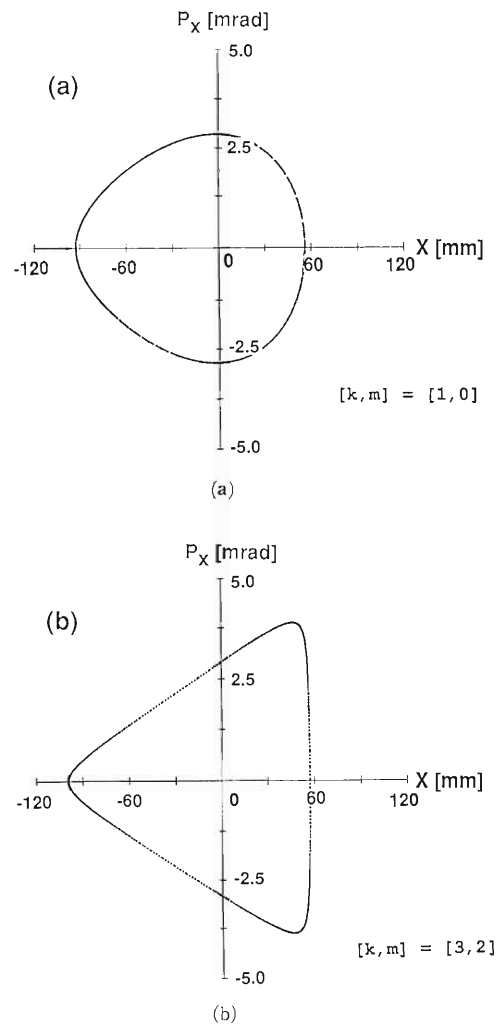


Fig. 2. Phase space obtained from the tracking calculation with HRMTRC. Horizontal-vertical coupling is taken to be 1%. (a) Effect of harmonic  $[k, m] = [1, 0]$  (1st-order resonance). (b) Effect of harmonic  $[k, m] = [3, 2]$  (3rd-order resonance).

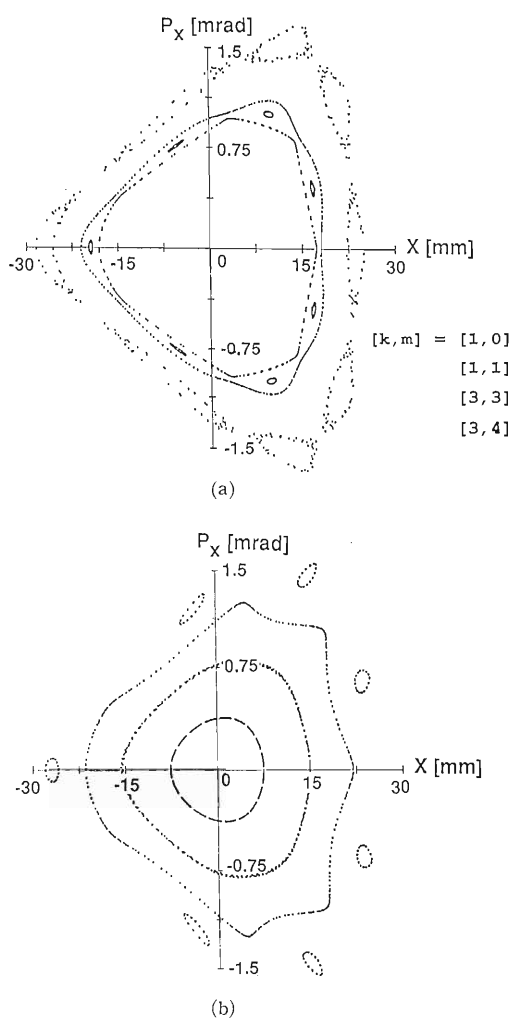


Fig. 3. Phase space with a combined effect of several different harmonics. (a) "Fictitious" tracking result with HRMTRC. Four components  $[k, m] = [1, 0], [1, 1], [3, 3]$ , and  $[3, 4]$  are included. (b) "Real" tracking result with DYNAM.<sup>3)</sup> Horizontal-vertical coupling is 1% in both cases. Calculations are done with the Triple Bend Achromat (TBA) lattice.<sup>4)</sup>

for an ideal lattice. The cpu time measured is roughly 60 s for 250 turn tracking using the computer machine FACOM M780.

In Fig. 1 we show the dynamic apertures calculated by HRMTRC, which demonstrate the effect of single harmonics for two cases. A Chasman-Green lattice in its "high beta" mode is used as an example.<sup>1)</sup> Corresponding phase space structures are observed in Fig. 2. Characteristics of the first-order (a), and the third-order (b) resonances can be seen. Compared in Fig. 1 by the solid lines are the theoretical predictions in the single resonance approximation. The very good agreement with the results of HRMTRC ensures the validity of both approaches.

The phase space in Fig. 3 provides an example in which several harmonics altogether determine the behavior of a large amplitude motion. In this particular case, effects of harmonics are combined to induce higher-order resonances (7th and 8th); this is also confirmed by DYNAM.<sup>4)</sup> Here we find the significance of HRMTRC: The analysis of higher-order resonances is usually quite tedious in the perturbation theory. Finally, we also refer to the apparent limitation of HRMTRC. It can be an especially helpful tool when the influence of the harmonics are not widely spread. The analysis might be difficult, for instance, in case the dynamics involves tune shifts with amplitude caused by a large number of harmonics, even though the stability limit is determined by only few of them.

## References

- 1) R. Nagaoka, H. Tanaka, and M. Hara: *RIKEN Accel. Prog. Rep.*, **21**, 228 (1987).
- 2) E. A. Crosbie: ANL-HEP-CP-87-21 (1987).
- 3) R. Nagaoka, H. Tanaka, K. Yoshida, K. Tsumaki, and M. Hara: This Report, p. 248.
- 4) R. Nagaoka, K. Yoshida, H. Tanaka, K. Tsumaki, and M. Hara: This Report, p. 242.
- 5) R.D. Ruth: *IEEE Trans. Nucl. Sci.*, **NS-30**, 2669 (1983).

## V-2-7. Computer Code CATS: A Code for Sextupole Optimization

R. Nagaoka, H. Tanaka, K. Yoshida, K. Tsumaki, and M. Hara

The goal of the lattice design in storage rings is to attain a magnet arrangement which, with fulfillment of the required performance of the machine, is capable of a long term beam accumulation. The design procedure is roughly divided into two parts: (1) Construction of linear optics; (2) Verification of dynamical properties by tracking a particle in computer simulation. Steps 1 and 2 continue repeatedly until a satisfactory solution is found. There are many computer codes with which to do these jobs. Codes such as Synch and Magic are for optics designing,<sup>1)</sup> and Racetrack,<sup>2)</sup> Patricia, and Teapot<sup>3)</sup> are for particle tracking.

One big reason for the need of step 2 is the strong nonlinearity of the machine due to sextupole magnets: Sextupoles are introduced in step 1 for chromaticity correction, but since they inevitably limit the transversal stability, the dynamic aperture is measured in step 2. In low-emittance machines where the strength of sextupoles tends to be large, the reduction of the dynamic aperture becomes above all serious. What one does for the cure is to include additional sextupoles, *i.e.* the "harmonic" sextupoles, in the lattice to cancel the origin of instability.<sup>4,5)</sup> This is not trivial in general, since with sextupoles, the problem is by nature nonlinear. Optimization of the sextupoles is therefore not only important but also accounts for a large portion of the work in the lattice design.

Being prompted by the necessity, we have developed a computer code that would mediate between the two groups of codes mentioned above: A code that optimizes the strength of harmonic sextupoles to enlarge the dynamic aperture. "CATS" is what we named for the code, since "Correction of Amplitude-dependent Tune Shifts" was initially the main purpose of it. As seen in Fig. 1, the stream of the procedure using CATS is composed of two parts: the sextupole optimization and the tracking. This is because, as already stated, the sextupole optimization being a complicated nonlinear problem, it

has no definite recipe; it must be done more or less by trial and error. There are also several graphic routines at each step. Below we explain main features of the code as well as the functions of supplementary graphic routines.<sup>†</sup>

### (I) CATS and related graphic routines

CATS is composed of more than 20 small subroutines. Some of them are used to calculate the quantities needed for the optimization: The linear optics, linear chromaticity and its correction, harmonics of the sextupole potential, distortion functions, second-order amplitude-dependent tune shifts, and so on. Basically, calculation in CATS is done for a unit superperiodic cell of the ring. In the input file must be included the information on the magnet arrangement as well as the specification of the sextupoles to be optimized.

The optimization is performed by making a least-square fit of a certain function defined in the routine "MODLFN" which is to be linked with CATS. MODLFN is provided with common blocks of harmonics of the sextupole potential and coefficients for the second order tune shifts

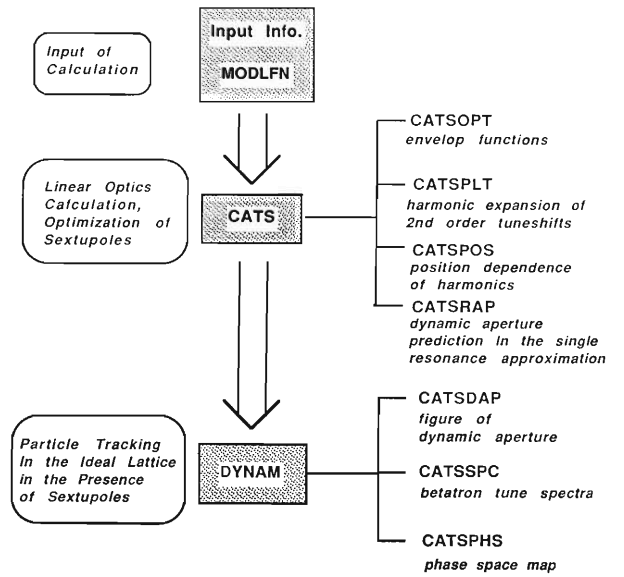


Fig. 1. Stream of optimization procedure with CATS.

<sup>†</sup> All the graphic figures take the 8 GeV Chasman-Green lattice in its hybrid mode<sup>7)</sup> as an example.

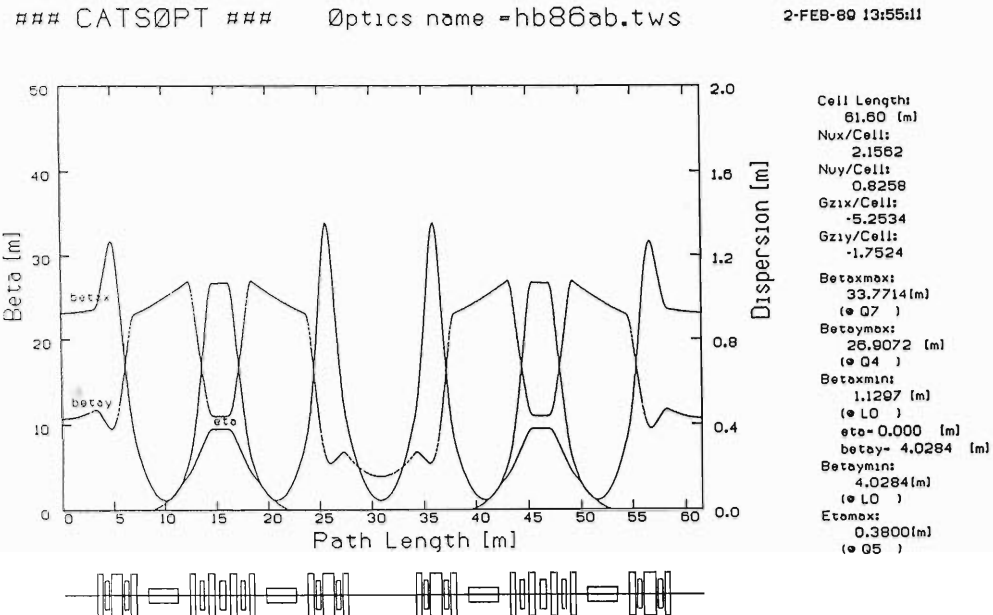


Fig. 2. Linear optics function over a superperiodic cell.

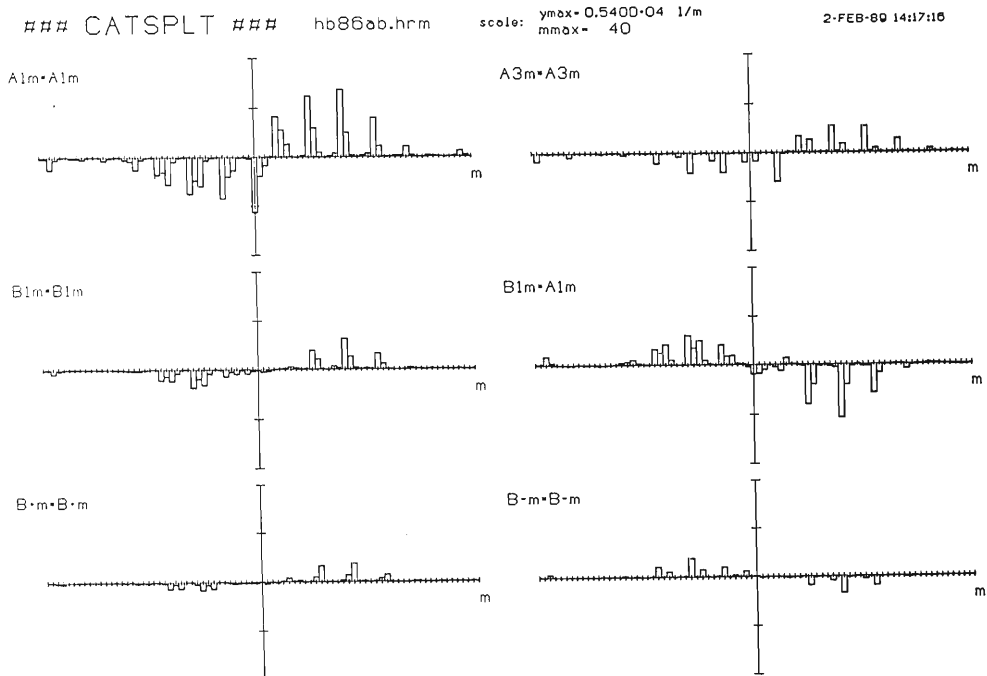


Fig. 3. Harmonic expansion of the second order tune shifts with amplitude.

with amplitudes. Depending on the situation, one then defines, in terms of these quantities, a "best" form of the model function to be least-square fitted. By this way, one can make an attempt either to minimize tune shifts with amplitudes or to eliminate the selected harmonics or any combination of these two.

In addition to the fitting result, CATS provides output files with which one can execute following graphic routines: (i) CATSOPT: Draws a figure of the envelope functions over a superperi-

odic cell (Fig. 2). Some of the useful information as regards the optics are also listed aside. (ii) CATSPLT: Draws a figure that demonstrates how each of the harmonics contributes to the coefficients describing the second-order amplitude-dependent tune shifts (Fig. 3).<sup>4)</sup> This helps identifying the individual harmonics responsible to the tune shifts. (iii) CATSPOS: For a given integer specifying the harmonics, draws a figure over a superperiodic cell that displays the position dependence of the harmonics (Fig. 4). This is

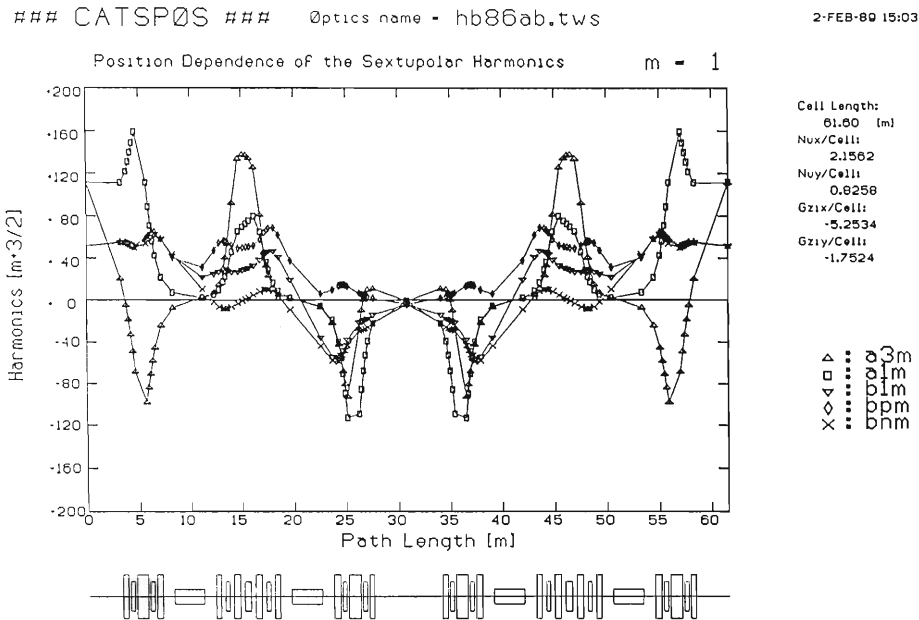


Fig. 4. Position dependence of the harmonics for a given  $m$ . The figure takes  $m=1$ .

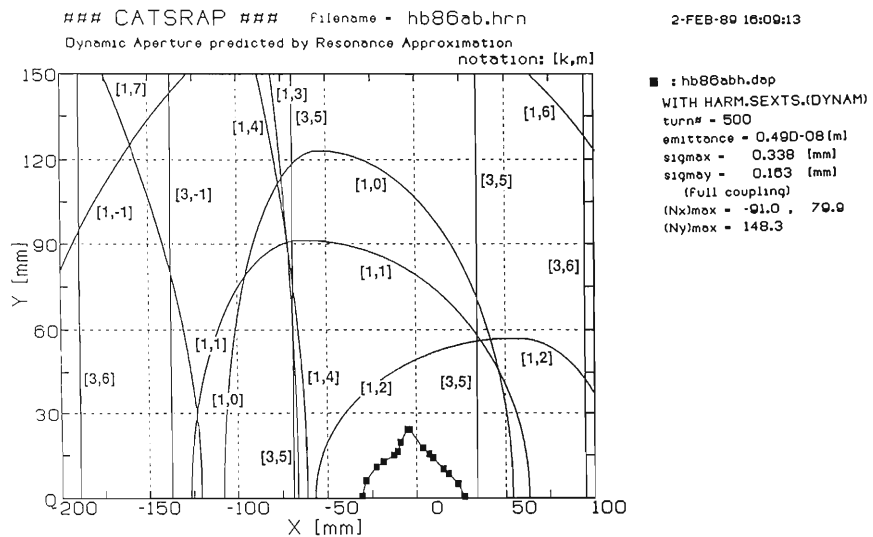


Fig. 5. Comparison of the dynamic aperture between the theory and the tracking. Theoretical predictions rely on the single resonance approximation (solid lines). Dark squares are the tracking results calculated by DYNAM.

useful in determining the optimal location of the sextupoles in case one wishes to eliminate the effect of a certain harmonic. (iv) CATSRAP: Calculates stability limits brought about by each of the harmonics using the single resonance approximation,<sup>6)</sup> and draws them in the  $x$ - $y$  plane in comparison with the actual dynamic aperture (Fig. 5). Although the calculation includes only the contribution of the lowest-order resonances (1st and 3rd), this provides another view of the effect of harmonics on the dynamics which may not be clear from the tune shift analysis using CATSPLT.

## (II) DYNAM and related graphic routines

Owing to the trial and error nature of the optimization procedure, the effectiveness of optimization must be checked at once in terms of the dynamic aperture. This is readily done by DYNAM which reads the output file of CATS containing necessary information for particle tracking: Strength and location (betatron phase advance) of the sextupoles. DYNAM is a tracking code, but it is merely organized to calculate the dynamic aperture of an ideal lattice in the presence of sextupoles. More realistic tracking with Closed-Orbit Distortions (COD), or correc-

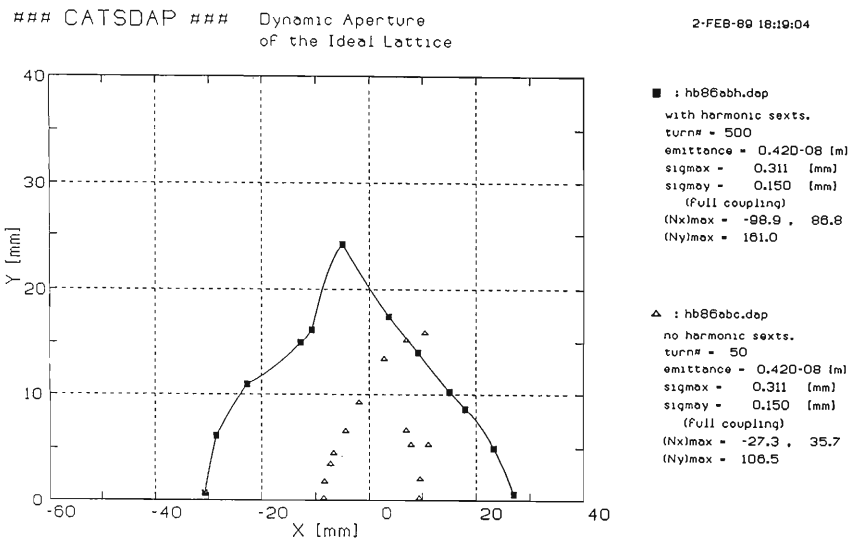


Fig. 6. Figure of the dynamic aperture calculated by DYNAM.

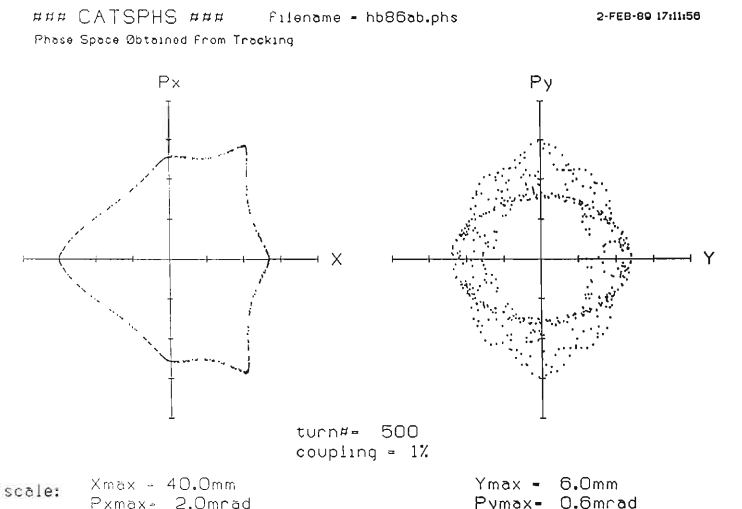


Fig. 7. Phase space map obtained from the tracking result of DYNAM.

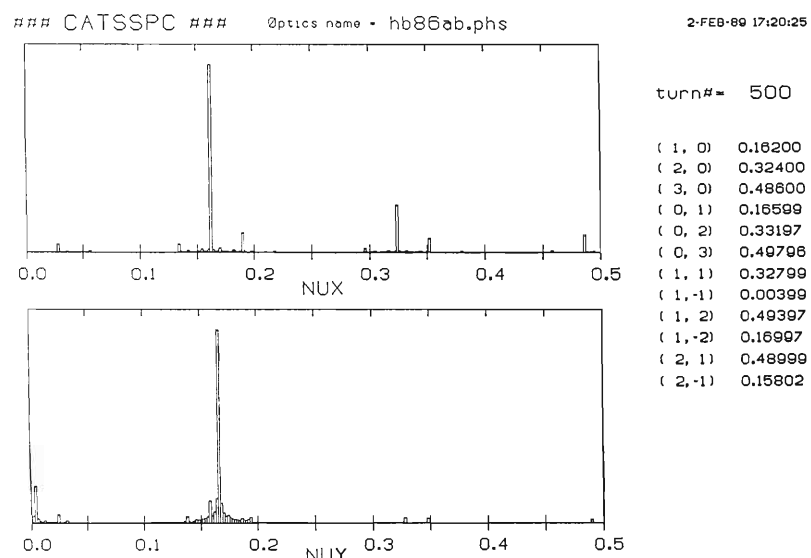


Fig. 8. Betatron tune spectra. Fourier analysis is made on the turn by turn phase space data calculated by DYNAM.

tion of COD, etc. must be done with codes such as RACETRACK in step 2.

Like other kick codes, DYNAM treats sextupoles as thin elements. Courant-Snyder coordinates are employed in two dimensions and the integration scheme is quite simple: Multiplication of a sinusoidal matrix between the sextupoles, and addition of amplitude-dependent kicks on the gradients at the sextupoles. Following RECETRACK,<sup>2)</sup> the dynamic aperture is pursued *via* iteration using the bisection method. Tracking calculation is preceded by preparing an input file controlling the conditions of the computation. Dynamic apertures can also be calculated for a number of couplings in a single run. The cpu time needed to obtain the outer curve of the dynamic aperture shown in Fig. 6 (Condition: 500 revolutions and 10 iterations each for 12 couplings) is, for example, 37 s with MICROVAX 3600.

There are three graphic routines that can be executed with the output files of DYNAM: (i) CATSDAP: Draws a figure of dynamic apertures in the  $x$ - $y$  plane (Fig. 6). (ii) CATSPHS: Reads the turn by turn data on  $(x, x', y, y')$  and draws a figure of the phase space mapping (Fig. 7). (iii) CATSSPC: This also reads the phase space data and performs Fourier analysis of the betatron

tunes to provide the plot shown in Fig. 8. CATSPHS and CATSSPC are particularly useful in analyzing the dynamics of large amplitude motions.

We have shown the structure and the capability of the computer code CATS developed for the sextupole optimization. The main feature of the code is that procedure for the optimization is supported by several supplementary routines, including the particle tracking, which help to find the right direction in the trial and error work. The code has been quite useful in our lattice design,<sup>7)</sup> and we still hope to extend its capability in future.

## References

- 1) A.A. Garren, A.S. Kenney, E.D. Courant, and M.J. Syphers: FN-420, 0170.000 (1985); A.S. King, M.J. Lee, and W.W. Lee: SLAC Report No. 183 (1975).
- 2) A. Wrulich: DESY Report-84-026 (1984).
- 3) H. Wiedemann: PEP-220 (1976); L. Schachinger and R. Talman: SSC-52 (1985).
- 4) R. Nagaoka, H. Tanaka, and M. Hara: *RIKEN Accel. Prog. Rep.*, **21**, 228 (1987).
- 5) E.A. Crosbie: ANL-HEP-CP-87-21 (1987).
- 6) E. Courant, R. Ruth, and W. Weng: SLAC PUB-3415 (1984).
- 7) R. Nagaoka, H. Tanaka, K. Yoshida, K. Tsumaki, and M. Hara: This Report, p. 227.

## V-2-8. Study of the Beam Injection to a 6 GeV Storage Ring

H. Tanaka, R. Nagaoka, K. Yoshida, K. Tsumaki, and M. Hara

The beam injection to a 6 GeV storage ring was studied and the main parameters of the beam injection were determined.

It is planned that electrons and positrons are repeatedly injected into a 6 GeV storage ring from an injector synchrotron to storage high (about 100 mA) currents. To perform multi-injection efficiently, we adopt an off-axis injection method. This method requires strong (a few kGauss) bump magnets that are capable of on-and-off within a few  $\mu$ s and have a more than 1  $\mu$ s flat top (the circulating period of this ring is about 4  $\mu$ s). In case when we find these requirements are too severe to design bump magnets, we will introduce following two concepts to overcome difficulty of the magnet design. One is a "fractional betatron tune," which allows the change of the on-and-off period to be easy, about 10–15  $\mu$ s corresponding to the period that an injected beam returns to a septum magnet. The other is the use of "many bump magnets," which reduces the strength of a bump magnet.

As an injection point, a dispersion-free long straight section of 7 m was selected because no other long section with high  $\beta_x$  was found. The basic design of the beam injection and a lattice<sup>1)</sup> configuration of one cell are shown in Table 1 and Fig. 1.

Assuming that a beam has a Gaussian distribution, we calculated the relative beam positions around a thin septum and the amplitude of a bump orbit from the standpoint that a beam loss at the septum is only due to the static beam distribution. The beam loss consists of three parts. First, loss occurs when an injected beam passes through the outside of the septum only at once (beam loss 1). Second, loss occurs when an

injected beam passes through the inside of the septum repeatedly, damping its transient large emittance to equilibrium one (beam loss 2). Third, loss occurs when the beam stored and damped passes through the inside of the septum repeatedly (beam loss 3). The beam loss 2 and 3 are estimated under the condition that a beam diffusion rate is sufficiently fast to recover a beam constant distribution during the beam circulating period. The results estimated for four

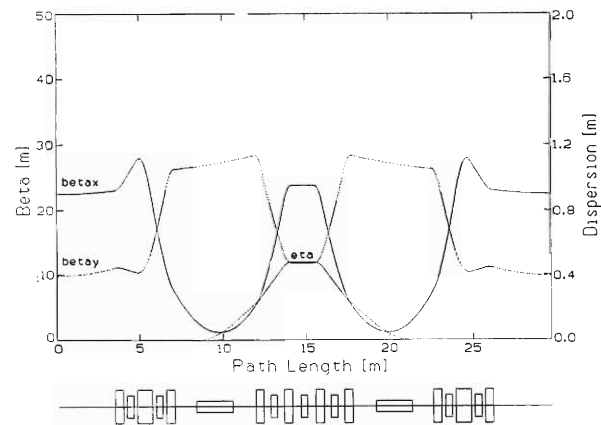


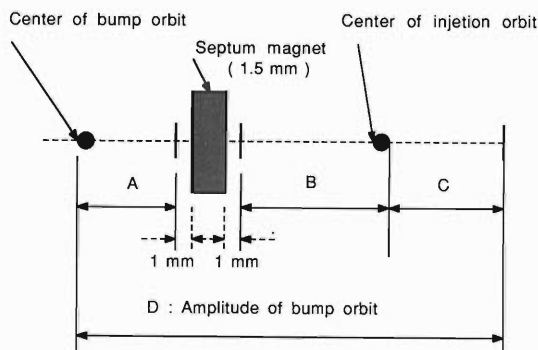
Fig. 1. Lattice configuration of one cell.

different beam losses are shown in Fig. 2. Though a large amplitude of the bump orbit insures a small static beam loss, we need a large dynamic aperture. A large amplitude, on the other hand, reduces a dynamic aperture significantly and increases dynamic beam loss. That is, a realistic injection efficiency depends on the balance of a static beam loss and a dynamic beam loss. The relative beam positions and the amplitude of the bump orbit should therefore be decided considering the reduction in the dynamic aperture, as described later.

The bump magnet arrangement was determined in consideration of the strength of a bump magnet and easiness of the installation of equipment. For the current lattice structure and to minimize the number of magnets, we examined the three cases in which with two pairs of the bump magnets are used as shown in Fig. 3. The strength of the bump magnet was calculated by an original computer code "INJECT," which was

Table 1. Basic conditions of the injection system.

Injection method	off-axis
Bump orbit recovery period	1 turn (about 4 $\mu$ s)
...Option "fractional betatron tune"	3–4 turn (10–15 $\mu$ s)
Beam injection point	Dispersion free long straight section (7 m)
Number of bump magnets	4 (2×2)
...Option "many bump magnets"	6 (3×3) or 8 (4×4)



Case	Total static loss (%)	$A$ (mm) [ $\sigma_0$ ]	$B$ (mm) [ $\sigma_1$ ]	$C$ (mm) [ $\sigma_1$ ]	$D$ (mm)
a	0.03	2.06 [4.8]	6.56 [4.0]	8.53 [5.2]	18.59
b	1.5	1.68 [3.9]	4.26 [2.6]	7.22 [4.4]	14.98
c	3.0	1.59 [3.7]	3.72 [2.3]	6.89 [4.2]	14.11
d	9.0	1.51 [3.5]	3.12 [1.9]	6.56 [4.0]	13.18

$\sigma_1$ :  $\sigma_{(\text{injected beam})} = 1.64 \text{ mm}$ ,  $\sigma_0$ :  $\sigma_{(\text{stored beam})} = 0.43 \text{ mm}$ .  
Thickness of septummagnet = 1.5 mm.

1 mm allowance is taken at both sides of septum magnets.

$D$  is defined as the distance between center of reference orbit and center of bump orbit.

Fig. 2. Results of calculated beam losses due to static beam distribution.

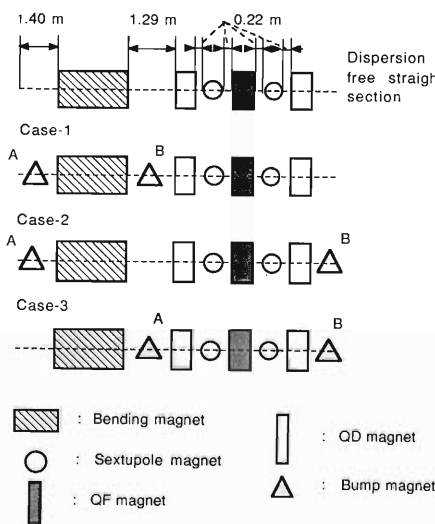


Fig. 3. Three kinds of bump magnets arrangements.

confirmed to work correctly with the result of "RACETRACK."<sup>2)</sup> The calculations are shown in Fig. 4, from which the strength of a magnet is found the best in case-1 (a pair of bump magnets is located with a bending magnet between). The

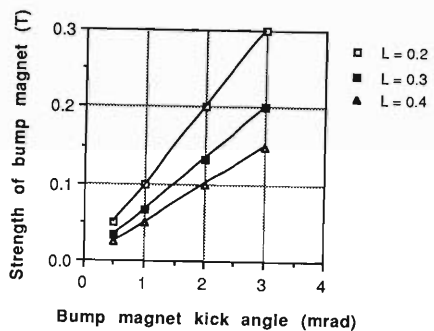
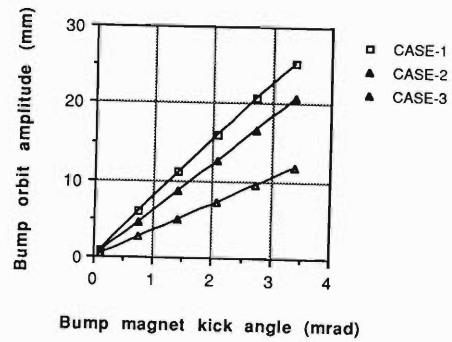


Fig. 4. Correlations between bump magnet kick angles and bump orbit amplitudes (upper diagram) and between bump magnet kick angles and strength of bump magnets (lower diagram).

difference between case-1 and case-2 (one bump magnet is located in the long drift space next to the bending magnet and the other in the long straight section) is not substantial. From easiness of installation of equipment, case-2 is the best because a crotch absorber of about 1 m should be installed besides the bending magnet. It is quite tight to locate both crotch and bump magnet in a short drift space besides a bending magnet of 1.29 m (see Fig. 2; two drift space besides the bending magnet have different lengths, 1.40 and 1.29 m). After all, we selected case-2 especially to avoid difficulty in installation.

We suspected that generating a bump orbit would influence beam dynamics, because a few sextupole magnets exist on the orbit. The sextupoles induce a linear tune shift in accordance with the amplitude of the bump orbit at their positions to shift a workpoint. A simulation subroutine of off-axis injection was added to "RACETRACK" to study the effect of the bump orbit on beam dynamics. Figure 5 shows the relation between the dynamic aperture and the bump orbit existing time in the turn number. Although the dynamic aperture is much reduced at the constant bump orbit, the reduction of the dynamic aperture is a little under the condition that the bump orbit only remains at a few turns from injection. Since the fractional tune of hori-

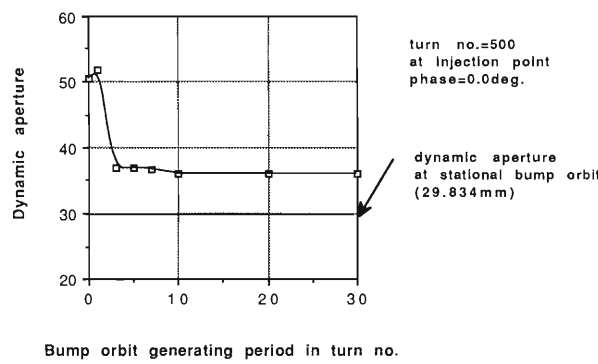


Fig. 5. Dependence of the dynamic aperture on the bump orbit existing time in a turn number. X-Y coupling is 0.01 and the tracking turn number is 500. The calculating point is at the center of the straight section. The amplitude of the bump orbit is 20.6 mm.

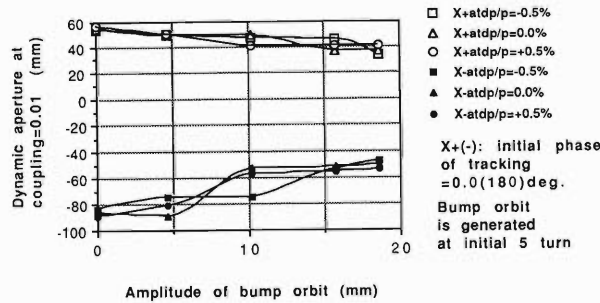


Fig. 6. Dependence of the dynamic aperture on the amplitude of the bump orbit. X-Y coupling is 0.01 and the tracking turn number is 500. The calculating point is at the center of the straight section. Existing time of the bump orbit in a turn number is 5.

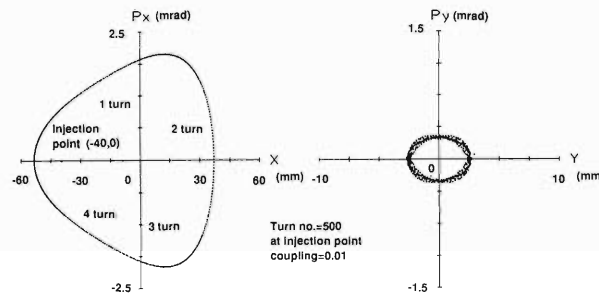


Fig. 7. Phase space of a particle injected at 40 mm amplitude from the inside of the ring. The amplitude of the bump orbit is 18.59 mm and existing time in a turn number is 5. This phase space represents coherent betatron oscillation. Amplitudes of oscillation are calculated under the condition that the bump orbit is a center of oscillation while the bump orbit is on and under the condition that the reference orbit is a center of oscillation while the bump orbit is off.

horizontal betatron oscillation is about 0.20, the maximum turn number under existence of the bump orbit is 5 turns even if a “fractional betatron tune” concept is taken. The dynamic

aperture with momentum errors was investigated under the bump orbit condition mentioned above. The dependence of the dynamic aperture on the amplitude of the bump orbit for three kinds of momenta is shown in Fig. 6, from which the dynamic aperture is found to be kept 40 mm in the injection side even at the largest bump amplitude (about 20 mm). Although only the effect of the bump orbit on an ideal ring was studied here, it was found, from other error analysis,<sup>3)</sup> that practical gradient errors did not greatly reduce the dynamic aperture. This means that the 6 GeV high  $\beta$  solution is not sensitive to the relation of a betatron phase advance among the sextupoles and that a high recovery ratio will be achieved by sufficient correction of closed orbit distortion (COD). Thus we adopted the bump orbit with an amplitude of 18.59 mm. In Fig. 7, an aspect of the phase space around 40 mm amplitude is shown. Although emittance growth due to bump orbit off is found, the phase space is clean and no micro-structure is found as expected.

In addition, we investigated whether the energy aperture was enough for an injected beam from the synchrotron. It is expected that the longitudinal condition of the injected beam is  $dP/P_0 = 0.001$ ,  $\sigma_z = 2.0$  cm. The energy aperture

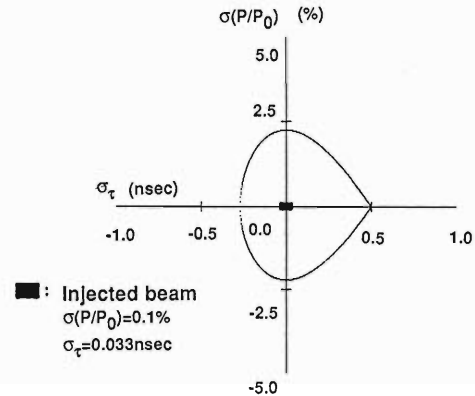


Fig. 8. Energy aperture with the injected beam.

Table 2. List of the final parameters for beam injection.

Amplitude of the bump orbit:	18.59 mm
Distance between the bump orbit and the inside of septum:	3.06 mm
Distance between the injection orbit and the outside of septum:	7.56 mm
Distance between the injection orbit and the inside of septum:	9.53 mm
Arrangement of bump magnets:	Case-2
Strength of bump magnets magnet-A	3.046 mrad
magnet-B	0.573 mrad

calculated at 10 MeV<sup>4)</sup> RF maximum voltage of the storage ring is shown with the injected beam in Fig. 8, indicating sufficiently large for the injected beam.

The parameters decided for the injection system are listed in Table 2.

The injection efficiency has not been calculated yet, but an injection efficiency calculation subroutine is being added to "RACETRACK" and it will be estimated soon. Moreover, we hope to investigate the effect of the bump orbit on the practical ring with errors under the condition

that the COD is corrected in the ring by the extension of the injection simulation subroutine.

#### References

- 1) H. Tanaka, R. Nagaoka, and M. Hara: *RIKEN Accel. Prog. Rep.*, **21**, 225 (1987).
- 2) A. Wrulich: DESY Report, 84-026 (1984).
- 3) RIKEN Accel. Group Synchrotron Radiation Facility Planning Section: CDR of STA 6GeV SR Project, 2-1 (1988).
- 4) T. Yoshiyuki, T. Kusaka, and M. Hara: *RIKEN Accel. Prog. Rep.*, **21**, 235 (1987).

## V-2-9. Beam Lifetime of the 6 GeV Electron Storage Ring

K. Tsumaki

In an electron storage ring for a synchrotron radiation source, the beam lifetime of several tens of hours is required. The beam lifetime in an electron storage ring depends on the gas pressure in a vacuum chamber, a vacuum chamber aperture, and a beam density. We then need to know the relation between the beam lifetime and these quantities. Thus, the beam lifetime has been studied by using a computer code ZAP.<sup>1)</sup>

Physical processes which determine the beam lifetime are gas scattering, single Coulomb scattering within a bunch (Touschek scattering), and a quantum effect. Since the quantum lifetime can be easily controlled by RF cavity voltage and the RF voltage can be determined to have an enough lifetime, calculation of the quantum lifetime is excluded. In this paper, we report the calculation results of the gas scattering lifetime and the Touschek lifetime.

### (1) Gas scattering lifetime

When an electron beam circulates in a vacuum chamber, it collides with residual gas and some of electrons are lost. There are two processes of scattering. One is the elastic scattering by nuclei and the other is the Bremsstrahlung by nuclei. An electron scattered by nuclei changes its direction of movement and a large change in the movement direction leads to a collision with a vacuum chamber. On the other hand, electrons which lose more energy than some limiting energy by Bremsstrahlung leave the energy aperture and get lost.

The beam lifetime affected by elastic scattering is determined by the smallest size of an aperture which is the aperture where an undulator is installed. The lifetimes determined by elastic scattering and Bremsstrahlung are calculated as a function of a chamber aperture under the conditions listed in Table 1. Residual gases

Table 1. Conditions for calculation of the gas scattering lifetime.

Momentum half-aperture $\Delta E/E$	2.2%
Averaged beta value $\beta_y$	18.39 m
Beta value at undulator section $\beta_y$	9.82 m
Gas species	H <sub>2</sub>
	CO
Pressure	$10^{-9}$ Torr

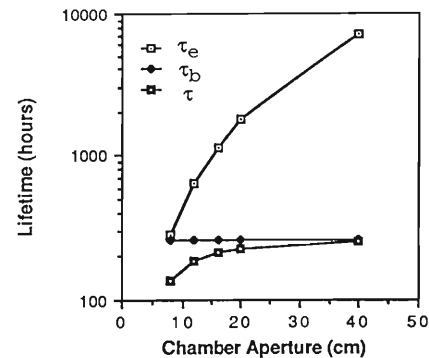


Fig. 1. Gas scattering lifetime as a function of a chamber aperture.  $\tau_e$ , the lifetime determined by elastic scattering;  $\tau_b$ , the lifetime by Bremsstrahlung;  $\tau$ , the total lifetime by gas scattering.

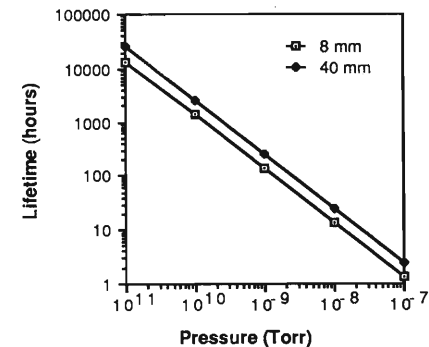


Fig. 2. Gas scattering lifetime as a function of gas pressure.

are assumed to be H<sub>2</sub> and CO. In both elastic and inelastic scatterings, the scattering cross section is almost proportional to the square of the atomic number  $Z$ , and thus the lifetimes are almost governed by CO gas.

Calculated results are shown in Fig. 1. The lifetime determined by elastic scattering is almost the same as the lifetime of inelastic scattering for an 8 mm chamber aperture. For a larger chamber aperture, the lifetime is almost governed by inelastic scattering; however, very long lifetimes are realized for chamber apertures larger than 8 mm. Figure 2 shows the lifetimes for an 8 mm and a 40 mm chamber aperture as a function of residual-gas pressure. Chamber apertures of 8 mm and 40 mm correspond to the

narrowest undulator section and the normal chamber section, respectively. Even at  $1 \times 10^{-8}$  Torr, lifetimes are more than 10 hours. Actually the vacuum system is designed to maintain the pressure of  $10^{-10}$  Torr under the beam-on conditions; therefore, no problems are found for the gas scattering lifetime.

## (2) Touschek lifetime

When an electron collides with another electron within a bunch, a momentum change occurs. If the momentum change exceeds a given upper limit, the electron leaves from the stable RF bucket and gets lost. This lifetime is inversely proportional to the electron density within a bunch: The lifetime is proportional to a bunch volume and inversely proportional to a bunch current. When the bunch current changes, the bunch length also changes due to the microwave instability.

Lifetimes are calculated as a function of the bunch current taking the effect of bunch lengthening into account. Conditions for the calculation are shown in Table 2. Since the broad-band impedance ( $|Z/n|$ ) that is the cause of bunch

Table 2. Conditions for calculation of the Touschek lifetime.

Emittance	$\epsilon_x$	$8.14 \times 10^{-9} \pi \text{ m}\cdot\text{rad}$
	$\epsilon_y$	$8.14 \times 10^{-11} \pi \text{ m}\cdot\text{rad}$
Momentum half-aperture	$\Delta E/E$	$2.2 \times 10^{-2}$
Bunch length	$\sigma_t$	3.7 mm ( $ Z/n  = 0 \Omega$ ) 26.3 mm ( $ Z/n  = 5 \Omega$ , $I_b = 5 \text{ mA}$ )

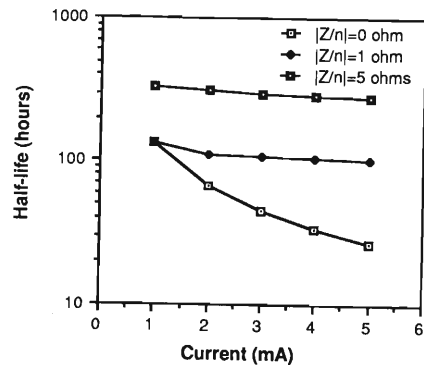


Fig. 3. Touschek lifetime as a function of a bunch current.

lengthening has not yet been evaluated precisely, impedances are assumed for the calculation of the bunch length.<sup>2)</sup> Calculated results are shown in Fig. 3. Without bunch lengthening ( $|Z/n| = 0 \Omega$ ), the lifetime is reduced to 27 hours for a 5 mA bunch current. However, with bunch lengthening, the lifetime is almost constant even if the bunch current increases: For impedances of 1 ohm and 5 ohms, lifetimes are 100 h and 300 h, respectively. Since the real machine will have broad-band impedance larger than 1 ohms, the Touschek lifetime will be more than 100 h.

## References

- 1) M.S. Zisman, S. Chattpadhyay, and J.J. Bisognano: ZAP User's Manual, LBL-21270 (1986).
- 2) Conceptual Design Report of STA 6 GeV SR Project (1988).

## V-2-10. Beam Stability of the 8 GeV Electron Storage Ring

K. Tsumaki, R. Nagaoka, H. Tanaka, K. Yoshida, and M. Hara

In a storage ring, beam performance depends greatly on a beam current. When the beam current is considerably low, no beam instability occurs and the beam characteristics are readily obtained by linear optics calculation programs such as Synch or Magic. When the beam current exceeds certain values, however, the beam instability occurs and bunch lengthening or emittance growth is induced. If the beam current is further increased, the bunch is brown up and the beam is lost.

These current-dependent phenomena are closely related to environmental devices such as RF cavities, bellows, and a vacuum chamber. Because an RF cavity has narrow-band and high- $Q$  impedances, it mainly induces coupled bunch instabilities. For bellows and a vacuum chamber, broad-band and low- $Q$  impedances are dominant, which correspond to the short range wake fields inducing single-bunch instabilities.

There are several methods to avoid these coupled bunch instabilities: the setting of a higher-order mode damper in RF cavities or the employment of a feedback system or the change of an operating point. For the single bunch instabilities, broad-band impedance should be decreased by smoothing chamber structures or bellows. However, the beam instabilities are inevitable even by these cures, and the machine performance is reduced greatly by these instabilities. We studied the instabilities by using ZAP<sup>1)</sup> that is a program for instability calculation.

### (1) Impedance

Since broad-band impedance is not evaluated precisely, it is treated as a parameter in the calculation of instabilities. As for the cavity impedance, KEK cavity results<sup>2)</sup> are adopted.

### (2) Single bunch instabilities

Because ring broad-band impedance limits the stored current for a single bunch operation, it is necessary to estimate acceptable impedance to store the current of a designed value. The threshold currents  $I_b$  of longitudinal instability for a bunch are calculated as a function of ring broad band impedance  $|Z_{\parallel}/n|$ , where  $Z_{\parallel}$  is the longitudinal impedance and  $n = \omega/\omega_0$  ( $\omega$  is the frequency of electro-magnetic field and  $\omega_0$  is the

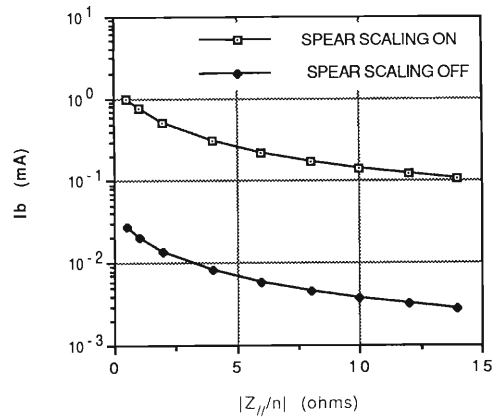


Fig. 1. Threshold current of longitudinal instability.

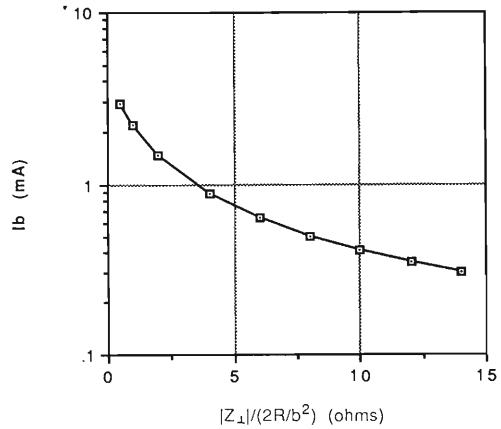


Fig. 2. Threshold current of transverse instability.

angular revolution frequency of electron beam).

The threshold currents  $I_b$  of transverse instability are also calculated as a function of transverse broad band impedance  $|Z_{\perp}|$  which is converted from longitudinal impedance using the following relation.

$$|Z_{\perp}| = 2R/b^2 |Z_{\parallel}/n| \quad (1)$$

where  $R$  and  $b$  are the radii of ring and beam pipe, respectively. Calculated results are shown in Figs. 1 and 2. In calculation, a SPEAR scaled and non SPEAR scaled impedances are used. The SPEAR scaled impedance is expressed by,

$$\begin{aligned} |Z_{\parallel}/n| &= |Z_{\parallel}/n|_0 \quad (\omega < \omega_c) \\ |Z_{\parallel}/n| &= |Z_{\parallel}/n|_0 (\omega/\omega_c)^{-1.68} \quad (\omega > \omega_c) \end{aligned} \quad (2)$$

where  $\omega_c = c/b$  ( $c$  is the velocity of light).

The threshold currents of the longitudinal instability are the threshold values at which bunch lengthening occurs owing to microwave instability. Microwave instability does not lead to a beam loss. Transverse threshold is the transverse mode-coupling threshold. Above these threshold currents, particles are blown up. From Fig. 2, the ring broad-band impedance should be suppressed to less than 1 ohm to obtain a beam current of few milliamperes. However, this threshold current may be pessimistic, because the effective impedance for a short bunch is smaller than that of a long bunch and, in this calculation, this effect is not taken into consideration. A real threshold current is probably two or three times larger than the value obtained in this calculation. Anyway, to obtain beam current of 3 or 5 mA,

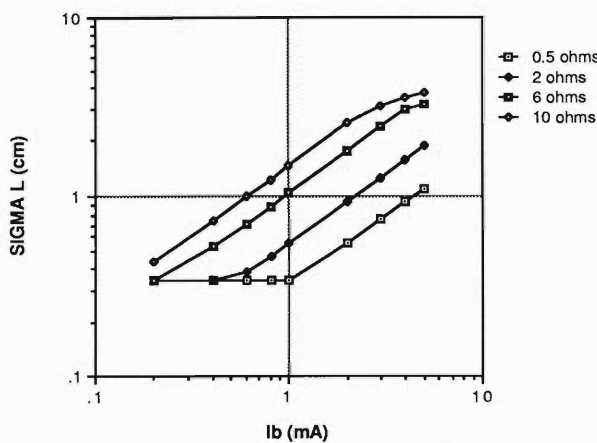


Fig. 3. Bunch lengthening due to microwave instability for SPEAR scaled impedance.

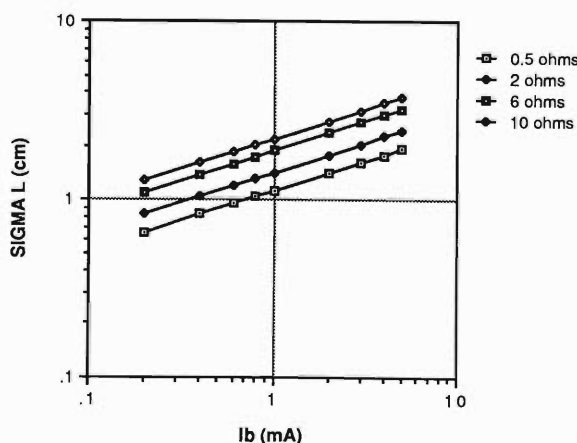


Fig. 4. Bunch lengthening due to microwave instability for non SPEAR scaled impedance.

impedance should be reduced to less than 1 or 2 ohms.

Figures 3 and 4 show the bunch lengthening due to microwave instability. The bunch length of 0.3 cm increases to about 1.9 cm as the current increases to 5 mA for the impedance of 2 ohm with a SPEAR scaling.

### (3) Coupled bunch instability

For multi-bunch operation, coupled bunch instability limits a stored current. If the growth rate is shorter than the radiation damping time, the bunch is brown up and the beam is lost. The growth rates of coupled bunch instabilities for the longitudinal and transverse motions are calculated under the conditions listed in Table 1, where the bunch lengths are calculated by assum-

Table 1. Conditions for calculations of coupled bunch instabilities.

Current	$I$	100 mA
Synchrotron tune	$\nu_s$	0.0095
Betatron tune	$\nu_x$	51.75
	$\nu_y$	19.82
Bunch length	$\sigma_1$	2.56 cm (22 bunches) 1.52 cm (44 bunches) 0.91 cm (88 bunches) 0.52 cm (176 bunches) 0.34 cm (2,464 bunches)
Number of cell		32

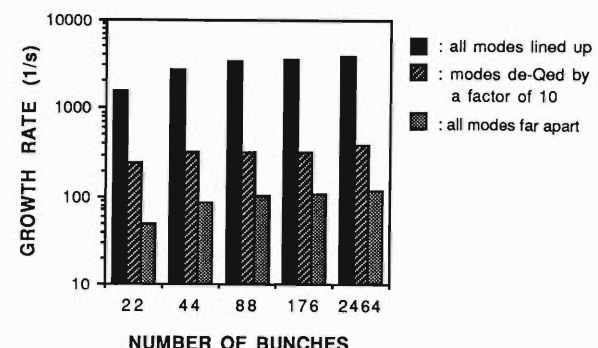


Fig. 5. Growth rate of longitudinal coupled bunch instability.

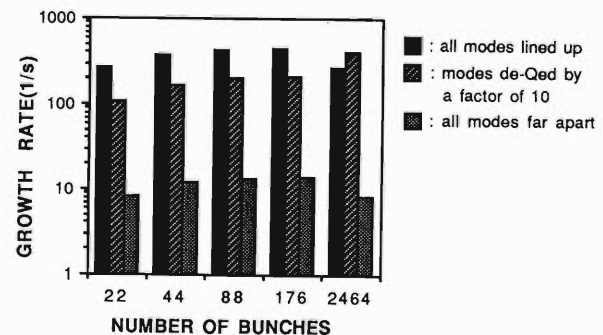


Fig. 6. Growth rate of transverse coupled bunch instability.

ing 4 ohm as impedance. Calculations are carried out for three cases. (1) All higher-order modes in different cells of accelerating cavity are lined up; the shunt impedances are  $32 \times R_{s0}$  and  $Q$  values are the same as for a single cell, where  $R_{s0}$  is the shunt impedance of a single cell. (2) All higher-order modes are de-Qed by a factor of 10; the shunt impedance are  $3.2 \times R_{s0}$  and the  $Q$  values are  $Q_0/10$ , where  $Q_0$  is the  $Q$  value for a single cell. (3) All higher-order modes in different cells are sufficiently far apart so that there is no superposition among the modes in different cells; the shunt impedance and the  $Q$  values have the same values as in the case of single cells. The first case is the most pessimistic assumption and the last one is the most optimistic assumption. Real cavities have the shunt impedances and  $Q$  values between the two cases.

Figures 5 and 6 show the calculated growth rates of the coupled bunch instabilities. Only a dipole mode is calculated, because the growth

rates of the other modes are much smaller than that of the dipole mode. Radiation damping times for the longitudinal and transverse motions are about 5 ms and 10 ms, respectively. Corresponding growth rates are 200/s and 100/s, respectively, and these values are smaller than the growth rates of the longitudinal and transverse instabilities for the cases of all modes lined up and mode de-Qed by a factor of 10. This result indicates that a beam current of 100 mA will not be achieved without the help of a feedback system or higher order mode dampers or a Landau cavity or any other effective cures if the de-Qing factor is less than 10.

#### References

- 1) M.S. Zisman, S. Chattopadhyay, and J.J. Bisognano: ZAP User's Manual, LBL-21270 (1986).
- 2) Y. Yamazaki, K. Takata, and S. Tokumoto: *IEEE Trans. Nucl. Sci.*, **NS-28**, 2915 (1981).

## V-2-11. Design of the Sextupole Magnets for the 8 GeV Storage Ring

J. Ohnishi, E.S. Park, and S. Motonaga

A Chasman-Green magnet lattice will be applied to the 8 GeV storage ring. In this type of lattice, 7 sextupole magnets are used per one cell for chromaticity and harmonics correction.<sup>1)</sup> These sextupole magnets have two distinctive features. One is that some sextupole magnets have asymmetrical yokes. Since this ring is utilized as a synchrotron radiation source, a light beam is extracted from bending magnets and insertion devices at a small angle and is passed through a part of the magnets located downstream. Therefore, yokes are designed to extend in one horizontal direction in order to make room for the light beam. Another feature is that the sextupole magnets include the capability to provide horizontal and vertical steering fields.

The configuration of the sextupole magnets is shown in Fig. 1 and the principal parameters are listed in Table 1. The magnets can be operated at more than 360 T/m<sup>2</sup> for the maximum strength of sextupole field. The magnet yokes and poles are constructed from 0.5-mm thick silicon steel laminations. One magnet consists of six sections. They are assembled after all coils are fitted to the pole and the yoke. The bore diameter is 110 mm decided from the size of a beam chamber.

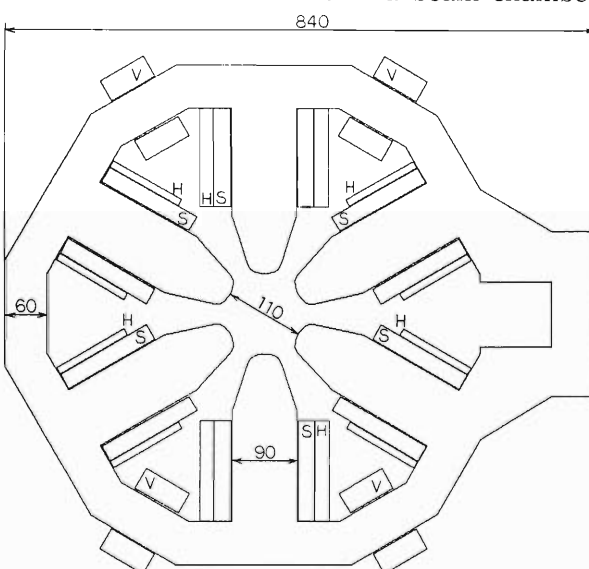


Fig. 1. Cross-sectional view of the sextupole magnet with steering elements. S: Sextupole coils, H: Horiz. steering coils, V: Vert. steering coils.

Table 1. Sextupole parameters for the 8 GeV storage ring (48 cells).

Number of magnets	336
Physical length	0.45 m
Magnet aperture radius	55.0 mm
Good field radius	40.0 mm
Strength $B''$ , max	360 T/m <sup>2</sup>
Number of turns per pole	18
Current	445 A
Current density	3.5 A/mm <sup>2</sup>
Conductor size	10×14 mm <sup>2</sup> , #4 mm
Voltage drop per magnet	10.0 V
Power	4.5 kW
Water flow	1.1 l/min
Water pressure drop	2.0 kg/cm <sup>2</sup>
Water temperature rise	10°C

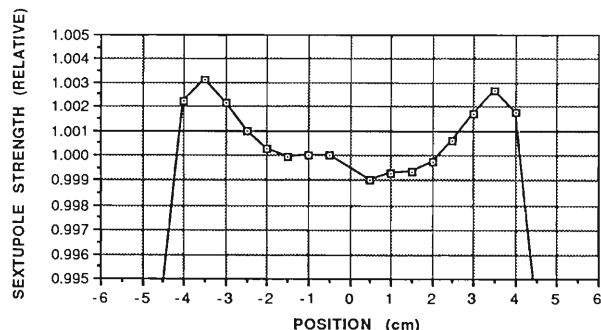


Fig. 2. Calculated sextupole field distribution of the sextupole magnet on a median plane normalized by  $B'' = 360 \text{ T/m}^2$  at  $x = -0.5 \text{ cm}$ .

The contour for all pole tips is the same,  $r^3 \cos 3\theta$  with shims. The width of poles and yokes is designed thick enough so that the reluctance in iron may be especially small because the dipole field for steering is excited additionally. The coils for the sextupole field are wound with 18 turns per pole of OFC hollow conductor.

The configuration of an iron yoke was decided from the numerical calculation of field distribution using a second dimensional code LINDA. The calculated distribution of the normalized sextupole field on a horizontal median plane is shown in Fig. 2. The field lines are shown in Fig. 3. The difference in the field strength between the left- and right-hand sides which is generated

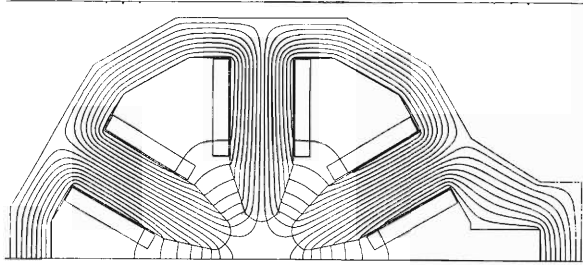


Fig. 3. Field lines of the asymmetrical sextupole magnet.

by the asymmetrical yokes could be suppressed to within  $2 \times 10^{-3}$ , small enough, by choosing a good thickness for the asymmetrical parts of the yokes. The shape of radial shims was also optimized so that a good field region can extend as wide as possible. The sextupole field is made stronger around both sides of the aperture because its integral value along the beam direction is expected to be smaller than in the central

region.

These sextupole magnets have extra coils for providing horizontal or vertical dipole fields which steer a beam in order to correct the closed orbit distortion. Two of the seven sextupole magnets in one cell provide horizontal dipole fields while another four provide vertical ones. Only the one remaining magnet operated with the strongest sextupole field have no steering function. It was checked by computer tracking simulation<sup>2)</sup> that these six sextupole steering elements and six usual steering magnets can correct the closed orbit distortion to be enough small. Then it was found out that the maximum required kick angle value on the beam is about 1 mrad.

The vertical dipole fields for horizontal steering is provided by excitation of the respective upper and lower three poles with opposing polarity. The six vertical dipole coils of the magnet

Table 2. Parameters of steering coils in sextupole magnets (48 cells).

	Horiz. steering (2 circuits)	Vert. steering (1 circuit)
Number of magnets	192	96
Physical length	0.45 m	0.45 m
Kick angle	1 mrad	1 mrad
Peak field	0.059 T	0.059 T
Number of turns per pole	100,40	90
Current, max.	42 A	42 A
Current density, max.	1.7 A/mm <sup>2</sup>	1.7 A/mm <sup>2</sup>
Conductor size	5×5 mm <sup>2</sup>	5×5 mm <sup>2</sup>
Voltage drop per circuit	9.6, 7.7 V	14.7 V
Power per circuit	0.40, 0.32 kW	0.62 kW

are powered by two current sources. One source powers two series coils around the two poles which face each other along the perpendicular direction and another powers the other four coils in series. The best field quality is generated by adjusting the current ratio between these two circuits. In contrast, the horizontal dipole field is provided by excitation of the two left-hand side poles with one polarity and the right-hand side ones with opposite polarity. For the excitation, the four series coils which are wound about return yokes are used. Table 2 shows the parameters of the sextupole steering elements. These elements can be operated up to 0.059 tesla in bipolarity as a maximum strength of the field. This value gives a 1 mrad kick angle to the beam.

Figure 4 shows the distribution of horizontal and vertical dipole fields  $B_x(y)$ ,  $B_y(x)$  on each symmetrical plane. This result was calculated

by the LINDA. The distribution of the vertical dipole in the figure was obtained by exciting the two central poles 2.5 times more strongly than

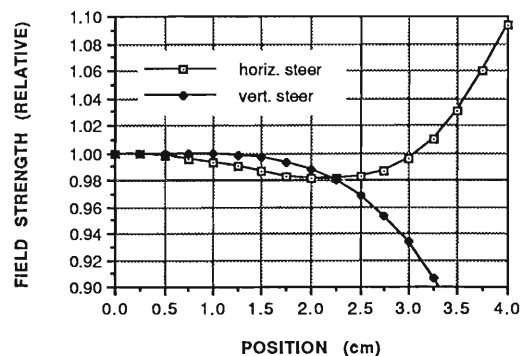


Fig. 4. Dipole field distribution calculated for horizontal and vertical steering in the sextupole magnet.  $B_y(x)/B_y(x=0)$  on a  $y=0$  plane for horiz. steering and  $B_x(y)/B_x(y=0)$  on  $x=0$  for vert. steering are shown. The  $B_y(x=0)$ ,  $B_x(y=0)$  are both 0.059 T.

the other poles. In this calculation the main coils for the sextupole field are not excited. However, both sextupole and dipole coils are simultaneously excited in real magnets. The field distribution is expected to be different from a simple superposition of dipole and sextupole fields because of the non-linearity in iron magnetic properties. Therefore, we have to calculate multipole field components from the sextupole magnets with steering elements under realistic conditions. Furthermore, we need to execute beam tracking simulation by using the result and make sure that the undesirable multipole field components are

small enough to obtain the required dynamic aperture size. These analyses are the subject of the study from now.

At present, we are designing a sextupole magnet mechanically. We are scheduled to construct a model magnet and measure its magnetic qualities.

#### References

- 1) R. Nagaoka, H. Tanaka, K. Yoshida, K. Tsumaki, and M. Hara: This Report, p. 227.
- 2) H. Tanaka, R. Nagaoka, K. Tsumaki, K. Yoshida, and M. Hara: This Report, p. 231.

## V-2-12. RF System for 8 GeV SR

T. Yoshiyuki, T. Kusaka, and M. Hara

In previous work,<sup>1)</sup> we designed the RF system for 6 GeV SR. We have now chosen to set the design energy of this SR facility at 8 GeV. This report describes an approach to designing the 8 GeV RF system.

The RF design parameters for the storage ring are listed in Table 1. Several advantages in machining cavities and the technical and commercial development for almost all the circuit devices in TRISTAN and PF (KEK) make the choice of the operating frequency of around 500 MHz. The nominal RF frequency is determined to be 508.58 MHz, the same frequency as TRISTAN, and the harmonic number is 2,424.

There are three kinds of energy losses for the storage ring. The first is due to synchrotron radiation from dipole magnets and amounts to 8.3 MeV at 8 GeV beam energy and the magnetic strength of 0.61 T. The second is due to synchrotron radiation from insertion devices and depends on the exact distribution of undulators and wigglers and their characteristics. Since insertion devices aren't designed yet, the loss is overestimated at 3.2 MeV. The last loss is calculated from the average beam current and the total impedance for higher-order cavity modes

and vacuum chamber components except the cavity. These impedances depend on the bunch length and the conditions of the bunch operation. The longer the bunch length, the smaller the energy loss. The loss also decreases with the number of bunches. The impedances for cavities and the vacuum chamber are important for energy loss and beam stabilities. Here this loss is estimated at 0.5 MeV for multi-bunch operation. Since total energy loss per turn amounts to about 12 MeV, the RF system for the storage ring should be capable of providing 12 MV.

An overvoltage is required for a long quantum lifetime, which is also a function of a momentum compaction factor and a beam energy spread besides the main RF parameters. The momentum compaction factor and the beam energy spread are  $1.373 \times 10^{-4}$  and  $3 \times 10^{-3}$ , respectively. The overvoltage factor of 1.33 gives more than one day for the quantum lifetime when the accelerating voltage is 12 MV. As a result, the maximum peak voltage in the cavity should be 16 MV.

The generator power  $P_g$  is the sum of the cavity power dissipation  $P_c$ , the power transferred to the beam  $P_b$ , and the reflected power  $P_r$ . Here, we estimate these powers when the average beam current  $I_0$  is 0.1 A and the shunt impedance is 22.5 MΩ/m. The cavity power per cell is limited to about 50 kW due to the problems in voltage breakdown and a vacuum. The cell number is thus determined to be about 35. In the case of 35 cells, the total cavity power  $P_c$

Table 1. RF parameters of the storage ring.

Beam energy	8 GeV
Circumference	1,428.7 m
Bending radius	43.75 m
Momentum compaction factor	$1.373 \times 10^{-4}$
Natural energy spread	0.3%
Radio frequency	508.58 MHz
Harmonic number	2,424
Synchrotron radiation loss per turn	8.3 MeV
Energy loss for insertion devices	3.2 MeV
Parasitic energy loss per 100 mA	0.5 MeV
Nominal RF voltage	12 MV
Maximum RF voltage	16 MV
Shunt impedance	22.5 MΩ/m
Quantum lifetime	>1 day
Number of cells	~35
Radiation damping time	$3.17 \times 10^{-3}$ s
Beam current	100 mA
Beam power	1.08 MW
Cavity power	1.20 MW
Klystron power	1 MW
Number of klystrons	4

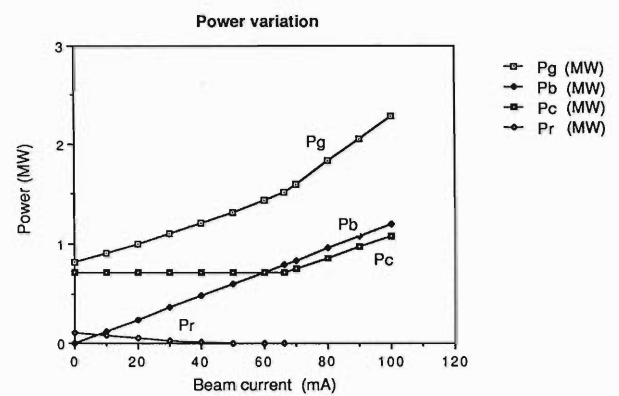


Fig. 1. Power variations as a function of beam current.

becomes 1.08 MW and the beam power  $P_b$  1.20 MW. From the viewpoint of the symmetry of arrangement and the margin of power, four klystrons will be set symmetrically around the storage ring. Each power variation is shown in Fig. 1 as a function of the beam current.

Four straight sections of each 6.5 m long will be needed for the arrangement of the RF cavities. In designing the cavity, two types of cavity structures are investigated: one is a single-cell cavity

and the other is a multi-cell cavity. The single-cell cavity has fewer higher-order modes than the multi-cell cavity. It is also easier to analyze the properties of the resonant modes. Since the power is fed to each cell, the power per cell gets large; therefore, the cell number could be reduced and an attainable beam current will increase. Since each cell has its own cavity component, however, the system needs more components and will be costly and complicated. Compared with

Table 2. Comparison between a single-cell cavity and a 3-cell cavity.

Cavity type	Single-cell	3-cell
Cell number	32	42
Number of units	32	14
Arrangement of units	$8_{\text{units}} \times 4_{\text{s.s.}}$	$4_{\text{units}} \times 3_{\text{s.s.}}$ $2_{\text{units}} \times 1_{\text{s.s.}}$
$P_c/\text{unit}$	37 kW	21 kW
$(P_c + P_b)/\text{unit}$	75 kW	150 kW
Number of couplers/unit	1	1
$I_{\max}$	0.2A	0.15A
		(0.2A)

s.s: straight sections, ( ): another case for a 3-cell cavity.

the single-cell cavity, the multi-cell cavity has large shunt impedance per cavity length and the configuration of the transmission lines will be simple, but it is liable to cause beam instabilities due to multiple higher-modes. In the case of the multi-cell cavity, both 3-cell and 5-cell cavities are studied. In the 5-cell cavity, two RF windows are needed to fill the power into the cavity, because of the limit of power per window of about 200 kW, but the power cannot be fed well to the cavity through two windows owing to reflection and transmission of the power. Therefore, for the storage ring, the 3-cell cavity is preferable to the 5-cell cavity. The relations of the cell number and the power for the single-cell and the 3-cell cavities are shown in Table 2. The final specifications of the cavity will be determined after the tests of a 1/6-model cavity and a life-sized model cavity<sup>2,3)</sup> and high power tests as mentioned later.

A higher harmonic RF system may be combined with the fundamental RF system for the storage ring. Adjustment of the slope of the superposed RF wave at the bunch center leads to control of a bunch length and a spread of synchrotron frequency. The resulting large spread of synchrotron frequency across the bunch together with the reduced peak current eliminates longitudinal coupled bunch instabilities and the head-tail effect. The third harmonic system is considered here and fixed at a frequency of 1,525.74 MHz. Figure 2(a) shows the superposition of RF waveforms in the 508.58

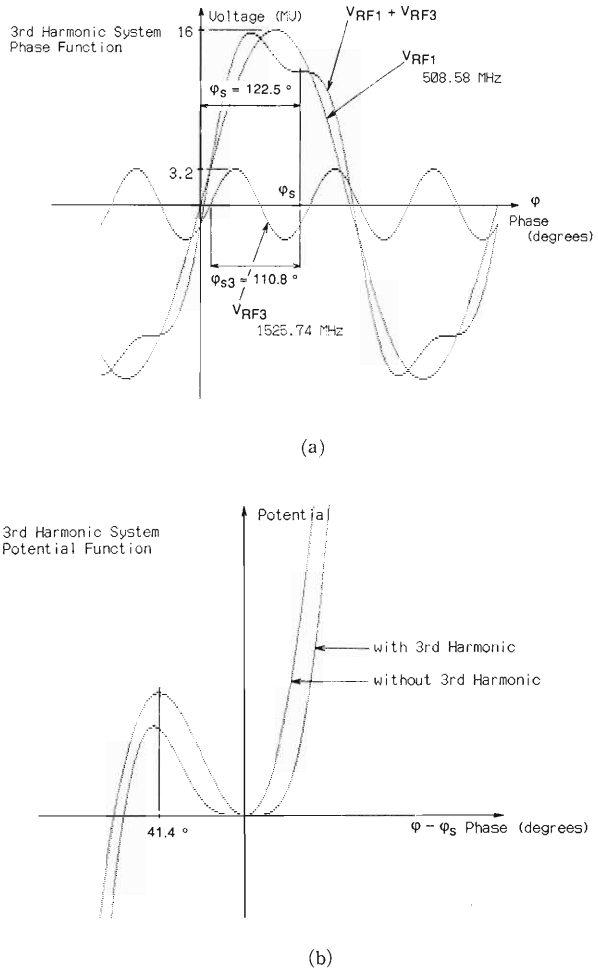


Fig. 2. 3rd harmonic RF system; a) RF waveforms, b) potential functions with and without harmonic system.

MHz and the 1,525.74 MHz systems. Figure 2(b) shows the potential functions with and without the properly adjusted 3rd harmonic system. It turns out that it is reasonable to utilize the 3rd harmonic system to get a sufficiently long bunch length. Table 3 shows the typical parameters of the 3rd harmonic system. When the fundamental RF peak voltage is 16 MV, the 3rd harmonic RF peak voltage comes to 3.23 MV. As for the cavity, 5-cell cavities with an on-axis coupled structure are applicable. The shunt impedance is about 30 MΩ/m. The cell length is  $\lambda/2$  (9.9 cm), where  $\lambda$  is the wavelength of the 3rd harmonic RF. Four 5-cell cavities would be considered to provide the impedance of about 60 MΩ. In order to produce the necessary voltage, a total power

Table 3. Parameters of the 3rd harmonic RF system for the storage ring.

Frequency	1,525.74 MHz
Number of cavities	4
Number of cells per cavity	5
Peak voltage of the 3rd harmonic RF	3.23 MV
Peak voltage of the fundamental RF	16 MV
$v^*$	0.75
$k^{**}$	0.202
Shunt impedance	30 MΩ/m
Cavity power	176 kW
$\lambda/2$ ( $\lambda$ : wavelength of RF)	9.9 cm
Phase angle (in terms of 508.58 MHz)	110.8 degrees

\*  $v = (\text{operation voltage}) / (\text{peak voltage of the fundamental RF system})$

\*\*  $k = (\text{peak voltage of the 3rd harmonic RF system}) / (\text{peak voltage of the fundamental RF system})$

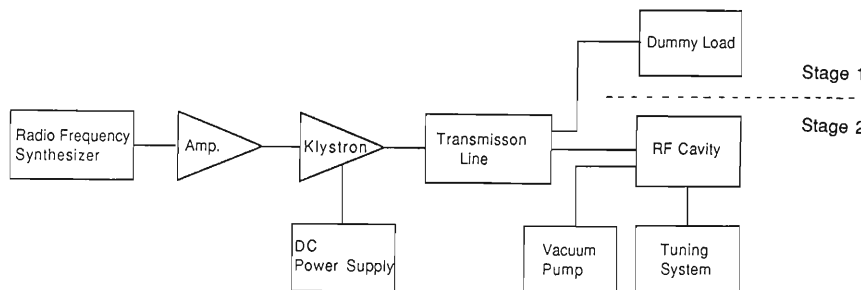


Fig. 3. Block diagram of high power test.

of 176 kW would be required.

Now, we plan high power tests in order to determine the final specifications of the RF system for the storage ring. The block diagram is shown in Fig. 3. The tests are performed in two stages. In the first stage, the experiments of a 1-MW klystron and a transmission line are conducted to supply the high power stably. The control system for the klystron will be established by using a dummy load. Several test cavities for high power will be examined in the next

stage. These tests give design limitations such as the maximum accelerating voltage and the maximum power coupled through the RF window.

#### References

- 1) T. Yoshiyuki, T. Kusaka, and M. Hara: *RIKEN Accel. Prog. Rep.*, **21**, 235 (1987).
- 2) T. Kusaka, T. Yoshiyuki, and M. Hara: This Report, p. 271.
- 3) T. Kusaka, K. Inoue, T. Yoshiyuki, A. Miura, and M. Hara: This Report, p. 268.

### V-2-13. 500 MHz Model Cavities for the 8 GeV SR Ring

T. Kusaka, K. Inoue,\* T. Yoshiyuki, A. Miura,\*\* and M. Hara

In the 8 GeV storage ring, it is planned to use a 508 MHz RF system. Two model cavities of a single-cell type and a 3-cell type have been fabricated to evaluate their electromagnetic properties and determine the specifications of a practical cavity. The inner shape was determined on the basis of numerical calculations<sup>1)</sup> and measurements of a 1/6 scale test cavity.<sup>2)</sup> The resonant frequency of the fundamental mode is designed to be 500 MHz in the single-cell cavity.

The 3-cell cavity is shown in Fig. 1. Figure 2 shows the disk configuration with re-entrant nose cones and two inductive coupling slots. The single-cell cavity is assembled by using the center cell of the three cells and two end plates. The fabrication process of the model cavity was divided into four steps as follows. RF characteristics were measured in each process.

In the first step, the model cavities were machined out of 6061 aluminum alloy. The overall machinery accuracy was within  $\pm 0.1$  mm. In this case, the maximum deviation of the resonant frequency of the fundamental mode is calculated to be about 0.6 MHz in the single-cell cavity. Each cell has the same diameter and small holes for measuring probes. Resonant frequencies and  $Q$ -values were measured by the reflection method with a network analyzer. Eighteen resonant modes were observed below 1.5 GHz in the single-cell cavity. Four modes were measured precisely because they were found to have high impedance values from HAX<sup>3)</sup> and URMEL<sup>4)</sup>

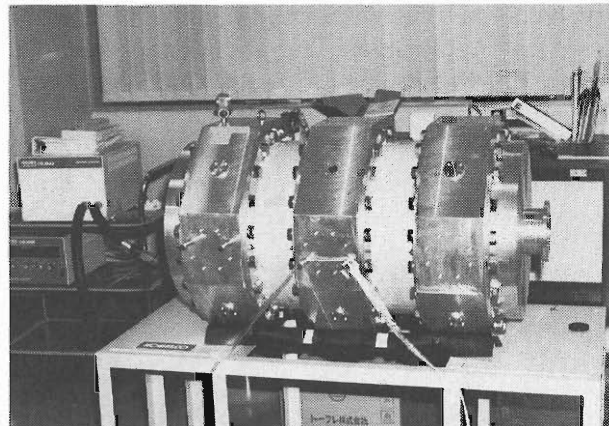


Fig. 1. Photograph of the assembled 3-cell cavity.

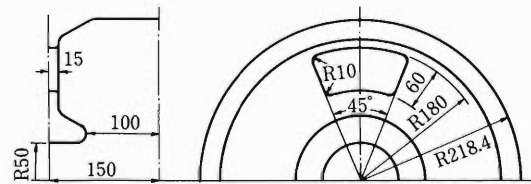


Fig. 2. Disk configuration with re-entrant nose cones and inductive coupling slots.

calculations. Table 1 shows the results of measurement and calculation. The longitudinal and transverse impedances were computed from the electromagnetic field distribution along the beam axis. The method of calculation is described in Ref. 5. The electric and magnetic field

Table 1. RF characteristics of the single-cell cavity.

Mode	Frequency (MHz)		Unloaded $Q$		$R_{\parallel}$ (MΩ) or $R_{\perp}$ (MΩ m <sup>-1</sup> )	
	Exp.	Calc.	Exp.	Calc.	Exp.	Calc.
TM <sub>010</sub>	499.6	500.5	22,000	26,000	5.1	6.0
TM <sub>011</sub>	747.2	749.2	18,300	22,000	0.99	1.2
TM <sub>110</sub>	844.8	844.1	28,900	36,000	9.0	14
TM <sub>111</sub>	1,050.4	1,053	21,000	28,000	13	16

\* Kobe Steel, Ltd.

\*\* College of Humanities and Sciences, Nihon University.

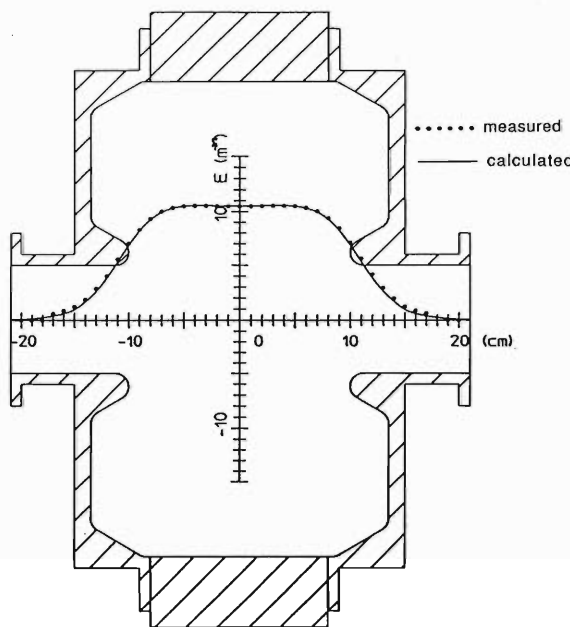


Fig. 3. Measured electric field distribution of the accelerating mode with computed result in the single-cell cavity.

Table 2. RF characteristics of the 3-cell cavity when each cell has the same diameter.

Mode	Frequency (MHz)	Unloaded Q	$R_{\parallel}/(M\Omega)$ or $R_{\perp}(M\Omega m^{-1})$
$TM_{0\ 1\ 0}$	$\pi$	492.7	20,100
	$\pi/2$	496.6	21,400
	0	498.0	21,600
$TM_{0\ 1\ 1}$	0	719.6	16,900
	$\pi/2$	736.3	18,600
	$\pi$	742.2	19,300
$TM_{1\ 1\ 0}$	$\pi$	832.8	24,700
	$\pi/2$	840.9	26,700
	0	844.2	24,600
$TM_{1\ 1\ 1}$	0	1,005.1	17,300
	$\pi/2$	1,026.2	18,600
	$\pi$	1,048.2	21,500

distributions were measured by a perturbation method.<sup>6)</sup> A metal sphere and a teflon sphere whose diameters were 20 mm were used as perturbing objects. Figure 3 shows the longitudinal electric field of the accelerating mode in the single-cell cavity. The electric field  $E$  is normalized so that the integral of  $|E|^2$  over the cavity is unity. The measured values agree well with the calculated values. In the 3-cell structure, triple modes were examined, whose phase shifts per cell were 0,  $\pi/2$ , and  $\pi$ . The results are listed in Table 2. In the accelerating mode, which was the  $\pi$  mode of the fundamental mode, the field

Table 3. RF characteristics of the 3-cell cavity with "flat"  $\pi$ -mode.

Mode	Frequency (MHz)	Unloaded Q	$R_{\parallel}/(M\Omega)$ or $R_{\perp}(M\Omega m^{-1})$
$TM_{0\ 1\ 0}$	$\pi$	491.0	19,900
	$\pi/2$	492.6	22,400
	0	495.7	22,000
$TM_{0\ 1\ 1}$	0	719.9	17,200
	$\pi/2$	737.8	20,000
	$\pi$	743.6	19,800
$TM_{1\ 1\ 0}$	$\pi$	830.1	24,800
	$\pi/2$	834.3	29,000
	0	840.3	30,000
$TM_{1\ 1\ 1}$	0	1,004.2	17,300
	$\pi/2$	1,024.0	17,600
	$\pi$	1,047.4	21,500

ratio of the center cell to the end cell was measured to be about -2.3. During one to three minutes of measurements, the temperature changes of the cavity led to resonant frequency drifts. It was compensated numerically by assuming the drifts were in proportion to time.

In the second step, the radius of end cells was enlarged to make a "flat" electric field in the 3-cell cavity. The cutting allowance of the cell body was calculated to be 3.2 mm by substituting the measured resonant frequencies into an equivalent circuit.<sup>2)</sup> The results are listed in Table 3. The shunt impedance of the accelerating mode increased from 12 MΩ to 15 MΩ, which was nearly three times as high as the one in the single-cell cavity. The coupling factor between adjacent cells was calculated to be 1.3% from measured frequencies.

In the third step, ports were machined in each cell. The center cell had four ports which were used for an input coupler, a frequency tuner, and damping couplers. Axially-asymmetric modes were split into two orthogonal modes because the degeneracy was broken by the ports whose diameters were different from each other. The direction of the field was measured by rotating a small flat metal plate at the center of the cavity. In this step, the  $Q$ -values in the higher-order modes were damped by the gap between a filler and a port. A damping factor of 4 was measured in a  $TM_{111}$ -like mode. The optimization of the gap size will be necessary to increase the damping factor and reduce the effect of higher-order modes on electron bunches.

The surface roughness is related to the surface resistance, which is proportional to the power dissipation in the cavity. In the final step, the inner surface of the cavity was buffed to increase

the  $Q$ -value. The roughness was improved from 3  $\mu\text{m}$  to better than 0.5  $\mu\text{m}$ . As a result, the  $Q$ -value in the accelerating mode is increased by 5%.

The impedances of the single-cell cavity and the 3-cell cavity were measured in four modes. Although the shunt impedance of the accelerating mode in the 3-cell cavity was almost three times as high as the one in the single-cell cavity, the maximum impedance of the higher-order modes was about 1.5 times as high as that of the single-cell cavity. A damping coupler will be developed to suppress the impedances of higher-order modes and increase the threshold current of coupled-bunch instabilities. Furthermore, a

prototype of cavity for tests using a 1-MW klystron will be designed on the basis of the present results.

#### References

- 1) T. Kusaka, T. Yoshiyuki, N. Kawasaki, and M. Hara: *RIKEN Accel. Prog. Rep.*, **21**, 237 (1987).
- 2) T. Kusaka, T. Yoshiyuki, and M. Hara: This Report, p. 271.
- 3) M. Hara, T. Wada, A. Toyama, and F. Kikuchi: *Sci. Papers I.P.C.R.*, **75**, 143 (1981).
- 4) T. Weiland: *Nucl. Instrum. Methods*, **216**, 329 (1983).
- 5) Y. Yamazaki, K. Takata, and S. Tokumoto: KEK 80-8, Aug. (1980).
- 6) L.C. Maier, Jr. and J.C. Slater: *J. Appl. Phys.*, **23**, 1 (1952).

## V-2-14. Study of Multi-Cell Cavity with Inductive Coupling Slots for the 8 GeV SR Ring

T. Kusaka, T. Yoshiyuki, and M. Hara

It is necessary for RF cavities in the 8 GeV SR ring to accelerate electrons with high efficiency of RF power and beam stability. In general, cavities of a standing-wave type used in electron machines are classified into single-cell structures and multi-cell ones. Multi-cell cavities have an advantage of higher shunt impedance per unit length than single-cell cavities and the RF system using multi-cell cavities includes a simpler transmission line from an RF power source to cavities than the RF system using single-cell cavities. However, the design of a multi-cell cavity is more difficult because of a coupling problem between cells and its dispersion property. Many types of multi-cell cavities have been operated in the  $\pi$  or  $\pi/2$  mode. In the  $\pi$  mode, higher shunt impedance is achieved, but tuning errors perturb the electric field more sensitively than in the  $\pi/2$  mode as the cell number of a cavity increases.<sup>1)</sup> Because the cell number needs to be small in the 8 GeV storage ring,<sup>2)</sup> a model of a 3-cell  $\pi$ -mode cavity with two inductive coupling slots was fabricated to study RF characteristics quantitatively. This report describes an approach to the calculation of the behavior of the 3-cell cavity and the comparison with the experimental results.

An equivalent circuit of the 3-cell cavity with inductive coupling slots is shown in Fig. 1,<sup>3)</sup> in which  $C$  is the capacitance between the end plates and  $L$  and  $L'$  are the inductances of the outer regions where the magnetic field is predominant. Inductive coupling between cells is represented by a parallel inductance  $L_c$ . The coupling factor, which is the ratio of a mutual inductance between cells to a self-inductance of a

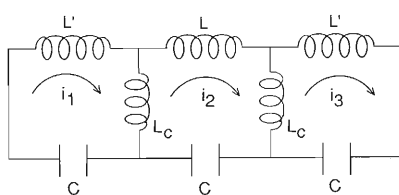


Fig. 1. Equivalent circuit for a 3-cell cavity with inductive coupling slots.

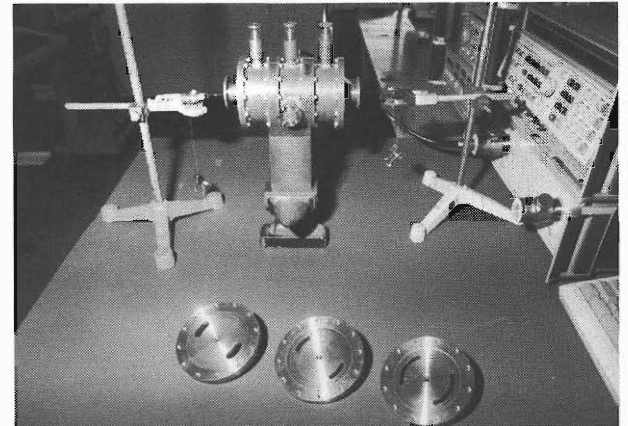


Fig. 2. 1/6 scale test cavity with several kinds of coupling disks.

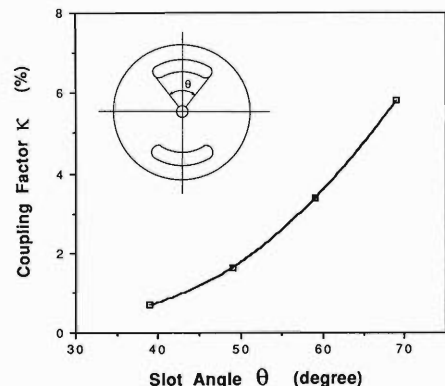


Fig. 3. Coupling factor as a function of slot angle in the 1/6 scale test cavity.

cell, is an important parameter to design a multi-cell cavity. A 1/6 scale test cavity was fabricated to investigate the influence of coupling slots. Several kinds of coupling disks shown in Fig. 2 were examined. The result of measurement is shown in Fig. 3. The coupling factor increases as the slot angle increases, but the shunt impedance decreases because of the power dissipation in the slots.<sup>4)</sup>

A life-sized model cavity was fabricated based on the experimental results on the 1/6 scale test cavity. The cavity structure is described in Ref. 5. Two coupling slots whose azimuthal angle is 45 degrees are machined to achieve more than 1% coupling with suppressing the extreme drop

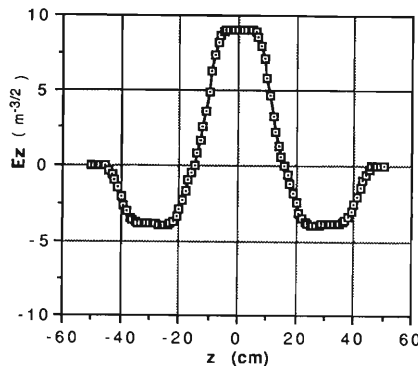


Fig. 4. Electric field distribution measured on the beam axis in the accelerating mode, when the 3 cells of the full-scale model cavity have the same diameter.

of the shunt impedance. When three cells have the same diameter, the electric field distribution of the accelerating mode is shown in Fig. 4. The electric field ratio of the center cell to the end cell is  $-2.3$ . On the other hand, applying the Kirchhoff's law to the three loops in Fig. 1, one obtains following equations.

$$(j\omega L' + 1/j\omega C) i_1 + j\omega L_c (i_1 - i_2) = 0 \quad (1a)$$

$$(j\omega L + 1/j\omega C) i_2 + j\omega L_c (2i_2 - i_1 - i_3) = 0 \quad (1b)$$

$$(j\omega L' + 1/j\omega C) i_3 + j\omega L_c (i_3 - i_2) = 0 \quad (1c)$$

Solving the eigenvalue problem, we have three resonant frequencies;

$$W = \{(W_0 + W_0') + 3W_c \pm \sqrt{(W_0 - W_0')^2 + 2(W_0 - W_0')W_c + 9W_c^2}\} / 2 \quad (2a)$$

$$W = W_0' + W_c \quad (2b)$$

$$W = 1/\omega^2,$$

$$W_0 = 1/\omega_0'^2 = LC,$$

$$W_0' = 1/\omega_0'^2 = L'C,$$

and

$$W_c = 1/\omega_c^2 = L_c C.$$

The current ratio  $r = i_2/i_1$  in the  $\pi$  mode is given by

$$r = \{(W_0' - W_0) - W_c \pm \sqrt{(W_0 - W_0')^2 + 2(W_0 - W_0')W_c + 9W_c^2}\} / 2W_c \quad (3)$$

When  $L$  is equal to  $L'$ , the ratio  $r$  is computed to be  $-2$ , where the minus sign means that the direction of the current flow is opposite. Compar-

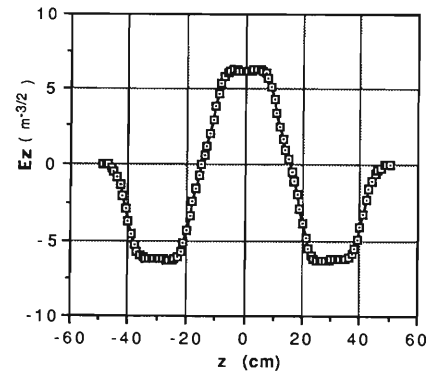


Fig. 5. Measured electric field distribution of the full-scale 3-cell cavity with a “flat”  $\pi$  mode.

ed with the measured ratio  $-2.3$ , it is found that  $L$  is larger than  $L'$ . By substituting the measured three frequencies of the fundamental modes into Eqs. 2, the value of  $L'$  is calculated to be  $0.997L$ .

In the multi-cell cavity, it is important to obtain a “flat”  $\pi$  mode, where the electric field strength is the same in all cells, in order to achieve high efficiency of the acceleration and stabilize the operation. The condition of a “flat”  $\pi$  mode is obtained by substituting  $i_1 = -i_2 = i_3$  into Eqs. 1, that is  $L' = L + 2L_c$ . As a result of calculation, the resonant frequency of the end cells  $\omega_0'/2\pi$  must be lowered by 4.12 MHz. After the end cell radius is enlarged by 3.2 mm, the electric field distribution of the accelerating mode is changed as is shown in Fig. 5. The electric field ratio is improved to be  $-0.986$  and the shunt impedance increases by 25%. The resonant frequency of the accelerating mode is measured to be 490.97 MHz, which is nearly equal to the frequency calculated with the equivalent circuit. The coupling factor, which is given by  $\kappa = 2L_c/(L + 2L_c)$ , is calculated to be 1.3% with the “flat”  $\pi$  mode. Throughout the experiment of the 3-cell cavity, the analysis using the equivalent circuit is useful in the fundamental mode. Further, it is expected that this design method can be applied to a 5-cell or 7-cell cavity for the booster synchrotron.

## References

- 1) P. B. Wilson: *IEEE Trans. Nucl. Sci.*, **NS-16**, 3, 1092 (1969).
- 2) T. Yoshiyuki, T. Kusaka, and M. Hara: This Report, p. 265.
- 3) J. R. Rees: PEP-255, Oct. (1976).
- 4) T. Kusaka, T. Yoshiyuki, A. Miura, and M. Hara: 1989 Particle Accelerator Conf., D33.
- 5) T. Kusaka, K. Inoue, T. Yoshiyuki, A. Miura, and M. Hara: This Report, p. 268.

## V-2-15. Calculation of the RF Electromagnetic Field for 8 GeV SR Ring Components

T. Kusaka, A. Miura,\* T. Wada, and M. Hara

In designing an 8 GeV storage ring, it is necessary to investigate the RF characteristics of ring components, especially high- $Q$  components, such as a cavity and bellows. Computer programs MAX3D and H2DB using a finite element method were developed to evaluate RF properties in two- and three-dimensional analysis.<sup>1,2)</sup> We calculated the changes in resonant properties by a frequency tuner in a cylindrical cavity and the shielding effect of a test bellows with these programs.

- (1) Three-dimensional analysis of a cylindrical cavity with a tuner

A frequency tuner is necessary to adjust the resonant frequency of an accelerating cavity for mechanical errors in the fabrication, the thermal effect due to the power dissipated in the cavity, and the phase correction between a generator voltage and an accelerating voltage. A plunger type of tuner mounted in the cylindrical cavity is tested. Because of the tuner structure, it is necessary to solve a three-dimensional problem.

Figure 1 shows the cavity structure. The cross sectional area of the tuner is 19.2 cm<sup>2</sup>. The half cavity is divided into 16 elements along the longitudinal direction and 9 elements along the radial direction as shown in Fig. 2. The TM<sub>0 1 0</sub>, TM<sub>0 1 1</sub>, TM<sub>1 1 0</sub>, and TM<sub>1 1 1</sub> modes are studied precisely because they are found to have high impedance values from calculations. In the case of no tuner, the calculated resonant frequencies are listed with analytical values in Table 1. The error is estimated at less than 1.3% below 1 GHz. The CPU time is about 26 minutes for a FACOM M-780 computer.

When the tuner is inserted, the calculation is carried out by eliminating the corresponding elements of the tuner from the region under analysis. An axially-asymmetric mode is split into two orthogonal modes suffixed V and P, because the degeneracy is removed by the tuner. The changes in the resonant frequency are shown in Fig. 3. When magnetic energy is stronger than electric energy at the tuner position, the

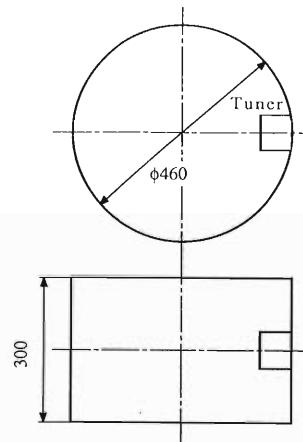


Fig. 1. Structure of a cylindrical cavity with a tuner.

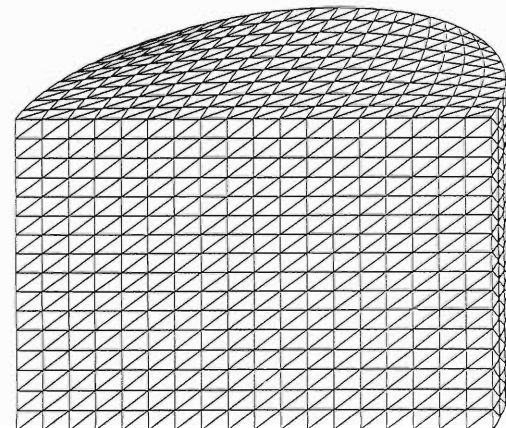


Fig. 2. Subdivisions of a half cylindrical cavity.

Table 1. Comparison between calculated resonant frequencies and analytical ones.

Mode	TM <sub>0 1 0</sub>	TM <sub>0 1 1</sub>	TM <sub>1 1 0</sub>	TM <sub>1 1 1</sub>
Calculated frequency (MHz)	499.31	707.42	793.78	950.96
Analytical frequency (MHz)	498.88	706.07	794.87	938.88

\* College of Humanities and Sciences, Nihon University.

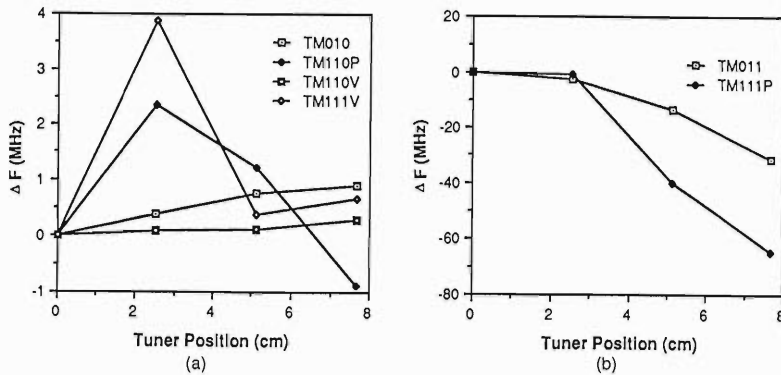


Fig. 3. Variation of resonant frequencies as a function of tuner position.

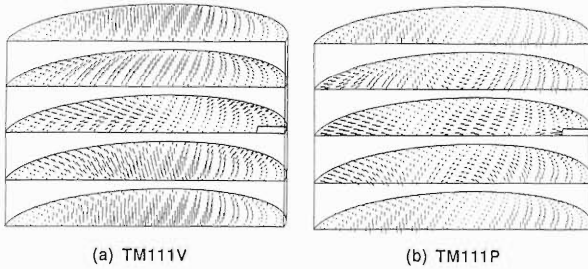


Fig. 4. Three-dimensional electric field distribution of orthogonal TM<sub>111</sub> modes. Bars indicate the strength and the direction of the electric field at each element.

resonant frequency increases, and *vice versa*. The calculated results agree with this theorem. The resonant frequency of the TM<sub>010</sub> mode goes up by about 0.8 MHz with a stroke of 5 cm. This result agrees with the experimental result using a 1/6 scale test cavity by considering the scaling factor.

As a typical result of the field calculation, the electric field distributions in the TM<sub>111V</sub> and TM<sub>111P</sub> modes are shown in Fig. 4, when the tuner is inserted by 5 cm. Next, the distribution of the RF electromagnetic field along the beam axis is examined. The accelerating electric field in the TM<sub>010</sub> mode hardly changes by the tuner insertion. When the tuner is inserted by 5 cm, the deviation of the accelerating field is less than 1%. In the TM<sub>011</sub> mode, a transverse electric field is induced which causes beam deflection. Figure 5 shows the strength of the electric field along the beam axis. The TM<sub>111</sub> modes shown above also have transverse fields. The effect of these fields in higher-order modes on the beam motion can be investigated on the basis of these calculations. From now on, the three-dimensional analysis will be applied to a model cavity for the 8 GeV SR ring.

## (2) Two-dimensional analysis of a test bel-

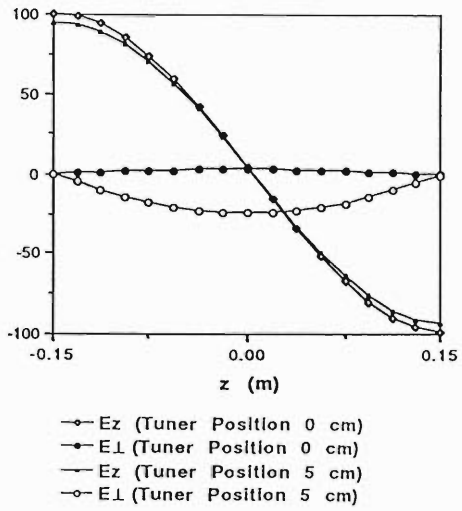


Fig. 5. Electric field distribution of TM<sub>011</sub> mode on the beam axis.

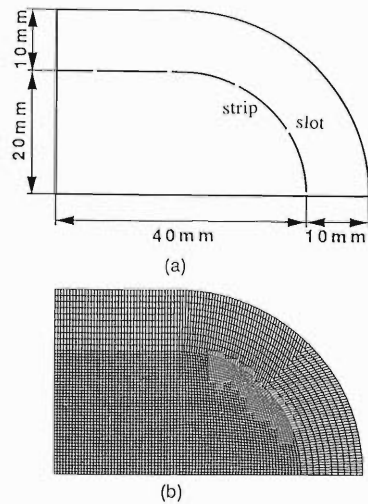


Fig. 6. Two-dimensional model of a test bellows.  
(a), a quarter of a bellows ; (b), mesh diagram.

lows

A new type of bellows is designed to get an electrical connection between an RF contact and

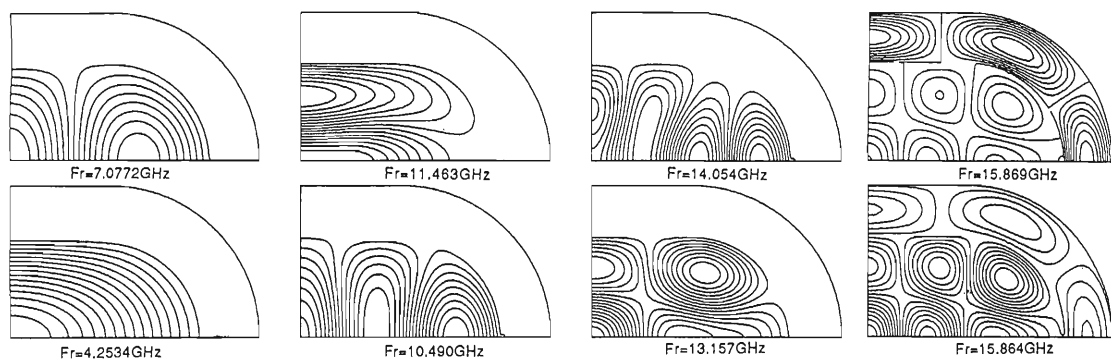


Fig. 7. Calculated magnetic field lines for TM modes.

flanges.<sup>3)</sup> It includes an inner conductor with slots along the beam axis and an outer conductor which is a conventional type of a bellows. A quarter of a cross section shown in Fig. 6 is the region under analysis. The total number of elements is about 4,500. A strip of the inner conductor is 1 cm wide and its thickness is assumed to be zero. The width of a slot is 1 mm.

The electromagnetic wave induced by a bunched beam can propagate along the inner region. The frequency of the wave depends on the bunch shape and the number of bunches in the ring. The propagating mode is mainly a transverse magnetic mode because the image current of the beam flows along the chamber. The magnetic field lines and the cutoff frequencies of TM modes are shown in Fig. 7, when the natural boundary condition is imposed on the axes of

symmetry. The magnetic fields hardly change under 15 GHz compared with the results of no slots. At higher frequencies, however, a mode in the inner region couples a mode in the outer region. It might cause an energy loss of an electron and overheating in a bellows.

To avoid the coupling, the reduction in the gap between conductors is considered. When the gap is shortened from 10 mm to 5 mm, the frequency of the mode coupling goes up above 19 GHz. It is also effective to increase the thickness of the inner conductor. Figure 8 shows the distribution of the longitudinal electric field along the horizontal axis. When the thickness of the strip increases from zero to 0.1 mm, the leakage of the field is decreased by 86% at a frequency of 15.9 GHz.

The two-dimensional electromagnetic field in a bellows is calculated. Since the bellows has a finite length along the chamber, it is necessary to extend the calculation into three-dimensional analysis. Furthermore, an experiment is planned to measure the properties of the bellows by transmitting a current pulse through a thin wire along the beam axis. The calculated results will be compared with experimental results.

#### References

- 1) M. Hara, T. Wada, A. Toyama, and F. Kikuchi: *Sci. Papers I.P.C.R.*, **75**, 143 (1981).
- 2) M. Hara, T. Wada, K. Mitomori, and F. Kikuchi: Proc. 11th Int. Conf. Cyclotron and Their Applications, p. 337 (1987).
- 3) S. Yokouchi, H. Sakamoto, Y. Morimoto, and S.H. Be: This Report, p. 279.

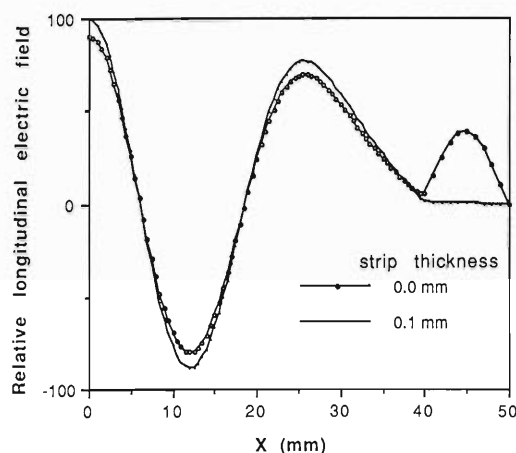


Fig. 8. Electric field distribution along the horizontal axis in a bellows at 15.9 GHz.

## V-2-16. Estimate of the Coupling Impedance for the Storage Ring

T. Yoshiyuki, T. Kusaka, J. Ohnishi, and S.H. Be

The most important ingredient to evaluate the stability of a particle beam in a storage ring is a longitudinal coupling impedance  $Z/n$  and a transverse impedance  $Z_\perp$ , the latter of which is usually related to the former. The storage ring has various elements which contribute to the impedance: a vacuum chamber, bellows, step changes, box-like objects, vacuum ports, slits of RF contacts, and RF cavities. In particular a vacuum chamber is designed so as to have a racetrack geometry of 8 cm wide and 4 cm high with a slot-isolated antechamber in which NEG pumping strips are installed.

The waveguide modes of this chamber were estimated by using numerical EM (electromagnetic) field programs, and the impedance of some vacuum elements was analytically estimated.

### (1) Electromagnetic properties of the vacuum chamber

The TE and TM modes of the vacuum chamber were investigated by using a computer program H2DB.<sup>11</sup> The calculation results of the TM modes for the vacuum chamber geometry with and without an antechamber are shown in Figs. 1 and 2. The H-field lines at a cutoff frequency of the first TM mode are shown in Fig. 1. The EM fields were confined to the beam chamber and

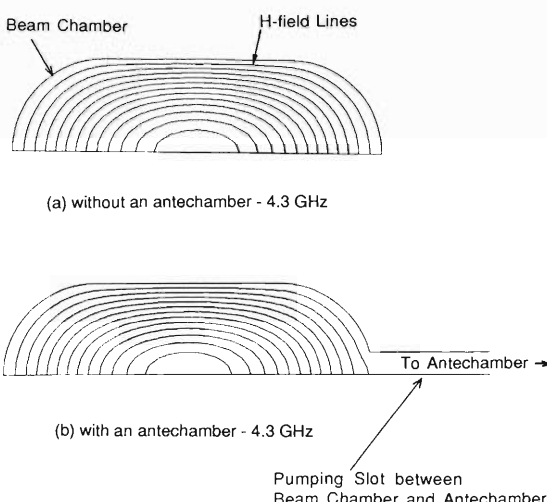


Fig. 1. Calculation of the H-field lines for the first TM mode, 4.3 GHz, of the beam chamber region. a, without an antechamber; b, with an antechamber.

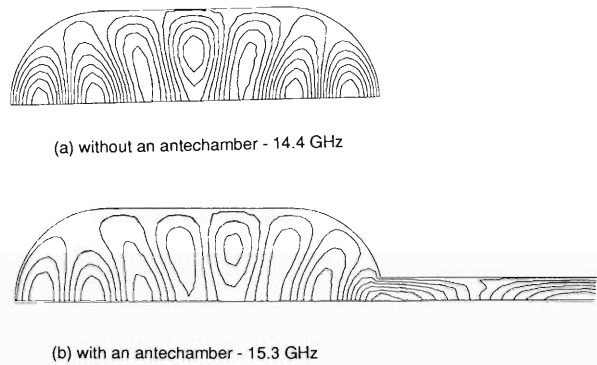


Fig. 2. Calculation of the H-field lines for higher-order TM mode of the beam chamber region. a, without an antechamber (14.4 GHz); b, with an antechamber (15.3 GHz).

respective cutoff frequencies for both geometries were 4.3 GHz. Figure 2 shows the H-field lines for a TM mode of about 15 GHz. As shown in Fig. 2 (b), when the beam chamber had an antechamber, deep penetration into the pumping slot occurred at frequencies above about 15 GHz and a distortion of the H-field lines was remarkable compared with the beam chamber without an antechamber.

The loss parameter  $k(\sigma_l)$  is given by

$$k(\sigma_l) = \sum_n k_n(0) \exp[-(\omega_n \sigma_l / c)^2]$$

where  $k_n(0) = \omega_n R_n / (4Q_n)$ ,  $R_n$  is the shunt impedance,  $Q_n$  the quality factor,  $\omega_n$  the frequency of  $n$ -th mode, and  $\sigma_l$  rms bunch length. Above 15 GHz, the slot has significant effects: 1) when a long bunch is above 1 cm in length, the loss parameter will be little dependent on the modes above 15 GHz; 2) when a short bunch is about 5 mm in length, the contribution to the modes near 15 GHz will be comparable with that near 1 GHz. The loss parameter for the vacuum chamber with an antechamber will significantly differ from that without an antechamber.

### (2) Analytical estimation of vacuum chamber components

We try to compute each contribution of various parts to the impedance. Before quantitative estimation of the impedance, we must first get an idea how much it can be reasonably allowed. The

impedance to be allowed is, in a classical stability criterion,<sup>2)</sup>

$$\left| \frac{Z}{n} \right| \leq \frac{\alpha E}{eI_P} \left( \frac{\Delta E}{E} \right)^2$$

where  $\alpha$  is the momentum compaction factor,  $E$  the total particle energy,  $\Delta E/E$  the FWHM of relative energy distribution, and  $I_P$  the peak current defined by

$$I_P = I_{AV} \frac{2\pi R}{3M\sigma_t}$$

with  $I_{AV}$  the average current in  $M$  bunches, with rms bunch length of  $\sigma_t$  and over a circumference of  $2\pi R$ .  $n$  is the ratio of the storage ring circumference of the wavelength of perturbation traveling around the bunch. Using the parameters of our storage ring;  $E = 8$  GeV,  $\alpha = 1.3 \times 10^{-4}$ ,  $\Delta E/E = 3 \times 10^{-3}$ ,  $I_{AV} = 100$  mA,  $2\pi R = 1,400$  m,  $M = 100$  bunches, and  $\sigma_t = 2$  cm, we obtain  $|Z/n| \leq 0.4 \Omega$ . This allowance is relatively small compared with other rings. This means that the impedance problem of our ring is more serious.

Assuming a cylindrical symmetry, we analytically estimated the impedance of different elements: free space, space charge, resistive wall, bellows, flange, pick-up electrodes, radius discontinuities, slits and holes, and RF cavity. The method we used to estimate the impedance is the one outlined by A.G. Ruggiero.<sup>3)</sup> Here we estimate the impedances of bellows, flanges, and step changes which show the most critical values. We also estimate the impedance of the slits for RF contacts which screen the bellows. The RF cavities have a large impedance, but that of the cavities is not included here.

In our ring, there are about 800 bellows of a circle and a racetrack types. In the low frequency range, impedance is pure inductance

$$Z = -iZ_0 \left( \frac{Ml}{2\pi R} \right) \ln \frac{d}{b}$$

where  $M$  is the number of bellows,  $l$  the length per bellows,  $d$  the average radius of bellows,  $b$

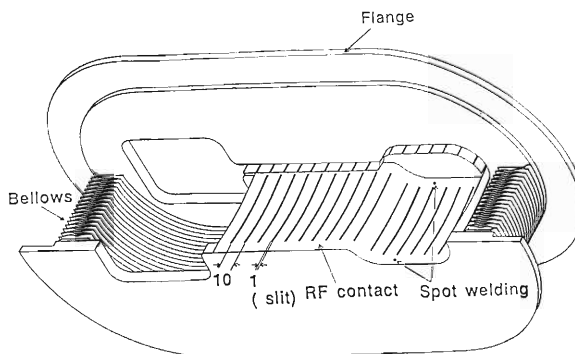


Fig. 3. RF contacts by which the bellows are screened on the vacuum chamber with the antechamber.

the average pipe radius of 30.15 mm, and  $Z_0 = 377 \Omega$ . We obtain  $Z/n = -i 15.7 \Omega$  for 576 race-track type bellows with  $d = 133$  mm,  $l = 60$  mm and 192 circle type bellows with  $d = 74$  mm,  $l = 60$  mm in our ring. The bellows must be shielded because this impedance is much larger than the allowance of the impedance obtained above.

For this purpose we screen the bellows by RF contacts as shown in Fig. 3. The RF contact has many slits around the beam chamber. The impedance from a slit is caused by the diffraction of electromagnetic wave through it. We estimated the slit impedance for a frequency  $\omega = n\omega_0$  from the following equation, where  $\omega_0$  is the revolution frequency.

$$\frac{Z}{n} = \frac{2Z_0\alpha^2}{3\pi^3 R^4 b^2} \left[ n^3 - i \frac{8}{\pi} \left( n^2 n_c + \frac{1}{3} n_c^3 \right) \right] \quad n \leq n_c$$

$$\alpha = \frac{\pi}{16} l w^2$$

where  $l \gg w$  for a rectangular slit of dimensions and  $b$  is the pipe radius. Also  $n_c \sim 2\pi R/l$ . The impedance  $|Z/n|$  for the RF contacts with slits of 60 mm long and 1 mm wide is shown in Fig. 4. The maximum impedance is  $1.64 \times 10^{-5} \Omega$  when the frequency is 5 GHz. This shows that the impedance due only to bellows is steeply diminished by screening the bellows with the RF contacts.

Flanges also contribute to the impedance. We assume that there are 20 flanges per cell in the storage ring. The impedance is calculated in the same fashion as for bellows. In the case of 48 cells,  $Z/n = i 2.29 \Omega$ , for  $l = 4$  mm,  $d$  (the outer radius of a gap between flanges) = 174 mm, and  $b = 32$  mm.

In the storage ring, the transition between different chambers is made with step changes. We shall take the most pessimistic look and consider the step changes in the vacuum chamber without tapering. Define  $S$  as the ratio of the

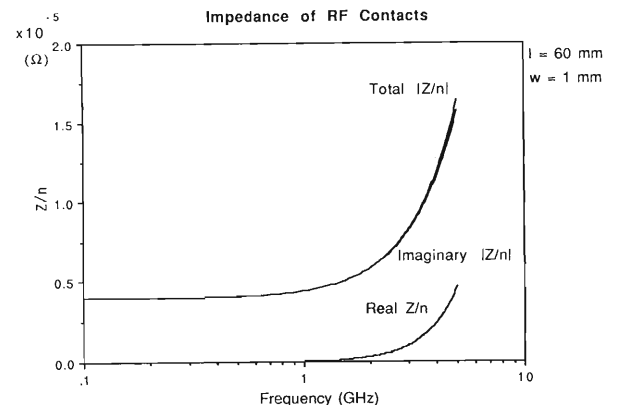


Fig. 4. Impedance of RF contacts.

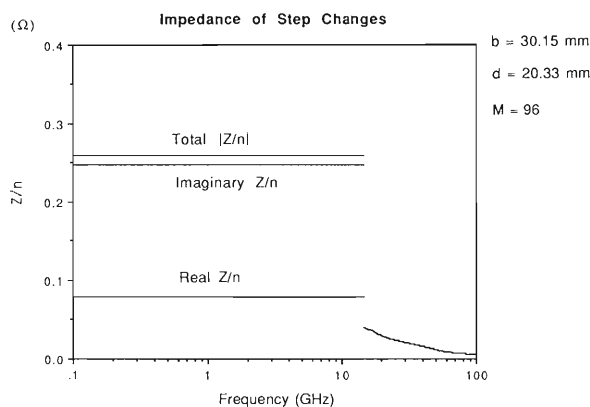


Fig. 5. Impedance of step changes.

outer dimension to the inner dimension  $d$ . We take  $S = 1.5$ . The impedance per the step change is

$$\frac{Z}{n} = (1 + i\pi) \frac{2Z_0}{\pi} (S-1)^2 \frac{d}{2\pi R}$$

for  $n \leq \frac{4\pi R}{4d(S-1)} = n_w$

$$= (1 + i\pi) 8.25 \times 10^{-4} \Omega$$

If  $n > n_w$ ,

$$\frac{Z}{n} = \frac{Z_0}{2\pi} \frac{(S-1)}{n} = \frac{30}{n} \Omega$$

Since there are 96 steps in the ring, the impedance gets  $0.26 \Omega$  at maximum as shown in Fig. 5. This value must become an issue, but in practice the steps are soften by long tapering sections to preserve matching from one side to another.

The preliminary calculations show that the most critical elements are bellows, flanges, and step changes. For bellows, the impedance is sufficiently decreased by screening them with RF contacts. The step changes are in practice tapered smoothly and the impedance becomes small. The effect of flanges on impedance must be studied in more details. Thus we need the way to decrease the impedance of flanges. The next step is to test these parts in simulation programs. The impedance measurements are also necessary to check the estimation.

#### References

- 1) M. Hara, T. Wada, A. Toyama, and F. Kikuchi: *Sci. Papers I. P. C. R.*, **75**, 143 (1981).
- 2) E. Keil and W. Schnell: CERN ISR-TH-RF 69/48.
- 3) A. G. Ruggiero: BNL Informal Report, Aug. (1979).

## V-2-17. Pumping System for the 8 GeV Storage Ring

S. Yokouchi, H. Sakamoto, Y. Morimoto, and S.H. Be

In order to obtain a beam lifetime of 20 h, the vacuum system of the 8 GeV storage ring must maintain a CO partial pressure of  $10^{-10}$  Torr all over the ring. A gas load in the vacuum system depends on synchrotron radiation (SR)-induced gas desorption and thermal desorption. SR-induced gas desorption decreases with an integrated photon flux. This is directly related to the integrated electron beam currents. The gas load,  $Q$ , can be expressed by  $Q = 2.49 \times 10^{-4} D^{-2/3}$  Torr l/s for 0.1 A at 8 GeV, where  $D$  is an integrated electron beam current in Ah unit. The total thermal gas load is  $8.5 \times 10^{-5}$  Torr l/s. In this estimation, we considered an extruded aluminum alloy as a chamber material and an oxygen-free copper as a crotch<sup>1)</sup> material. For the outgassing rate of these materials, we assumed  $5 \times 10^{-12}$  Torr l/s cm<sup>2</sup>. The total inner surface area of the chamber and crotch is  $1.7 \times 10^7$  cm<sup>2</sup>. The gas load is summarized in Table 1.

Figure 1 shows the pumping system per cell of the ring. The main pumping system is based on a non-evaporable getter (NEG) strip whose details are described in this report.<sup>2)</sup> The distributed NEG strips are used in both straight and bending chambers, but distributed ion pump (DIP) is equipped only in a bending chamber. In a straight chamber, a sputter ion pump (SIP) and a titanium sublimation pump (TSP) are mounted on an absorber where many gas molecules are produced by SR. SIP, TSP, and Lumped NEG pump are installed at the crotch where a heavy gas load is expected by SR. SIP and the Lumped NEG pump are attached to a trapping room to pump almost all the SR-induced gas molecules before they have a chance to bounce around in

Table 1. Gas load in the ring.

$D$ (Ah)	SR-induced gas load (Torr l/s)	Thermal gas load (Torr l/s)	Total gas load (Torr l/s)
1	$2.5 \times 10^{-4}$	$8.5 \times 10^{-5}$	$3.4 \times 10^{-4}$
10	$5.4 \times 10^{-5}$	↑	$1.4 \times 10^{-4}$
100	$1.2 \times 10^{-5}$	↑	$9.7 \times 10^{-5}$

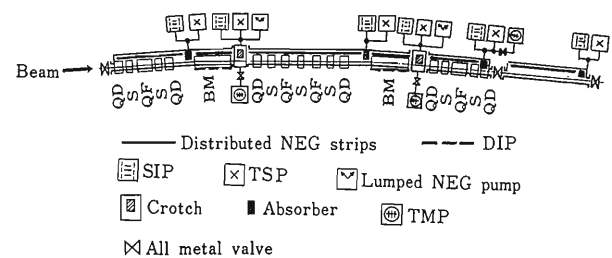


Fig. 1. Pumping system per cell of the ring.

Table 2. Effective pumping speed per cell of the ring.

Section	NEG strip	DIP	TSP	SIP	unit 1/s	
					Lumped NEG pump	Total
Straight chamber	1,130	—	—	—	—	1,130
Bending chamber	300	420	—	—	—	720
Absorber	—	—	1,940	680	—	2,620
Crotch	—	—	1,940	680	2,200	4,820
Total	1,430	420	3,880	1,360	2,200	9,290

the beam chamber. Our main pumping system is based on the NEG strip but a feature of the pumping system is a mixed pumping one which consists of a distributed NEG strip, DIP, SIP, TSP, and a Lumped NEG pump.

The effective pumping speed (CO) per cell is listed in Table 2. The values of SIP and a Lumped NEG pump in the crotch are those at the trapping room and the others at the beam chamber. The total pumping speed of the ring is  $9,290 \times 44$  (cell), *i.e.*,  $4.1 \times 10^5$  l/s. Since the total gas load in the ring is  $9.7 \times 10^{-5}$  Torr l/s (see Table 1), the expected average pressure becomes  $\sim 2 \times 10^{-10}$  Torr (CO equivalent) at 100 Ah  $D$ . The calculated pressure gradient profile over one cell is presented in this report.<sup>3)</sup>

As the NEG materials, two types (St 101 and St 707) are available. They are different in operating temperature. In our ring, St 707 is favored. The reasons are as follows: (1) Activation temperature is higher for St 101 ( $\sim 700^\circ\text{C}$ ) than for St 707 ( $\sim 450^\circ\text{C}$ ). (2) The number of thermal cycles

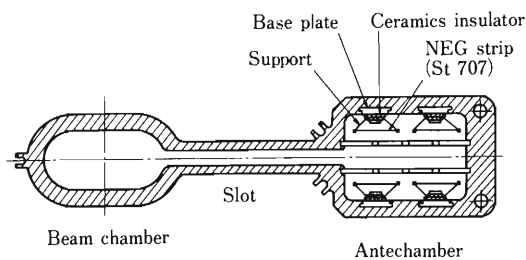


Fig. 2. Cross section of the vacuum chamber with NEG strips.

(i.e. lifetime) for heat treatment is limited in case of St 101 compared with St 707. (3) More electrical power for heating is required for St 101 than for St 707. (4) Thermal affection to the chamber is more serious for St 101. (5) Because of a larger thermal expansion of NEG strips, an installation of the strips in the narrow space (as shown in Fig. 2) is difficult.

The sorption capacity of NEG is sufficient for H<sub>2</sub> since its sorption is reversible. The interval of regeneration cycle is expected to be about 2.5 y at a ring operation pressure of  $1 \times 10^{-9}$  Torr. Although CO is permanently sorbed in the getter material, the lifetime for CO is estimated at about 20 y. For this duration the reactivation cycle will be required about 20 times.

Figure 2 shows an assembly of NEG strips in the chamber. The support holds both sides of the NEG strip, where getter materials are not deposited. The employment of this supporting method is to prevent the getter materials from exfoliation during the heating; the exfoliation of the getter materials originates in temperature ununiformity. Each support insulated with ceramics insulator is discretely fixed on the baseplate.

A turbo-molecular pump (TMP) is to be used for backup pumping. TMP is a ultra-high vacuum pump which can dynamically pump a large quantity of gases. Therefore, the TMP will be run in the range of low pressure before each pump of the main pumping system starts up.

All aluminum alloy gate valves with an RF contact are mounted for isolating the chambers at each end of the cell. By closing them, each cell can independently be pumped after venting to atmospheric pressure and subjected to leak check.

Bellows with an RF contact are used for compensating misalignments during installation of the chambers, valves, and other components,

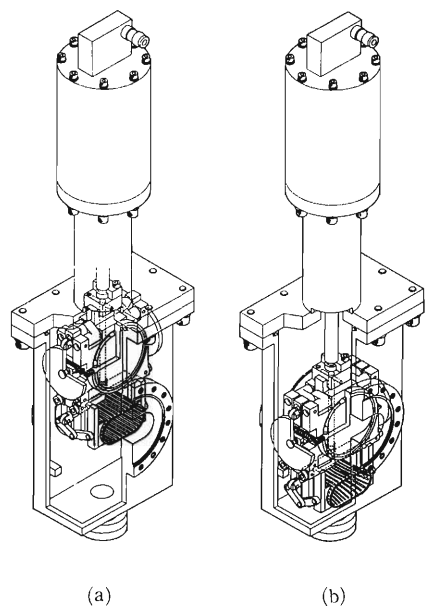


Fig. 3. Isometric drawing of all aluminum alloy gate valve with an RF contact (a) at open position and (b) at closed position.

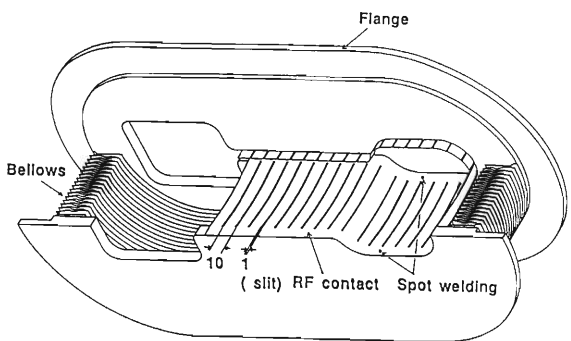


Fig. 4. Isometric drawing of bellows with an RF contact.

and thermal expansion during ring operation and bakeout.

The aluminum alloy gate valve and bellows were specially designed to minimize RF impedance. These are shown in Figs. 3 and 4. Further development of a valve and bellows with a smoother, simpler, and more conductive wall is strongly required.

Aluminum gaskets are used for connection of the flanges.

## References

- 1) Y. Morimoto, S. Yokouchi, H. Sakamoto, and S.H. Be: *RIKEN Accel. Prog. Rep.*, 21, 247 (1987).
- 2) S. Yokouchi, H. Sakamoto, Y. Morimoto, and S.H. Be: This Report, p. 283.
- 3) H. Sakamoto, S. Yokouchi, Y. Morimoto, S.H. Be, and I. Aoki: This Report, p. 288.

### V-2-18. Stress Analysis of the Vacuum Chamber for the 8 GeV Storage Ring

T. Nishidono,\* H. Kakui,\* S.H. Be, H. Sakamoto,  
S. Yokouchi, Y. Morimoto, and Y. Oikawa

The vacuum chamber consists of two chambers with different shapes. We used aluminum alloy chambers (A6063-T6) to minimize synchrotron radiation (SR) -induced desorption as well as thermal outgassing.

The cross-sectional view of the vacuum chambers for the straight sections is shown in Fig. 1.

This vacuum chamber consists of a beam chamber and a slot-isolated antechamber in which non-evaporable getter (NEG) strips are

installed.

The cross-sectional view of the vacuum chambers for the bending magnet is shown in Fig. 2.

This vacuum chamber consists of beam chamber, a slot-isolated antechamber, and a pump chamber. We install a distribution ion pump (DIP) and a NEG strip pump on opposite sides of the beam chamber.

These chambers contain cooling channels for removing the thermal load of SR light.

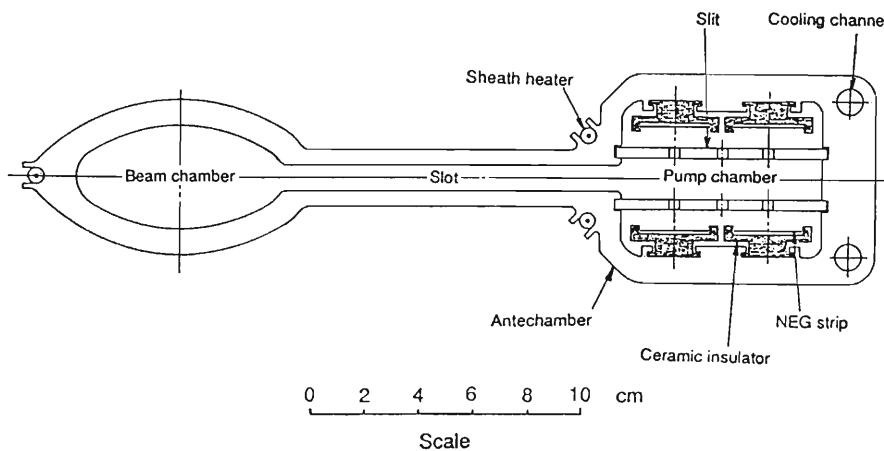


Fig. 1. Cross-sectional view of the vacuum chamber for the straight sections.

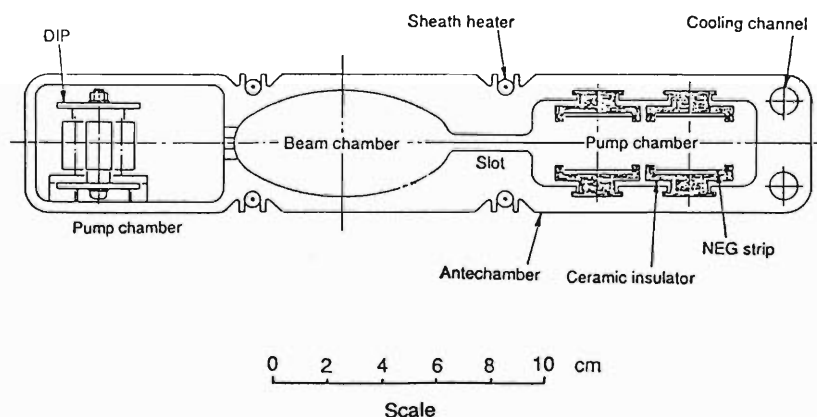
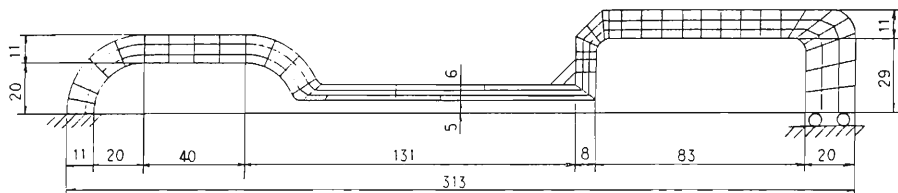
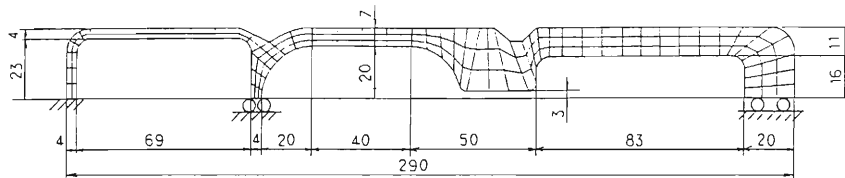


Fig. 2. Cross-sectional view of the bending magnet vacuum chamber.

\* Ishikawajima-Harima Heavy Industry Co., Ltd.



The vacuum chamber for the straight sections.



The vacuum chamber for the bending magnet.

Fig. 3. Analytical model.

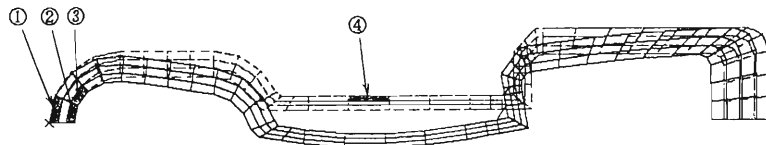
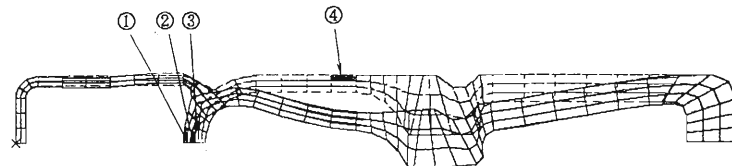
The vacuum chamber for straight sections. Displacement (mm)—MAG MIN: 0.00E+00 MAX: 4.50E-01. Stress (kg/mm<sup>2</sup>)—①: 2.1, ②: -2.6, ③: -2.4, ④: -1.9.The vacuum chamber for bending magnet. Displacement (mm)—MAG MIN: 0.00E+00 MAX: 1.03E-01. Stress (kg/mm<sup>2</sup>)—①: 1.7, ②: -2.4, ③: -1.5, ④: -1.3.

Fig. 4. Calculation results of stress analysis.

Flexible sheathed heaters are inserted into baking channels. Further, these chambers are thermally insulated with Kapton films.

The chambers must be designed so as to stand the pressure difference between the atmospheric pressure and the vacuum.

The stress of the vacuum chambers was calculated, on the base of the analytical model shown in Fig. 3. Calculated results are shown in Fig. 4, which shows that 1) in the vacuum chamber for straight sections, the maximum displacement ( $\Delta Y$ ) is 0.45 mm at the slot, and the maximum stress ( $\sigma$ ) is 2.6 kg/mm, and 2) in the vacuum chamber for the bending magnet, the  $\Delta Y$  is 0.1 mm at the slot, and the  $\sigma$  is 2.4 kg/mm. The value of the stress of these vacuum chambers are

less than the allowable stress of 6.8 kg/mm for materials to be used as a chamber. Thus, these vacuum chambers will withstand the pressure difference between the atmosphere and the vacuum. However the displacements are larger than the mounting accuracy required for beam position monitors. In our storage ring, monitors must be mounted with a high accuracy of 0.1 mm on the vacuum chambers.

This means that a proper countermeasure for reducing displacements must be taken.

These problems will be discussed, and results will be checked with prototype model chambers which are now under fabrication. Calculations of a thermal stress are in progress.

## V-2-19. Pumping Characteristics of NEG Strip

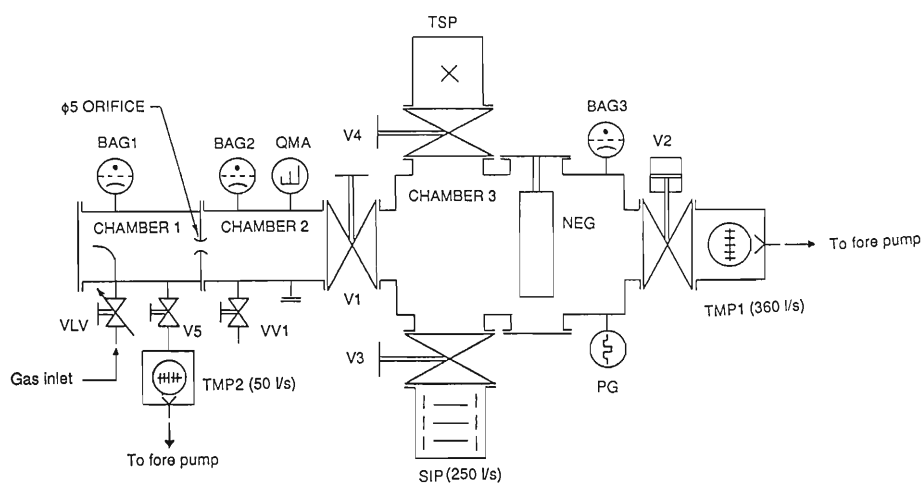
S. Yokouchi, H. Sakamoto, Y. Morimoto, and S.H. Be

We experimentally investigated the pumping speed of a non-evaporable getter (NEG) strip (trade name St 707), which is planned to be used as a main pump in the pumping system for the 8 GeV storage ring (details of the pumping system are described in this report<sup>1)</sup>).

### NEG Material

The NEG material available for a strip is a 84%Zr-16%Al alloy (St 101 supplied by SAES GETTERS S. p. A) or a 70%Zr-24.6%V-5.4%Fe alloy (St 707). These alloys are deposited on a support strip of constantan in powder form. The getter alloy is suitable for pumping active gases, but not for methane and noble gases. The alloy reacts with active gases such as CO, CO<sub>2</sub>, O<sub>2</sub>, and N<sub>2</sub> to form stable chemical compounds. Hydrogen and its isotopes, however, form a solid solution in the alloy and can thus be reversibly sorbed. NEG develops its pumping characteristics after heat treatment called "activation". The heat treatment diffuses a thin surface layer, which is formed by exposing to air during the manufacturing steps, into the bulk and makes the surface of the getter clean and enable to sorb.

Another heat treatment called "reactivation" is needed to recover the pumping speed of NEG which has fallen to low values by sorbing active gases. The optimum treatment for full activation recommended by the manufacturer is heating for  $\sim 45$  min under vacuum at  $\sim 700^\circ\text{C}$  for St 101 and at  $\sim 450^\circ\text{C}$  for St 707. Hydrogen sorbed in NEG can be released from the getter by the regeneration treatment, which is necessary when the pumping speed for H<sub>2</sub> is fallen below an acceptable limit or H<sub>2</sub> quantity sorbed is approaching an embrittlement limit of 20 Torr l/g. The time necessary for the regeneration of NEG is obtained from  $t = M \times (1/q_f - 1/q_i) \times 10^{-(A-B/T)} / F$  s, where  $M$  is the weight of a getter material in g,  $q_f$  the final H<sub>2</sub> concentration in Torr l/g,  $q_i$  the initial H<sub>2</sub> concentration in Torr l/g,  $A$  and  $B$  the constants,  $T$  the regeneration temperature in kelvin, and  $F$  the pumping speed of a backing pump in l/s. The regeneration process, however, should not be performed times without number because of the development of thermal fatigue effects in the getter-coated strips. The thermal fatigue, which depends mainly on the tempera-



NEG : Non-evaporable getter (St 707) strip

SIP : Sputter ion pump

TSP : Titanium sublimation pump

TMP : Turbo molecular pump

QMA : Quadrupole mass analyzer

BAG1,2,3 : Bayard-Alpert nude gauge

PEG : Penning gauge

PG : Pirani gauge

V1,2,3,4,5 : Manual gate valve

VLV : Variable leak valve

VV1,2 : Venting valve

Fig. 1. Schematic diagram of the device with test instruments.

ture and the duration of regeneration, causes peeling-off of the getter powder.

#### Measurement

Figure 1 shows a schematic diagram of the test device. The chambers are made of extruded aluminum alloy (A6063-T6). Chambers 1 and 2 form a test dome for measuring the pumping speed. In chamber 3, NEG strips were installed as shown in Fig. 2, and a sputter ion pump and a titanium sublimation pump, which would be used in the 8 GeV storage ring, were set up to investigate a vacuum performance of the mixed pumping system. A turbo-molecular pump (TMP2) were installed in chamber 1 to prevent the partial pressure buildup of gases such as  $\text{CH}_4$  and Ar which cannot be pumped with NEG. The effective surface area of the NEG strips is  $506 \text{ cm}^2$  and the total weight of the getter material is 21.5 g.

Pumping speeds of the NEG strip were measured for  $\text{H}_2$  at room temperature and  $275^\circ\text{C}$ , and for CO at room temperature by following procedures. For  $\text{H}_2$ , the initial  $\text{H}_2$  quantity sorbed ( $\text{H}_2$  concentration) is given by  $\log p = 4.8 + 2\log q - 6,166/T$ ,<sup>2)</sup> where  $p$  is the equilibrium pressure of  $\text{H}_2$  in Torr after appropriate regeneration,  $q$  the  $\text{H}_2$  concentration in Torr l/g, and  $T$  the regeneration temperature in kelvin. The pumping speeds were measured by two methods: (1) Gases are introduced at a constant throughput, and the

pumping speeds were measured periodically, and (2) gases were introduced at various throughputs, and the pumping speeds were measured.

For CO, the initial CO quantity sorbed is regarded as zero after activation at  $\sim 450^\circ\text{C}$  for  $\sim 10$  min. The pumping speed was also measured by the same method as (1) for  $\text{H}_2$ . The quantity of sorbed gas is calculated by adding the integrated throughput to the initial gas quantity sorbed. The pumping speed is given by  $S = C \times (p_1 - p_2)/p_2$  l/s, where  $C$  is the conductance of an orifice in l/s,  $p_1$  the pressure at BAG 1 in Torr,  $p_2$  that at BAG 2 in Torr.

The pumping speeds of the NEG strip (St 707) for  $\text{H}_2$  are plotted in Fig. 3, in which curve 1 (obtained by the measuring method (1)) shows

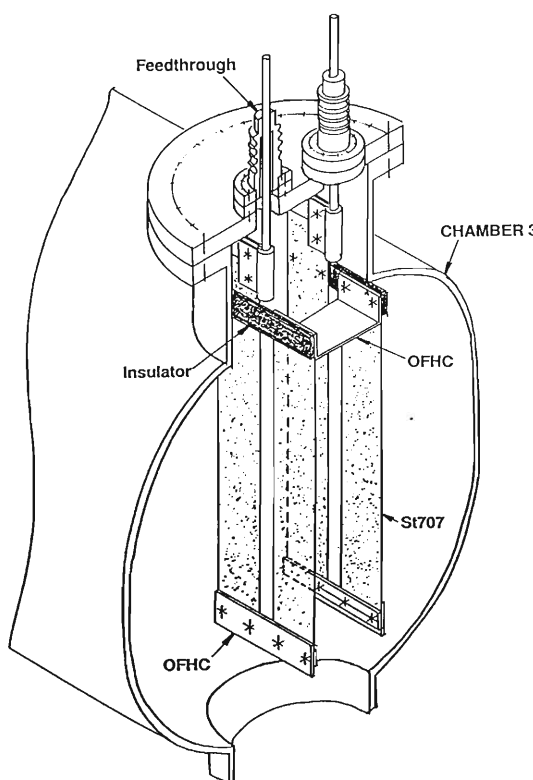


Fig. 2. Assembly of NEG strips in the chamber.

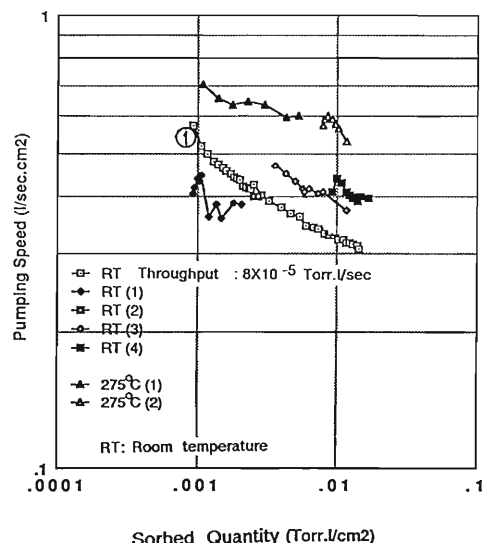


Fig. 3. Pumping speeds of the NEG strip (St 707) for  $\text{H}_2$  at room temperature and  $275^\circ\text{C}$ .

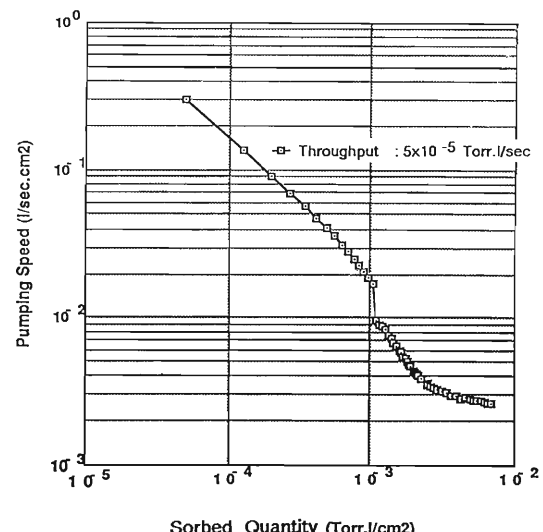


Fig. 4. Pumping speeds of the NEG strip (St 707) for CO at room temperature.

that the pumping speed for  $H_2$  does not decrease rapidly. This means that the  $H_2$  gas adsorbed on the surface diffuses into the bulk of the getter, and the pumping speed decreases gradually owing to the reduction in the bulk diffusion with an increase in  $H_2$  concentration. Other curves were obtained by the measuring method (2). Fluctuation in the data is due to the change in the throughput during the measurement. It has been reported<sup>3)</sup> that the pumping speed for  $H_2$  depends on the throughput. The pumping speed at 275°C is higher than that at room temperature, because the bulk diffusion is promoted at high temperature.

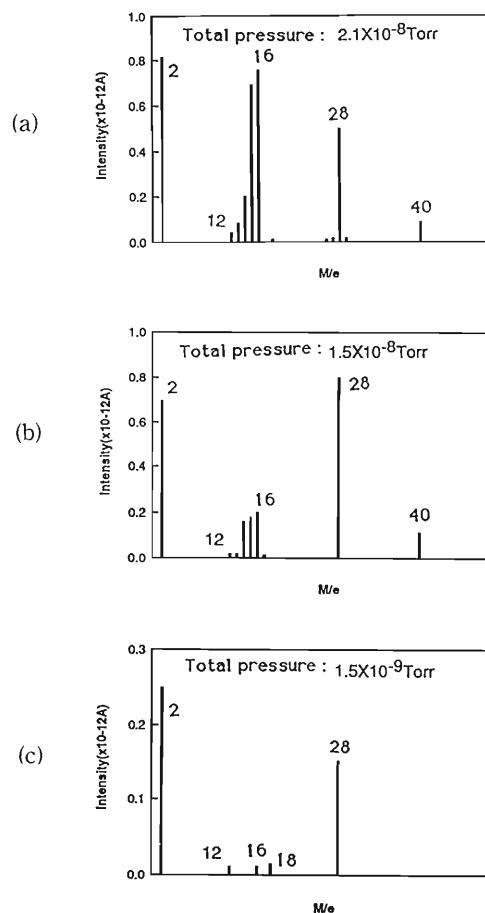


Fig. 5. Mass spectra of the residual gases, (a) with only NEG strip (at room temperature), (b) with a combination of NEG strip (at room temperature) and TMP2, and (c) with NEG strip (at room temperature), TMP1, and TMP2.

ture.

Figure 4 shows the pumping speed for CO. The pumping speed decreases rapidly owing to an increase in the quantity of CO sorbed because of little diffusion at room temperature. A slope,  $\sim -1$ , of the curve is in agreement with the results of Benvenuti, et al.<sup>3)</sup> A drastic change at the sorbed quantity of  $\sim 1 \times 10^{-3}$  Torr  $l/cm^2$  was ascribed to an error due to a change in the measuring range of the gauge (BAG 2).

The results of residual gas analysis are shown in Figs. 5 and 6. In Fig. 5, where only a NEG strip was used, significant peaks of  $CH_4$  ( $M/e = 16$ ) and Ar ( $M/e = 40$ ) appeared, these results indicate that the NEG strip has no pumping capacity for  $CH_4$  and Ar.

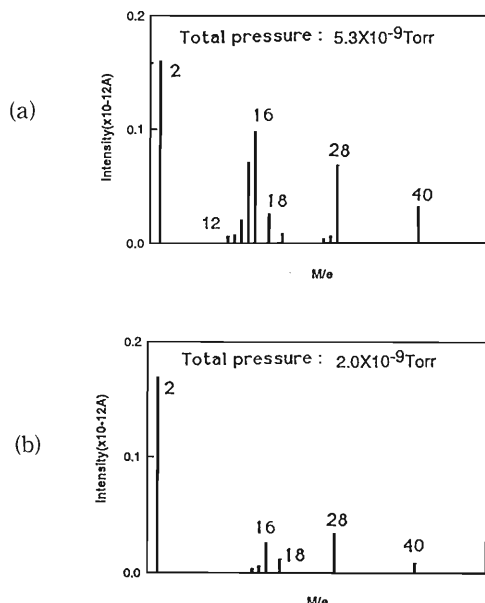


Fig. 6. Mass spectra of the residual gases, (a) with a combination of NEG strip (at 275°C) and TMP2, (b) with a combination of NEG strip (at 275°C), TMP1, and TMP2.

## References

- 1) S. Yokouchi, H. Sakamoto, Y. Morimoto, and S.H. Be: This Report, p. 279.
- 2) SAES GETTERS: St 707 (Catalogue).
- 3) C. Benvenuti and F. Francia: *J. Vac. Sci. Technol. A*, 6, 2529 (1988).

## V-2-20. Synchrotron Radiation Power Distribution at the 8 GeV Storage Ring

Y. Morimoto, H. Sakamoto, S. Yokouchi, and S.H. Be

Synchrotron radiation (SR) power distribution along the 6 GeV storage ring was described.<sup>1)</sup> Later, a beam energy was increased from 6 GeV, to 8 GeV, and many other design parameters were changed with an increase in the beam energy. SR power distributions along the 8 GeV storage ring are calculated under the new design conditions. At present, the cell number of a lattice is not fixed; however, we chose a 44-cell lattice to estimate a thermal load, and SR-

induced outgassing loads for the vacuum chambers and their components.

The layout of various components of the 8 GeV storage ring is shown in Fig. 1. SR power distributions are calculated at the positions of a crotch (CR) and an absorber (AB), and from the geometry of a vacuum chamber. The crotch and absorber are placed so as to intercept most of the SR beam emitted from a bending magnet (BM), and thereby protect the vacuum chamber from SR

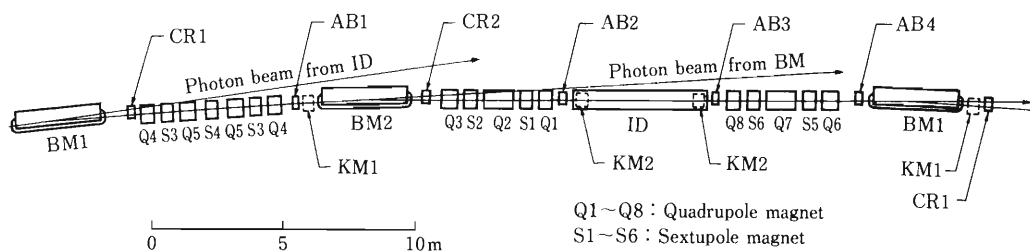


Fig. 1. Schematic layout of a cell of the 8 GeV storage ring.

radiation. Particularly, the crotch has a highly concentrated pumping speed to evacuate SR-induced outgas. The crotch is positioned just downstream of the bending magnet and selectively separate an SR beam which should be transported to the experimental facility. The absorber is positioned just upstream of the bending magnet and the insertion device (ID), and absorbs the SR beam except that entering the electron beam passageway. A power density on the crotch is extremely high, but that on the absorber is relatively low. The structure of the crotch is more complicated than that of the absorber because of the higher power and power density of the crotch. Details of the crotch along with the thermal analysis and geometry of the vacuum chamber are presented in this progress reports.<sup>2)</sup>

Four kicker magnets (KM) to be used to inject an electron beam from the synchrotron into the storage ring are installed in a section of the storage ring; one is between BM1 and CR1, one between AB1 and BM2, and two in the straight section where ID is normally installed. Therefore, CR1 and AB1 are located at a distance of approximately 1 m from the end of BM1 and

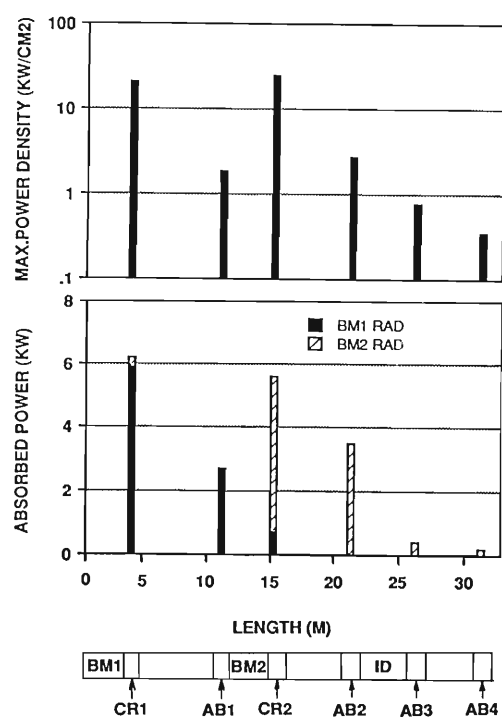


Fig. 2. Absorbed power and maximum power density distributions.

BM2, respectively. Thus we take a space for installation of the kicker magnets. Furthermore, AB3 is added just downstream of the ID for protecting the valve positioned at the back of the ID.

The SR power,  $P_r$  in kW, is given by  $P_r = 26.6E^3BI$ , where  $E$  is the electron energy in GeV,

Table 1. Absorbed powers and power densities.

Area	% Absorbed	Absorbed power (kW)	Max. power density (kW/cm <sup>2</sup> )
a) BM1 Radiation			
CR1	63.0	5.9	21.3
AB1	29.1	2.7	1.8
CR2	7.9	0.7	0.7
Total	100.0	9.3	
b) BM2 Radiation			
CR2	52.9	4.9	25.3
AB2	37.3	3.5	2.7
AB3	4.6	0.4	0.8
AB4	1.6	0.2	0.4
CR1	3.6	0.3	0.2
Total	100.0	9.3	

$B$  the magnetic field in T, and  $I$  the electron current in A. In the design parameters of  $E=8$  GeV,  $B=0.6$  T, and  $I=0.1$  A, the total SR power from 88 BM in our storage ring corresponds to about 820 kW. Thus the SR power emitted from each BM becomes approximately 9.3 kW.

The calculated SR power distributions including power densities along the 8 GeV storage ring are shown in Fig. 2; Table 1 lists the numerical values. The maximum power density on the crotch is 25.3 kW/cm<sup>2</sup> and the total SR power emitted from each bending magnet is 9.3 kW. In our 8 GeV storage ring, no SR beam strikes the wall of vacuum chambers.

The crotch which can withstand the high power density of 25.3 kW/cm<sup>2</sup> is under construction. The design of the absorber has not been started yet, but a trapping structure similar to that of the crotch will be considered for AB1 and AB2, because of their high absorbed powers.

## References

- 1) Y. Morimoto, H. Sakamoto, S. Yokouchi, and S.H. Be: *RIKEN Accel. Prog. Rep.*, **21**, 245 (1987).
- 2) Y. Morimoto, S. Yokouchi, H. Sakamoto, S.H. Be, and T. Shirakura: This Report, p. 292.

## V-2-21. Pressure Gradient Profile in the 8 GeV Storage Ring

H. Sakamoto, S. Yokouchi, Y. Morimoto, S.H. Be, and I. Aoki\*

The method of calculating pressure distribution in our storage ring and results are described below. This calculation is strongly required in designing the pumping system for the storage ring.

### 1) Analytical model of pressure distribution

On the basis of the analytical model shown in Fig. 1, a fundamental expression<sup>1)</sup> for the pressure distribution is given by

$$C_u \frac{d^2P}{dx^2} + q_u - S_u P = 0 \quad (1)$$

where  $C_u$  is the conductance against unit length,  $q_u$  the outgassing rate per unit length, and  $S_u$  the distributed pumping speed per unit length.

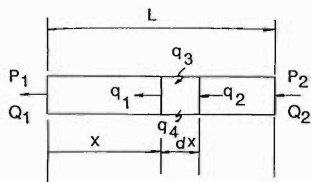


Fig. 1. Analytical model of pressure distribution.

Here we made following assumptions:

- [1] The cross-sectional shape of the chamber is constant;
- [2] The thermal outgassing rate is constant; and
- [3] The distributed pumping speed is constant.

By solving Eq. 1, the relation between the pressure  $P$  and the flow rate  $Q$  is given by

$$\begin{pmatrix} P_2 \\ Q_2 \end{pmatrix} = \begin{pmatrix} A_{11} & A_{12} \\ A_{14} & A_{15} \end{pmatrix} \begin{pmatrix} P_1 \\ Q_1 \end{pmatrix} + \begin{pmatrix} A_{13} \\ A_{16} \end{pmatrix}$$

where  $P_1$  and  $P_2$  are the pressures at the entrance and the exit of each element, respectively,  $Q_1$  and  $Q_2$ , the flow rate at the entrance and exit of each element, respectively,  $A_{11}$ ,  $A_{12}$ ,  $A_{13}$ ,  $A_{14}$ ,  $A_{15}$ , and  $A_{16}$ , the constants determined by the elements.

### 2) Calculation method

Since the vacuum chamber is devided into elements owing to the difference in the distributed pumping speed and the outgassing rate per unit length, the relation between the pressure and the flow rate is given by

$$\begin{pmatrix} P_{i+1} \\ Q_{i+1} \end{pmatrix} = \begin{pmatrix} A_{ii} & A_{i2} \\ A_{i4} & A_{i5} \end{pmatrix} \begin{pmatrix} P_i \\ Q_i \end{pmatrix} + \begin{pmatrix} A_{i3} \\ A_{i6} \end{pmatrix}$$

where  $i=1-n$ .

In a closed vacuum system like a storage ring,  $P_1=P_{n+1}$  and  $Q_1=Q_{n+1}$ . Then we obtain  $2n$  simple equations as follows

$$\begin{aligned} A_{11} \times P_1 + A_{12} \times Q_1 - 1 \times P_2 + 0 \times Q_2 &= -A_{13} \\ A_{14} \times P_1 + A_{15} \times Q_1 + 0 \times P_2 - 1 \times Q_2 &= -A_{16} \\ -1 \times P_1 + 0 \times Q_1 + A_{n1} \times P_n + A_{n2} \times Q_n &= -A_{n3} \\ 0 \times P_1 - 1 \times Q_1 + A_{n4} \times P_n + A_{n5} \times Q_n &= -A_{n6} \end{aligned}$$

The above equations can be rewritten to a matrix of  $(2n+1)$ ,  $(2n)$ -type as given by

$$\begin{pmatrix} A_{11} & A_{12} & -1 & 0 & \cdot & -A_{13} \\ A_{14} & A_{15} & 0 & -1 & \cdot & -A_{16} \\ \cdot & \cdot & A_{21} & A_{22} & -1 & 0 & \cdot & \cdot & \cdot & \cdot & \cdot & \cdot & -A_{23} \\ \cdot & \cdot & A_{24} & A_{25} & 0 & -1 & \cdot & \cdot & \cdot & \cdot & \cdot & \cdot & -A_{26} \\ \vdots & \vdots & & & & & & & & & & & \vdots \\ -1 & 0 & \cdot & \cdot & \cdot & \cdot & & & & & & & A_{n1} & A_{n2} & -A_{n3} \\ 0 & -1 & \cdot & \cdot & \cdot & \cdot & & & & & & & A_{n4} & A_{n5} & -A_{n6} \end{pmatrix}$$

The pressure at each element and the flow rate are obtained by solving this matrix.

If a front end for photon beam lines is set along a line tangential to the electron orbit in the storage ring, the matrix is further rewritten to the following matrix of  $(2n+3)$ ,  $(2n+2)$ -type,

$$\begin{pmatrix} A_{11} & A_{12} & -1 & 0 & \cdot & -A_{13} \\ A_{14} & A_{15} & 0 & -1 & \cdot & -A_{16} \\ \cdot & \cdot & A_{21} & A_{12} & -1 & 0 & \cdot & \cdot & \cdot & \cdot & \cdot & \cdot & -A_{23} \\ \cdot & \cdot & A_{24} & A_{25} & 0 & -1 & \cdot & \cdot & \cdot & \cdot & \cdot & \cdot & -A_{26} \\ \cdot & \cdot & & & & & \cdot & \cdot & \cdot & \cdot & \cdot & \cdot & \vdots \\ & & & & & & & & & & & & A_{n1} & A_{n2} & -1 & 0 & -A_{n3} \\ & & & & & & & & & & & & A_{n4} & A_{n5} & 0 & -1 & -A_{n6} \\ & & & & & & & & & & & & \cdot & \cdot & -1 & 0 & -P_0 \\ & & & & & & & & & & & & \cdot & \cdot & 0 & -1 & -Q_0 \end{pmatrix}$$

Table 1. Parameters for the 8 GeV SOR.

Beam energy	8 GeV
Beam current	100 mA
Dipole field	0.6 T
Circumference	1,500 m
No. of cell	44

\* Osaka Vacuum, Ltd.

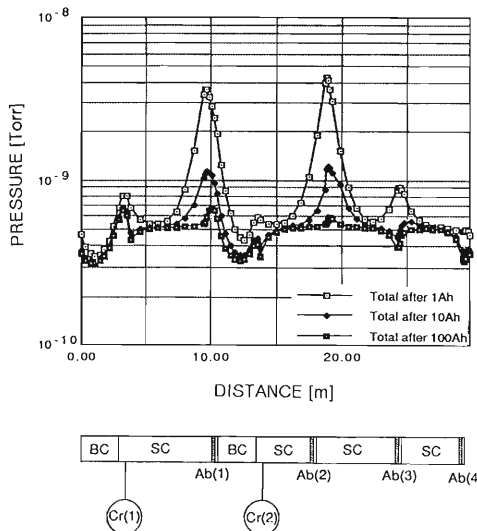


Fig. 2. Pressure gradient profile.

when  $P_0$  and  $Q_0$  are the initial conditions, i.e., the pressure and the flow rate at a connection point between the storage ring and the front end.

### 3) Results

A pressure gradient profile is calculated based on the pumping system<sup>2)</sup> and the synchrotron radiation (SR) power distribution.<sup>3)</sup> The main parameters for the 8 GeV storage ring are shown in Table 1. The SR induced outgassing rate ( $Q_{SR}$ ) is given by  $Q_{SR} = 2n^{\circ}\eta K$ , where  $n^{\circ}$  is the number of photons per second ( $=1 \times 10^{18} E [\text{GeV}] I [\text{mA}]$ ),  $\eta$  is the number of molecules per photon ( $=5.0 \times 10^{-6} D^{-2/3} [\text{Ah}]$ ,  $D$  the integrated stored current), and  $K = 3.11 \times 10^{-20} [\text{Torr l/molecule}]$ .

In this calculation, we assumed that the distribution of the SR induced outgassing rate is in proportion to the rate of SR power deposited at crotches and absorbers, and that the compositions of residual gases are 80% H<sub>2</sub>+20% CO.

Calculated pressure gradient profiles over one cell are shown in Fig. 2. Three curves show respective pressure profiles after the integrated stored current of 1, 10, and 100 Ah. From Fig. 2 we can see that an average pressure over the ring decreases with an increase in the integrated stored current. The area where absorbers Ab(1) and Ab(2) are placed shows the highest pressure in the ring. This means that pumping capabilities at the absorbers are not enough. After 100 Ah,

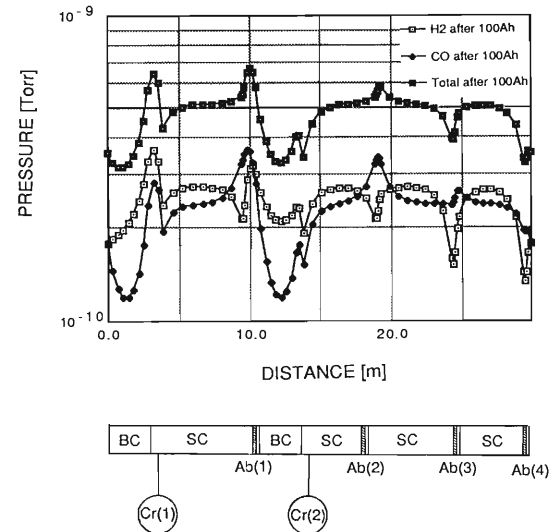


Fig. 3. Partial gradient profile.

however, the average pressure is about 0.2 nTorr and a beam lifetime of about 20 h is expected to be achieved easily. Further, Fig. 2 shows that the pressures at the bending magnet and straight sections, except the area where the crotches and absorbers are placed, are not affected appreciably by the integrated stored current. Thus, we conclude that the pressures at the bending magnet sections and the straight sections are mainly governed only by the thermal outgassing rate. For a mixture of 80% H<sub>2</sub> and 20% CO, partial gradient profiles for H<sub>2</sub> and CO gases are also calculated and the results are shown in Fig. 3. In this calculation we considered the pumping speed and conductance for respective gases. From Fig. 3 we can find that the beam lifetime must be estimated for CO gas because the lifetime is in inverse proportion to the square atomic number of the gas atoms. The lifetime of greater than 20 h can be ensured even with the partial pressure of CO calculated above.

### References

- 1) T. Ikeguchi, M. Matumoto, S. Ueda: KEK Rep., 87 8 Aug. (1987).
- 2) S. Yokouchi, H. Sakamoto, Y. Morimoto, and S.H. Be: This Report, p. 279.
- 3) Y. Morimoto, H. Sakamoto, S. Yokouchi, and S.H. Be: This Report, p. 286.

## V-2-22. Outgassing Rate of an Extruded Aluminum Alloy Chamber

H. Sakamoto, S. Yokouchi, Y. Morimoto, and S.H. Be

The outgassing rate of various vacuum materials is important factor in the design of a vacuum system. In a storage ring, particular, the materials of low outgassing rates are required. Thus we are considering to use an extruded aluminum alloy (A6063T6) for the material of vacuum chambers. The chemical composition of A6063T6 is 0.55 w/o of Mg, 0.44 w/o of Si, and the rest is Al. This aluminum alloy is extruded in the atmosphere of Ar + O<sub>2</sub> and no surface treatment for using in the vacuum is necessary. To measure the outgassing rate of the extruded aluminum alloy, we constructed an experimental device as shown in Fig. 1. This device consists of three chambers made of extruded aluminum alloy. The outgassing rate is obtained by estimating the gas quantities from the inner surface of the chamber 1. The specific method will be described later. On the respective outsides of the chambers, sheathed heaters are welded for bak-

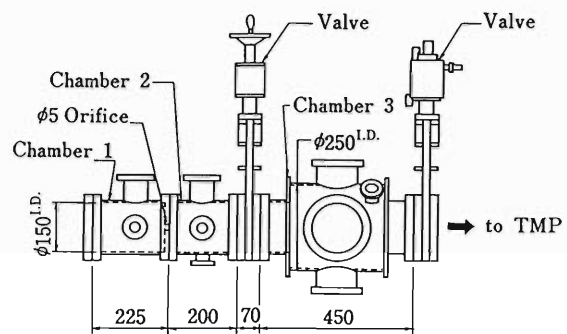
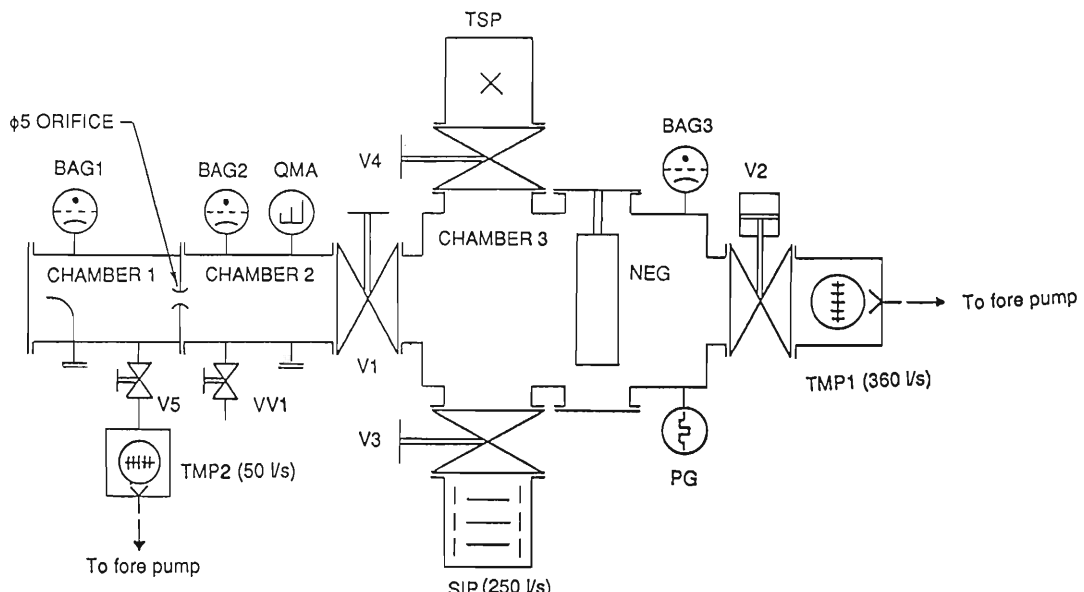


Fig. 1. Outline of the device.

ing the chambers, and chromel-alumel thermocouples are also attached for measuring the baking temperature.

A schematic diagram of the device with test instruments is shown in Fig. 2. A Bayard-Alpert (BA) nude gauge (BAG1) in the chamber 1, a BA nude gauge (BAG2), and a quadrupole mass



NEG : Non-evaporable getter (St 707) strip  
SIP : Sputter ion pump  
TSP : Titanium sublimation pump  
TMP : Turbo molecular pump  
QMA : Quadrupole mass analyzer

BAG1,2,3 : Bayard-Alpert nude gauge  
PEG : Penning gauge  
PG : Pirani gauge  
V1,2,3,4,5 : Manual gate valve  
VV1,2 : Venting valve

Fig. 2. Schematic diagram of the device with instruments.

analyzer (QMA) in the chamber 2 are installed. A sputter ion pump (SIP), a titanium sublimation pump (TSP), non-evaporable getter (NEG) strips, and a turbo molecular pump (TMP) are mounted on the chamber 3 with gate valves (V2,V3,V4). Thus, it is possible to combine these pumps by opening or closing the gate valves.

The outgassing rate ( $Q$ ) of the chamber 1 was obtained from  $Q = C (P_1 - P_2)/S$ , where  $P_1$  is the pressure of the chamber 1,  $P_2$  that of the chamber 2, and  $C$  is the conductance (2.28 l/s) of the orifice of 5 mm in diameter. This orifice is placed between the chamber 1 and 2.

Measured outgassing rates for the chamber 1 as a function of the pumpdown time are shown in Fig. 3. At first, the chambers were evacuated for about 190 h with 300 l/s TMP and then 250 l/s SIP instead of TMP. The increase in the outgassing rate after 20 h is due to the prebaking effect of the chamber for 50 h at 80°C. This prebaking was carried out to check the leak between flanges. After prebaking, the minimum outgassing rate was  $8.0 \times 10^{-12}$  Torr l/s cm<sup>2</sup>. Figure 3 shows that the outgassing rate keeps constant during approximately 700 h after prebaking. This means that the baking at 80°C is not enough to decrease the outgassing rate of the chamber. After checking leak, the chambers was baked for

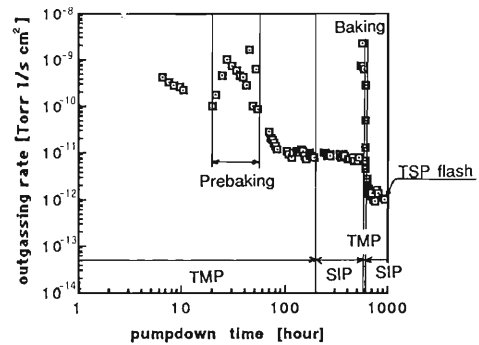


Fig. 3. Outgassing rate of the extruded aluminum alloy chamber.

40 h at 150°C. After the baking, the outgassing rate decreased from  $8.0 \times 10^{-12}$  Torr l/s cm<sup>2</sup> after prebaking to  $9.0 \times 10^{-13}$  Torr l/s cm<sup>2</sup> at about 150 h after the baking. This outgassing rate is in approximate agreement with the results reported so far. Evacuating with only SIP, the minimum pressure of the chambers 1 and 2 were  $1.6 \times 10^{-9}$  Torr and  $8.8 \times 10^{-10}$  Torr, respectively. Furthermore, by evacuating with TSP in addition to SIP, the pressure of the chambers 1 and 2 ultimately decreased to  $1.2 \times 10^{-9}$  Torr and  $4.2 \times 10^{-10}$  Torr, respectively, with no variation in the outgassing rate.

## V-2-23. Thermal Analysis of the Crotch at the 8 GeV Storage Ring

Y. Morimoto, S. Yokouchi, H. Sakamoto, S.H. Be, and T. Shirakura\*

The design of a crotch which can absorb high power density ( $\sim 25\text{ kW/cm}^2$ ) is one of the most difficult and urgent problems in the vacuum system of the 8 GeV storage ring. We designed a new type crotch. The essential feature of our crotch is its structure, in which particles such as photo-electrons, reflected photons, and SR-induced outgasses from the crotch are efficiently trapped. Furthermore, three different pumps (see Fig. 1) provided in the crotch evacuate gas molecules before they have a chance to bounce into an electron beam chamber.

An isometric view of the crotch is shown in Fig. 1. The main body, which is made of oxygen-free copper (OFHC), consists of two rooms: one is for an electron beam passageway, which was fabricated to match a cross section of an electron beam chamber, thereby minimizing higher order mode losses. The other is for trapping particles as described above. The trapping room is isolated from the electron beam channel except the region of a slit with low conductance. An SR beam from a bending magnet enters the trapping room through the slit and strikes absorber 1 (AB1) and absorber 2 (AB2), which are also made of OFHC and inserted into the main body. Not only AB1 and AB2 on which SR beam strikes directly but also the main body is made of OFHC, because (1) SR-induced desorption is caused by photo-electrons which bounce in the space around AB1 and AB2 at random, (2) photo-electrons are produced by reflected photons besides the photons which strike AB1 and AB2 directly, and (3) OFHC has low photo-electron yield under SR irradiation and a low outgassing rate compared with other materials. Cooling is achieved by flowing water through a cooling channel in AB1 and AB2.

The SR power from the bending magnet is concentrated within a small vertical angle ( $\sim 1/\gamma$ ), thus resulting in large power densities at the surface irradiated with SR beams; here  $\gamma$  is the ratio of the electron beam energy to the electron rest-mass energy. For 8 GeV, 100 mA, and  $B = 0.6\text{ T}$ , the power and its density at the crotch are

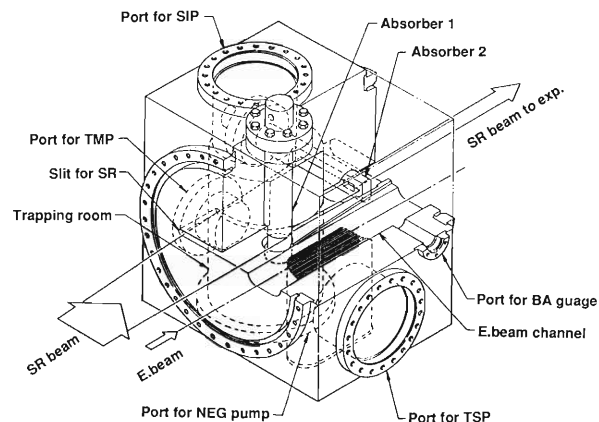


Fig. 1. Isometric view of the crotch.

Table 1. Absorbed powers and power densities at the crotch.

Area	Absorbed power (kW)	Max. power density (kW/cm <sup>2</sup> )
a) Crotch 1		
Absorber 1	1.08	21.3
Absorber 2	5.09	13.8
Total	6.17	
b) Crotch 2		
Absorber 1	1.17	25.3
Absorber 2	4.48	15.5
Total	5.65	

given in Table 1. The difference in thermal loads between crotch 1 (CR1) and crotch 2 (CR2) is due to the difference in these positions. CR1 and CR2 are located at a distance of approximately 1 m and 0.5 m from each end of the bending magnet, respectively. We chose a thermal load at CR2 as the boundary conditions for thermal analysis because it is higher than that at CR1. Two model regions as shown in Fig. 2 are considered for AB1 and AB2. We performed thermal analysis in three dimensions for AB1 and in two dimensions for AB2 because of the inherent symmetry of the thermal problem. Furthermore, the geometry of the model regions is simplified on a conservative side. Heat inputs are distributed over a strip of

\* Kobe Steel, Ltd.

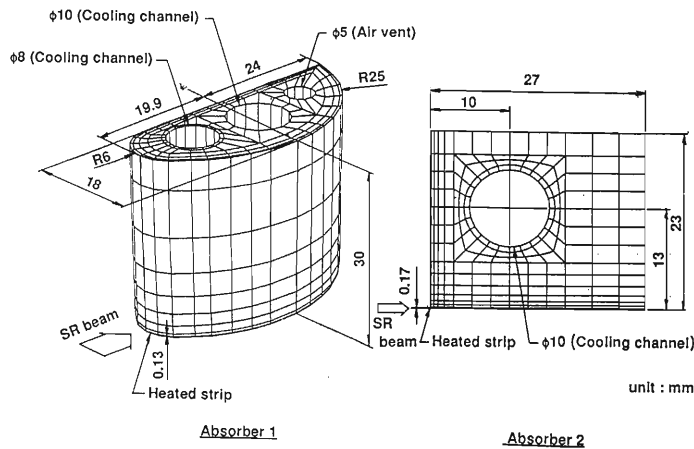


Fig. 2. Simplified heat transfer model to calculate temperature distributions.

0.13 mm in height for AB1 and 0.17 mm for AB2. Here we assume that the heat inputs are deposited just on the surface. The power densities perpendicular to the SR direction are 25.3 kW/cm<sup>2</sup> (peak power density: 52kW/cm<sup>2</sup>) for AB1 and 15.5 kW/cm<sup>2</sup> (peak power density: 32 kW/cm<sup>2</sup>) for AB2. In calculation, we assumed that heat transfer occurs only at the surfaces along which cooling-water flows, and other surfaces are insulated.

The heat flux per unit area,  $Q$ , at the water-cooled surface is given by

$$Q = h(T_w - T_c) \quad T_w < T_s \quad (1)$$

$$Q = h(T_w - T_c) + A_o^3 f_p^2 f_\xi^2 (\lambda_l^2 C_{pl} \rho_l^2$$

$$/ P_o M^2 \sigma L \rho_v) (T_w - T_s)^3$$

$$T_w > T_s \quad (2)$$

where  $h$  is the heat transfer coefficient,  $T_w$  the

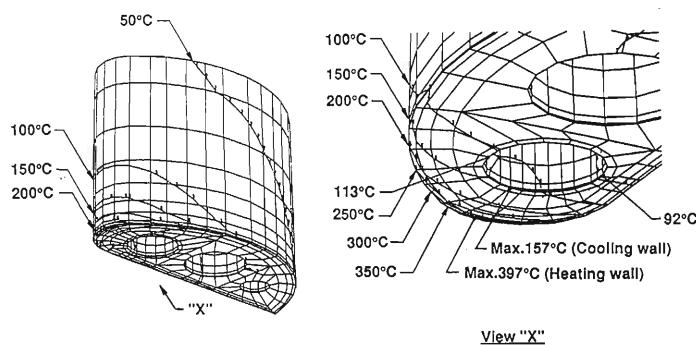


Fig. 3. Temperature distributions computed for absorber 1.

wall temperature,  $T_c$  the water temperature,  $A_o$  the coefficient decided by the boundary layer condition,  $f_p$  the pressure coefficient,  $f_\xi$  the degree of bubble,  $P_o$  and  $M$  the constant,  $\sigma$  the surface tension,  $L$  the latent heat,  $\rho_v$  the vapor density,  $\rho_l$  the liquid density,  $\lambda_l$  the liquid thermal conductivity,  $C_{pl}$  the liquid specific heat at constant pressure, and  $T_s$  the boiling point. Equation 1 for forced convection heat transfer and Eq. 2 is for fully developed nucleate boiling. The second term in Eq. 2 is given by Nishikawa and Yamagata.<sup>1)</sup> The water temperature and pressure are set to be 30°C and 4 kg/cm<sup>2</sup> absolute (boiling point is 143°C), respectively. To simulate the heat flow within the model regions, a finite

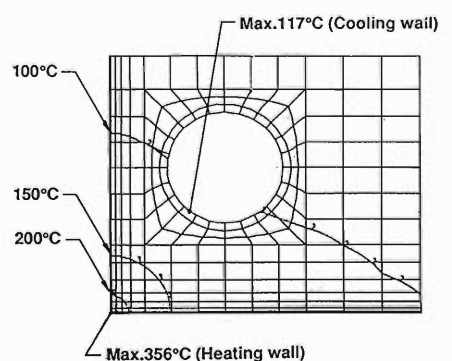


Fig. 4. Temperature distributions computed for absorber 2.

element program MARK-IBM was used, which is capable of solving the Poisson or Laplace equation in three dimensions.

Figures 3 and 4 shows the calculation results for the two model regions. The calculated maximum temperatures on the surface irradiated with an SR beam are 397°C for AB1 and 356°C for AB2. The maximum temperatures on the cooling wall are 157°C for AB1 and 117°C for AB2. These results indicate that our crotch withstands the high power density of 25.3 kW/cm<sup>2</sup>. As seen from Fig. 3, the maximum temperature on the cooling wall for AB1 shows that nucleate boiling occurs on a part of the cooling wall. The maximum temperature of 157°C on the cooling wall is less than the wall temperature of 167°C corresponding to "burn out."<sup>2,3)</sup> This means that the heat flux in the area, where uncleanate boiling is observed, does not exceed a critical value above which "burn out" occurs. If the heat flux exceeds the

critical value, the wall temperature increase rapidly because of the reduction in heat transfer. It is caused by film boiling and at worst the wall may be melted down. This is called "burn out." To avoid "burn out," we must pay much attention not to give excessive heat flux through the wall-water interface.

A prototype model of the crotch is under construction, which is scheduled to be completed by the end of March 1989. Using an electron beam as a source of thermal loads, we plan experiments to confirm our design.

#### References

- 1) K. Nishikawa and K. Yamagata: *Int. J. Heat Mass Transfer*, **1**, 219 (1960).
- 2) N. Zuber, M. Tribus and J.W. Westwater: *Int. Develop. Heat Transfer*, ASME, 230 (1961).
- 3) S.S. Kutateladze: *Zh. Tekh. Fiz.*, **20**, 1389 (1950).

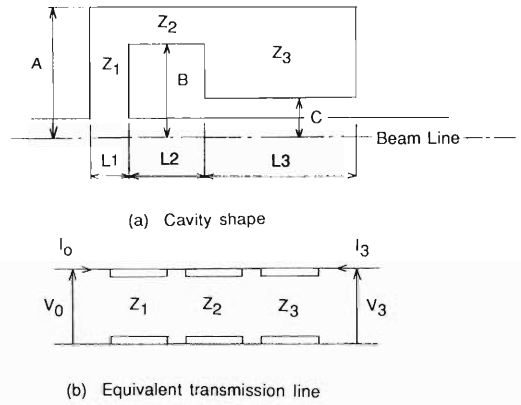
## V-2-24. Design of the Low-Frequency Cavity for the Synchrotron

T. Yoshiyuki, T. Kusaka, and M. Hara

A two-RF system is investigated for the synchrotron of the STA (Science and Technology Agency) SR facility. Acceleration in the synchrotron is performed at two different frequencies. The low-frequency system (20–50 MHz) is used to capture long macro-pulses from the 1.5 GeV linac. The RF bucket of this system is wider than 15 ns. Injected bunch is accelerated to 2.7 GeV, and then the bunch length is shortened to about 1 ns by radiation damping. The high-frequency system (508 MHz) is then turned on to accelerate the beam up to 6 GeV. This is why a two-RF system is necessary.

There is only a small space for the low-frequency cavity in the synchrotron, because it is an injection ring for the storage ring and must be designed compactly and because the 508 MHz RF system occupies large room in the RF section. The low-frequency cavity also needs a large shunt impedance because the peak RF voltage is high (250 kV). In this report, we show the design of the low-frequency cavity whose frequency is 42 MHz and find the optimum shape with a small size and a large shunt impedance.

A capacitively-loaded coaxial type of cavity as shown in Fig. 1(a) is considered for the low-frequency system. The cavity has a circular tuning plate on the high voltage end and a capacitive loading plate across the gap. In the design of this cavity, a circuit model equivalent to the cavity makes the design easy and optimizes the structure. To calculate the cavity size and the shunt impedance we can dissect the cavity into different parts.<sup>1)</sup> In the calculation of the cavity size, the cavity is divided into three parts: a gap between the tuning plate and the capacitive plate (axial length:  $L_1$ ), a part between the capacitive plate and the outer wall ( $L_2$ ), and a coaxial line ( $L_3$ ). These parts are approximated to three transmission lines whose characteristic impedances are  $Z_1$ ,  $Z_2$ , and  $Z_3$  as shown in Fig. 1(b). They are analyzed using the boundary conditions by which voltage and current are continuous at each boundary. In this resonator, the current  $I_0$  on the beam line is zero because the voltage  $V_0$  is the largest, and the voltage  $V_3$  at the shorted end is zero because of



$Z_1, Z_2, Z_3$  : Characteristic impedance

Fig. 1. Calculational geometry and equivalent transmission lines for the capacitively-loaded coaxial type of cavity.

the resonant condition. The cavity length ( $L$ ) is calculated under the condition of a fixed resonant frequency ( $f$ ):

$$L = L_1 + L_2 + L_3 = L_1 + L_2 + \frac{1}{\beta} \left( \frac{\pi}{2} - \alpha \right)$$

where  $\tan \alpha = \frac{Z_3 Q}{P}$ ,  $\beta = \frac{2\pi f}{c}$ ,  $c$  is the velocity of light.

$$P = \cos \beta A \cos \beta L_2 - \frac{Z_2}{Z_1} \sin \beta A \sin \beta L_2$$

$$Q = \frac{1}{Z_2} \cos \beta A \sin \beta L_2 + \frac{1}{Z_1} \sin \beta A \cos \beta L_2$$

In the calculation of the shunt impedance, the cavity is divided into five parts: the previous three parts in the calculation of the cavity size, short circuit on the coaxial line, and the rapid change of the cross-section of an inner conductor. The losses ( $P_{\text{loss}, i}$ ) are calculated in each part of a resonator. The shunt impedance ( $R_s$ ) is calculated from these losses.

$$R_s = \frac{V_0^2}{\sum_i P_{\text{loss}, i}}$$

The comparison of the calculation results using this model with those obtained by SUPERFISH<sup>2)</sup> is shown in Table 1. The calculations of the cavity size and the shunt impedance provide reasonable results compared with those by

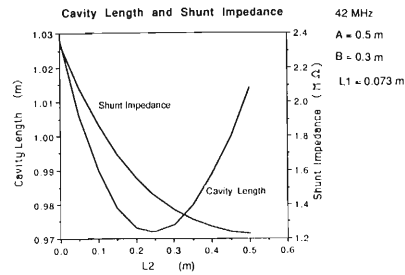


Fig. 2. Calculation results of the cavity length and the shunt impedance.

Table 1. Comparison of the calculation results obtained by a circuit model and SUPERFISH.

(a) Calculation geometries.

Case	A	B	C	L1	L2	L3	Cavity length (=L1+L2+L3)
1	0.5	0.3	0.15	0.073	0.03	0.91	1.013
2	0.5	0.3	0.15	0.073	0.24	0.65	0.963
3	0.5	0.4	0.15	0.073	0.03	0.53	0.693
4	0.4	0.3	0.15	0.073	0.32	0.56	0.953
5	0.5	0.4	0.15	0.10	0.35	0.65	1.10

(all units: m)

(b) Calculation results.

Case	Frequency (MHz)		Shunt impedance (MΩ)	
	Circuit model	SUPERFISH	Circuit model	SUPERFISH
1	42.0	41.6	2.18	2.13
2	42.0	41.6	1.47	1.66
3	42.0	41.6	1.01	1.29
4	42.0	41.8	0.625	0.890
5	42.0	40.8	1.57	1.76

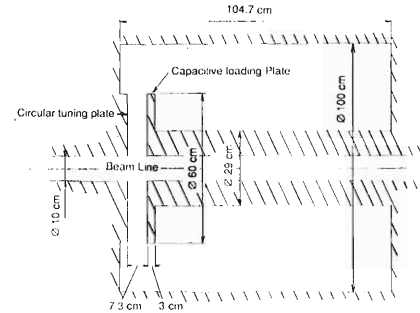


Fig. 3. Shape of the 42 MHz cavity.

SUPERFISH. The results using this model as a function of the thickness of the capacitive plate ( $L_2$ ) are also shown in Fig. 2. When  $L_2$  is 0.25 m, the total cavity length is the shortest, but a decrease in the length is about 5% at most and the shunt impedance is reduced to about 60% of the maximum. To obtain a sufficiently large shunt impedance and a reasonable size, the cavity dimensions are chosen to case 1 in Table 1 in view of the easiness to fabricate and the cooling of the capacitive plate. The shape of the cavity is shown in Fig. 3.

In conclusion, a circuit model shows a good approximation for the cavity design. The low-frequency cavity for the synchrotron is designed with a reasonable size and a large shunt impedance by using this model.

#### References

- W. Ebeling, H. Gerke, H. Hartwig, M. Nagl, H.P. Scholz, M. Sommerfeld, and A. Zolfaghari: DESY M-79/28, Dec. (1979).
- K. Halbach and R.F. Holsinger: *Part. Accel.*, 7, 213 (1976).

## V-2-25. Conceptual Design of Linac for the RIKEN SR

K. Yamasu, H. Miyade, and M. Hara

The RIKEN SR ring uses an injector linac system for acceleration of electrons or positrons up to 1.5 GeV. This injector system consists of three parts<sup>1)</sup>:

1) Electron part: Electrons generated by an electron gun at a current of 100 mA are bunched through a bunching system. They are accelerated up to 250 MeV in the electron linac.

2) Positron part: Electrons of their peak current of 5A are accelerated up to 200 MeV and hit a positron converter. Generated positrons are then accelerated up to 250 MeV in a positron linac.

3) Common part: Electrons or positrons accelerated up to 250 MeV are then injected into a common linac and accelerated up to 1.5 MeV.

Design parameters of this injector are summarized in Table 1.

Because many breakdowns are expected to occur in such a complex system, we hope to reduce the number of klystrons and accelerating structures to simplify a high power RF circuit.

To optimize an accelerating unit, we calculate an average accelerating field. The loaded field gradient  $E(z)$  of a constant gradient (C.G.) section is expressed by the symbols listed in Table 1.<sup>3)</sup>

$$E(z) = \sqrt{\frac{r_0 P_0}{L}} \sqrt{1 - e^{-2\tau}} + \frac{i r_0}{2} \ln \left( 1 - (1 - e^{-2\tau}) \frac{z}{L} \right)$$

where  $z$  is the distance along the structure.

If we use a long structure to accelerate a beam, the attenuation constant becomes large and we must reduce the diameter of an exit iris, called  $2a$  in general, to keep the field gradient constant. In this investigation we suppose that the shunt-impedance and the merit of  $Q$  is constant and the exit ' $2a$ ' is 20 mm $\phi$  for the beam size.

Figure 1 shows the dependence of the average field gradient on the C.G. structure length when the input power to a structure is changed and the peak beam current is 100 mA.

The high power RF (radio frequency) source generates a high field gradient. The most powerful pulsed klystron available today provides 35-MW output at peak. Because power loss in the

Table 1. Linac parameters.

General			
Energy	$i$	1.5	GeV
Beam current		$i$	
e mode		100	mA
e <sup>+</sup> mode		10	mA
Repetition rate		50	pps
Pulse length		15	ns
Regular section			
Frequency	$f$	2.856	GHz
Accelerating mode		Travelling wave, $2/3\pi$	
Structure type		Disk loaded	
Structure length	$L$	2.836	m
No. of cells		81	
Attenuation	$\tau$	0.427	Np
Shunt impedance	$r_0$	54.0	MΩ/m
Filling time	$t_f$	0.628	μs
Merit of $Q$	$Q$	13,200	
Range of iris diameter	$2a$	26.00~20.00	mm $\phi$
Group velocity	$v_g/c$	0.022~0.009	
Field gradient (100 mA)		17.38	MV/m
No. of structures		31	
Effective length		86.31	m
Klystron			
Peak power (effective)	$P_0$	30	MW
Pulse width		6.0	μs
Duty factor		0.04	%
Efficiency (max.)		44.0	%
Gain (max.)		47	dB
No. of klystrons		31	

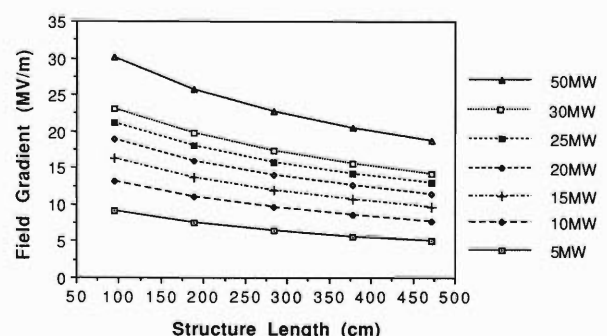


Fig. 1. Dependence of average field gradient on the structure length (100 mA loaded) in the C.G. structure.

high-power RF circuit is about 5 MW, and RF power of 30 MW is supplied to an accelerating structure.

We chose a 3-m long accelerator structure driven by a 30-MW klystron as a unit structure, in which the field gradient is about 18 MV/m. The beam is accelerated up to 1.5 GeV by the linac which has 31 klystrons and 31 structures, and the effective length of the linac is 86.3 m.

The field gradient in this unit is shown Fig. 2. Since we cannot calculate the loaded field gradient of a quasiconstant gradient (Q.C.G.) section analytically, we must calculate it by a numerical

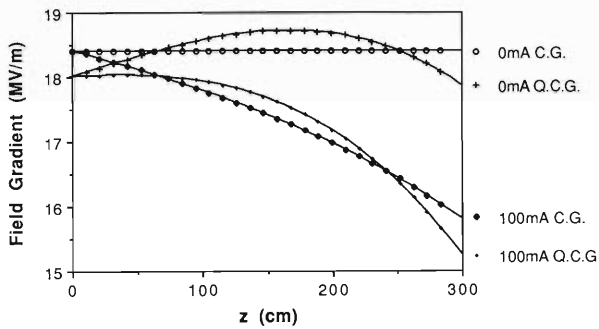


Fig. 2. Field gradient along the structure.

analysis method using a computer.

It is required that a beam at the exit of this injector is stable and its energy spread is small. A bunching system is the most important system to decide the beam characteristics. Figure 3 shows the trajectory of the bunching beam in our buncher. It is clear that electrons distributed in the phase of  $140^\circ$  to  $-170^\circ$  are bunched.<sup>3)</sup> In acceleration of a pulsed beam, the accelerating voltage in a linac decreases with time in a transient period which corresponds to a filling time of the beam pulse after the injection of the front of it. This causes an additional energy spread of the beam. The energy gain,  $V(t)$  for electrons coming  $t$  s after the pulse front is given by the following equation;<sup>2)</sup>

$$V(t) = \sqrt{r_0 P_0 L} \sqrt{1 - e^{-2\tau}} - \frac{i r_0 L}{2} (1 - e^{-2\tau}) + \frac{i r_0 L}{2} \frac{\omega t}{Q} e^{-2\tau} + e^{-\frac{\omega t}{Q}}$$

where  $\omega$  is the phase frequency.

Energy gain per one structure in the transient state is calculated from this equation. Figure 4 shows the result in a short time scale and Fig. 5 in a long time scale. When the width of the pulsed beam is shorter enough than the structure's filling time, it is clear that the rate of the energy spread is 0.3%/15 ns at 100 mA and, therefore,

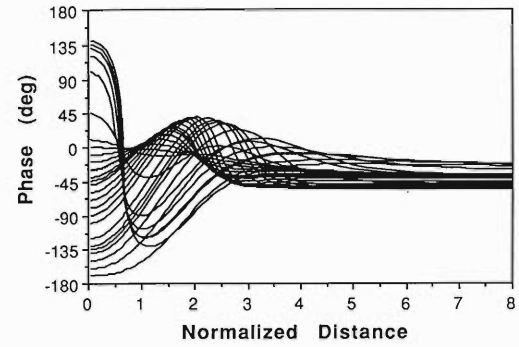


Fig. 3. Phase orbits through the our bunching system.

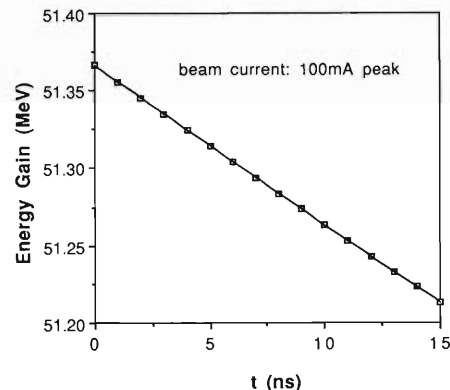


Fig. 4. Transient energy gain per one structure in short time scale.

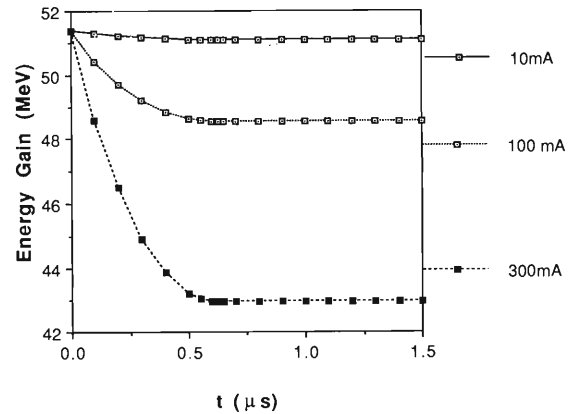


Fig. 5. Transient energy gain per one structure in long time scale.

the beam energy gain is nearly equal to the 'unloaded' beam energy gain.

## References

- 1) H. Miyade, K. Yoshida, K. Tsumaki, and M. Hara: *RIKEN Accel. Prog. Rep.*, **21**, 233 (1987).
- 2) P.B. Neal: *M.L. Rep.*, No. 388 (1957).
- 3) J.M. Ponce de Leon and E.L. Ginzton: *M.L. Rep.*, No. 265 (1955).

## V-2-26. Positron Injection System for RIKEN SR

H. Miyade, K. Yamasu, and M. Hara

In the RIKEN SR the requirements for the positron injection system are:

- 1) Energy of injection into a booster synchrotron is 1.5 GeV and its energy spread is less than 0.5%;
- 2) Efficiency of conversion from electron to positrons greater than about 0.5%; and
- 3) Emittance is less than 2.6 mm·mrad at 1.5 GeV.

On the basis of these requirements, a positron injection system was studied on the structure shown in Fig. 1. The system has two solenoid magnets; one is between a target and an accelerating section, and the other is around the accelerating section. The magnetic fields are 1.2 T and 0.2 T respectively,<sup>1)</sup> and the field distributions are assumed to be rectangular shaped. The electric field in the accelerating section is 16.66 MV/m.<sup>2)</sup> The iris diameter is 20 mm.<sup>2)</sup> The distance between the target and the first solenoid ( $l_1$ ) is set

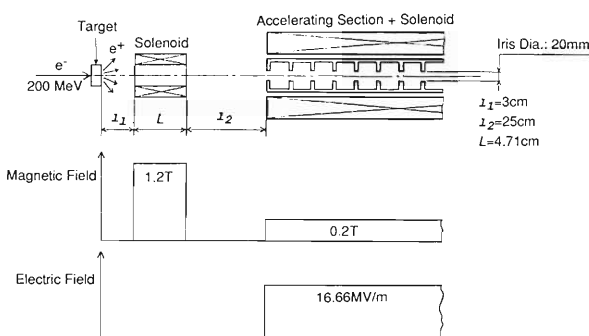


Fig. 1. Structure of the positron injection system.

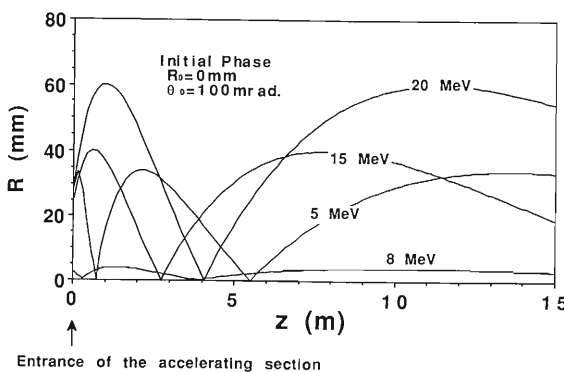


Fig. 2. Positron orbits in the accelerating section.

to 3 cm and that between the first and the second solenoid ( $l_2$ ) is set to 25 cm tentatively,<sup>1)</sup> but they will be optimized later. The length of the first solenoid ( $L$ ) is chosen so that the acceptance is maximum for the positron at an emission energy of 8 MeV. When  $l_1=3$  cm and  $l_2=25$  cm,  $L$  is 4.71 cm.

Positrons emitted from the center of a target with an emission angle of 100 mrad are in the orbits as shown in Fig. 2. When the maximum deviation from the central axis is greater than the iris radius of 10 mm, the positron cannot pass through the accelerating section. Figure 3 shows the energy dependence of the maximum emission angle of the positron which can pass through the accelerating section. For a positron with an emission energy of 8 MeV, the maximum emission angle is 256 mrad and the acceptance, which is defined as a solid angle, is 0.205 sr.

The acceptance of the positron emitted at the position apart from the target center is less than that at the center. Figure 4 shows the relation between the acceptance and the distance from

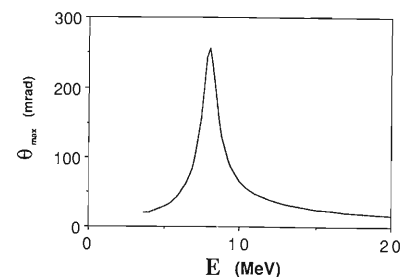


Fig. 3. Energy dependence of the maximum emission angle.

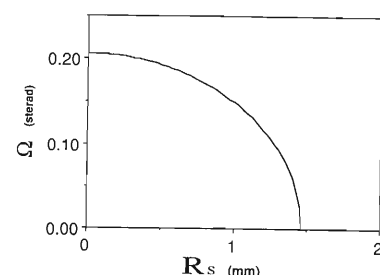


Fig. 4. Dependence of the acceptance on the emitting position.

the target center to the position where the positrons are emitted. The acceptance is 0 at the distance of 1.46 mm from the center, *i.e.*, a positron emitted from the position apart more than 1.46 mm from the target center cannot pass through the accelerating section.

When an electron with an energy of  $E^-$  (MeV) impinges the target, the number of positrons emitted from the target in a unit solid angle with energies between  $E^+$  (MeV) and  $E^+ + dE^+$  (MeV) is expressed by

$$NdE^+ = 2 \times 10^{-4} E^- \exp(-\theta/0.35) dE^+ / (1/\text{sr})$$

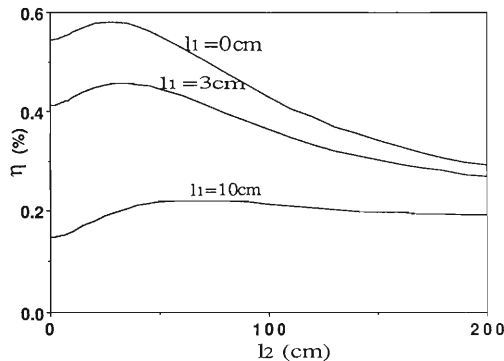


Fig. 5. Dependence of the conversion efficiency on  $l_2$ .

where  $\theta$  is the emission angle.<sup>4)</sup> When the emission energy range of the accepted positrons is  $8 \pm 1.5$  MeV<sup>3)</sup> and the energy of the impinging electrons is 200 MeV, we obtain the conversion efficiency of 0.45%.

For a positron with an emission energy of 8 MeV, the emittance on the target is

$$1.46 \text{ mm} \times 256 \text{ mrad} = 374 \text{ mm} \cdot \text{mrad}$$

Upon acceleration up to 1.5 GeV it becomes

$$374 \text{ mm} \cdot \text{mrad} \times 8 \text{ MeV} / 1.5 \text{ GeV}$$

$$= 2.0 \text{ mm} \cdot \text{mrad}$$

Furthermore, assuming a dilution factor of 12%,<sup>3)</sup> we obtain the emittance of  $2.0 \text{ mm} \cdot \text{mrad} \times 1.12 = 2.2 \text{ mm} \cdot \text{mrad}$ .

Finally, we mention the optimization of  $l_1$  and  $l_2$ . For  $l_1$  it is clear that the smaller  $l_1$  makes the acceptance greater, *i.e.*, the optimized value of  $l_1$  is 0. Figure 5 shows the dependence of the conversion efficiency on  $l_2$ . When  $l_1$  is 0–3 cm, the optimized value of  $l_2$  is 25–40 cm.

## References

- 1) R. Chehab, S. Fukuda, and A. Asami: KEK preprint, 87-169, Mar. (1988).
- 2) K. Yamasu, H. Miyade, and M. Hara: Proc. 13th Linear Accelerator Meeting in Japan, p. 236 (1988).
- 3) Conceptual Design Report, ANL-87-15, Apr. (1987).
- 4) J. Haissinski: *Nucl. Instrum. Methods*, **51**, 181 (1967).

## VI. RADIATION MONITORING

### 1. Routine Monitoring of the Cyclotron, RILAC, and TANDETRON

I. Sakamoto, S. Fujita, M. Yanokura, T. Kobayashi,  
 O. Kurihara, T. Katou, M. Miyagawa, S. Kagaya,  
 S. Shinohara, M. Iwamoto, and I. Kohno

The present report describes the results of routine radiation monitoring carried out for the cyclotron, RILAC, and TANDETRON from January to December 1988.

Aspects of the leakage radiation from the cyclotron are described in a succeeding report.<sup>11</sup>

#### (1) Residual activities of the cyclotron

In August 1988, the dose rates due to residual activities of the machine were measured 19 days after the scheduled shutdown; the maximum irradiation dose rates measured was 10 mR/h at 50 cm apart from a septum. No external exposure doses were detected for two workers during replacement of the septum.

#### (2) Contamination in the cyclotron building

The surface contamination has been kept below  $10^{-5} \mu\text{Ci}/\text{cm}^2$  on the floors of the cyclotron building. The radioactive nuclides found by

$\gamma$ -ray spectrometry were  $^{183}\text{Re}$  and  $^{65}\text{Zn}$  in the cyclotron vault, and  $^{137}\text{Cs}$  in the waste-storage room. The contamination was wiped off twice a year. Immediately after this decontamination, the activities on the floor of most of the above places were reduced below  $10^{-7} \mu\text{Ci}/\text{cm}^2$ .

When radioactive substances were handled in the hot laboratory and chemical laboratories, the air in a draft chamber was activated. The air in the draft chamber was exhausted; and the radioactivity in the exit was found to be  $10^{-13} \mu\text{Ci}/\text{cm}^3$ .

#### (3) Drainage

The radioactivities in drain water from the cyclotron and the linac buildings were found to be of the order of  $10^{-8}$ – $10^{-7} \mu\text{Ci}/\text{cm}^3$ . The total activity in aqueous effluents was  $1.2 \mu\text{Ci}$ , in which the main radioactive nuclide was  $^{137}\text{Cs}$ , the

Table 1. Annual external exposure doses received by RIKEN accelerator workers from January to December 1988.

Workers	Dose undetectable	Number of persons			Collective dose (mrem)
		10–100 (mrem)	>100 (mrem)	Total	
Ring cyclotron operation and maintenance groups	8	0	0	8	0
Cyclotron operation and maintenance groups	7	2	0	9	30
Linac operation and maintenance groups	8	0	0	8	0
Nuclear physicists	59	3	0	62	30
Accelerator physicists	19	1	1	21	180
Physicists in other fields	54	2	0	56	40
Nuclear chemists	20	13	0	33	570
Radiation chemists	4	0	0	4	0
Biological chemists	14	0	0	14	0
TANDETRON workers	13	0	0	13	0
Health physicists	6	0	0	6	0
Total	212	21	1	234	850

Average annual dose per person, 3.6 mrem; Maximum individual annual dose was 110 mrem.

radioactivity was  $0.4 \mu\text{Ci}$ , and the other nuclides found by  $\gamma$ -ray spectrometry were  $^{71}\text{As}$  and  $^{57}\text{Co}$ .

(4) Radiation monitoring for RILAC and TANDETRON

The leakage radiation during operation of RILAC was measured outside the linac building every three months. No leakage of  $\gamma$  rays and neutrons from the linac building was detected. No contamination due to residual activities was found on the floor of control area and conditioning air in the linac building.

X-ray monitoring was carried out for TANDETRON, when a copper target was bombarded with 1.6 MeV  $\text{H}^+$  ions of 0.1 nA, the maximum irradiation dose rates measured around TANDETRON was 0.2 mR/h. No leakage X-rays were detected around the target chamber and outside the TANDETRON room.

(5) Personnel monitoring

The number of RIKEN accelerator workers increased to 2 times of that in the preceding period.

The external exposure dose for personnel were measured by using  $\gamma$  ray and neutron film badges. The dose received by accelerator workers from January to December 1988 are shown in Table 1. The collective  $\gamma$ -ray doses to all workers was 850 man-mrem. The collective dose owing to thermal and fast neutron exposures was below the detection limit. Because nuclear chemists began experiments in the hot laboratory in February, the collective dose for the workers in this period increased to 4.7 times of the value in the preceding period.

Reference

- 1) I. Sakamoto, S. Fujita, and I. Kohno: This Report, p. 303.

## VI-2. Leakage-Radiation Measurements in the Cyclotron Building

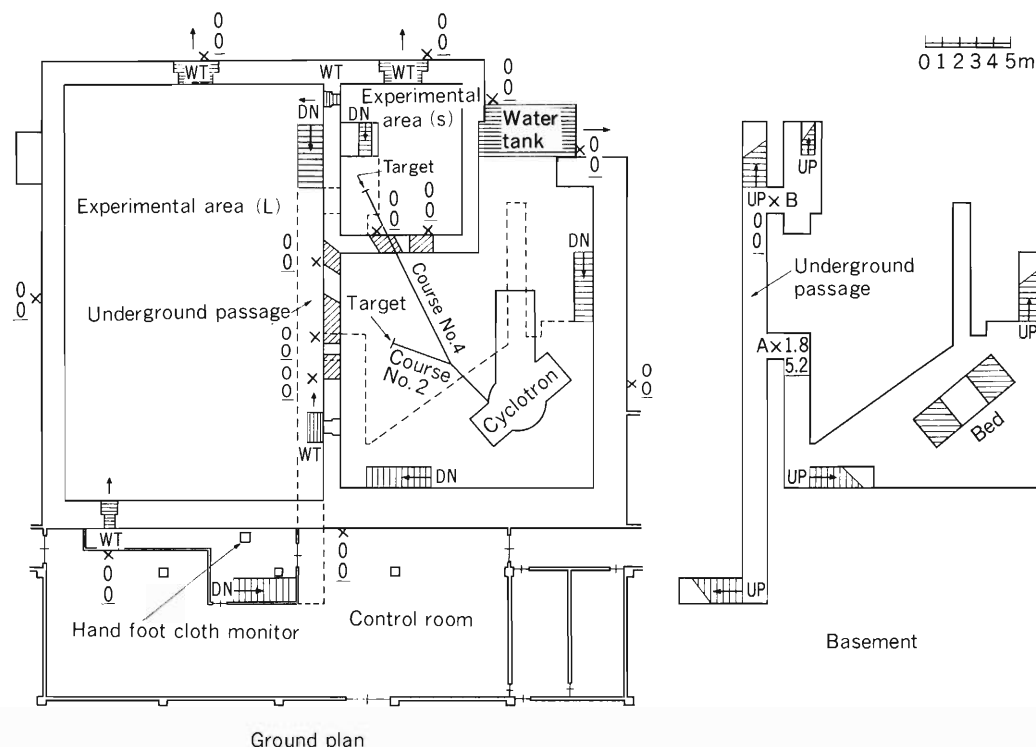
I. Sakamoto, S. Fujita, and I. Kohno

Leakage radiation was measured at various points in the cyclotron building in July 1988, when a target placed on the beam line No. 2 was bombarded with 40-MeV helium ions at a beam intensity of 2  $\mu$ A.

$\gamma$ -Ray dose rates were measured with an ionization chamber survey meter, and dose-equivalent rates for fast and slow neutrons were measured with a "rem counter."\* The results are shown in Fig. 1.

The leakage doses measured during January and December 1988 with  $\gamma$ -ray and neutron film badges placed at two positions (point A and B in Fig. 1) on the underground passage are shown in Table 1.

Of the dose values at point B measured every month, the maximum total dose of 1,300 mrem was observed in November, when the values for  $\gamma$ -rays, and thermal and fast neutrons were 290, 30, and 980 mrem, respectively.



Operating conditions		Dose unit
$E\alpha$	: 40 MeV	$\gamma$ ray: mR/h
Beam line	: No. 2	Neutron: mrem/h (underlined value)
Target	: Ir	

Fig. 1. Leakage-radiations (neutrons and  $\gamma$  rays) in the cyclotron building.

\* A Neutron Rem Counter NSN1 manufactured by Fuji Electric Co., Ltd. Japan.

Table 1. Leakage-radiation doses (in mrem) on the underground passage of the cyclotron building during January and December 1988.

Month	Point A*				Point B*			
	$\gamma$ rays (mrem)	Thermal neutrons (mrem)	Fast neutrons (mrem)	Total (mrem)	$\gamma$ rays (mrem)	Thermal neutrons (mrem)	Fast neutrons (mrem)	Total (mrem)
1.88'	310	10	10	330	0	0	0	0
2	50	10	30	90	0	0	0	0
3	320	10	60	390	0	0	10	10
4	350	10	40	400	0	0	20	20
5	280	20	100	400	0	0	10	10
6	50	0	30	80	0	0	0	0
7	490	20	70	580	0	0	10	10
8	0	0	0	0	0	0	0	0
9	40	0	20	60	0	0	0	0
10	320	30	70	420	0	0	0	0
11	20	0	0	20	290	30	980	1,300
12	270	20	40	330	0	0	0	0
Total	2,500	130	470	3,100	290	30	1,030	1,350

\* See Fig. 1.

The high fast-neutron doses observed at point A in May, June, and October and at point B in November were 100, 70, 70, and 980 mrem, respectively. The increase in the neutron dose at point B was due to high intensity irradiation in the beam line No. 4 which was bombarded with 22-MeV helium ions at a beam intensity of 250

nA; the beam intensity cyclotron users frequently use on this beam line was 7-8 nA. At point A, the high fast-neutron doses were due mainly to activation analysis and radioisotope production carried out on the beam line No. 2 during these periods.

### VI-3. Shielding Calculation for the Facility of RIKEN Ring Cyclotron Using RILAC as an Injector

T. Shikata, N. Nakanishi, T. Kosako, and H. Kamitsubo

Since December 1986, RIKEN Ring Cyclotron has been operated with a linear accelerator for heavy ions, RILAC, as an injector. This report describes a calculation of the shielding design for this coupled operation.

Neutrons emitted by  $^{12}\text{C}$  (75 MeV/u,  $6 \times 10^{12}$  pps) on a thick  $^{56}\text{Fe}$  target was chosen as a source for the shielding calculation. The energy spectrum is given in Refs. 1 and 2. This energy of carbon ions is slightly higher than the utmost energy in the coupled operation. A one-dimensional discrete ordinate code ANISN-JR<sup>3</sup> was used in the calculation.

Shielding is executed by an iron-concrete berm-dump combined with a concrete wall. The dose rate at the distance  $L$  from a point source can be

obtained by multiplying the dose rate for the normal incidence on a iron-concrete double layer slab by  $1/L^2$  (calculation by a slab model); the results are shown in Fig. 1. These charts were made for designing neutron shielding. The summed thickness of the concrete part of a beam dump and a wall is taken as the abscissa and the dose rate at  $L$  multiplied by  $L^2$  is taken as the ordinate. Using this chart, we can estimate the thickness of a concrete part and an iron part to suppress the dose rate below an allowable level, with an arbitrary thickness ratio. When a source is surrounded with a shield, the calculation by a slab model using ANISN does not give a correct result. For instance, considering isotropic neutron sources which have an energy distribution

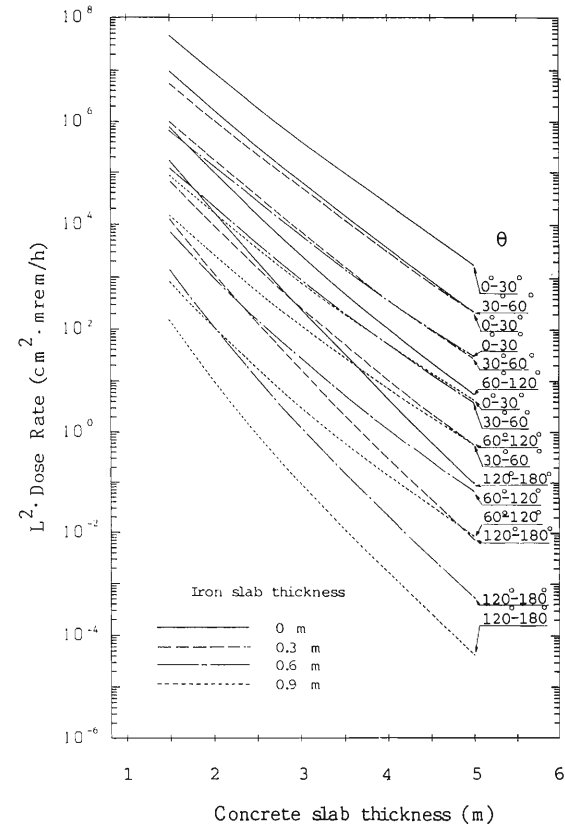
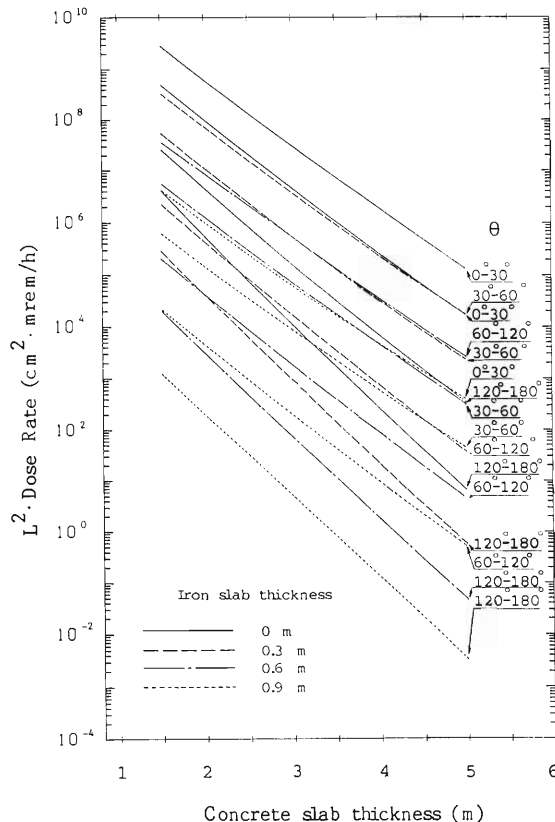


Fig. 1. (a) Neutron dose rates for a point source outside the concrete wall.  $L$  is the distance from the source and  $\theta$  is a specified angular interval. (b) Photon dose rates for a point source outside the concrete wall.

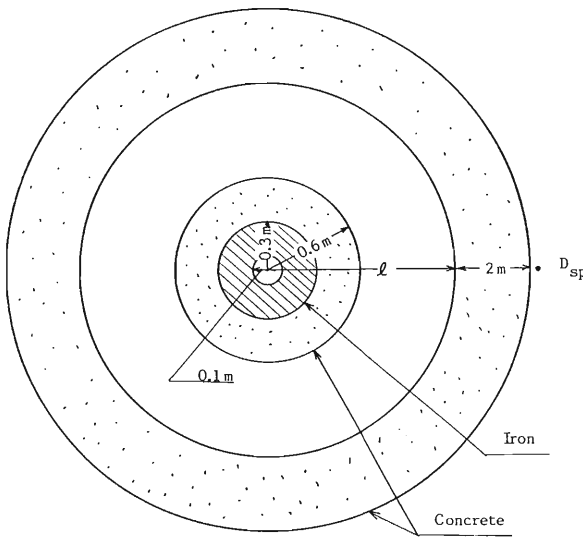


Fig. 2. Concentric spherical shell.

of neutrons ejecting into angular ranges  $0^\circ$ - $30^\circ$ ,  $30^\circ$ - $60^\circ$ ,  $60^\circ$ - $120^\circ$ , and  $120^\circ$ - $180^\circ$ , we carried out following calculation. We considered a spherical shell of an inner radius of  $l$ , which has a beam dump composed of a vacancy of 10 cm in radius, an iron shell of 20 cm in thickness, and a concrete shell of 30 cm in thickness at the center, as illustrated in Fig. 2. The calculated neutron dose rate outside the shell,  $D_{sp}$ , which can be obtained exactly by using ANISN-JR, was compared with that obtained from the slab model described above,  $D_{sl}$ . A similar calculation was also carried out for a monochromatic neutron sources. Neutron dose rates outside the shell were denoted as  $D_{sp}'$  and  $D_{sl}'$ , corresponding to the dose rates for the spherical system and from the slab model, respectively. The ratios,  $D_{sp}/D_{sl}$  and  $D_{sp}'/D_{sl}'$ , are shown in Fig. 3. In this shielding system, the dose rate obtained from the slab model are underestimated, especially for low-energy neutrons. Thus, in general, the dose rate calculated by means of the slab model must be multiplied by a proper factor, which cannot always be obtained correctly and has to be determined by a physical consideration suited to each shielding system.

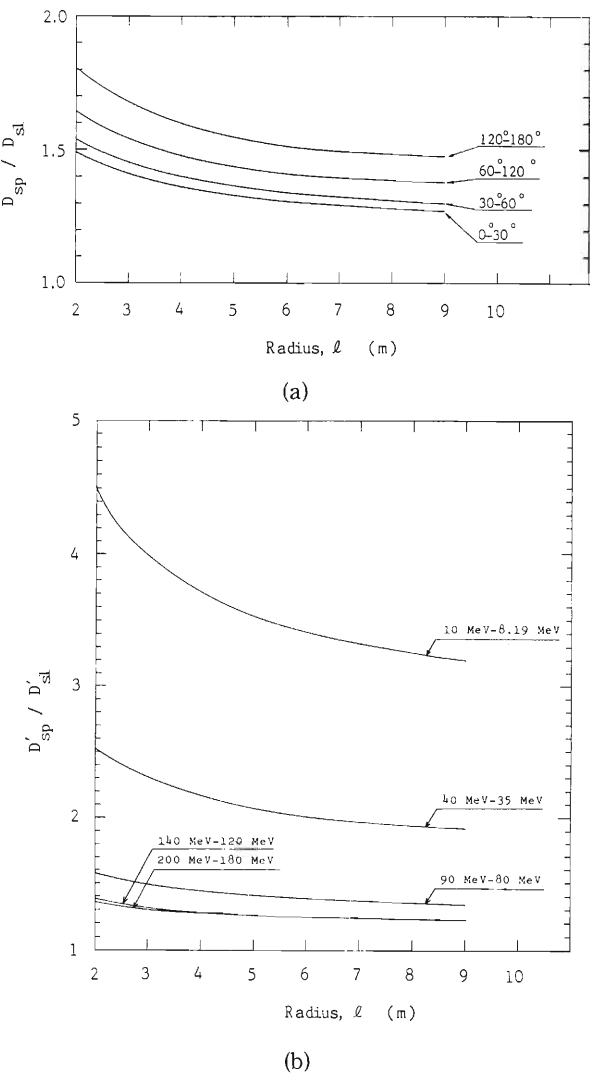


Fig. 3. (a)  $D_{sp}/D_{sl}$ .  $D_{sp}$  stands for the neutron dose rate outside a concrete shell of 2 m in thickness, which encloses a beam dump composed of a vacancy of 10 cm in radius, an iron shell of 20 cm in thickness, and a concrete shell of 30 cm in thickness.  $D_{sl}$  stands for the neutron dose rate at the same point calculated by means of the slab model. (b)  $D_{sp}'/D_{sl}'$ .  $D_{sp}'$  and  $D_{sl}'$  have similar meanings as  $D_{sp}$  and  $D_{sl}$ , respectively, for monochromatic neutron source.

#### References

- 1) T.A. Gabriel, R.T. Santro, H.W. Bertini, and N.M. Larson: ORNL-TM-4334 (1973).
- 2) T. Nakamura: INS-NUMA-5 (1977).
- 3) K. Koyama, Y. Taji, K. Minami, T. Tsutsui, T. Ideta, and S. Miyasaka: JAERI-M 6954 (1977).

## VI-4. Radiation Monitoring in RIKEN Ring Cyclotron Facility

S. Fujita, I. Sakamoto, T. Inamura, and H. Kamitsubo

The Radiation Safety Control System (RSCS) worked steadily from January to December 1988, performing radiation monitoring continuously and automatically.

Additional beam lines became available for experiments in the experimental vaults D, E2, E3, and E7. Figure 1 shows the indoor monitoring positions and the beam lines in the RIKEN Ring Cyclotron facility.

On November 24-29, an experiment was carried out with a  $^{14}\text{N}$  beam of 42 MeV/u, the highest energy used this year, in an experimental vault E7. Figure 2 shows the daily variations in dose rates during this experiment recorded on: (a) an ionization chamber in the RIKEN Ring Cyclotron vault; (b) an ionization chamber in an

experimental vault E7; (c) an ionization chamber in the AVF Cyclotron vault; (d) a  $\text{BF}_3$  counter in an experimental vault E7; and (e) a  $\text{BF}_3$  counter in the AVF Cyclotron vault. Slight leakage neutrons were recorded in the AVF vault (Fig. 2(e)), but no leakage gamma rays were detected (Fig. 2(c)). No leakage gamma rays and no neutrons from RIKEN Ring Cyclotron and E1, D, E2, E3, and E7 vaults were detected by environmental monitors.

Here we shall present a typical example of residual activities measured in the facility. Strongest residual activities were detected on the beam lines. Table 1 summarizes dose rates on the beam lines, measured with a NaI-scintillation survey meter and an ionization-chamber survey meter.

On December 14-16, 11 days after the experiment performed with a  $^{14}\text{N}$  beam of 42 MeV/u, the dose rates due to residual activities of RIKEN Ring Cyclotron were measured with an ionization-chamber survey meter. The results

Table 1. Summary of residual activities measured along the beam lines. Alphabets indicate detection points. (See Fig. 1.)

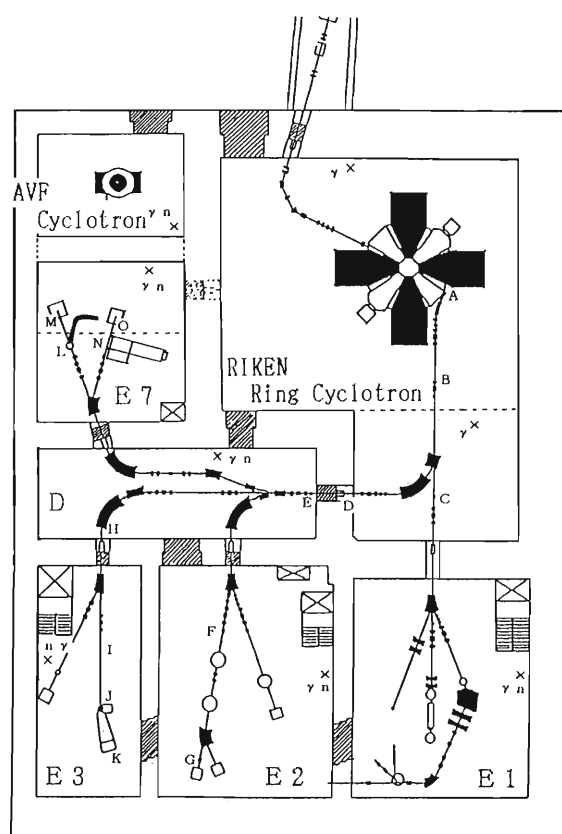


Fig. 1. Layout of RIKEN Ring Cyclotron facility as of 1988. Monitoring positions are denoted by  $\times$ . Residual-activity detection points on the beam lines are denoted by alphabets.

Detection point	NaI <sup>3</sup> <sub>131</sub> scintillation survey meter (mR/h)	Ionization-chamber survey meter (mR/h)	Date
A	—	1.7	Nov. 19
B	—	3.0	Nov. 19
C	1.5	—	Aug. 1
D	0.03	—	Dec. 5
E	0.4	—	Dec. 5
F	0.01	—	Aug. 1
G	0.3	—	Nov. 19
H	0.25	—	Dec. 5
I	0.25	—	Dec. 5
J	0.15	—	Dec. 5
K	0.6	—	Dec. 5
L	0.05	—	Nov. 7
M	0.02	—	Nov. 7
N	0.4	—	Nov. 7
O	3.0	1.0	Nov. 7

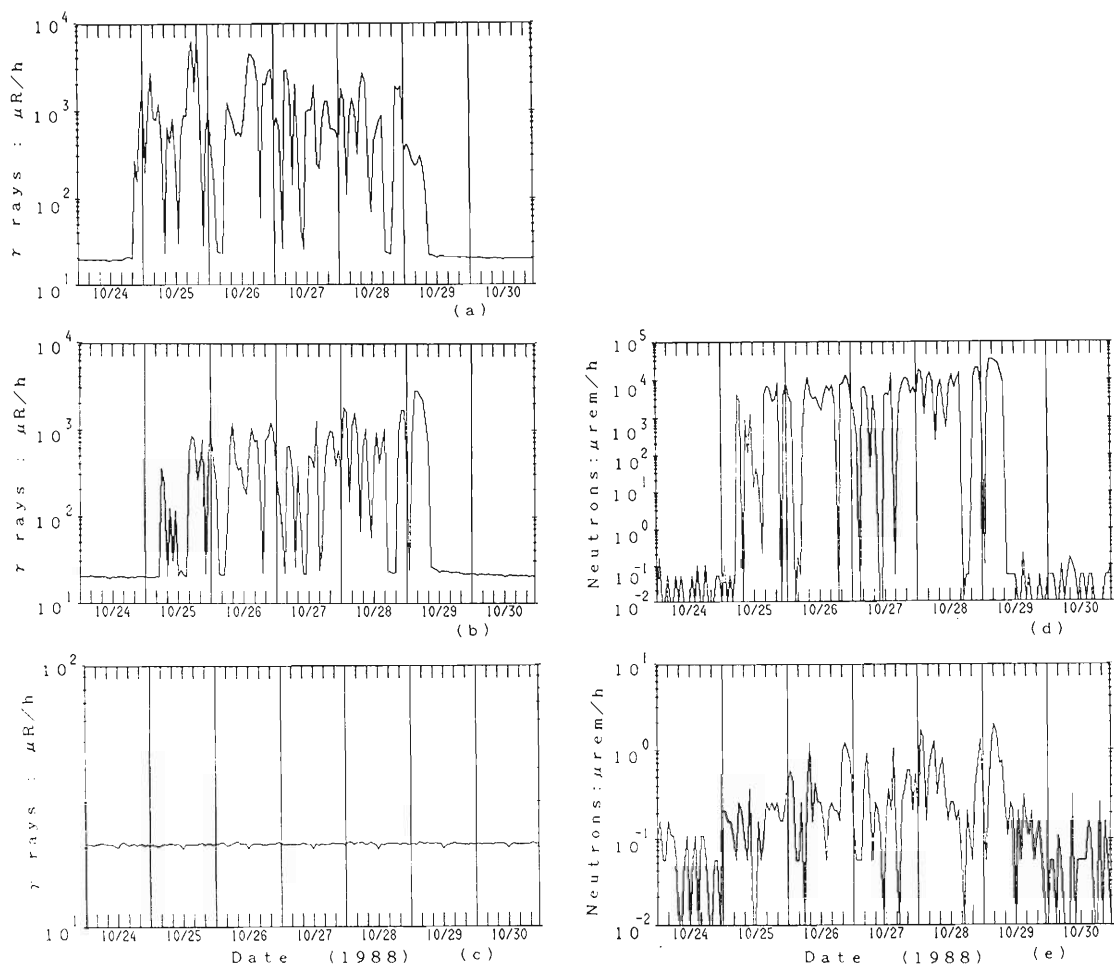
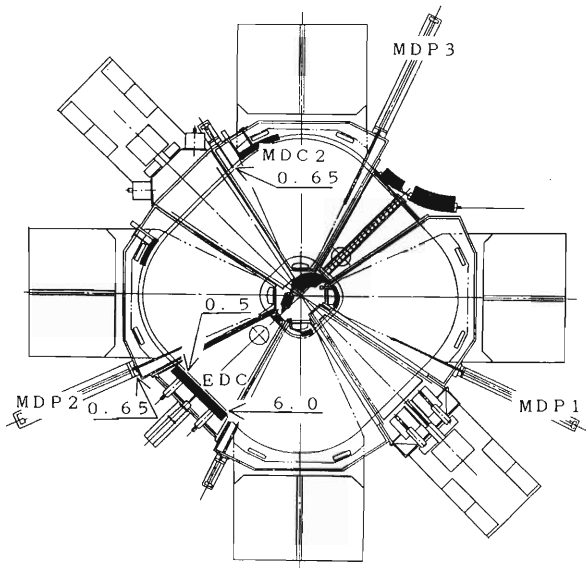


Fig. 2. Daily variations in the radiation level measured in RIKEN Ring Cyclotron facility. Detectors are (a) an ionization chamber in RIKEN Ring Cyclotron vault, (b) an ionization chamber in the experimental vault E7, (c) an ionization chamber in the AVF Cyclotron vault, (d) a  $\text{BF}_3$  counter in the experimental vault E7, and (e) a  $\text{BF}_3$  counter in the AVF Cyclotron vault.



are shown in Fig. 3, together with the detection positions. The dose rates increased about 2-10 times that of a previous report,<sup>1)</sup> depending on the positions. The maximum dose rate was found to be 6.0 mR/h at EDC, an electrostatic deflection

Fig. 3. Detection points around RIKEN Ring Cyclotron. EDC, an electrostatic deflection channel; MDC2, a magnetic deflection channel; MDP1, a main differential probe 1; MDP2, a main differential probe 2; MDP3, a main differential probe 3. Figures indicated are dose rates in units of mR/h.

channel of the beam extraction region.

#### Reference

- 1) S. Fujita, I. Sakamoto, T. Inamura, and H. Kamitsubo: *RIKEN Accel. Prog. Rep.*, **21**, 258 (1987).

## VII. LIST OF PUBLICATIONS

1. Accelerator development and accelerator physics
  - 1) S.H. Be, Y. Morimoto, H. Sakamoto, and S. Yokouchi: "Conceptual Design of the Vacuum System for the 6 GeV Storage Ring," American Vacuum Society Series 5, Upton, N. Y., p. 7 (1988).
  - 2) Y. Morimoto, H. Sakamoto, S. Yokouchi, and S.H. Be: "Conceptual Design and Thermal Analysis of the Crotch at the 6 GeV Storage Ring," American Vacuum Society Series 5, Upton, N. Y., p. 327 (1988).
  - 3) S.H. Be, S. Nakajima, K. Ikegami, N. Ohsako, K. Morimoto, T. Kikuchi, and S. Morishita: "New Cryopumps for a Resonator of the RIKEN Ring Cyclotron," *Vacuum*, **38**, 543 (1988).
  - 4) Y. Yano: "Initial Operation of RIKEN Ring Cyclotron," Proc. 3rd Jpn.-Chin. Jt. Symp. Accelerators for Nuclear Science and Their Applications, Wako, Nov. 1987, p. 6 (1988).
2. Nuclear physics and nuclear instrumentation
  - 1) S. Yamaji, H. Hofmann, and R. Samhammer: "Self-Consistent Transport Coefficients for Average Collective Motion at Moderately High Temperatures," *Nucl. Phys.*, **A475**, 487 (1988).
  - 2) S. Kato and 16 others including T. Suzuki: "Neutrino Mass Studied by Measuring Tritium Beta-Decay with an Iron-Free Beta-Ray Spectrometer," *Nucl. Phys.*, **A478**, 433 (1988).
  - 3) I. Tanihata: "Nuclear Structure Studies Using High-Energy Radioactive Beams," *Nucl. Phys.*, **A478**, 795c (1988).
  - 4) T. Motobayashi, S. Satoh, H. Murakami, H. Sakai, N. Matsuoka, T. Saito, T. Noro, K. Hosono, A. Okihana, M. Ishihara, H. Okamura, and A. Hatori: "Tensor Analyzing Power Measurement of  $^1\text{H}(\text{d}, ^2\text{He})\text{n}$  Reaction at 70 MeV," *Nucl. Phys.*, **A481**, 207 (1988).
  - 5) K. Asahi, M. Ishihara, T. Ichihara, M. Fukuda, T. Kubo, Y. Gono, A.C. Mueller, R. Anne, D. Bazin, D. Guillemaud-Mueller, R. Bimbot, W.-D. Schmidt-Ott, and J. Kasagi: "Production of Spin-Aligned Unstable Nuclei in the Projectile Fragmentation at Intermediate Energies," *Nucl. Phys.*, **A488**, 83c (1988).
  - 6) I. Tanihata: "Nuclear Studies with Secondary Radioactive Beams," *Nucl. Phys.*, **A488**, 113c (1988).
  - 7) H. Kawakami and 20 others including T. Suzuki: "Study of Energy Loss of 18 keV  $\beta$ -Rays in a Langmuir-Blodgett Thin Film," *Nucl. Instrum. Methods Phys. Res. A*, **264**, 511 (1988).
  - 8) T. Doke, H.J. Crawford, A. Hitachi, J. Kikuchi, P.J. Lindstrom, K. Masuda, E. Shibamura, and T. Takahashi: "LET Dependence of Scintillation Yields in Liquid Argon," *Nucl. Instrum. Methods Phys. Res. A*, **269**, 291 (1988).
  - 9) T. Motobayashi, S. Satoh, H. Murakami, H. Sakai, and M. Ishihara: "A Silicon Counter Array for  $^2\text{He}$  Detection," *Nucl. Instrum. Methods A*, **271**, 491 (1988).
  - 10) T. Nakagawa and W. Bohne: "A Compact and Gridless Channel Plate Start Detector," *Nucl. Instrum. Methods A*, **271**, 523 (1988).
  - 11) T. Kajino, H. Toki, K.-I. Kubo, and I. Tanihata: "Nuclear Matter Radii of  $^7\text{Be}$  and  $^7\text{Li}$  and Astrophysical S-factor for Radiative Alpha-Capture Reactions," *Phys. Lett. B*, **202**, 475 (1988).
  - 12) I. Tanihata, T. Kobayashi, O. Yamakawa, S. Shimoura, K. Ekuni, K. Sugimoto, N. Takahashi, T. Shimoda, and T. Sato: "Measurement of Interaction Cross Sections Using Isotope Beams of Be and B, and Isospin Dependence of the Nuclear Radii," *Phys. Lett. B*, **206**, 592 (1988).
  - 13) H. Harada, T. Murakami, K. Yoshida, J. Kasagi, T. Inamura, and T. Kubo: "Intruder Deformed Bands in  $^{110}\text{Sn}$  and  $^{112}\text{Sn}$ ," *Phys. Lett. B*, **207**, 17 (1988).
  - 14) M. Oshima, E. Minehara, S. Ichikawa, H. Iimura, T. Inamura, A. Hashizume, H. Kusakari, and S. Iwasaki: "Signature Dependence of M1 and E2 Transition Probabilities for the  $i_{13/2}$  Rotational Band in  $^{161}\text{Dy}$ ," *Phys. Rev. C*, **37**, 2578 (1988).
  - 15) R. J. Peterson, M. Yasue, M.H. Tanaka, T. Hasegawa, N. Nishimura, H. Ohnuma, H. Shimizu, K. Ieki, H. Toyokawa, M. Iwase, J. Iimura, and S.I. Hayakawa: " $^{25}\text{Mg}(^3\text{He}, \text{d})^{26}\text{Al}$  to High Spin States," *Phys. Rev. C*, **38**, 1130 (1988).
  - 16) S. Hayashi, Y. Miake, T. Nagae, S.

- Nagamiya, H. Hamagaki, O. Hashimoto, Y. Shida, I. Tanihata, K. Kimura, O. Yamakawa, T. Kobayashi, and X.X. Bai: "Production of Pions and Light Fragments in 0.8 A GeV La+La Collisions," *Phys. Rev. C*, **38**, 1229 (1988).
- 17) R.J. Peterson, M. Yasue, M.H. Tanaka, T. Hasegawa, N. Nishimura, H. Ohnuma, H. Shimizu, K. Ieki, H. Toyokawa, M. Iwase, J. Iimura, and S.I. Hayakawa: "Forbidden (p, d) Pickup to Stretched States of  $^{26}\text{Al}$ ," *Phys. Rev. C*, **38**, 2026 (1988).
- 18) T. Kobayashi, O. Yamakawa, K. Omata, K. Sugimoto, T. Shimoda, N. Takahashi, and I. Tanihata: "Projectile Fragmentation of the Extremely Neutron Rich Nuclei  $^{11}\text{Li}$  at 0.79 GeV/nucleon," *Phys. Rev. Lett.*, **60**, 2599 (1988).
- 19) Y. Nojima, K. Matsuta, T. Minamisono, K. Sugimoto, K. Takeyama, K. Omata, Y. Shida, I. Tanihata, T. Kobayashi, S. Nagamiya, K. Ekuni, S. Shimoura, J.R. Alonso, G.F. Krebs, and T.J.M. Symons: "Polarization Creation by Beam-Foil Interactions for Projectile Fragments Produced in High-Energy Heavy-Ion Collisions and NMR Detection of Short-Lived  $\beta$ -Emitting  $^{39}\text{Ca}$ ," *Nucl. Instrum. Methods Phys. Res. B*, **33**, 193 (1988).
- 20) K. Sato and S. Yoshida: "Studies of Nuclear Second Moments for Pre-Equilibrium Nuclear Reaction Theories—Extension to Finite-Range Residual Interaction," *Z. Phys. A*, **330**, 265 (1988).
- 21) N. Hasebe, Y. Ezawa, H. Yoshii, and T. Yanagimachi: "Charge Waveform of a New Two-Dimensional Position Sensitive Silicon Detector," *Jpn. J. Appl. Phys.*, **27**, 816 (1988).
- 22) H. Kawakami and 19 others including T. Suzuki: "Preparation of Low-Energy Reference Electron Source with  $^{169}\text{Yb}$ ," *J. Appl. Phys.*, **27**, 1488 (1988).
- 23) T. Motobayashi, S. Satoh, H. Murakami, H. Sakai, N. Matsuoka, T. Saito, T. Noro, K. Hosono, A. Okihana, M. Ishihara, H. Okamura, and S. Hatori: "Tensor Analyzing Power of the (d,  $^2\text{He}$ ) Reaction on  $^{12}\text{C}$  at 70 MeV," *J. Phys. G*, **14**, L137 (1988).
- 24) H. Kawakami and 16 others including T. Suzuki: "Neutrino Mass and End-Point Energy of  $^3\text{H}$   $\beta$ -Decay," *J. Phys. Soc. Jpn.*, **57**, 2873 (1988).
- 25) I. Tanihata: "Nuclear Structure Studies Using Beams of Radioactive Nuclei," Proc. 5th Int. Conf. Nuclei Far from Stability, Rosseau Lake, Ontario, Canada, Sep. Proc., **164**, 213 (1988).
- 26) W. Bohne, H. Morgenstern, K. Grabisch, T. Nakagawa, and S. Proschitzki: "Critical Excitation Energy in Fusion Evaporation Reaction," Proc. JAERI Int. Symp. Heavy Ion Reaction Dynamics in Tandem Energy Region, Universal Press, Tokyo, p. 227 (1988).
- 27) M. Yasue and T. Wada: "A Guid Note for Spectral Analysis in the S-3500 System," INS-Report, p. 670 (1988).
- 28) I. Tanihata: "Nuclear Structure Studies Using Beams of Radioactive Nuclei," Proc. RIKEN-IN2P3 Symp. Heavy-Ion Collisions, Shimoda, Oct. 1987, eds. M. Ishihara and S. Yamaji, p. 82 (1988).
- 29) T. Shinozuka and K. Asahi: "Report on the Fifth International Conference on Nuclei Far from Stability," *Butsuri*, **43**, 637 (1988) (in Japanese).
3. Atomic and solid-state physics
- 1) Y. Kanai, T. Kambara, Y. Awaya, B. Sulik, N. Stolterfoht, and Y. Yamazaki: "K-LL Auger Spectra of Nitrogen Projectiles," *At. Collision Res. Jpn.*, **14**, 64 (1988).
  - 2) T. Kambara, T. Mizogawa, Y. Awaya, Y. Kanai, R. Schuch, and K. Shima: "Impact Parameter Dependent Probabilities of Au L<sub>3</sub>-Shell Ionization by 1 MeV/amu Ar Ions," *At. Collision Res. Jpn.*, **14**, 66 (1988).
  - 3) T. Mizogawa, Y. Awaya, T. Kambara, Y. Kanai, M. Kase, H. Kumagai, and K. Shima: "Charge-Equilibration Processes of 50-MeV Ar Ions Passing through Solid (C Foils) and Gaseous ( $\text{CH}_4$ ) Targets," *At. Collision Res. Jpn.*, **14**, 68 (1988).
  - 4) Y. Awaya, K. Hino, Y. Kanai, A. Hitachi, H. Vogt, K. Kuroki, and Y. Yamazaki: "Momentum Distribution of Be 2s Electrons Measured by a Radiative Electron Capture Process," *At. Collision Res. Jpn.*, **14**, 71 (1988).
  - 5) Y. Kanai, T. Kambara, T. Chiba, and Y. Awaya: "Facilities for Atomic Physics at RIKEN Ring Cyclotron," *At. Collision Res. Jpn.*, **14**, 91 (1988).
  - 6) H. Tawara, T. Tonuma, and T. Matsuo: "Multiply Charged Ions from Solid Produced under Energetic Heavy Ion Impact," *Nucl. Instrum. Methods B*, **30**, 603 (1988).
  - 7) K. Shima, E. Nakagawa, T. Kakita, M. Yamanouchi, Y. Awaya, T. Kambara, T. Mizogawa, and Y. Kanai: "Projectile

- Atomic Number Dependence of Equilibrium Charge States for 1 and 2 MeV/u Ions Passing through a Carbon Foil," *Nucl. Instrum. Methods B*, **33**, 212 (1988).
- 8) S. Karashima, K. Hino, and T. Watanabe: "Charge Equilibrium of Relativistic Uranium Ions in Matter," *Nucl. Instrum. Methods B*, **33**, 227 (1988).
  - 9) K. Ando, S. Kohmoto, Y. Awaya, H. Kumagai, T. Tonuma, and S. Tsurubuchi: "Beam-Foil Experiments on Lifetime and Spectra of Highly Ionized Aluminum Ions," *Nucl. Instrum. Methods B*, **33**, 239 (1988).
  - 10) A. Koyama, H. Ishikawa, and Y. Sasa: "Energy Spectra of Al-LVV Auger Electrons Induced by Grazing Angle Incident Fast Heavy Ion Impact," *Nucl. Instrum. Methods B*, **33**, 308 (1988).
  - 11) K. Hino and T. Watanabe: "Angular Distribution and Linear Polarization of X-Rays Induced by Radiative Electron Capture Process," *Nucl. Instrum. Methods B*, **33**, 314 (1988).
  - 12) A. Koyama, H. Ishikawa, Y. Sasa, O. Benka, and M. Uda: "Depression of Yields of Low Energy Secondary Electrons Induced by Impact of Heavy Ions with High Electric Charges," *Nucl. Instrum. Methods B*, **33**, 338 (1988).
  - 13) A. Koyama, H. Ishikawa, Y. Sasa, O. Benka, and M. Uda: "High Charge Effects on Electron Excitations in Metal Targets for AR<sup>12+</sup> Impact Compared with Those for He<sup>2+</sup> Impact," *Nucl. Instrum. Methods B*, **33**, 341 (1988).
  - 14) K. Fujima, H. Adachi, and M. Kimura: "The Charge Transfer Collision between a Low Energy Ion and a Solid Surface," *Nucl. Instrum. Methods B*, **33**, 455 (1988).
  - 15) K. Aono, M. Iwaki, and S. Namba: "Luminescence During Eu-Implantation Into Calcium Fluoride," *Nucl. Instrum. Methods Phys. Res. B*, **32**, 321 (1988).
  - 16) E. Yagi, M. Iwaki, K. Tanaka, I. Hashimoto, and H. Yamaguchi: "Behavior of Krypton Atoms in Aluminium," *Nucl. Instrum. Methods Phys. Res. B*, **33**, 724 (1988).
  - 17) S. Nakamura, E. Yagi, T. Osaka, and M. Iwaki: "Lattice Disorder and Behavior of Implanted Atoms in In-Implanted TiO<sub>2</sub> (Rutile)," *Nucl. Instrum. Methods Phys. Res. B*, **33**, 733 (1988).
  - 18) E. Yagi, H. Sakairi, A. Koyama, and R.R. Hasiguti: "Recovery and Reverse Annealing of Proton- and  $\alpha$ -Particle-Irradiated Cu<sub>3</sub>Au at Low Temperatures" (Extended Abstract), Proc. 3rd Sino-Jpn. Symp. Metal Physics and Physical Metallurgy, Shanghai Iron and Steel Res. Inst., Shanghai, p. 1 (1988).
  - 19) E. Yagi, S. Nakamura, F. Kano, T. Kobayashi, K. Watanabe, Y. Fukai, and T. Matsumoto: "Hydrogen Trapping by Solute Atoms in Nb-Mo Alloys as Observed by the Channeling Method" (Extended Abstract), Proc. 3rd Sino-Jpn. Symp. Metal Physics and Physical Metallurgy, Shanghai Iron and Steel Res. Inst., Shanghai, p. 49 (1988).
  - 20) H. Kawakami and 20 others including T. Suzuki: "Precise Measurement of Ag KLM and KLN Auger Spectra," *Phys. Lett. A*, **127**, 175 (1988).
  - 21) S. Hara, H. Fukuda, T. Ishihara, and A.V. Matveenko: "Hyper-Radial Adiabatic Expansion for a Muonic Molecule dt $\mu$ ," *Phys. Lett. A*, **130**, 22 (1988).
  - 22) R. Kadono, K. Nishiyama, K. Nagamine, and T. Matsuzaki: "Muon Diffusion in Pure Bismuth: Evidence for an Extended Muonic State," *Phys. Lett.*, **132**, 195 (1988).
  - 23) T. Watanabe and K. Hino: "Photon Emission Processes Induced by Ion-Atom Collisions," *Indian J. Phys.*, **62B**, 278 (1988).
  - 24) S. Kubota, M. Itoh, J. Ruan, S. Sakuragi, and S. Hashimoto: "Observation of Interatomic Radiative Transition of Valence Electrons to Outermost-Core-Hole States in Alkali Halides," *Phys. Rev. Lett.*, **60**, 2319 (1988).
  - 25) S.M. Younger, A.K. Harrison, K. Fujima, and D. Griswold: "Quantum Calculations of the Electronic Structure of a Many-Atom Plasma," *Phys. Rev. Lett.*, **61**, 962 (1988).
  - 26) M. Iwai, I. Shimamura, and T. Watanabe: "Structure of the Integral Cross Sections for Excitation in Ion-Atom Collisions Calculated in the Plane-Wave Born Approximation," *Phys. Rev. A*, **37**, 729 (1988).
  - 27) X. Fang, X. Zhang, Q. Ma, Y. Liu, and T. Watanabe: "Calculation of the Electron-Stripping Cross Sections of Ne Charged Ions by Proton Impact," *Phys. Rev. A*, **38**, 497 (1988).
  - 28) E. Yagi, H. Sakairi, A. Koyama, and R.R. Hasiguti: "Isochronal Annealing of Proton- or  $\alpha$ -Particle-Irradiated Cu<sub>3</sub>Au at Low Temperatures," *Phys. Rev. B*, **38**, 3189 (1988).
  - 29) T. Matsuo, T. Tonuma, M. Kase, T. Kam-

- bara, H. Kumagai, and H. Tawara: "Production of Multiply Charged Ions from CO and CO<sub>2</sub> Molecules in Energetic Heavy-Ion Impact," *Chem. Phys.*, **121**, 93 (1988).
- 30) H. Sato, M. Kimura, and K. Fujima: "Elastic and Momentum Transfer Cross Sections in Electron Scattering by Water Molecules," *Chem. Phys. Lett.*, **145**, 21 (1988).
- 31) T. Matsuo, H. Shibata, J. Urakawa, M. Sekiya, T. Kambara, M. Kase, and Y. Awaya: "Ar L-MM Auger Spectra in Energetic Ar<sup>4+</sup> + Ar Collisions," *J. Phys. B: At. Mol. Opt. Phys.*, **21**, 1791 (1988).
- 32) T. Munakata and T. Watanabe: "Studies of Chemical Reactions by Molecular Beams," *Parity*, **3**, 38 (1988) (in Japanese).
- 33) K. Yano, H. Oyama, Y. Sakamoto, and M. Yanokura: "Erosion of Graphite by Atomic Hydrogen," *J. Vac. Soc. Jpn.*, **31**(5), 445 (1988).
- 34) M. Wakasugi, T. Horiguchi, M. Koizumi, and Y. Yoshikawa: "Hyperfine Structure near 13-1 Band Head in the B-X Transition of <sup>127</sup>I<sub>2</sub>," *J. Opt. Soc. Am. B*, **5**, 2298 (1988).
- 35) K. Hino and T. Watanabe: "Radiative Electron Capture Processes in the Relativistic Incident Energy Region," *Butsuri*, **43**, 759 (1988) (in Japanese).
- 36) T. Matsuzaki, K. Ishida, K. Nagamine, Y. Hirata, and R. Kadono: "Obsevation of Radiative Transition Photons in the  $\mu$ -Transfer Process for Liquid D<sub>2</sub> with <sup>4</sup>He Impurity," *Muon Catalyzed Fusion*, **2**, 217 (1988).
- 37) T. Tonuma, T. Matsuo, M. Kase, T. Kambara, H. Kumagai, S.H. Be, I. Kohno, and H. Tawara: "Multiple Ionization by Energetic Heavy Ion Collisions—An Evidence of the Innershell Electron Transfer in Highly Charged Recoil Ion Production," in High Energy Ion-Atom Collisions, eds. D. Berenyi and G. Hock, Springer, p. 488 (1988).
- 38) Q.-C. Ma, X.-X. Zhang, Y.-Y. Liu, and T. Watanabe: "Formation of ( $\mu^+ \mu^-$ ) in  $\mu^+$ -( $\mu^-$ p) Collision and the Scaling Rule," *Chin. J. Nucl. Phys.*, **9**, 351 (1988) (in Chinese).
- 39) E. Yagi: "Application of Ion Beam Analisis to Materials Science," *Bull. Jpn. Inst. Met.*, **27**, 241 (1988) (in Japanese).
- 40) K. Hino, and T. Watanabe: "Radiative Electron Capture Processes in Relativistic Impact Energy Region," *Bull. Phys. Soc.* *Jpn.*, **43**, 759 (1988) (in Japanese).
- 41) K. Fujima: "Atomic Models for Hot Dense Plasmas," *Inst. Plasma Phys., Nagoya Univ., Rep. IPPJ-AM-57*, p. 1 (1988).
4. Radiochemistry, radiation chemistry and radiation biology
- 1) T. Takahashi, F. Yatagai, T. Katayama, S. Konno, K. Nakano, I. Kaneko, and T. Kasuya: "Position Determination by Laser Marks of Biological Samples Placed on a Plastic Track Detector and Inactivation of *B. Subtilis* Spores by a Single Heavy Ion," *Jpn. J. Appl. Phys.*, **27**, 2181 (1988).
  - 2) H. Sunaga, T. Agematsu, R. Tanaka, K. Yoshida, and I. Kohno: "Dosimetry by a Cellulose Triacetate Film Dosimeter in Proton-Beam Irradiation," *Radioisotopes*, **37**, 84 (1988) (in Japanese).
  - 3) T. Takahashi, T. Katayama, F. Yatagai, S. Konno, I. Kaneko, T. Kasuya, T. Doke, and H. Ohashi: "The Inactivation of Bacterial Spores by a Single Heavy Ion and Preparation for Experiments in a Spacecraft," *J. Radiat. Res.*, **29**, 37 (1988).
  - 4) T. Takahashi, F. Yatagai, T. Katayama, and I. Kaneko: "Biological Effects of HZE Particles in Cosmic Rays and Experimental Programme," *Space Environ. Monit.*, **5**, 115 (1988) (in Japanese).
  - 5) I. Kaneko, K. Eguchi-Kasai, T. Kosaka, T. Nakano, K. Maruhashi, and T. Takahashi: "DNA Lesion and Cell Death by  $\alpha$ -Particles and Nitrogen Ions," COSPAR —Molecular and Cellular Effects of Heavy Ions, **27**, 56 (1988).
  - 6) S. Ambe, T. Okada, F. Ambe, I. Tanaka, S. Nasu, and F.E. Fujita: "*In and Ex Situ* Emission Mössbaur Spectra of No-Carrier-Added <sup>119</sup>Sb Electrodeposited on Gold," *J. Electrochem. Soc.*, **135**, 949 (1988).
  - 7) K. Maeda, Y. Sasa, M. Maeda, H. Yusuyama, and M. Uda: "Applecation of PIXE to Biological Materials in Daily Life," Proc. 12th Int. Symp. Hosei Univ., p. 453 (1988).
  - 8) H. Kusuyama, K. Okada, T. Kawai, K. Maeda, Y. Sasa, and M. Uda: "Trace Elemental Analysis of Renal Cell Carcinoma Using Particle Induced X-Ray Emission (PIXE)," *Trace Met. Metab., Its Abnorm. Treat.*, **16**, 51 (1988).
  - 9) K. Kimura, T. Kataoka, T. Azuma, Y. Aoki, Y. Ito, and Y. Tabata: "New Emission Bands at High Density Excitation of Dense Gas and Liquid of Helium Irradiat-

ed by N-Ions," *Phys. Lett. A*, **133**, 91 (1988).

### (Papers Presented at Meetings)

1. Accelerator development and accelerator physics
  - 1) H. Sakamoto, Y. Morimoto, S. Yokouchi, and S.H. Be: "Power Distribution of Synchrotron Radiation at the 6 GeV Storage Ring," 43th Annu. Meet. Phys. Soc. Jpn., Kooriyama, Apr. (1988).
  - 2) S.H. Be, Y. Morimoto, H. Sakamoto, and S. Yokouchi: "Conceptual Design of the Vacuum System for the 6 GeV Strange Ring," Advanced Synchrotron Light Source Conf., N. Y., May (1988).
  - 3) Y. Morimoto, H. Sakamoto, S. Yokouchi, and S.H. Be: "Conceptual Design and Thermal Analysis of the Crotch at the 6 GeV Storage Ring," Advanced Synchrotron Light Source Conf., N. Y., May (1988).
  - 4) T. Fujisawa, K. Ogiwara, S. Kohara, I. Yokoyama, M. Nagase, Y. Chiba, and Y. Kumata: "Radio-Frequency System of the RIKEN Ring Cyclotron," 1st Eur. Particle Accelerator Conf., Rome, Jun. (1988).
  - 5) A. Goto: "Injector AVF Cyclotron at RIKEN," 1st Eur. Particle Accelerator Conf., Rome, Jun. (1988).
  - 6) Y. Yano: "Status Report on RIKEN Ring Cyclotron," 1st Eur. Particle Accelerator Conf., Rome, Jun. (1988).
  - 7) K. Yamasu, H. Miyade, and M. Hara: "The Coceptual Design of the Linac for the RIKEN-SR," 13th Linear Accelerator Meet. Jpn., Tsukuba, Sep. (1988).
  - 8) K. Yamasu, H. Miyade, and M. Hara: "The R&D of the 1.5 GeV Linac for the RIKEN SR," 13th Linear Accelerator Meet. Jpn., Tsukuba, Sep. (1988).
  - 9) H. Miyade, K. Yamasu, and M. Hara: "The Study of the Positron Injection System for the RIKEN SR," 13th Linear Accelerator Meet. Jpn., Tsukuba, Sep. (1988).
  - 10) S.H. Be: "Design of Vacuum Chamber Components Including Step Changes for the 6 GeV Storage Ring," Workshop on Impedance and Current Limitations, Grenoble, France, Oct. (1988).
  - 11) A. Nishide, S. Yokouchi, M. Iguchi, and S.H. Be: "Effects of Magnetic Fields on Turbomolecular Pumps for RIKEN Ring Cyclotron," 29th Vacuum Symp. Proc., Osaka, Nov. (1988).
- 12) T. Kikuchi, K. Morimoto, N. Ohsako, K. Ikegami, S. Nakajima, and S.H. Be: "New Cryopumps for a Resonator of the RIKEN Ring Cyclotron," 29th Vacuum Symp. Proc., Osaka, Nov. (1988).
- 13) S. Yokouchi, Y. Morimoto, H. Sakamoto, and S.H. Be: "Pumping Characteristics of NEG Strip," 29th Vacuum Symp. Proc., Osaka, Nov. (1988).
2. Nuclear physics and nuclear instrumentation
  - 1) T. Minowa, T. Suzuki, C. Yoneyama, H. Katsuragawa, and M. Shimazu: "Detection of Laser Cooling Effect by Resonance Ionization Spectroscopy," 43th Annu. Meet. Phys. Soc. Jpn. Kooriyama, Mar. (1988).
  - 2) H. Katsuragawa, M. Otsuki, K. Nishiyama, Minowa, S. Kawamura, H. Sonobe, and M. Shimazu: "Resonance Ionization Spectroscopy of Neutral Atoms Generated by Laser Ablation Method," 43th Annu. Meet. Phys. Soc. Jpn. Kooriyama, Mar. (1988).
  - 3) T. Minowa, H. Katsuragawa, and M. Shimazu: "Highly Sensitive Detection of the Laser Cooling Effect of Na Atoms Using Multiphoton Ionization Method," 1988 Conf. Lasers and Electro-Optics, Anaheim, Apr. (1988).
  - 4) M. Matsuo, F. Sakata, and Y. Zhuo: "Microscopic Derivation of Transport Equation in the TDHF Theory," 43th Annu. Meet. Phys. Soc. Jpn., Kooriyama, Apr. (1988).
  - 5) K. Ieki, S.M. Lee, M. Ishihara, S. Shirato, J. Ruan (Gen), T. Motobayashi, H. Murakami, Y. Ando, N. Iwasa, M. Ogiwara, Y. Nagashima, S.C. Jeong, and H. Fujiwara: "Angular Momentum Transfer and Spin Alignment in the  $^{40}\text{Ar} + ^{209}\text{Bi}$  Reaction at 26 MeV/u," 43th Annu. Meet. Phys. Soc. Jpn., Kooriyama, Apr. (1988).
  - 6) T. Motobayashi, K. Ieki, S. Shirato, J. Ruan (Gen), H. Murakami, Y. Ando, M. Ogiwara, N. Iwasa, S. Shibuya, J. Kasagi, H. Hama, K. Yoshida, M. Sakurai, M. Ishihara, and T. Ichihara: "Nuclear Unbound States Observed in Two Particle Correlation Measurements," 43th Annu. Meet. Phys. Soc. Jpn., Kooriyama, Apr. (1988).
  - 7) K. Asahi, M. Ishihara, T. Ichihara, M. Fukuda, T. Kubo, Y. Gono, A.C. Mueller, R. Anne, D. Bazin, D. Guillemaud-Mueller, R. Bimbot, W.-D. Schmidt-Ott, and J.

- Kasagi: "Spin Alignment in Projectile Fragmentation at Intermediate Energies," 43th Annu. Meet. Phys. Soc. Jpn., Koriyama, Apr. (1988).
- 8) M. Ishihara, M. Fukuda, K. Asahi, T. Ichihara, T. Kubo, I. Tanihata, M. Adachi, and M. Koguchi: "Measurement of Total Reaction Cross Section Using Secondary Beams," 43th Annu. Meet. Phys. Soc. Jpn., Koriyama, Apr. (1988).
  - 9) I. Tanihata: "Nuclear Studies with Secondary Radioactive Beams," 3rd Int. Conf. Nucleus-Nucleus Collisions, Saint-Malo, France, Jun. (1988).
  - 10) M. Fukuda, M. Adachi, K. Asahi, T. Ichihara, M. Ishihara, M. Koguchi, T. Kubo, H. Kumagai, T. Nakagawa, and I. Tanihata: "Measurement of Interaction Cross Sections at Intermediate Energies Using Particle Telescope," 3rd Int. Conf. Nucleus-Nucleus Collisions, Saint-Malo, France, Jun. (1988).
  - 11) I. Tanihata: "Nuclear Structure Studies with Radioactive Beams," Gordon Research Conf. Nuclear Chemistry Colby-Sawyer College, New London, New Hampshire, USA, Jun. (1988).
  - 12) K. Asahi, M. Ishihara, T. Ichihara, M. Fukuda, T. Kubo, Y. Gono, A.C. Mueller, R. Anne, D. Bazin, D. Guillemaud-Mueller, R. Bimbot, W.-D. Schmidt-Ott, and J. Kasagi: "Production of Spin-Aligned Unstable Nuclei in the Projectile Fragmentation at Intermediate Energies," 3rd Int. Conf. Nucleus-Nucleus Collisions, Saint-Malo, France, Jun. (1988).
  - 13) M. Fukuda, M. Adachi, K. Asahi, T. Ichihara, M. Ishihara, M. Koguchi, T. Kubo, H. Kumagai, T. Nakagawa, and I. Tanihata: "Measurement of Interaction Cross Section at Intermediate Energies Using Particle Telescope," 3rd Int. Conf. Nucleus-Nucleus Collisions, Saint-Malo, France, Jun. (1988).
  - 14) I. Tanihata: "Radii of Light Neutron-Rich Nuclei," Int. Symp. Heavy Ion Physics and Nuclear Astrophysical Problems, Tokyo, Jul. (1988).
  - 15) K. Asahi, M. Ishihara, T. Ichihara, M. Fukuda, T. Kubo, Y. Gono, A.C. Mueller, R. Anne, D. Bazin, D. Guillemaud-Mueller, R. Bimbot, W.-D. Schmidt-Ott, and J. Kasagi: "Spin Alignment in Projectile Fragmentation at Intermediate Energies," Int. Symp. Heavy Ion Reactions and Nuclear Astrophysical Problems, Tokyo, Jul. (1988).
  - 16) M. Koguchi, M. Fukuda, K. Asahi, H. Kumagai, M. Adachi, I. Tanihata, and M. Ishihara: "Rotating Catcher System for Beta Decay Studies of Projectile Fragments," Int. Symp. Heavy Ion Reactions and Nuclear Astrophysical Problems, Tokyo, Jul. (1988).
  - 17) H. Katsuragawa, T. Minowa, T. Suzuki, and M. Shimazu: "Isotopic Enrichment Using Laser Cooling of Atomic Beam," 25th Annu. Meet. Radioisotopes in the Physical Sciences and Industries, Tokyo, Jul. (1988).
  - 18) S. Yamaji: "Self-Consistent Transport Coefficients for Damped Motion," Lanzhou Int. Summer Sch. Heavy Ion Collisions, Lanzhou, China, Aug. (1988).
  - 19) M. Matsuo, F. Sakata, T. Marumori, and Y. Zhuo: "Master Equations in the Microscopic Theory of Nuclear Collective Dynamics," Lanzhou Int. Summer Sch. Heavy Ion Reaction Theory, Lanzhou, China, Aug. (1988).
  - 20) K. Asahi: "Measurement of  $g$ -Factors for Nuclei Far from Stability," 1988 Fall Meet. Phys. Soc. Jpn., Matsuyama, Oct. (1988).
  - 21) K. Ieki, S.M. Lee, M. Ishihara, S. Shirato, J. Ruan (Gen), T. Motabayashi, H. Murakami, Y. Ando, N. Iwasa, M. Ogiwara, Y. Nagashima, S. Okumura, S.C. Jeong, F. Fujiwara, Y.H. Pu, T. Mizota, and T. Murayama: "Angular Momentum Transfer and Spin Alignment in the  ${}^{40}\text{Ar} + {}^{209}\text{Bi}$  Reaction at 26 MeV/u II," 1988 Fall Meet. Phys. Soc. Jpn., Matsuyama, Oct. (1988).
  - 22) T. Nakagawa, W. Bohne, H. Morgenstern, K. Grabisch, and S. Proschitzki: "Maximum Excitation Energy of Compound Nucleus," 1988 Fall Meet. Phys. Soc. Jpn., Matsuyama, Oct. (1988).
  - 23) M. Oshima, S. Ichikawa, H. Iimura, E. Minehara, H. Kusakari, T. Inamura, A. Hashizume, and M. Sugawara: "Ground-state Rotational Bands in  ${}^{157}\text{Gd}$  and  ${}^{173}\text{Yb}$ ," 1988 Fall Meet. Phys. Soc. Jpn., Matsuyama, Oct. (1988).
  - 24) K. Sueki, H. Nakahara, and I. Kohno: "Nuclear Charge Distribution in Deep Inelastic Scattering Process on Heavy Ion Reaction between Light Mass Nuclei," 1988 Fall Meet. Phys. Soc. Jpn., Matsuyama, Oct. (1988).
  - 25) M. Otsuki, T. Minowa, H. Nakahama, H. Katsuragawa, and T. Inamura: "Reson-

- nance Ionizaiton Spectroscopy Using Laser Ablation—Thermal Armonic Beam," 1988 Fall Meet. Phys. Soc. Jpn., Hiroshima, Oct. (1988).
- 26) T. Suzuki, T. Minowa, H. Horibe, and H. Katsuragawa: "Detection of Laser Cooling Effect by Resonance Ionization Spectroscopy II," 1988 Fall Meet. Phys. Soc. Jpn., Hiroshima, Oct. (1988).
  - 27) T. Suzuki, I. Tanihata, T. Kubo, T. Ichihara, T. Kobayashi, and M. Fujiwara: "Subthreshold Pion Production in Heavy-Ion Collisions," 43th Annu. Meet. Jpn. Phys. Soc. Kooriyama, Oct. (1988).
  - 28) I. Tanihata, W.P. Liu, T. Kubo, T. Suzuki, M. Yanokura, T. Doke, Y. Yamaguchi, T. Murakami, T. Yanagimachi, and N. Hasebe: "Test Experiment for New Isotope Search at RRC," 43th Annu. Meet. Jpn. Phys. Soc., Kooriyama, Oct. (1988).
  - 29) M. Ishihara, K. Asahi, T. Ichihara, T. Kubo, I. Tanihata, M. Fukuda, M. Adachi, and M. Takada: "Interaction Cross Section Measurement Using Secondary Radioisotope Beams," 43th Annu. Meet. Jpn. Phys. Soc., Kooriyama, Oct. (1988).
  - 30) T. Kobayashi, I. Tanihata, T. Shimoura, K. Matsuta, Y. Miyatake, K. Sugimoto, H. Wieman, D. Olson, W. Müller, and J. Symons: "Target Mass Dependence of Total Interaction Cross Sections for Drip-line Nuclear," 43th Annu. Meet. Jpn. Phys. Soc., Kooriyama, Oct. (1988).
  - 31) M. Matsuo: "Microscopic Approach to Nuclear Collective Dynamics in Highly Excited Region," INS Symp. Vibration and Rotation in Nuclei, Tokyo, Nov. (1988).
  - 32) M. Matsuo: "Microscopic Approach to Dissipative Large Amplitude Collective Motions," RIFP Symp. Non-Linear Dynamics in Nuclear Collective Motions, Kyoto, Dec. (1988).
  - 33) T. Inamura: Laser Nuclear Spectroscopy," Symp. Laser Sciences, Wako, Dec. (1988).
3. Atomic and solid-state physics
- 1) A. Koyama: "Characteristics of Metal Electron Excitation by Fast High Charge Ions," RIKEN Symp., Wako, Mar. (1988).
  - 2) H. Ishikawa, Y. Sasa, and A. Koyama: "Energy Spectrum of Al-LVV Auger Electrons Induced by Grazing Angle Incident Fast Heavy Ion Impact," RIKEN Symp., Wako, Mar. (1988).
  - 3) A. Koyama: "Characteristics of Metal Electron Excitation by Fast High Charge Ions," RIKEN Symp., Wako, Mar. (1988).
  - 4) H. Ishikawa, Y. Sasa, and A. Koyama: "Energy Spectrum of Al-LVV Auger Electrons Induced by Grazing Angle Incident Fast Heavy Ion Impact," RIKEN Symp., Wako, Mar. (1988).
  - 5) Aono Keiko, Iwaki Masaya, and Namba Susumu: "Ion Implantation in  $\text{CaF}_2$  (III)," 19th Symp. Ion Implantation and Sub-micron Fabrication (RIKEN Symp.), Wako, Mar. (1988).
  - 6) Y. Awaya, T. Mizogawa, Y. Kanai, H. Kumagai, M. Kase, and K. Shima: "Charge-State Distribution of Fast Heavy Ions after Passing through Solid Targets," Symp. Interactions between Ion Beam and Solids, Tokyo, Mar. (1988).
  - 7) E. Yagi: "Lattice Location Study on Hydrogen in Metals by Means Ion Beam Analysis," Symp. Ion Beam Interactions with Solids, Tokyo, Mar. (1988).
  - 8) K. Ishida, T. Matsuzaki, and K. Nagamine: "Radiative Transition in Muon Transfer Reaction," Atomic Physics Forum, Nagoya, Mar. (1988).
  - 9) Y. Sakamoto, K. Yano, H. Oyama, and S. Itoh: "Erosion of  $\text{MoS}_2$  by Irradiation of Hydrogen Plasma I," 1988 Spring Meet. Jpn. Soc. Plasma Science and Nuclear Fusion Research, Tsukuba, Mar. (1988).
  - 10) H. Tawara: "Production Processes of Highly Charged Ions," 43th Annu. Meet. Phys. Soc. Jpn., Kooriyama, Mar. (1988).
  - 11) H. Mitsuya, K. Nakamura, I. Hashimoto, H. Yamaguchi, E. Yagi, and M. Iwaki: "Motion of Kr Bubbles in Kr-Implanted Aluminum," 43th Annu. Meet. Phys. Soc. Jpn., Kooriyama, Apr. (1988).
  - 12) E. Yagi, T. Kobayashi, S. Nakamura, F. Kano, K. Watanabe, Y. Fukai, and T. Matsumoto: "Trapping of Hydrogen in Nb-Mo Alloys," 43th Annu. Meet. Phys. Soc. Jpn., Kooriyama, Apr. (1988).
  - 13) K. Ishida, T. Matsuzaki, and K. Nagamine: "Design of a Superconducting Secondary Beam Course with Large Acceptance Using Axi-Symmetric Magnetic Field," 43th Annu. Meet. Phys. Soc. Jpn., Kooriyama, Mar. (1988).
  - 14) T. Watanabe: "Theoretical Aspects of Electron Capture by  $\text{C}^{6+}$  and  $\text{O}^{8+}$  from  $\text{H}$ ,  $\text{H}_2$ , and  $\text{He}$ ," IAEA Specialists' Meet. Carbon and Oxygen Collision Data for Fusion Plasma Research, Vienna, May (1988).

- 15) Y. Sakamoto, K. Yano, H. Oyama, H. Kokai, A. Itoh, and A. Miyahara: "Deterioration of Molybdenum ( $\text{MoS}_2$ ) by Hydrogen Plasma Irradiation," 8th Int. Conf. Plasma-Surface Interactions in Controlled Fusion Devices, Jülich, May (1988).
- 16) E. Yagi: "Lattice Location Study on Kr Atoms in Aluminium by Means of the Channelling Method," 6th Int. Conf. Ion Beam Modification of Materials, Tokyo, Jun. (1988).
- 17) T. Fujihana, Y. Okabe, and M. Iwaki: "Effects of Implantation Temperature on The Hardness of Iron Nitrides Formed with High Nitrogen Dose," 6th Int. Conf. Ion Beam Modification of Materials, Tokyo, Jun. (1988).
- 18) I. Kohno: "Production of Fast Switching Power Thyristor by Proton Irradiation," 7th Int. Conf. Ion Implantation Technology, Kyoto, Jun. (1988).
- 19) K. Kobayashi: "Effect of Incident Angles of N-Implantation on Recrystallization of  $\text{AlN}_x$  Thin Films, 7th Int. Conf. Ion Implantation Technology, Kyoto, Jun. (1988).
- 20) T. Watanabe: "Theories of Electron Capture by Ion-Atom Collisions," Semin. Atomic Physics Group in ATOMKI, Inst. Nucl. Res. Hung. Acad. Sci., Debrecen, Hungary, Jun. (1988).
- 21) T. Watanabe: "Radiative Processes Induced by Ion-Atom Collisions," Semin. Atomic Physics Group in ATOMKI, Inst. Nucl. Res. Hung. Acad. Sci., Debrecen, Hungary, Jun. (1988).
- 22) S. Karashima, K. Hino, and T. Watanabe: "Equilibrium Charge States of Relativistic Uranium Projectile Ions in Matter," 11th Int. Conf. Atomic Physics, Paris, Jul. (1988).
- 23) K. Hino, and T. Watanabe: "Photon Angular Distribution of the Ultra-Relativistic K-Shell Radiative Electron Capture by Heavy Ion Collisions," 11th Int. Conf. Atomic Physics, Paris, Jul. (1988).
- 24) K. Hino, and T. Watanabe: "Angular Distribution and Linear-Polarization of X Rays Induced by Radiative Electron Capture," 11th Int. Conf. Atomic Physics, Paris, Jul. (1988).
- 25) Y. Awaya, K. Hino, Y. Kanai, A. Hitachi, H. Vogt, K. Kuroki, and Y. Yamazaki: "Momentum Distribution of Be 2s Electrons Measured by Radiative Electron Capture in Heavy Ion Collisions," 11th Int. Conf. Atomic Physics, Paris, Jul. (1988).
- 26) T. Mizogawa, Y. Awaya, T. Kambara, Y. Kanai, M. Kase, H. Kumagai, and K. Shima: "Charge-Equilibration Processes of 50-MeV Ar Ions Passing through Solid (C Foils) and Gaseous ( $\text{CH}_4$ ) Targets," 11th Int. Conf. Atomic Physics, Paris, Jul. (1988).
- 27) T. Fujimoto and I. Shimamura: "Electronic States in High Density Plasma and Charge Equilibrium," 13th, Res. Meet. Soc. Atomic Collision Research, Tokyo, Jul. (1988).
- 28) T. Kambara: "Experiments of RTE in GSI," 13th Res. Meet. Soc. Atomic Collision Research, Tokyo, Jul. (1988).
- 29) E. Yagi: "Study on a State of Hydrogen in Metals by the Channelling Method," Symp. Tandem Accelerator and Related Technique, Tokyo, Jul. (1988).
- 30) T. Watanabe: "The Report of the Visit to France," Jt. Semin. on "Radiative and Collisional Process in High Density Plasma" and on "Elementary Theory for Diagnosis of High Density Plasma," Nogoya Univ., Jul. (1988).
- 31) Y. Awaya, T. Kambara, Y. Kanai, T. Mizogawa, A. Hitachi, and B. Sulik: "Systematics of Multiple Inner-Shell Ionization of Target Atoms by 0.8-26 MeV/u Heavy Ion Impact," Spectroscopy and Collisions of Few Electron Ions, Bucharest, Aug. (1988).
- 32) E. Yagi, S. Nakamura, F. Kano, T. Kobayashi, K. Watanabe, Y. Fukai, and T. Matsumoto: "Hydrogen Trapping by Solute Atoms in Nb-Mo Alloys as Observed by the Channelling Method," Int. Symp. Metal-Hydrogen Systems—Fundamentals and Applications, Stuttgart, Sep. (1988).
- 33) E. Yagi, S. Nakamura, F. Kano, T. Kobayashi, K. Watanabe, Y. Fukai, and T. Matsumoto: "Hydrogen Trapping by Solute Atoms in Nb-Mo Alloys as Observed by the Channeling Method," 3rd Sino-Jpn. Symp. Metal Physics and Physical Metallurgy, Shanghai, Sep. (1988).
- 34) E. Yagi, H. Sakairi, A. Koyama, and R.R. Hasiguti: "Recovery and Reverse Annealing of Triton- or  $\alpha$ -Particle-Irradiated  $\text{Cu}_3\text{Au}$  at Low Temperatures," 3rd Sino-Jpn. Symp. Metal Physics and Physical Metallurgy, Shanghai, Sep. (1988).
- 35) I. Shimamura: "Rydberg Series of Doubly Excited Resonance States of  $\text{H}_2$ ," Okazaki Conf. Theoretical Chemistry of Excited Molecules, Okazaki, Sep. (1988).

- 36) Y. Awaya, T. Kambara, and T. Kanai: "Experimental Studies of Heavy Ion-Atom Collisions at RIKEN Ring Cyclotron," Int. Semin. Atomic and Molecular Physics—2nd Chin.-Jpn. Jt. Semin., Fuji-Yoshida, Oct. (1988).
- 37) I. Shimamura: "Doubly Excited Rydberg Series of Molecular Repulsive States: H<sub>2</sub>," Int. Semin. Atomic and Molecular Physics—2nd Chin.-Jpn. Jt. Semin., Fuji-Yoshida, Oct. (1988).
- 38) T. Watanabe: "Rearrangement Processes of Coulomb Interacting Three-Body Systems," Int. Semin. Atomic and Molecular Physics—2nd Chin.-Jpn. Jt. Semin., Fuji-Yoshida, Oct. (1988).
- 39) T. Tonuma, T. Mukoyama, T. Koizumi, T. Matsuo, H. Shibata, K. Shima, H. Tawara, and A. Yagishita: "Multiple-Photoionization of Xe in the Vicinity of L Edges," Int. Semin. Atomic and Molecular Physics—2nd Chin.-Jpn. Jt. Semin., Fuji-Yoshida, Oct. (1988).
- 40) H. Tawara, T. Tonuma, H. Kumagai, and T. Matsuo: Charge Distributions of Recoil Ions Accompanied with Multiple Ionization of Heavy Projectile Ions: 1.05 MeV/amu Ne<sup>q+</sup> and Ar<sup>q+</sup> + Ne and Ar Collisions," Int. Semin. Atomic and Molecular Physics—2nd Chin.-Jpn. Jt. Semin., Fuji-Yoshida, Oct. (1988).
- 41) T. Tonuma, T. Mukoyama, T. Koizumi, T. Matsuo, H. Shibata, K. Shima, H. Tawara, and A. Yagishita: "Multiple-Photoionization of Xe in the Vicinity of L Edges," Int. Semin. Atomic and Molecular Physics—2nd Chin.-Jpn. Jt. Semin., Fuji-Yoshida, Oct. (1988).
- 42) H. Tawara, T. Tonuma, H. Kumagai, and T. Matsuo: Charge Distributions of Recoil Ions Accompanied with Multiple Ionization of Heavy Projectile Ions: 1.05 MeV/amu Ne<sup>q+</sup> and Ar<sup>q+</sup> + Ne and Ar Collisions," Int. Semin. Atomic and Molecular Physics—2nd Chin.-Jpn. Jt. Semin., Fuji-Yoshida, Oct. (1988).
- 43) A. Keiko, I. Masaya, and N. Susumu: "Luminescence during Ion-Implantation into CaF<sub>2</sub> (III)," 1988 Fall Meet. Jpn. Soc. Appl. Phys., Toyama, Oct. (1988).
- 44) K. Tanaka, T. Takahashi, K. Kawakami, and E. Yagi: "Characterization of Crystallinity of Thin Ge Layer Epitaxially Grown on Si," 1988 Fall Meet. Jpn. Soc. Appl. Phys., Toyama, Oct. (1988).
- 45) A. Koyama: "Secondary Electron Emission from Metals Induced by Fast Ion Impact," Physikkolloq. Johanes Kepler Univ., Linz, Oct. (1988).
- 46) H. Tawara: "Production of Highly Charged Ions in Particle and Photon Impact," Meet. "Research of Multiply Charged Ion Science," Takehara, Oct. (1988).
- 47) H. Maeda, A. Suzuki, Y. Mizugai, Y. Matsumoto, and M. Takami: "Resonance Ionization Spectroscopy of Heavy Metal Elements," Fall Meet. Atomic Energy Meet., Kobe, Oct. (1988).
- 48) A. Koyama, H. Ishikawa, and Y. Sasa: "Energy Spectra of Al-LVV Auger Electrons Induced by Grazing Angle Incident Fast Heavy Ion Impact," 1988 Fall Meet. Phys. Soc. Jpn., Hiroshima, Oct. (1988).
- 49) A. Koyama, H. Ishikawa, and Y. Sasa: "Excitation of Convoy-Like Electrons by Glancing Angle Incident Heavy High Charge Ions," 1988 Fall Meet. Phys. Soc. Jpn., Hiroshima, Oct. (1988).
- 50) A. Koyama, H. Ishikawa, and Y. Sasa: "Energy Spectra of Al-LVV Auger Electrons Induced by Grazing Angle Incident Fast Heavy Ion Impact," 1988 Fall Meet. Phys. Soc. Jpn., Hiroshima, Oct. (1988).
- 51) I. Shimamura, C.J. Noble, and P.G. Burke: "Doubly Excited Resonant Rydberg Series in Hydrogen Molecules," 1988 Fall Meet. Phys. Soc. Jpn., Hiroshima, Oct. (1988).
- 52) E. Yagi: "Behaviour of Kr Atoms Implanted into Al," 1988 Fall Meet. Phys. Soc. Jpn., Hiroshima, Oct. (1988).
- 53) M. Koizumi, T. Horiguchi, M. Wakasugi, H. Sakata, and Y. Yoshizawa: "Rotational Quantum-Number Dependence of Hyperfine Spritting in <sup>127</sup>I<sub>2</sub>," 1988 Fall Meet. Phys. Soc. Jpn., Hiroshima, Oct. (1988).
- 54) Y. Mizugami, H. Maeda, Y. Matsumoto, A. Suzuki, and M. Takami: "Resonance Ionization Spectroscopy of Lantanoid Elements," 1988 Fall Meet. Phys. Soc. Jpn., Hiroshima, Oct. (1988).
- 55) T. Watanabe, and L. Végh: "Dynamic Electron Correlation in Charged-Particle Collision and Photoionization," 1st Asian-Pac. Conf. Atomic and Molecular Physics, Taipei, Nov. (1988).
- 56) T. Watanabe, K. Hino, Y. Awaya, T. Kambara, and Y. Kanai: "Studies of Heavy Ion-Atom Collisions at RIKEN Ring Cyclotron," 1st Asian-Pac. Conf. Atomic and Molecular Physics, Taipei, Nov. (1988).

- 57) Y. Awaya, T. Kambara, and Y. Kanai: "Experimental Studies of Heavy Ion-Atom Collisions at RIKEN Ring Cyclotron," 1st Asian-Pac. Conf. Atomic and Molecular Physics, Taipei, Nov. (1988).
- 58) K. Ando, S. Kohmoto, Y. Awaya, T. Tonuma, and S. Tsurubuchi: "Analysis of Mg IX 2s3d-2s4f Transition of Beam-Foil Spectra," 1st Asian-Pac. Conf. Atomic and Molecular Physics, Taipei, Nov. (1988).
- 59) T. Watanabe and L. Végh: "Scattering Correlation in Multiple Ionization by Proton, Anti-Proton and Multi-Charged Ion Impact," 10th Conf. Application of Accelerators in Research and Industry, Denton, Nov. (1988).
- 60) K. Hino and T. Watanabe: "Intensities and Angular Distribution of X-Rays by Radiative Electron Capture in Ultra-Relativistic Ion-Atom Collisions," 10th Conf. Application of Accelerators in Research and Industry, Denton, Nov. (1988).
- 61) T. Watanabe: "Experimental and Theoretical Studies of Radiative Electron Capture in Ion-Atom Collisions," 4th Int. Workshop Cross Sections of Fusion and Other Applications, College Station, Nov. (1988).
- 62) T. Fujihana, Y. Okabe, and M. Iwaki: "The Relationship between Crystal Structure and Hardness of Nitrogen Implanted Iron Surface Layers," Fall Meet. Materials Research Soc., Boston, USA, Nov. (1988).
- 63) T. Tawara, T. Tonuma, T. Matsuo, A. Yagishita, H. Shibata, T. Koizumi, K. Shima, and T. Mukoyama: "Multiply Photoionization of Rare Gas Atoms Resulting in Production of Multiply Charged Ions," Kansas Univ. Semin., Nov., Manhattan, Kansas (1988).
- 64) K. Yano, Y. Sakamoto, H. Oyama, H. Kokai, S. Itoh, T. Banno, and S. Baba: "Erosion of MoS<sub>2</sub> by Irradiation of Hydrogen Plasma II," 3rd Symp. Plasma Science and Nuclear Fusion Research and Related Societies, Tokyo, Nov. (1988).
- 65) Y. Kanai, T. Kambara, and Y. Awaya: "Beam Line for Atomic Physics and Results of Test Experiments," RIKEN Symp. Studies of Solid State Physics and Materials, Atomic Processes, Nuclear Chemistry, and Biology and Medical Science by Using Ring Cyclotron, Wako, Dec. (1988).
- 66) K. Ishida, T. Matsuzaki, and K. Nagamine: "Test Experiments at the Solid State Physics and Materials Beam Course," RIKEN Symp. Studies of Solid State Physics and Materials, Atomic Processes, Nuclear Chemistry, and Biology and Medical Science by Using Ring Cyclotron, Wako, Dec. (1988).
- 67) H. Maeda, Y. Mizugai, Y. Matsumoto, A. Suzuki, and M. Takami: "Multistep and Multiphoton Resonance Ionization Spectroscopy of Lantanoids," RIKEN Symp. Laser Science, Wako, Dec. (1988).
- 68) H. Maeda: "Resonance Ionization Spectroscopy of Lanthanoid Elements," RIKEN Symp. Laser Nuclear Spectroscopy, Wako, Dec. (1988).
- 69) I. Shimamura: "Application of the R-Matrix Method to Doubly Excited Molecular States," 7th Indian Natl. Workshop and Conf. Atomic and Molecular Physics, Aligarh, India, Dec. (1988).
- 70) I. Shimamura: "Theory of Electron-Molecule Collisions," Symp. Atomic, Collisions, Kalyani, India, Dec. (1988).
4. Radiochemistry, radiation chemistry, and radiation biology
- 1) T. Takahashi and S. Nagaoka: "Radiation Environment in Space," Symp. Manned Space Flight, Tokyo, Jan. (1988).
  - 2) T. Takahashi, M. Uehara, E. Watanabe, T. Katayama, K. Nakano, T. Kusaya, I. Kaneko, and F. Yatagai: "Plastic Track Detector for the Investigation of Inactivation of Bacterial Spores by a Single Heavy Ion," 35th Spring Meet. Jpn. Soc. Appl. Phys. and Related Societies, Tokyo, Mar. (1988).
  - 3) T. Doke and T. Takahashi: "Dosimetry and Biological Experiments in Space Environment," 35th Spring Meet. Jpn. Soc. Appl. Phys. and Related Societies, Tokyo, Mar. (1988).
  - 4) T. Takahashi, F. Yatagai, T. Katayama, T. Kasuya, and T. Doke: "Improvement in the Position Accuracy and Viability for the Inactivation of *B. subtilis* Spores by a Single Heavy Ion," 6th Track Detector Symp., Tokyo, Apr. (1988).
  - 5) I. Kaneko, K. Eguchi-Kasai, T. Kosaka, and K. Nakano: "Effects of Charged Particle Beam on DNA in Human Melanoma Cells," Int. Conf. Large Dose Ionizing and Non-Ionizing Radiation, Hanzo, China, Apr. (1988).
  - 6) K. Kimura: "Electronic Excitation by

- Heavy Ions," Ann. Meet. Chem. Soc. Jpn., Tokyo, Apr. (1988).
- 7) K. Kimura: "Roles of Rydberg Transitions to Ionization Potential, Electron Mobility, and Rate of Excitation Transfer in Condensed Matter," 5th Semin. Radiat. Chem. Jpn., Wako, May (1988).
  - 8) I. Kaneko, K. Eguchi-Kasai, T. Kosaka, K. Nakano, A. Maruhashi, and T. Takahashi: "DNA Lesion and Cell Death by  $\alpha$ -Particles and Nitrogen Ions," COSPAR 27th Plenary Meet., Helsinki, Jul. (1988).
  - 9) H. Sunaga, T. Agematsu, R. Tanaka, T. Sasaki, K. Yoshida, and I. Kohno: "Thin Cellulose-Triacetate Film Dosimeter," 25th Annu. Meet. Radioisotopes in the Physical Sciences and Industries, Tokyo, Jul. (1988).
  - 10) I. Kaneko, K. Eguchi-Kasai, T. Kosaka, K. Nakano, A. Maruhashi, and T. Takahashi: "DNA Lesion and Cell Death by  $\alpha$ -Particles and Nitrogen Ions," 27th Plenary Meet. Committee on Space Research, Helsinki, Finland, Jul. (1988).
  - 11) T. Kosaka, K. Eguchi-Kasai, and I. Kaneko: "DNA Damages Induced by Heavy Ions and Its Repair," RIKEN Symp., Yokohama, Aug. (1988).
  - 12) K. Suzuki, M. Watanabe, M. Suzuki, and I. Kaneko: "Lethal and Neoplastic Transforming Effects of High LET Radiations," RIKEN Symp., Yokohama, Aug. (1988).
  - 13) K. Maeda, Y. Sasa, K. Yoshida, H. Kusuyama, and M. Uda: "Multielemental Analysis of Human Spermatozoa and Seminal Plasma Using Particle Induced X-Ray Emission (PIXE) Spectroscopy," 57th Natl. Meet. Chem. Soc. Jpn., Sendai, Sep. (1988).
  - 14) Y. Sasa, K. Maeda, T. Kitamura, and M. Uda: "Application of PIXE to Materials Science, (1) Analysis of Thin Al Foils," 57th Natl. Meet. Chem. Soc. Jpn., Sendai, Sep. (1988).
  - 15) I. Kaneko, M. Watanabe, M. Suzuki, and K. Suzuki: "Transformation Effect of  $\alpha$ -Particles and Nitrogen Ions," 14th L.H. Fray Conf.—Low Dose Radiation-Biological Bases of Risk Assessment, Oxford, Sep. (1988).
  - 16) I. Kaneko, K. Eguchi-Kasai, T. Kosaka, and K. Sato: "A Comparison of DNA Double Strand Breaks Among Four Different Radiation-Sensitive Mammalian Cells," 47th Annu. Meet. Jpn. Cancer Soc., Tokyo, Sep. (1988).
  - 17) Y. Itoh, K. Kadota, H. Fukushima, N. Nonaka, and K. Tachi: "Study on Carbon, Boron and Oxygen in LEC-GaAs," 49th Fall Meet. Jpn. Soc. Appl. Phys., Toyama, Oct. (1988).
  - 18) M. Tachibana, T. Mukouyama, H. Adachi, K. Fuwa, Y. Sasa, and M. Uda: "Analysis of F K Satellite Spectra," '88 Fall Meet. Phys. Soc. Jpn., Hiroshima, Oct. (1988).
  - 19) M. Suzuki, K. Suzuki, M. Watanabe, and I. Kaneko: "Cellular Transformation Transformation by Heavy Ions," 31st Annu. Meet. Jpn. Radiation Research Soc., Hiroshima, Oct. (1988).
  - 20) T. Takahashi, F. Yatagai, T. Katayama, N. Imamura, and I. Nozaki: "Interpretation of Inactivation Cross of *E. coli* K-12 Series," 31th Annu. Meet. Jpn. Radation Research Soc., Hiroshima, Oct. (1988).
  - 21) K. Kimura, T. Suzuki, K. Uehara, and K. Watanabe: "Decay Measurement of Fast Emission of BaF<sub>2</sub> Single Crystal Excited by Heavy Ions," Fall Meet. Phys. Soc. Jpn., Hiroshima, Oct. (1988).
  - 22) K. Nakagawa, K. Kimura, A. Ejiri, and M. Nishikawa: "Photoionization Process of Anthracene in Super Critical State of Xe: Roles of Rydberg States," Fall Meet. Phys. Soc. Jpn., Hiroshima, Oct. (1988).
  - 23) K. Nakagawa, A. Ejiri, M. Nishikawa, and K. Kimura: "Solvation Effect of Super Critical Xe on Rydberg States and on Photoionization of Anthracene," Meet. Mol. Struc., Tokyo, Oct. (1988).
  - 24) M. Watanabe, M. Suzuki, K. Suzuki, I. Kaneko, and K. Nakano: "Neoplastic Transformation of Cultured Mammalian Cells by Cosmic Rays," 2nd Annu. Meet. Jpn. Soc. Biological Sciences in Space, Tokyo, Nov. (1988).
  - 25) I. Kaneko, K. Eguchi-Kasai, T. Kosaka, G. Okada, and K. Nakano: "Effects of Heavy Ions on DNA in Mammalian Cells," 2nd Annu. Meet. Jpn. Soc. Biological Sciences in Space, Tokyo, Nov. (1988).
  - 26) H. Kusuyama, K. Okada, K. Yoshida, K. Maeda, Y. Sasa, and M. Uda: "Trace Element Analysis of Human Spermatozoa and Seminal Plasma," 33rd Annu. Meet. Infertility Sod. Jpn., Kyoto, Nov. (1988).
  - 27) K. Kimura, K. Uehara, T. Suzuki, and K. Watanabe: "Measurement Technique of Fast Emission Decay by Heavy Ion Excitation," 31th Meet. Radiat. Chem. Jpn., Tokyo, Nov. (1988).
  - 28) K. Kimura: "Phenomena of Ionization and

- Excitation at High Density by Heavy Ion Irradiation," 2th Workshop Application of Radiation, Tokyo, Nov. (1988).
- 29) T. Takahashi, F. Yatagai, T. Kosaka, K. Nakano, and T. Kanai: "Dosimetry at RRC Biology Facility," RIKEN Symp. Studies on Materials Sciences, Atomic Processes, Nuclear Chemistry, and Radiobiology by RIKEN Ring Cyclotron, Wako, Dec. (1988).
  - 30) M. Suzuki, I. Kaneko, S. Yamashita, and S. Hashimoto: "The Combined Effects of *Cis*-Dichlorodiammineplatinum and Heavy Ions," RIKEN Symp., Wako, Dec. (1988).
  - 31) M. Watanabe, K. Suzuki, M. Suzuki, and I. Kaneko: "Neoplastic Transformation by Heavy Ions," RIKEN Symp., Wako, Dec. (1988).
  - 32) I. Kaneko, G. Okada, and H. Mitsui: "Mutation-Modifying Effects of Nicotin Nicotinamide and Inhibitors of Poly (ADP-ribose) Polymerase in Mammalian Cells," 3rd Int. Conf. Mechanisms of Antimutagenesis and Anticarcinogenesis, Ohito, Dec. (1988).
  - 33) K. Tachi, M. Aratani, T. Kato, M. Yanokura, T. Sato, M. Otsuka, and M. Tsujiguchi: "Light Element Depth Profiling by RILAC Applied to the Study on the Composition of Anodic Oxide Films on Titanium," 7th Symp. Ion Beam Technology, Tokyo, Dec. (1988).

## VIII. LIST OF OUTSIDE USERS AND THEIR THEMES

(Jan.-Dec. 1988)

- |   |  |
|---|--|
| 1) N. Nonaka<br>"Radiochemical Analysis of $^{16}\text{O}$ , $^{14}\text{N}$ ,<br>and $^{12}\text{C}$ in Si Crystal and GaAs" | Japan Chemical Analysis Center                               |
| 2) S. Hokuyo<br>"Radiation Damage of GaAs Solar Cells"  | Mitsubishi Electric Co., Ltd.                                |
| 3) H. Okazaki<br>"Radiation Damage of InP Solar Cells"  | Nippon Mining Co., Ltd.                                      |
| 4) T. Ohga<br>"Radiation Damage of Solar Cells"   | Nippon Telephone Telegram Co., Ltd.                          |
| 5) K. Tomii<br>"Improvement of Thyristors by Proton Irradiation"  | Semiconductor R & D Lab., Matsushita Electric Work Co., Ltd. |
| 6) H. Akiyama<br>"Improvement of Thyristors by Proton Irradiation"  | LSI Lab., Mitsubishi Electric Co., Ltd.                      |
| 7) M. Kitagawa<br>"Improvement of Thyristors by Proton Irradiation"   | Toshiba Co., Ltd.  |
| 8) Y. Shimizu<br>"Improvement of Thyristors by Proton Irradiation"  | Hitachi Co., Ltd.  |
| 9) A. Morio<br>"Study of Single Event Upset in Micro-processors by Bombarding $^{14}\text{N}$ Particles"                      | Japan Trust Center for Electronic Parts                      |
| 10) K. Ogura<br>"Test of Sensibility of CR39 Track Detector for High Energy Protons"  | Faculty of Engineering, Nippon University                    |
| 11) H. Arai<br>"Radiation Damage of Solar Cells"  | NEC Co., Ltd.  |

## IX. LIST OF SEMINARS

- (Jan.-Dec. 1988)
- 1) T. Tachibana, Waseda Univ. (Tokyo), 27 January  
“New Mass Formula and Improved Gross Theory of  $\beta$  Decay”
  - 2) S. Kinouchi, Tsukuba Univ. (Ibaraki), 10 February  
“Cranking Term Arising from Velocity-Dependent Potential and Comments on Super-Deformed Band”
  - 3) T. Kajino, Tokyo Metropolitan Univ. (Tokyo), 15 April  
“Big Bang Nucleosynthesis and the Role of Unstable Nuclei”
  - 4) S. Matsui, Hiroshima Univ. (Hiroshima), 27 April  
“Precise Measurement of  $^{177m}\text{Lu}$   $\gamma$  Rays by Means of Pulser”
  - 5) S. Tasaka, Gifu Univ. (Gifu), 25 May  
“Calibration of CR-39 Solid-State Detector by Means of RRC Beam”
  - 6) S.S. Kapoor, Bhabha Atomic Research Center (India), 31 May  
“Heavy-Ion Induced Fission and Fission-Like Reaction”
  - 7) H. Shengnian, Inst. Atomic Energy (China), 4 June  
“Neutron Induced Fission and Spontaneous Fission”
  - 8) S. Iida, Inst. Nuclear Study (Tokyo), 7 June  
“Berry Phase”
  - 9) D.H. Feng, Drexel Univ. (USA), 16 June  
“Dynamical Pauli Effect, Saturation of Nuclear Collectivity  $\alpha$  and the Fermion Dynamical Symmetry Model”
  - 10) Z. Yizhong, Inst. Atomic Energy (China), 22 June  
“Recent Progress in Fission Theory Based on Diffusion Model”
  - 11) Y. Miake, Brookheaven Natl. Lab. (USA), 29 July
  - 12) K. Kuroda, LAPP (France), 2 August  
“Development of Position Sensitive Photo-Multiplier”
  - 13) T. Murakami, Michigan State Univ. (USA), 3 August  
“Can We Measure the Temperature from the Population of Particle Unbound States ?”
  - 14) R.H. Siemssen, KVI (Netherlands), 3 August  
“Probing the Dynamics of Asymmetric Heavy-Ion Reactions with the K X-Ray Method”
  - 15) C.Y. Wong, Oakridge Natl. Lab. (USA), 30 August  
“Anomalous Positron Peaks in Heavy Ion Collisions”
  - 16) S. Yoshida, Yamagata Univ. (Yamagata), 20 September  
“Pre-Equilibrium Processes”
  - 17) N. Tajima, Univ. Tokyo (Tokyo), 11 October  
“K-Isomerism and  $\gamma$ -Softness”
  - 18) J. Alstad, Univ. Oslo (Norway), 11 November  
“New Development in the SISAK—Techniques for Studying Short Lived Nuclei—”
  - 19) K. Kimura, Kyushu Univ. (Fukuoka), 16 November  
“An Approach to Heavy Ion Particle Identification in Terms of Gas Counter”
  - 20) H. Wollnik, Univ. Giessen (West Germany), 21 November  
“Mass Separation of Short-Lived Nuclei by Recoil- and Ion-Source Separators”
  - 21) B. Heush, C.R.N. Strasbourg (France), 7 December  
“Study of Peripheral Collision for the  $^{40}\text{Ar} + ^{27}\text{Ag}$ ,  $^{\text{nat}}\text{Ti}$  at 44 MeV/n and  $^{40}\text{Ar} + ^{\text{nat}}\text{Ag}$  at 30 and 60 MeV/n by Inclusive and Exclusive Measurements at GANIL”
  - 22) S. Kinouchi, Inst. Nuclear Study (Tokyo), 13

- December  
"Effect of Velocity-Dependent Terms in Super-Deformed Nuclei"
- 23) Y. Yamamoto, Tsukuba Univ. (Ibaraki), 13 December  
"Quantum Theory of the Selfconsistent Collective Coordinate Method and Stability Problem"
- 24) T. Muto, Kyoto Univ. (Kyoto), 13 December  
"Pion Condensation in High Density Nuclear Matter and Neutron Star Phenomena"
- 25) K. Saotome, Tohoku Univ. (Miyagi), 13 December  
"Finite Temperature Nuclear Matter in TFD Formalism"

## X. LIST OF PERSONNEL

### Members of the Board

AMBE Fumitoshi 安部文敏  
 CHIBA Yoshiaki 千葉好明  
 INAMURA Takashi 稲村卓  
 KAMITSUBO Hiromichi 上坪宏道  
 KATSUMATA Koichi 勝又紘一  
 KOHNO Isao 河野功  
 MATSUOKA Masaru 松岡勝  
 SAKURAI Akira 桜井成  
 TANIHATA Isao 谷畠勇夫  
 YOKOO Hisaaki 横尾久明

AWAYA Yohko 栗屋容子  
 HASHIZUME Akira 橋爪朗  
 ISHIHARA Masayasu 石原正泰\*  
 KANEKO Ichiro 金子一郎  
 KIRA Akira 吉良爽  
 KURIHARA Osamu 栗原修  
 NAGAMINE Kanetada 永嶺謙忠  
 TAKAMI Michio 高見道生  
 WATANABE Tsutomu 渡部力

\* Chairman

### Cyclotron Operation and Maintenance Group

FUJITA Shin 藤田新  
 KAGEYAMA Tadashi 影山正  
 KOHNO Isao 河野功  
 TAKEBE Hideki 武部英樹

IKEGAMI Kumio 池上九三男  
 KOHARA Shigeo 小原重夫  
 OGAWARA Kiyoshi 萩原清

### Linac Operation and Maintenance Group

CHIBA Yoshiaki 千葉好明  
 IKEZAWA Eiji 池沢英二  
 KAMBARA Tadashi 神原正  
 KUBO Toshiyuki 久保敏幸  
 YANOKURA Minoru 矢野倉実

HEMMI Masatake 逸見政武  
 INOUE Toshihiko 井上敏彦  
 KASE Masayuki 加瀬昌之  
 MIYAZAWA Yoshitoshi 宮沢佳敏

### Scientific and Engineering Personnel

#### Cosmic Radiation Laboratory

IMAI Takashi 今井喬  
 MUNAKATA Kazuoki 宗像一起

KOHNO Tsuyoshi 河野毅

#### (Visitors)

HASEBE Nobuyuki 長谷部信行 (Fac. Gen. Educ., Ehime Univ.)  
 MURAKAMI Hiroyuki 村上浩之 (Fac. Sci., Rikkyo Univ.)  
 NAGATA Katsuaki 永田勝明 (Fac. Eng., Tamagawa Univ.)

NAKAMOTO Atsusi 中本 淳 (Fac. Sci., Rikkyo Univ.)  
 NISHIJIMA Kyoshi 西嶋恭司 (Sci. Eng. Res. Lab., Waseda Univ.)  
 YANAGIMACHI Tomoki 柳町朋樹 (Fac. Sci., Rikkyo Univ.)

## (Student)

KASHIWAGI Toshisuke 柏木利介 (Sci. Eng. Res. Lab., Waseda Univ.)

## Cyclotron Laboratory

BE Suck Hee 裴 碩喜  
 FUJITA Jiro 藤田二郎  
 GOTO Akira 後藤 彰  
 HATANAKA Kichiji 畑中吉治  
 INAMURA Takashi 稲村 卓  
 KAMITSUBO Hiromichi 上坪宏道  
 KOHNO Isao 河野 功  
 MORITA Kosuke 森田浩介  
 NAGASE Makoto 長瀬 誠  
 NAKANISHI Noriyoshi 中西紀喜  
 SAITO Motozo 斎藤始三  
 SHIKATA Takashi 四方隆史  
 TOYAMA Mitsuru 遠山 満  
 YAMAJI Shuhei 山路修平  
 YOKOYAMA Ichiro 横山一郎

FUJISAWA Takashi 藤沢高志  
 FUJITA Shin 藤田新  
 HARA Masahiro 原雅弘  
 IKEGAMI Kumio 池上九三男  
 KAGEYAMA Tadashi 影山正  
 KOHARA Shigeo 小原重夫  
 MATSUO Masayuki 松尾正之  
 NAGAOKA Ryutaro 長岡隆太郎  
 NAKAJIMA Shunji 中島諄二  
 OGAWARA Kiyoshi 萩原清  
 SASAKI Shigeki 佐々木茂樹  
 TAKEBE Hideki 武部英樹  
 WADA Takeshi 和田雄  
 YANO Yasushige 矢野安重

## (Visitors)

ANAYAMA Hiroshi 穴山汎 (Reliability Cent. Electronic Components of Japan)  
 CHOE Byung-Ha 趙炳夏 (KAIST, Korea)  
 EGUCHI-KASAI Kiyomi 江口(笠井)清美 (Inst. Basic Med. Sci., Univ. Tsukuba)  
 EJIRI Hiroyasu 江尻宏泰 (Dep. Phys., Osaka Univ.)  
 FUKUMOTO Sadayoshi 福本貞義 (KEK)  
 FURUNO Kohei 古野興平 (Inst. Phys. Tandem Accel. Cent., Univ. Tsukuba)  
 GOKA Tateo 五家建夫 (NASDA)  
 HARADA Kichinosuke 原田吉之助 (Nippon Energy K.K.)  
 HARADA Minoru 原田稔 (Reliability Cent. Electronic Components of Japan)  
 HAYASHI Nobuyuki 林伸行 (Electro Tech. Lab.)  
 HIRAKI Akio 平木昭夫 (Fac. Eng., Osaka Univ.)  
 HORIGUCHI Takayoshi 堀口隆良 (Dep. Phys., Hiroshima Univ.)  
 IKEDA Kiyomi 池田清美 (Dep. Phys., Niigata Univ.)  
 IKEGAMI Hidetsugu 池上栄胤 (RCNP, Osaka Univ.)  
 INOUE Makoto 井上信 (RCNP, Osaka Univ.)  
 ISOYA Akira 磯矢彰 (Sch. Sci., Tokai Univ.)  
 IWAMOTO Akira 岩本昭 (Japan Atomic Energy Res. Inst.)  
 IWASHITA Yoshihisa 岩下芳久 (Inst. Chem. Res., Kyoto Univ.)  
 KADOYA Shingo 角矢真吾 (Japan Gasoline Co.)  
 KANEKO Kumetaro 金子条太郎 (Inst. Nucl. Study, Univ. Tokyo)

KASAI Shunichi 河西俊一 (Japan Atomic Energy Res. Inst.)  
 KATAYAMA Ichiro 片山一郎 (RCNP, Osaka Univ.)  
 KATORI Kenji 鹿取謙二 (Dep. Phys., Osaka Univ.)  
 KATSURAGAWA Hidetsugu 桂川秀嗣 (Dep. Phys., Toho Univ.)  
 KIKUCHI Fumio 菊地文男 (Coll. Arts Sci., Univ. Tokyo)  
 KISHIMOTO Teruo 岸本照夫 (Dep. Phys., Univ. Tsukuba)  
 KOBAYASHI Shinsaku 小林晨作 (Dep. Phys., Kyoto Univ.)  
 KOHMOTO Susumu 河本進 (Univ. Electro-Commun.)  
 KONDO Michiya 近藤道也 (RCNP, Osaka Univ.)  
 KOSAKO Toshiso 小佐古敏莊 (Atomic Energy Res. Cent., Univ. Tokyo)  
 KOWATA Mitsuyoshi 小綿光喜 (Reliability Cent. Electronic Components of Japan)  
 KUDO Hisaaki 工藤久昭 (Dep. Chem., Niigata Univ.)  
 KUSAKA Takuya 日下卓也 (Kobe Steel, Ltd.)  
 LEE Young Pak 李英白 (RIST, Korea)  
 MATSUKI Seishi 松木征史 (Inst. Chem. Res., Kyoto Univ.)  
 MINOWA Tatsuya 箕輪達哉 (Dep. Phys., Toho Univ.)  
 MIURA Iwao 三浦 岩 (RCNP, Osaka Univ.)  
 MIYADE Hiroki 宮出宏紀 (Sumitomo Heavy Ind., Ltd.)  
 MIYATAKE Hiroari 宮武宇也 (Fac. Sci., Osaka Univ.)  
 MORIMOTO Yoshihide 森本佳秀 (Kobe Steel, Ltd.)  
 MORIO Atsuo 森尾篤夫 (Reliability Cent. Electronic Components of Japan)  
 MUKHOPADHYAY, N.K. (V.E.G. Cent., B.A.R.C., India)  
 MURAYAMA Toshiyuki 村山利幸 (Tokyo Univ. Mercantile Marine)  
 NAGAI Yasuki 永井泰樹 (Dep. Appl. Phys., Tokyo Inst. Technol.)  
 NAGAMIIYA Shoji 永宮正治 (Dep. Phys., Univ. Tokyo)  
 NAKAHARA Hiromichi 中原弘道 (Dep. Chem., Tokyo Metrop. Univ.)  
 NAKAI Koji 中井浩二 (KEK)  
 NAKAJIMA Kazuhisa 中島一久 (KEK)  
 NAKAMURA Shinya 中村慎也 (Reliability Cent. Electronic Components of Japan)  
 NAKAMURA Takashi 中村尚司 (Cyclotron Radioisot. Cent., Tohoku Univ.)  
 NAKAMURA Yoshiteru 中村義輝 (Japan Atomic Energy Res. Inst.)  
 NISHII Masanobu 西井正信 (Japan Atomic Energy Res. Inst.)  
 NOMURA Toru 野村亨 (Inst. Nucl. Study, Univ. Tokyo)  
 NONAKA Hideki 野中英生 (Sumitomo Heavy Ind., Ltd.)  
 ODERA Masatoshi 小寺正俊 (Sci. Eng. Res. Lab., Waseda Univ.)  
 ONISHI Jun-ichi 大西純一 (KAWASAKI Heavy Ind., Ltd.)  
 ONISHI Naoki 大西直毅 (Dep. Phys., Coll. Gen. Educ., Univ. Tokyo)  
 ONUMA Hajime 大沼甫\* (Dep. Phys., Tokyo Inst. Technol.)  
 OTA Shigemi 太田滋生 (KEK)  
 PARK Eng Soo (POSTECH, Korea)  
 SAKAI Hideyuki 酒井英行 (RCNP, Osaka Univ.)  
 SAKAMOTO Hiroyuki 坂本浩幸 (Ishikawajima-Harima Heavy Ind., Co., Ltd.)  
 SAKAMOTO Isao 坂本勲 (Electro Tech. Lab.)  
 SAKURADA Yuzo 桜田勇三 (ULVAC Co.)  
 SASUGA Tsuneo 賴家恒男 (Japan Atomic Energy Res. Inst.)  
 SATO Kenichi 佐藤憲一 (Div. Phys., Tohoku Coll. Pharm.)

- SHIMANO Yosuke 島野洋介 (NASDA)  
 SHIMAZU Mitsuyoshi 島津備愛 (Dep. Phys., Toho Univ.)  
 SHINOZUKA Tsutomu 篠塚勉 (Cyclotron Radioisot. Cent., Tohoku Univ.)  
 SHIRAI SHI Haruki 白石春樹 (Natl. Res. Inst. Metals)  
 SUEKI Keisuke 末木啓介 (Inst. Nucl. Study, Univ. Tokyo)  
 SUGAI Isao 菅井勲 (Inst. Nucl. Study, Univ. Tokyo)  
 SUNAGA Hiromi 須永博美 (Japan Atomic Energy Res. Inst.)  
 TAKEGOSHI Hidekuni 竹腰秀邦 (Inst. Chem. Res., Kyoto Univ.)  
 TAKEMASA Tadashi 武政尹士 (Dep. Phys., Saga Univ.)  
 TAKI, G.S. (V.E.G., B.A.R.C., India)  
 TAKIGAWA Noboru 滝川昇 (Dep. Phys., Tohoku Univ.)  
 TAMAGAKI Ryozo 玉垣良三 (Dep. Phys., Kyoto Univ.)  
 TANAKA Hitoshi 田中均 (Japan Gasoline Co.)  
 TANAKA Jinichi 田中仁市 (Inst. Nucl. Study, Univ. Tokyo)  
 TANAKA Koki 田中幸基 (Nippon Steel Corp.)  
 TASAKA Shigeki 田坂茂樹 (Fac. Educ., Gifu Univ.)  
 TOMIMASU Takio 富增多喜夫 (Electro Tech. Lab.)  
 TORIYAMA Tamotsu 鳥山保 (Dep. Appl. Phys., Tokyo Inst. Technol.)  
 TORIZUKA Kanji 鳥塚莞爾 (Fac. Med., Kyoto Univ.)  
 TSUKIJI Masaru 築地優 (NEC Corp.)  
 TSUMAKI Koji 妻木孝治 (Hitachi, Ltd.)  
 TSUNEMOTO Hiroshi 常元博 (Natl. Inst. Radiol. Sci.)  
 VALLI Kalevi (Dep. Phys., Jyvaskyla Univ., Finland)  
 WAKISHIMA Susumu 脇島進 (Reliability Cent. Electronic Components of Japan)  
 WANG Zhen (Inst. Mod. Phys., Acad. Sin., China)  
 WATANABE Hiroshi 綿鍋博志 (Electro Tech. Lab.)  
 YAMASU Kazushige 弥益和重 (Mitsubishi Heavy Ind., Ltd.)  
 YAMAZAKI Takashi 山崎魏 (RCNP, Osaka Univ.)  
 YOKOTA Wataru 横田涉 (Japan Atomic Energy Res. Inst.)  
 YOKOUCHI Shigeru 横内茂 (Osaka Vacuum, Ltd.)  
 YOSHIDA Katsuhisa 吉田克久 (Mitsubishi Electric, Co.)  
 YOSHIDA Nobuaki 吉田宣章 (Dep. Phys., Univ. Tokyo)  
 YOSHIDA Shiro 吉田思郎 (Dep. Phys., Tohoku Univ.)  
 YOSHINAGA Naotaka 吉永尚孝 (Comput. Cent., Univ. Tokyo)  
 YOSHIYUKI Takeshi 吉行建 (Toshiba, Co.)

---

\* Visiting Professor

(Students)

- HARADA Shigenobu 原田重信 (Dep. Appl. Phys., Tokyo Inst. Technol.)  
 ISHII Yasuyuki 石井保行 (Coll. Hum. Sci., Nihon Univ.)  
 KOBAYASHI Takayuki 小林貴之 (Fac. Sci., Tokyo Metrop. Univ.)  
 KUNIHIRO Kazuaki 国弘和明 (Dep. Appl. Phys., Tokyo Inst. Technol.)  
 KOIZUMI Mitsuo 小泉光生 (Dep. Phys., Hiroshima Univ.)  
 MIURA Atsushi 三浦厚 (Coll. Hum. Sci., Nihon Univ.)  
 OSAKI Mitsuhiro 大崎光洋 (Fac. Sci. Eng., Chuo Univ.)

SHIMOMURA Koichiro 下村浩一郎 (Dep. Phys., Kyoto Univ.)  
 SUZUKI Mitsuru 鈴木 充 (Fac. Sci., Toho Univ.)  
 TORII Yoshinari 鳥居良成 (Dep. Appl. Phys., Tokyo Inst. Technol.)  
 YOSHIDA Atsushi 吉田 敦 (Dep. Appl. Phys., Tokyo Inst. Technol.)

#### Linear Accelerator Laboratory

CHIBA Toshiya 千葉利哉	CHIBA Yoshiaki 千葉好明
HEMMI Masatake 逸見政武	INOUE Toshihiko 井上敏彦
KAMBARA Tadashi 神原 正	KASE Masayuki 加瀬昌之
KUBO Toshiyuki 久保敏幸	KUMAGAI Hidekazu 熊谷秀和
MIYAZAWA Yoshitoshi 宮沢佳敏	NAKAGAWA Takahide 中川孝秀
SUZUKI Takeshi 鈴木 建	TAKEUCHI Sachiko 竹内幸子
TANIHATA Isao 谷畑勇夫	TONUMA Tadao 戸沼正雄
YANOKURA Minoru 矢野倉 実	YOSIDA Koichi 吉田光一

#### (Visitors)

FUJIWARA Ichiro 藤原一郎 (Inst. Atomic Energy, Kyoto Univ.)  
 ITO Noriaki 伊藤憲昭 (Dep. Cryst. Mater., Nagoya Univ.)  
 KIKUCHI Jun 菊地順 (Sci. Eng. Res. Lab., Waseda Univ.)  
 LIU Wei Ping 柳平 (Inst. Atomic Energy, China)  
 NONAKA Hideki 野中英生 (Sumitomo Heavy Ind., Ltd.)  
 SUGAWARA Masahiko 菅原昌彦 (Fundam. Sci., Chiba Inst. Technol.)  
 YAMAGUCHI Hiromi 山口裕美 (Sci. Eng. Res. Lab., Waseda Univ.)

#### (Students)

FUKUDA Mitsunori 福田光順 (Fac. Sci., Tokyo Inst. Technol.)  
 ITO Tatsuya 伊藤達也 (Sci. Eng. Res. Lab., Waseda Univ.)

#### Radiation Laboratory

ASAHI Koichiro 旭耕一郎	GONO Yasuyuki 郷農靖之
HASHIZUME Akira 橋爪朗	ICHIHARA Takashi 市原卓
ISHIHARA Masayasu 石原正泰	IZUMO Koichi 出雲光一
KONNO Satoshi 金野智	TAKAHASHI Tan 高橋旦
TENDO Yoshihiko 天道芳彥	

#### (Visitors)

ABE Yasuhisa 阿部恭久 (Res. Inst. Fundam. Phys., Kyoto Univ.)  
 ADACHI Minoru 足立 實 (Dep. Appl. Phys., Tokyo Inst. Technol.)  
 ANDO Yoshiaki 安藤嘉章 (Dep. Phys., Rikkyo Univ.)  
 Didier Beaumel (Inst. Phys. Nucl., Orsay, France)  
 DOKE Tadayoshi 道家忠義 (Sci. Eng. Res. Lab., Waseda Univ.)  
 ENDO Saburo 遠藤三郎 (Fac. Eng., Sci. Univ. Tokyo)  
 FUJIOKA Manabu 藤岡学 (Dep. Phys., Tohoku Univ.)  
 HAMA Hiroyuki 浜広幸 (Dep. Phys., Tokyo Inst. Technol.)

HASEGAWA Takeo 長谷川武夫 (Inst. Nucl. Study, Univ. Tokyo)  
 HITACHI Akira 月出 章 (Sci. Eng. Res. Lab., Waseda Univ.)  
 HWANG Han Yull 黃 翰悅 (Dep. Phys., Yonsei Univ. Korea)  
 ICHIMURA Munetake 市村宗武 (Coll. Gen. Educ., Univ. Tokyo)  
 IEKI Kazuo 家城和夫 (Fac. Sci., Rikkyo Univ.)  
 KAGEYAMA Mayumi 影山眞弓 (Hoyo Corp.)  
 KASAGI Jirota 笠木治郎太 (Fac. Sci., Tokyo Inst. Technol.)  
 KATO Norihisa 加藤哲久 (Dep. Phys., Kyushu Univ.)  
 KATO Seigo 加藤静吾 (Fac. Lib. Arts, Yamagata Univ.)  
 KATORI Kenji 鹿取謙二 (Fac. Sci., Osaka Univ.)  
 KAWAKAMI Hirokane 川上宏金 (Inst. Nucl. Study, Univ. Tokyo)  
 KITAO Kensuke 喜多尾憲助 (Natl. Inst. Radiol. Sci.)  
 KUBONO Sigeru 久保野 茂 (Inst. Nucl. Study, Univ. Tokyo)  
 KUBOTA Shinzou 奎田信三 (Fac. Sci., Rikkyo Univ.)  
 KUSAKARI Hideshige 草刈英榮 (Fac. Educ., Chiba Univ.)  
 LEE Sang Mu 李 相茂 (Inst. Phys., Univ. Tsukuba)  
 MASUDA Kimiaki 増田公明 (Sch. Sci. Eng., Waseda Univ.)  
 MOTOBAYASHI Tohru 本林 透 (Fac. Sci., Rikkyo Univ.)  
 MURAKAMI Takeshi 村上 健 (Dep. Phys., Tokyo Inst. Technol.)  
 NAGAI Yasuki 永井泰樹 (Fac. Sci., Tokyo Inst. Technol.)  
 NAGASHIMA Yasuo 長島泰夫 (Dep. Phys., Univ. Tsukuba)  
 NAKAYAMA Shintarou 中山信太郎 (Coll. Gen. Educ., Univ. Tokushima)  
 OHNUMA Hajime 大沼 甫 (Fac. Sci., Tokyo Inst. Technol.)  
 ORIHARA Hikonojo 織原彥之亟 (Cyclotron and Rakioisot. Cent., Tohoku Univ.)  
 OSHIMA Masumi 大島真澄 (Japan Atomic Energy Res. Inst.)  
 OYAIZU Mitsuhiro 小柳津充広 (Inst. Nucl. Study, Univ. Tokyo)  
 RUAN (GEN) Jian-zhi 阮 建治 (Dep. Phys., Rikkyo Univ.)  
 SAKAGUCHI Harutaka 坂口治隆 (Dep. Phys., Kyoto Univ.)  
 SAWAMOTO Takeyuki 泽本健之 (Hoya Corp.)  
 SHIBAMURA Eido 柴村英道 (Saitama Coll. Health)  
 SHIMIZU Hajime 清水 肇 (Fac. Sci., Tokyo Inst. Technol.)  
 SHIMOURA Susumu 下浦 享 (Fac. Sci., Univ. Tokyo)  
 SHIRATO Shoji 白土鉢二 (Dep. Phys., Rikkyo Univ.)  
 SUGAWARA Masahiko 菅原昌彦 (Fundam. Sci., Chiba Inst. Technol.)  
 TAKAHASHI Noriaki 高橋憲明 (Coll. Gen. Educ., Osaka Univ.)  
 TAKIGAWA Noboru 滝川 昇 (Dep. Phys., Tohoku Univ.)  
 TOKI Hiroshi 土岐 博 (Dep. Phys., Tokyo Metrop. Univ.)  
 YAMAYA Takashi 山屋 堯 (Dep. Phys., Tohoku Univ.)  
 YASUE Masaharu 安江正治 (Inst. Nucl. Study, Univ. Tokyo)  
 YOSHIZAWA Yasukazu 吉沢康和 (Dep. Phys., Hiroshima Univ.)

## (Students)

FUJIWARA Hideaki 藤原英明 (Inst. Phys., Univ. Tsukuba)  
 FUKUDA Mitsunori 福田光順 (Fac. Sci., Tokyo Inst. Technol.)  
 ICHINOSE Hideo 市之瀬秀夫 (Grad. Sch. Sci. Eng., Waseda Univ.)  
 ITO Tatsuya 伊藤達也 (Grad. Sch. Sci. Eng., Waseda Univ.)

IWASA Naohito 岩佐直仁 (Dep. Phys., Rikkyo Univ.)  
 JEONG S.C. 鄭淳讚 (Inst. Phys., Univ. Tsukuba)  
 KOGUCHI Masanari 高口雅成 (Dep. Appl. Phys., Tokyo Inst. Technol.)  
 MIZOTA Takeshi 溝田武志 (Inst. Phys., Univ. Tsukuba)  
 NAKAMURA Takashi 中村隆司 (Fac. Sci., Univ. Tokyo)  
 OGIWARA Masahiro 萩原正弘 (Dep. Phys., Rikkyo Univ.)  
 OGIWARA Mitsuhiro 萩原光彦 (Inst. Phys., Univ. Tsukuba)  
 OKUMURA Susumu 奥村進 (Inst. Phys., Univ. Tsukuba)  
 PU Y.H. 蒲越虎 (Inst. Phys., Univ. Tsukuba)  
 SAKURAI Mikio 桜井幹夫 (Dep. Phys., Tokyo Inst. Technol.)  
 SHIBUYA Shinji 渋谷真二 (Dep. Phys., Rikkyo Univ.)  
 TAKANASHI Hidehiko 高梨英彦 (Fac. Sci., Tokyo Inst. Technol.)  
 TAMURA Akitoshi 田村彰敏 (Grad. Sch. Ookayama, Tokyo Inst. Technol.)  
 UTSUMI Motoharu 内海資元 (Grad. Sch. Sci. Eng., Waseda Univ.)

## Atomic Processes Laboratory

ANDO Kozo 安藤剛三	AWAYA Yohko 粟屋容子
HINO Kenichi 日野健一	KAMBARA Tadashi 神原正
KANAI Yasuyuki 金井保之	NISHIDA Masami 西田雅美
SHIMAMURA Isao 島村勲	WATANABE Tsutomu 渡部力

## (Visitors)

FUJIMA Kazumi 藤間一美 (Dep. Phys., Chuo Univ.)  
 HARA Shunsuke 原俊介 (Dep. Phys., Univ. Tsukuba)  
 HITACHI Akira 月出章 (Inst. Sci. Technol., Waseda Univ.)  
 ISHII Keishi 石井慶之 (Dep. Eng. Sci., Kyoto Univ.)  
 ISOZUMI Yasuhito 五十樓泰人 (Radioisot. Res. Cent., Kyoto Univ.)  
 ITO Shin 伊藤真 (Radioisot. Res. Cent., Kyoto Univ.)  
 ITOH Yoh 伊東陽 (Fac. Sci., Josai Univ.)  
 IWAI Masahiro 岩井正博 (Theor. Div., Inst. Mol. Sci.)  
 KARASHIMA Shosuke 唐島照介 (Dep. Electron. Eng., Tokyo Univ. Sci.)  
 KAWATSURA Kiyoshi 川面澄 (Japan Atomic Energy Res. Inst.)  
 KIMURA Mineo 季村峯生 (Argonne Natl. Lab.)  
 KOIKE Fumihiro 小池文博 (Sch. Med., Kitasato Univ.)  
 KOIZUMI Tetsuo 小泉哲夫 (Dep. Phys., Rikkyo Univ.)  
 KOYAMA Naoto 小山直人 (Dep. Eng. Phys., Univ. Electro-Commun.)  
 KUROKI Kenro 黒木健郎 (Natl. Res. Inst. Police Sci.)  
 MATSUO Takashi 松尾崇 (Dep. Pathol., Tokyo Med. Dent. Univ.)  
 MATSUZAWA Michio 松澤通生 (Dep. Eng. Phys., Univ. Electro-Commun.)  
 MIZOGAWA Tatsumi 溝川辰巳 (Fac. Sci., Saitama Univ.)  
 NOBLE J. Cliff (Daresbury Lab., England)  
 OHSAKI Akihiko 大崎明彦 (Inst. Mol. Sci.)  
 OHTANI Shunsuke 大谷俊介 (Inst. Plasma Phys., Nagoya Univ.)  
 OKUNO Kazuhiko 奥野和彦 (Dep. Phys., Tokyo Metrop. Univ.)  
 SATO Hiroshi 佐藤浩史 (Dep. Phys., Ochanomizu Univ.)

SATO Kuninori 佐藤国憲 (Inst. Plasma Phys., Nagoya Univ.)  
 SCHMIDT-BÖCKING Horst (Inst. Kern Phys., Univ. Frankfurt)  
 SHIBATA Hiromi 柴田裕美 (Res. Cent. Nucl. Sci. Technol., Univ. Tokyo)  
 SHIMA Kunihiro 島 邦博 (Tandem Accel. Cent., Univ. Tsukuba)  
 SHIMAKURA Noriyuki 島倉紀之 (Gen. Educ. Dep., Niigata Univ.)  
 SUZUKI Hiroshi 鈴木 洋 (Dep. Phys., Sophia Univ.)  
 TAKAGI Shoji 高木祥示 (Dep. Phys., Toho Univ.)  
 TANIAS Monterio (Dep. Math., Royal Holloway and Bedfrod New Coll., England)  
 TAWARA Hiroyuki 傑 博之 (Inst. Plasma Phys., Nagoya Univ.)  
 TERASAWA Michitaka 寺沢倫孝 (Himeji Inst. Technol.)  
 TSURUBUCHI Seiji 鶴淵誠二 (Fac. Technol., Tokyo Univ. Agric. Technol.)  
 URAKAWA Junji 浦川順治 (Natl. Lab. High Energy Phys.)  
 VOGT Hans G. (Max Planck Inst., Heidelberg)  
 WAKIYA Kazuyoshi 脇谷一義 (Dep. Phys., Sophia Univ.)  
 YAMAZAKI Yasunori 山崎泰規 (Res. Lab. Nucl. Reactor, Tokyo Inst. Technol.)

## (Students)

NISHIMURA Hisashi 西村 久 (Dep. Phys., Tokai Univ.)  
 OHTA Ken 太田 賢 (Dep. Phys., Sophia Univ.)  
 SAKAUE Hiroyuki 坂上裕之 (Dep. Phys., Sophia Univ.)

## Metal Physics Laboratory

ISHIDA Katsuhiko 石田勝彦	KOYAMA Akio 小山昭雄
MATSUZAKI Teiichiro 松崎禎市郎	NAGAMINE Kanetada 永嶺謙忠
SHIOTANI Nobuhiro 塩谷亘弘	YAGI Eiichi 八木栄一

## (Visitors)

MIYAKE Yasuhiro 三宅康博 (Meson Sci. Lab., Univ. Tokyo)  
 TANAKA Koki 田中幸基 (Nippon Steel Corp.)  
 TORIKAI Eiko 鳥養映子 (Fac. Eng., Yamanashi Univ.)

## (Student)

ISHIKAWA Hiroshi 石川 浩 (Fac. Sci., Sci. Univ. Tokyo)

## Magnetic Materials Laboratory

OKADA Takuya 岡田卓也	SAKAI Nobuhiko 坂井信彦
-------------------	---------------------

## (Visitors)

YAMADAYA Tokio 山田谷時夫 (Fac. Lit. Sci., Yokohama City Univ.)  
 ASAI Kichizo 浅井吉藏 (Fac. Technol., Univ. Electro-Commun.)

## Plasma Physics Laboratory

ISHIBE Yukio 石部行雄	ISHII Shigeyuki 石井成行
-------------------	----------------------

OKAZAKI Kiyohiko 岡崎清比古  
SAKAMOTO Yuichi 坂本 雄一

OYAMA Hitoshi 大山 等  
YANO Katsuki 矢野勝喜

(Visitors)

SUGIYAMA Kazuo 杉山和男 (Fac. Eng., Saitama Univ.)  
YAMASHINA Toshiro 山科俊郎 (Fac. Eng., Hokkaido Univ.)

#### Semiconductor Laboratory

(Visitor)

AONO Keiko 青野桂子 (Coll. Lib. Arts, Kitasato Univ.)

#### Biophysical Chemistry Laboratory

(Visitor)

DAI Yisheng 戴 義生 (Inst. Opt. Electron., Acad. Sin., China)

#### Inorganic Chemical Physics Laboratory

KOBAYASHI Masayoshi 小林雅義  
SASA Yoshihiko 佐々嘉彦

MAEDA Kuniko 前田邦子  
TAKAMI Michio 高見道生

(Visitors)

ISHII Keizo 石井慶造 (Cyclotron Radioisot. Cent., Tohoku Univ.)  
KUSUYAMA Hiroyuki 楠山弘之 (Saitama Med. Sch.)  
MUKOUYAMA Takashi 向山毅 (Inst. Chem. Res., Kyoto Univ.)  
UDA Masayuki 宇田応之 (Dep. Mater. Sci., Waseda Univ.)  
FUKUDA Yukio 福田行男 (Coll. Lib. Arts, Kobe Univ.)  
MIZUGAI Yoshihiro 水谷由宏 (Dep. Phys., Sophia Univ.)  
SUZUKI Atsuyuki 鈴木篤之 (Dep. Nucl. Eng., Univ. Tokyo)

(Student)

MAEDA Haruka 前田はるか (Dep. Eng., Tokyo Univ.)

#### Radiochemistry Laboratory

AMBE Fumitoshi 安部文敏  
ARATANI Michi 荒谷美智  
IWAMOTO Masako 岩本正子

AMBE Shizuko 安部静子  
ITOH Yoshiko 伊東芳子  
OHKUBO Yoshitaka 大久保嘉高

(Visitors)

ENDO Kazutoyo 遠藤和豊 (Fac. Sci., Tokyo Metrop. Univ.)  
FUKUSHIMA Hiroto 福嶋浩人 (Japan Chemical Analysis Cent.)  
IMAI Masato 今井正人 (Komatsu Electronic Metals Co., Ltd.)  
IMURA Ryo 井村亮 (Cent. Res. Lab., Hitachi, Ltd.)

KADOTA Yoshinori 角田佳績 (Sumitomo Metal Mining Co., Ltd.)  
 KATADA Motomi 片田元己 (Fac. Sci., Tokyo Metrop. Univ.)  
 KATO Hajime 加藤 一 (Fac. Educ., Yamanashi Univ.)  
 NONAKA Nobuhiro 野中信博 (Japan Chemical Analysis Cent.)  
 OOHIRA Shigeo 大平重男 (Nikkei Techno Res. Co., Ltd.)  
 SAITO Kazuo 斎藤和男 (Toshiba Corp., R & D Cent.)  
 SAKAI Youichi 酒井陽一 (Fac. Sci., Univ. Tokyo)  
 SUEHIRO Makiko 末広牧子 (Tokyo Metrop. Geriatric Hospital)  
 SUGAI Isao 菅井 黙 (Inst. Nucl. Study, Univ. Tokyo)  
 TOMINAGA Takeshi 富永 健 (Fac. Sci., Univ. Tokyo)  
 WATANABE Yasuo 渡辺裕夫 (Fac. Sci., Tokyo Metrop. Univ.)

## (Students)

KOBAYASHI Yoshio 小林義男 (Fac. Sci., Tokyo Metrop. Univ.)  
 KUBO Kenya 久保謙哉 (Fac. Sci., Univ. Tokyo)  
 MISHIMA Kenji 三嶋謙二 (Fac. Sci., Univ. Tokyo)  
 NAKADA Masami 中田正美 (Fac. Sci., Tokyo Metrop. Univ.)  
 Qui Qi 邱 齐 (Res. Lab. Nucl. React., Tokyo Inst. Technol.)  
 TACHI Kouju 館 弘樹 (Fac. Metall., Shibaura Inst. Technol.)  
 YU Byon Gon 俞 炳坤 (Res. Lab. Nucl. React., Tokyo Inst. Technol.)

## Chemical Dynamics Laboratory

KIMURA Kazuie 木村一宇

## (Visitor)

ITO Yasuo 伊藤泰男 (Res. Cent. Nucl. Sci. Technol., Univ. Tokyo)

## (Students)

SUZUKI Takayoshi 鈴木隆敬 (Dep. Phys., Chuo Univ.)  
 UEHARA Keiji 上原桂二 (Dep. Phys., Chuo Univ.)  
 WATANABE Kazuhiro 渡辺一弘 (Dep. Phys., Chuo Univ.)

## Radiobiology Laboratory

KANEKO Ichiro 金子一郎

NAKANO Kazushiro 中野和城

## (Visitors)

BAVERSTOCK Keith F. (Rasiobiol. Unit, Med. Res. Counc., U.K.)  
 EGUCHI-KASAI Kiyomi 江口(笠井)清美 (Inst. Basic Med. Sci., Univ. Tsukuba)  
 KANAI Tatsuaki 金井達明 (Natl. Inst. Radiol. Sci.)  
 MARUHASHI Akira 丸橋晃 (Inst. Clin. Med., Univ. Tsukuba)  
 McINTYRE Cindy L. (Radiobiol. Unit, Med. Res. Counc., U.K.)  
 SUZUKI Keiji 鈴木啓司 (RI Cent., Fac. Med., Yokohama City Univ.)  
 WATANABE Masami 渡辺正己 (RI Cent., Fac. Med., Yokohama City Univ.)  
 YAMASHITA Shoji 山下昌次 (Natl. Saitama Hospital)

(Students)

KOSAKA Toshifumi 小坂俊文 (Dep. Vet. Radiol., Nihon Univ.)  
SUZUKI Masao 鈴木雅雄 (Fac. Med., Keio Univ.)

Safety Control Affairs Office

KAGAYA Satoru 加賀屋 悟  
KURIHARA Osamu 栗原 修  
MIYAGAWA Makoto 宮川真言  
SAWA Hiroshi 澤 宏  
USUBA Isao 薄葉 勲

KATOU Takeo 加藤武雄  
MATSUZAWA Yasuhide 松沢安秀  
SAKAMOTO Ichiro 坂本一郎  
SHINOHARA Shigemi 篠原茂己

Surface Characterization Center

IWAKI Masaya 岩木正哉  
SAKAIKI Hideo 坂入英雄

(Visitor)

FUJIHANA Takanobu 藤花隆宣 (Advanced Technology Inc.)

(Student)

KOBAYASHI Kenzo 小林健三 (Fac. Eng. Sci., Osaka Univ.)

Laser Science Research Group

NAMBA Susumu 難波 進

## AUTHOR INDEX

- ABE Ryo 阿部 亮 2,215  
AIHARA Toshimitsu 藍原利光 4  
AKAGI Hiroyasu 赤木宏安 2  
AMBE Fumitoshi 安部文敏 83,121,122,124,125,  
127,150,152  
AMBE Shizuko 安部静子 125,127,150  
ANDO Kozo 安藤剛三 70  
ANDO Yoshiaki 安藤嘉章 18,174  
AOKI Ichiro 青木伊知郎 288  
AONO Keiko 青野桂子 99  
AONO Masakazu 青野正和 91  
ARAI Eiichi 新井栄一 109  
ARATANI Michi 荒谷美智 109,111,113,115  
ASAI Kichizo 浅井吉蔵 84,121,122,125  
AWAYA Yohko 粟屋容子 54,55,62,68,70,72,  
74,149  
BE Suck Hee 裴 碩喜 199,276,279,281,283,286,  
288,290,292  
BARVERSTOCK K.F. 139  
BOHNE Wolfgang 164  
CHIBA Toshiya 千葉利哉 149  
CHIBA Yoshiaki 千葉好明 4  
CHIHARA Teiji 千原貞次 124  
DOKE Tadayoshi 道家忠義 10,168,170,172  
EGUCHI-KASAI Kiyomi 江口(笠井)清美 133  
EKUNI Katsuaki 江国克昭 12  
ENDO Kazutoyo 遠藤和豊 121,152  
FUJIHANA Takanobu 藤花隆宣 93,95  
FUJIMA Kazumi 藤間一美 45  
FUJIMOTO Takashi 藤本 孝 52  
FUJISAWA Takashi 藤沢高志 196,211,222,225  
FUJITA Jirou 藤田二郎 184  
FUJITA Shin 藤田 新 301,303,307  
FUJIWARA Hideaki 藤原英明 18,157,166  
FUKUDA Mitsunori 福田光順 8,10  
FUKUSHIMA Hiroto 福嶋浩人 107  
GOTO Akira 後藤 彰 2,202,203,205,207,209,  
211,213,215  
227,231,235,238,  
242,245,248,253,  
259,265,268,271,  
273,295,297,299  
HARA Masahiro 原 雅弘 49  
HARA Shunsuke 原 俊介 49  
HASEBE Hiroo 長谷部裕雄 4  
HASEBE Nobuyuki 長谷部信行 10,168,170,172  
HASHIMOTO Hirokazu 橋本宏和 115  
HASHIMOTO Iwao 橋本 巍 86  
HASHIZUME Akira 橋爪 朗 20,21,187,189,  
191,194  
HATA Kazuhiro 泰 和博 18  
HATANAKA Kichiji 畑中吉治 2,133,148,202,  
219,222,225  
HAYAKAWA Shun-ichiro 早川俊一郎 148  
HAYASHI Nobuyuki 林 伸行 105  
HEMMI Masatake 逸見政武 4  
HINO Ken-ichi 日野健一 35,38,40  
HITACHI Akira 月出 章 54,55  
HOSHINO Tetsuro 星野哲郎 178  
ICHIHARA Takashi 市原 卓 8,144,148  
ICHIKAWA Shinichi 市川進一 20,21  
IEKI Kazuo 家城和夫 18,174  
IMURA Hideki 飯村秀紀 20,21  
IKEGAMI Kumio 池上九三男 199,202,213  
IKEGAMI Yuji 池上祐二 133,152  
IKEZAWA Eiji 池沢英二 4,219  
IMAI Takashi 今井 喬 168,172  
IMURA Ryo 井村 亮 109  
INABA Takayuki 稲葉貴之 74  
INAMURA Takashi 稲村 卓 20,21,144,176,  
178,180,182,307  
INOUE Koji 井上浩司 268  
INOUE Toshihiko 井上敏彦 4  
ISHIDA Katsuhiko 石田勝彦 153,155  
ISHIHARA Masayasu 石原正泰 18,148  
ISHIHARA Takeshi 石原 武 49  
ISHII Keizo 石井慶造 60  
ISHII Shigeyuki 石井成行 222,225  
ISHIKAWA Hiroshi 石川 浩 79,81  
ISHIKAWA Toshiyuki 石川俊行 2  
ISSHIKI Hiroshi 一色 博 2  
ITO Tatsuya 伊藤達也 10  
ITO Susumu 伊藤 進 102  
ITOH Yoshiko 伊東芳子 107  
IWAKI Masaya 岩木正哉 86,91,93,95,99  
IWAMOTO Masako 岩本正子 83,121,122,127,  
150,152,301  
IWASA Naohito 岩佐直仁 18,174  
JEONG S.C. 鄭 淳讚 18  
KADOTA Yoshinori 角田佳績 107  
KAGAYA Satoru 加賀屋悟 301  
KAGEYAMA Tadashi 影山 正 6,202,203,  
207,211  
KAJINO Toshitaka 梶野敏貴 16  
KAKUI Hideo 角井日出雄 281  
KAMBARA Tadashi 神原 正 54,55,57,62,68,  
72,74,149  
KAMITSUBO Hiromichi 上坪宏道 305,307  
KANAI Tatsuaki 金井達明 133

- KANAI Yasuyuki 金井保之 54, 55, 62, 68, 72, 74, 149
- KANEKO Ichiro 金子一郎 133, 137, 139, 141
- KARASHIMA Shosuke 唐島照介 45
- KASE Masayuki 加瀬昌之 2, 4, 62, 200, 202, 217
- KASHIWAGI Toshisuke 柏木利介 10, 170, 172
- KATADA Motomi 片田元己 83, 122, 124
- KATAYAMA Toshiko 片山敏子 133
- KATO Hajime 加藤一 113
- KATO Seigo 加藤静吾 148
- KATO Takeshi 加藤毅 111, 113
- KATOU Takeo 加藤武雄 301
- KATSURAGAWA Hidetsugu 桂川秀嗣 75, 176, 178, 180
- KAWAHARA Hiroyuki 河原博之 105
- KAWANISHI Shunichi 河西俊一 131
- KAWASE Yoichi 川瀬洋一 125
- KIKUCHI Jun 菊地順 10, 168, 170, 172
- KIMURA Kazue 木村一宇 128
- KITAO Kensuke 喜多尾憲助 187, 189, 191, 194
- KITAZAWA Hideaki 北澤英明 153
- KOBAYASHI Kenzo 小林健三 93
- KOBAYASHI Takane 小林峰 7, 91, 93, 97, 301
- KOBAYASHI Toshio 小林俊雄 8, 12, 14
- KOBAYASHI Yoshio 小林義男 83, 121, 122, 124
- KOHARA Shigeo 小原重夫 6, 196, 202, 209, 211, 215
- KOHMOTO Susumu 河本進 70
- KOHNO Isao 河野功 6, 105, 121, 130, 131, 301, 303
- KOHNO Tsuyoshi 河野毅 168, 172
- KOIZUMI Mitsuo 小泉光生 180, 182
- KOKAI Hideki 小海秀樹 102
- KOSAKA Toshifumi 小坂俊文 133, 135, 139, 141
- KOSAKO Toshiso 小佐古敏莊 305
- KOYAMA Akio 小山昭雄 79, 81
- KUBO Ken-ichi 久保謙一 16
- KUBO Kenya 久保謙哉 121, 152
- KUBO Toshiyuki 久保敏幸 8, 10, 148, 170
- KUBONO Shigeru 久保野茂 148
- KUMAGAI Hidekazu 熊谷秀和 10, 21, 62, 65, 128, 135
- KUMATA Yukio 熊田幸生 196, 202, 203, 209, 211
- KURIHARA Osamu 栗原修 301
- KURIMOTO Kazuya 栗本一哉 115
- KURIYAMA Kazuo 栗山一男 105
- KUSAKA Takuya 日下卓也 265, 268, 271, 273, 276, 295
- KUSAKARI Hideshige 草刈英栄 20, 21
- KUSUYAMA Hiroyuki 楠山弘之 119
- LEE S.M. 李相茂 18, 147, 157, 166
- LIU Wei Ping 柳衛平 10, 170
- MAEDA Haruka 前田はるか 77
- MAEDA Kazushige 前田和茂 148
- MAEDA Kuniko 前田邦子 60, 117, 119
- MARUMORI Toshio 丸森寿夫 27, 31
- MATSUKI Seishi 松木征史 182
- MATSUMOTO Takehiko 松本武彦 97
- MATSUMOTO Yoshiyasu 松本吉泰 77, 180
- MATSUO Masayuki 松尾正之 27, 29, 31
- MATSUO Takashi 松尾崇 65
- MATSUZAKI Teiichiro 松崎禎市郎 153, 155
- McCINTYRE Cindy 139
- MINEHARA Eisuke 峰原英介 20, 21
- MINOH Arimichi 箕曲在道 222, 225
- MINOWA Tatsuya 箕輪達哉 75, 176, 178
- MISHIMA Kenji 三嶋謙二 121
- MIURA Atsushi 三浦厚 268, 273
- MIYADE Hiroki 宮出宏紀 297, 299
- MIYAGAWA Makoto 宮川真言 301
- MIYAHARA Akira 宮原昭 102
- MIYAKE Yasuhiro 三宅康博 153
- MIYAZAWA Yoshitoshi 宮沢佳敏 4
- MIZOGAWA Tatsumi 溝川辰巳 54, 55, 62
- MIZOTA Takeshi 溝田武志 18, 157, 166
- MIZUGAI Yoshihiro 水谷由宏 77
- MOKLER P.H. 57
- MORIMOTO Yoshihide 森本佳秀 279, 281, 283, 286, 288, 290, 292
- MORITA Susumu 森田右 60
- MOTOBAYASHI Tohru 本林透 18
- MOTONAGA Shoushichi 元永昭七 262
- Müller Alex C. 57
- MUNAKATA Kazuoki 宗像一起 168, 172
- MURAKAMI Hiroyuki 村上浩之 10, 18, 168, 170, 172, 174
- MURAYAMA Toshiyuki 村山利幸 18, 180, 182
- NAGAMINE Kanetada 永嶺謙忠 153, 155
- NAGAOKA Ryutaro 長岡隆太郎 227, 231, 235, 238, 242, 245, 248, 253, 259
- NAGASE Makoto 長瀬誠 200, 202, 211
- NAGASHIMA Yasuo 長島泰夫 18
- NAGATA Katsuaki 永田勝明 168, 172
- NAKADA Masami 中田正美 121
- NAKAGAWA Takahide 中川孝秀 8, 10, 147, 157, 159, 162, 164, 166
- NAKAHARA Hiromichi 中原弘道 121
- NAKAJIMA Mitsuo 中島充夫 115
- NAKAJIMA Shunji 中島淳二 199

- NAKAMOTO Atsushi 中本 淳 170,172  
NAKAMURA Takashi 中村 尚司 148  
NAKANISHI Noriyoshi 中西 紀喜 203,305  
NAKANO Kazushiro 中野 和城 133,135,137,  
139,141  
NAMBA Susumu 難波 進 93,99  
NISHI Katsuji 西 克夫 152  
NISHIDONO Toshirou 西殿 敏郎 281  
NISHII Masanobu 西井 正信 131  
NISHIJIMA Kyoshi 西嶋 恭司 170,172  
NONAKA Hideo 野中 英生 2,219  
NONAKA Nobuhiro 野中 信博 107  
NOZAKI Tadashi 野崎 正 107  
OGAWA Masao 小川 雅生 115  
OGIHARA Mitsuhiro 萩原 光彦 18,157,166  
OGIWARA Kiyoshi 萩原 清 6,196  
OGIWARA Masahiro 萩原 正弘 18,174  
OHKI Tomonori 大木 智則 4  
OHKUBO Yoshitaka 大久保嘉高 125,127,150,  
187,189,191,  
194  
OHNISHI Jun-ichi 大西 純一 262,276  
OHNUMA Hajime 大沼 甫 148  
OHTA Ken 太田 賢 74  
OHTANI Syunsuke 大谷 俊介 74  
OIKAWA Yoshifumi 老川 嘉郁 281  
OKABE Yoshio 岡部 芳雄 95  
OKADA Takuya 岡田 卓也 83,84,121,122,124,  
125  
OKUMURA Susumu 奥村 進 18  
OMATA Kazuo 小俣 和夫 14  
ORIHARA Hikonojo 織原彦之丞 148  
OSHIMA Masumi 大島 真澄 20,21  
OSHIRO Yukimitsu 大城 幸光 222  
OTSUKA Masahisa 大塚 正久 111  
OTSUKA Shozo 大塚省三 2  
OTSUKI Masayoshi 大槻 昌義 176,178  
OYAMA Hitoshi 大山 等 102  
PARK Eung Soo 朴 應秀 262  
PU Y.H. 蒲 越虎 18,157,166  
QIU Qi 邱 齐 109  
REUSCH Stefan 57  
RUAN (GEN) Jian-Zhi 阮 建治 18  
SAITO Motozo 斎藤 始三 202,211,215,217  
SAKAI Nobuhiko 坂井 信彦 84,121  
SAKAI Yoichi 酒井 陽一 121  
SAKAIRI Hideo 坂入 英雄 7,91  
SAKAMOTO Hiroyuki 坂本 浩幸 279,281,283,  
286,288,290,  
292  
SAKAMOTO Ichiro 坂本 一郎 301,303,307  
SAKAMOTO Isao 坂本 獻 105  
SAKAMOTO Yuichi 坂本 雄一 102  
SAKATA Fumihiko 坂田 文彦 27,29,31  
SAKAUE Hiroyuki 坂上 裕之 74  
SANO Hirotoshi 佐野 博敏 83,121,122,124  
SASA Yoshihiko 佐々嘉彦 60,79,81,84,117,119  
SASUGA Tsuneo 貴家 恒男 131  
SATO Kenichi 佐藤 憲一 33  
SATO Toshihiko 佐藤 敏彦 111  
SCHMIDT-BÖCKING Horst 72  
SCHUCH Reinhold 57  
SEGUCHI Tadao 濑口 忠男 131  
SHIBUYA Shinji 渋谷 真二 18  
SHIKATA Takashi 四方 隆史 305  
SHIMA Kunihiro 島 邦博 54,62  
SHIMAMURA Isao 島村 獻 47,52  
SHIMANO Yosuke 嶋野 洋介 104  
SHIMIZU Hajime 清水 肇 148  
SHIMODA Tadashi 下田 正 12  
SHIMOMURA Kohichiro 下村 浩一郎 182  
SHIMOURA Susumu 下浦 亨 12  
SHINOHARA Shigemi 篠原 茂己 301  
SHIRAKURA Takao 白倉 貴雄 292  
SHIRATO Shoji 白土 鈴二 18  
STACHURA Zbigniew 57  
STOLTERFOHT Nikolaus 68  
SUEKI Keisuke 末木 啓介 187  
SUGAI Isao 菅井 獻 113,180  
SUGAWARA Masahiko 菅原 昌彦 20,21  
SUGIMOTO Kenzo 杉本 健三 12,14  
SULIK Bela 55,68  
SUNAGA Hiromi 須永 博美 130  
SUZUKI Atsuyuki 鈴木 篤之 77  
SUZUKI Hiroshi 鈴木 洋 74  
SUZUKI Keiji 鈴木 啓司 141  
SUZUKI Masao 鈴木 雅雄 137,141  
SUZUKI Takayoshi 鈴木 隆敬 128  
SUZUKI Takayuki 鈴木 隆之 75  
SUZUKI Takeshi 鈴木 健 8,10,170  
TACHI Kouju 館 弘樹 107,111  
TACHIKAWA Toshiki 立川 敏樹 203  
TAJIMA Norio 田島 典夫 135  
TAKAHASHI Noriaki 高橋 憲明 12  
TAKAHASHI Shigeo 高橋 成夫 200  
TAKAHASHI Tan 高橋 旦 133,135  
TAKAMI Michio 高見道生 60,77,180  
TAKAYANAGI Toshinobu 高柳 俊暢 74  
TAKEBE Hideki 武部 英樹 2,200,202,203  
TAKEKAWA Shunji 竹川 俊二 91

TANAKA Hitoshi 田中 均 227, 231, 235, 238,  
242, 245, 248, 253,  
259  
TANAKA Koki 田中幸基 100  
TANAKA Ryuichi 田中隆一 130  
TANIGUCHI Yoshiki 谷口美樹 196, 222, 225  
TANIHATA Isao 谷畑勇夫 8, 10, 12, 14, 16, 147,  
159, 170  
TAWARA Hiroyuki 傑博之 65  
TENDOW Yoshihiko 天道芳彦 187, 189, 191,  
194  
TOKI Hiroshi 土岐博 16  
TOMINAGA Takeshi 富永健 121  
TONUMA Tadao 戸沼正雄 65, 70  
TORIKAI Eiko 鳥養映子 153  
TOYOKAWA Hidenori 豊川秀訓 148  
TSUMAKI Koji 妻木孝治 227, 231, 235, 238, 242,  
245, 248, 253, 257, 259  
TSURUBUCHI Seiji 鶴淵誠二 70  
UDA Masayuki 宇田応之 60, 117, 119  
UEHARA Keiji 上原桂二 128  
UEHARA Shin-ichi 上原進一 125  
URAI Teruo 浦井輝夫 7  
VEGH Lászlé 42  
VOGT Hans 72  
WADA Takeshi 和田雄 144, 186, 273  
WAKASA Shuichiro 若狭秀一郎 148  
WAKIYA Kazuyoshi 脇谷一義 74  
WARCZAK Amdrzej 57  
WATANABE Hiroshi 綿鍋博志 105  
WATANABE Kazuhiro 渡辺一弘 128  
WATANABE Masami 渡辺正己 141  
WATANABE Shu 渡部秀 133  
WATANABE Tokuji 渡辺徳治 133  
WATANABE Tsutomu 渡部力 35, 38, 40, 42,  
45  
WATANABE Yasuo 渡辺裕夫 121, 152  
WINTERMEYER Gerd 57

YAGI Eiichi 八木栄一 7, 86, 88, 97, 100  
YAMADA Yutaka 山田豊 133, 135  
YAMADAYA Tokio 山田谷時夫 84  
YAMAGUCHI Hiromi 山口裕美 10  
YAMAGUCHI Hiroyuki 山口弘之 86  
YAMAJI Shuhei 山路修平 23, 25  
YAMAKAWA Osamu 山川修 14  
YAMASHITA Shoji 山下昌次 137  
YAMASU Kazushige 弥益和重 297, 299  
YAMAZAKI Hiroshi 山崎博史 124  
YAMAZAKI Yasunori 山崎泰規 68  
YANAGIMACHI Tomoki 柳町朋樹 10, 168,  
170, 172  
YANO Katsuki 矢野勝喜 102  
YANO Yasushige 矢野安重 2, 148, 202  
YANOKURA Minoru 矢野倉実 4, 10, 102, 109,  
111, 113, 150,  
170, 301  
YASUE Masaharu 安江正治 148, 186  
YATAGAI Fumio 谷田貝文夫 133, 135  
YOKOTA Wataru 横田渉 219  
YOKOUCHI Shigeru 横内茂 279, 281, 283, 286,  
288, 290, 292  
YOKOYAMA Ichiro 横山一郎 200, 217  
YONEDA Akira 米田晃 168  
YOSHIDA Hyogo 吉田兵吾 148  
YOSHIDA Katsuhisa 吉田克久 227, 231, 235,  
238, 242, 245,  
248, 253, 259  
YOSHIDA Kenichiro 吉田謙一郎 119  
YOSHIDA Kenzo 吉田健三 130  
YOSHIDA Koichi 吉田光一 8  
YOSHIDA Shiro 吉田思郎 33  
YOSHINAGA Naotaka 吉永尚孝 23, 25  
YOSHIYUKI Takeshi 吉行健 265, 268, 271,  
276, 295  
YUASA-NAKAGAWA Keiko 中川恵子 157,  
159, 162, 166  
ZHUO Yizhong 卓益忠 27, 31

## **RIKEN Accelerator Progress Report**

理化学研究所加速器年次報告 第22巻 (1988)

---

印刷 平成元年(1989) 8月25日

発行 平成元年(1989) 8月31日

発行者 理化学研究所

代表者 小田 稔

〒351-01 埼玉県和光市広沢2番1号

電話 (0484) 62-1111

編集者 理化学研究所加速器研究施設運営委員会

印刷所 勝美印刷株式会社

〒112 東京都文京区小石川1丁目3番7号

---

定価 5,000円  
(消費税別)



**理化学研究所**

埼玉県 和光市 広沢